2022 Global Fluid Power Society Ph.D. Symposium

October 12-14, 2022 in Naples, Italy



Welcome Message from the General Chairs

On behalf of the Organizing Committee, we welcome you to the *Conference Proceedings of the 2022 Global Fluid Power Society PhD Symposium (GFPS2022)*. The Symposium is a bi-annual event organized by the Global Fluid Power Society (GFPS) to showcase and brainstorm on research carried out by junior investigators in fluid power. GFPS Society was created in 2016 to merge two long-lasting fluid power organizations: Fluid Power Net International (FPNI) and Network of Fluid Power Centres in Europe (FPCE). GFPS inherits the spirit of both FPNI and FPCE and currently represents the world's largest scientific network of fluid power institutions.

Since its first edition, the *GFPS PhD Symposium* represents an international meeting place in the world of research in the field of Fluid Power involving national and international institutions, academia, and companies in a discussion on the most recent results of scientific and technological research for the fluid power industry, with particular emphasis to applications and new trends. Attention is paid to, but not limited to, new technology in the fluid power, power transmissions and motion control fields.

The first edition of the *GFPS PhD Symposium* was hosted by the University of Samara, Russia, in 2018; then, after two years of emergency, the COVID-19 outbreak forced the edition 2020 expected in Guilin, China, and organized by the Harbin Institute of Technology di Harbin, to be held online. 2022 is finally coming back to normality!

In 2022, our expectation of hosting you all in Italy and its world-famous Naples has been realized! The program is arranged to offer the possibility of visiting Naples before, during and after the Symposium!

The University of Naples and the University of Sannio coordinate the organization.

The *GFPS2022* Program is highly varied, including plenary sessions, regular technical sessions with 61 oral presentations, two industry panel sessions, and special events devoted to students, young professionals, professors, and industries, scheduled over three days.

Presentations are organized in 2 General Sessions and 14 Special Sessions. Special Sessions aim to create a focus on specific topics, where researchers can gain knowledge, familiarize themselves, exchange ideas, and build cooperation.

The received papers were submitted for peer review. Relevance, quality, significance, and novelty of the scientific contribution were the main attributes for acceptance and publication in the Proceedings. The International Journal of Fluid Power publishes the Proceedings. We want to thank all the reviewers who actively contributed to the selection and quality improvement of the presented works.

GFPS PhD Symposium 2022 is honoured to have experts in Fluid Power as Invited Speakers.

- Prof. Rudolf Scheidl, from Johannes Kepler University, Austria, will present the first day of “Symbiotic Fluid Power”.
- Prof. Katharina Schmitz, from RWTH Aachen University, Germany, will present “Fluid Power – A sustainable motion technology” on October 13.
- Prof. Kim A. Stelson, from the University of Minnesota, US, will give a talk on “Energy Saving Fluid Power Technology for Off-Highway Vehicles” on the last day of the Symposium.

We are grateful to the Invited Speakers for joining the Symposium.

To recognize the most outstanding papers presented at the bi-annual *2022 Global Fluid Power Society PhD Symposium*, a Backé Medal sponsored by the Global Fluid Power Society, a Best Conference Paper Award sponsored by MDPI Fluids Journal, and a Best Conference Paper Award sponsored by the Symposium Organizers will be assigned.

We sincerely want to thank all the sponsors and the patronages who made this event possible.

The *2022 Global Fluid Power Society PhD Symposium* is about to begin. Students, professors, and engineers enjoy the Workshop!

October 10, 2022

Adolfo Senatore, University of Naples, Italy



Emma Frosina, University of Sannio, Italy

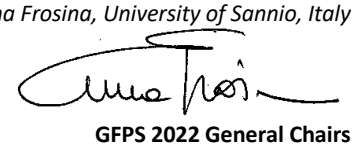

GFPS 2022 General Chairs

GENERAL CHAIRS

Adolfo Senatore, University of Naples Federico II, Italy

Emma Frosina, University of Sannio, Benevento, Italy

ORGANIZING COMMITTEE MEMBERS

Antonella Bonavolontà, University of Naples Federico II, Italy

Pasquale Borriello, University of Naples Federico II, Italy

Raffaele De Rosa, University of Naples Federico II, Italy

Pietro Mazzei, University of Naples Federico II, Italy

Luca Romagnuolo, University of Naples Federico II, Italy

ACADEMIC COMMITTEE MEMBERS

Riccardo Amirante, Politecnico di Bari, Italy

Eric J. Barth, Vanderbilt University, USA

Eric Bideaux, INSA Lyon, France

Massimo Borghi, University of Modena and Reggio Emilia, Italy

Paolo Casoli, University of Parma, Italy

Victor Juliano De Negri, Federal University of Santa Catarina, Brazil

William Durfee, University of Minnesota, USA

Heikki Handroos, Lappeenranta University of Technology, Finland

Nigel Johnston, University of Bath, UK

Petri Kuosmanen, Aalto University, Finland

Perry Y. Li, University of Minnesota, USA

Songjing Li, Harbin Institute of Technology, China

Alarico Macor, University of Padova, Italy

Bernhard Manhartsgruber, Johannes Kepler University Linz, Austria

Pietro Marani, STEMS CNR, Italy

Massimo Milani, University of Modena and Reggio Emilia, Italy

Tatiana Minav, Tampere University of Technology, Finland

Hubertus Murrenhoff, RWTH Aachen University, Germany

Damiano Padovani, Guangdong Technion-Israel Institute of Technology, China

Andrew Plummer, University of Bath, UK

Antonio Rossetti, ITC CNR, Italy

Massimo Rundo, Politecnico di Torino, Italy

Kazushi Sanada, Yokohama National University, Japan

Rudolf Scheidl, Johannes Kepler University Linz, Austria

Katharina Schmitz, RWTH Aachen University, Germany

Andrzej Sobczyk, University of Technology, Poland

Kim A. Stelson, University of Minnesota, USA

Victor Sverbilov, Sarmara University, Russia

Paolo Tamburrano, Politecnico di Bari, Italy

Andrea Vacca, Purdue University, USA

James D. Van de Ven, University of Minnesota, USA

Feng Wang, Zhejiang University, China
Jürgen Weber, Technische Universitat Dresden, Germany
Travis Wiens University of Saskatchewan, Canada
Barbara Zardin, University of Modena and Reggio Emilia, Italy

Index

WELCOME MESSAGE FROM THE GENERAL CHAIRS **2**

GENERAL CHAIRS **3**

ORGANIZING COMMITTEE MEMBERS **3**

ACADEMIC COMMITTEE MEMBERS **3**

INDEX **5**

1. PUMPS AND MOTORS **7**
1.1 31 Analysis of Compensation Ratios and Control Torques of an Axial Piston Pump with Rotated Valve Plates 7
1.2 37 Validated Efficiency Improvements by Implementation of Structures on the Slipper Surface of an Axial Piston Pump 7
1.3 47 Analyses of Engineered Surfaces for Performance Improvements of External Gear Pumps 7
1.4 4 Numerical Modeling of Helical External Gear Pump Through a Novel CFD Approach Using Simerics MP+ 7
1.5 Numerical Modeling of Helical External Gear Pump Through a Lumped Parameter Approach 7
1.6 34 High Fidelity Data Generation and Fault Diagnosis of a Gear Pump 7
1.7 8 Simulation Model of a Helical Gear Pump for the Evaluation of the Filling Capability 7
1.8 33 Modelling and Experimental Validation of the Dynamic Startup Behavior of External Spur Gear Motor 7
1.9 54 Design, Modeling, and Experimental Characterization of a Fast Additively Manufacturable MRI-Compatible Pneumatic Motor for Surgical Robots 7
1.10 38 A Study on a Twin-Screw Pump for Thermal Management Systems by means of CFD using SimericsMP+®: experimental validation and focus on Pressure Pulsation 7
2. FLUID POWER COMPONENTS, ARCHITECTURES AND SYSTEMS **7**
2.1 30 An Efficient Simulation Approach to Determine the Thermal Equilibrium of Drive Systems in Mobile Machinery 7
2.2 46 Digital Electro Hydraulic Actuator with Variable Speed Digital Hydraulic Pump: A Design Overview 7
2.3 A Piezo-Electrically Actuated Valve for Hydraulic Exoskeleton Drives - Modelling and Measurement of a Prototype 7
2.4 50 Different solutions for the achievement of Variable Margin Load Sensing systems: energy saving and increased performance 7
2.5 32 Numerical Simulations of a High Frequency Switching 4/2 ON/OFF Valve for Pulse Modulation Switching Digital Circuits 7
2.6 52 Design for Structural Durability of an Hydraulic Main Valve for Mobile Applications 7
2.7 22 Generation and Validation of a Real Time Multibody Model for Off-Highway Vehicles, Aiming at the Design of Suspension Systems 7
2.8 3 A Parametric Study on Architectures Using Common-Pressure Rail Systems and Multi-Chamber Cylinders 8
2.9 36 Challenges in the Designing Process of Hydraulic Cylinders Made of Plastics 8
2.10 14 Identifying the Future Research Trend for Using Speed-Controlled Hydraulic Cylinders in Offshore Applications through Literature Survey 8
3. CONTROL METHODOLOGIES FOR FLUID POWER SYSTEMS AND APPLICATIONS **8**
3.1 9 Loading System for Wind Turbine Drivetrain Test Bench with Model-Based Compensation Control Strategy 8
3.2 10 Cartesian Damping Controller with Nonlinear Control for a Floating-Base Hydraulic Manipulator 8
3.3 11 Real-Time Trajectory Scaling Algorithm for Hydraulic Manipulators Subject to Limited On-Board Power 8
3.4 Lionel Hulttinen and Jouni Mattila, Tampere University, Finland 8
3.5 7 Compliance Motion Control of the Hydraulic Dual-Arm Manipulator Based on Virtual Decomposition Control 8
3.6 23 Pressure Feedback Control of Electro-Hydraulic Actuators Using Fixed Displacement Hydraulic Machines 8
3.7 51 Energy Saving Enhancement Through 3-Way Downstream Compensator Main Valve, a Viable Option for Efficient Off-Highway Applications 8
4. NOVEL ENERGY EFFICIENT COMPONENTS AND SYSTEMS **8**
4.1 53 System for Recovering Energy in Hydraulic Circuit by Using a Small Pelton Turbine 8
4.2 25 A Practical Numerical Method to Map the Energy Efficiency of Individual Electro-Hydraulic Drives 8
4.3 27 Development of a Bi-Stable Mechanism for Efficiency Optimization of Pneumatic Pressure Boosters 8
5. TRIBOLOGY **8**
5.1 44 Influence of the Pressure-Viscosity Behavior of Different Base Oils on the Formation of Lubricating Films in Tribological Contacts 8
5.2 43 Topology Optimization of Fluid Cooling Systems for Machine Tools 8
5.3 18 Elastodynamic Performance Evaluation and Comparison in Hydraulic and Electromechanical Linear Actuator Driven Heavy-Duty Manipulators 8
6. GENERAL SESSION **8**
6.1 42 Evaluation of Nonlinear MIMO Controllers for Independent Metering in Mobile Hydraulics 8

6.2 13 Combined Multidimensional Approaches for the Simulation of Flow Trough a Wall-Flow Particulate Filter 9
6.3 1 Using Nonlinear Observers as Virtual Sensors in Hydraulically Actuated Equipment in Industrial IoT Systems 9
6.4 6 Dynamic Fluid Simulation of Hydraulic Oil Flow Inside Fatigue Cracks During Transient Loads 9
6.5 12 Implementation of a Variational Autoencoder for Dimension Reduction of a Hydraulic System 9
6.6 21 CFD Simulations of Flow Field in Flapper-Nozzle Pilot Valve with Vortex Generators 9
6.7 39 Study of a Dual Layout Input-To-Output Coupled Hydromechanical Transmission 9
6.8 40 Simulation Model of Hydraulic Generator with Variable Flow Direction 9

1. PUMPS AND MOTORS

1.1 *Analysis of Compensation Ratios and Control Torques of an Axial Piston Pump with Rotated Valve Plates*
Thomas Heeger, Stephan Wegner, Liselott Ericson

1.2 *Validated Efficiency Improvements by Implementation of Structures on the Slipper Surface of an Axial Piston Pump*
Svenja Horn, Roman Ivantysyn, Jürgen Weber

1.3 *Analyses of Engineered Surfaces for Performance Improvements of External Gear Pumps*
Paolo Casoli, Fabio Scolari, Carlo Maria Vescovini, Carlo Rossi, Antonio Lettini

1.4 *Numerical Modeling of Helical External Gear Pump Through a Novel CFD Approach Using Simerics MP+*
Pietro Mazzei, Adolfo Senatore, Emma Frosina, Simone Bulleri

1.5 *Numerical Modeling of Helical External Gear Pump Through a Lumped Parameter Approach*
Pietro Mazzei, Emma Frosina, Simone Bulleri, Adolfo Senatore

1.6 *High Fidelity Data Generation and Fault Diagnosis of a Gear Pump*
Kayal Lakshmanan, Fabrizio Tessicini, Antonio Gil, Ferdinando Auricchio

1.7 *Simulation Model of a Helical Gear Pump for the Evaluation of the Filling Capability*
Alessandro Corvaglia, Massimo Rundo, Sara Bonati, Manuel Rigosi

1.8 *Modelling and Experimental Validation of the Dynamic Startup Behavior of External Spur Gear Motor*
Ajinkya J Pawar, Andrea Vacca, Manuel Rigosi

1.9 *Design, Modeling, and Experimental Characterization of a Fast Additively Manufacturable MRI-Compatible Pneumatic Motor for Surgical Robots*
Mengtang Li, Jing Zhang, Xiyun Wu, Jieting Yuan, Xiyu Wang, Yongyin Ye, Beichen Ding

1.10 *A Study on a Twin-Screw Pump for Thermal Management Systems by means of CFD using SimericsMP+®: experimental validation and focus on Pressure Pulsation*
Pasquale Borriello, Emma Frosina, Pierpaolo Lucchesi, Adolfo Senatore

2. FLUID POWER COMPONENTS, ARCHITECTURES AND SYSTEMS

2.1 *An Efficient Simulation Approach to Determine the Thermal Equilibrium of Drive Systems in Mobile Machinery*
Eric Pohl, Sven Osterland, Jürgen Weber

2.2 *Digital Electro Hydraulic Actuator with Variable Speed Digital Hydraulic Pump: A Design Overview*
Dimitri O Silva, Marcos Paulo Nostrani, Rodrigo S Lopes Junior, Gierri Waltrich, Petter Krus, Victor Juliano De Negri

2.3 *A Piezo-Electrically Actuated Valve for Hydraulic Exoskeleton Drives - Modelling and Measurement of a Prototype*
Philipp Zagar, Rudolf Scheidl

2.4 *Different solutions for the achievement of Variable Margin Load Sensing systems: energy saving and increased performance*
Davide Mesturini, Mattia Scolari, Francesco De Martino, Ulderico Busani

2.5 *Numerical Simulations of a High Frequency Switching 4/2 ON/OFF Valve for Pulse Modulation Switching Digital Circuits*
Francesco Sciatti, Paolo Tamburrano, Andrew Plummer, Elia Distaso, Pietro De Palma, Riccardo Amirante

2.6 *Design for Structural Durability of an Hydraulic Main Valve for Mobile Applications*
Filippo Ciardo, Giovanni Meneghetti, Edoardo Caldesi, Cesare Dolcin, Alessandro Cervi, Davide Mesturini

2.7 *Generation and Validation of a Real Time Multibody Model for Off-Highway Vehicles, Aiming at the Design of Suspension Systems*
Andrea Fornaciari, Barbara Zardin, Massimo Borghi

2.8 *A Parametric Study on Architectures Using Common-Pressure Rail Systems and Multi-Chamber Cylinders*
Mateus Bertolin, Andrea Vacca

2.9 *Challenges in the Designing Process of Hydraulic Cylinders Made of Plastics*
Piotr Stryczek

2.10 *Identifying the Future Research Trend for Using Speed-Controlled Hydraulic Cylinders in Offshore Applications through Literature Survey*
Wei Zhao, Morten Kjeld Ebbesen, Torben Ole Andersen

3. CONTROL METHODOLOGIES FOR FLUID POWER SYSTEMS AND APPLICATIONS

3.1 *Loading System for Wind Turbine Drivetrain Test Bench with Model-Based Compensation Control Strategy*
Danyang Li, Yajing Gu, Yonggang Lin, Jiajun Song, Xiangheng Feng, Hongwei Liu

3.2 *Cartesian Damping Controller with Nonlinear Control for a Floating-Base Hydraulic Manipulator*
Pauli Mustalahti, Jouni Mattila

3.3 *Real-Time Trajectory Scaling Algorithm for Hydraulic Manipulators Subject to Limited On-Board Power*
Lionel Hulttinen, Jouni Mattila

3.4 *Compliance Motion Control of the Hydraulic Dual-Arm Manipulator Based on Virtual Decomposition Control*
Bolin Sun, Min Cheng, Ruqi Ding, Bing Xu, Jouni Mattila

3.5 *Pressure Feedback Control of Electro-Hydraulic Actuators Using Fixed Displacement Hydraulic Machines*
Shaoyang Qu, Hassan Assaf, Andrea Vacca, Enrique Busquets

3.6 *Energy Saving Enhancement Through 3-Way Downstream Compensator Main Valve, a Viable Option for Efficient Off-Highway Applications*
Cesare Dolcin, Gianluca Ganassi, Ulderico Busani, Francesco De Martino

4. NOVEL ENERGY EFFICIENT COMPONENTS AND SYSTEMS

4.1 *System for Recovering Energy in Hydraulic Circuit by Using a Small Pelton Turbine*
Marco Rizzoli, Giovanni Cillo, Barbara Zardin, Danilo Manfredi, Massimo Borghi

4.2 *A Practical Numerical Method to Map the Energy Efficiency of Individual Electro-Hydraulic Drives*
Damiano Padovani

4.3 *Development of a Bi-Stable Mechanism for Efficiency Optimization of Pneumatic Pressure Boosters*
Matthias Schmid, Olivier Reinertz, Katharina Schmitz

5. TRIBOLOGY

5.1 *Influence of the Pressure-Viscosity Behavior of Different Base Oils on the Formation of Lubricating Films in Tribological Contacts*
Sebastian Deuster, Achill Holzer, Katharina Schmitz

5.2 *Topology Optimization of Fluid Cooling Systems for Machine Tools*
Christoph Steiert, Juliane Weber, Jürgen Weber

5.3 *Elastodynamic Performance Evaluation and Comparison in Hydraulic and Electromechanical Linear Actuator Driven Heavy-Duty Manipulators*
Aleksi Vesterinen, Goran R. Petrovic ́, Jouni Mattila

6. GENERAL SESSION

6.1 *Evaluation of Nonlinear MIMO Controllers for Independent Metering in Mobile Hydraulics*
Lukas Bachmann, André Sitte, Jürgen Weber

6.2 *Combined Multidimensional Approaches for the Simulation of Flow Trough a Wall-Flow Particulate Filter*
Andrea Natale Impiombato, Gabriele Discepoli, Fabrizio Paltrinieri, Massimo Milani, Luca Montorsi

6.3 *Using Nonlinear Observers as Virtual Sensors in Hydraulically Actuated Equipment in Industrial IoT Systems*
Victor Zhidchenko, Yashar Shabbouei Hagh, Egor Startcev, Heikki Handroos

6.4 *Dynamic Fluid Simulation of Hydraulic Oil Flow Inside Fatigue Cracks During Transient Loads*
Lukas Michiels, Marcus Geimer

6.5 *Implementation of a Variational Autoencoder for Dimension Reduction of a Hydraulic System*
Faras Brumand-Poor, Faried Makansi, Jiakun Liao, Katharina Schmitz

6.6 *CFD Simulations of Flow Field in Flapper-Nozzle Pilot Valve with Vortex Generators*
Tong Li, Jinghui Peng, Songjing Li

6.7 *Study of a Dual Layout Input-To-Output Coupled Hydromechanical Transmission*
Antonio Rossetti, Nicola Andretta, Alarico Macor

6.8 *Simulation Model of Hydraulic Generator with Variable Flow Direction*
Kacper Da ̨bek, Krzysztof Ke ̨dzia, Piotr Osin ́ski

Analysis of Compensation Ratios and Control Torques of an Axial Piston Pump with Rotated Valve Plates

Thomas Heeger[1], Stephan Wegner, Liselott Ericson[1]

[1]*The Division of Fluid and Mechatronic Systems, The Department of Management and Engineering, Linköping University,* thomas.heeger@liu.se

Abstract

Conventionally, variable hydraulic axial piston machines vary displacement by adjusting the length of the piston stroke. Another method to achieve variable displacement is to rotate the valve plate and thus adjust the effective use of the piston stroke. This paper provides an analytical methodology to calculate control torques for valve plate rotation. This methodology considers compensation ratios in the contact between the valve plate and the piston plate, and compensation ratios in the contact between the valve plate in the housing. This paper adds the consideration of a spring force, pressure-dependent viscosity, and a surrogate model for the compensation force from the area between high-pressure and low-pressure to the traditional calculation of the compensation ratio. The influence of the cylinder barrel's rotation angle and the valve plate rotation angle is taken into account. The calculation results for an exemplary pump of floating piston type reveal that the main share of the required control torque originates from the contact between the valve plate and the housing. A hydrostatic compensation force in that interface can reduce this torque, but it is illustrated that a full compensation is not possible. For large valve plate rotation angles, the risk of valve plate tipping caused by the axial ports in the housing is shown, which shows that valve plate rotation is not suitable for displacement control to small displacement levels when using axial ports.

River Journal, 1–27.
© 2024 *River Publishers. All rights reserved.*

Keywords: axial piston pump, variable displacement, valve plate rotation, compensation ratio, control torque, double pump.

1 Introduction

Variable displacement in hydraulic machines can avoid the delivery of hydraulic excess power and enable the downsizing of the prime mover. Typically, the displacement is varied by adjusting the length of the piston stroke, e.g., by adjusting the angle of the swash plate in swash plate machines. Another possibility to achieve variable displacement is to rotate the valve plate (VP) and thus adjust the effective use of the piston stroke.
Expected benefits of VP rotation are small control torques and low actuation power, and thus an easy control [1]. The power required for the displacement control can have a significant share of the system losses, as the overall efficiency of displacement controlled pumps can be significantly reduced by their control power [12].
The idea of VP rotation is not new, and the concept has already been studied decades ago. Small VP rotations, by only a couple of degrees, have been considered in order to adjust the effective pre-compression in a pump (e.g. [4,8]), while large VP rotations have been considered in order to vary pump displacement by reducing the effective piston stroke [7, 15]. Unfortunately, the same pre and de-compression angles provide a higher effective pre and de-compression when commutation takes place at a greater distance to the dead centres. When pre and de-compression angles cannot be modified for different operating points and displacement settings, issues such as cavitation and high-pressure (HP) peaks [3] as well as noise and backflow [5] occur. Using a double pump with opposing pistons as sketched in Fig. 1 offers the potential to overcome these obstacles: as visualised in Fig. 2, the displacement can be adjusted by joint rotation of both VPs, and the effective pre and de-compression can be adjusted by relative rotation of the VPs. [9]

When rotating a VP, all of its tasks need to be considered: VPs are used to separate the inlet from the outlet as well as to provide a smooth pressure transition for each piston chamber as it passes over the valvelands between inlet and outlet. Furthermore, they provide an axial journal to balance the piston forces, which needs to provide a good compromise between frictional and leakage losses. Conventionally, on the backside of the VP, no relative movement to the housing takes place, and thus the focus is solely on avoiding leakage losses, which means that a compensation of the piston forces is not desired in that interface. [13] When rotating the VP, of course, this needs to

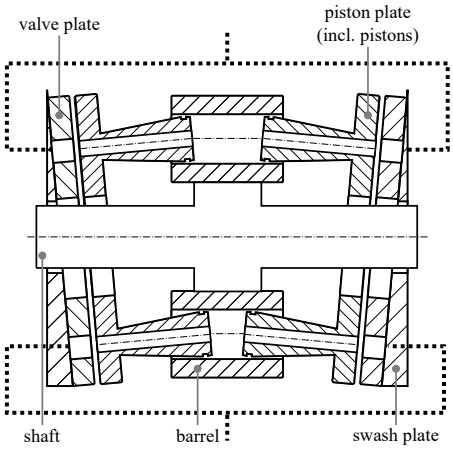

Figure 1: Floating piston pump with opposing pistons. Two opposing pistons share one bore in the cylinder barrel, and therefore they communicate with one another.

be revisited. A (partial) compensation of the piston forces is then desired in order to reduce the torque required to move the VP.
The required control torque is dependent on the cylinder barrel (CB) rotation angle and the VP rotation angle. This paper presents an analytical methodol-

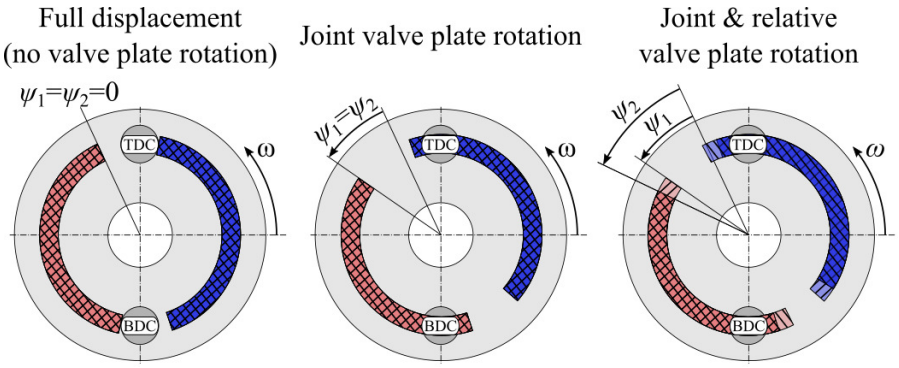

Figure 2: Joint and relative VP rotation. Left: both VPs are in the same position (at maximum displacement). Center: both VPs have been rotated by the same angle, reducing the displacement. Right: VP2 has been rotated by an additional angle, reducing the pre- and de-compression angle.

ogy to calculate compensation ratios and quantify the required control torque for different CB and VP rotation angles. This is done on the example of a floating piston pump [6] with opposing pistons. For this purpose, the consideration of a spring force, pressure-dependent viscosity and a surrogate model for the compensation force from the area between HP and low-pressure (LP) are added to the traditional calculation of the compensation ratio. Furthermore, the balance point (BP) of the uncompensated force is calculated to evaluate the risk of VP tipping and a VP modification for decreased control torques is suggested.

2 Methodology

Forces in axial piston machines can be distinguished between pressure-dependent and pressure-independent forces. Pressure-dependent forces occur due to the pressurisation of an area and are the dominant type of force in hydrostatic machines. Even frictional forces are dominantly pressure-dependent. Typically, it is attempted to compensate pressure-dependent forces in contacts with relative motion by hydrostatic bearings. [10]

2.1 Analysis of Compensation Ratios

Traditionally, the compensation ratio ζ is defined as the ratio between loading forces and compensating fluid forces in the important contact between VP and cylinder block, see (1). The equivalent contact in the machine sketched in Fig. 1 is the contact between VP and piston plate (PP). The VPs are parallel to the swash plates, and the piston forces act normal to the VPs. Therefore, compensation ratios for the pump sketched in Fig. 1 and for traditional swash plate pumps can be calculated with the same methodology.

$$\zeta = \frac{F_{\mathrm{comp}}}{F_{\mathrm{load}}} \tag{1}$$

A compensation ratio larger than 1 indicates that the cylinder block resp. PP can lose contact to the VP, leading to uncontrolled leakage of HP fluid which can cause a loss of functionality. Compensation ratios far below 1 indicate solid body contact, which leads to the risk of wear and fretting. [4] Therefore, compensation ratios slightly below 1 are targeted in the design process (see [10, 17]).
As the calculation methods for ζ in the literature differ, the correct interpretation of the numerical value of the compensation ratio depends on the used

method. Wegner et al. [17] summarises and compares different methods for analytical calculation of the compensation ratio of the contact between VP and cylinder block.

2.1.1 Assumptions and Simplifications

As summarised in [18], numerical models can take into account non-uniform gap heights, elastic and thermal deformation as well as hydrodynamic and squeezing effects. However, when attempting to calculate compensation ratios analytically, some assumptions and simplifications are typically made (see [13, 17]):

- All pressurised pistons are at the same pressure level.
- The contact surfaces are flat and parallel to one another. The gap height is constant over time and there is no tipping of the cylinder block resp. PP. Therefore, no squeeze flows are present.
- There is no relative motion between the contact surfaces. Therefore, no shear flows are present.
- The fluid has a constant density (i.e., it is incompressible) and a constant viscosity. This simplifies the expression for the pressure flow. However, in this paper, pressure-dependency of the viscosity is considered using (7).
- Only forces generated by static pressure are considered. Other forces (e.g., hydrodynamic forces) are neglected. However, in this paper, the spring force pressing the PP against the VP is also considered.

Some of the assumptions are further elaborated and justified in [4]. In this paper, effects such as elastic and thermal deformation, and production influences are not considered.
The PP is floating and its position is affected by the contact points between PP and CB. However, this is neglected in this paper. Instead it is assumed that the centre of gravity of the PP remains at the same location, i.e., the PP only moves around its axis and does no translational movement relative to the VP.

2.1.2 Load Force

Fig. 3 sketches the piston force and the compensation force for the contact PP-VP. The load force for this contact is created by the pressurised pistons. Wegner et al. [17] emphasizes that some methods consider the passage opening area as loaded area, i.e., a pressure force from this area is used both for the calculation of F_{comp} and F_{load}. However, in the passage opening of a kidney, no load on the PP-VP contact is created. Therefore, there is no physical

equivalent to this calculated pressure force, and compensation ratios would be overestimated. [17] Thus, (2) considers that no load on the PP is created at the passage areas A_{pass} through the piston bores. Furthermore, the spring force F_{S} pressing the PP against the VP is considered.

$$F_{\mathrm{load,PP-VP}} = \sum_i p_i \left(A_{\mathrm{piston}} - A_{\mathrm{pass}}\right) + F_{\mathrm{S}} \tag{2}$$

The same methodology can be applied to calculate the load force in the

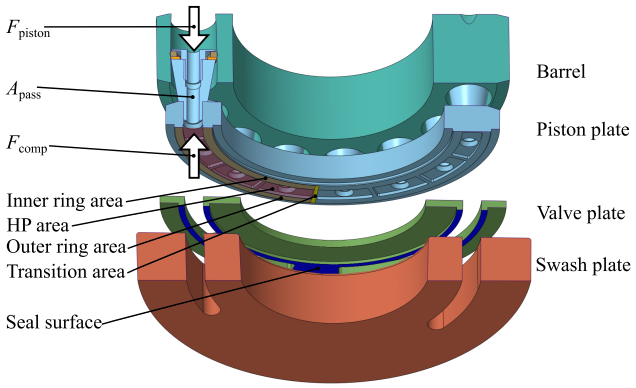

Figure 3: Overview of relevant pump parts and pressure zones for the contact PP-VP.

contact between the VP and the housing (contact VP-H), which is sketched in Fig. 4. The pressurised area in the HP kidney does not lead to a force in this contact, as that pressure force is taken by the housing. Hence the load force is calculated acc. to (3).

$$F_{\mathrm{load,VP-H}} = \left(\sum_i p_i A_{\mathrm{piston}}\right) - p_H A_{\mathrm{kidney}} + F_{\mathrm{S}} \tag{3}$$

2.1.3 Compensation Force

To calculate the compensation force, the pressure distribution in the different contact areas needs to be known. Thus different areas are defined, in which the pressure distribution can be described. For the contact PP-VP, these areas are marked in Fig. 3 and 5. The compensation force is calculated in (4):

$$F_{\mathrm{comp}} = F_{\mathrm{HP}} + F_{\mathrm{rings}} + F_{\mathrm{trans}} \tag{4}$$

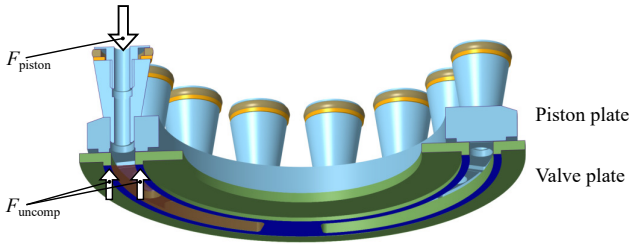

Figure 4: The contact VP-H is typically not compensated and acts as a seal. The load force is created by the pistons, and the kidney opening reduces the force in the contact.

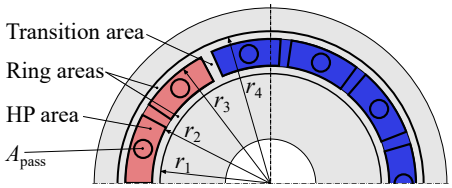

Figure 5: Relevant areas in contact PP-VP and definition of r_1 to r_4.

For calculation of F_{HP} in the contact PP-VP, HP is present in the areas covered by a pocket connected to the HP kidney. At the passage areas A_{pass} no compensation force is created.

$$F_{\text{HP,PP-VP}} = p_{\text{H}} \left(r_3^2 - r_2^2\right) \left(\varphi_{\text{E}} - \varphi_{\text{S}}\right)/2 - \sum_i p_i A_{\text{pass}} \tag{5}$$

In the contact VP-H, conventionally no compensation force is desired. The high piston forces are actually appreciated as they guarantee a good sealing in this contact, which avoids leakage losses. Typically, the backside of the VP provides no area for HP to act upon. However, this changes for increased VP rotation angles, see sec. 2.2.3.
Besides the calculation of F_{HP}, the forces at the ring areas F_{rings} and the transition areas between the HP and LP zones F_{trans} need to be calculated. When calculating these forces for the contact VP-H, two different assumptions can be made:

1. The load force strongly dominates over the compensation force, thus the contact is perfectly sealed and no hydrostatic force is present, i.e.,

$F_{\mathrm{rings,VP-H}} = 0$ and $F_{\mathrm{trans,VP-H}} = 0$. This assumption applies for very low compensation ratios.

2. There is leakage between the housing and the VP, which enables communication of pressure. The pressure distribution is similar to the one in the contact between PP and VP. This assumption applies for higher compensation ratios.

For the calculation of F_{rings} for the contact VP-PP, or contact VP-H with assumption 2, the Reynolds equation (6) can be simplified and an analytical solution is possible. Equation (6) consists of terms for squeeze flow, shear flow and pressure flow [17].

$$\frac{\partial\left(\rho h\right)}{\partial t} + \nabla \cdot \left(\frac{\rho h}{2}\left(\vec{v_{\mathrm{t}}} + \vec{v_{\mathrm{b}}}\right)\right) - \nabla \cdot \left(\frac{\rho h^3}{12\eta}\nabla p\right) = 0 \tag{6}$$

With the assumptions given in sec. 2.1.1 and the pressure-dependent viscosity as in (7) [14], only the term for pressure flow remains and is simplified to (8).

$$\eta = \eta_0\, e^{bp} \tag{7}$$

$$\nabla \cdot e^{-bp}\,\nabla p = 0 \tag{8}$$

Equation (8) written in cylinder coordinates, and a constant pressure over φ and z, yield in (9).

$$\frac{\partial^2 p}{\partial r^2} - b\left(\frac{\partial p}{\partial r}\right)^2 = 0 \tag{9}$$

Integrating twice, and the boundary values ($p(R_{\mathrm{O}}) = p_{\mathrm{O}}$, $p(R_{\mathrm{I}}) = p_{\mathrm{I}}$), yield in (10).

$$p\left(r\right) = p_{\mathrm{O}} - \frac{1}{b}\ln\left(\frac{(R_{\mathrm{O}} - r)e^{b(p_{\mathrm{O}} - p_{\mathrm{I}})} + r - R_{\mathrm{I}}}{R_{\mathrm{O}} - R_{\mathrm{I}}}\right) \tag{10}$$

An example for the resulting pressure distribution is shown in Fig. 6.

The pressure force and its BP can generally be calculated using (11) and (12), and if desired the BP be converted to polar coordinates using (13).

$$F = \int_{\varphi_{\mathrm{S}}}^{\varphi_{\mathrm{E}}} \int_{R_{\mathrm{I}}}^{R_{\mathrm{O}}} p(r)\, r\, dr\, d\varphi \tag{11}$$

$$x_{\mathrm{bp}} = \left(\int_{\varphi_{\mathrm{S}}}^{\varphi_{\mathrm{E}}} \int_{R_{\mathrm{I}}}^{R_{\mathrm{O}}} p(r) r^2 \cos\varphi\, dr\, d\varphi\right)/F \tag{12a}$$

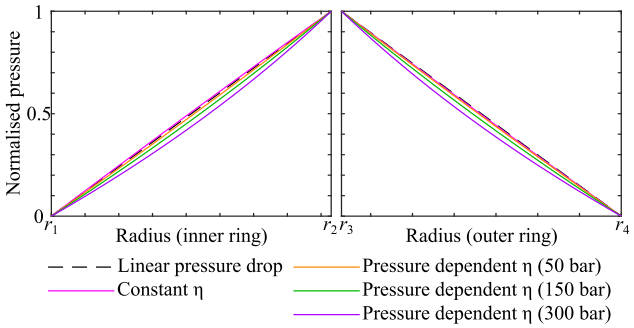

Figure 6: Normalised pressure distribution over ring areas.

$$y_{\mathrm{bp}} = \left(\int_{\varphi_{\mathrm{S}}}^{\varphi_{\mathrm{E}}} \int_{R_{\mathrm{I}}}^{R_{\mathrm{O}}} p(r) r^2 \sin\varphi \, dr \, d\varphi \right) / F \tag{12b}$$

$$r_{\mathrm{bp}} = \sqrt{x_{\mathrm{bp}}^2 + y_{\mathrm{bp}}^2} \tag{13a}$$

$$\varphi_{\mathrm{bp}} = \mathrm{arctan2}(x_{\mathrm{bp}}, y_{\mathrm{bp}}) \tag{13b}$$

The estimation of the pressure field in the transition zones underlies a high degree of uncertainty. Thus it is often not considered for the calculation of the compensation ratio, or different assumptions are made to calculate the pressure force. [17]
In this paper, the pressure distribution in the contact VP-H is calculated using the EHD simulation program described in [16], utilizing the basic functionality of modelling the geometry and solving the Reynolds equation using the finite volume method discretised model. It allows to add features like kidneys and bores as boundary conditions to a disc-shaped simulation domain. In this work, it is used as a tool to calculate the pressure distribution in the transition zones where analytical calculations cannot be applied. The simulation results are condensed in a surrogate model in order to enable analytical calculations. More details are presented in sec. 2.2.3.

2.2 Cylinder Barrel Rotation and Valve Plate Rotation Dependent Compensation Ratios

Typically, the compensation ratio is only calculated for one rotational position of the CB. However, the compensation ratio varies over the cylinder block rotation angle [11] resp. the CB rotation angle, and also over the VP rotation angle.

2.2.1 Load Force

Firstly, the load force needs to be calculated. Hence, the pressure in each chamber needs to be known. Lee et al. [11] assumes the piston chamber pressures to remain at the pressure of the last kidney the chamber was in contact with, i.e., the chamber reaches HP when entering the HP kidney and remains at this pressure level until entering the LP kidney. This approach can also be applied for rotated VPs.

Figure 7a shows the start and end of the HP kidney (α_S, α_E) and the LP kidney (β_S, β_E). The kidney angles need to reflect the current kidney angles under consideration of the VP rotation. As the two sides of the pump communicate with one another through the CB, relative valve plate rotation needs to be considered. For the contact PP-VP, the effective VP angles are to be used, see Fig. 2.

At commutation from LP to HP, a chamber reaches HP as soon as it gets in contact with a HP kidney at α_S. The pocket in the PP then extends the HP area by the angle θ_3, and over the angle θ_4 the pressure drops to LP level. At commutation from HP to LP, the chamber pressure drops to LP as soon as the chamber gets in contact with a LP kidney at β_S. Thus the HP area reaches at least to the angle $\beta_{\mathrm{S}'} = \beta_\mathrm{S} - 2\pi/z$, which is one period before the start of the LP kidney at β_S. The HP area on the interface VP-PP is extended beyond $\beta_{\mathrm{S}'}$ by the angle θ_1, and over the angle θ_2 the pressure drops to LP level.

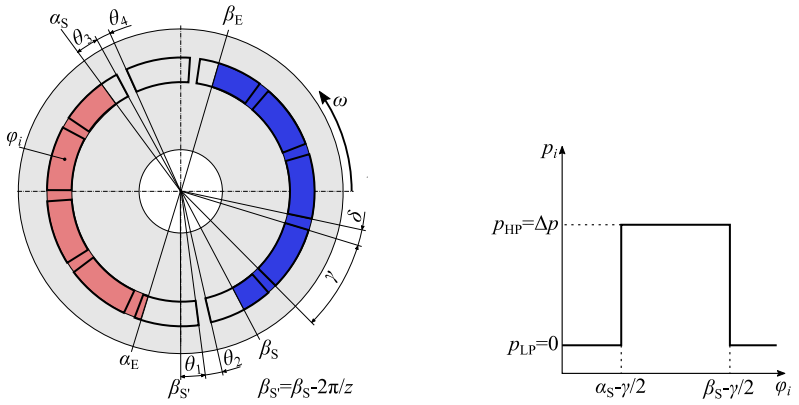

(a) Definition of relevant angles around commutation. The HP kidney is marked in red, the LP kidney is marked in blue.

(b) Pressure p_i in one chamber i over rotational angle of the chamber φ_i.

Figure 7: View of VP and port plate angles as well as chamber pressure.

2.2.2 Compensation Force in Contact between Piston Plate and Valve Plate

Lee et al. [11] introduces case differentiations for different situations around commutation. In this paper, a lower number of cases is required as both the pockets in the PP and the kidneys are rectangular. For each commutation, four different situations are possible as shown in Fig. 8 and 9. For each of the cases, two angles can be calculated: the angle extending the length of the HP area (θ_1, θ_3), and the angle of the transition area between HP and LP (θ_2, θ_4). These angles are used to provide inputs to (5), (11) and (16) for different CB and VP rotation angles. The equations for the calculation of the angles are shown in tab. 1. For the calculation of F_{trans}, case 1 of the surrogate model developed for the contact VP-H is used, see sec. 2.2.3.
Furthermore, cross-porting can be considered. When cross-porting occurs, it is assumed that the kidneys keep their pressure levels, and that in the chamber connecting HP and LP, the pressure is $(p_{\mathrm{H}} + p_{\mathrm{L}})/2$. Cross-porting can occur for large relative VP rotation angles, and small cross-porting angles might be desired in some operating points in order to reduce HP peaks and the risk of cavitation [9].

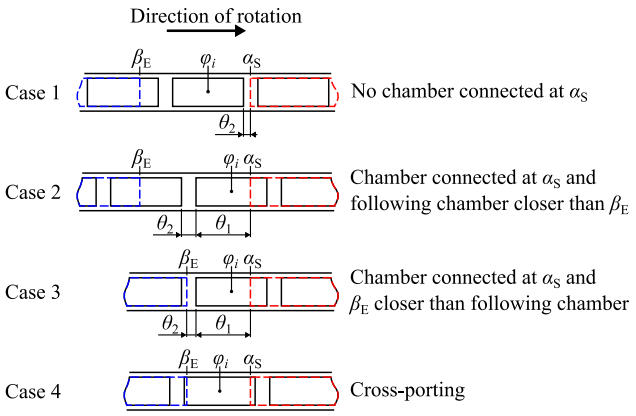

Figure 8: PP pocket position relative to effective kidney angles around commutation from LP to HP, visualised on unrolled VP.

2.2.3 Compensation Force in Contact between Valve Plate and Housing

The compensation force in the contact VP-H depends on the VP rotation angle. The different cases are shown in tab. 2 and Fig. 10. For large VP

Table 1: Constraints and variables for cases of piston pocket position relative to kidney angles around commutation.

Case	**Constraints for φ_i**	$\boldsymbol{\theta_1}$	$\boldsymbol{\theta_2}$	$\boldsymbol{\theta_3}$	$\boldsymbol{\theta_4}$
1	$\beta_{\mathrm{S}} - \gamma/2 - \delta < \varphi_i < \beta_{\mathrm{S}} - \gamma/2$	0	$\alpha_{\mathrm{S}} - (\varphi_i + \gamma/2)$	n/a	n/a
2	$\lvert\beta_{\mathrm{S}} - \varphi_i\rvert < \gamma/2$ & $\varphi_i - \gamma/2 - \delta > \alpha_{\mathrm{E}}$	$\alpha_{\mathrm{S}} - (\varphi_i - \gamma/2)$	δ	n/a	n/a
3	$\lvert\beta_{\mathrm{S}} - \varphi_i\rvert < \gamma/2$ & $\varphi_i - \gamma/2 - \delta < \alpha_{\mathrm{E}}$	$\alpha_{\mathrm{S}} - (\varphi_i - \gamma/2)$	$(\varphi_i - \gamma/2) - \beta_{\mathrm{E}}$	n/a	n/a
4	$\beta_{\mathrm{S}} - \gamma/2 < \varphi_i < \alpha_{\mathrm{E}} + \gamma/2$	0	0	n/a	n/a
5	$\alpha_{\mathrm{S}} - \gamma/2 - \delta < \varphi_i < \alpha_{\mathrm{S}} - \gamma/2$	n/a	n/a	$\varphi_i - \beta_{\mathrm{S}'} + \gamma/2$	$\beta_{\mathrm{S}} - (\varphi_i + \gamma/2)$
6	$\lvert\alpha_{\mathrm{S}} - \varphi_i\rvert < \gamma/2$ & $\varphi_i - \gamma/2 - \delta > \beta_{\mathrm{E}}$	n/a	n/a	$\varphi_i - \beta_{\mathrm{S}'} - \gamma/2 - \delta$	δ
7	$\lvert\alpha_{\mathrm{S}} - \varphi_i\rvert < \gamma/2$ & $\varphi_i - \gamma/2 - \delta < \beta_{\mathrm{E}}$	n/a	n/a	$\alpha_{\mathrm{E}} - \beta_{\mathrm{S}'}$	$(\varphi_i - \gamma/2) - \alpha_{\mathrm{E}}$
8	$\alpha_{\mathrm{S}} - \gamma/2 < \varphi_i < \beta_{\mathrm{E}} + \gamma/2$	n/a	n/a	$\alpha_{\mathrm{E}} - \beta_{\mathrm{S}'}$	0

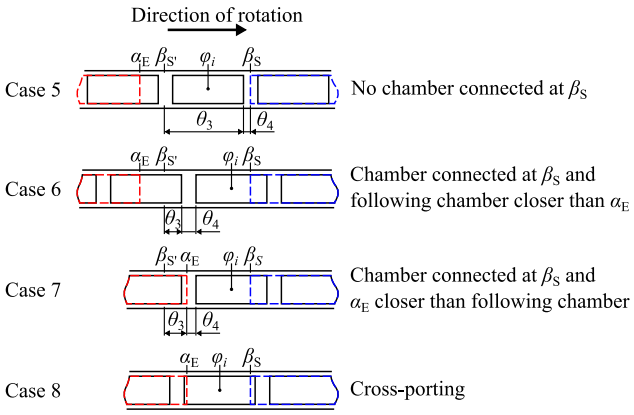

Figure 9: PP pocket position relative to effective kidney angles around commutation from HP to LP, visualised on unrolled VP.

rotation angles, the HP port in the housing partially is under the valve land as sketched in case 3 to 5, resulting in (14):

$$F_{\mathrm{HP,VP-H}} = p_{\mathrm{H}}\, A_{\mathrm{overlap}} \tag{14}$$

F_{rings} and F_{trans} are 0 when assuming perfect sealing (see sec. 2.1.3). Under

Table 2: Cases of housing ports relative to kidney for commutation from LP to HP (HP to LP is analogue).

Case	**Constraints for kidney position rel. to housing ports**	$\boldsymbol{\theta_5}$	$\boldsymbol{\theta_6}$
1	$\alpha_{\mathrm{HS}} > \alpha_{\mathrm{S}}$ & $\alpha_{\mathrm{S}} - \beta_{\mathrm{HE}} > \varphi_{\mathrm{c}}$	0	$\alpha_{\mathrm{S}} - \beta_{\mathrm{E}}$
2	$\alpha_{\mathrm{S}} - \beta_{\mathrm{HE}} < \varphi_{\mathrm{c}}$		
3	$\alpha_{\mathrm{HS}} < \alpha_{\mathrm{S}}$ & $(\alpha_{\mathrm{S}} - \alpha_{\mathrm{HS}}) < \varepsilon$	$\alpha_{\mathrm{S}} - \alpha_{\mathrm{HS}}$	$\alpha_{\mathrm{HS}} - \beta_{\mathrm{E}}$
4	$\alpha_{\mathrm{HS}} < \alpha_{\mathrm{S}}$ & $(\alpha_{\mathrm{S}} - \alpha_{\mathrm{HS}}) < \varepsilon$ & $(\alpha_{\mathrm{HS}} - \beta_{\mathrm{E}}) \geq \varphi_{\mathrm{c}}$		
5	$\alpha_{\mathrm{HS}} < \alpha_{\mathrm{S}}$ & $(\alpha_{\mathrm{HS}} - \beta_{\mathrm{E}}) < \varphi_{\mathrm{c}}$		
6	$(\alpha_{\mathrm{HS}} < \alpha_{\mathrm{E}}$ & $\alpha_{\mathrm{HE}} > \beta_{\mathrm{S}})$ or $(\alpha_{\mathrm{HS}} < \beta_{\mathrm{E}}$ & $\alpha_{\mathrm{HE}} > \alpha_{\mathrm{S}})$	n.a.	n.a.

the assumption of the presence of an oil film, F_{rings} can be calculated using (11).
Numerical calculations were carried out to calculate F_{trans} for various VP rotation angles and pressure levels for the geometry described in 3.1. This was

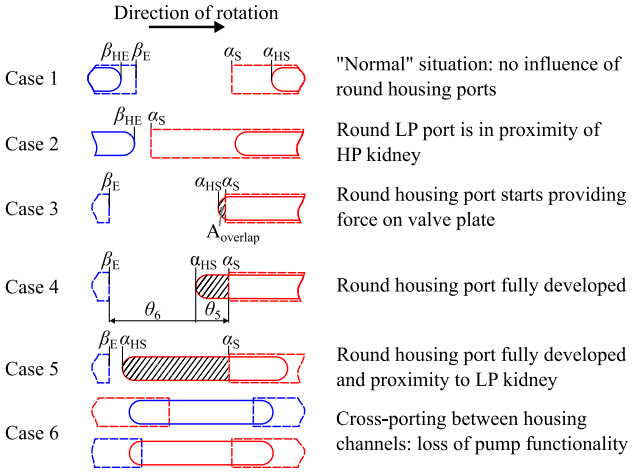

Figure 10: Position of the unrolled kidneys relative to the channels in the housing, for commutation from LP to HP (cases for HP to LP analogue). When the channels are below the valve land zone, a hydrostatic force acts on the VP.

done using the EHD simulation program described in [16], utilizing the basic functionality of modelling the geometry and solving the Reynolds equation using the finite volume method. The pressure distribution in the transition zones is extracted from the results. Fig. 11 visualises exemplary results. The results reveal that F_{trans} and its BP are scalable with the angle of the transition zone, which enables a normalisation of the results.
Attempting to generalise the results of the numerical calculations, so that forces can also be accurately calculated analytically for slightly different pump geometries (e.g., different kidney opening angles), the force of the transition area and its BP were normalised and a surrogate model was created. This surrogate model includes different equations, depending on which case in Fig. 10 is active. For cases 3 to 5 in Fig. 10, the surrogate model provides parameters for a separate calculation of the force around the round port (in the direction of θ_5) and the force in the transition area (in the direction of θ_6), see Fig. 11b.

The basis for the normalisation of the force is a fully pressurised transition area. However, (15a) considers that for large transition angles in the contact VP-H, the pressure close to the LP port is negligible, see Fig. 11. φ_{c} is the angle on which the distance on the VPs mean radius is equivalent to the

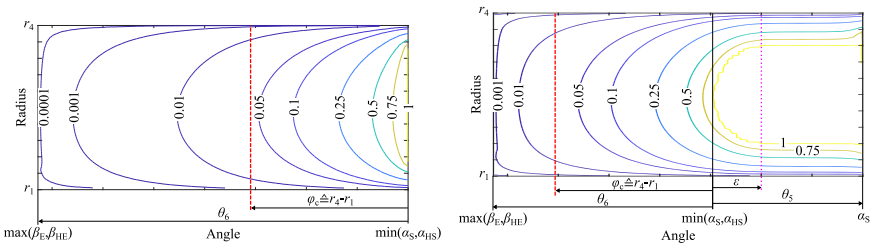

(a) Pressure distribution between two rectangular kidney ports.

(b) Distribution of normalised pressure for partially uncovered housing port. On the right hand side of the magenta colored dotted line, the pressure distribution ($p(r)$) is acc. to (10).

Figure 11: Distribution of normalised pressure in transition zone from LP to HP in VP-H contact acc. to numerical calculation, visualised on unrolled VP. The characteristic angle φ_c is the equivalent to the distance $r_4 - r_1$ on the mean radius $(r_1 + r_4)/2$. The surrogate model neglects the pressure to the left of the red dashed line.

distance between the VPs inner and outer radius. Transition areas at greater distance than φ_c are neglected.
When θ_5 is larger than the angle covered by the round end of the housing port ε, the part exceeding ε is calculated as a ring acc. to (10). Thus the angle for this area is limited to ε, see (15b). Furthermore, only the area not covered by the HP port is considered, as the area covered by the HP port is already taken into account in (14).

$$\varphi_\mathrm{p,trans} = \begin{cases} \theta_6, & \text{for } \theta_6 \leq \varphi_\mathrm{c} \\ \varphi_\mathrm{c} = (r_4 - r_1)/(\frac{r_1+r_4}{2}), & \text{for } \theta_6 > \varphi_\mathrm{c} \end{cases} \tag{15a}$$

$$\varphi_\mathrm{p,port} = \begin{cases} \theta_5, & \text{for } \theta_5 \leq \varepsilon \\ \varepsilon, & \text{for } \theta_5 > \varepsilon \end{cases} \tag{15b}$$

The surrogate model in tab. 3 provides the normalised parameters σ_F and σ_φ. Using (16), the forces and their BPs can be calculated. For the radius, no normalisation is required, as it remains almost unchanged for different φ_p. However, it needs to be considered that the housing ports of the examplary pump are not fully centred in relation to the kidney, thus the BP of the force around the port is slightly off-centre, see (16c).

$$F = \sigma_\mathrm{F}\, p_\mathrm{H}\, A \tag{16a}$$

$$\varphi_{\mathrm{F}} = \sigma_{\varphi}\, \varphi_{\mathrm{p}} \tag{16b}$$

$$r_{\mathrm{F}} = \begin{cases} \frac{r_1+r_4}{2}, & \text{for transition land} \\ \frac{r_1+r_4}{2} + 0.07\frac{r_4-r_1}{2}, & \text{for area around port} \end{cases} \tag{16c}$$

2.2.4 Influence of Valve Plate Rotation

Relative VP rotation affects the effective valve land and thus the amount of pistons loaded with HP. The pockets in the PP are directly connected to the pistons, thus the compensation force in the contact PP-VP directly reacts to an increased amount of pressurised pistons. Therefore, in the contact PP-VP, all calculations are made based on the *effective* VP angles.
In the contact VP-H, the load force is affected by relative VP rotation as it affects the amount of pressurised pistons. However, the compensation force is not affected by relative VP rotation. Thus, for the compensation force in the contact VP-H, the calculations are made based on the *total* rotation angle of each VP. In order to simplify the visualisation, the figures in sec. 3 show results for 0 deg relative VP rotation.

2.2.5 Balance Point of Uncompensated Force

The load forces are not fully compensated. The uncompensated force's magnitude can be calculated with a force balance. Its location can be calculated with a torque balance around the load force, revealing that for high compensation ratios, the compensation force can be at a significant distance from the load force (as a small compensation force requires a large lever to maintain the torque balance). The uncompensated force needs to be within the outer radius of the VP's contact surface with its contact partner in order to avoid tipping [2].

2.3 Friction Torque

The friction torque for each interface of the VP is calculated using (17). A torque needs to be provided in order to overcome this friction torque and rotate the VP.

$$T_{\mathrm{fric}} = F_{\mathrm{uncomp}}\, r_{\mathrm{fric}}\, \mu \tag{17}$$

The correct friction coefficient μ for each interface will need to be established with measurements, and even then it will not be constant over the full operating range.
Due to the different level of hydrostatic compensation, the friction coefficient

Table 3: Surrogate models for transition land force, the force from the land around the housing port and their angular location of their BPs.

Case	**Zone**	$\boldsymbol{\sigma}_{\mathrm{F}}$	$\boldsymbol{\sigma}_{\varphi}$
1	transition land	$0.243 - 1.13 \cdot 10^{-9} \cdot p/\mathrm{Pa}$	$0.267 - 5.25 \cdot 10^{-10} \cdot p/\mathrm{Pa}$
	around round port	0	n.a.
2	transition land	$0.243 - 1.13 \cdot 10^{-9} \cdot p/\mathrm{Pa} + 0.0125 \cdot (\varphi_{\mathrm{c}} - \theta_5)/\mathrm{deg}$	$0.267 - 5.25 \cdot 10^{-10} \cdot p/\mathrm{Pa} + 0.0075 \cdot (\varphi_{\mathrm{c}} - \theta_5)/\mathrm{deg}$
	around round port	0	n.a.
3	transition land	$0.243 - 1.13 \cdot 10^{-9} \cdot p/\mathrm{Pa} - 0.0109 \cdot \theta_5/\mathrm{deg}$	$0.267 - 5.25 \cdot 10^{-10} \cdot p/\mathrm{Pa} - 0.0025 \cdot \theta_5/\mathrm{deg}$
	around round port	$0.721 - 1.58 \cdot 10^{-9} \cdot p/\mathrm{Pa} - 0.0395 \cdot \theta_6/\mathrm{deg}$	$0.492 - 0.0116 \cdot \theta_6/\mathrm{deg}$
4	transition land	$0.185 - 1.13 \cdot 10^{-9} \cdot p/\mathrm{Pa}$	$0.254 - 5.25 \cdot 10^{-10} \cdot p/\mathrm{Pa}$
	around round port	$0.509 - 1.58 \cdot 10^{-9} \cdot p/\mathrm{Pa}$	0.430
5	transition land	$0.185 - 1.13 \cdot 10^{-9} \cdot p/\mathrm{Pa} + 0.0055 \cdot (\varphi_{\mathrm{c}} - \theta_5)/\mathrm{deg}$	$0.254 - 5.25 \cdot 10^{-10} \cdot p/\mathrm{Pa} - 0.0061 \cdot (\varphi_{\mathrm{c}} - \theta_5)/\mathrm{deg}$
	around round port	$0.509 - 1.58 \cdot 10^{-9} \cdot p/\mathrm{Pa}$	0.430

μ is expected to differ between the two investigated interfaces. The overall friction torque is the sum of friction torques on both interfaces. When the CB rotates at higher speed than the VP, it needs to be considered that the direction of the friction torque in the contact between VP and PP is the same as the CB rotation.
When calculating the lever/radius of the friction torque, it needs to be considered that forces can only be transmitted where contact between the parts is possible (i.e., between r_1 and r_4). Thus, the friction radius r_{fric} is approximated as the radius r_{appr} between two axial rings between r_1 and r_4 as derived in [16]. When the BP's radius r_{bp} is larger than the approximated radius, it is used instead, see (18).

$$r_{\mathrm{fric}} = \begin{cases} r_{\mathrm{appr}} = \frac{2}{3}\frac{r_4^3 - r_1^3}{r_4^2 - r_1^2}, & \text{for } r_{\mathrm{bp}} <= r_{\mathrm{appr}} \\ r_{\mathrm{bp}}, & \text{for } r_{\mathrm{appr}} < r_{\mathrm{bp}} <= r_4 \end{cases} \tag{18}$$

3 Results and discussion

3.1 Inputs

The methodology presented in sec. 2 is applied on a 35 cm^3/rev pump with 11 pistons on each side and the geometric parameters shown in tab. 4. The spring force F_{S} is 90 N and the parameter b for the pressure-dependent viscosity is set to $1.7{\cdot}10^{-8}$/Pa.

Table 4: Geometry parameters for exemplary pump.

Angles in deg	**in VP**	**in housing**	**in PP**
$\alpha_{\mathrm{S}}, \alpha_{\mathrm{HS}}, \gamma$	119.2	152.3	28.0
$\alpha_{\mathrm{E}}, \alpha_{\mathrm{HE}}, \delta$	255.2	207.7	4.7
$\beta_{\mathrm{S}}, \beta_{\mathrm{HS}}$	295.5	27.7	
$\beta_{\mathrm{E}}, \beta_{\mathrm{HE}}$	77.5	332.3	
Radii in mm	**PP-VP**	**VP-H**	**Housing ports**
r_1	26.2	27	n.a.
r_2	28.7		29
r_3	35.7		35
r_4	38.2	37	n.a.
Areas in mm^2	A_{piston}	A_{pass}	A_{kidney}
A	178.5	38.5	534.4

3.2 Compensation Ratio

Fig. 12 shows the compensation ratio for the contact PP-VP. The compensation ratio is slightly affected by the varying size of the transition area during commutation, and by the amount of pressurised pistons. VP rotation has the same effect as CB rotation on the compensation ratio.
In comparison to the analytical approaches to calculate compensation ratios which are summarised in [17], the spring force F_{S} increases the load force, and the pressure-dependent viscosity decreases the compensation force. Thus these two effects lead to a decreased result for the compensation ratio.

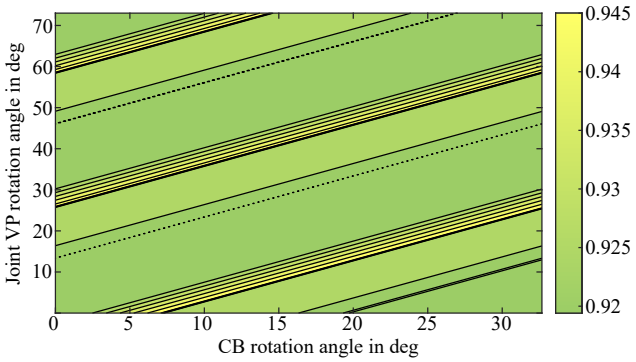

Figure 12: Compensation ratio for the contact PP-VP.

Fig. 13 shows the compensation ratio in the contact VP-H. When assuming perfect sealing (Fig. 13a), no compensation force is present until the VP reaches case 3 (see Fig. 10). With increasing VP rotation, the compensation force increases. The compensation ratio varies with the amount of pressurized pistons.
When assuming the existence of an oil film (see Fig. 13b), the compensation ratio is increased by 27 to 40%, depending on the amount of pressurised pistons. That indicates that the compensation ratio drastically increases as soon as an oil film is present between VP and housing. This case needs to be considered when targeting compensation ratios close to 1.

3.3 Location of Forces

Fig. 14 shows the location of the load force, the hydrostatic compensation force and the uncompensated force in the contact PP-VP for three different VP positions over one CB revolution. It shows that the BPs of the load force

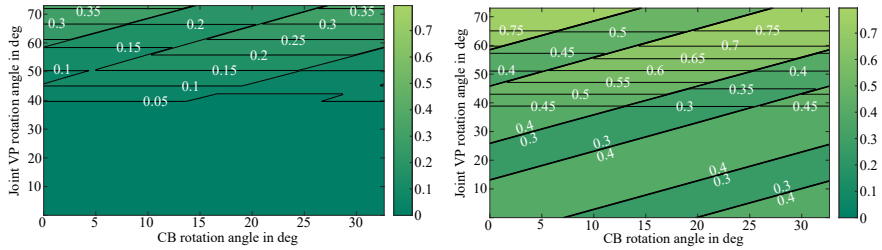

(a) Assuming perfect sealing. (b) Assuming existence of an oil film.

Figure 13: Compensation ratio in PP-H contact.

and the compensation force follow the VP rotation, and thus the uncompensated force remains inside the area of possible contact without tipping.

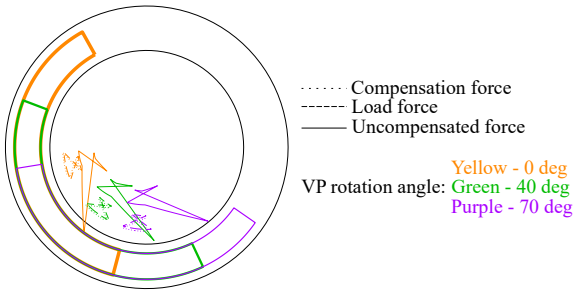

Figure 14: Location of load force, hydrostatic compensation force and uncompensated force for the contact PP-VP.

Fig. 15 shows the location of the load force, the hydrostatic compensation force and the uncompensated force in the contact VP-H for three different VP positions over one CB revolution.
Assuming perfect sealing (Fig. 15, left), there is no compensation force for small VP rotation angles. For larger VP rotation angles, the only hydrostatic compensation force is created by the pressure force from the HP port acting on the VP. The BP of this compensation force remains at a constant position over the CB rotation angle. The BP of the compensation force has a large distance to the load force. However, as the compensation force is rather small, the uncompensated force remains in proximity of the load force and within the area of possible contact for small to medium VP rotation angles. For

large VP rotation angles, the uncompensated force's BP is outside the area of possible contact, leading to VP tipping.
Assuming the existence of an oil film (Fig. 15, right), the compensation force's BP rotates with the VP. The uncompensated force's BP carries out a larger movement than the load force. When the housing port creates a pressure force on the VP, the compensation force's BP no longer fully follows the rotation of the VP. Thus, the movement of the uncompensated force's BP is increased. Even though the compensation force's BP is in closer proximity to the load force than in the scenario with perfect sealing, the BP of the uncompensated force can be even further away, as the uncompensated force's magnitude is lower and the torque balance needs to be maintained. Likewise, for large VP rotation angles, the uncompensated force's BP is outside the area of possible contact, so that tipping is expected. This reveals that VP rotation is not suitable for small displacement levels when using axial ports.

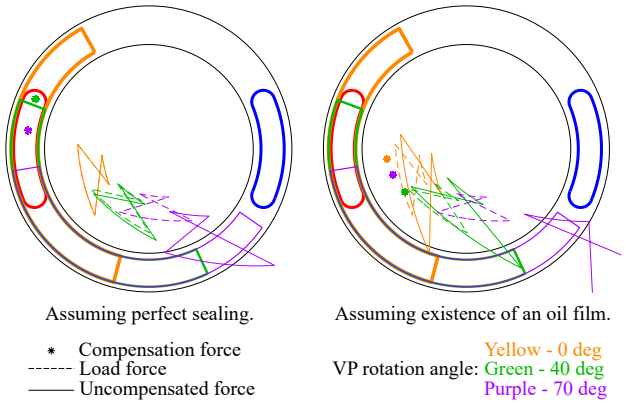

Figure 15: Location of load force, hydrostatic compensation force and uncompensated force for the contact between VP-H.

3.4 Friction Torque

Fig. 16 shows the friction torque in the contact PP-VP for an assumed friction coefficient of μ=0.06. The friction torque varies over the VP rotation angle and the CB rotation angle due to the varying amount of pressurised pistons.

Fig. 17 shows the friction torque in the contact VP-H for a friction coefficient of μ=0.12. The friction coefficient in this contact is assumed to be significantly higher than in the contact PP-VP, as the lubrication conditions

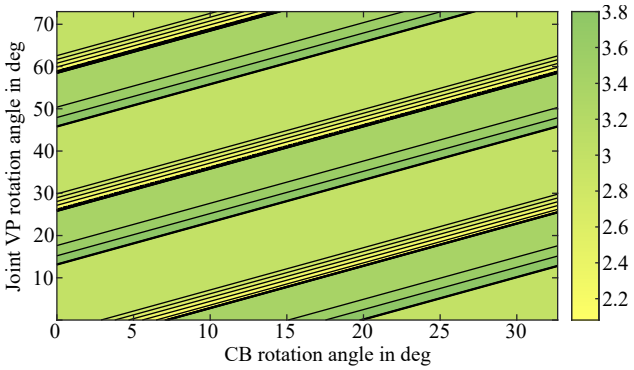

Figure 16: Friction torque in Nm at 300 bar in contact PP-VP, assuming μ=0.06.

are significantly worse (no hydrodynamic lubrication, and this contact works as seal for high compensation ratios). The friction torque strongly depends on the amount of pressurised pistons, and it decreases with increasing VP rotation angles due to increased compensation forces.
The friction torque in the contact VP-H dominates over the friction torque in the contact PP-VP.

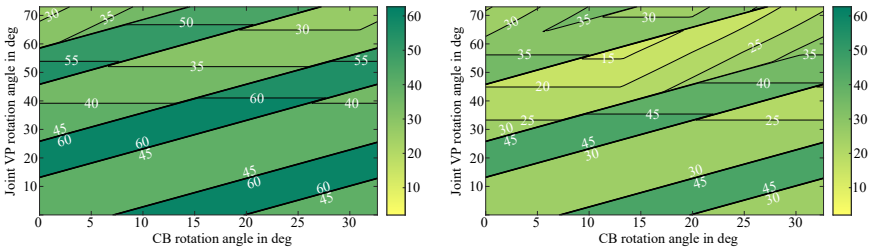

(a) Assuming perfect sealing. (b) Assuming existence of an oil film.

Figure 17: Friction torque in Nm at 300 bar in contact VP-H, assuming μ=0.12.

3.5 Possible Valve Plate Design Improvement

In the considered exemplary pump, high friction torques occur in the contact VP-H, as compensation ratios are low. Increased compensation ratios could

decrease the friction torque. A possibility to increase the compensation ratio is shown in Fig. 18: pockets on the housing side of the VP are located adjacent to the HP kidney, providing a hydrostatic compensation force. An advantage of this pocket design is that the pockets increase the angle in which the compensation force fully follows the movement of the VP, thus keeping the BP of the unbalanced force stable over a larger VP rotation range. Furthermore, the BP of the compensation force can be moved closer to the load force. However, an (almost) full compensation of the forces in this contact is not possible, as the BP of the uncompensated force needs to remain within the outer radius of possible contact even though the compensation force does not follow the load force, and the load force varies over one revolution.

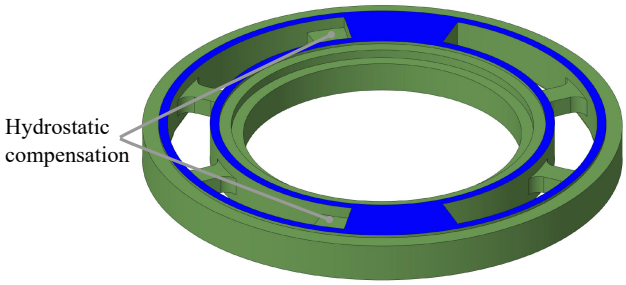

Figure 18: Partial pressure compensation with pockets on the housing side of the VP.

4 Conclusion

An analytical approach to calculate compensation ratios and friction torques for VP rotation has been presented. This has been done on the example of a double pump of floating piston type, but the approach can also be used for traditional swash plate pumps. The main share of the friction torque originates from the contact between VP and housing. Pockets for hydrostatic compensation can increase the compensation ratio and reduce this torque. However, due to the varying amount of HP pistons and the location of the compensation force does not follow the location of the load force over one revolution, a full compensation is not possible.

For large VP rotation angles, a hydrostatic force from the housing port acts on the valve plate. This force does not follow the VP rotation, leading to VP tipping. This reveals that while VP rotation provides a stable force balance

for high displacement levels, it is not suitable for small displacement levels when using axial ports.

Acknowledgment

This research was funded by the Swedish Energy Agency (Energimyndigheten, Grant Number 50181-1).

Nomenclature

Abbreviation / index	Meaning
BP	Balance point
CB	Cylinder barrel
E	End
H	Housing
HP	High-pressure
LP	Low-pressure
PP	Piston plate
S	Start
VP	Valve plate

Designation	Denotation	Unit
b	Parameter for pressure dependency of viscosity	1/Pa
h	Film height	m
p	Pressure	Pa
p_{H}	High-pressure	Pa
r, r_x	Radius	m
r_{F}	Radius of F_{trans}	m
t	Time	s
v	Velocity	m/s
A_{piston}	Piston area	m^2
A_{pass}	Area of passage in piston	m^2
A_{overlap}	Area charging the backside of the VP with HP	m^2
F_{comp}	Hydrostatic compensation force	N
F_{load}	Load force	N
F_{rings}	Compensation force from radial seal rings	N
F_{trans}	Comp. force from transition area	N
F_{HP}	Compensation force from area charged with HP	N
F_{S}	Spring force	N
T_{fric}	Friction torque	Nm
α	Angle related to HP kidney	rad
β	Angle related to LP kidney	rad
$\beta_{\mathrm{S}'}$	Angle which is $2\pi/z$ earlier than β_{S}	rad
γ	Angle covered by one pocket	rad
δ	Angle between two pockets	rad
ε	Angle covered by circular end of housing port	rad
ζ	Compensation ratio	-
η	Dynamic viscosity	Pa s
θ_x	Angular length of specific area	rad
μ	Friction coefficient	-
ρ	Oil density	$\mathrm{kg/m}^3$
σ_{p}	Factor for force in transition area / around port	-
σ_{φ}	Factor for angle of BP of force	-
φ_c	Characteristic angle	rad
φ_{F}	Angle between HP zone and BP of F_{trans}	rad
φ_i	Rotational position of piston i	rad
φ_{p}	Reference for σ_{p}	rad
φ_{E}	Angle of end of seal ring zone	rad
φ_{S}	Angle of start of seal ring zone	rad
ψ	Angle of rotation of VP	rad

References

[1] P.A.J. Achten, Z. Fu, and G.E.M. Vael. Transforming future hydraulics: a new design of a hydraulic transformer. In *The Fifth Scandinavian International Conference on Fluid Power (SICFP '97), Sweden, Linköping*, 1997.

[2] Peter Achten and Sjoerd Eggenkamp. Barrel tipping in axial piston pumps and motors. In *Proceedings of the 15:th Scandinavian International Conference on Fluid Power, June 7-9, 2017, Linköping, Sweden*, 2017.

[3] Peter A. J. Achten and Zhao Fu. Valving land phenomena of the Innas hydraulic transformer. *International Journal of Fluid Power*, 1(1):39–47, Jan 2000.

[4] Eckhard Brangs. *Über die Auslegung von Axialkolbenpumpen mit ebenem Steuerspiegel*. PhD thesis, RWTH Aachen, 1965.

[5] Junhee Cho, Xiaoping Zhang, Noah D. Manring, and Satish S. Nair. Dynamic modelling and parametric studies of an indexing valve plate pump. *International Journal of Fluid Power*, 3(3):37–48, Jan 2002.

[6] Liselott Ericson and Jonas Forssell. A novel axial piston pump/motor principle with floating pistons: Design and testing. In *BATH/ASME 2018 Symposium on Fluid Power and Motion Control*. American Society of Mechanical Engineers, Sep 2018.

[7] Liselott Ericson, Samuel Kärnell, and Martin Hochwallner. Experimental investigation of a displacement-controlled hydrostatic pump/motor by means of rotating valve plate. In *Proceedings of 15:th Scandinavian International Conference on Fluid Power, (SICFP'17), Linköping, Sweden*. Linköping University Electronic Press, Dec 2017.

[8] Thomas Grahl. Geräuschminderung an Axialkolbenpumpen durch variable Umsteuersysteme. *O+P Ölhydraulik und Pneumatik*, 33(5):437–443, 1989.

[9] Thomas Heeger and Liselott Ericson. A new degree of freedom for variable axial piston pumps with valve plate rotation. In *Proceedings of the 17:th Scandinavian International Conference on Fluid Power, SICFP21, June 1-2, 2021, Linköping, Sweden*, 2021.

[10] Jaroslav Ivantysyn and Monika Ivantysynova. *Hydrostatic pumps and motors: principles, design, performance, modelling, analysis, control, and testing*. Akademia Books International, New Delhi, 2001.

[11] Seong-Ryeol Lee, Stephan Wegner, Hubertus Murrenhoff, and Katharina Schmitz. Analytical approach to calculate the rotational angle-dependent compensation ratio of the cylinder block - valve plate contact in axial piston machines. In *16th Scandinavian International Conference on Fluid Power, SICFP'19, 2019-05-22 - 2019-05-24, Tampere, Finland*, 2019.

[12] Jan Lux and Hubertus Murrenhoff. Experimental loss analysis of displacement controlled pumps. In *10th International Fluid Power Conference, Dresden*, pages 441–452, 2016.

[13] Noah D. Manring. *Fluid Power Pumps and Motors: Analysis, Design and Control*. McGraw Hill Book CO, 2013.

[14] Hubertus Murrenhoff. *Grundlagen der Fluidtechnik, Teil 1: Hydraulik*. Shaker Verlag GmbH, Aachen, 2016. Lecture notes.

[15] Société Anonyme André Citroën. Perfectionnement aux pompes à barillet, 1959.

[16] Stephan Wegner. *Experimental and Simulative Investigation of the Cylinder Block/Valve Plate Contact in Axial Piston Machines*. PhD thesis, RWTH Aachen, 2020.

[17] Stephan Wegner, Stefan Gels, and Hubertus Murrenhoff. Vergleich analytischer Berechnungsmethoden des Entlastungsgrades im Kolbentrommel-Steuerspiegel-Kontakt in Axialkolbenmaschinen. *O+P Fluidtechnik*, pages 60–69, 11-12 2017.

[18] Jiang'ao Zhao, Yongling Fu, Jiming Ma, Jian Fu, Qun Chao, and Yan Wang. Review of cylinder block/valve plate interface in axial piston pumps: Theoretical models,

experimental investigations, and optimal design. *Chinese Journal of Aeronautics*, 34(1):111–134, 2021.

Biography



Thomas Heeger received his M.Sc. degree in mechanical engineering at RWTH Aachen University, Germany, in 2018. He is currently doing his doctoral studies in Fluid and Mechatronic Systems at Linköping University, Sweden. Research interests include pumps and their electrification.



Stephan Wegner received his Ph.D. in hydraulics from the Institute for Fluid Power Drives and Systems at RWTH Aachen University, Germany, in 2021.



Liselott Ericson received her Ph.D. in hydraulics at Linköping University (LiU), Sweden, in 2012. She currently works as a professor at Fluid and Mechatronic Systems at LiU. The areas of interest include pump and motor design, electro-hydraulic systems, modelling and simulation.

Validated efficiency improvements by implementation of structures on the slipper surface of an axial piston pump

Svenja Horn, Roman Ivantysyn, Jürgen Weber

Institute of Mechatronic Engineering, TU Dresden, svenja.horn@tu-dresden.de, roman.ivantysyn@tu-dresden.de, juergen.weber@tu-dresden.de

Abstract.

New application areas such as compact drives and displacement control using variable electric motors require that hydrostatic machines exhibit good performance also at very low relative speeds without being damaged during critical mixed friction conditions. Low relative speeds result in a drop of the hydrodynamic pressure in the lubricating gaps and therefore to friction losses, wear and a higher probability of failures. The aim of this paper is to present a novel approach to reduce the viscous friction losses and wear during critical operating conditions, by increasing the hydrodynamic pressure build-up and modify the hydrostatics of the slippers of an axial piston pump. To achieve this goal structured surface profiles on the slipper surface are investigated, both in simulation and measurement. The measurement results and simulation validation are shown in this paper.

Keywords. Axial piston pump, slippers, surface structures, lubricating gap, numerical simulation, tribology**.**

1 INTRODUCTION

Electrification and compact drives are becoming popular due to environmental benefits and their ease of operation and plug-and-play. However, the pumps in these drives are exposed to very critical mixed friction conditions, especially at low speeds and high pressures. Low relative speeds result in a drop of the hydrodynamic pressure in the lubricating gaps and therefore to friction losses, wear and a higher probability of failures. Usually, material combinations of leaded bronze or brass and steel are used to ensure good run-in behavior and thus good dry-running performance under mixed friction. However, EU regulations require that lead-containing materials should no longer be used in the future. This makes it necessary to find other materials and structures that can withstand the tougher operating conditions despite the absence of lead containing metals. In order to avoid lead in the lubrication gaps, new designs must be investigated to reduce wear in the first place.

The research goal was to develop a novel approach to reduce the viscous friction losses and wear during critical operating conditions by increasing the hydrodynamic pressure build-up of the slippers of an axial piston pump. In order to achieve this objective, structured surface profiles are investigated to be adapted to the slipper surface, which is one of the three main

lubricating interfaces, see Figure 1.1, and significantly contributes to the pumps powerlosses. In cooperation with the Fraunhofer IWU Chemnitz the manufacturing limitations for series production of the structured surface are analyzed for different materials. This paper presents the measurement results of the developed designs.

On the right side of Figure 1.1 the optimization problem of the lubrication interfaces is shown. A trade-off arises due to the conflicting requirements on the gap to allow good bearing properties while reducing leakage at the same time. The powerloss curve on the right of the figure depicts this correlation with a theoretical parallel gap height. Unfortunately, the optimum gap height changes with each operating condition, further increasing the complexity of the design process.

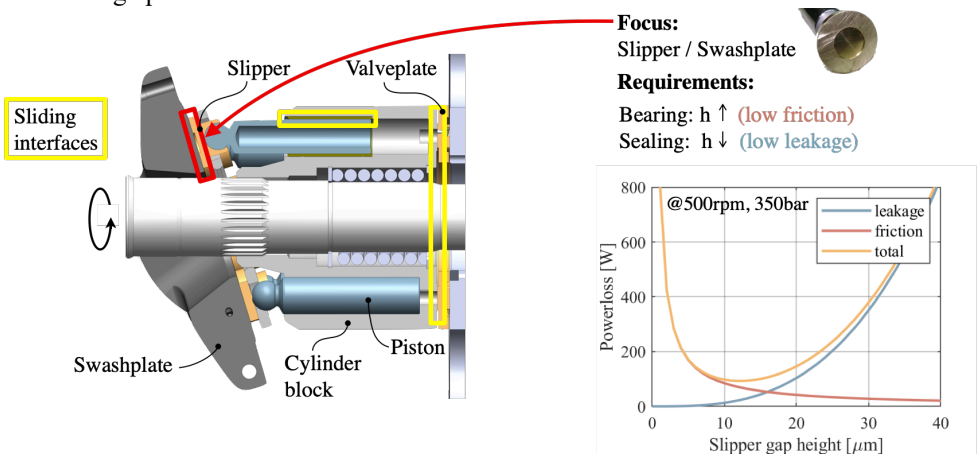

Figure 1.1. Sliding interfaces of the axial piston pump (left) and calculation of the powerlosses of a single slipper (right)

2 RESEARCH GOAL AND APPROACH

There are two main physical mechanisms that affect the gap height that occurs at a certain operating condition (OC), which apply to both the slipper/swash plate and valve plate/cylinder block interfaces. First the hydrostatic pressure that is directly correlating to the pressure in the piston and the area they act on. Second, the hydrodynamic pressure that is essentially resulting from the rotational speed. A pump designer needs to choose a certain speed range for his design, which defines the amount of hydrodynamics. The hydrostatics are adjusted to the hydrodynamics. However, this implies that for certain operating conditions (OCs) with low pressures and low speeds, insufficient hydrodynamic and hydrostatic forces are present to ensure an adequate fluid film to be formed. As shown in Figure 2.1, this can lead to mixed friction and wear. Using traditional approaches, such as increasing the pocket size or changing the orifice of the slipper, one can change the distribution of the powerlosses, either having a well performing slipper at low speeds and pressures or having optimal powerlosses at high speeds and high pressures, but typically not both. Surface structures open-up the possibility to perform well at all regimes.

Using simulation three designs were selected and manufactured. This paper shows the measurement results as well as the comparison to simulation results as validation.

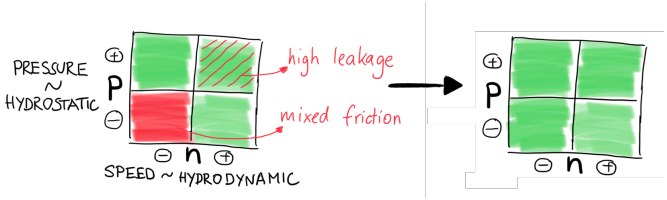

Figure 2.1. Research goal: Increase of load capacity especially at low speeds without worsening at high speeds and pressures

3 LITERATURE

In the past there have been quite a few researchers that investigated surface structures and modifications on hydrodynamic bearings, not that many have incorporated these also on surfaces used for hydrostatics. Due to space limitations the next section only covers the ones that built and tested these structures on hydrostatic bearings. One can distinguish the efforts in structural regimes. Micro, meso and macro structures. Micro structures usually have a depth to length ratio of 1:10 both being in the µm range. First efforts of these kinds were tested in the automotive industry to reduce friction between the piston and the bore of combustion engines. They can lead to friction reductions of up to 55% [1]. In hydraulic pumps this was tested by [2], [3]. Here various micro dimples were tested on many parts such as bearings, gear pumps, pistons and valve plates. It was shown that these micro holes were beneficial for purely hydrodynamic bearings such as the piston. However, for hydrostatic bearings they are contra-productive as they disturb the pressure field of the hydrostatics, which was not accounted for in the simulation models. In contrast, Baker used an earlier version of Caspar, a more sophisticated simulation tool that is also used for the simulations of this paper, to design waved like structures on a valve plate. Those were in the meso-region, meaning depth were in micrometer range but wave lengths in millimeter (1:1000). Baker developed a very promising design and demonstrated up to 10% decrease in powerlosses while also showing a tremendous reduction in wear [4]. These meso-structures turned out to be more successful with hydrostatic sealings as shown in simulation in the piston-cylinder interface by Ivantysynova, Lasaar, Ernst, and Wondergem [5]–[7]. The proposed step design in this paper could be mistaken with a step design patented by Ivantysyn in 1997 [8]. While this step height is similar in size, it serves a different purpose. Here the pocket diameter is self-adjusting with small gap heights, essentially increasing the pocket diameter when gap heights decrease to only a few µm. This step is in the opposite direction as the proposed step, removing material at the inner diameter instead of adding to it. Macro structures, meaning depth and length in millimeter range, have been found to be beneficial in hydrodynamic thrust bearings as demonstrated by some companies [9]. However, their use in hydraulics is not applicable due to their deep grooves and therefore total loss of hydrostatics.

4 OVERVIEW OF PREVIOUS SIMULATION RESULTS

4.1 Methodology

For the development of a wear free slipper that is well performing in low and also high speed regimes, an extensive simulation effort was expended (over 4400 simulations / 36,000 CPU hours) using the latest version of Caspar FSTI, which includes deformations due to pressure

and temperature. First a competitive baseline with no structure was designed using computational design methods. The test pump was a Parker PV series (92cc) with a decreased slipper outer diameter to reflect the mean of five leading pump manufacturers to give these results a more general foundation. This baseline represents the very best possible single land design for this given piston size (21 mm diameter) and will serve as a reference. A single land design was chosen to accorporate the largest possible surface area, which is beneficial for low-speed applications. The optimization goals were minimization of overall powerloss due to leakage and friction and the minimization or total avoidance of material wear. The whole design process is illustrated in [10].

Using the same criteria but adding multiple forms of freedom in the surface topology different surface structures were designed and analyzed, the very best being a waved structure and a step structure. These three designs (flat reference, wave and step) were manufactured using state of the art series manufacturing methods such as turning or stamping and are shown in Figure 4.1. These slippers were tested in the same run-in pump and compared to each other.

4.2 Selected Operating Conditions (OCs)

In order to reduce simulation time while retaining a representative operational space, the number of investigated OCs were limited to a distinct selection. Table 4.1 shows the selected four OCs with different speeds n, pressure drops Δp and swashplate angles β, inducing crucial conditions in the operation of a pump. OC1 with low speed and low working pressure represents start-up or idle situation. During these conditions it is most likely that mixed friction and abrasion can occur due to insufficient hydrodynamic pressure built up. OC2 with low speed but high pressure is typical for load holding situations, a typical condition for high leakage losses, which need to be prevented. High speed and low pressure for OC3 result in high centrifugal forces that tend to tilt the slipper such that wear is to be feared. An additionally low swashplate angle induces lift off and high leakages, which needs to be prevented. OC4 with maximum power from high speed and high pressure is usually resulting in higher leakage values and often generates high thermal load, making it prone to temperature and pressure deformations, which need to be accounted for. OC4 also represents a very significant OC for the OEMs and their customers.

Table 4.1 Definition of operating conditions (OCs)

OC	n [rpm]	Δp [bar]	β [%]	represents
1	500	50	100	Idle
2	500	350	100	Low flow high load
3	1800	50	20	Prevent slipper lift-off
4	1800	350	100	Max. power

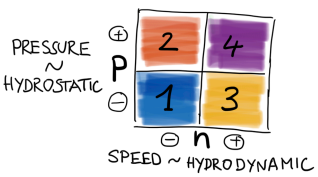

4.3 Final designs and comparison to reference design

Figure 4.1 shows pictures of the final manufactured designs, which were the outcome of the simulation optimization. On the left is the reference slipper with a balance of 99%. The balance factor is an indicator of the slipper's pocket size and is described along with the entire design process in more detail in [10], [11] and given in (1). It is calculated by dividing the hydrostatic force F_{fz}, that is estimated as logarithmic pressure drop over the sealing land, by the force of the piston on the slipper F_{SK}:

$$B = \frac{F_{fz}}{F_{SK}} \tag{1}$$

The wave slipper is shown in the centre of Figure 4.1. The structure is visible with the naked eye, but is mainly due to stepped surface topology, which was easier to manufacture and had no significant effect on the performance according to simulation studies. The balance of the wave slipper is at 102%, indicating that the pocket of the sealing land is larger than the reference. The pressure drop is influenced by the wave, otherwise the slipper would lift off and have an excessive amount of leakage at higher pressures. To the right side of Figure 4.1 is the step slipper. For this slipper the inner sealing land is 6 µm higher than the outer one. The step in between the two sealing lands can barely be seen, its only indicated by the 6 radial lines around the centre of the sealing land. Each line represents a 1 µm increase. The balance is even higher here at 105%, making this indicator purely a pocket size rather than a performance factor.



Figure 4.1. Final structured designs with optimized parameters and reference design

The optimization of the slippers was performed for the 4 OCs mentioned earlier in this chapter. The 4 OCs were weighted equally, therefore the optimization was the reduction of the sum of the powerlosses. Figure 4.2 shows the simulated performance gains from the two structured designs in comparison to the reference. In sum over all four OCs the wave design shows powerloss reductions by 9% and the step design by even 38%. The overall aim of the study, to improve low speed performance (OC1) without a significant efficiency decrease at higher speeds and pressures, has already been reached with the wave design. This is indicated by the plot on the right of Figure 4.2, which shows the individual powerlosses at each OC. An 85% reduction in powerlosses at low speed and low pressure (OC1) can be achieved by adding a waved surface to the slipper. The step design achieves a similar powerloss reduction of 88% for OC1, while performing better at the other OCs as well, which greatly surpasses the initial goal. Both, wave and step design achieve an improvement of over 10% of the total

pump efficiency for OC1. A possible reason for the great performance of both the wave and the step design at low speeds and low pressures (OC1) is the increased hydrodynamics due to the surface structures. Further investigations for a better understanding of the underlying physics are in progress. A comparison of the designs with the same pocket size to show the isolated influence of the shaping itself has been shown in [10].

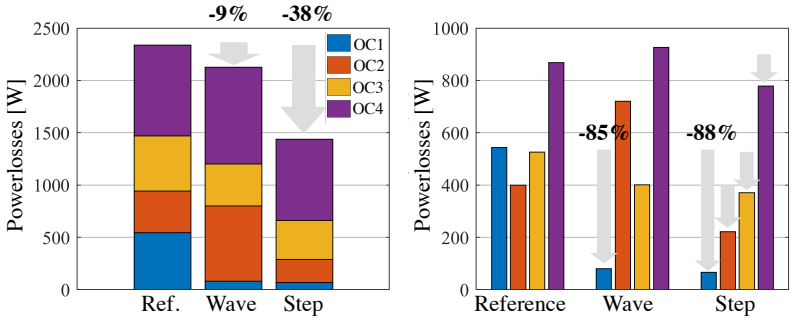

Figure 4.2. Comparison of powerlosses for the final designs and the reference in cumulation (left) and individually by operating condition (OC) (right)

5 EFFICIENCY MEASUREMENTS OF STRUCTURED SLIPPERS IN COMPARISON TO A FLAT REFERENCE SLIPPER

5.1 Steady state test rig and measurement procedure

The pump used in this study was a Parker PV 92cc series, which is an open circuit pump with a variable swash plate. The test rig used for these tests along with the used sensors is illustrated in Figure 5.1 and Table 5.1.

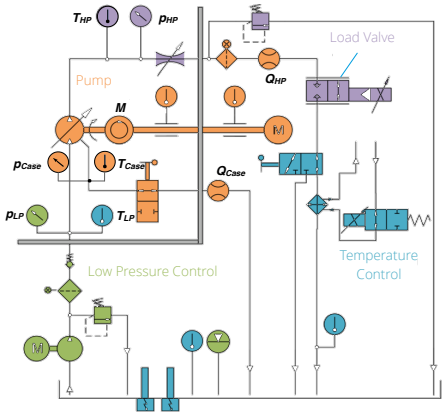

Figure 5.1. Test rig schematic

The next section shows the measurement results for various designs of the slippers. All measurements were performed in a stationary manner, meaning the conditions were held until temperature, flow and torque stabilized. When performing pump test rig measurements, it is obvious that the resulting leakage and torque reflect the entire pump, not just the slippers. Therefore, improvements can only be measured relative to each other, and it is necessary to have a solid baseline to which these design changes can be compared to. Pumps and their

lubricating gaps typically go through a wear-in process, during which the efficiency also changes.

Table 5.1. Electronic sensors and accuracies

Para-meter	Sensor data		
	Sensor	***Type***	***Accuracy***
M	Torque meter	HBM T10F (1 kN)	<0.1% FS
Q_{HP}	Flow meter	Kracht VC12 (600 l/min)	± 0.3%
Q_{Case}	Flow meter	VSE VS1 (80 l/min)	± 0.3%
p_{HP}	Pressure transducer	KELLER PA-23SY (400 bar)	± 0.25% FS
p_{LP}	Pressure transducer	KELLER (30 bar)	± 0.15% FS
p_{Case}	Pressure transducer	HYDAC (16 bar)	± 0.15% FS
T_{HP}	Temperature sensor	HYDAC, -25..+100 °C	± 0.8% FS
T_{LP}	Temperature sensor	HYDAC, -25..+100 °C	± 0.8% FS
T_{Case}	Temperature sensor	HYDAC, -25..+100 °C	± 0.8% FS

To avoid that this run-in interferes with the slipper study, the entire pump was run-in at each OC for a total of over eight hours. Previous studies by the authors have shown that the cylinder block/valve plate gap typically takes up to 30 min to run-in per pressure and speed level [12]. The 8 hours of the standard pump were determined to be sufficient to cover this running-in period. After this running-in period, the flat reference slipper was implemented. To avoid any potential influence from the disassembly, all modifications were carried out by a Parker specialist. Each design was tested multiple times in over 120 OCs, ranging from 500-2300 rpm, 50-350 bar and 25–100 % displacement. These 120 OCs built a Design of Experiment (DOE) set that can be compared to simulation and to each other. In between the measurements of the DOE sets, the pump was also tested to speeds down to 0.1 rpm with (50 and 300 bar) and without pressure to capture low speed and start-up behavior. These ultra-low speed tests were run in between the DOE sets, in order to see if the performance changed after multiple hours at low speed. This process was repeated until no more changes in efficiency were observed between the sets. Then the pump was disassembled, and the next nine slippers (and attached pistons) were replaced. The swash plate was changed only for the step design, as more than expected leakage was observed for the wave design, which could have been due to a worn and therefore not perfectly flat swash plate.

5.2 Full DOE measurement results of the waved slipper at 100% displacement and run-in performance

Although the pump was assumed to be fully run-in, there were still small differences in efficiency at some OCs for each slipper. The variation for the flat reference slipper was small, decreasing by <1% for the 50 bar series, with the largest deviation at 50 bar and 500 rpm being 0.9 percentage points. After disassembly, it was observed that the entire surface of the slipper showed minor wear in the <2µm roughness range. A more detailed analysis of the surface wear can be found in the authors' second paper at this conference.

The waved slipper experienced more pronounced wear. A total of 4 full DOE-sets were measured and are shown in Figure 5.2. The graph shows the total efficiency over speeds from 500-2300 rpm and pressures from 50 to 350 bar, all at 100% displacement. Differently dashed lines indicate different measurement durations ranging from the first measurement after 8 hours to the last measurement after 35 hours. In the low to medium pressure ranges, there were virtually no changes in efficiency. Only at high pressures, increased leakage led to a drop in efficiency. In particular, at low speed and high pressure, changes in the order of 4-5 percentage points were observed in the overall efficiency between the first and last measurement. In contrast to the flat reference design, the changes were in a positive direction, i.e. the overall efficiency increased over time.

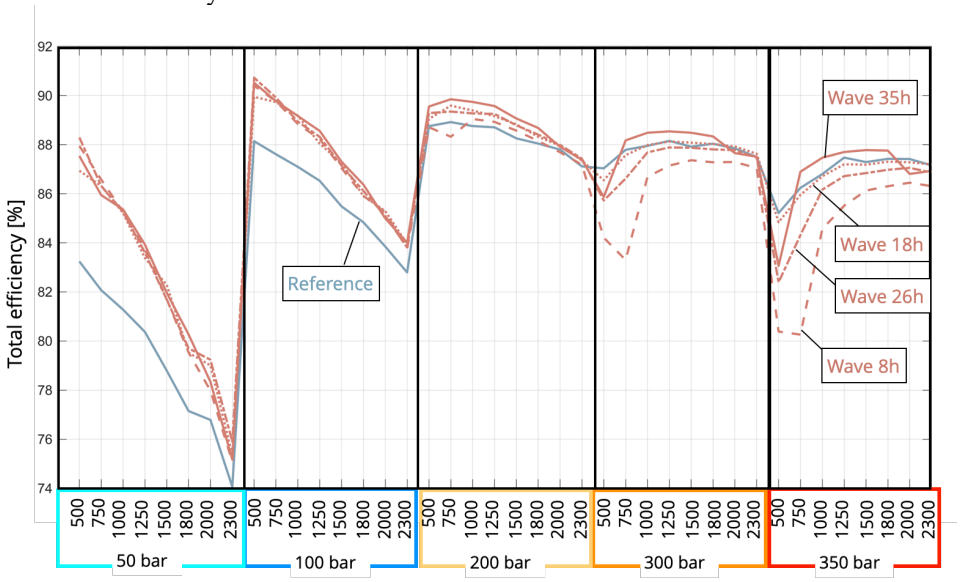

Figure 5.2. Total efficiency for multiple DOE sets of the waved slipper at 100% displacement after different test hours

Unfortunately, after disassembly, the slipper was more worn than expected. Simulation only indicated minor wear at the edges, but not to the extend presented in the surface topology measurements in Figure 5.3. The plot shows 5 µm total wear at the inner edge of the slipper. However, on a positive note, the 6 µm wave was not completely worn off after the tests and the increasing efficiency suggests that the structure will not wear off further. As the valleys (e.g. the lowest part of the wave) were not worn (also indicated by the color in the photos), it was possible to measure the total material loss. This is not possible for the flat slipper as the entire surface has experienced some form of wear. Because of the unaffected valleys, another interesting finding can be observed by the shape of the valleys of the wave. When new, they were perfectly level. After the 35 hours of use, the valleys were shifted by a total of 1.5 µm as indicated by the dotted line in Figure 5.3. This observation can only be explained by a plastic deformation. At the time, it was not known that slippers undergo this type of plastic deformation, so it was never included in any of the simulation models and could have been the cause of the higher than expected wear. Based on the results, it is possible to further improve the wave design and possibly reduce the wear even further.

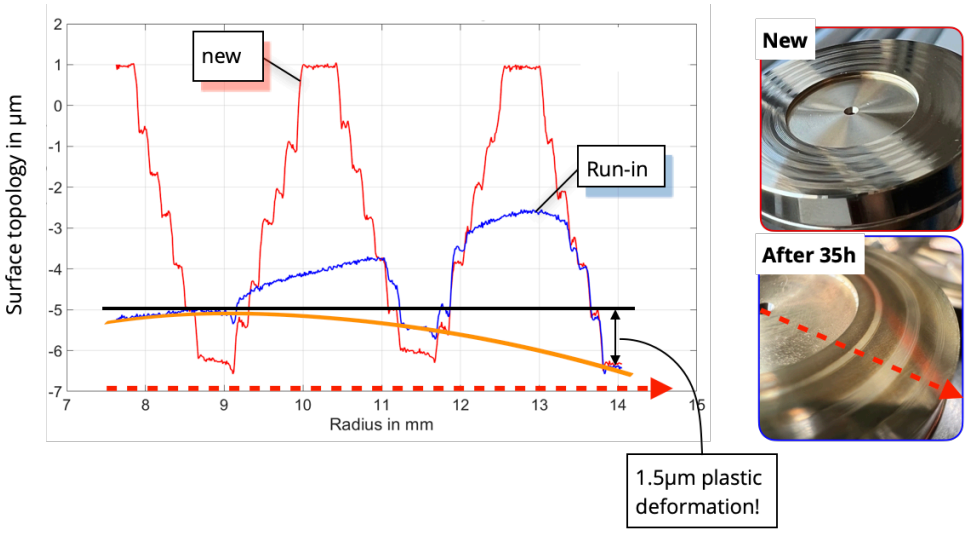

Figure 5.3. Surface topology and photos of the waved slipper new and run-in

5.3 Full DOE measurement results of the step slipper at mutliple displacements in comparison to the reference slipper

The total efficiency map for both the reference and the step slipper for three displacement levels are shown in Figure 5.4. The y-axis represents the pressure level and the shared x-axis the pump speed. Each displacement level has its corresponding color legend. For 100% displacement (top two figures) it is clearly visible, that the step design increases the efficiency predominantly in the lower left corner (low pressure and low speed), while also increasing the dark green area ($\eta_{tot} \geq 90\%$) to medium pressures and speeds.

The efficient area at high speed and low pressure also improved slightly, however this area can usually be improved with the valve plate / cylinder block interface, as this is its most critical OC. The step design greatly improves the efficiencies at low displacements. At 50% displacement (middle figures) the efficiencies below 75% completely disappeared with the step design, while most of the operating conditions now experience efficiencies well above 80%. The drastic rise in efficiency is even more noticeable at 25% displacement (lower figures). Here the reference slipper had no OC with a total efficiency above 70%. After implementing the step slipper the pump now is able to perform at close to 80% total efficiency at low to medium speed and pressures.

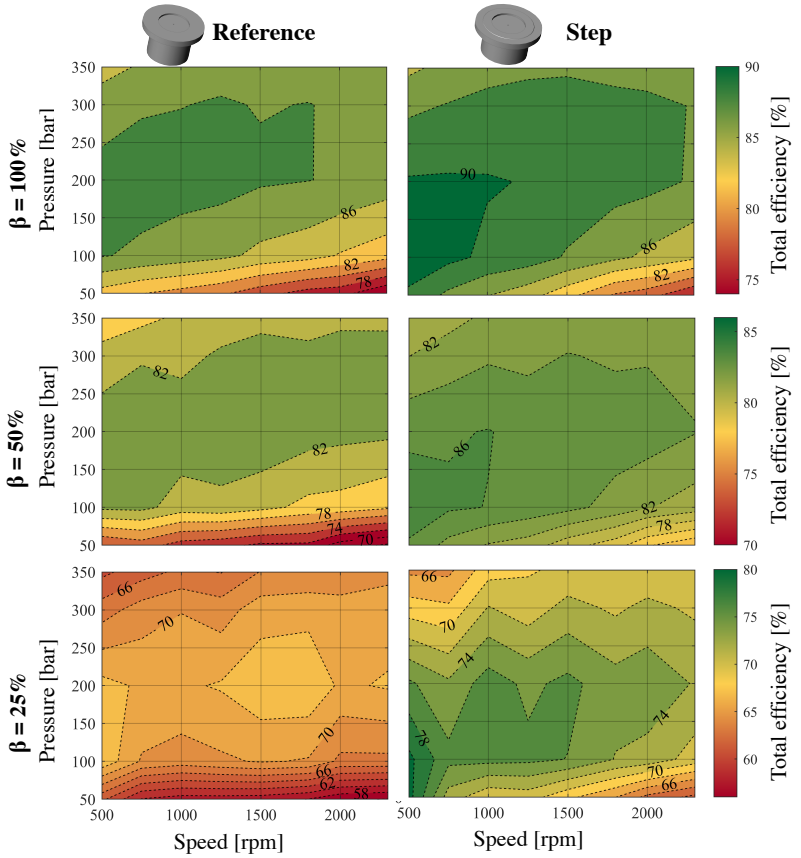

Figure 5.4. Total efficiency characteristic maps of the step design in comparison to the reference for three different swashplate angles

The step design had virtually no run-in. Even after 46 hours of rigorous pump testing the 6µm step had only 1.5 µm of wear on the inner diameter, again due to reduction in surface roughness. A 565 hours endurance test was completed for all designs just prior to publication visual inspection shows that both structures, the wave and the step, are still intact. A more detailed analysis of the run-in of the step-slipper and the manufacturing process is presented in the second paper at this conference by the same authors.

5.4 Efficiency improvements of the structured designs in comparison to the flat reference

Figure 5.5 shows the total efficiency at 100% displacement for the entire operating range for the three tested slipper designs: flat, wave and step. When comparing the waved slipper with the flat reference slipper it can be concluded that the waved slipper has much better low pressure and low speed performance, with an increase of up to 5 percentage points. At low speeds and high pressures the performance of the waved slipped did not increase compared to the flat reference design. At 500 rpm and 350 bar the reference has an advantage of up to 2 percentage points.

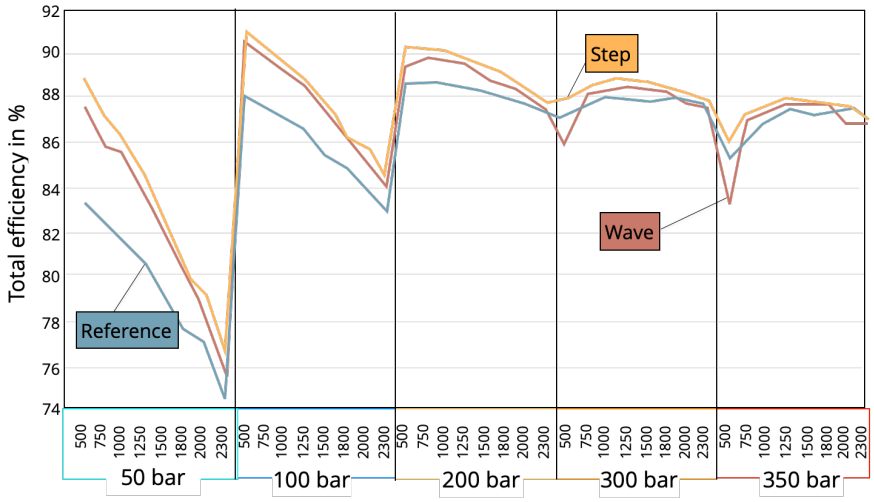

Figure 5.5. Total efficiency of the three different slipper designs at 100% displacement

The slipper with the 6 µm step had the best performance across all operating conditions topping even that of the wave slipper at low pressures and low speeds, while still outperforming the flat reference design at high pressures and high speeds.

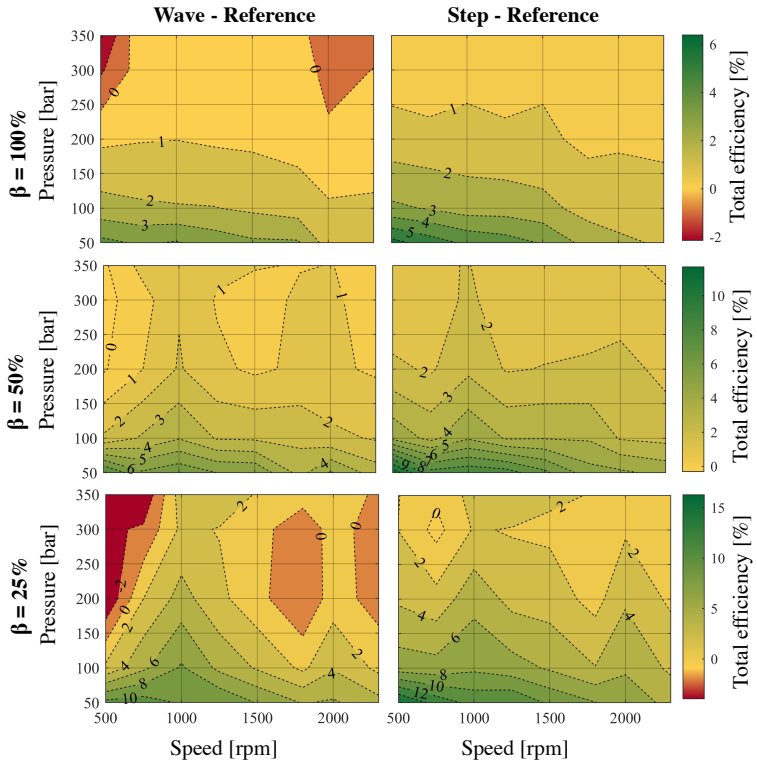

Figure 5.6. Total efficiency differences of the structured designs subtracting the reference at 100%, 50% and 25% displacement

For lower swash plate angles the efficiency gain was even more drastic as can be seen in the change in the efficiency maps shown in Figure 5.6. Here the difference between the total efficiency between the wave and reference slipper (left) and step and reference slipper (right) is shown. The higher the values the more total efficiency point gain was achieved by the design. While the waved slipper achieved great results at low pressure, it also led to up to 2 percentage point losses at 100% and high pressure. The step design had no OC where it had a noticeable efficiency drop compared to the reference design. The overall efficiency point increase from the step design compared to the flat design is 6 percentage points at 100%, 11 percentage points at 50% displacement and up to 16 percentage points at 25% displacement, all at 500 rpm and 50 bar.

5.5 Performance at extremely low speeds

Both the wave and the step slipper had an exceptionally good low and ultra-low speed performance. Figure 5.7 shows the measured torque loss at 50 bar for all three slipper designs (left) and the correspoding leakage losses (right). An additional measurement of the step slipper in lead-free material with a lead content of <0.1% has been carried out. The speed is shown on a logarithmic scale to highlight the ultra-low speed torque. The wave slipped and the step slipper outperform the reference slipper across the entire speed range for 50 bar. Both the wave and step design have a similar low torque loss, reducing the torque loss up to 80%. To recollect, the shown torque loss reflects the losses for the entire pump, which highlights how much influence the slipper has for low speed performance in axial piston pumps.

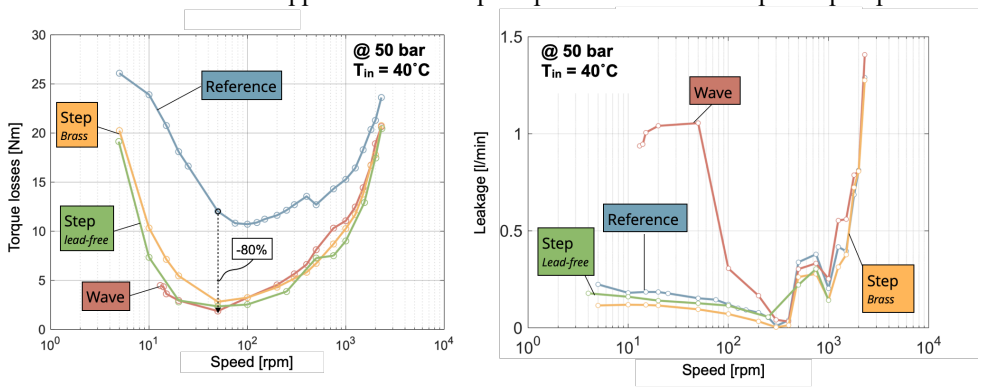

Figure 5.7. Torque loss (left) and leakage (right) at 50 bar for the different designs

The brass and lead-free step slipper have an even lower leakage than the reference, even though having a larger pocket size. This can be explained by overall lower gap heights and a reduction in tilt. The wave design however has a much higher leakage at low rpm (<200 rpm). This was not predicted by the simulation and will be further investigated.

The torque loss at 300 bar is shown in Figure 5.8 left with the corresponding leakage losses in the right. At 300 bar the step design outperforms the flat design starting at 100 rpm with a maximum torque reduction of 16%. However, below 100 rpm the two slipper designs have a very similar torque curve. In contrast to that, the wave slipper design exhibits an essentially flat torque curve from 30 to 500 rpm, leading to a 60 % reduction of torque at 30 rpm. It is not clear, why the lead-free step slipper has such a different torque and leakage curve compared to the brass step slipper. It could be due to the short operating time of only 10 hours.

The leakage results are similar to the trends of the 50 bar measurements. The wave slipper leaks 2 l/min at 30 rpm, whereas the reference pump produces 1 l/min leakage. For more low speed analysis including cold start-up and wear measurements refer to the second paper of the authors in this conference.

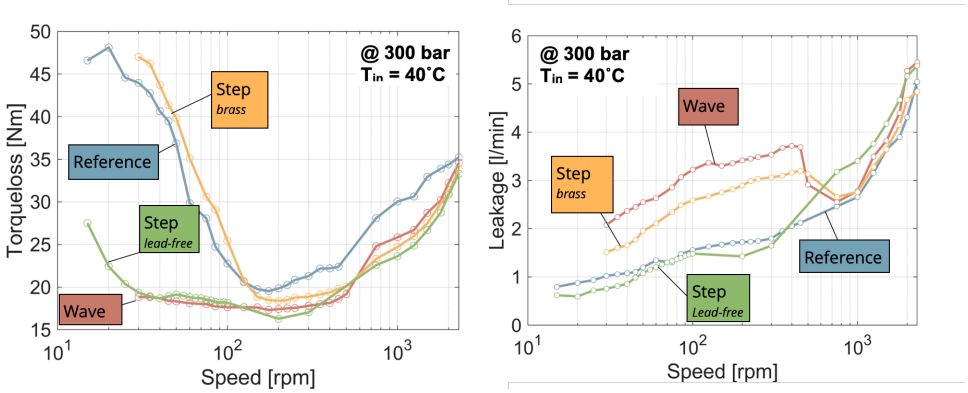

Figure 5.8. Torque loss (left) and leakage (right) at 300 bar for the different designs

6 COMPARISON TO SIMULATION RESULTS

The comparison between the designs is only possible in relation to each other, as the entire pump is measured instead of just the slippers. A similar problem is faced with comparing the simulation with measurement. In order to compare the 4 OC the wave and step design power losses were subtracted from flat design. This was done for both the simulation and measurement and compared in Figure 6.1. The two columns are the wave slipper (left) and the step slipper (right). In each column there are simulation results (compare to Figure 4.2) and measurement results. The waved design was predicted to have a 12% increase in efficiency at OC1 in comparison to the reference slipper. Similarly, the simulation predicted a slightly lower increase at OC3 while having a small efficiency reduction at OC2 and virtually unchanged at OC4. In measurement the trend is the same, but with more improvement at OC3 but also worse at OC2. The waved slipper has virtually no effect on OC4 both in simulation and measurement

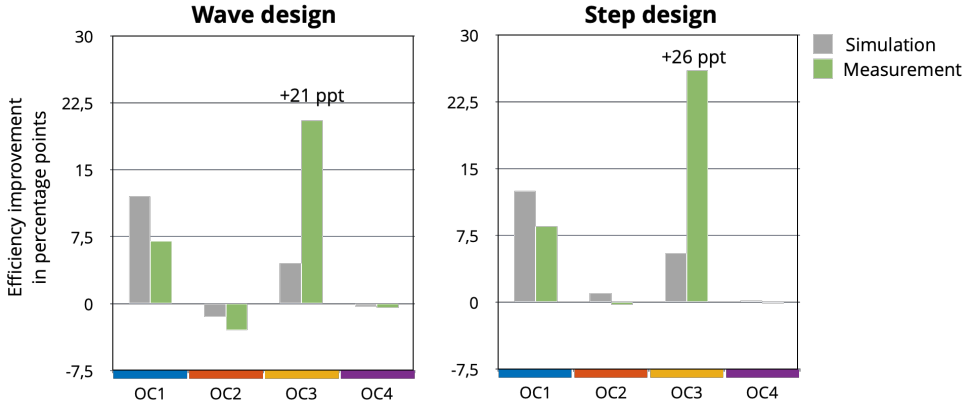

Figure 6.1. Comparison between simulation and measurement

For the step design the simulation expected a large increase in efficiency at OC1 and OC3 and a small to no increase for OC2 and OC4. The measurement confirms the simulated trend. However, OC3 highly outperforms expectations and OC1 has slightly less improvements. OC3 has small reduction in efficiency instead of an increase and OC4 is essentially unchanged as predicted. Overall there is a very good match between the simulation results and the measurement, further increasing the confidence in using numerical simulation tools such as Caspar FSTI as the only necessary design tool, and using measurements only as confirmation rather than a step in the design chain.

7 SUMMARY AND CONCLUSION

Surface structures have a potential to increase hydrostatic machines performance. This was shown in the past for example for the valve plate by Baker [7]. This paper presents the measurement results of two viable surface structures of the slipper. A wave like structure, leaning on the results from Baker has shown to be able to reduce the friction at low pressure and high pressure across the entire operating range. However, the powerlosses increased due to leakage at high pressure and the design showed wear and plastic deformation, leaving room for improvement if such a structure should be used for future pump types. The torque loss at 300 bar is very impressive, staying nearly constant from 30 to 500 rpm. The plastic deformation could be incorporated in the future simulation results further improving this design.

A new step-like structure has shown tremendous potential for slipper and, by extension, other hydrostatic bearings. This 6 µm step has not only reduced the start-up torque by more than half, but has also improved performance in almost all operating conditions, particularly under partial load conditions such as low speed, low pressure or low displacement. This design has virtually no wear, with only 1.5 µm on the inner surface, after rigorous testing over the entire operating range. This was confirmed by a 565 hour accelerated lifetime test, where the slipper showed similar wear to the tests after 35 hours. It is also very easy to manufacture, at least compared to the wave-type structure. These results open up new possibilities for pumps at low speeds and especially lead-free designs, as this slipper essentially does not have to withstand metal to metal contact. Such a lead-free slipper has been successfully tested with the step design and the results are presented in the second paper at this conference from the same author, entitled “Design of a Lead-Free Slipper Bearing for Low Speed Axial Piston Pump Applications”. In the future, all lubrication gaps could benefit from such structures, further increasing efficiency and allowing virtually any speed operation in combination with electric drives.

8 ACKNOWLEDGMENT

The presented research activities are part of the project “Tribologieoptimierung von Pumpensystemen durch fertigungsgerechte Einbringung von Mesostrukturen” (Ref. No. 20757 BR/1). The authors would like to thank the Fluid Power Research Fund of the VDMA for the funding and support.

9 REFERENCES

[1] B. Kim, Y. H. Chae, and H. S. Choi, “Effects of surface texturing on the frictional

behavior of cast iron surfaces," *Tribol. Int.*, vol. 70, pp. 128–135, 2014.

[2] H. Murrenhoff and A. Hoppermann, "Verbessertes Verschleiß- und Reibgungsverhalten hydraulischer Komponenten durch laserstrukturierte Kontaktflächen," 2004.

[3] M. VDMA, "Abschlussbericht Mathematische Modellierung , Optimierung und Herstellung mikrostrukturierter Kontaktflächen für hydraulische Verdrängereinheiten - OptiKonS," 2010.

[4] J. Baker and M. Ivantysynova, "Advanced Surface Design for Reducing Power Losses in Axial Piston Machines," *11th Scand. Int. Conf. Fluid Power, SICFP*, 2009.

[5] M. Ivantysynova and R. Lasaar, "An investigation into micro- and macrogeometric design of piston/cylinder assembly of swash plate machines," *Int. J. Fluid Power*, vol. 5, no. 1, pp. 23–36, 2004.

[6] M. Ernst, A. Vacca, M. Ivantysynova, and G. Enevoldsen, "Tailoring the Bore Surfaces of Water Hydraulic Axial Piston Machines to Piston Tilt and Deformation," pp. 1–29, 2020.

[7] A. M. Wondergem and M. Ivantysynova, "The Impact of the Surface Shape of the on Power Losses," in *FPNI*, 2014, pp. 1–12.

[8] J. Ivantysyn, "Sliding bearing with self-adjusted load bearing capacity," US5983781A, 1997.

[9] N. R. Kane, J. Sihler, and A. H. Slocum, "A hydrostatic rotary bearing with angled surface self-compensation.," *Precis. Eng. 27.2*, pp. 125–139, 2003.

[10] S. Horn, R. Ivantysyn, and J. Weber, "Tribo-optimized lubricating interfaces in hydrostatic pumps with surface shaped slippers," 2022.

[11] J. Ivantysyn and M. Ivantysynova, *Hydrostatic Pumps and Motors*. Academic Books International, 2001.

[12] R. Ivantysyn, A. Shorbagy, and P. J. Weber, "Analysis of the Run-in Behavior of Axial Piston Pumps," in *IEEE GFPS 2018*, 2018.

Biographies



Svenja Horn received her diploma degree in aircraft construction from Technical University of Dresden in 2018. Since 2018 she is working as a research assistant at the Chair of Fluid-Mechatronic Systems on the efficiency and lifetime improvement and optimization of axial piston pumps. Her research focus on the tribological phenomena of the slipper/swashplate interface as well as the implementation of machine learning algorithms to monitor the pump's service life. Her PhD thesis deals with increasing efficiency through meso-structured surfaces and examines the physical effects and functioning of structuring in more detail



Roman Ivantysyn received his bachelor's and master's degrees in mechanical engineering from Purdue University in 2008 and 2011, respectively. Since 2011, he has been working as a research assistant at the Chair of Fluid-Mechatronic Systems (Fluidtronics) at the Technical University of Dresden, focusing on systems and components. His research topics include open circuit displacement control in mining excavators, pump design and thermal gap analysis in axial piston pumps. He is set to submit his PhD thesis, titled "Thermal Investigation of the Lubricating Gaps of an Axial Piston Pump with Respect to Efficiency and Wear," this year.

Analyses of engineered surfaces for performance improvements of external gear pumps

Paolo Casoli[1], Fabio Scolari[1], Carlo Maria Vescovini[1], Carlo Rossi[2], Antonio Lettini[2]

[1]*Department of Engineering and Architecture, University of Parma, Italy*
paolo.casoli@unipr.it, fabio.scolari@unipr.it, carlomaria.vescovini@unipr.it

[2]*Casappa S.p.A., Parma, Italy rossic@casappa.com, lettinia@casappa.com*

Abstract.

In the field of fluid power systems the research is constantly aimed at the development of more efficient components. Electro-hydraulic solutions present an interaction between hydraulic and electrical machine, often with the aim of controlling the delivered flow rate by changing the pump shaft speed over a possibly wide range; these solutions pose new challenges for the design of hydraulic machines. This work focuses on the possibility of extending the working range of external gear pumps by increasing the hydrodynamic bearing capacity in the meatus between gear wheels and lateral plates. The goal is to accomplish this result through the introduction of a textured surface on the lateral plates. Starting from the results of CFD simulations, some physical prototypes have been realized to carry out an experimental verification activity. Bench tests have been then conducted to measure the efficiency of pumps with textured lateral plates, to be compared with the efficiency of standard pumps. The results obtained, showing different behaviours between the samples compared, create the basis for future developments.

Keywords. Textured surfaces, gear pump, laser texturing, dynamic cavitation.

1. INTRODUCTION

In hydraulic systems most of the fixed displacement machines used to generate flow are external gear pumps, since they have high reliability and low cost due to the small number of components. Although they are conceptually simple machines, the design is often difficult, such as the lateral plates, which are crucial to ensure high efficiency for the entire pump [1]. Recently, electro-hydraulic solutions have become a major research topic. These solutions consist in coupling hydraulic and electric machines in order to control the flow rate required by the users by varying the speed of the pump over a wide operating range [2, 3]. Electro-hydraulic solutions could further favour the diffusion of gear pumps, but also pose design challenges, since the components are subjected to more severe working conditions.

This work investigates the possibility of extending the working range of external gear pumps by increasing the hydrodynamic bearing capacity between gear wheels and lateral plates, by means of textured surfaces. A textured surface provides several improvements [4]. Firstly, it allows to generate a greater bearing capacity due to an increased average pressure for hydrodynamic effects. Moreover, a lower coefficient of friction can be achieved by reducing the contact surface. Finally, the textured surface can generate oil wells that ensure greater lubrication of the meatus. All these effects allow to reduce the overall wear and increase the useful life of the machine. In scientific literature there are interesting studies regarding textured surfaces applied to thrust bearings. Rahmani et Al. [5] achieved good improvements in the bearing capacity and frictional force of an axial bearing thanks to numerical study of textured surfaces. Etsion et Al. [6, 7] achieved good numerical results, experimentally validated on a parallel bearing. In order to achieve the benefits of a textured surface, an accurate definition of the geometry is essential. The large number of involved variables that influence performance makes the design phase complex: some of these are the geometric characteristics of the texture, the type of contact, the properties of the fluid and the operating conditions. The study of the fluid meatus has been performed by means of CFD simulations. In previous articles [8, 9], the influence on the bearing capacity of the main geometric characteristics of the texture and the best distribution of the dimples to maximize performances have been studied numerically on a simple reference domain. Starting from previous results, in this work further fluid dynamics simulations were carried out, extending the domain to the meatus between gear wheels and lateral plates inside external gear pumps. Great importance has been attributed to the fluid model. In hydraulic circuits, local cavitation phenomena could occur in particular working conditions that could compromise the operation of the machines. A detailed cavitation model has been implemented to consider both the effect of gaseous and vapor cavitation. The next step was the physical realization of the prototypes. The textures on the lateral plates samples have been made by laser marking, since it is a very flexible technology with an excellent repeatability. The samples have been subsequently measured by means of an optical profilometer to verify the geometric characteristics obtained and to calibrate the process parameters. An experimental test bench activity was then conducted to measure the efficiency of pumps with textured lateral plates, to be compared with the efficiency of standard pumps. The results are very encouraging, since they show different behaviours between standard pumps and pumps with textured components and put the foundations for future developments and insights. The paper is structured as follows. Section II describes the case study, highlighting the advantages and criticalities of external gear pumps; in section III the geometric configuration chosen to carry out the numerical simulations is discussed. Section IV describes the fluid model adopted with particular attention to the cavitation phenomenon. Section V reports the results of the numerical simulations, while section VI describes the experimental activity, both the physical production of the prototypes and the experimental layout of the test bench.

2. CASE STUDY

External gear pumps are conceptually simple machines, but the design is often difficult, especially to ensure good performances at high working pressures. Among the internal components, the lateral plates are two important elements that strongly affect the performances of the machine. They are axial compensation plates that allow for minimum

gap heights with the gear wheels to reduce losses due to leakage, improving the volumetric efficiency. They also prevent the lateral plates from coming into direct contact with the gear wheels, avoiding excessive wear of the elements. The equilibrium position of the lateral plates depends on the acting forces, given by the operating conditions of the machine, such as the delivery pressure and the rotational speed. In order to limit leakages from high to low pressure, the lateral plates are usually designed to be inclined more towards the low pressure area: this means that the gap height in the suction area is lower, making the portion of the lateral plate in low pressure critical. Variations in the working conditions can reduce the gap height between the lateral plates and the gear wheels to the point of allowing direct contact between the two components, which is normally avoided due to the establishment of a hydrodynamic bearing capacity that counterbalances the approach of the two surfaces. The direct contact between the aluminum lateral plates and the steel gear wheels generates wear of the lateral plates, risking to seriously damage the component causing a decrease in pump performance.

3. TEXTURED SURFACES

The aim of this research activity is to generate an additional hydrodynamic bearing capacity by means of textured surfaces to avoid, or at least to limit, direct contact between gear wheels and lateral plates. A textured surface has a precise and ordered micro geometry designed to increase some properties, in this case tribological ones. The study focuses on the fluid gap between the gear wheels and the lateral plates, highlighted in Fig. 3.1. Since the low pressure area is the critical one, the texture has been introduced only on this portion of the lateral plates. To investigate the hydrodynamic effects of a textured surface, a numerical CFD study has been performed in the ANSYS® CFX environment. The gap geometry is complex to define due to the position assumed by the lateral plates while the pump is working. It was therefore assumed that the gap is delimited by two parallel surfaces. Previous research [8, 9] have shown that the best geometric layout of the dimples within the domain to maximize the bearing capacity is a configuration called partial texturing. The dimples are placed only on a portion of the entire domain and the best condition is when the textured portion is equal to 45-60% of the entire domain.

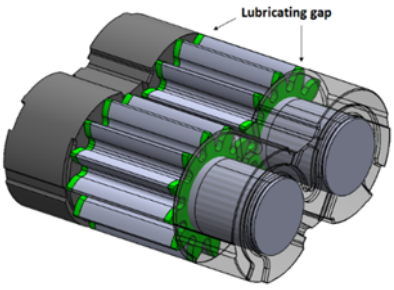

Figure 3.1. Assembly of gear wheels and lateral plates. The fluid gap is highlighted in green.

In this work, a grid of channels defines a sectoral structure where each sector has been partially textured. Figure 3.2 shows a portion of the aforementioned surface: the dimples are highlighted in green, while the channels, with greater depth, are in blue. The size of the sectors has been defined considering the geometry of the tooth, which, being an involute

profile, narrows towards the extremity: for this reason, the sectors at greater distance from the rotation axis have a smaller angular dimension. Geometric dimensions cannot be disclosed for confidentiality reasons.

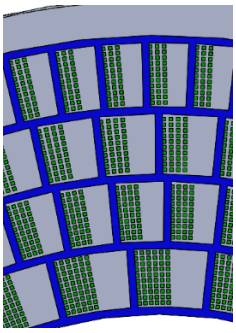

Figure 3.2. Geometry characterized by the sequence of dimples (in green) and channels (in blue).

4. FLUID MODEL

A three-phase fluid model, consisting of liquid, gas and vapor, has been adopted in the simulations. In accordance with the law of mass conservation, the sum of the mass fractions of each phase must be unitary. To also include the effects of gaseous cavitation, the liquid phase was modelled as a variable composition mixture of oil and dissolved air.

4.1. Gaseous cavitation

Since non-condensable gases can be dissolved in liquid or in free form, it is required to know the variation of the mass fractions of both free and dissolved air. So, two additional convection-diffusion equations have been added to the CFD code, one for non-condensable gases in the gaseous phase and one for those dissolved in liquid. The discussion of the model is reported in [8]. ρ is the fluid density and U the velocity.

$$\frac{\partial(\rho f_{g,g})}{\partial t} + \nabla \cdot \left(\rho \, \vec{U} \, f_{g,g} - D_{g,g}(\nabla f_{g,g})\right) = \dot{S}_{DA} \tag{4.1}$$

$$\frac{\partial(\rho f_{g,l})}{\partial t} + \nabla \cdot \left(\rho \, \vec{U} \, f_{g,l} - D_{g,l}(\nabla f_{g,l})\right) = -\dot{S}_{DA} \tag{4.2}$$

The source term $\dot{S}_{DA}$ controls the transition between the two states:

$$\dot{S}_{DA} = R_d - R_a = \begin{cases} C_d \rho_g (p_{equil} - p_g)(1 - f_{g,g}) f_{g,l} \\ C_a \rho_g (p_g - p_{equil})(f_{g,l,lim} - f_{g,l}) f_{g,g} \end{cases} \tag{4.3}$$

R_d and R_a are the mass rate for desorption and absorption. The equilibrium pressure p_{equil} controls the process and is given by the sum of the vapor pressure and the partial pressure of the gas. The release of air occurs when the partial pressure of the gas is lower than the equilibrium one, while the reabsorption when the pressure is higher. C_d and C_a are empirical coefficients that influence the speed with which the associated phenomenon occurs.

4.2. Vapor cavitation

To also include the effects of vapor cavitation, a transport equation for vapor was used, starting from the Rayleigh-Plesset equation. The complete description of the model is given in [7]. The equation that expresses the interphase mass transfer rates for condensation is:

$$\dot{m}_{fgc} = F\frac{3r_g\rho_g}{R_B}\sqrt{\frac{2}{3}\frac{|p_v - p|}{\rho_l}}\ sign(p_v - p) \tag{4.4}$$

And for vaporization:

$$\dot{m}_{fgv} = F\frac{3R_{nuc}(1 - r_g)\rho_g}{R_B}\sqrt{\frac{2}{3}\frac{|p_v - p|}{\rho_f}}\ sign(p_v - p) \tag{4.5}$$

where R_B represents the bubble radius, p_v is the pressure in the bubble, p is the pressure in the liquid surrounding the bubble, ρ_f is the liquid density, and σ is the surface tension coefficient between the liquid and air, R_{nuc} is the volume fraction of the nucleation sites. F is a parameter that determines the speed of the process and can be different in case of condensation, F_c, or vaporization, F_v. The liquid modelled in the CFD simulations is an ISO VG-46 hydraulic oil, which is a complex mixture of hydrocarbons, the main properties are: density 850 kg/m^3 and kinematic viscosity 46 mm^2/s at 40°C. The parameters of the cavitation model are reported in Table I and have been identified through a previous experimental activity, focused on the flow through a fixed orifice [10].

Table I Cavitation parameters used in numerical simulations

Vapor pressure	**R_b**	**R_{nuc}**	**F_v**	**F_c**	**C_d**	**C_a**
0.2 bar	0.5 μm	5e-4	0.9	0.01	2	-0.1

5. NUMERICAL RESULTS

During the rotation of the gear wheel the portion of the textured surface changes in the domain: the simulations were performed considering different angular positions of the tooth, spaced 2° from each other. The boundary conditions are open boundary with zero relative pressure for the perimeter walls of the domain, while the upper plane is a moving wall with a no slip condition. The rotational speed of the moving plane is assumed to be 2500 r/min. The fluid motion is assumed to be laminar, due to the low height of the gap and the high viscosity of the hydraulic oil, assumed at 40 °C. The fluid domain has been discretized using a structured mesh, whose characteristics have been established following a sensitivity analysis. Figure 5.1 shows the absolute pressure contours relating to one angular position with a gap height equal to 10 μm. The rotational direction of the moving plane is clockwise. In the configuration of partial texturing, in each sector an increasing pressure ramp is generated to achieve an overall overpressure. The grid of channels permits to make each sector independent from the others by restoring the boundary conditions: in this way all sectors provide a contribution that allows the entire surface to generate a positive bearing capacity, calculated as the integral of pressure on the moving plane.

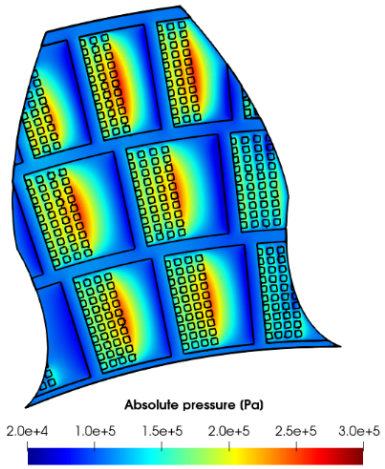

Figure 5.1. Pressure contours. Gap 10 μm and rotating speed 2500 r/min

Figure 5.2 shows the force generated by the surface in different positions assumed by the tooth during rotation. For confidentiality reasons, the bearing capacity was normalized with respect to the maximum value. The bearing capacity changes according to the angular position of the tooth. The reason for this trend is due to the number of sectors present in the computing domain which is not always constant in the various positions considered. This trend is maintained for all the gap heights but intensifies as the gap decreases.

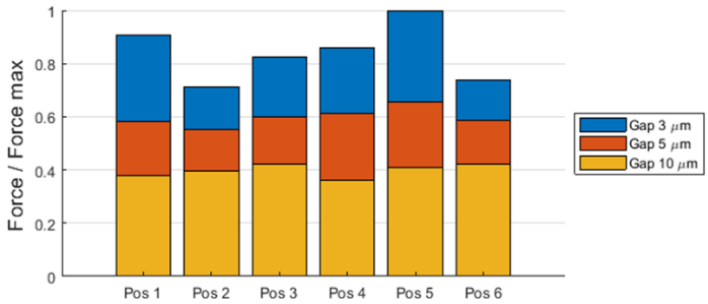

Figure 5.2. Bearing capacity for different values of the gap.

The graph of Fig. 5.2 also indicates that the force increases as the gap decreases. To better quantify this feature, Fig. 5.3 shows the dimensionless force averaged over the various positions considered: the trend as the gap decreases rises more than linearly and represents a very useful aspect capable of limiting the further approach between the two coupled surfaces.

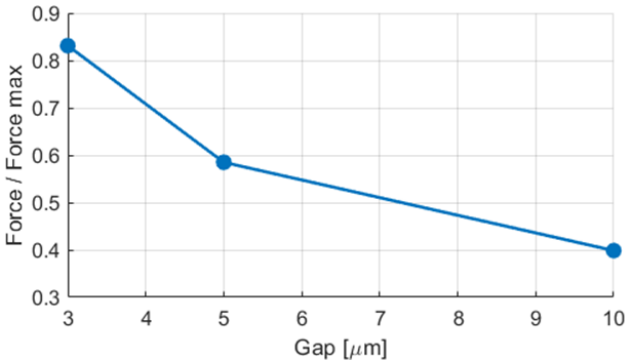

Figure 5.3. Bearing capacity averaged over the six angular positions as a function of the gap.

5.1. Cavitation consideration

The numerical model allows to calculate the distribution of the gaseous phase, both of vapor and of free air. The Fig. 5.4 shows the volume fraction of vapor generated in the case of a 3 µm gap. Vapor is generated locally in small portions of the domain. Since, as shown in the pressure contour, the channels represent the area where the pressure is lower, the vapor tends to be generated in this portion of the domain where the saturation pressure is reached. In the angular position considered (also representative of the other positions), vapor is formed only in the channels towards the outlet, since there is no subsequent sector that contributes to increasing the pressure. The sectors in the centre of the domain increase the pressure in the adjacent channels sufficiently not to reach the saturation pressure.

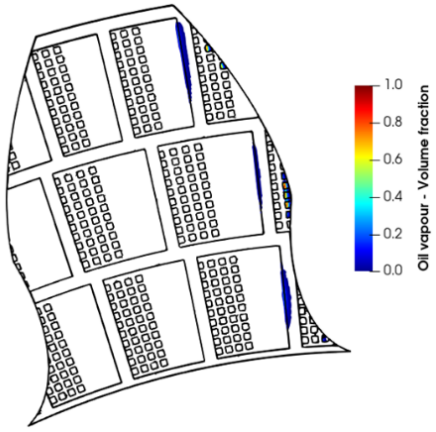

Figure 5.4. Oil vapor volume fraction. Gap 3 µm, rotating velocity 2500 r/min. Only the portions of the mesh where the volume fraction of vapor is greater than 10% are highlighted.

Free air also tends to be concentrated more in the channels, since the pressure is the lowest within the domain, as shown in Fig. 5.5. Since the free air reabsorption process is not instantaneous, part of the free air is dragged inside the sectors before being completely reabsorbed by the pressure increase.

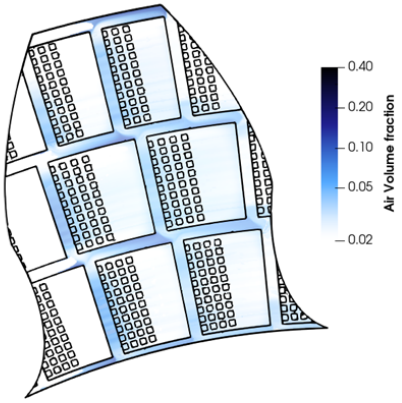

Figure 5.5. Air volume fraction. Gap 3 μm, rotating velocity 2500 r/min. Only the portions of the mesh where the volume fraction of air is greater than 2% are highlighted.

The model permits to verify that the chosen texture configuration allows to minimize the effects of vaporous cavitation, confining its onset locally, without negative effects on the pressure field generated by the texture. Furthermore, even the gaseous cavitation manifests itself with low intensity and does not affect the pressure profile given by the texturing.

6. EXPERIMENTAL ACTIVITY

6.1. Samples manufacturing

The texture has been created on the portion of lateral plates corresponding to the suction area by means of laser marking technology. For this task a 20W fiber laser source in pulsed regime has been adopted. Details regarding the processing parameters cannot be disclosed for confidentiality reasons. The samples have been measured, before the experimental tests, using an optical profilometer in order to verify that the geometry obtained is the desired one. The profilometer, available at the Department of Engineering and Architecture of the University of Parma, is a Taylor Hobson CCI MP-L. In Fig. 6.1 a picture of a textured lateral plate sample is presented: the textured sectors delimited by the grid of channels can be seen.



Figure 6.1. Photo of the lateral plate.

Fig. 6.2 shows the 3D profile of the surface obtained by the profilometer. The measurements of the surface are essential to calibrate the process parameters to obtain a geometry as close as possible to the theoretical one. Laser marking leaves burrs in correspondence with the removed surface, which have been almost totally eliminated by a subsequent mechanical finishing process.

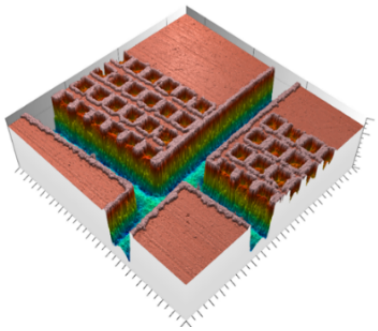

Figure 6.2 3D profile measured after the mechanical finishing process.

The textured samples have been then assembled into external gear pumps made by Casappa S.p.A.

6.2. Test

The tests have been performed on the test bench present in the Laboratory of the Department of Engineering and Architecture of the University of Parma. Figure 6.3 shows a picture of the test bench set up and the respective ISO layout diagram is reported in Fig. 6.4.

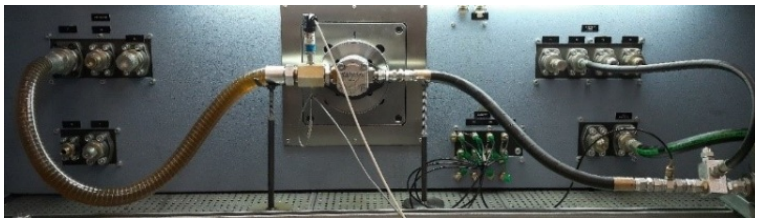

Figure 6.3. Picture of the test bench set up.

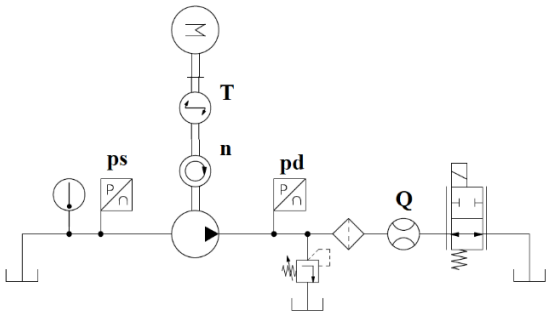

Figure 6.4. ISO scheme of the circuit layout.

Table II lists the sensors models used and their main characteristics. The overall efficiency was calculated by measuring: torque, inlet pressure, delivery pressure, flow rate and shaft speed.

Table II Sensors installed in the test bench and relative features

Variable	Sensor	Model	Main Features
ps	Pressure Transducer	Wika S-10	0 – 10 barA ±0.5%FS
pd	Pressure Transducer	Danfoss MBS 1250	0 – 400 bar ±0.5%FS
Q	Flow Meter	VSE VS 1	0-80 l/min ± 0.3% measured value
n	Speed sensor	HMB T10FS	accuracy class 0.05
T	Torque sensor	HMB T10FS	accuracy class 0.05

6.3. Results

To assess whether the pumps with textured components have better performances than the traditional ones, it is necessary to carry out tests in severe conditions. In normal operating conditions, the wear on the lateral plates does not occur, even after long-term tests. Therefore, tests conducted under out-of-specification conditions, where a direct contact between the lateral plates and the gear wheels takes place, would be necessary. However also in this case, a decrease in the overall efficiency of the pump is difficult to associate exclusively to the textured components, because they are also affected by other effects (for examples by radial clearances). Moreover, depending on the type of tests and the test conditions, a measurable wear on the lateral plates due to the direct contact can be observed only after many working cycles, for the progressive removal of material in seizure conditions. In order to achieve the direct contact with the gear wheels also at normal operating conditions, to emphasize the effect of textured plates and to reduce the test time, the lateral plates have been specially modified, in order to increase the axial and tilting

forces. The test method consists in characterizing the performances of the machine in fixed pressure points (ranging from 120 bar to 240 bar, 20 bar step) at increasing pump speed (from 1000 r/min to 3000 r/min, 500 r/min step). The contact, and the associated seizure of plates, is then reached at a certain combination of pressure and speed. The test procedure has been repeated twice to show possible marked differences between the two cycles. Figure 6.5 shows the trend of the overall efficiency of a pump with modified lateral plates, but without texturing: the efficiency of the first cycle is represented in a continuous line, the second in dashed line. The values have been divided by a reference value for confidentiality reasons. To make the comparison between the two data series clearer, curves of only three speeds are shown. As the rotation speed decreases, the difference between the efficiencies increases, such that the efficiency of the machine after two cycles is significantly lower than in the first cycle. This is a clear consequence of components internal wear and represents a proof that the test is such as to reach critical conditions.

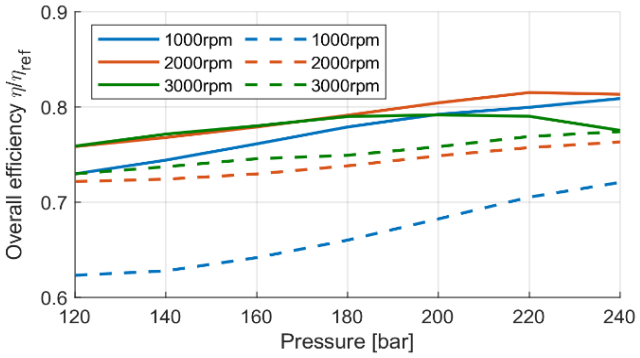

Figure 6.5. Overall efficiency of a pump with modified lateral plates, but without texturing. Solid line represents Cycle I; Dashed line represent Cycle II

Similarly, Fig. 6.6 shows the overall efficiency of a pump with modified lateral plates, but with textured surface. In this case, the differences between the efficiencies obtained in the two cycles are very slight. This means that despite the severe test conditions, textured side plates pumps are not as damaged as traditional ones.

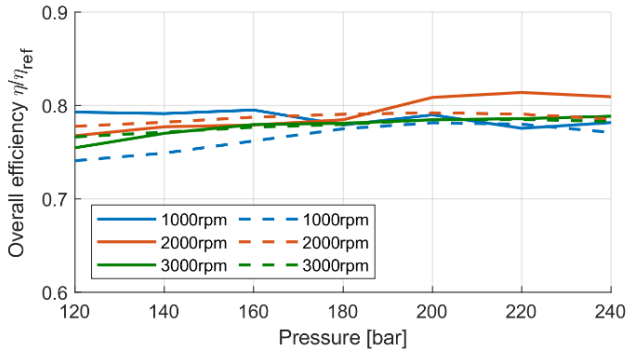

Figure 6.6. Overall efficiency of a pump with textured lateral plates. Solid line represents Cycle I; Dashed line represent Cycle II

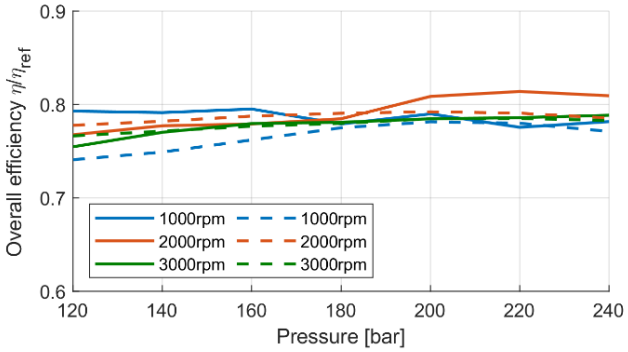

Figure 6.7. Overall efficiency of a pump with modified lateral plates and with textured surface. Solid line represents Cycle I; Dashed line represent Cycle II

Figure 6.7 shows the comparison between the results of pumps without textured components, and pumps with textured lateral plates. The results shown are the average of those obtained on all tested samples. A synthetic parameter has been introduced to quickly assess if there are significant differences between the two cycles: the parameter is the average of the overall efficiency calculated for each test point of each cycle. For confidentiality reasons, the result has been divided by a reference value.

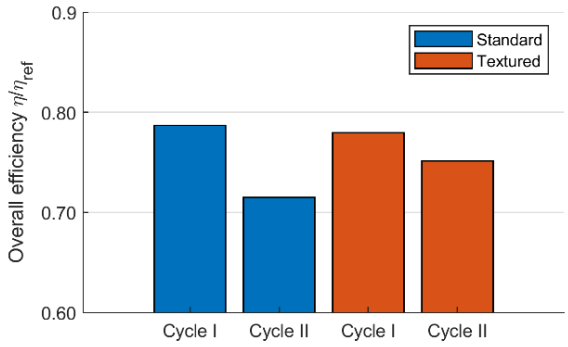

Figure 6.8. Comparison between pumps without textured lateral plates and pumps with textured lateral plates: the values are averaged between all samples tested.

The chart, Fig. 6.8, confirms and clarifies what observed on the graphs of Fig. 6.6 and Fig. 6.7. The traditional pumps show a very marked reduction in efficiency, equal to -7%. This is a sign that the configuration of the components and the test conditions were such as to reach seizure conditions. Under the same test conditions, the pumps with textured lateral plates show only a slight decrease in efficiency, equal to -2.7%. These results are very encouraging because they show that the introduction of a textured surface promotes better performances and create the basis for future developments. Further validation tests will be performed to confirm the repeatability of the results, while also varying the operating conditions.

7. CONCLUSIONS

In this work, the results of a research activity on the application of textured surfaces applied to gear pumps are presented. The texture was made on the lateral plates to generate an additional bearing capacity with the aim of avoiding or at least limiting the approach between gear wheels and lateral plates, in order to reduce wear of the components and increase the useful life of the machine. A numerical study with CFD simulations permits to define the best geometric configuration to set up an experimental verification campaign. The samples were made by laser marking, since it is a very versatile technology with excellent repeatability. Bench tests were carried out to compare the performances between pumps with traditional lateral plates and pumps with textured components. The results showed that the two configurations behave differently: in general, pumps with textured lateral plates show better performances, which in any case will require further checks in the future.

ACKNOWLEDGMENT

The authors would like to thank Simone Mazzucato (Sisma S.p.A, Italy) for the support given in the laser marking processes on the tested prototypes.

8. REFERENCES

[1] J. Ivantysyn, M. Ivantysynova, Hydrostatic Pumps and Motors, Principles, Designs, Performance, Modelling, Analysis, Control and Testing. Akademia Books International. New Delhi, India, 2002.

[2] A. Malvasi, R. Squarcini, G. Armenio, A. Brömmel, Design process of an electric powered oil pump. Autotechreview. 2014. Doi: 10.1007/s38313-012-0236-0.

[3] J. H. Kim, S. G. Kim, The Flow Rate Characteristics of External Gear Pump for EHPS. Proceedings of the 4th International Conference on Intelligent Systems, Modelling and Simulation, Bangkok, Thailand. 2013. Doi: 10.1109/ISMS.2013.113.

[4] T. Ibatan, M. S. Uddin, M. A. K. Chowdhury. Recent development on surface texturing in enhancing tribological performance of bearing sliders, Surface & Coatings Technology, 2015, Volume 272, pp 102–120. Doi: 10.1016/j.surfcoat.2015.04.017

[5] R. Rahmani, A. Shirvani, H. Shirvani, Optimization of Partially Textured Parallel Thrust Bearings with Square-Shaped Micro-Dimples, Tribology transactions, 2007, 50:3, 401-406. Doi: 10.1080/10402000701429261

[6] I. Etsion, G. Halperin, V. Brizmer, Y. Klingerman, Experimental investigation of laser surface textured parallel thrust bearings, Tribology Letters, 2003, Volume 17, pp 295–300.

[7] Brizmer V, Kligerman Y, Etsion I, A Laser Surface Textured Parallel Thrust Bearing, Tribology transactions, 2003, 46:3, 397-403, DOI: 10.1080/10402000308982643

[8] P. Casoli, F. Scolari, C. Rossi, M. Rigosi, A cfd design of engineered surface for tribological performance improvements in hydraulic pumps, 12th International Fluid Power Conference (12. IFK). Dresden, October 12 – 14, 2020. Doi: 10.25368/2020.41

[9] P. Casoli, F. Scolari, M. Rundo, A. Lettini, M. Rigosi, CFD Analyses of Textured Surfaces for Tribological Improvements in Hydraulic Pumps. Energies 2020, 13(21), 5799. Doi: 10.3390/en13215799

[10] P. Casoli, F. Scolari, M. Rundo, Modelling and Validation of Cavitating Orifice Flow in Hydraulic Systems. Sustainability 2021, 13(13), 7239. Doi:10.3390/su13137239

Biographies



Paolo Casoli received M.S. degree in mechanical engineering at the University of Bologna (Italy) in 1990. He became associate professor in 2001 and currently is a full Professor of Fluid Machinery at the Department of Systems Engineering and Industrial Technologies at the University of Parma (Italy). His research interests include modelling and experimental analysis of positive displacement pumps for fluid power applications. The research is focused on both the machines and the circuits connected to the machines.



Carlo Maria Vescovini received M.S. degree in Mechanical Engineering at the University of Parma (Italy) in April 2021. He currently is an Industrial Engineering Ph.D. student at the Department of Systems Engineering and Industrial Technologies University of Parma (Italy). His research concerns power hydraulics systems and machines. In particular, his work focuses on positive displacement pumps, their modelling and testing. Furthermore, part of its commitment is aimed at reducing the noise and pulsations produced by of volumetric machines through passive and active devices.



Fabio Scolari received Ph.D. in Industrial Engineering at the University of Parma (Italy) in 2022. His fields of research are hydraulic systems and components. His main research

activity consists in the study of techniques for increasing the hydrodynamic bearing capacity between lubricated couplings inside hydraulic pumps.



Antonio Lettini graduated in Mechanical Engineering at the Polytechnic University of Turin (Italy) in 2000 and specialized in the field of Fluid Power at the Fluid Power Research Laboratory in Turin before joining Casappa SpA in 2003. Since 2008 he is in charge of the R&D Department Management, now as Group R&D Director. He earned an MBA at Bologna Business School in 2010.



Carlo Rossi graduated in Mechanical Engineering in 1998 at the University of Parma (Italy). He started his professional career first dealing with the management of maintenance in manufacturing companies, then with aluminium die-casting in the field of electric motors. Starting from 2007, he moved to the fluid power field joining Casappa SpA and since 2018 he has been focusing on new technologies and production processes for gear pumps and piston pumps.

Numerical Modeling of Helical External Gear Pump Through a Novel CFD Approach Using Simerics MP+

Pietro Mazzei[1], Emma Frosina[2], Simone Bulleri[3], Adolfo Senatore[1].

[1]Department of Industrial Engineering, University of Naples Federico II, Via Claudio, 21, 80125 Naples, Italy, pietro.mazzei2@unina.it (P.M.), senatore@unina.it (A.S.).

[2]Department of Engineering, University of Sannio, Piazza Roma, 21, 82100 Benevento, Italy, frosina@unisannio.it.

[3]Research Department, Hydreco Hydraulics Italia, Vignola, Modena, Italy, sbulleri@hydreco.com

Abstract.

External Gear Pumps (EGPs) are positive displacement machines with excellent performances and very competitive costs. A particular typology of EGPs is Helical Gear Pump, where the teeth present an inclination along the axial direction, permitting a progressive meshing with consequent lower vibration and noise emission.
Three-dimensional CFD numerical analysis of these pumps has proven to be quite complex. More recently some analyses have been proposed however, to obtain realistic results, approximations regarding the helical angle along the axial dimension have been applied. Those models consisted of a high number of grid cells, leading to high computational time request. In this article, it is explored the use of a novel CFD approach through the use of the commercial code Simerics MP+, already used with success by the research group. This new method permits to evaluate the geometry of the pump without any geometrical approximation, leading to more accurate results and less computational time required if compared with other 3D-CFD tools. An accurate numerical model has been built up on a reference pump with helical gears; the model has been then compared with the results of an experimental campaign.
Finally, a new design of the pressure relief grooves inside the wear plates has been investigated and simulated with the objective of reducing the fluid-borne noise emission, as well as to improve the volumetric efficiency of the pump and to reduce the flow ripple fluctuation, pressure spikes and crossflow optimization.

Keywords. Helical EGPs, Helical Gears, 3D CFD modelling, flow ripple, fluid-borne noise, design optimization.

1. INTRODUCTION

Helical external gears pumps (EGPs) are a type of positive displacement machines that have similar volumetric performances of traditional spur gears EGPs while producing less vibrations and lower noise emissions thanks to the more progressive meshing permitted by their geometry design. The same design sets some additional challenges respect to traditional spur gear, though. The particular gear design generates a variable axial force during the meshing that make the design of the balancing surfaces of the wear plates more demanding.

The desire to harness these advantages have pushed the scientific community to search ways to better understand and accurately simulate this EGP typology. One way to simulate the working condition is through the use of a three-dimensional CFD numerical modeling. The three-dimensional CFD numerical modeling of helical gears pumps has always proven to be a challenging matter due to the difficulty in following the helical angle along the axial direction that requires the implementation of a number of geometry approximation.

Until recent times, the only way to simulate those pumps through a three-dimensional CFD analysis was to slice up the gears along the axial direction and treat every slice as spur gears in connection to the adjacent slices. This methodology allows to obtain a good accuracy, as it can be seen in other similar works found in scientific literature [1,2], but require a high number of grid cells and mismatched grid interface with consequent higher computational time.

In this paper, a novel three-dimensional CFD approach has been applied by using a new capability available in the commercial code Simerics MP+, developed by Simerics Inc. This approach implements the use of a body-fitted binary tree grid generator that accurately follows the fluid volume extracted along the gears' helical angle. The parent-child tree architecture permits to obtain expandable data structure with reduced memory storage, generating thus an accurate and efficient grid, hence eliminating the needs of geometry approximations.

This novel approach has then been validated through experimental tests performed on a test rig of Duplomatic MS Group. After this validation process, a new design of the pressure relief grooves inside the wear plate has been investigated with the objective of improving the volumetric efficiency while reducing the flow ripple fluctuation.

2. PUMP ANALYZED AND EXPERIMENTAL TEST SETUP

The new mentioned numerical methodology has been applied on a reference external helical gear pump produced by Hydreco Hydraulics Italia with a displacement of 14.5 cm3/rev.

The basic technical data of the pump are listed in Table 1.

The pump has a housing made from die-cast alloy, making it ideal for mobile application. An assembly vision of the pump is visible in Figure 2.1. a); while in Figure 2.1. b) there is the exploded view.

Table 1. PUMP TECHNICAL DATA

Description	*Value*	*Unit*
Nominal displacement	14.5	cm^3/rev
Max. continuous pressure	260	bar
Max. intermitted pressure	290	bar
Max. peak pressure	310	bar
Min. rotational speed	500	rev/min
Max. rotational speed	3500	rev/min

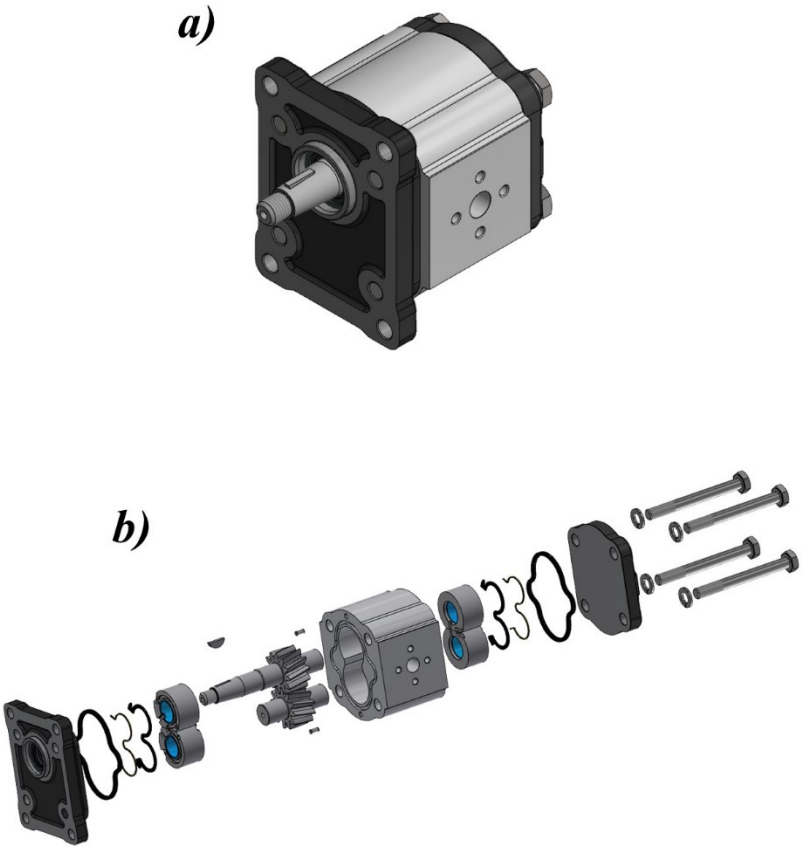

Figure 2.1. a) Assembly of the reference helical gears pump; b) Exploded view

The experimental campaign to validate the model has been executed on a dedicated test bench at Duplomatic MS. The test bench layout is shown in Figure **2.2**. There are two strain gauge sensors, P1 at the inlet side (Duplomatic model PTH, scale: -1÷10 bar and ±0.25% FS) and P2 at the delivery side (Duplomatic model PTH, scale: 0÷400 bar and ±0.25% FS). The flow-rate meter Q1 is a VSE VS 0.4 (VSE.flow®, Neuenrade, Germany), scale 0.03÷40 L/min, 0.3% measured value accuracy.

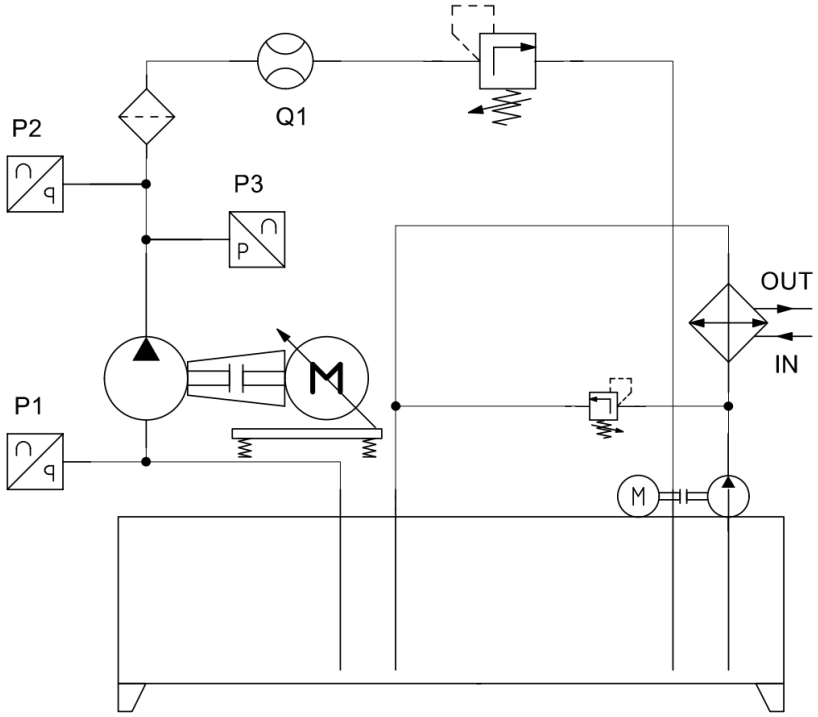

Figure 2.2. Test bench layout

The tests have been carried out with an oil ISO 46, grade HL, maintained at a temperature of 40° C ± 1°C. The pump has been tested varying the delivery pressure at different fixed speeds.

Pressure ripples have been also acquired by adding a fixed orifice after the P2 strain gauge sensors to impose the load and a P3 high frequency pressure sensor (PCB® model 113B26, PCB Piezotronics, Inc.,NY, USA) between the tested pump and the P2 strain gauge.

The experimental campaign has involved the analysis of a numbers of working conditions with the additional measurement of the noise levels. Being the numerical model focused on the fluid dynamic aspect, only some of the experimental data has been compared to the results obtained from the numerical model, as shown in section 4.

3. THE THREE-DIMENSIONAL CFD NUMERICAL MODEL

3.1. Numerical Model Description

The numerical model has been developed using the commercial code Simerics MP+®, developed by Simerics Inc. This tool has been specifically designed to analyze hydraulic components, offering a variety of templates for specific case of pumps, motors and valves.

The pump fluid domain utilized has been extracted from the CAD files of the pump, as it can be seen in Figure 3.1.

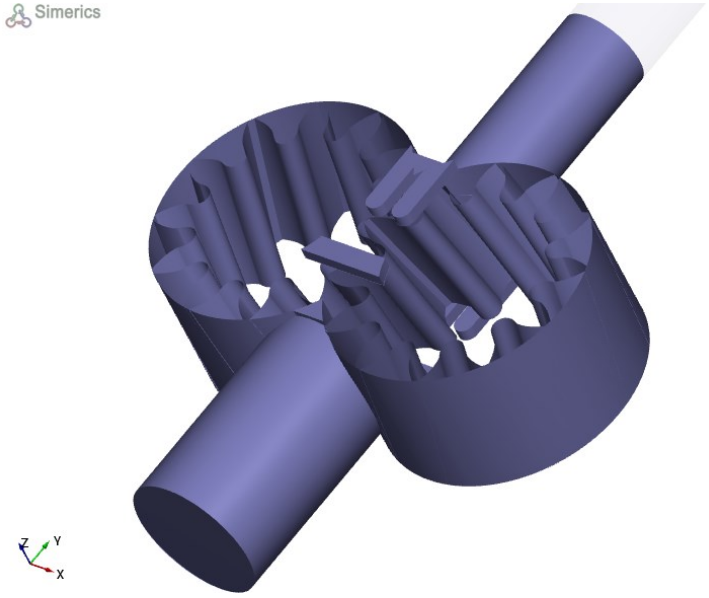

Figure 3.1. Helical pump fluid domain

It has been meshed using a body-fitted binary tree approach with the use of the rotor template Mesher to implement the rotation of the helical gears. An analysis with coarser and finer mesh has also been explored; the results obtained from the first ones have proved to have too low accuracy, while the latter have a precision increase such that it is not justified by the higher computational power and time required to reach the converge of the solution.

The final model with the selected grid contains around 950,000 cells and it is shown in Figure 3.2.

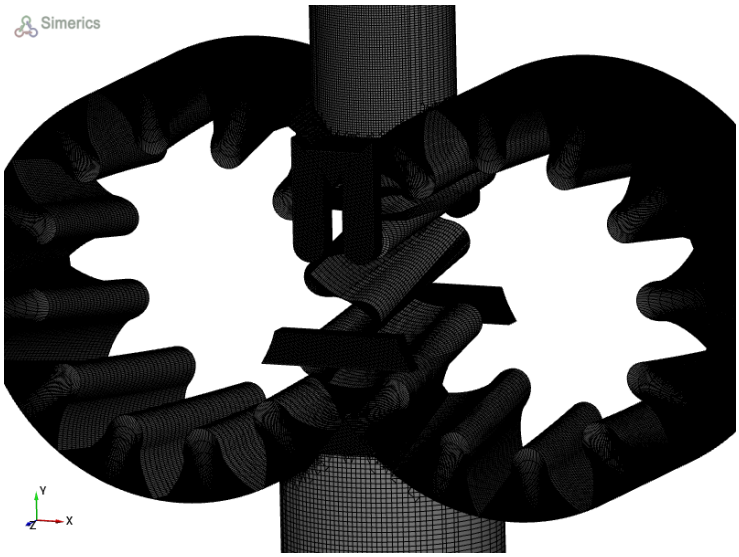

Figure 3.2. Mesh grid of pump's fluid domain

The simulations have been run on a workstation equipped with an Intel® Xeon® CPU E5-2640v2 @ 2.00 GHz (two processors) with 192 GB RAM. The computational time required to complete a simulation with an angular step size of 0.5 degree of gear shaft rotation is about 72 hours for two pump revolutions.

The gears in the model have been translated along the vertical axis to consider the effect of the pressure forces acting on the gears. The driven gear has also been rotated to reproduce the contact with the Driving gear. The numerical simulation does not permit to evaluate a zero gap, so the choice of the minimal value of the gap is of utmost importance to replicate real working conditions.

A value of 27 µm has been initially selected for the gap between the teeth and the one between the teeth and the housing. This initial value led to unrealistic crossflow values during the meshing. Thus, a more restrictive value of 5 µm has been chosen as minimal gap value, as shown in Figure 3.3. This resulted in an increase of the cell required to reach a stable solution.

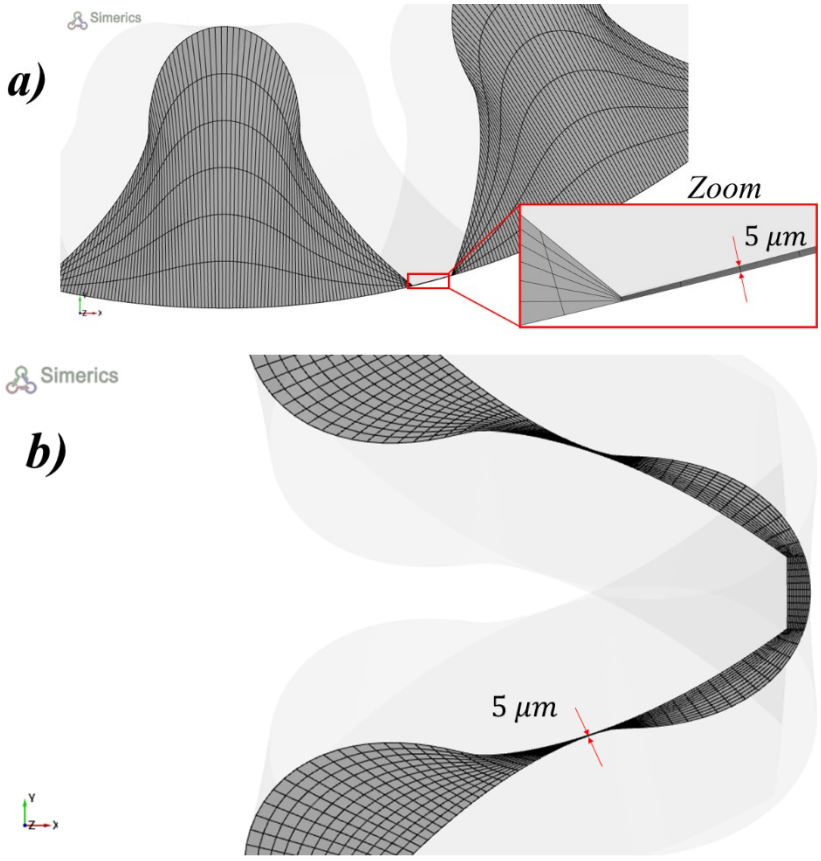

Figure 3.3. a) Minimum size gap housing-tooth contact; b) minimum size gap meshing teeth contact

The numerical model includes the evaluations of turbulence and cavitation. The turbulence has been predicted by the use of a standard k-ε turbulence model. Despite the presence in the literature of more accurate model than the k-ε, for this application where the losses due to the viscous stresses are negligible compared to pressure forces, this model permits to obtain a good accuracy requiring only a minimal amount of additional computational power. The reliability of this methodology implemented can be seen in numerous works available in literature [3-7].

3.2. Cavitation Model Description

The cavitation model utilized is directly available in the code and is able to predict cavitating conditions with high accuracy. It is built on the work of Singhal et al., based on the Rayleigh-Plesset equation [6] and appraises for cavitation, aeration and liquid compressibility. This model describes the vapor distribution using the following formulation:

$$\frac{\partial}{\partial t}\int_{\Omega(t)} \rho\, f_v d\Omega + \int_{\sigma} \rho\big((\vec{v} - \overrightarrow{v_\sigma}) \cdot \vec{n}\big) f_v d\sigma = \int_{\sigma} \left(D_f + \frac{\mu_t}{\sigma_f}\right)(\nabla f_v \cdot \vec{n}) d\sigma + \int_{\Omega} (R_e - R_c) d\Omega \tag{3.1}$$

Where D_f is the diffusivity of the vapor mass fraction and σ_f is the turbulent Schmidt number. In the following study, these two numbers are set equal to the mixture viscosity and unity, respectively. The vapor generation term, R_e, and the condensation rate, R_c, are characterized as:

$$R_e = C_e \frac{\sqrt{k}}{\sigma_l} \rho_l \rho_v \left[\frac{2}{3}\frac{(p - p_v)}{\rho_l}\right]^{\frac{1}{2}} \left(1 - f_v - f_g\right) \tag{3.2}$$

$$R_c = C_c \frac{\sqrt{k}}{\sigma_l} \rho_l \rho_v \left[\frac{2}{3}\frac{(p - p_v)}{\rho_l}\right]^{\frac{1}{2}} f_v \tag{3.3}$$

The Singhal's cavitation theory has been extended to also include non-condensable gases (NCG) in the liquid [7]. The unsteady mixture (liquid, liquid vapor and NCG) density ρ is evaluated in according to the equation (3.4):

$$\frac{1}{\rho} = \frac{f_v}{\rho_v} + \frac{f_g}{\rho_g} + \frac{(1 - f_v - f_g)}{\rho_l} \tag{3.4}$$

The NCG in the hydraulic fluid can be found as a free and a dissolved state. The model utilized for this activity implement an Equilibrium Dissolved Gas Model approach, which assumes that the free NCG mass fraction is not constant. Its evaluation is obtained by the resolutions of an additional transport equation for the mass fraction of the dissolved gas (3.5).

$$\frac{\partial}{\partial t}\int_{\Omega(t)} \rho\, f_d d\Omega + \int_{\sigma} \rho\left(\left(\left(\vec{v} - \overrightarrow{v_\sigma}\right)\cdot\vec{n}\right) f_d d\sigma\right) = \int_{\sigma}\left(D_{f_d} + \frac{\mu_t}{\sigma_f}\right)(\nabla f_d \cdot \vec{n}) d\sigma \int_{\Omega} \frac{\rho\left(f_d - f_{d,equil}\right)}{\tau} d\Omega + \int_{\Omega}\left(S_{f_d}\right) d\Omega \quad (3.5)$$

Where the equilibrium gas mass fraction $f_{d,equil}$ depends on the active cell pressure and is evaluated through the following equation:

$$f_{d,equil} = \frac{p}{p_{f_{d,equil\,ref}}} \cdot f_{d,equil\,ref} \quad (3.6)$$

Hereby, the NCG_{tot}, sum of the free gas mass fraction and the dissolved gas mass fraction is constant:

$$NCG_{tot} = f_g + f_d \; = const. \quad (3.7)$$

Under these assumptions, only one equation must be resolved for the dissolved gas f_d; the free gas f_g is subsequently evaluated based on the assumption of the NCG_{tot} being constant.

4. MODEL VALIDATION

The experimental tests have been conducted on the test bench described previously. The pump has been tested under four different pump speeds: 1000, 1500, 1800 and 2200 rev/min. The values of the delivery flow rate have been for all the delivery pressure conditions in the range of 20÷240 bar.

Due to the high computational time required to complete a simulation, only two discrete single delivery pressure points for three different pump speeds have been completely simulated. In detail, the simulations have been run at a delivery pressure of 100 bar and 200 bar with a pump speed of 1000 and 1500 rev/min. In Figure 4.1 is shown a comparison between the numerical model and the experimental results for the delivery flow-rate values (normalized to reference value, Q_{ref}) of the reference pump.

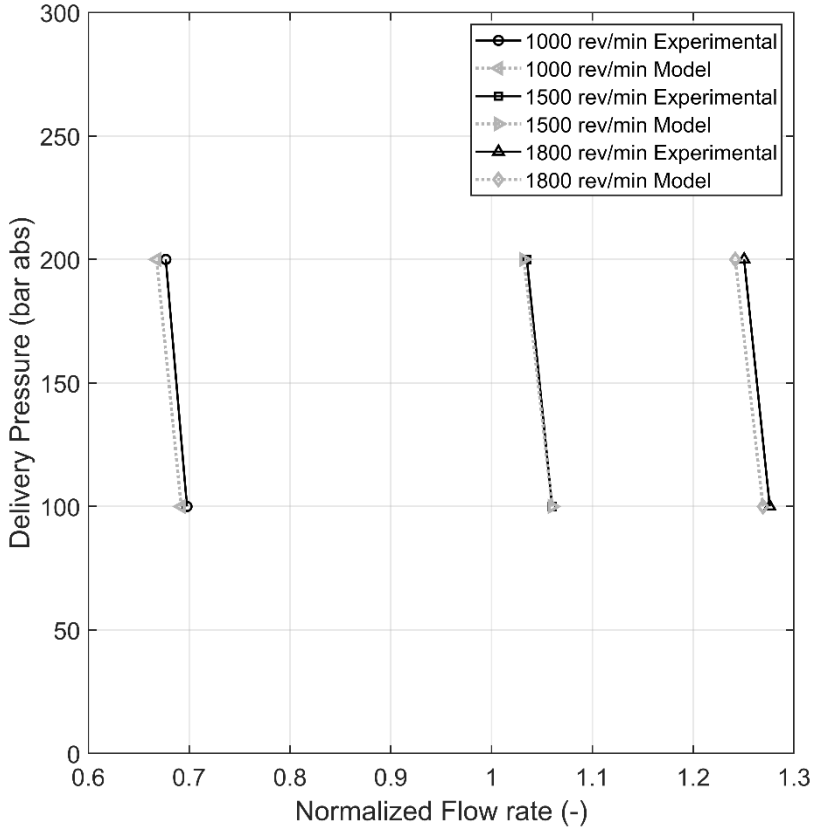

Figure 4.1. Pressure vs. normalized delivery flow rate comparison at different pump speed: 1000 rev/min, 1500 rev/min and 1800 rev/min

It can be noted that the numerical model correctly predicts the flow-rate trends for all the simulated pump speeds; the error percentage between model and experimental data is always below 1%, staying thus within the uncertainty range of the experimental measurements.

A study of the pressure ripple at the delivery side of the pump has been also conduced to further validate the numerical model. To reproduce the same conditions of the experimental campaign, the numerical model has been modified introducing a duct and an orifice both shown in Figure 4.2.

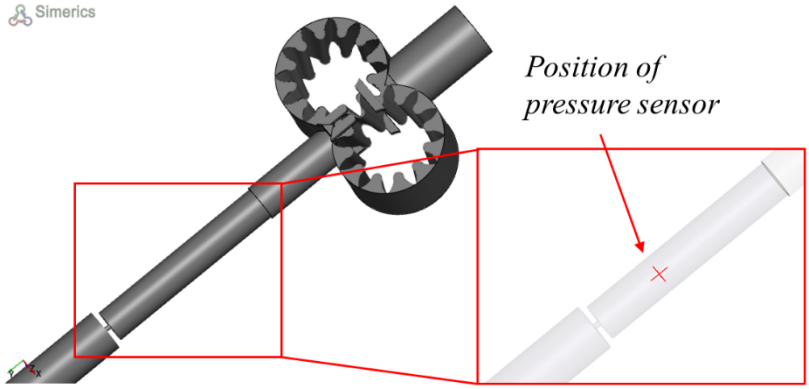

Figure 4.2. Pressure ripple analysis: Fixed orifice and the monitoring point

The comparison between model and experimental data are presented in Figure 4.3 for a single working condition. The pressure ripple values are normalized against a pressure reference value, p_{ref}. The chart reveals that there is good accordance between the experimental data and the results obtained from the numerical model. The small disagreement presents on the peaks of the pressure ripples is most likely due to the presence of high frequency noise in the experimental measurements due to the test bench setup not been perfectly isolated.

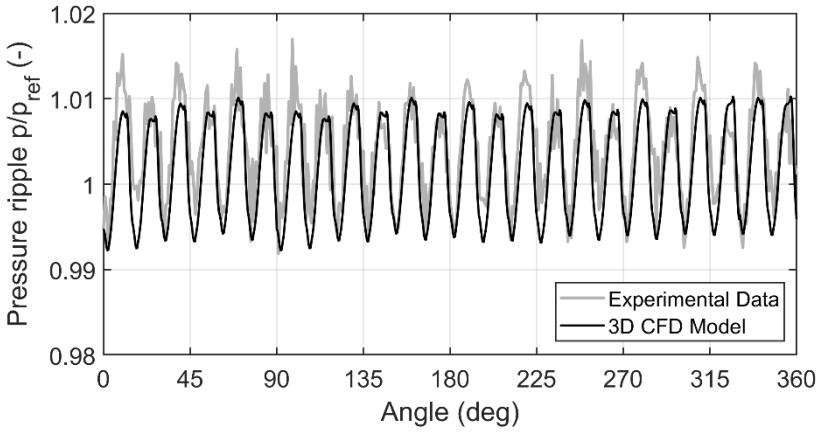

Figure 4.3. Normalize pressure ripples comparison at n=1500 rev/min

The performed comparisons have permitted to verify the high accuracy of the developed 3D numerical model for both steady-state and transient output parameters.

5. PUMP DESIGN OPTIMIZATION INVESTIGATION

After the process of validating the numerical model, a new design of the pressure relief grooves in the wear plate has been investigated. The relief grooves act as noise reducers by realizing a gradual switch between the displacing chambers and their connections with the outlet and inlet ports, thereby limiting pressure spikes and flow ripple fluctuations but also

generating an undesirable cross-flow between the suction and the delivery volumes. The new design proposed has the objective to improve the volumetric efficiency while reducing the fluid-borne noise emissions.

This new design has been developed with the idea of exploiting the offset angle between front and rear gears' faces due to the helical angle, implementing thus an asymmetrical design. This is in contrast with the current design, which presents a symmetrical geometry between the front and the rear for lean production and assembly reasons (Figure 5.1 a).

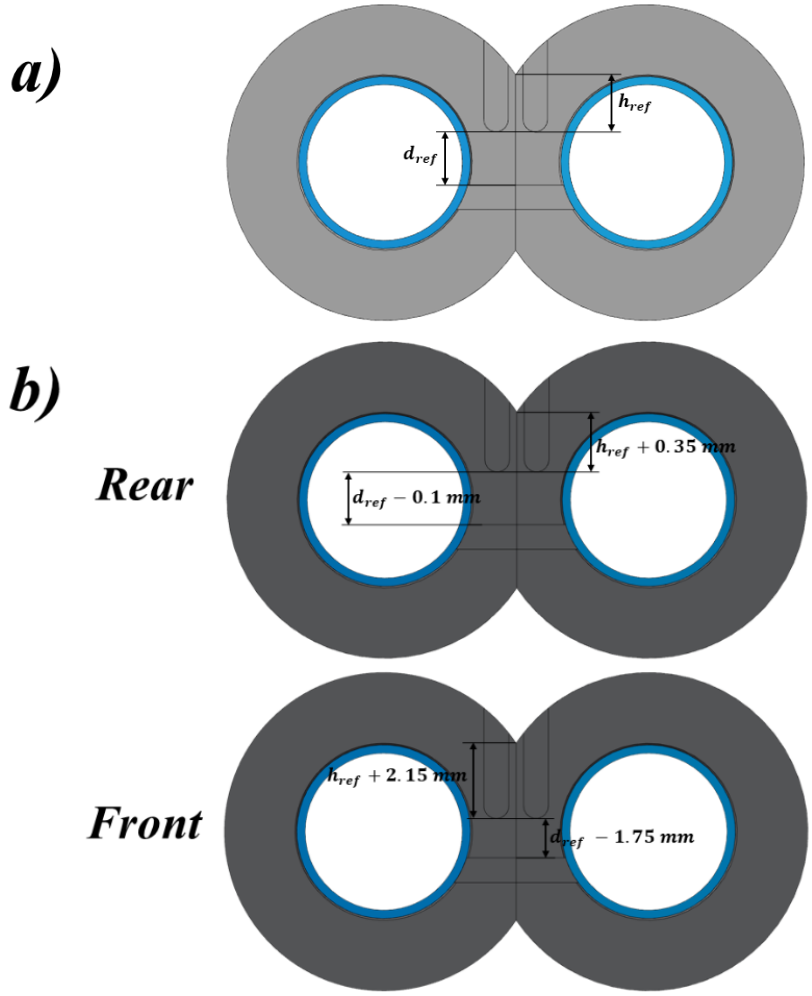

Figure 5.1. a) Relief grooves design of the standard pump; b) Proposed new design of the relief grooves

The asymmetrical design allows to control the pump timings through the length of the delivery relief grooves of the rear face and the position of the suction relief groove of the front face. This permits increased freedom for the remaining relief grooves; their length and position could then be chosen to improve the volumetric efficiency, to reduce pressure spikes and flow ripple fluctuations or a mix of both effects. The final geometry tested is shown in Figure 5.1. b).

The preliminary nature of the investigation coupled with the high computational time required to run a simulation has led to the complete simulation of this new pump design geometry for only one pump speed, 1500 rev/min, and one delivery pressure, 200 bar.

The results comparison between the standard design and the new prototyped design for the same test condition are shown in Figure 5.2 and in Table 2, where the numerical flow ripple and the numerical mean flow rate comparisons are presented with values normalized to a reference value, Q_{ref}.

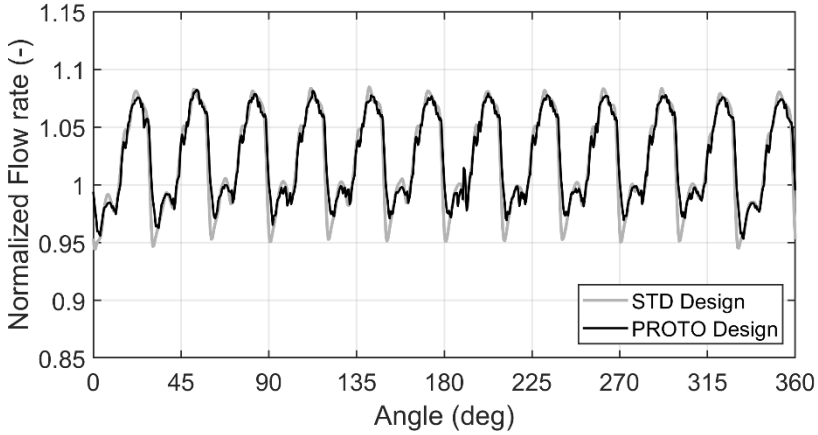

Figure 5.2. Numerical flow ripple comparison at n=1500 rev/min, Δp=200 barA

Table 2. RELIEF GROOVES DESIGN COMPARISON N=1500 REV/MIN ΔP=200 BARA

Description	***Value***	***Unit***
Mean flow rate STD Design	1.021	Q_{ref}
Mean flow rate PROTO Design	1.024	Q_{ref}

It can be appreciated from the table that the new design has a small advantage regarding the mean delivery flow, exhibiting a value increase of about 0.5%, pointing the way to a small improvement of the volumetric efficiency.

The analysis of Figure 5.2 reveals that the new investigated design permits to reduce the flow ripple, with a significant reduction of the crossflow rate. The non-uniformity rate of the

flow ripple is reduced of around 8%, confirming the increment of the average delivery flow rate. Another significative result is presented in Figure 5.3 where it is shown the comparison of the pressure evolution inside a chamber in rotation for each gear for the two tested designs. In particular, Figure 5.3. a) refers to a chamber of the driving gear, while the Figure 5.3. b) corresponds to one of the driven gear.

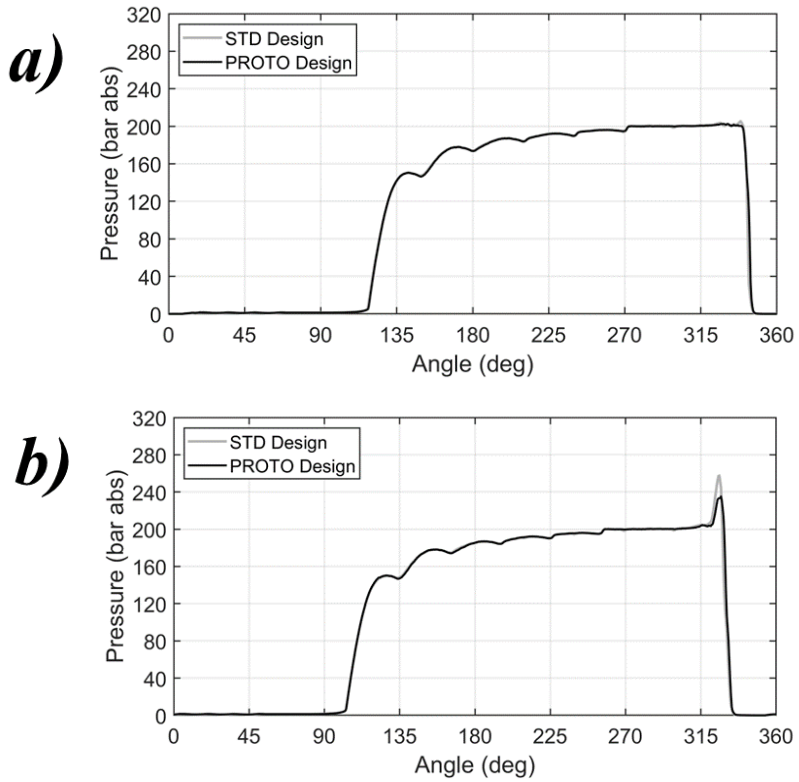

Figure 5.3. Numerical pressure evolutions comparison at n=1500 rev/min, Δp=200 barA: a) driving gear; b) driven gear.

Pressure spikes visible in Figure 5.3 are zoomed in Figure 5.4. a) and Figure 5.4. b). In particular, Figure 5.4. a) presents the zoomed view of the pressure spikes that occurs during meshing inside a chamber of the driving gear, while Figure 5.4. b) is the corresponding view in a chamber of the for the driven gear.

The examination of these results shows that the new proposed design presents lower pressure spikes during gears' meshing inside the chambers for both driving and driven gears. These results, coupled with the reduction of the non-uniformity rate of the flow ripple, suggest that the new design of the pressure relief grooves in the wear plate could provide reduction in the vibrations produced hence diminished noise emissions.

It is expected that for higher rotational speeds the pressure peaks inside a chamber during meshing will be more intense, so the advantages shown by the new proposed design could

be more relevant. For this reason, a simulation at 1800 rev/min has been executed on both new proposed design and the standard design.

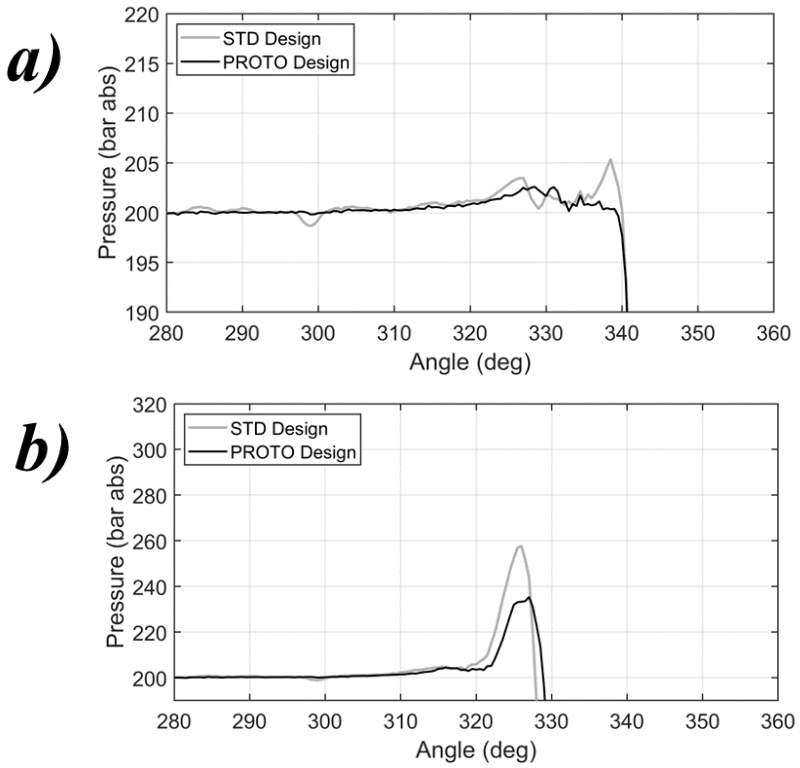

Figure 5.4. Zoomed view of numerical pressure evolutions comparison at n=1500 rev/min, Δp=200 barA: a) driving gear; b) driven gear.

The results obtained are reported in Figure 5.5 and Table 3, where the numerical flow ripple and the numerical mean flow rate comparisons are presented with values normalized to a reference value, Q_{ref}.

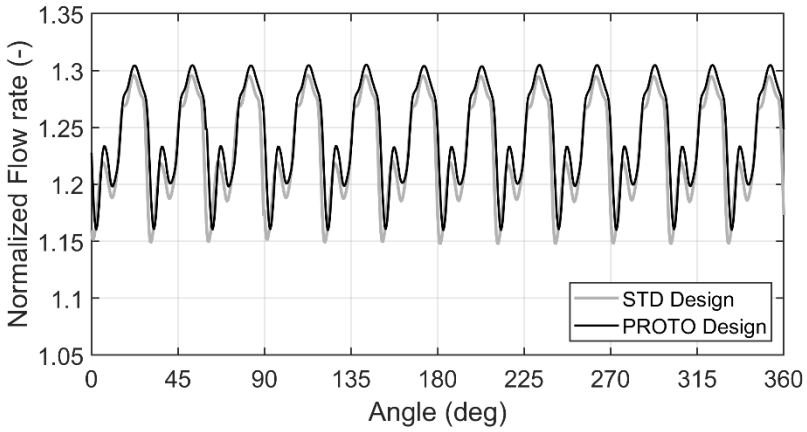

Figure 5.5. Numerical flow ripple comparison at n=1800 rev/min, Δp=200 barA

In Figure 5.6 a zoomed view of the pressure evolution inside a chamber in rotation for each gear in the meshing zone is presented for the two tested designs.

Table 3. RELIEF GROOVES DESIGN COMPARISON N=1800 REV/MIN ΔP=200 BARA

Description	***Value***	***Unit***
Mean flow rate STD Design	1.231	Q_{ref}
Mean flow rate PROTO Design	1.247	Q_{ref}

The analysis of Figure 5.5 and Table 3 demonstrate that for a higher angular speed the new design continues to improve the volumetric efficiency and the non-uniformity rate, albeit in a lesser percentage.

The investigation of Figure 5.6 shows that the pressure spikes are again less intense than the standard design, with a percentage difference more conspicuous, hence confirming the expected hypothesis.

Thus, to reach a conclusive evaluation regarding this new proposed design, it is necessary to simulate and analyze other pump working conditions to discover if this improved behavior appears as well or if it is only an isolate case of the specific pump working condition simulated.

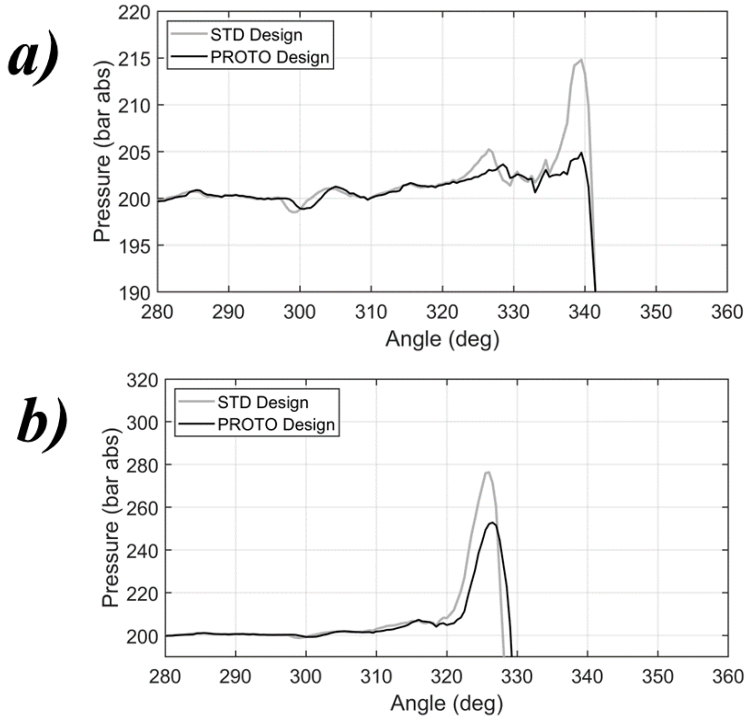

Figure 5.6. Zoomed view of numerical pressure evolutions comparison at n=1800 rev/min, Δp=200 barA: a) driving gear; b) driven gear

6. CONCLUSIONS

A novel three-dimensional CFD approach for the study of an external helical gear pump has been described in this article. This approach has been used to develop a numerical model using the commercial code Simerics MP+®, developed by Simerics Inc. The model has been realized based on a geometry of a reference pump manufactured by Hydreco Hydraulics Italia and include accurate tools to predict flow-rate, turbulence and cavitation.

An experimental test campaign, to compare and validate the results of the developed model, has been carried out on a dedicated test bench on the pump used as reference. The comparison has proved good agreement between model and experimental data under a number of working conditions, demonstrating the accuracy of the simulated model. Therefore, the approach can be used to study and optimize design of External helical gear pump.

For this reason, the approach has been applied studying a new design of the geometry of the pressure relief grooves. The results obtained from this first analysis has given interesting results and represent the first step for a further geometry optimization.

ACKNOWLEDGMENT

The authors would like to thank Simerics Inc. for providing them Simerics MP+® licenses. The authors appreciate the technical support from Roberto Maddalon of Duplomatic MS and Simone Bulleri from Hydreco Hydraulics Italia.

NOMENCLATURE

Acronym	*Description*
EGP	External Gear Pump
CFD	Computational Fluid Dynamic
CAD	Computer Aided Drafting
NCG	Non-Condensable Gas

Symbol	*Description*	*Unit*
C_c	Cavitation Condensation coefficient	[-]
C_e	Cavitation Evaporation coefficient	[-]
D_f	Diffusivity of the vapor mass fraction	[m^2/s]
D_{f_d}	Diffusivity of the dissolved NCG	[m^2/s]
f_g	Mass fraction of free NCG	[-]
f_d	Mass fraction of dissolved NCG	[-]
$f_{d,equil}$	Equilibrium gas mass fraction of dissolved NCG	[-]
$f_{d,equil\,ref}$	Equilibrium mass fraction of the dissolved NCG at the reference pressure	[-]
f_v	Mass fraction of the vapor	[-]
k	Turbulent Kinetic Energy	[J/kg]
n	Pump speed	[rad/s]
$\vec{n}$	Surface normal	[-]
NCG_{tot}	Total non-condensable gas mass fraction	[-]
p	Pressure	[Pa]
p_v	Phase-change threshold pressure	[Pa]
$p_{f_{d,equil\,ref}}$	Reference pressure for the dissolved gas equilibrium mass fraction	[Pa]

Q_{ref}	Reference flow rate	[L/min]
R_e	Vapor generation rate	[-]
R_c	Vapor condensation rate	[-]
S_{fd}	Source of dissolved NCG	[kg/m^3]
$\vec{v}$	Fluid velocity vector	[m/s]
v_σ	Fluid velocity vector	[m/s]

Greek letter	***Description***	***Unit***
μ_t	Turbulent viscosity	[Pa·s]
ρ	Density of mixture	[kg/m^3]
ρ_g	Density of gas	[kg/m^3]
ρ_l	Density of liquid	[kg/m^3]
ρ_v	Density of vapor	[kg/m^3]
σ	Surface of control volume	[m^2]
Ω	Control volume	[m^3]
σ_f	Turbulent Schmidt number	[-]
σ_l	Surface tension	[N/m]

7. REFERENCES

[1] Heisler, A.S., Moskwa, J.J., Fronczak, F.J. "Simulated Helical Gear Pump Analysis Using a New CFD Approach." Proceedings of the ASME 2009 Fluids Engineering Division Summer Meeting. Volume 1: Symposia, Parts A, B and C. Vail, Colorado, USA. August 2–6, 2009. pp. 445-455. ASME. https://doi.org/10.1115/FEDSM2009-78472.

[2] Zhao, X., Vacca, A., Dhar, S. "Numerical Modeling of a Helical External Gear Pump With Continuous-Contact Gear Profile: A Comparison Between a Lumped-Parameter and a 3D CFD Approach of Simulation." Proceedings of the BATH/ASME 2018 Symposium on Fluid Power and Motion Control. BATH/ASME 2018 Symposium on Fluid Power and Motion Control. Bath, UK. September 12–14, 2018. V001T01A053. ASME. https://doi.org/10.1115/FPMC2018-8903.

[3] Pellegri, M., Vacca, A., Frosina, E., Buono, D., Senatore, A. Numerical analysis and experimental validation of Gerotor pumps: A comparison between a lumped parameter and a computational fluid dynamics-based approach. Proceedings of the Institution of Mechanical Engineers, Part C: Journal of Mechanical Engineering Science. 2017;231(23):4413-4430. https://doi.org/10.1177/0954406216666874.

[4] Frosina, E., Senatore, A., Buono, D., Stelson, K.A., Wang, F., Mohanty, B., Gust, M.J. "Vane Pump Power Split Transmission: Three Dimensional Computational Fluid Dynamics Modeling." Proceedings of the ASME/BATH 2015 Symposium on Fluid Power and Motion Control. ASME/BATH 2015 Symposium on Fluid Power and Motion Control. Chicago, Illinois, USA. October 12–14, 2015. V001T01A011. ASME. https://doi.org/10.1115/FPMC2015-9518.

[5] Borghi, M., Zardin, B. "Axial Balance of External Gear Pumps and Motors: Modelling and Discussing the Influence of Elastohydrodynamic Lubrication in the Axial Gap." Advances in Multidisciplinary Engineering. Ed. Jahanmir, S, Saka, N, Tucker, C, & Kim, S. ASME Press, 2016. https://doi.org/10.1115/1.861080_ch8.

[6] Schleihs, C., Viennet, E., Deeken, M., Ding, H., Xia, X., Lowry, S., Murrenhoff, H. 3D-CFD simulation of an axial piston displacement unit. In Proceedings of the 9th International Fluid Power Conference, Aachen, Germany, 24–26 March 2014; pp. 332–343.

[7] Zhou, J., Vacca, A., Casoli, P. A novel approach for predicting the operation of external gear pumps under cavitating conditions, Simulation Modelling Practice and Theory, Volume 45, 2014, Pages 35-49, ISSN 1569-190X, https://doi.org/10.1016/j.simpat.2014.03.009.

[8] Singhal, A. K., Athavale, M. M., Li, H., Jiang, Y. (August 19, 2002). "Mathematical Basis and Validation of the Full Cavitation Model ." ASME. J. Fluids Eng. September 2002; 124(3): 617–624. https://doi.org/10.1115/1.1486223.

[9] Simerics Inc. Simerics MP+'s User Manual - v 5.0.11; Simerics: Bellevue, WA, USA, 202

Biographies



Pietro Mazzei received his B.Sc and M.Sc of Mechanical Engineering degree at Federico II of Naples University, Italy in 2021. He received his Ph.D. degree on Industrial Engineering in 2023, focusing on the development of numerical models to analyze and optimize the performances and the noise emissions of external gear machines. Currently he is employed at CIRA (Centro Italiano Ricerche Aerospaziali) on the development of hybrid LTA vehicle as a pressure and thermal modeling expert.

Numerical Modeling of Helical External Gear Pump Through a Lumped Parameter Approach

Pietro Mazzei[1], Emma Frosina[2], Simone Bulleri[3], Adolfo Senatore[1].

[1]Department of Industrial Engineering, University of Naples Federico II, Via Claudio, 21, 80125 Naples, Italy, pietro.mazzei2@unina.it (P.M.), senatore@unina.it (A.S.).

[2]Department of Engineering, University of Sannio, Piazza Roma, 21, 82100 Benevento, Italy, frosina@unisannio.it.

[3]Research Department, Hydreco Hydraulics Italia, Vignola, Modena, Italy, sbulleri@hydreco.com

Abstract.

External gear pumps are a type of positive displacement machines that combine excellent performances with very competitive costs. These characteristics unfold the necessity of tools to accurately simulate their performance. In this article, a numerical methodology based on a lumped parameter approach has been developed for helical External Gear Pumps (EGPs). The methodology is based on the usage of a tool, that, starting from the pump drawing, thanks to different subroutines developed in different interconnected environments, allows to fully analyze EGPs with Helical. The tool is based on a tool called EgeMATor developed by the research group for spur gears and described in a precedent works [1]. The tool has been further expanded in its functionality and optimized becoming EgeMATor MP+. Indeed, the new release has been expanded not only to include helical gears but also to simulate the bearings' reaction and consequently the gears' eccentricity variations. Results obtained from the simulations have been compared with data obtained thanks to an experimental campaign carried on a series of reference pumps done to further validate the numerical model and the new implemented functionalities.
Then, a new methodology that, for a defined tooth gears profile, is able to automatically obtain an optimized design of the pressure relief grooves of the wear plate has been studied. This methodology, through a flow ripple fluctuation, pressure spikes and crossflow optimization based on geometric assumptions, has the objective to characterize a design that permits to improve the volumetric efficiency as well as to reduce the fluid-borne noise emission of the pump analyzed.

Keywords. Helical EGPs, lumped parameter numerical approach, fluid-borne noise, flow ripple reduction, design optimization.

1. INTRODUCTION

External gear pumps (EGPs) are a type of positive displacement machines. They are usually chosen thanks to their high resistance and volumetric efficiency combined with simple working principle and low manufacturing cost. Those pumps are widely used in the fluid power field for both industrial and mobile applications. Despite their simple operating principle, obtaining high efficiency levels coupled with low noise emissions is a more arduous task. To assist in reaching these objectives, the scientific community have come with two different approaches. The first utilizes a three-dimensional CFD approaches to analyze the local pressurization and the overall flow behavior. Frosina et al. [2] used 3D-CFD approach to investigate the performance of a high-pressure EGP with spur gears. Heisler et al. [3] and Qi et al. [4] used different approaches to predict the behavior of a helical EGP. This methodology has proved to obtain a comprehensive understanding of those pumps, with excellent prevision of the working characteristics. These results come at the cost of a substantial computational power and time required; thus, to reduce the resources required simplifications are usually employed.

The second methodology implements lumped parameter approaches, where interconnected control volumes with constant properties are chosen to capture pressure variation within the pump. This analysis requires only a small fraction of the computational expenses required by a 3D-CFD approach, permitting to execute rapid simulations. Borghi et al. [5] have developed and validated a lumped parameter model that predicts the general behavior of the EGP. Mucchi et al. [6] have built up a similar model based on the same approach that is also capable to analyze helical gears. Ransegnola et al. [7] compare helical and spur EGPs through a lumped parameter approach in a multi-domain system, demonstrating its flexibility and accuracy.

This research group also has explored the analysis of EGPs by means of a lumped parameter approach, developing a new release of a simulation tool already presented in a previous work [1], called EgeMATor. The tool already permitted to completely analyze and predict both the fluid dynamics and the mechanical properties of EGPs with spur gears. Thus, in this paper, the authors have carried on improvements of such tool with the objective of further optimize it and also to expand the analyses that it could execute. Thus, the EgeMATor tool has been further developed firstly to automatically predict the gear positions, by evaluating the bearings' force reactions, and then to include the analysis on EGPs with helical gears. The new tool release that includes both features has been called EgeMATor MP+.

The novel approach has been also validated comparing the results obtained from the simulations with the experimental data got on a reference helical EGP manufactured by the company Hydreco Hydraulics Italia using a test bench provided by Duplomatic MS, both companies involved in the research.

Finally, the validated approach has been used to devise an optimal pressure relief grooves design based on geometric assumptions.

2. PUMP ANALYZED AND EXPERIMENTAL TEST SETUP

The analysis proposed in this paper has been performed on a reference external helical gear pump designed by the company Hydreco Hydraulics Italia; the pump has a displacement of 14.5 cm3/rev.

The basic technical data of the pump are listed in Table 1.

The pump has a housing made from die-cast alloy, making it ideal for mobile application. The exploded view of the pump geometry is shown in Figure 2.1.

Table 1. PUMP TECHNICAL DATA

Description	*Value*	*Unit*
Nominal displacement	14.5	cm^3/rev
Max. continuous pressure	260	bar
Max. intermitted pressure	290	bar
Max. peak pressure	310	bar
Min. rotational speed	500	rev/min
Max. rotational speed	3500	rev/min

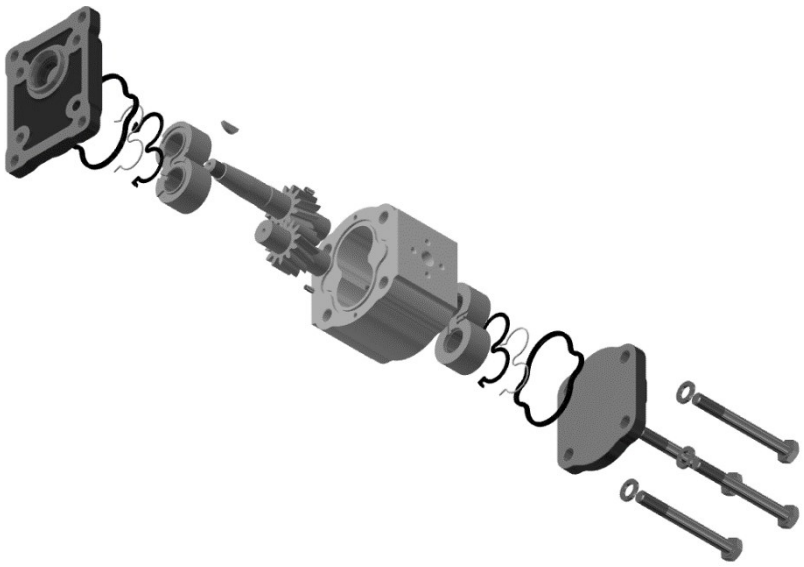

Figure 2.1. Exploded view of the reference pump

The experimental campaign to validate the model has been done on a dedicated test rig of the Italian company Duplomatic MS, involved in the research project. The test bench layout is shown in Figure **2.2**. There are two strain gauge sensors, P1 at the inlet side (Duplomatic model PTH, scale: -1÷10 bar and ±0.25% FS) and P2 at the delivery side (Duplomatic model

PTH scale: 0÷400 bar and ±0.25% FS). The flow-rate meter Q1 is a VSE VS 0.4 (VSE.flow®, Neuenrade, Germany), scale 0.03÷40 L/min, 0.3% measured value accuracy.

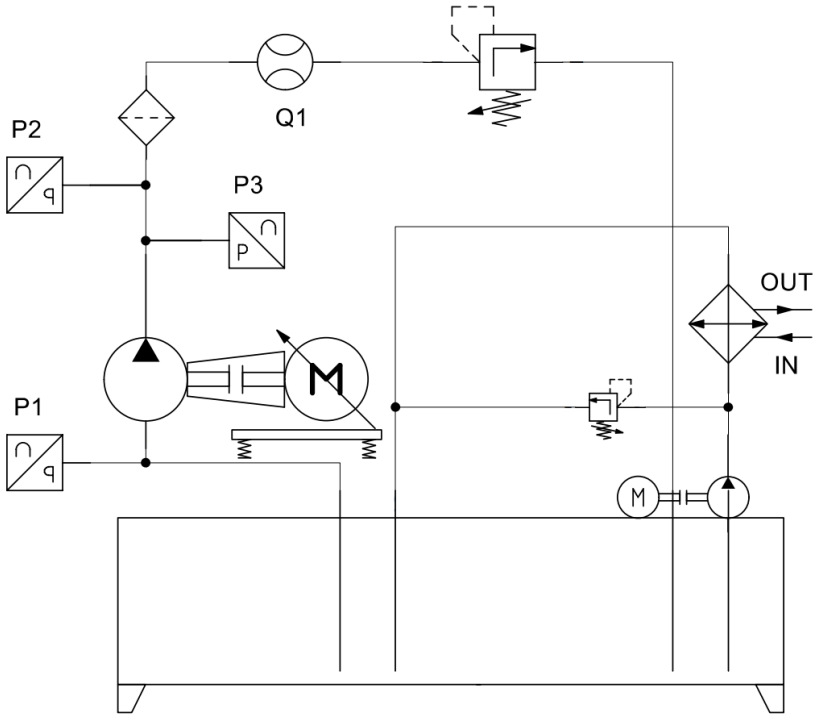

Figure 2.2. Test bench layout

The tests have been carried out with an oil ISO 46, grade HL, maintained at a temperature of 40° C ± 1°C. The pump has been tested varying the delivery pressure at different speeds. The experimental data has been compared to the results obtained from EgeMATor MP+, results will be presented in the section 4.

The experimental campaign to validate the model has been executed on a dedicated test bench at Duplomatic MS. The test bench layout is shown in Fig 2. There are two strain gauge sensors, P1 at the inlet side (Duplomatic model PTH, scale: -1÷10 bar and ±0.25% FS) and P2 at the delivery side (Duplomatic model PTH, scale: 0÷400 bar and ±0.25% FS). The flow-rate meter Q1 is a VSE VS 0.4 (VSE.flow®, Neuenrade, Germany), scale 0.03÷40 L/min, 0.3% measured value accuracy.

3. THE TOOLS: EGEMATOR AND EGEMATOR MP+

3.1. Overview

EgeMATor (External Gear Machine Multi Tool Simulator) is a tool completely developed by the authors for numerical simulations of external gear machines. In particular, the tool is

composed of different subroutines developed in different environments, interconnected to each other, as visible from its workflow Figure 3.1, to study the EGMs in depth.

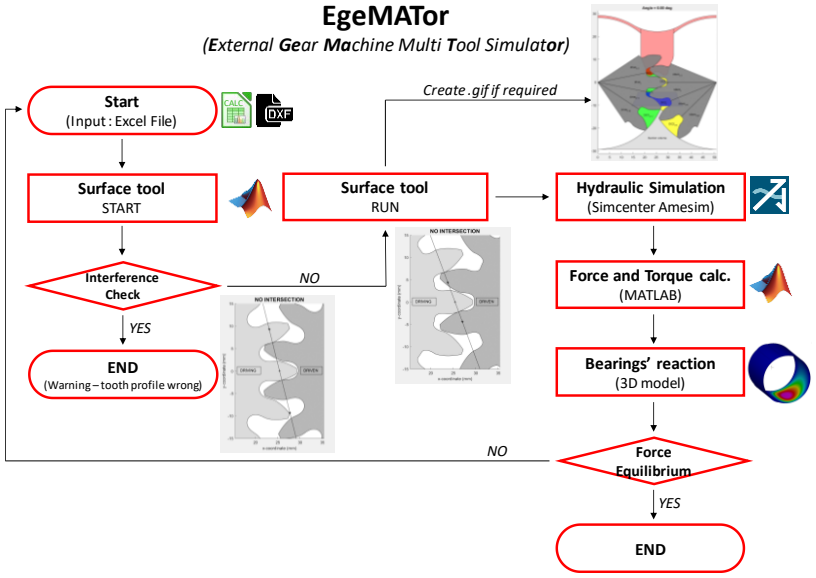

Figure 3.1. The EgeMATor's (External Gear Machine Multi Tool Simulator) workflow

The hydraulic simulation main subroutine, visible in Figure 3.1, runs a numerical simulation of the pump in Simcenter Amesim®, using a lumped parameter method based on the control volume approach. This step is preceded by a code, written by the authors in MATLAB®, called Surface Tool, that provides all the information requested by the hydraulic simulation subroutine. The Surface Tool [1] generates automatically tables with all the inputs requested by the code developed in Simcenter Amesim® like the displacement volumes as the gears rotate and their connection with the contiguous elements.

EgeMATor works in closed loop, therefore, after the hydraulic simulation, it is possible to activate a subroutine that calculates gears' forces and torques. Next, another subroutine runs the bearings' reaction calculation through a 3D-CFD numerical model; finally, results are compared and, if a different gear positioning is necessary, the Surface Tool starts the process again. Further details are available in [1].

3.2. The new bearings' model approach

The bearings' reaction subroutine included in the first release of EgeMATor was based on a 3D-CFD numerical approach using the commercial code Simerics MP+®. This subroutine required considerably more computational time than all the other subroutines included in EgeMATor. To remove this limitation and to gain more flexibility, a new subroutine has been studied and implemented in the tool.

This subroutine has been written in MATLAB®; it needs as input the geometrical data of the bearings and the load applied on them, giving as output the force reactions, the eccentricity value, and the angle of minimum film thickness.

The approach is based on the application of the Reynolds equation (3.1) under an iso-viscous approximation [8-9]:

$$\frac{\partial}{\partial x}\left(h^3\frac{\partial p}{\partial x}\right)+\frac{\partial}{\partial y}\left(h^3\frac{\partial p}{\partial y}\right)=6U\eta\frac{dh}{dx} \tag{3.1}$$

where h is the hydrodynamic film thickness, p is the film pressure, U is the bearing entraining velocity and η is the dynamic viscosity.

The code implements a discretization of the solution domain and resolves, with a finite difference method, the Reynolds equation in its non-dimensional form:

$$\frac{\partial}{\partial x^*}\left(h^{*3}\frac{\partial p^*}{\partial x^*}\right)+\left(\frac{R}{L}\right)\frac{\partial}{\partial y^*}\left(h^{*3}\frac{\partial p^*}{\partial y^*}\right)=6U\eta\frac{\partial h^*}{\partial x^*} \tag{3.2}$$

where R is the bearing radius and L is the bearing axial length.

To further improve the accuracy of the numerical solutions, a numerical parameter developed by Vogelpohl [10] has been implemented. This parameter, M_v, is defined as follows:

$$M_v=p^*h^{*1.5} \tag{3.4}$$

Substitution into the non-dimensional form of Reynolds equation (3.1) yields the so called "Vogelpohl equation":

$$\frac{\partial^2 M_v}{\partial x^{*2}}+\left(\frac{R}{L}\right)^2\frac{\partial^2 M_v}{\partial y^{*2}}=FM_v+G \tag{3.5}$$

where parameters F and G are evaluated as follows:

$$F=\frac{0.75\left[\left(\frac{\partial h^*}{\partial x^*}\right)^2+\left(\frac{R}{L}\right)^2\left(\frac{\partial h^*}{\partial y^*}\right)^2\right]}{h^{*2}}+\frac{1.5\left[\frac{\partial^2 h^*}{\partial x^{*2}}+\left(\frac{R}{L}\right)^2\frac{\partial^2 h^*}{\partial y^{*2}}\right]}{h^*} \tag{3.6}$$

$$G=\frac{\left(\frac{\partial h^*}{\partial x^*}\right)}{h^{*1.5}} \tag{3.7}$$

Therefore, giving as input the geometrical data of the bearing, the pump speed rotation and load, the subroutine evaluates the pressure field along the bearings, as it can be seen in Figure 3.2.

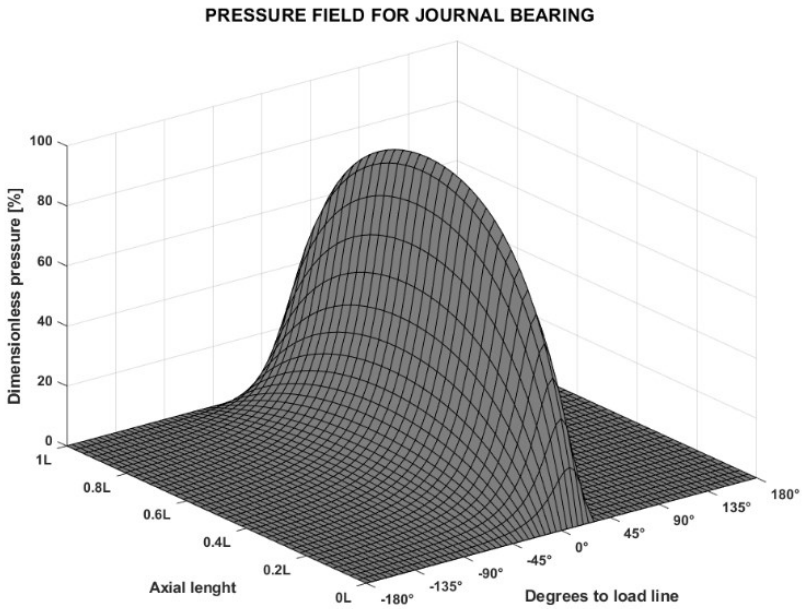

Figure 3.2. The non-dimensional pressure field evaluated by the new MATLAB® subroutine

The computational time required to resolve the numerical solution with a residual inferior to 10^{-5} is lower than a minute, streamlining considerably the iterative procedure to verify the force equilibrium condition present on the EgeMATor's workflow and, thus, identifying the real position of the gears inside the housing.

3.3. EgeMATor MP+

As said, the EgeMATor was capable to study only EGPs with spur gears; this limitation had to be overcome. The new release of the tool, named EgeMATor MP+ (External Gear Machine Multi Tool Simulator for Multiple Gears' Profiles), permits to simulate also pumps with a gears' profile that shifts along the axial dimension, like the helical gears profile.

The new tool has a different workflow described in Figure 3.3. The new capability can be seen in figure after the interference check, the tool now, in fact, verifies also the gears' profile typology: in presence of spur gears, the workflow proceeds as in the older version; while, if gears are helical, the new approach is activated running the new subroutines of the Surface Tool developed in EgeMATor MP+.

This new approach is based on considering gears as composed of a series of slices, with a limited axial extension, and each slice is shifted of a certain degree compared to the others. The relation between the slice axial extension dz) and its angular shift ($d\varphi$) against a reference slice is the following:

$$dz = \frac{b}{\beta} \cdot d\varphi \tag{3.8}$$

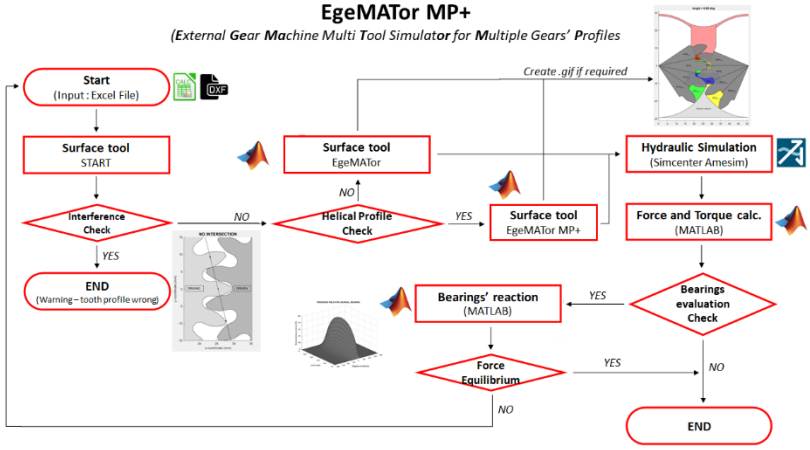

Figure 3.3. The EgeMATor MP+ (External Gear Machine Multi Tool Simulator for Multiple Gears' Profiles) workflow

where b is the axial length of the gears and β is the total helical angle. To obtain the total values of the geometric characteristics of the pump analyzed, like for example the volume of the displacement chamber, an integration is performed:

$$V = \int_{z_1}^{z_2} A dz = \frac{b}{\beta} \int_{\varphi_1}^{\varphi_2} A(\varphi) d\varphi \tag{3.9}$$

where the z_1 and z_2 are respectively the top and bottom surfaces of the gear; φ_1 and φ_2 are their respective profile angle on the area curve, and the function $A(\varphi)$ is the area curve, that could represent a displacement area or a variable area.

When the new subroutine included in the *Surface Tool* has terminated the evaluation of the geometrical properties of helical gears' profile, the workflow processes with the same iterations done in the previous version of the tool, giving to the hydraulic simulation the requested inputs.

At the present time, the evaluations of the force and torque in the case of the helical gears' profile is still incomplete because the script does not yet evaluate the component along the axial dimension of the pump, that is present on this typology of gear profiles. Therefore, following the workflow in Figure 3.3, at the stage "bearing evaluation check", in case of spur gears, EgeMATor MP+ works like EgeMATor evaluating the bearing reaction; in case of helical gears, the evaluation of the bearings' reaction is excluded, leading to termination.

Consequently, in the validation phase presented in the next section of this paper, the iterative process to find the force equilibrium has not been executed and the gears are positioned in contact with the housing along the vertical direction.

4. MODEL VALIDATION

To validate the new tool EgeMATor MP+, an experimental campaign on the previously mentioned reference helical EGP have been conducted on the test bench already described. The pump has been tested under four different pump speeds: 1000, 1500, 1800 and 2200 rev/min. The values of the delivery flow rate have been acquired for all the delivery pressure conditions in the range of 20÷240 bar. Simulations have been run for a fixed temperature of the hydraulic oil of 40°C.

The low computational time required to complete a simulation permits to run a high number of working conditions; therefore, for each pump speed six discrete value of delivery pressure have been simulated.

In detail, the simulations have been run for delivery pump pressure values of: 20, 50 100, 150, 200 and 240 bar.

In Figure 4.1 the comparison between the numerical model and the experimental results is presented; the flow-rate has been normalized to reference value, Q_{ref}.

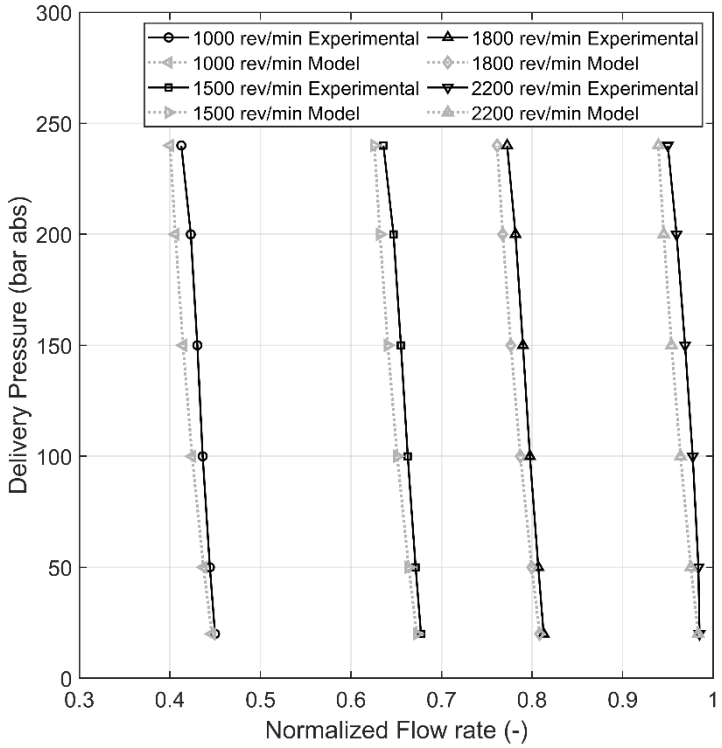

Figure 4.1. Pressure vs. normalized delivery flow rate comparison at different pump speed: 1000 rev/min, 1500 rev/min, 1800 rev/min and 2200 rev/min

It can be noted that EgeMATor MP+ correctly predicts the experimental with percentage errors between model and experimental data always below 3%, staying thus within the uncertainty range of the experimental measurements.

5. OPTIMAL GROOVE DESIGN RESEARCH METHODOLOGY

The validated numerical model for studying helical EGPs has been designed to include further capabilities such as optimization procedures. This section presents a preview of an under-development procedure that, for a given gears profile, will be able to optimize the pressure relief grooves inside the pump's wear plates. It is based on geometric assumptions to minimize the crossflow between delivery and suction while limiting pressure spikes. To better understand the methodology of this new procedure, a brief description of the considered internal connections is needed. Figure 5.1 shows a schematization of all the internal connection that have been implemented in the mode.

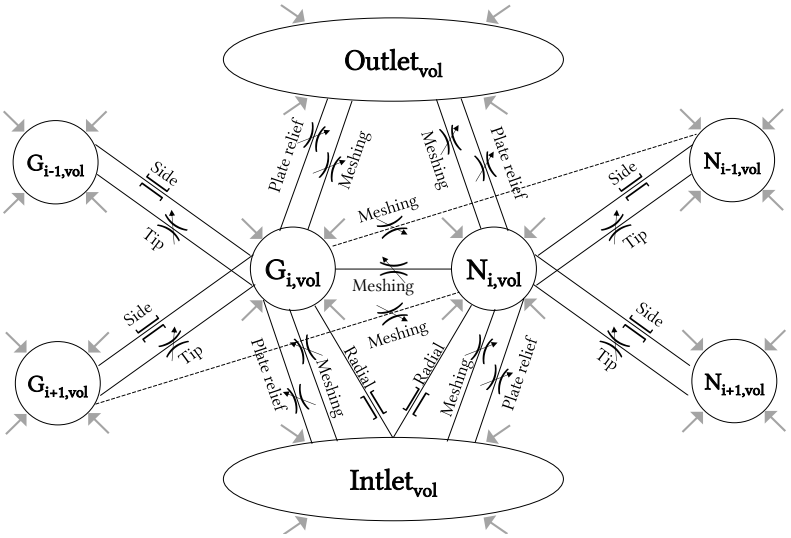

Figure 5.1. Schematized internal connection modeled in the *Surface Tool*

As it shown, the connections between the displacement chamber volumes ($G_{i,vol}$ - $N_{i,vol}$) and the plate relief grooves are modeled as variable orifice. The opening and closing timings paired with the cross-sectional area values of these connections are the characteristics that mainly affect the EGP performance and behavior.

The previously described *Surface Tool*, as said, estimates the volume of a displacement chamber as function of the rotation angle, φ. The new procedure implements a subroutine to find the rotation angle value that correspond the minimum chamber volume. This identified angle, $\varphi_{DC\ MIN}$, is of utmost importance since represents the angle when the instantaneous commutation between the delivery and suction pressure takes place. The optimization of the wear plate design in this area is fundamental for preventing unwanted pressure spikes.

After that, an iterative procedure can start. Since the procedure is under-development, at this stage only a simple rectangular shaped groove designs could be tested for both the delivery

and inlet groove. These shapes are characterized by a series of parameters, as shown in Figure 5.2. The parameters are normalized respect to the gear module *m* and vary between an interval of values, which can be seen in the Table 2.

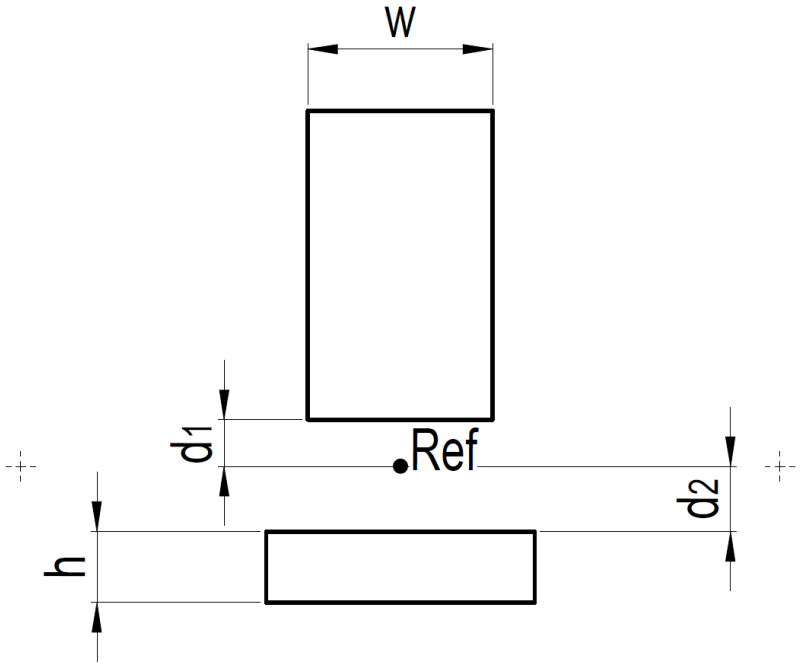

Figure 5.2. Reference parameters for the groove shape design search

Table 2. GROOVES PARAMETRIZATION

Description	***Value***	***Min***	***Max***
Delivery Groove width	W	1	3
Suction Groove height	h	0.5	2
Delivery Groove reference distance	d_1	0	3
Suction Groove reference distance	d_2	0	3

The designs obtained are tested against a series of target functions:

$$TF_1 = \left|\varphi_{DC_MIN} - \varphi_{GRV}\right| \tag{5.1}$$

$$TF_2 = \frac{1}{n}\sum_{i=1}^{n} A\left(\varphi_{DC_MIN} \mp n\Delta\varphi\right) - A_g\left(\varphi_{DC_MIN} \mp n\Delta\varphi\right) \tag{5.2}$$

The target function TF_1 in (5.1) has the objective to obtain higher volumetric efficiency. To achieve this objective, the TF_1 has to be minimized, that means minimize the angular difference between the rotation angle value of minimum chamber volume $\varphi_{DC\,MIN}$ and the characteristics rotation angle value for the grooves φ_{GRV}. In particular, for the delivery groove, φ_{GRV} represents the rotation angle value of connection closure between the groove and the delivery chamber, while φ_{GRV} represents the rotation angle value of connection opening between the groove and the delivery chamber for the suction groove.

The target function TF_2 in (5.2) has the objective of minimize the internal pressure peaks occurring during the meshing in proximity of $\varphi_{DC\,MIN}$. To accomplish this target, TF_2 has to be minimized, that is the difference between the cross-sectional area of the groove A_g (in dark red in Figure 9) and the projection area of the displacement chamber volumes on the lateral side A (in green in Figure 9) for a number n of points with an angular pitch distance from $\varphi_{DC\,MIN}$ equal to $\Delta\varphi$. This ensures a more gradual passage between the high and low pressure zones around the $\varphi_{DC\,MIN}$, reducing the pressure peaks. The minus or plus sign in (5.2) are respectively for the delivery or suction groove.

In this way, the design that minimize both target functions represent the best choice for the simplified geometry utilized. In the next steps, the procedure will be implemented to be executed for typical groove geometries. With this implementation, EgeMATor MP+ will be not only able to fully characterize EGPs with helical gears but also to optimize them by acting on the wear plates geometries. It can be appreciated from the table that the new design has a small advantage regarding the mean delivery flow, exhibiting a value increase of about 0.5%, pointing the way to a small improvement of the volumetric efficiency.

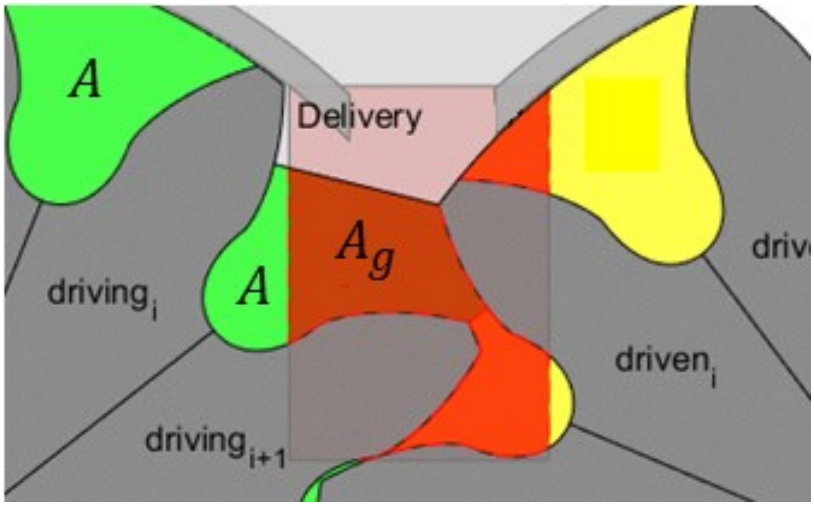

Figure 5.3. Areas evaluated in the optimal groove design methodology

6. CONCLUSIONS

A novel lumped parameter approach for studying external helical gear pumps has been described in this article. The tool, called *EgeMATor MP+*, has been developed to extend the functionalities of *EgeMATor*, a tool previously developed by the authors for the simulation of EGPs with spur gears.

Two important capabilities have been implemented. The first one was developed to include the bearing reactions and, consequently, to estimate the gears' eccentricity. This feature, developed in MATLAB®, substitutes a previous one executes by using a 3D-CFD approach with higher computational time. Secondly, the tool has been implemented to be applied to EGPs with helical gears.

The new tool has been run on a reference EGP geometry with helical gears. Model results have been compared with experimental data with errors always below 3%.

Finally, an under-development procedure has been firstly presented; it will allow the optimization of the wear plate designs avoiding pressure spikes in the transition area between suction and delivery.

NOMENCLATURE

Acronym	*Description*
EGP	External Gear Pump
CFD	Computational Fluid Dynamic
EGM	External Gear Machine

Symbol	*Description*	*Unit*
A	Area of displacement chamber	[m^2]
A_g	Cross-sectional area of groove	[m^2]
b	Axial length of the gears	[m]
F	First coefficient of the Vogelpohl equation	[-]
G	Second coefficient of the Vogelpohl equation	[-]
h	Hydrodynamic film thickness	[m]
h^*	Non-dimensional hydrodynamic film thickness	[-]
L	Bearings axial length	[m]
M_v	Vogelpohl parameter	[-]
p	Pressure	[Pa]
p^*	Non-dimensional pressure	[-]

Q_{ref}	Reference flow rate	[L/min]
R	Bearings radius	[m]
U	Bearings entraining velocity	[m/s]
x^*	Non-dimensional x-coordinate of the hydrodynamic film	[-]
y^*	Non-dimensional y-coordinate of the hydrodynamic film	[-]
z	Axial extension of the slices	[m]
z_1	Axial start position for the reference profile	[m]
z_2	Axial finish position for the reference profile	[m]

Greek letter	***Description***	***Unit***
β	Total helix rotation angle	[rad]
φ	Gear profile rotation angle	[rad]
φ_1	Axial profile angle start position for the reference profile	[rad]
φ_2	Axial profile angle finish position for the reference profile	[rad]
$\varphi_{DC\ MIN}$	Gear profile rotation angle of instantaneous commutation (minimum chamber volume)	[rad]
φ_{GRV}	Groove rotation angle characteristics	[rad]
$\Delta\varphi$	Angular pitch value for optimization function	[Pa · s]
η	Dynamic viscosity of the hydrodynamic film	[-]

7. REFERENCES

[1] Marinaro, G., Frosina, E., Senatore, A. "A Numerical Analysis of an Innovative Flow Ripple Reduction Method for External Gear Pumps." Energies. 2021; 14(2):471. https://doi.org/10.3390/en14020471.

[2] Frosina, E., Senatore, A., Rigosi, M. "Study of a High-Pressure External Gear Pump with a Computational Fluid Dynamic Modeling Approach." Energies. 2017; 10(8):1113. https://doi.org/10.3390/en10081113.

[3] Heisler, A. S., Moskwa, J. J., Fronczak, F. J. "Simulated Helical Gear Pump Analysis Using a New CFD Approach." Proceedings of the ASME 2009 Fluids Engineering Division Summer Meeting. Volume 1: Symposia, Parts A, B and C. Vail, Colorado, USA. August 2–6, 2009. pp. 445-455. ASME. https://doi.org/10.1115/FEDSM2009-78472

[4] Qi, F., Dhar, S., Nichani, V., Srinivasan, C. et al., "A CFD study of an Electronic Hydraulic Power Steering Helical External Gear Pump: Model Development, Validation and Application," SAE Int. J. Passeng. Cars - Mech. Syst. 9(1):346-352, 2016, https://doi.org/10.4271/2016-01-1376.

[5] Borghi, M., Zardin, B., Specchia, E., "External Gear Pump Volumetric Efficiency: Numerical and Experimental Analysis," SAE Technical Paper 2009-01-2844, 2009, https://doi.org/10.4271/2009-01-2844.

[6] Battarra, M., Mucchi, E., "A method for variable pressure load estimation in spur and helical gear pumps." Mechanical Systems and Signal Processing, Volumes 76–77, 2016, Pages 265-282, ISSN 0888-3270, https://doi.org/10.1016/j.ymssp.2016.02.020.

[7] Ransegnola, T., Zhao, X., Vacca, A. "A comparison of helical and spur external gear machines for fluid power applications: Design and optimization." Mechanism and Machine Theory, Volume 142, 2019, 103604, ISSN 0094-114X, https://doi.org/10.1016/j.mechmachtheory.2019.103604.

[8] Stachowiak, G. W., Batchelor, A. W., "4 - Hydrodynamic Lubrication", Editor(s): Stachowiak, G. W., Batchelor, A. W., Engineering Tribology (Third Edition), Butterworth-Heinemann, 2006, Pages 103-204, ISBN 9780750678360, https://doi.org/10.1016/B978-075067836-0/50005-5.

[9] Stachowiak, G. W., Batchelor, A. W., "5 – Computational Hydrodynamics", Editor(s): Stachowiak, G. W., Batchelor, A. W., Engineering Tribology (Third Edition), Butterworth-Heinemann, 2006, Pages 205-259, ISBN 9780750678360, https://doi.org/10.1016/B978-075067836-0/50006-7.

[10] Prandtl, L. (1938), Dr.-Ing. G. Vogelpohl Vdi, Beiträge zur Kenntnis der Gleitlagerreibung. Mitteilung aus dem Institut für Techn. Strömungsforschung a. d. Techn. Hochschule Berlin, Leitung; Prof. Dr.-Ing. H. Föttinger VDI (VDI-Forschungsheft 386, Beilage zu „Forschung auf dem Gebiete des Ingenieurwesens", Ausgabe B, Bd. 8, Sept./Okt. 1937.) 28 S. m. 38 Abb. u. 6 Zahlentafeln. Berlin 1937, VDI-Verlag, GmbH. Preis 5 M. Z. angew. Math. Mech., 18: 313-314. https://doi.org/10.1002/zamm.19380180507.

Biographies



Pietro Mazzei received his B.Sc and M.Sc of Mechanical Engineering degree at Federico II of Naples University, Italy in 2021. He received his Ph.D. degree on Industrial

Engineering in 2023, focusing on the development of numerical models to analyze and optimize the performances and the noise emissions of external gear machines. Currently he is employed at CIRA (Centro Italiano Ricerche Aerospaziali) on the development of hybrid LTA vehicle as a pressure and thermal modeling expert.

High fidelity data generation and fault diagnosis of a gear pump

Kayal Lakshmanan[1], Fabrizio Tessicini[2], Antonio J. Gil[1], Ferdinando Auricchio[3]

[1] *Faculty of Science and Engineering Swansea University Swansea, UK*
k.lakshmanan@swansea.ac.uk
[2] *Innovation Head F-Lab Milano, Italy*
[3] *Department of Civil Engineering and Architecture University of Pavia Pavia, Italy*

Abstract

The sudden failure of industrial components can adversely affect an organisation regarding time, cost, and workflow. To prevent downtime that could result in a major disruption, it is crucial to keep equipment components in optimal condition. Hence developing a system that can detect an equipment failure early is essential. The present work proposes a computational strategy of fault diagnosis using Machine Learning (ML) algorithms for an external gear pump. Due to the lack of sufficient experimental data, a novel approach of creating a high-fidelity in-silico data using a Computational Fluid Dynamic (CFD) model of the gear pump in both normal and defective working conditions (viscosity variations, radial gap variations, speed variations, etc.) is introduced. A novel synthetic data generation technique is implemented by perturbing the frequency content of the time series to recreate other working conditions. These synthetically generated datasets are used to train the underlying ML metamodel. Three different ML classification algorithms are used for fault diagnosis, namely Multilayer Perceptron (MLP), Naive Bayes (NB),and Support Vector Machine (SVM).

River Journal, 1–16.
© 2024 *River Publishers. All rights reserved.*

1 Introduction

Gear pumps are comprised of sophisticated gear arrangements used to pump fluid under a variety of working conditions. For example, the Fluid-o-tech external gear pump has been used within medical equipment, ink-jet printing systems, cooling systems, sanitisation applications, etc. [1]. Due to a sophisticated and compact design, external gear pumps can be easily fit inside complex industry equipment reducing the manufacturing time and associated cost. However, the sudden failure of any industry component can have negative consequences on the industry in terms of time and workflow. As a result, Predictive Maintenance has emerged as a necessary tool to predict failure and minimise industrial downtime and associated cost. Predictive Maintenance techniques help determine the condition of in-service equipment to predict when maintenance should be performed. It is crucial to monitor the actual mechanical condition of the machine's health regularly to avoid sudden failure.

In order to perform fault diagnosis using data-driven approaches, the actual condition of the gear pump needs to be monitored. Additionally, the availability of a sizable collection of high-fidelity data is crucial for ML predictive capabilities [2]. High-fidelity in-silico data can be used to replace experimental data in cases where it is unavailable or not sufficient [3, 4]. In this work, the gear pump operations are accurately modelled using a CFD model that can simulate both normal and varied fault cases such as radial gap variations, clogging, viscosity variations, etc. From these simulations, pressure, flow rate, and torque are monitored for several working conditions of the pump.

A noise perturbation method is introduced by increasing noise function in specific frequency components monotonically to reproduce potential environmental fluctuations of the working pump from the in-silico data [5, 6]. Finally, the synthetically generated datasets are used to extract the features that will eventually be used to train an ML model.

The nearest neighbour algorithm, SVM, probabilistic-based algorithms like the Bayesian network, and Naive Bayes are traditionally used for fault detection [7]. Currently, Artificial Neural Networks, fuzzy–neural networks, evolutionary algorithms, and deep learning algorithms are widely used ML techniques for fault diagnosis [8, 9, 10]. The recurrent neural network and the convolutional neural network models have demonstrated enhanced performance over time in the field of fault diagnostics [11, 12, 13, 14].

This industry-academia collaboration sought to address one specific bottleneck: finding an efficient strategy to create a reliable dataset with the same properties of the real-world data and perform fault diagnosis of the external gear pump with insufficient availability of experimental data. As a result, this work has proposed a fault diagnosis methodology using supervised learning ML algorithms MLP, SVM and NB and synthetic data generation methods to support ML algorithms.

Following the introduction, Section 2 introduces the generation of high-fidelity in silico data using a Computational Fluid Dynamics (CFD) model of a gear pump, Section 3 describes the synthetic generation method, Section 4 presents the framework fault diagnosis, and Section 5 summarises the conclusions.

2 Generation of High-fidelity data using Computational fluid dynamics simulation of an external gear pump

The CFD model is developed utilising the commercial code 'Simerics MP+' that numerically solves the mass, momentum, and energy conservation equations. Also incorporates precise physical models for turbulence and cavitation. The mathematical model and governing equations are detailed in [15].

2.1 Geometry

Gear pumps are rotating positive displacement external gear pumps, where the fluid is displaced from the inlet side of the pump to the outlet side of the pump due to the intermeshing of the drive and the slave gear's teeth. The geometry of the external gear pump, which is of main interest to this work, is shown in Figure 1. However, some specific geometry features have been hidden due to commercial sensitivity.

The lubrication channel is connected to the gears through the top channel with rotating shafts, and the gears are sealed inside a tight, leak-free housing. Likewise, a bottom channel with rotating shafts connects the rear side of the gear to the magnet. The inlet and outlet ports are connected to the sides of the gear. The inlet and outlet sensors are placed in the inlet and outlet ports. The outlet sensor is placed away from the end to avoid reversing the flow and accurately measure the pressure distribution in the outlet port. During the operation, these types of pumps are noiseless, pulsation-free and capable of

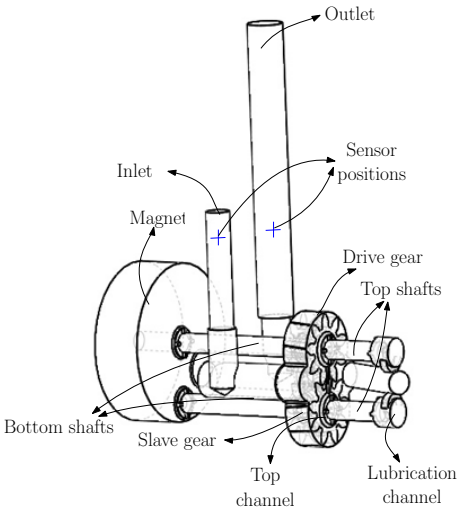

Figure 1 Geometry of the external gear pump. Specific features of the geometry and the measurements have been hidden due to commercial sensitivity.

handling liquids up to 95 °C with pressure up to 12 bar and flow rate up to 210 l/h [1].

2.2 Model attributes

The fluid domain of the external gear pump is extracted from the Computer-Aided Design (CAD) of the pump, which is provided by the industrial partner F-Lab and the geometry is imported into Simerics MP+. For extremely curved sections or narrow cut portions, high-quality hexahedral cells are produced using the binary tree unstructured mesh. Additionally, Simerics MP+ features a specialised tool for meshing the interior geometry of the gear using a rotor gear template mesh, resulting in highly structured hexahedral cells of excellent quality [16]. The entire fluid domain's mesh is created utilising Simerics MP+ with 446393 cells (see Figure 2). High-quality hexahedral cells are generated using the unstructured mesh for high-curved or narrowly cut sections, such as shafts and magnets.

The simulation of an external gear pump running in healthy conditions use the conditions presented in Table 2.2. The boundary condition for the inlet pressure is atmospheric pressure and for the outlet is 3.15 bar.

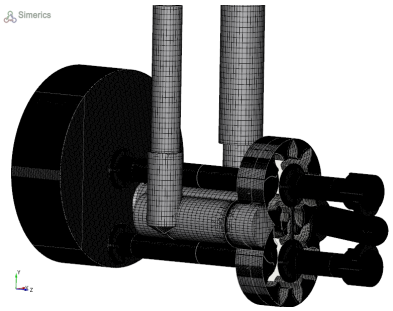

Figure 2 Mesh of the external gear pump (the entire fluid domain) created using Simerics MP+.

Table 1 Properties of a healthy (normal working condition) gear pump.

Operating conditions of the gear pump	
Speed	1450 rpm
Radial gap	0.03 mm
Number of drive gear teeth	9
Number of slave gear teeth	9
Material properties of the gear pump	
Viscosity	0.0383 Pa-s
Density	800 kg/m^3
Temperature	300 K

2.2.1 Mesh sensitivity analysis

A mesh sensitivity analysis is carried out, whereby a finer and finer mesh is used until a threshold of accuracy is passed going from one model to the next [17]. For simplicity and to optimise the number of cells, a simpler geometry is considered with the inlet port, the outlet port, and external gear in Figure 1. Simulations are performed for fixed time step with four different grid sizes (h_1, h_2, h_3, h_4) ranging from coarse to fine mesh. The properties of different grid sizes and their commutation time are displayed in Table 2. Figure 3 illustrates the relative error percentage of pressure, flow rate, and torque at a fixed time step for the various cell counts, and it can be seen that the relative error reduces as the cell count increases. Due to the effectiveness of the Simerics MP+, even though the discretisation accuracy in the case of the h3 mesh is of first order, the accuracy of the solution is above second order. As an outcome of this investigation, all CFD analyses are carried out using mesh size h3.

Table 2 Mesh sensitivity analysis: execution time is in a dimensionless quantity, where h_1 is used as reference.

	h_1	h_2	h_3	h_4
No of elements	44518	247495	446393	4605699
Max cell size	0.1	0.07	0.03	0.018
Min cell size	0.005	0.005	0.002	0.001
Execution time	1	3.24	7.57	182.76

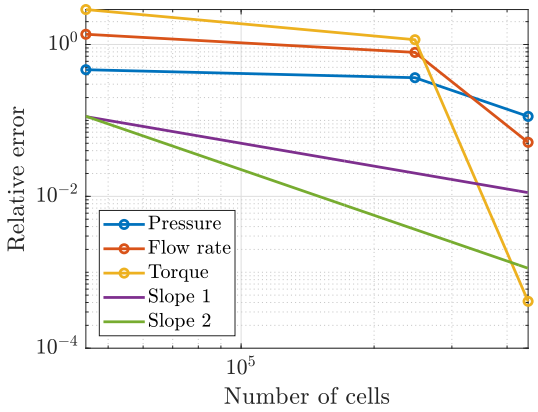

Figure 3 Relative error of pressure, flow rate and torque (fixed time step) in relation to finest mesh (h_4).

2.3 CFD model validation against experimental data

To validate the CFD model, our industrial partner provided the experimental results of the external gear pump (Figure 1) with the exact specifications mentioned in Section 2.2. The gear pump experiment was carried out by setting speed and viscosity levels for various outlet pressure values from 1 to 9 bar. The inlet pressure is assumed to be atmospheric pressure (1.01325 bar) for all the experiments. The discharge flow rate has been measured for each experiment, and the average of these values has been used to validate the CFD model. Particularly, the investigations were performed out for the gear's two distinct rotational speed values, 1450 rpm and 2900 rpm. For the 1450 rpm speed, two different viscosity values, 0.001 Pa-s and 0.075 Pa-s and for the 2900 rpm, three different viscosity values, 0.001 Pa-s, 0.02 Pa-s and 0.075 Pa-s are considered. CFD simulations with the healthy scenario, different speed scenarios, and different viscosity scenarios are validated against experimental

values. The following results are standardised using standardisation or z-score normalisation technique for the confidentiality purpose. Standardisation is expressed as $\boldsymbol{x} - \mu/\sigma$, where $\boldsymbol{x}$ is data vector and μ and σ is mean and standard deviation of $\boldsymbol{x}$.

Figure 4 compares the standardised average experimental outlet flow rate of a gear pump with a rotating speed of 1450 rpm to the CFD simulation models for various pressure levels and two different viscosity levels of 0.001 Pa-s and 0.075 Pa-s. The relative pressure, that is, the difference between outlet and inlet pressure values are shown in x-axis. Figure 5 compares the standardised average experimental outlet flow rate of a gear pump with a rotating speed of 2900 rpm to the CFD simulation models for various pressure levels and two different viscosity levels of 0.001 Pa-s and 0.075 Pa-s. From Figures 4 and 5, it can be seen that the simulation results are in very good agreement with experiments. Additionally, a greater viscosity value leads to a high discharge flow rate.

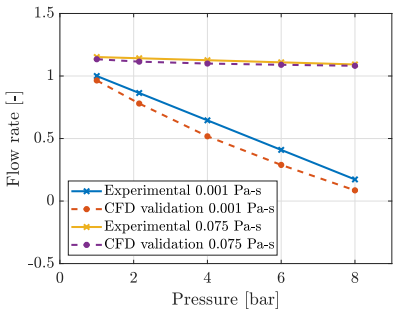

Figure 4 Standardised average outlet flow rate of experimental results against CFD model of gear pump with speed of 1450 rpm for different relative pressure values.

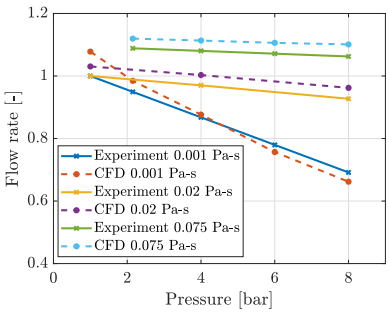

Figure 5 Standardised average outlet flow rate of experimental results against CFD model of gear pump with speed of 2900 rpm for different relative pressure values.

2.4 Implementation of fault conditions in the external gear pump

After validating various viscosity values and two different speed values in the CFD simulations with experimental values, we have built potential fault scenarios which can cause the pump to degrade or even fail. The fault scenarios are built to understand the pump's complete behaviour when running in an abnormal condition. Finally, various working conditions are recreated based on the validated CFD models and the experience of the industrial partner, including, radial gap degradation, axial gap degradation, speed variations(validated

experimentally), viscosity variations(validated experimentally), temperature variations and clogging (or blocking) variations, as depicted in Figure 6.

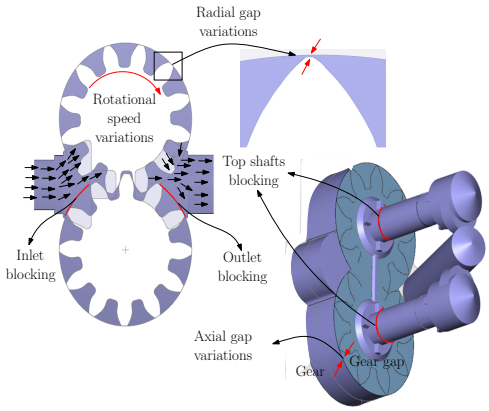

Figure 6 Developed fault scenarios using the gear pump's normal operating state as a benchmark.

The fault variables and their various cases (in percentage) are displayed in Table 2.4. The percentage is calculated considering the healthy working conditions parameters of the gear pump as a reference. Following Section 2.2, all fault scenarios are simulated.

Table 3 Implemented fault scenarios; the percentage is calculated considering healthy working conditions parameters of gear pump as reference.

Fault scenarios	Different cases
Radial gap degradation (G)	66.66%, 133.33%, 200%
Axial gap degradation (A)	2.5%, 5%, 7.5%
Speed variations (S)	1.78%, 3.57%, 5%
Viscosity variations (V)	0.8%, 1.6%, 2.4%
Temperature variations (T)	2.5%, 5%, 7.5%
Clogging variations (C)	blocked inlet, outlet, top shafts

For all cases, the gear pump is run for five gear revolutions (1450 rpm) with an atmospheric (1.01325 bar) inlet pressure and outlet pressure of 3.15 bar. The first revolution is for the initialisation of flow, and the second to fifth revolution is considered for the results. For data acquisition, pressure at the outlet sensor (sensor shown in Figure 1), the discharge flow rate and the sum of drive and slave gear's torque have been considered primary sensor variables.

For instance, fault scenarios due to radial gap degradation are created based on the concept that mass particles can enter the pump, causing the gear teeth and the gear case to erode, as displayed in Figure 6. In our work, the radial gap faults are generated by increasing the gap between the gear and the gear case and re-running appropriate CFD simulations. Step-by-step degradation behaviour is generated, namely G1, G2 and G3, to understand the erosion behaviour between the gear teeth and gear case. The standardised discharge flow rate of the scenarios (G1, G2, G3) compared with the healthy scenario (H) is shown in Figure 7. The mean flow rate of G1, G2 and G3 is decreased by 21%, 40% and 56%, respectively, concerning the healthy scenario; this concludes that increasing the gap size decreases the mean flow rate.

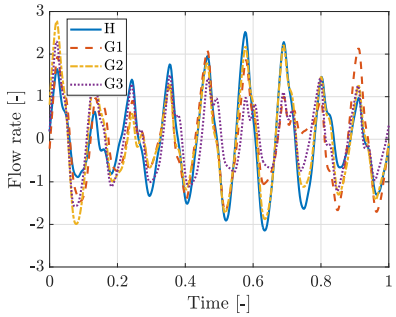

Figure 7 Discharge flow rate with respect to time of radial gap fault scenarios.

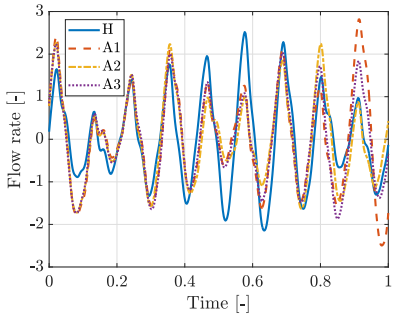

Figure 8 Discharge flow rate with respect to the time of axial gap fault scenarios.

The axial gap degradation are designed to understand the impact of flow leakage inside the fluid volume. They are produced by widening the axial gap (side leakage) between the gear and the gear perimeter without moving the gear centre, as shown in 6. Similar to radial gap fault scenarios, the discharge flow rate decreases with the incremental increase of axial gap size. The standardised discharge flow rate of scenarios (A1, A2, A3) compared with the healthy scenario (H) is shown in Figure 8. Comparing to the healthy scenario, the mean flow rate of axial gap variations (A1, A2 and A3) is decreased by 2%, 4% and 6.3%, respectively.

The fault scenarios due to speed variations are introduced by increasing the rotational speed (in RPM) of the gear pump to find out the flow behaviour. The speed variations are created to validate that for positive displacement pumps, as the rotational speed increases, the discharge flow rate increases in linear trend, which is proven in [16] for an external gear pump. The step-by-

step increase in speed variations (S1, S2 and S3) increases the mean flow rate by 2%, 4.5% and 6.3%, respectively, concerning the healthy scenario.

The fault scenarios due to viscosity variations are produced to learn the pump's flow performance in the change of viscosity values. Gear pumps are best suitable for high viscosity applications. When the fluid viscosity decreases, slip increases; the slip is when the pump recirculates from the outlet to the inlet side as it escapes through machined clearances while the pump tries to progress forward. The amount of slip is determined by the fluid's viscosity and discharge pressure. A thin fluid with a low viscosity can squeeze through the clearances more easily than thicker fluids, where high discharge pressure can force thinner fluids back through the pump, causing more slipping. Because thin fluids slip, the pump's efficiency decreases as less product progress with the forward movement, hence the lower discharge flow rate. As a result, the mean flow rate of viscosity variations (V1, V2 and V3) is increased by 0.4%, 1% and 1.5%, respectively, compared to the healthy scenario.

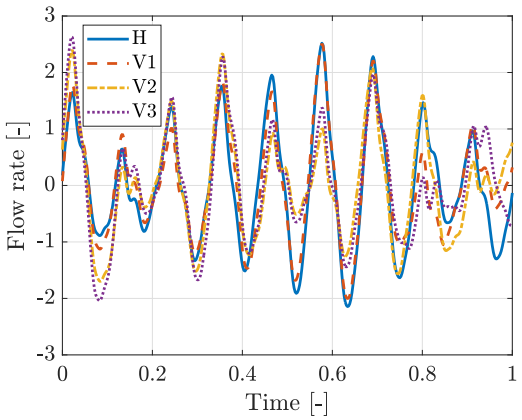

Figure 9 Discharge flow rate with respect to the time of radial gap fault scenarios.

The fault scenarios due to temperature variations are generated to comprehend the changes in the gear pump's performance with respect to temperature variations. An increase in temperature heats up the fluid transported through the pump, which reduces the fluid viscosity. As discussed above, an increase in viscosity increases the discharge flow rate. So, due to an increase in temperature, the viscosity decreases, which implies that the discharge flow rate decreases. Considering the healthy scenario, the mean flow rate of temper-

ature variations (T1, T2 and T3) is decreased by 0.16%, 0.25% and 0.33%, respectively.

The fault scenarios due to clogging or blocking are implemented to validate the sudden disturbances due to any blockages in the pump. For this reason, various parts of the pump, the outlet (C1), the inlet (C2) and the top shafts (C3), are partially blocked. The CFD simulation is performed, and the discharge flow rate can be measured. Blocking a part of the outlet (C1) and part of the inlet (C2), the discharge flow rate is decreased by 4% and 0.5%, and however, when blocking the top shafts (C3), the discharge flow rate is increased by 0.19%.

The results of the faulty scenarios are extracted in time series, which will be used perform the fault diagnosis in Section 4.

3 Synthetic data generation method for fault diagnosis using a noise perturbation method

A large amount of data is a prerequisite for any ML algorithm in order to better the learning phase. Using a noise perturbation method, the high-fidelity data generated by the CFD model is modified to simulate potential environmental fluctuations of the working pump settings. The addition of noise is carried out by perturbing the frequency content by an error function constructed in the following manner

$$\hat{x}^{mod}(\tilde{\omega_j}) = \hat{x}(\tilde{\omega_j})[1 + \alpha\epsilon(\tilde{\omega_j})] \tag{1}$$

where $\hat{x}(\tilde{\omega_j})$ is the original frequency content (for a selected frequency ω_j) obtained from a discrete Fourier transform, α is a scalar parameter tuned depending on the amount of noise added and $\epsilon(\omega_j)$ is a monotonically increasing function of the frequency ω (larger noise added in larger frequencies).

4 Fault diagnosis results

The present section presents a fault diagnosis (fault detection) of the external gear pump by means of the three alternative ML algorithms, namely MLP, SVM and NB. The overview of the designed fault diagnosis simulation process is depicted in Figure 10.

The availability of huge collections of high-fidelity data is essential for ML predictive performance [2]. In case of limited experimental data avail-

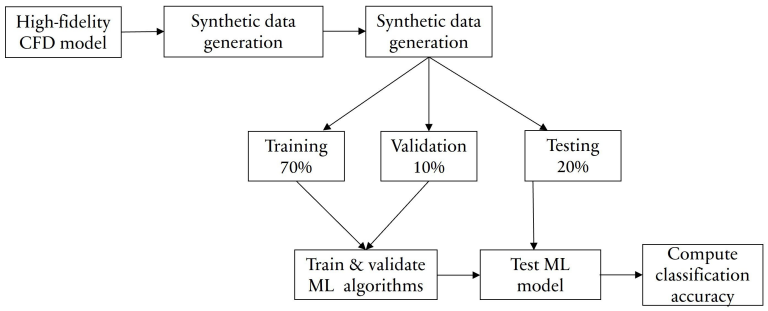

Figure 10 Overview process of fault diagnosis using ML classification algorithms.

ability (or absence), these can be superseded using high-fidelity in-silico data. The aspect of high-fidelity data generation has been discussed in Section 2. Large volumes of data are typically required to improve any ML algorithm's predicted response. A synthetic data generation method is implemented to facilitate the gathering of data greatly (see Section 3).

Once the dataset is gathered, it is divided into a training dataset (used to fit the model) comprised of 70%, validation comprised of 10%, and a test dataset (used to provide an unbiased evaluation of a final model fit on the training dataset) comprised of the remaining 20% randomly. The training dataset is used to train each ML algorithm, which is tested against the test dataset, and the accuracy of the model is computed. In this work, the optimisation of these hyper-parameters is performed using a random search for all the methods.

For this example, we consider the healthy dataset (H) and all six types of fault scenarios implemented with 18 different cases (C1, C2, C3, G1, G2, G3, S1, S2, S3, T1, T2, T3, W1, W2, W3 V1, V2, V3). Variables such as pressure, flow rate and torque are monitored for all the fault scenarios. These datasets are in the form of a discrete set of time values. The synthetic data generation approach is used to increase the availability of data needed to train the ML approach. The generated datasets are standardised and used as input datasets for training and testing ML algorithms. The output data is considered as labels (H, C1, C2,...V2, V3). The training dataset is trained using MLP, SVM and NB and tested against the test dataset, where the accuracy of the test dataset is calculated between model output and desired output. Following the overview designed process of fault diagnosis in Figure 10, a fault diagnosis is performed for the desired dataset.

The backpropagation technique is employed for the training of the MLP network to optimise the updating of the weights in accordance with the loss

function given during model development. The backpropagation algorithm requires that the network is trained for a specified number of epochs to the training dataset. Each epoch can be partitioned into groups called batches. The batch size determines how many patterns the network is exposed to in a single epoch before the weights are adjusted. The model loss is typically displayed in relation to the number of epochs. This plot can detect if the model is overfitting, underfitting or suitably fitting to the training dataset [18]. Furthermore, the Early Stopping Argument is utilised to terminate the training when the selected performance metric reaches a point of no further improvement [19]. For SVM classification, three hyper-parameters are considered: kernel function, kernel parameter, and regularisation parameter. A random search algorithm is utilised to ensure the optimal choice of hyper-parameters for SVM.

Table 4 Classification accuracy of pressure, flow rate and torque using MLP, SVM and NB.

	MLP	SVM	NB
Pressure	100.0 %	99.12 %	99.28 %
Flow rate	100.0 %	97.42 %	94.75 %
Torque	98.23 %	94.64 %	69.92 %

Table 4 shows the classification test accuracy of pressure, flow rate and torque using ML algorithms MLP, SVM and NB. The accuracy obtained using ML algorithms, compared to pressure and flow rate, torque provides relatively lower accuracy. In contrast, the use of a flow rate provides the highest fault diagnosis accuracy. Moreover, for almost all cases, the classification accuracy is high due to the discrete information of various fault cases, however, torque suffers from comparatively low accuracy with all three ML algorithms, especially with NB.

5 Conclusion and remarks

This paper has presented a novel methodology for fault diagnosis using Machine Learning (ML) algorithms for an external gear pump. In this regard, the main novelty of this work is the generation of high-fidelity data for the external gear pump, using CFD models and synthetic data generation methods, and a framework for a fault diagnosis strategy with the application of ML algorithms.

In-silico data generation techniques offer a long-term resolution to limited or missing experimental data and provide additional investigation through ML or other data analysis techniques. Moreover, the synthetic data generation method can be employed where data privacy can be of significant concern. Fault diagnosis of the gear pump has been performed using feature extraction methods and three types of ML classification algorithms: MLP, SVM, and NB.

The engineering sector is primarily interested in finding affordable ways to do these assessments. This would suggest the use of the torque as the magnitude to be most easily monitored because it is linearly related to current absorption, which can be monitored via the current sensor. Hence, torque analysis is performed for fault diagnosis. However, compared to pressure and flow rate, torque provides comparatively lower classification accuracy, which results in the question of accuracy versus cost. If the industry chooses to use torque to perform fault diagnosis, then there is a trade between the cost and accuracy.

References

[1] Fluid-o-tech. URL `https://www.fluidotech.it/en/products/technologies/external-gea` Accessed: 2021-04-03.

[2] Ziad Obermeyer and Ezekiel J Emanuel. Predicting the future—big data, machine learning, and clinical medicine. *The New England journal of medicine*, 375(13):1216, 2016.

[3] Yaomin Zhao, Harshal D Akolekar, Jack Weatheritt, Vittorio Michelassi, and Richard D Sandberg. Rans turbulence model development using cfd-driven machine learning. *Journal of Computational Physics*, 411: 109413, 2020.

[4] Faria T Zahura, Jonathan L Goodall, Jeffrey M Sadler, Yawen Shen, Mohamed M Morsy, and Madhur Behl. Training machine learning surrogate models from a high-fidelity physics-based model: Application for real-time street-scale flood prediction in an urban coastal community. *Water Resources Research*, 56(10):e2019WR027038, 2020.

[5] Kayalvizhi Lakshmanan, Antonio J Gil, Ferdinando Auricchio, and Fabrizio Tessicini. A fault diagnosis methodology for an external gear pump

with the use of machine learning classification algorithms: Support vector machine and multilayer perceptron. Loughborough University, 2020. doi: https://doi.org/10.17028/rd.lboro.12097668.v1.

[6] Kayal Lakshmanan, Fabrizio Tessicini, Antonio J Gil, and Ferdinando Auricchio. A fault prognosis strategy for an external gear pump using machine learning algorithms and synthetic data generation methods. *Applied Mathematical Modelling*, 123:348–372, 2023.

[7] B Samanta. Gear fault detection using artificial neural networks and support vector machines with genetic algorithms. *Mechanical systems and signal processing*, 18(3):625–644, 2004.

[8] Arfat Siddique, GS Yadava, and Bhim Singh. Applications of artificial intelligence techniques for induction machine stator fault diagnostics. In *4th IEEE International Symposium on Diagnostics for Electric Machines, Power Electronics and Drives, 2003. SDEMPED 2003*, pages 29–34. IEEE, 2003.

[9] Matheus F Torquato, Kayal Lakshmanan, Natalia Narożańska, Ryan Potter, Alexander Williams, Fawzi Belblidia, Ashraf A Fahmy, and Johann Sienz. Cascade optimisation of battery electric vehicle powertrains. *Procedia Computer Science*, 192:592–601, 2021.

[10] Kayal Lakshmanan, Eugenio Borghini, Arnold Beckmann, Cameron Pleydell-Pearce, and Cinzia Giannetti. Data modelling and remaining useful life estimation of rolls in a steel making cold rolling process. *Procedia Computer Science*, 207:1057–1066, 2022.

[11] Dawei W Dong, John J Hopfield, and KP Unnikrishnan. Neural networks for engine fault diagnostics. In *Neural Networks for Signal Processing VII. Proceedings of the 1997 IEEE Signal Processing Society Workshop*, pages 636–644. IEEE, 1997.

[12] C James Li and Tung-Yung Huang. Automatic structure and parameter training methods for modeling of mechanical systems by recurrent neural networks. *Applied Mathematical Modelling*, 23(12):933–944, 1999.

[13] Roberto M Souza, Erick GS Nascimento, Ubatan A Miranda, Wenisten JD Silva, and Herman A Lepikson. Deep learning for diagnosis and

classification of faults in industrial rotating machinery. *Computers & Industrial Engineering*, 153:107060, 2021.

[14] Kayal Lakshmanan, Davide Balatti, Hamed Haddad Khodaparast, Michael I Friswell, and Andrea Castrichini. Experimental and numerical gust identification using deep learning models. *Applied Mathematical Modelling*, 132:41–56, 2024.

[15] Hui Ding, FC Visser, Y Jiang, and M Furmanczyk. Demonstration and validation of a 3d cfd simulation tool predicting pump performance and cavitation for industrial applications. *Journal of fluids engineering*, 133 (1), 2011.

[16] Feng Qi, Sujan Dhar, Varun Haresh Nichani, Chiranth Srinivasan, De Ming Wang, Liang Yang, Zhonghui Bing, and Jinming Jim Yang. A cfd study of an electronic hydraulic power steering helical external gear pump: Model development, validation and application. *SAE International Journal of Passenger Cars-Mechanical Systems*, 9(2016-01-1376):346–352, 2016.

[17] Wu-Gui Jiang, Ren-Zhi Zhong, Qing H Qin, and Yong-Gang Tong. Homogenized finite element analysis on effective elastoplastic mechanical behaviors of composite with imperfect interfaces. *International journal of molecular sciences*, 15(12):23389–23407, 2014.

[18] Koushal Kumar and B Abhishek. *Artificial neural networks for diagnosis of kidney stones disease*. GRIN Verlag, 2012.

[19] François Chollet et al. Keras, 2015. URL `https://keras.io`. Accessed: 2020-09-06.

Simulation Model of a Helical Gear Pump for the Evaluation of the Filling Capability

Alessandro Corvaglia[1], Massimo Rundo[1,*], Sara Bonati[2], Manuel Rigosi[2]

[1] *Department of Energy, Politecnico di Torino, 10129 Turin, Italy*

[2] *Casappa S.p.A., 43044 Lemignano di Collecchio, Italy*

**Corresponding author: massimo.rundo@polito.it*

Abstract.

In this paper, a computational fluid dynamics model of a helical gear pump developed in SimericsMP+ is presented. The aim of the study is the analysis of the phenomena occurring in the suction side in conditions of incomplete filling at high velocity. The model was validated by measuring the delivered flow rate as function of the inlet pressure for different angular speeds. The experimental tests have demonstrated the capability of the model to detect with a good accuracy the operating conditions for which the delivered flow rate starts to decrease due to the partial filling of the inter-teeth chambers. Based on this study, the model seems accurate enough to be used as design tool for optimizing the pump in order to improve the filling capability.

Keywords. helical gear pump, incomplete filling, CFD, SimericsMP+.

1. INTRODUCTION

A current trend in the field of hydraulic power units is the control of the flow rate through variable speed electric prime movers driving a fixed displacement pump. In particular, the electro-hydrostatic actuators (EHA), initially developed for aeronautic applications, are mature enough to substitute the centralized hydraulic circuit in many off-road vehicles [1]. For instance, in the field of earth moving machines, many different layouts have been analyzed for achieving a fuel saving [2], including the use of individual electro-hydraulic drives for the main actuators [3]. The gear pumps are the most suitable units for such applications. The internal gear machines (crescent pumps) have the advantage that, at equal geometry of the driver gear, the kinematic flow ripple is almost an order of magnitude smaller than in an external gear pump [4]. Such a favorable characteristic leads to a lower noise, although in this aspect some technical improvements can be implemented also in the external gear units [5]. However external gear machines are the most used due to the higher maximum working pressure and the lower manufacturing cost [6]. In this context, helical gear type is more promising, being quieter than the corresponding one with straight teeth (spur gear).

Several studies have been conducted for developing simulation models of external gear pumps. Recent topics are the accurate evaluation of the mechanical-hydraulic efficiency [7, 8] and of the gears' micromotion [9]. However, the application with variable speed electric motors requires the increment of the maximum operating velocity, which can lead to incomplete filling and cavitation. The most evident effect is a saturation of the delivered flow rate with the increment of the angular speed. The phenomenon occurs when the pressure difference between the suction port and the rotating inter-teeth spaces is not enough for accelerating the fluid up to a proper velocity. The consequence is that the fluid has not enough time to completely fill the inter-teeth vanes before they leave the suction side. Such a working condition leads to two main problems: a significant decrease of the volumetric efficiency and a huge increment of the pressure ripple due to the sudden back flow when the partially filled inter-teeth chambers connect to the delivery volume. The latter problem is also responsible of an abnormal increase of the noise. Moreover, the implosion of the gaseous bubbles also generates erosion damage during time. The usual way of avoiding the incomplete filling consists in boosting the pump, but such a solution is not always feasible. All these problems are well known in the aeronautic field where the increment of the power-to-weight ratio needs the use of small displacement pumps, but with an extreme operating speed [10].

In this context, it is particularly important to develop a simulation model able to predict the filling capability in conditions of high speed, so that it can be used for the pump optimization. The phenomenon of the incomplete filling can be reproduced even with a 0D or 1D simulation model [11]. Moreover, a model tuned on experimental flow rate can reproduce correctly the characteristic huge pressure ripple generated by the intense backflow when the partially filled chambers connect to the delivery volume. However, a lumped parameter model is able to catch the influence of a geometric parameter on the pressure drop in the suction side only in an approximate way. The quantitative predictivity of the maximum flow rate can be achieved only with a CFD model, since the real 3D geometry, such as the spatial orientation of the chambers and the shape of the suction duct, must be considered without simplifications.

Some studies on the influence of the geometric parameters on the filling capability have been carried out using SimericsMP+® for gerotor [12] and vane pumps [13]. It has been demonstrated that the model is able to evaluate the beneficial or detrimental influence of a specific geometric modification. The main analyzed parameters were the number of chambers, the radius, and the axial thickness of the rotors. More recently, the capability of the software to predict the suction pressure at which the incomplete filling starts has been demonstrated for a straight teeth external gear pump [14].

Based on the best knowledge, simulation studies on the incomplete filling of helical gear pumps are not present in the open literature. In the present study, a CFD model of a high-speed pump prototype visible in Fig. 1 is described and validated experimentally with good results. The two gears are integral with the shaft and housed in the pump casing. The shafts are supported by journal bearings mounted in the balance plates. The aim of the balance plates is twofold: to compensate the axial gaps and to manage the connection of the trapped volume in the meshing region. The balance plates are also provided with peripheral channels for transferring the delivery pressure back in a number of inter-teeth volumes.

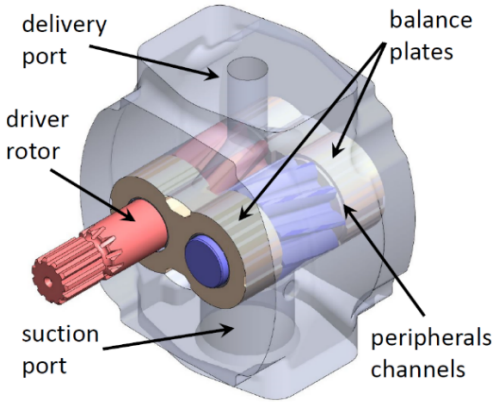

Fig. 1. 3D drawing of the helical gear pump

2. SIMULATION MODEL

2.1. Model structure

The model of the pump was developed at the Politecnico di Torino with the software SimericsMP+. Starting from the surfaces of the fluid domain, different volumes were identified, as shown in Fig. 2.

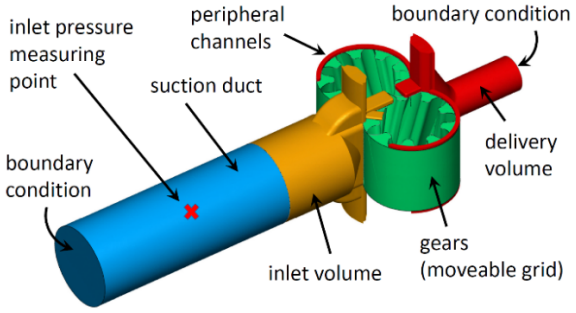

Fig. 2. Subdivision of the volumes with the location of the inlet pressure transducer

The inlet and delivery ducts are fixed; they also include the peripheral channels and the machining on the balance plates, while the green volumes rotate around the gears' axis. In addition, a fixed cylindrical volume was added for simulating the upstream portion of the inlet pipe. The position of the measuring point of the inlet pressure is the same as on the test rig. For the choice of the distance of the inlet boundary condition from the measuring point, it was verified that a longer length of the inlet pipe had no influence on the results, but only on the computational time. Despite the aim of the study is to correctly simulate the phenomena occurring at high speed in the suction side with low delivery pressure, a micro-shift of the gears along the horizontal and vertical axes was applied for obtaining a more reasonable value of the fluid leakages. In particular, to consider the mean direction of the

force acting on the rotors, the axes of the gears were shifted towards the suction side and the distance between the axes was reduced. The axial clearances were neglected because the gaps are compensated by the balance plates. Since it is not possible to have contact between the gears for the continuity of the mesh, a gap was left between the flanks of the teeth. However, since the study was performed at low delivery pressure, this additional leakage does not significantly affect the delivered flow rate of the pump.

The mesh of the rotating volumes was built with the template external gear that generates a structured hexahedral grid. During the rotation, the number of cells in the radial direction is kept constant and the mesh is compressed when a tooth of the opposite gear enters the tooth space. The outermost layer of the cells is made to slide with respect to the housing and to the grid of the opposite gear. The inlet and delivery volumes were meshed with the general mesh generator that generates an unstructured Cartesian grid with cubic elements. The mesh was refined locally in the grooves and in the peripheral channels. Finally, the grid of the inlet duct was created with a mesh generator specific for cylindrical geometries. A 3D view of the mesh is shown in Fig. 3.

For the simulation of aeration and cavitation, the transient for air release and dissolution can have an influence [15] and SimericsMP+ allows considering these transients [16]. However, the uncertainty on the amount of total air and on the values of time constants makes the use of the most detailed model questionable, therefore the model of fluid Equilibrium Dissolved Gas was chosen.

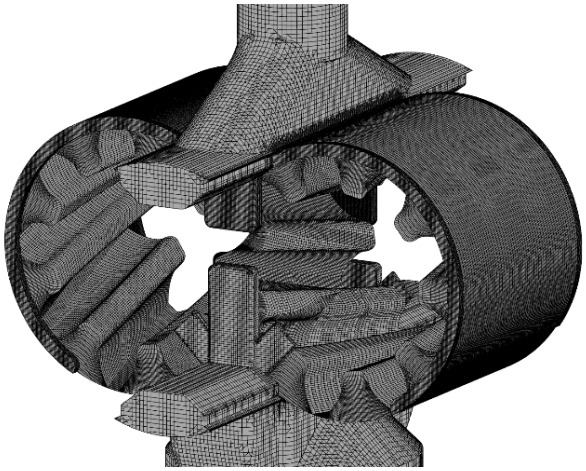

Fig. 3. View of the mesh of the variable volume chambers and of the inlet/outlet volumes.

The total volume fraction of air used in the simulation is equal to 6%. Such a percentage was selected because it was proved to be a good starting value, although obtained by tuning on a different test rig [13]. No turbulence model was applied since previous studies on fluid power pumps have demonstrated the negligible effects on the simulated results due to the high viscosity of the hydraulic oils [14, 17].

The software discretizes the governing equations with the finite volume method. In the present analysis, the first-order upwind interpolation scheme was used, while the SIMPLE-S method was employed for the pressure–velocity coupling. As boundary conditions,

pressures were imposed at the two ports (Fig. 2). Transient simulations were performed, and the moving average of the delivery flow rate calculated over a shaft revolution was monitored. The steady-state condition was considered reached when the difference between the mean flow rates calculated in two consecutive revolutions became lower than 1%. Starting from a new simulation, usually 3-4 revolutions are necessary to achieve the steady-state conditions. However, a couple of revolutions could be enough if the proper initial conditions are set, namely the final results of a previous simulation executed in a close operating point.

2.2. Model optimization

The mesh sensitivity analysis was carried out on the version of the pump with straight teeth. As far as the total number of cells is concerned, it was found that its increment from 0.5 to 1.6 million led to a variation of the calculated delivery flow rate of less than 0.5%. Hence a number of cells around 1 million is usually enough for this kind of study. However, the version with helical teeth needs a higher number of layers axially in the rotor domain. This increment is not necessary for improving accuracy, but for avoiding problems of convergence due to the interference of the gears. In fact, in order to reproduce the helical shape with good accuracy, the number of cells' layers must be high enough, otherwise an unrealistic stepped gap between the gear flanks is obtained. Based on these analyses, for each rotor 720 cells in the circumferential direction, 11 radially and 50 axially were set. It must be noticed that in a straight teeth pump 12 cells in the axial direction were instead enough. In Table 1 the detail of the number of cells used in the model is reported.

Table 1. Number of cells for each subdomain

Volume	Number of cells
2 Rotors	792.000
Delivery volume	760.143
Inlet volume	181.732
Suction duct	22.800
Total	1.756.675

In order to determine the angular step and the residual for the best trade-off between accuracy and computational time, the tests listed in Table 2 were performed. In SimericsMP+ the exponent of the residual drop is defined as the difference between the natural logarithm of the residual at the n-th iteration and maximum residual in all previous iterations from 1 to n-1. The volumetric efficiency is defined as the ratio between the calculated and the theoretical flow rates. For confidentiality reasons, the speed and delivery pressure used for such tests cannot be provided. The CPU time is expressed in hours per shaft revolution, and it was obtained on a workstation with Intel Xeon Platinum 8268 processor with 24 cores at 2.90 GHz. It can be observed that the use of a residual 0.1 leads to a significant underestimation of the volumetric efficiency, while with a residual 0.01 the reduction of the angular step does not give any improvement on the flow rate, but only increases the computational time. Therefore, the simulations were performed with an angular step of 1 degree and a residual drop of 0.01. With these settings the convergence is reached usually with 50-70 iterations.

Table 2. Influence of the angular step and of the residual

Configuration	Volumetric efficiency	CPU time (h/rev)
0.5 deg – residual 0.1	94.3 %	3.5
0.5 deg – residual 0.01	96.7 %	16.5
1 deg – residual 0.1	90.3 %	3
1 deg – residual 0.01	96.7 %	7

3. MODEL VALIDATION

The experimental tests were carried out at the Casappa SpA laboratory. The hydraulic scheme of the test rig is reported in Fig. 4. A variable speed electric motor drives two axial piston pumps Casappa MVP60. The pump labelled PU1 feeds a fixed displacement external gear motor Casappa PHM 20 that drives the pump under test. This solution allows working at a speed higher than the one that can be imposed by the electric motor. On the delivery port of the helical gear pump the only resistance is due to the filter and the flow meter F1. The pump with label PU2, along with the preloaded check valve, is used for controlling the inlet pressure of the pump under test. Since the flow rate delivered by the pump PU2 is always slightly higher than the flow rate sucked by the helical gear pump, an excess flow is continuously discharged by the check valve that imposes upstream its cracking pressure. By means of a manual restrictor R, the suction pressure can be reduced to the desired value measured by the transducer P4. The details of the transducers are listed in Table 3. The tests were performed with an ISO VG46 oil at the temperature of 50 °C.

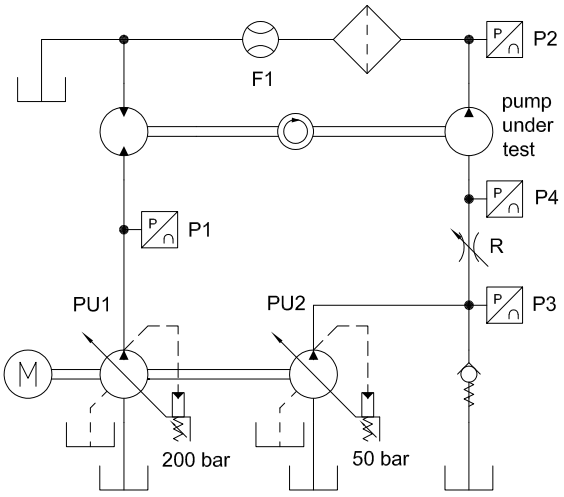

Fig. 4. Hydraulic scheme of the high-speed test rig

The test procedure consisted of imposing a value of angular speed and progressively reducing in steps the flow area of the variable restrictor R. For each value of the inlet pressure measured by the transducer P4, the flow rate was recorded. The results of the steady-state

tests at three angular speeds are reported in Fig. 5. For confidentiality reasons, the quantities have been normalized with respect to the maximum experimental values.

Table 3. Technical data of the transducers

Quantity	Transducer	Range	Accuracy
Pressures P1, P2	Trafag 8253	0÷400 bar	±0.3% F.S.
Pressures P3, P4	Trafag 8254	-1÷4 bar	±0.3% F.S.
Flow rate	VSE VS 4	1÷250 L/min	±0.3% Reading

It can be observed that for high values of the inlet pressure the delivered flow rate is insensitive to the flow area of the restrictor, while a noticeable reduction due to the incomplete filling occurs at low pressure levels. Moreover, it is evident that the inlet pressure at which the flow rate begins to decrease increases with the pump speed. Such a behavior can be explained considering that, with equal pressure measured at the inlet port, the higher speed implies a bigger energy spent by the fluid for entering the rotating chambers. The model can predict with good accuracy the critical suction pressure below which the incomplete filling occurs. Moreover, the gradual reduction of the flow rate visible at 4500 rpm in the pressure range 0.4 - 0.6 is also correctly reproduced. At 6000 rpm a slight overestimation of the flow rate in conditions of complete filling is visible. A possible reason for this discrepancy is because the micro-positioning of the gears was calibrated on the test at 3000 rpm and the same axes' position was maintained also for the other speeds. It is likely that at 6000 rpm, due to a higher load capacity of the bearings, a smaller shift towards the inlet volume occurs, leading to a higher leakage on the tips of the teeth. However, apart from this offset, the shape of the simulated curve reproduces very well the experimental trend. Fig. 6 shows a visualization of the air release in the meshing region of the suction side in operating point 1 indicated in Fig. 5. The cut-plot of the total gas volume fraction is taken in the midplane of the gears. Due to the rapid increment of the volume, a massive formation of gaseous phase is detected in the chambers of both gears at 0 degrees.

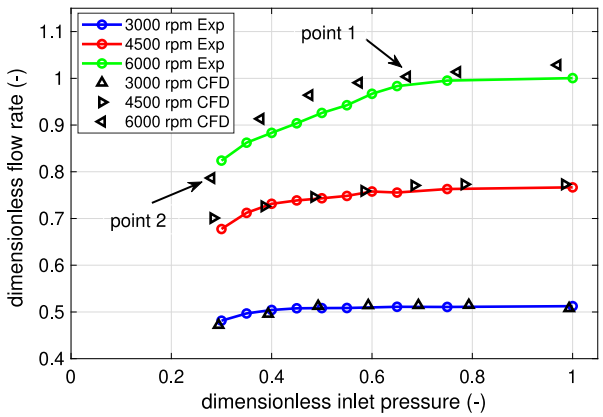

Fig. 5. Comparison between experimental and simulated normalized delivery flow rate vs. dimensionless absolute inlet pressure for three different shaft speeds

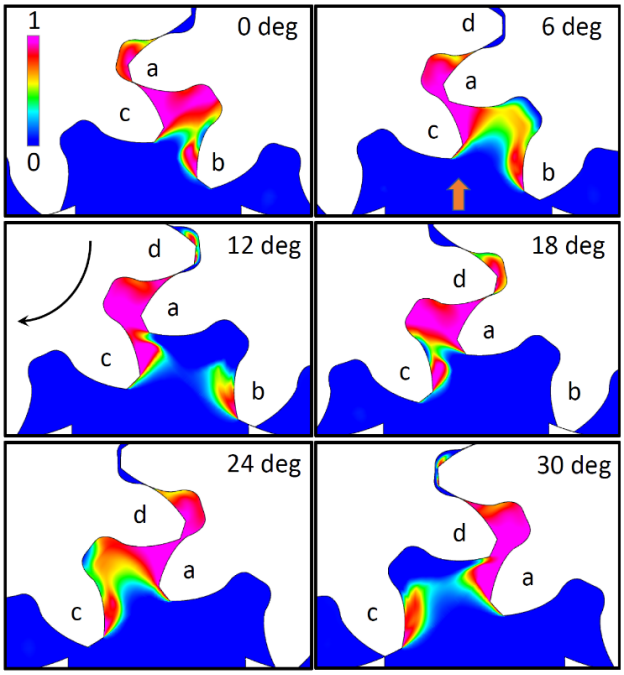

Fig. 6. Total gas volume fraction for 6 different angular positions of the gears in the operating point 1 in Fig. 5 (blue color indicates only liquid phase)

At 6 degrees the fraction of gas in the chamber between the teeth “a” and “b” of the driver gear progressively decreases for the following reasons.

- The derivative of chamber volume has become zero, since the tooth “c” has completely left the space between “a” and “b”.
- The area connection between the chamber and the suction volume has become quite large, since the distance between the tips of the teeth “b” and “c” has significantly increased.
- The chamber is favorability oriented with respect to direction of the incoming flow.

At 12 degrees the gaseous phase is only located behind the trailing flank of the tooth “b”, while at 18 degrees the filling of the chamber is complete. In a similar way the chamber between the teeth “c” and “d” of the driven gear is almost empty at 12 degrees due to the fast increment of the volume and the small flow area. The oil enters the chamber starting from the lower radius (24 degrees), where the peripheral velocity is smaller, and radially due to the favorable orientation of the chamber with respect to the inlet jet; at 30 degrees the air fraction is located only behind the tip of the tooth “c”.

In operating point 1 the delivered flow rate is very close to the maximum value, because the inlet pressure is high enough for recovering the missing oil volume in the inter-teeth spaces before they leave the suction side. Hence the local formation of gaseous phase in the meshing region has no effects on the overall behavior of the pump. On the contrary, if the

inlet pressure is further decreased the chambers remain partially empty up to the connection with the delivery volume. In Fig. 7 the gas volume fraction is shown for the case with severe incomplete filling (point 2 in Fig. 5). When the chambers are isolated, the centrifugal force pushes the liquid phase outwards, and the gas fraction is confined in the innermost part of the gears.

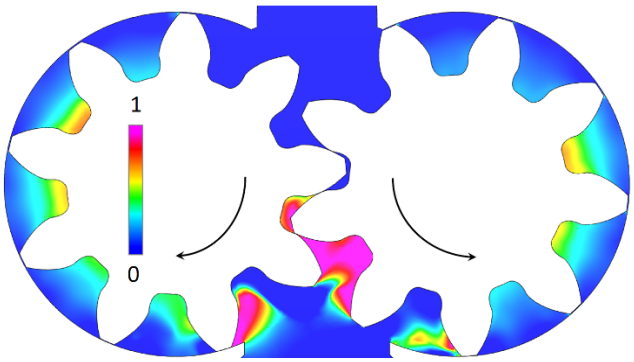

Fig. 7. Cut-plot of the total gas volume fraction in the operating point 2 in Fig. 5

In Fig. 8 the pressure distribution is shown. For confidentiality reasons the values on the color scale have been omitted. In the suction volume the lowest pressure level (dark blue) occurs in the meshing region and behind the trailing flank of the teeth, while an overpressure is detected in front of the leading flank. In the isolated chambers the pressure level remains low since the leakage on the tip of the teeth and the flow through the peripheral channels are not enough to compensate for the missing oil volume. Hence the chambers are abruptly pressurized when they are connected directly to the delivery volume. The generated backflow is the cause of the typical high pressure ripple and noise occurring in conditions of incomplete filling. Since the aim of the developed model is only the evaluation of the incomplete filling, the entire delivery line has not been simulated for limiting the computational time. Hence a reliable estimation of the pressure ripple is not possible. However, in the reference [18] the increment of the pressure pulsation in a gear machine in condition of incomplete filling can be appreciated.

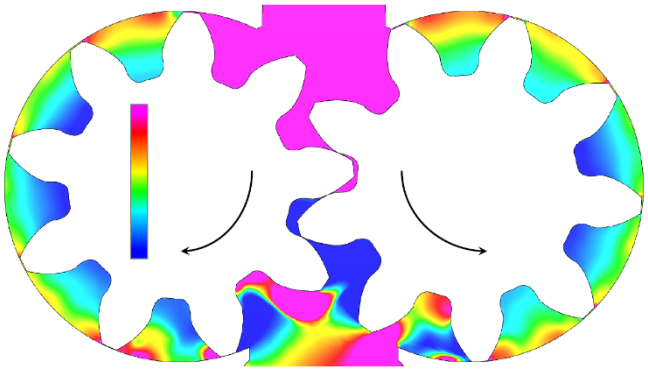

Fig. 8. Cut-plot of the pressure field in the operating point 2 in Fig. 5

4. CONCLUSIONS

The development of a fixed displacement pump for a direct connection to a variable speed electric motor represents a challenge due to the risk of incomplete filling and cavitation. The proper geometry of the casing and of the gears must be optimized in order to minimize the pressure drops in the suction side. The evaluation of the effect on the filling of a geometric modification needs a model able to consider the real 3D shape of the volumes and their relative motion. In this paper the reliability of the CFD model has been proved on a helical gear pump prototype. More specifically, the minimum suction pressure that still allows the complete filling of the chambers is estimated with good precision. Moreover, it has been verified that the limit suction pressure increases as the speed is increased. The outcomes allow being confident that the developed model can be used as design tool for optimization purposes. Possible future studies will involve the analysis of the influence of some geometrical parameters of the gears and of the suction port for extending the operating speed range of the pump.

5. REFERENCES

[1] S. Qu, D. Fassbender, A. Vacca, E. Busquets, 'A high-efficient solution for electro-hydraulic actuators with energy regeneration capability', Energy, 216, 2021, doi: 10.1016/j.energy.2020.119291.

[2] A. Bedotti, M. Pastori, P. Casoli, 'Modelling and energy comparison of system layouts for a hydraulic excavator', Energy Procedia, 148, pp. 26-33, 2018, doi: 10.1016/j.egypro.2018.08.015.

[3] P. Casoli, F. Scolari, T. Minav, M. Rundo, 'Comparative Energy Analysis of a Load Sensing System and a Zonal Hydraulics for a 9-Tonne Excavator', Actuators, 9(2), 2020, doi: 10.3390/ACT9020039.

[4] M. Rundo, 'Theoretical flow rate in crescent pumps', Simul. Model. Pract. Theory, 71, pp. 1-14, 2017, doi: 10.1016/j.simpat.2016.11.001.

[5] G. Marinaro, E. Frosina, A. Senatore, 'A Numerical Analysis of an Innovative Flow Ripple Reduction Method for External Gear Pumps', Energies, 14(2), 2021, doi: 10.3390/en14020471.

[6] J. Ivantysyn, M. Ivantysynova, 'Hydrostatic pumps and motors', Akademia Books International, New Delhi, 2001.

[7] B. Zardin, E. Natali, M. Borghi, 'Evaluation of the Hydro—Mechanical Efficiency of External Gear Pumps', Energies, 12(13), 2019, doi: 10.3390/en12132468.

[8] R. Rituraj, A. Vacca, M. Rigosi, 'Modeling and validation of hydro-mechanical losses in pressure compensated external gear machines', Mech. Mach. Theory, 161, 2021, doi: 10.1016/j.mechmachtheory.2021.104310.

[9] X. Zhao, A. Vacca, 'Multi-domain simulation and dynamic analysis of the 3D loading and micromotion of continuous-contact helical gear pumps', Mech. Syst. Signal Process., 163, 2022, doi: 10.1016/j.ymssp.2021.108116.

[10] Q. Chao, Z. Xu, J. Tao, C. Liu, J. Zhai, 'Cavitation in a high-speed aviation axial piston pump over a wide range of fluid temperatures', Proc. ImechE, Part A: J. Power and Energy, 2022, 236(4), pp. 727-737, doi: 10.1177/09576509211046998.

[11] D. Buono, F.D.S.D. Cola, A. Senatore, E. Frosina, G. Buccilli, J. Harrison, 'Modelling Approach on a Gerotor Pump Working in Cavitation Conditions', Energy Procedia, 101, pp. 701-709, 2016, doi: 10.1016/j.egypro.2016.11.089.

[12] G. Altare, M. Rundo, 'CFD analysis of gerotor lubricating pumps at high speed: Geometric features influencing the filling capability', ASME/BATH 2015 Symposium on Fluid Power and Motion Control, Chicago, USA, 2015, doi: 10.1115/FPMC2015-9539.
[13] M. Rundo, G. Altare, P. Casoli, 'Simulation of the filling capability in vane pumps', Energies, 12 (2), 2019, doi: 10.3390/en12020283.
[14] A. Corvaglia, M. Rundo, P. Casoli, A. Lettini, 'Evaluation of Tooth Space Pressure and Incomplete Filling in External Gear Pumps by Means of Three-Dimensional CFD Simulations', Energies, 14 (1), 2021, doi: 10.3390/en14020342.
[15] M. Rundo, R. Squarcini, F. Furno, 'Modelling of a Variable Displacement Lubricating Pump with Air Dissolution Dynamics', SAE Int. J. Engines, 11 (2), pp. 111-126, doi: 10.4271/03-11-02-0008.
[16] U. Stuppioni, A. Suman, M. Pinelli, A. Blum, 'Computational fluid dynamics modeling of gaseous cavitation in lubricating vane pumps: An approach based on dimensional analysis', J. Fluids Eng., 142 (7), 2020, doi: 10.1115/1.40464.
[17] M. Rundo, G. Altare, 'Lumped Parameter and Three-Dimensional Computational Fluid Dynamics Simulation of a Variable Displacement Vane Pump for Engine Lubrication', J. Fluids Eng., 140(6), 2018, doi: 10.1115/1.4038761.
[18] G. Altare, M. Rundo, 'Advances in simulation of gerotor pumps: An integrated approach', Proc. ImechE, Part C: J. Mech. Eng. Sci., 231 (7), pp. 1221-1236, 2017, doi: 10.1177/0954406217694663.

Biographies



Alessandro Corvaglia received his MSc degree in Mechanical Engineering (2016) from the Politecnico di Torino. After graduation, he joined the Fluid Power Research Laboratory of Politecnico di Torino as Research Fellow developing simulation models for axial piston and external gear pumps. In 2018 he started his PhD in Energetics focusing on the advanced modeling of lubricated gaps in axial piston pumps.



Massimo Rundo received his MSc degree in mechanical engineering from the Politecnico di Torino, Italy, in 1996. After graduation, he worked as a visiting researcher, and later as a research fellow, at the Fluid Power Research Laboratory of the Politecnico di Torino, contributing to extensive research projects on positive displacement pumps. In 2005 he joined the faculty at the Department of Energy as assistant professor. He is currently an associate professor of fluid power. His research activity is primarily focused on modelling, simulation and testing of fluid power components and systems.



Sara Bonati received her MSc degree in mechanical engineering from the University of Parma in 2016. At the same university, she carried out a research grant in 2016 in partnership with Fornovo Gas S.r.l concerning the development of lumped-parameter fluid dynamics models of positive displacement compressors. She has been working at Casappa Spa since 2017 in the R&D team as Simulation Engineer, focusing on research and product development activities through CAE tools.



Manuel Rigosi completed his MSc degree in Mechanical Engineering from the University of Parma, in 2011. After an internship, he joined Casappa R&D Department in the role of

Simulation Engineer, focused in replicating the physical phenomena within hydraulic gear and piston pumps through the usage of customized lumped parameter models and 3D simulations. In 2018 he took the responsibility for the development of new products with a team of engineers and designers. In recent years he has contributed to innovation by signing 4 patents regarding solutions already applied to the latest products Casappa is offering on the market today.

MODELLING AND EXPERIMENTAL VALIDATION OF THE DYNAMIC STARTUP BEHAVIOR OF EXTERNAL SPUR GEAR MOTOR

Ajinkya Pawar[1], Andrea Vacca[1], Manuel Rigosi[2]

Maha Fluid Power Research Center[1], Purdue University, Lafayette, IN, USA

Casappa S.P.A.[2], Parma, Italy

Abstract.

The sizing of fluid power systems controlling hydraulic motors is often affected by their dynamic start-up behavior. The start-up pressure that must be provided to initiate the rotation of a hydraulic motor is usually significantly higher that the corresponding pressure reached in steady operation, due to internal frictional effects. This important aspect, typically referred to as "startup torque" affects the motor shaft dynamic, as well as the power requested from the hydraulic supply. Despite the importance of this aspect, there are only few modelling techniques, mostly empirical, available to describe the start-up characteristics of hydraulic motors. This paper contributes to this field by presenting a model for the analysis of the dynamic operation of a spur gear motor. The model predicts the start-up pressure and torque, as well as the shaft speed evolution over time. The proposed model builds upon the HYGESim (HYdraulic GEar machine Simulator) developed by the authors' team in the past years. The modeling approach is refined to consider the torque contributions affecting the rotational dynamics of gears. To allow simulating many shaft revolutions in a complete hydraulic system, the torque losses at the lubricating interfaces are interpolated from pre-computed results of a detailed in-house multiphysics simulation model available to the authors. An experimental activity was performed on a commercial motor to validate the model. Experiments allowed to measure the instantaneous flow, pressure, and speed during a start-stop cycle typical of a fan drive system. The experimental and simulation results show very good qualitative and quantitative agreement. The proposed simulation approach can help designers in optimization studies to achieve better designs, owing to its accuracy and reduced simulation time.

Keywords. Gear motors, External Gear Machines, Dynamic modelling, Start-up torque, Hydromechanical Efficiency

1. INTRODUCTION

This paper addresses the topic of modeling the start-up behavior of hydraulic motors, namely the so-called "start-up torque" aspect of this kind of components. To briefly explain the

concept of start-up torque, it is useful to remind the relationship valid at steady state conditions:

$$\Delta p_m = \frac{2\pi T_m}{\eta_{hm} V_d} \tag{1}$$

In this equation T is torque at the motor shaft, and the torque efficiency, η_{hm} represents the steady state torque losses. During transient start-up, the higher friction present at the internal interfaces causes a much larger pressure drop required to induce the shaft rotation. According to Eq. (1), this overpressurization for Δp_m can be perceived as an additional torque present at the shaft, thus leading to a definition of a start-up torque larger than the corresponding steady state value. This start-up torque is a critical parameter for system using hydraulic motors. In fact, the hydraulic control system must be designed considering this more stringent start-up torque condition, rather than a nominal torque given by Eq. (1).

Studies were carried out in the past to understand the start-up process of hydraulic components. Many of these studies were focused upon modelling friction losses at different lubricating interfaces. Harnoy [1] proposed an analytical model to determine start-up torque loss from hydrodynamic journal bearings including stick-slip effects. Bouyer and Fillon [2] along with Henry [3] performed experimental measurements to determine the friction torque from journal and thrust bearings during start-up. In both cases, a high peak in coefficient of friction during start-up was observed. For line contacts a similar experimental study was carried out by Gasenfeit and Soom [4]. Garcia et al [5] presented effects of lubricants on static friction determination at lubricated line contacts. The torque loss during start-up of different types of hydraulic motors was experimentally captured by Michael et al. [6] to study the effects of lubricant chemistry and rheology on starting efficiency. The analytical modelling of the torque losses during start-up of hydraulic motors has been an unexplored area of research. Existing models are either interface specific as in [1] or entirely empirical in nature, as proposed by Merritt [7], Hibi and Ichikawa [8], and not very suitable for design purposes.

Modelling of frictional losses in steady-state operation in external gear pumps was recently presented by Rituraj et al. [9], who considered losses at various lubricating interfaces using analytical formulations, showing accuracy in the prediction of the machine hydromechanical efficiency. However, full film regime in all lubricating interfaces was assumed, which is an unsuitable assumption for start-up.

The present paper aims formulating a model for external spur gear machines (EGMs) suitable for both steady-state operation as well as start-up dynamics. While modelling and experimental analysis of EGMs has been a major area of research for the authors' research group over the past decade, the aspect of dynamic start-up is for the first time introduced. For the purposes of this research, the model is implemented in a Simcenter Amesim environment and is validated against start-up experimental data by comparing the start-up pressure and rotational speed of the motor. The reference machine used for the simulation and experiments is a Casappa Polaris gear motor. The unit is based on a pressure compensated axial balancing design using 4 journal bearings integrated in floating bearing blocks. Important design details of the reference unit are provided in table 1.

Table 1: Reference unit details

Displacement	4.95 cc/rev
Maximum operating pressure	260 bar
Maximum operating speed	4000 rpm
Number of teeth	12
Housing material	Aluminum

The structure of the paper is as follows: Section 2 presents the modelling methodology followed to evaluate the rotational dynamics of the motor. Section 3 includes the description of start-up experimental tests and details of simulation model setup. Results obtained from the simulation model and their comparison with experimental data are presented in Section 4. Additional capabilities of the model in terms of hydromechanical efficiency evaluation are also detailed in Section 4 while Section 5 includes conclusions and possible improvements to the current model that can be done in future

2. MODELING METHODOLOGY

Over the past decade, the authors' research group has developed an external gear machine simulation tool now called Multics-HYGESim. Figure 1 shows the schematic of different submodules of this tool which are used to simulate the operation of an EGM. For completeness, all modules are described here briefly. Further details on the simulation methodology followed by this tool can be found in [10]. The geometrical module extracts important information regarding the geometry of the machine using CAD files of important components such as gears, lateral bushings, and casing. The pressurization of fluid inside tooth space volumes (TSV) of an EGM is modelled by a DC solver using a lumped parameter approach which also considers, tooth tip leakages and cavitation. The Reynolds solver uses a CFD approach to study the details of lubricating interfaces (lateral gap fluid films and journal bearings). The forces calculated by DC and Reynolds solvers are used by Dynamics Solver to determine the instantaneous position of the involved bodies (gears and bushings), also allowing to account for wear-in of the housing. The Deformation Solver accounts for effects of fluid structure interaction by determining the deformation of bodies.

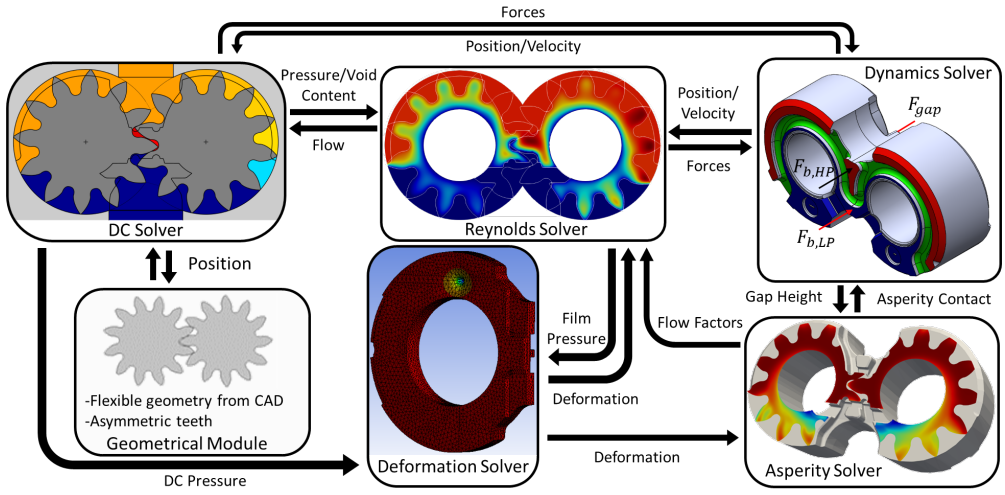

Fig. 2.1- Schematic of Multics-HYGESim

Finally, the asperity solver accounts for mixed lubrication effects at these interfaces. Various aspects of an EGM such as volumetric efficiency, pressure ripple, leakages are simulated and experimentally validated with this simulation tool as described in [10]. However, all these studies were carried out under steady state operating conditions. As Multics-HYGESim adopts a computational approach to simulate the coupled effects of the previously mentioned physical phenomena (CFD approach, mixed lubrication, and fluid structure interaction effects), the computational cost is high, resulting in relatively high simulation times (typically about one day for simulating few revolutions). Thus, simulating the transient behavior of the motor becomes challenging with this approach, as the transient simulation must consider many shaft revolutions. To overcome to this challenge, this paper proposes a reduced model derived from Multics-HYGESim, which considers the aforementioned effects in an analytical way. Additionally, the authors also propose methodology to calculate the start-up torque of the motor as well as to include frictional loss from different sealing interfaces inside the motor. Details of this reduced model (referred to as proposed model henceforth) are presented in the upcoming section focusing on methodology followed to solve the dynamic behavior of an external gear motor.

2.1. External Gear Motor Dynamic Modeling

The inlet side of the motor is connected to a high-pressure line while the outlet side of the motor is connected to a low-pressure line. The pressurized fluid exerts a rotary moment on both gears causing them to rotate in opposite directions. Thus, the fluid is displaced from the high-pressure side to low-pressure side while causing the actuation or generation of rotary motion during this process. Figure 2 depicts the moments acting on gears and their directions under assumed orientation of inlet and outlet, as well as the coordinate system which include moments due to fluid pressure and moments due to friction. Gear 1 is assumed to be driving an external load and thus, is subjected to additional moment due to the resistance and inertia of the load. Considering these moments, Newton's second law is applied to both gears (Eq. 2 and 3), which are assumed as rigid bodies:

$$M_{fp1} + M_{c1} - M_{f1} - M_l = (I_1 + I_l)\alpha_1 \qquad (2.2)$$

$$M_{fp2} - M_{c2} - M_{f2} = I_2\alpha_2 \qquad (2.2)$$

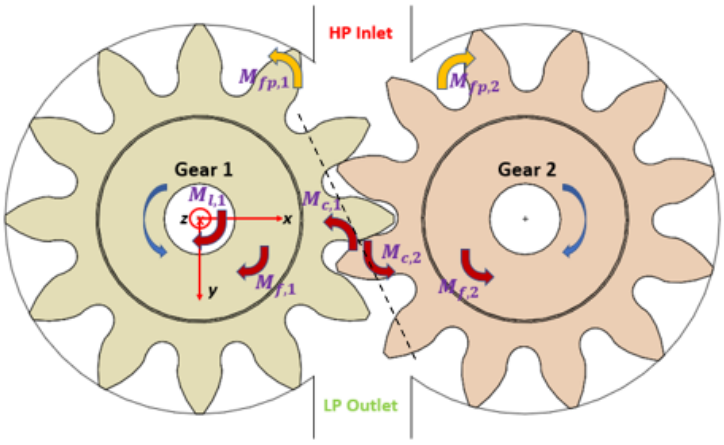

Fig. 2.2 - Loads determining rotational dynamics of gears

2.2. Moment due to fluid pressure

To determine the moment due to fluid pressure acting on the gears, the pressure inside each tooth space volume (TSV) chambers of both gears is first evaluated according to a lumped parameter approach first introduced by Vacca & Guidetti in [11]. This approach is based on the pressure buildup equation (4), and it is also used in the DC Solver of Multics-HYGESim, Fig. 2. The overall pressure distribution in all TSVs is then used to calculate forces and moments acting on both gears. The force loading is then used to describe the radial micromotion of the gears as described in in [11].

$$\frac{dp_i}{dt} = \frac{K_{oil}}{V_i}\left(\sum(Q_{in} - Q_{out}) - \frac{dV_i}{dt}\right) \tag{2.3}$$

It is worth mentioning that gear motors have different gear meshing conditions than gear pumps. In the case of a pump, gear 1 shown in Fig. 2 would be connected to an external prime-mover which rotates the gear such that the fluid is displaced from a low-pressure inlet (LP) to a high-pressure outlet (HP). With the port pressure conditions of Fig. 2, gear 1 would rotate clockwise and gear 2 would be driven by gear 1. Instead, in case of a motor, there is no prime mover. Due to its smaller inertia, gear 2 drives gear 1 which is connected to an external rotary load. This meshing difference must be carefully considered in this work for the accurate evaluation of fluid dynamic characteristics of the motor. To allow using the geometric model previously developed for pumps the current paper considers the inlet and outlet as shown in Fig. 2. Under these conditions, the contact location of both gears remains the same as it would have been if the EGM is operated in pumping mode.

2.3. Moment due to friction

Frictional losses in EGMs generally arise from friction acting at various interfaces which include journal bearings (JB), lateral gap (LG) fluid films, meshing, seals, drain leakage, and tooth tip leakage interfaces.

Differently from the past work [9], where full-film conditions were assumed, this work consider a CFD approach to determine losses at journal bearing and lateral fluid film interfaces by considering effects of mixed lubrication and solid to solid contact friction. Authors here have chosen an approach to account for these effects using independent CFD simulations for the JB and LG interface with the aim of obtaining an analytical implementation to reduce computational time for running motor transient simulations while maintaining accuracy of frictional loss prediction.

2.3.1. Friction at journal bearings

At each journal bearing, shear forces are generated at the shaft and fluid film interface due to presence of viscous as well as contact friction. For analytical implementation, the friction coefficient variation for the reference journal bearing is determined as a function of a suitable non-dimensional parameter by running standalone CFD simulations under operating conditions defined in table 2. This parameter is chosen to be Sommerfield number (Eq. 2.4). For these simulations, the shaft is treated as a rigid body which has free degrees of translational motion in x and y directions and rotating at the prescribed operating speed, while the bushing is treated as a fixed rigid body.

$$S = \frac{\eta N}{P}\left(\frac{r}{c}\right)^2 \tag{2.4}$$

Table 2: Parameters for the standalone journal bearing simulation

Model Parameters	Value [unit]
Shaft Velocity	10-3000 RPM
Load	5500 N
Working fluid	ISO VG 46
Operating Temperature	50^oC
Sommerfield Number Range	0.001-0.2

Simulations are run at a range of Sommerfield number values by varying the operating speed while keeping the applied load on the shaft as constant. The friction force on the shaft is evaluated by integrating the shear stress at the shaft surface. At very low values of Sommerfield number, the bearing operates in mixed lubrication regime. In this case, contribution of surface roughness to fluid film behavior cannot be ignored. To model this, a stochastic approach presented by Patir and Cheng [12] is used. In this regime, the fluid film cannot support the entire load and partial load support is offered by asperity contact. Thus, the friction force for this regime consists of the force due to shear stress in mixed lubrication (Eq. 6) and the friction force due to asperity contact (Eq. 7).

$$\tau_w = \varphi_{fp}\frac{h}{2}\frac{\partial p}{\partial x} + (\varphi_f + \varphi_{fs})\frac{\eta(U_2 - U_1)}{h} \tag{2.5}$$

$$F_{f,asp} = \mu_{asp}\int p_{asp} dA_{asp} \tag{2.6}$$

Based on simulation results, data for coefficient of friction variation with respect to Sommerfield number is acquired. This data is used to obtain a curve fit to calculate the coefficient of friction at the journal bearing analytically, Eq. (8). The torque loss at journal bearing is then obtained using Eq. (9).

$$\mu_{JB} = 0.04486 * e^{-\left(\frac{S}{0.002681}\right)} + 0.01897 * tanh\left(\frac{S}{1.085}\right) + 0.0006507 \tag{2.7}$$

$$M_{JB} = \mu_{JB} r_s F_s \tag{2.8}$$

2.3.2. Friction at lateral fluid film interface

The lateral fluid films in pressure compensated EGMs provide axial load support which is beneficial for axial balancing of such units. Past work by the authors' research group, such as [9], presented a fast analytical approach to calculate the torque loss at this lubricating interface. In particular, the friction moment generated due to shear stress was calculated also considering possible tilting of the floating bushings with respect to gears. Even though this approach is computationally suitable as it uses closed form solutions, it does not consider effects of gear and lateral bushing deformation, mixed lubrication and asperity contact friction, which instead heavily affect start up conditions. To capture these

effects, this work has considered complete simulations of the reference machine with the Multics–HYGESim introduced earlier.

Figure 7 shows the difference in predicted torque loss at lateral films obtained using the proposed approach and the analytical approach previously used in [9]. Torque loss values are non dimensionalized for confidentiality reasons. These plots clearly indicate how the analytical model described in [9] underpredicts friction losses at lateral films for all operating conditions. To capture the extra torque loss a term ΔM_{LG} is defined as in Eq. 10 and considered in the proposed model to avoid running computationally expensive CFD simulations.

$$\Delta M_{LG} = M_{CFD,lat} - M_{analytical,lat} \qquad (2.9)$$

To describe ΔM_{LG} in a model that does not evaluate the hydrodynamic effects in the lateral films as in Multics-Amesim, the gear side film pressure distribution is approximated using TSV chamber pressures. As a result, an unbalanced force in the axial direction of the bushing (F_z) and an unbalanced tilting moment about horizontal axis of the bushing (M_x) is observed on the lateral bushing. The approach taken is to model the extra torque loss ΔM_{LG} as a function of F_z and M_x. A lookup-table which outputs the value of ΔM_{LG} corresponding to values of F_z and M_x is obtained by interpolating the available data (Fig. 3).

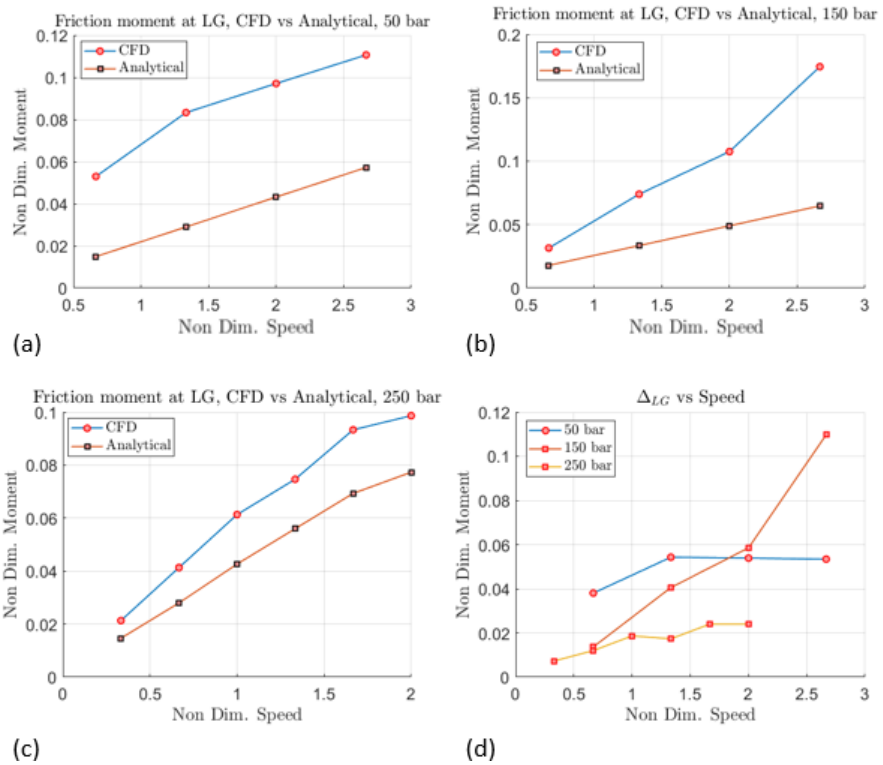

Fig. 2.3: Comparison of friction loss at lateral interfaces a) 50 bar b) 150 bar c) 250 bar inlet pressure d) Map of difference between torque loss predicted

2.3.3. *Friction at Meshing Interface*

During meshing, a rolling and sliding contact occurs between gears teeth, which leads to friction at this interface. In spur EGMs, this contact is non-conformal in nature. Due to high contact loads and small contact area, fluid pressure in this region is in the order of gigapascals causing local elastic deformation of the bodies and modifying the gap height distribution. Thus, meshing zone contact shows presences of Elasto-Hydrodynamic Lubrication (EHL). This work uses the same approach as in reference paper [9], which consists on using the Jacobson and Hamrock model [13] to determine coefficient of friction in EHL conditions.

.

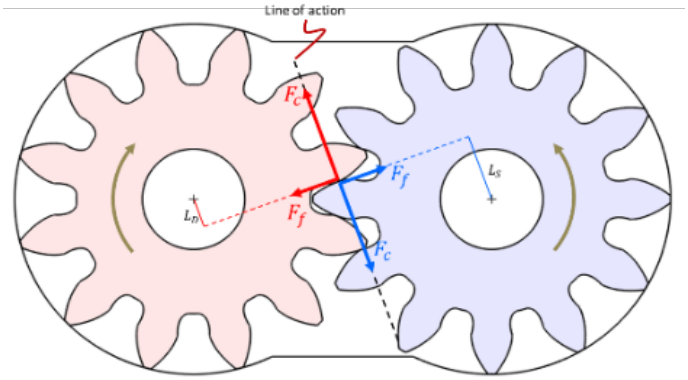

Fig 2.4: Friction moment at gear meshing interface

In particular, the friction force at meshing interface is determined by multiplying a coefficient of friction, Eq. (11) by the contact force. The moment due to this force is determined by multiplying it with a moment arm as shown in Fig. 4. The meshing friction moment on gears, can either support or oppose the motion. But the net effect always results in a torque loss.

$$\mu_1 = 0.6710^{-6}(U^*)^{0.81}U^{0.26}(WG^2)^{3.32} \text{ if } \mu_1 \leq 0.8\gamma$$
$$\mu_1 = 0.80\gamma + 0.021\tanh\left(\frac{\mu_1}{\gamma} - 0.8\right) \quad \text{if } \mu_1 > 0.8\gamma \tag{2.10}$$

2.3.4. *Friction at tooth tip interface*

The geometry of EGMs allows tooth tip leakages to be treated as laminar flow between parallel plates. The net friction force at these interfaces is calculated by integrating wall shear stress, which includes the contribution of both Couette and Poiseuille terms of laminar flow as indicated in reference [9]. Eq. (12) is used to determine the shear stress and in turn, frictional loss at this interface can be calculated using Eq. (13).

$$\tau_{w,i} = \frac{\omega r_g \eta}{h} + \frac{h(p_{i+1} - p_i)}{2L} \tag{2.11}$$

$$M_{tip} = \sum_i F_i r_g = Lbr_g \sum_i \tau_{w,i} \qquad (2.12)$$

2.3.5. Friction at seals in EGMs

To prevent leakages from different pressurized areas, the reference machine uses rubber seals are used as shown in Fig. 5. A shaft seals prevents leakage from the drive gear shaft to the outside of the unit. Seals on the balance side of the bearing blocks seal the environments between HP and LP balance areas. While assembly the EGMs, seals are subjected to pre-load to ensure proper operation which result in friction and torque loss at these interfaces.

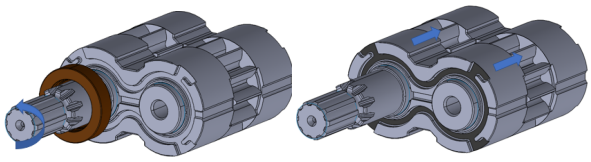

Fig 2.5: Major Seals inside the reference EGM a) Shaft Seal b) Bearing Block Seal

The shaft seal compresses against the drive shaft and the casing, which results in friction generation at the interface causing torque loss to occur. To estimate the value of this loss, a 2006 study by Nikas and Sayles [14] is referred. According to their study, the hydrodynamic friction force on the rotor and stator separated by a seal is dependent on penetration depth and temperature. The value of hydrodynamic friction force at shaft seal interface is determined based on Fig 6. This value is assumed to be constant. This assumption is valid because the load support from forces acting in radial direction on gears is provided by the journal bearings, which leads negligible change in radial forces at seal interface. The penetration depth at the seal does not change and can be assumed to be equal to the value established during the initial assembly. The torque loss from shaft seal is determined by multiplying the friction force value taken from [14] by shaft radius.

The bearing block seals contribute the torque loss of EGMs due to an initial pre-load. As shown in Fig. 5 b), the lateral bushings are pushed towards the gear side, due to forces from the balance side. The pre-load of the seal results in an additional force which causes a reduction in the lateral gap height. Thus, the pre-load at bearing block seal influences lateral fluid film behavior and its torque loss. The effect of this additional force is accounted for by including an additional force in axial direction from balance side which changes F_z and M_x on lateral bushings, thus changing the value of ΔM_{LG} of Eq. (10) obtained from interpolation. This additional pre-load is dependent on manufacturing tolerances and is assumed to be constant for the given reference machine.

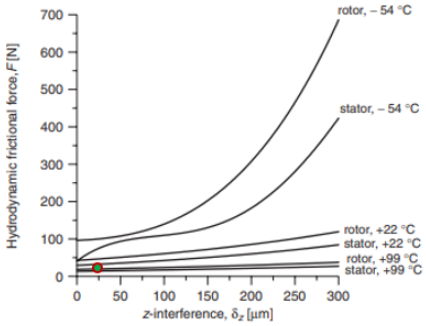

Fig 2.6: Friction force at flexible seals under motion as a function of temperature [14]

2.4. Start-up torque loss modeling

During start up, lubricating interfaces such as journal bearings and lateral films are in boundary lubrication regime leading to high torque loss. Similarly, friction meshing interface during start-up is also seen to be higher as the load is supported mainly by asperities due to lack hydrodynamic support. As the motors speed starts increasing, the operation of these lubricating interfaces transitions from boundary lubrication regime to mixed lubrication and subsequently full film region. This behavior can be modelled using a Stribeck curve.

Analytical modelling of Stribeck curve to predict the frictional force as a function of velocity has been presented in [15]. Thiagarajan et al. [16] used this model to predict the friction force (Eq. 14) at the lateral bushing-casing interface. The same friction model ([16]) is modified to calculate the start-up torque loss in an EGM (Eq. 15). To apply this equation for start-up torque loss, the moment is expressed as a function of angular speed of the motor. Term F_c in Eq. 14 represents the coulomb friction at the boundary lubrication interface.

$$F_f = \sqrt{2e}(F_{brk} - F_c) * \exp\left[-\left(\frac{v}{v_{st}}\right)^2\right] + F_c \tanh\left(\frac{v}{v_c}\right) + fv \tag{2.13}$$

$$M_s = \sqrt{2e}(M_{brk} - M_c) * \exp\left[-\left(\frac{\dot{\theta_m}}{\dot{\theta}_{st}}\right)^2\right] + M_c \tanh\left(\frac{\dot{\theta}}{\dot{\theta}_c}\right) + f\dot{\theta_m} \tag{2.14}$$

It is to be noted that Eq. (15) models the start-up torque to required overcome frictional resistance from all lubricating interfaces of the motor. From Eq. (14), as the velocity increases beyond v_{st}, the friction value is given by summation of coulomb friction component F_c and viscous friction component F_v. Similarly in Eq. (15), the term M_c can be equated to friction moment from shaft seal interface as it is independent of operating speed. Thus, Eq. (15) models the start-up torque loss when motor speed is lower than $\dot{\theta}_{st}$ and torque loss from shaft seal at higher speeds. Values of parameters $\dot{\theta}_{st}$, $\dot{\theta}_c$ and f in Eq. (15) are assumed based on equivalent values in [16]. The value of braking moment M_{brk}, which is the maximum frictional moment that must be overcome for the motor to start rotating, is the only key model parameter that requires tuning based on experimental data.

2.5. Moment due to load

While in operation, hydraulic motors are subjected to external loads which affect their dynamic behavior. Therefore, a dynamic model for these loads is required for modeling the dynamic behavior of the EGM. As it will be discussed in the next section, the reference tests are performed with the motor connected to a fan. The moment from such loads can be modeled as a viscous loss due to air resistance and inertia of the body. In the current model, the inertia of the load is added to the inertia of the gear 1 shaft as shown by Eq. (2). The air resistance is calculated using an empirical linear plus cubic relationship which is generally valid for loads such as a fan.

$$M_{fan} = k_{f1}\omega + k_{f2}\omega^3 \qquad (2.15)$$

The final structure of the reduced model as described in this section is shown in the Fig. 7.

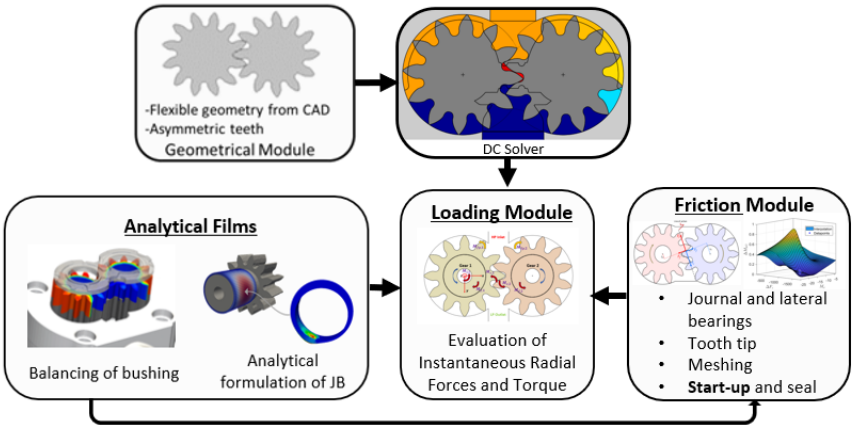

Fig 2.7: Schematic of reduced HYGESim model for transient simulations

3. EXPERIMENTAL SETUP AND SIMULATION MODEL

This section illustrates the experimental setup used to validate the model based on test performed on the reference EGM of table 1. The test schematic is provided in Fig. 8, and the main features of the sensors are provided in table 3. The test set up reproduces a typical hydraulic circuit for fan drive. The motor is supplied with a periodic flow by acting on the shaft speed of the speed pump, which varies from null to a given value. Consequently, the motor starts from rest, reaches a maximum speed and then comes again to rest.

Table 3: Summary of sensor specifications

Sensor	Model	Specifications	Accuracy
Pressure Transducer (P_1)	Parker SCPT-400	0-400 bar	±0.5% Full scale
Pressure Transducer (P_2)	Parker SCPT-400	0-400 bar	±0.5% Full scale
Flowmeter	Parker SCVF-060	0-60 L/min	±0.5% Full scale
Velocity Transducer (pump)	CCT transducers TR10	0-9000 RPM	±0.5% Full scale

Torque Transducer (pump)	CCT transducers TR10	0-250 Nm	±0.1% Full scale
Velocity transducer (motor)	Parker SCRPM-220	0-10000 RPM	±0.5% Full scale

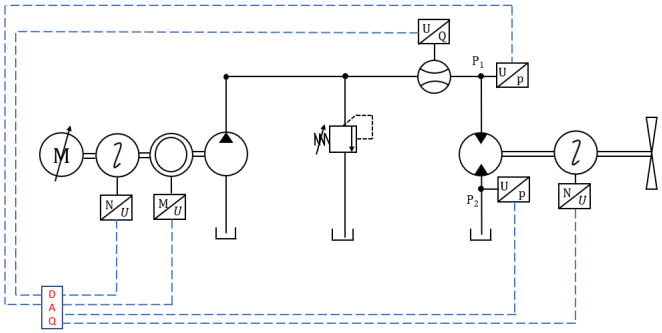

Fig. 3.1: Schematic of experimental setup

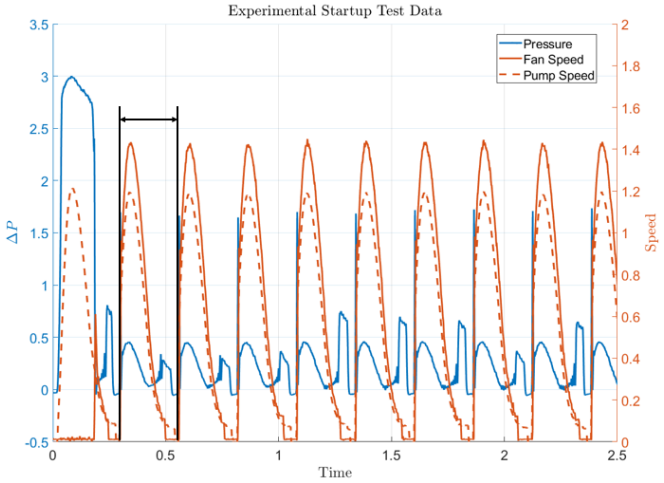

Fig. 3.2: Schematic of non dimensionalized experimental data

The measured pressure differential across the motor and the fan speed is used to validate the simulation model. The flow provided by the supply pump is estimated by the measured pump shaft speed and its volumetric efficiency map. The Hydraulic line connection between the pump and the motor is modelled by considering equivalent thickness and bulk modulus of the rubber hoses using pressure build-up equation (4). The load dynamic of the fun is governed by Eq. (16). As the experimental data is periodic, simulations are carried out for only one period of 20 seconds, marked in Fig. 9, which involves starting up and stopping of the motor.

4. RESULTS

This section provides comparison between experimental and simulated data for start-up pressure, motor pressure drop, and speed evolution over time. All results are non-

dimensionalized with respect to an undisclosed value of equivalent units for confidentiality. Table 4 shows the parameters which are used to obtain results presented in this section.

Figure 10 shows the comparison of motor fan transient speed obtained from simulation and experiments. Results for motor pressure drop comparison are shown in Figure 11. The simulation model captures the transience of fan speed and pressure accurately. The maximum pressure reached during this operation is defined as motor's startup pressure. The simulation predicts the start-up pressure to be almost 400% of maximum operational pressure during experimental cycle and agrees well with experimentally observed value.

Table 4: Motor simulation model calibrated parameters

Model Parameters	Value [unit]
Linear viscous loss coefficient (k_{f1})	0.0002 Nm/rpm
Cubic viscous loss coefficient (k_{f2})	4e-7 Nm/rpm
Braking friction moment (M_{brk})	1 Nm
Load moment of inertia (I_l)	0.0035 kgm^2
Seal friction loss (M_{seal})	0.15 Nm
Hydraulic line length (L)	2.5 m
Temperature	88^oC

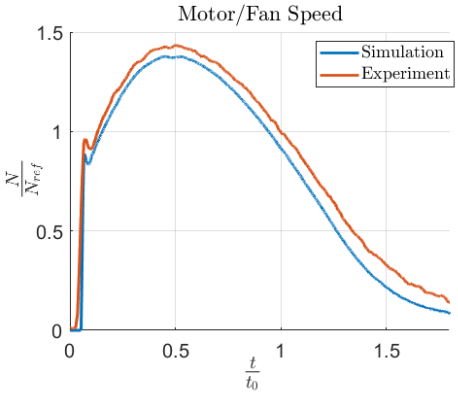

Fig. 4.1: Fan speed evolution with time – comparison between simulations and experiments

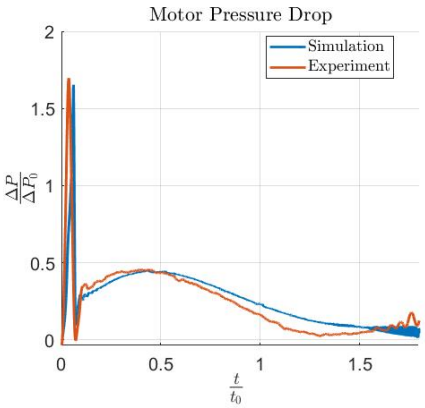

Fig. 4.2: Pressure evolution with time – comparison between simulations and experiments

An offset is seen in the predicted fan speed with respect to the experimental trend during transience. A possible reason can be given by inaccuracies in volumetric efficiency mapping which is used to estimate the inlet flow. During the start-up regime, the speed rise is seen to be more gradual in experimental case while the simulation shows a stiffer behavior. A similar effect is also seen in pressure plots leading to stiffer rise in start-up pressure. Regardless of small inaccuracies, the simulation model matches experimental behavior in terms of trends and magnitude in both start-up and transient regions. Thus, dynamic behavior of an external gear motor can be modelled using the simulation approach described in this paper.

4.1. Additional Model Capabilities – Prediction of hydromechanical efficiency

The presented model that predicts the moment loss due to friction at various interfaces can also be used to estimate the steady state hydromechanical efficiency of the reference unit. Example results for this parameter are compared with experimental data and are presented in a non-dimensionalized form in figure 12.

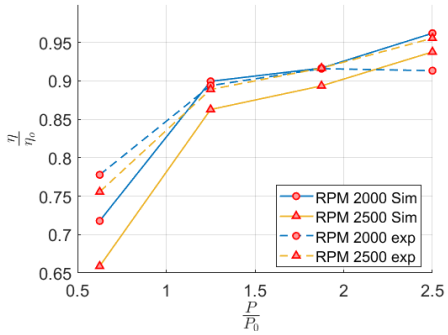

Figure 12: Hydromechanical Efficiency – comparison between simulations and experiments

The model captures the overall hydromechanical efficiency values and trends as seen in experimental data. The inaccuracies observed can be due to inaccurate estimation of seal loss with respect to different operating conditions. Another factor is the journal bearing model which does not account for deformation of shaft and bearing blocks, which can lead to inaccurate torque predictions at that interface.

5. CONCLUSIONS

This paper presents the modelling of the start-up transient features of external gear motors through a fast-modelling approach suitable for the analysis of the typical transient durations of such units. The modelling approach evaluates the net moment on both gear shafts arising from the pressurization of the tooth space volumes, as well as the frictional losses. The friction moments at the lubricating interfaces such as journal bearings and lateral films were determined using a CFD approach including effects of mixed lubrication and integrated in the reduced order model thought an analytical formulation to reduce computational time. Start-up torque loss was determined using a Stribeck curve-based approach, whose characteristics can be easily set by the user. Experiments were performed on a reference unit replicating a typical fan drive system, The predicted start-up pressure and motor speed results showed very good match with respect to experimental start-up test data.

As an additional capability, model shows the capability for predicting hydromechanical efficiency trends and levels at different operating conditions. The model has a potential for further refinements such as modelling the dynamics during stopping of motor. Effects of the solid body deformation of the shaft and the bearing block could be included in the torque loss determination at the journal bearing interface to further increase the model accuracy. Nevertheless, the fast computation time and high accuracy makes the proposed model suitable for performing system design analyses, and also component design optimization studies.

6. NOMENCLATURE

$M_{fp1,2}$	Moment due to fluid pressure on gears 1,2
$M_{f1,2}$	Moment due to friction on gears 1,2
$M_{c1,2}$	Moment due to contact of gear teeth on gears 1,2
M_l	Moment due to load
$I_{1,2}$	Moment of inertia of gears 1,2
I_l	Moment of inertia of load
$\alpha_{1,2}$	Angular acceleration of gears 1,2
p	Fluid pressure
K_{oil}	Bulk Modulus of working fluid
V_i	Volume of ith TSV chamber
$Q_{in,out}$	Flow entering, exiting TSV chamber
τ_w	Wall shear stress at lubricating interfaces
r_s	Shaft radius
η	Lubricant viscosity
$\varphi_{f,fp,fs}$	Flow factors in mixed lubrication model
μ	Coefficient of friction
F_f	Friction force
$U_{1,2}$	Surface velocities at top and bottom surface of lubricating interfaces
S	Sommerfield number
M_{tip}	Friction moment at tooth tip interface
h	Gap height
L,b	Depth, width of gear tooth
r_g	Gear outer radius
M_s	Torque loss at start-up
M_{brk}	Braking friction moment at start-up
M_c	Coulomb friction moment at start-up
f	Viscous friction loss coefficient at seals
$\dot{\theta}_m$	Motor angular speed
$\dot{\theta}_{st}$	Stribeck characteristic speed
$\dot{\theta}_c$	Coulomb characteristic speed
M_{fan}	Viscous torque loss for a fan drive

7. REFERENCES

[1] A. Harnoy, "Model-Based Investigation of Friction During Start-Up of Hydrodynamic Journal Bearings", J. Tribol. 1995, 117(4), pp. 667-673.

[2] Bouyer J, Fillon M. Experimental measurement of the friction torque on hydrodynamic plain journal bearings during start-up. Tribol Int 2011;44:772–81

[3] Y. Henry, J. Bouyer, M. Fillon, Experimental analysis of the hydrodynamic effect during start-up of fixed geometry thrust bearings. Tribology International 2018;120:299-308

[4] E. H. Gassenfeit, A. Soom, Friction Coefficients Measured at Lubricated Planar Contacts During Start Up. Journal of Tribology 1988; 110:533-538

[5] J. Garcia, J. Lumkes, B. Hecahman, A. Martini, Viscosity Dependence of Static Friction in Lubricated Metallic Line Contacts, Tribology Transactions 2011; 54: 333-340

[6] P. Michael, J. Garcia, S. Bair, M. Devlin and A. Martini, Lubricant Chemistry and Rheology Effects on Hydraulic Motor Starting Efficiency, Tribology Transactions 2012; 55:549-557

[7] H. E. Merritt, Hydraulic Control Systems, Wiley Publisher, New York, 1967

[8] A. Hibi, T. Ichikawa, Mathematical Model of the Torque Characteristics for Hydraulic Motors, Bulletin of JSME, 1977; 20-143:616-621

[9] R.Rituraj, A. Vacca, M. Rigosi, Modelling and validation of hydro-mechanical losses in pressure compensated external gear machines, Mechanism and Machine Theory 161 (2021) 104310

[10] T. Ransegnola, F. Zappaterra, A. Vacca, A strongly coupled simulation model for external gear machines considering fluid-structure induced cavitation and mixed lubrication, Applied Mathematical Modelling, Volume 104, 2022, Pages 721-749.

[11] A. Vacca, M. Guidetti, Modelling and Experimental Validation of external spur gear machines for fluid power applications, Simul. Model. Pract. Theory. 19 (2011), 2007-2031

[12] N. Patir, and H. S. Cheng, "An Average Flow Model for Determining Effects of Three-Dimensional Roughness on Partial Hydrodynamic Lubrication." ASME. *J. of Lubrication Tech*. January 1978; 100(1): 12–17. https://doi.org/10.1115/1.3453103

[13] B.O. Jacobson, B.J. Hamrock, Non-Newtonian fluid model incorporated into elastohydrodynamio lubrication of rectangular contacts, J. Tribol. 106 (1984) 275–281, doi:10.1115/1.3260901

[14] G. Nikas, R. Sayles, Study of leakage and friction of flexible seals for steady motion via a numerical approximation method, Tribology International 39 (2006) 921–936

[15] B. Armstrong and C. de Wit. Friction Modeling and Compensation. CRC Press, 1995 edition

[16] D. Thiagarajan, A. Vacca, S. Watkins, On the lubrication performance of external gear pumps for aerospace fuel delivery applications, Mechanical Systems and Signal Processing, Volume129, 2019, Pages 659-676.

Biographies



Ajinkya Pawar completed his bachelor's degree in mechanical engineering and master's degree in Robotics from Indian Institute of Technology Madras, in 2020. He started pursuing a doctorate degree in mechanical engineering at Purdue University under the guidance of Prof. Andrea Vacca. His interests are in numerical modeling of external gear machines considering deformation and thermal effects.



Andrea Vacca is the Maha Fluid Power Faculty Chair and a Professor at Purdue University. He currently leads the Maha Fluid Power Research Center which was established in 2004 by the late Prof. Monika Ivantysynova. Dr. Vacca completed his studies in Italy (Ph.D. from the University of Florence in 2005), and he joined Purdue University in 2010 after being an Assistant Professor at the University of Parma (Italy). Fluid power technology has been Dr. Vacca's major research interest since 2002. Dr. Vacca authored the textbook "Hydraulic Fluid Power" by Wiley and more than 150 technical papers, most of them published in international journals or referred conferences. He is chair of Fluid Power Systems and Technology Division (FPST) of the American Society of Mechanical Engineers (ASME), and a former chair of the Fluid Power Division of the Society of Automotive Engineers (SAE). Dr. Vacca is also one of the Directors of the Global Fluid Power Society (GFPS).



Manuel Rigosi completed his MSc degree in Mechanical Engineering from the University of Parma, in 2011. After an internship, he joined Casappa R&D Department in the role of Simulation Engineer, focused in replicating the physical phenomena within hydraulic gear and piston pumps through the usage of customized lumped parameter models and 3D simulations. In 2018 he took the responsibility for the development of new products with a team of engineers and designers. In recent years he has contributed to innovation by signing 4 patents regarding solutions already applied to the latest products Casappa is offering on the market today.

Design, Modeling, and Experimental Characterization of a Fast Additively Manufacturable MRI-Compatible Pneumatic Motor for Surgical Robots

Mengtang Li[1,#,*], Jing Zhang[1,#], Xiyun Wu[1], Jieting Yuan[1],

Xiyu Wang[1], Yongyin Ye[1], and Beichen Ding[1]

[1]School of Intelligent Systems Engineering, Sun Yat-Sen University, Shenzhen, China

Email: limt29@mail.sysu.edu.cn

#Contributed Equally

**Corresponding Author*

Abstract.

For robot assisted surgery under magnetic resonance imaging (MRI) guidance, constraints such as material limits, actuation method limits and available sensor limits have made the design and control of an actuation and transmission system the most challenging problem. Aiming at tackling the aforementioned issues, this paper proposes a novel pneumatic powered motor, which features few as two inputs, continuous and back-drivable motion outputs, integrated MRI-compatible speed sensor, compact modularly switchable down-speed components, and fast additively manufacture ability (22 components in total). It promisingly fills the gap between the current MRI-compatible surgical robots and available actuation methods and offers an alternative approach for the community to actuate various surgical robotic platforms. Detailed design methods for the pneumatic motor and integrated rotary encoder are developed first. Motor performances are experimentally evaluated next to analyse and demonstrate its characteristics under various pressures against different load torques. Finally, the proposed pneumatic motor is compared with recent MRI-compatible pneumatic actuators, illustrating the feasibility of the proposed fluid power motor for actuations of MRI surgical robots.

Keywords. Pneumatic systems, Pumps and motors, Fluid power components, Fluid power drives and transmissions, MRI (Magnetic Resonance Imaging)

1. INTRODUCTION

Compared with computed tomography (CT) and X-ray, magnetic resonance imaging technology can quickly and clearly generate human soft tissue imaging without exposing patients or physicians to ionizing radiation. These advantages make MRI guided surgical robot an appealing trend in the future of minimal invasive surgery [1]. However, the

magnetic environment strictly restricts the medical devices constructed of ferromagnetic materials and other specific materials from entering the magnetic scanner to prevent danger or degrade the imaging quality. The American Society for Testing and Materials (ASTM) [2] and the U.S. Food and Drug Administration (FDA) [3] have strictly defined standards for MR-compatible and MR-safe materials and driving methods. Considering the safety and imaging quality requirements, the design and construction of MR-compatible actuators are the foundation and critical technology of MRI guided surgical robot [4].

On the premise of MRI compatible materials, pneumatic actuators demonstrate noteworthy advantages in compact size, simpler structure, sterility and safety, compared with other actuation methods, such as hydraulics [5,6,7], shape memory alloy (SMA) [8], piezoelectric ceramics motor (also known as ultrasonic motor) [9,10], tendon (cable) drive [11,12], etc. Hence it is the most widely studied and applied actuation methods in the field of MRI guided surgical robot [13,14]. Among pneumatic methods, the turbine/fan-based air motor [15,16] illustrates attracting advantages in manufacturing simplicity and device compactness compared with the piston cylinder-based actuator [17,18,19]. It also has advantages in generating continuous and bidirectional motions compared with gear-based pneumatic stepper actuator that can only output unidirectional rotary motion with fixed steps [20,21,22,23]. A novel flexible fluidic actuator (FFA) for MRI surgical robots can dramatically simplify the manufacture progress via selective laser sintering (SLS) [24], yet it suffers from the same issues as the gear-based pneumatic actuators and is only able to produce step motions slowly. It can be seen that the pneumatic motor acts like a 'DC motor' for the joints of MRI guided surgical robots. However, only one design of MRI compatible pneumatic rotary motor has been designed and applied into surgical robot platforms according to a comprehensive literature review done in 2020 [4]. Adequate room for design improvement exists.

This paper proposes a new MRI compatible pneumatic motor based on strain wave harmonic mechanism, featuring the characteristics of 1) continuous and back-drivable motion outputs, 2) integrated MRI-compatible speed sensor, 3) compact modularly switchable down-speed components, and 4) fast additively manufacture ability. Preliminary motor performance tests are conducted to evaluate and analyze the design and working principle. The proposed actuator aims at offering the community with a new actuation method for the community to actuate various surgical robotic platforms. The remainder of this paper arranges as follows. Section 2 presents the mechanism design and working principle, and integrated rotary encoder. Section 3 describes the motor performance characterizations. Results discussion and actuator comparison are included as well. Section 4 draws conclusive remarks.

2. MATERIALS AND METHODS

2.1. Mechanism Design and Working Principle

The proposed MRI compatible pneumatic motor for surgical robots mainly consists a turbine and a strain wave gear box (also called harmonic drive) with necessary supporting cases. The turbine and all supporting cases are fast additively manufactured by a 3D printer using acrylonitrile butadiene styrene (ABS). Other MRI-compatible materials can also be used to improve the structure strength or to reduce motion friction. The proposed pneumatic motor differs from the conventional ones which adopt fix displacement architectures for example

a sliding vane structure. A modified Pelton turbine [25] is designed and utilized to allow bidirectional operation when pressurized air is supplied to the two inlet ports through long transmission air hoses from a standard medical gas tank placed in the safe room. The pressurized air pushes the turbine to rotate and dissipates from exhaust ports into the ambient environment, without any safety or sterility concerns. Necessary ball bearings are placed axially to support the shaft with low rotary frictions.

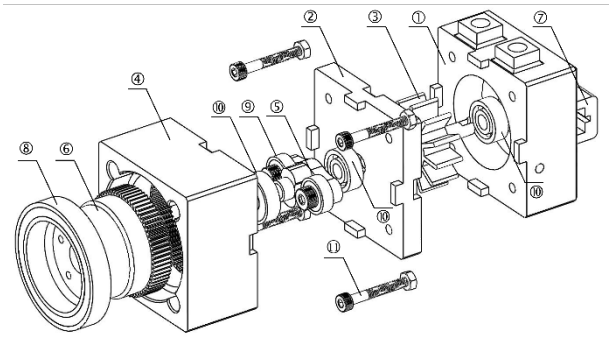

Figure 1 Exploded CAD view of the pneumatic motor assembly.

A harmonic drive system couples with the output shaft of the turbine to increase output torque while reducing speed. The circular spline is incorporated into the harmonic drive case. The flex spline is fabricated with soft material (thermplastic polyurethane, TPU) to permit some deformation. The wave generator is designed to install two ball bearings distributed evenly. As the wave generator rotates along with the turbine shaft, the outer cases of the two ball bearings push against and roll on the inner surface the deformable flex spine, causing the flex spline to rotate in the opposite direction at a reduced speed. The flex spine meshes with the circular spline, outputting torque for joints of surgical robots. A reduction ratio r can be obtained by the following equation:

$$r = \frac{n_{flex} - n_{cir}}{n_{flex}} \tag{1}$$

where n_{flex} and n_{cir} are the number of teeth of flex spline and circular spline, respectively. Normally, the circular spline involves two more teeth than the flex spline, leading to the result of:

$$r = \frac{-2}{n_{flex}} < 0 \tag{2}$$

Hence, the mechanism of the strain wave gear is capable of achieving a large down-gear ratio within a compact space. The negative sign tells the fact the output rotation is in the opposite with the input shaft. The detailed design of a first-generation prototype (60mm x 40mm x 40mm) is depicted in Figure 1, along with part descriptions listed in Table 1. Photographs of the first-generation prototype is shown in Figure 2. The working principle of the soft flex spline is demonstrated as well. Here a harmonic drive system with -1:40 gear ratio is designed. Other options can also be customed designed.

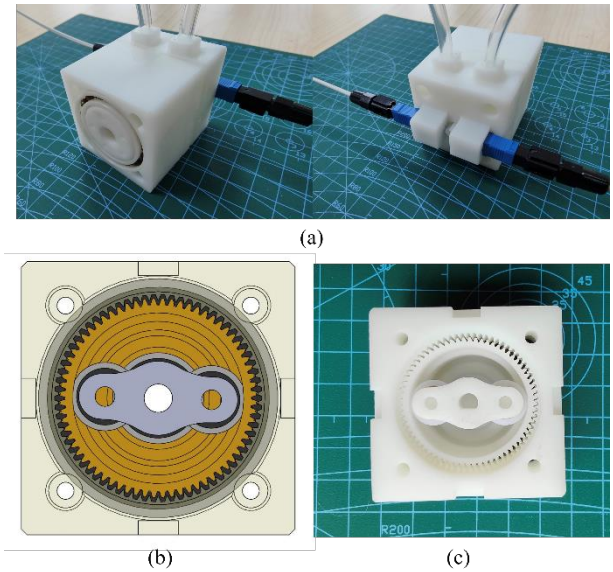

Figure 2 (a) Assembly of the proposed pneumatic motor. (b) CAD view of the strain wave gear system: the flex spline is designed in a circular manner (not deformed here). (c) Photo of the strain wave gear system: the flex spline is deformed because the two ball bearings push against it.

Table 1 Fabrication materials of the proposed pneumatic motor

Number	Part Name	Description	Material
1	Motor case 1	3D print	ABS
2	Motor case 2	3D print	ABS
3	Turbine	3D print	ABS
4	Circular spline	3D print	ABS
5	Wave generator	3D print	ABS
6	Flex spline	3D print	TPU-30
7	Rotary encoder (not plotted)	Internet fiber wire and wire connector	Optical fiber and plastic
8	Ball bearing 1	KIF®Φ30×Φ42×7	Polyamide and glass
9	Ball bearing 2	KIF®Φ4×Φ12×4	Polyamide and glass
10	Ball bearing 3	KIF®Φ5×Φ16×5	Polyamide and glass
11	Screws and Nuts	M3×252	Plastic

2.2. Integrated Rotary Encoder

Conventional rotary encoder relies on electrical signal to function and transmit measurement data, which inevitably involves danger inside the scanner and compromises MR imaging quality. Hence, an MRI compatible rotary encoder is necessarily needed. Inspired by the built-in encoder design in [16], two Internet optical fiber wires are used where one fiber carries a continuous light beam generated from a light source (e.g. a fiber wire visual fault locator, Cinyobo®) while the other one receives the light beam. A cutout at the end of the

shaft cyclically blocks the light beam when the shaft rotates, thus creating two binary pulses per revolution. The pulses of high/low light density can be captured by a photoresistor, transmitting the binary signal into useful rotary speed data. Another pair of optical fiber wires at $90\ deg$ angular offset can be added to increase the resolution and accuracy at the cost of a larger device size. The shaft speed $n\ [rpm]$ during a period of time $T\ [sec]$ can simply be obtained by:

$$n = \frac{n_{pulse}}{2T} \cdot \frac{1}{n_{optpair}} \cdot \frac{60sec}{1min} \tag{3}$$

where n_{pulse} is the number of pulses, $n_{optpair}$ is the number of optical fiber wire pairs. Introducing interrupts every time a high pulse comes and computing the time interval between each interrupt is another method to obtain instantaneous rotary speed and can significantly improve the accuracy. But methods similar to this would require higher sampling frequency.

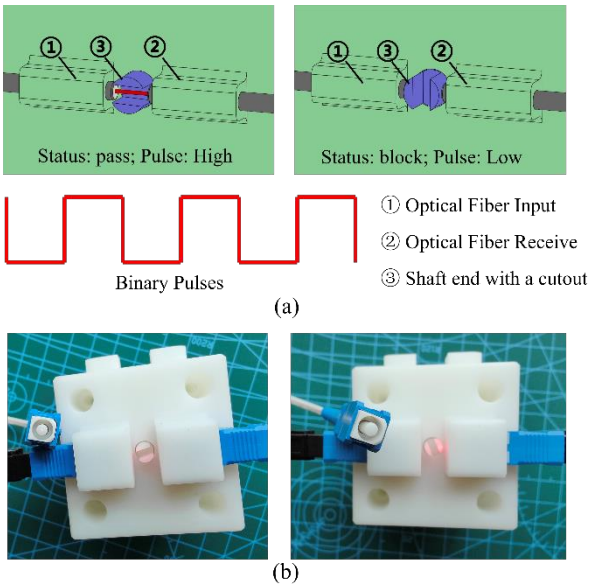

Figure 3 (a) Schematics of the integrated rotary encoder: Left: continuous light beam can pass through the cutout of the end of the shaft, leading to high light density; Right: light is blocked, resulting in low light density. (b) Photos of optical light beam passes (left) or is blocked (right).

Consider the fragility of optical fibers (the core of an optical fiber wire made of glass), and the potential miscounting due to misalignment of optical fiber wires, this paper improves the previous design by utilizing standard Internet optical fiber wire connectors. This not only protects the light transmitting optical fibers, but also provides pre-aligned click-on/off sockets. Figure 3 shows the detailed design and working principle of the integrated rotary encoder.

2.3. Minimally Invasive Steerable Needle Robot

The proposed MRI-compatible pneumatic motor serves as a fundamental power unit for joints of surgical robots. To straightforwardly illustrate the potential applications of the proposed motor, a minimally invasive steerable needle deployment robot, which can be used for percutaneous treatment for biopsy or delivered therapy, is shown in Figure 4.

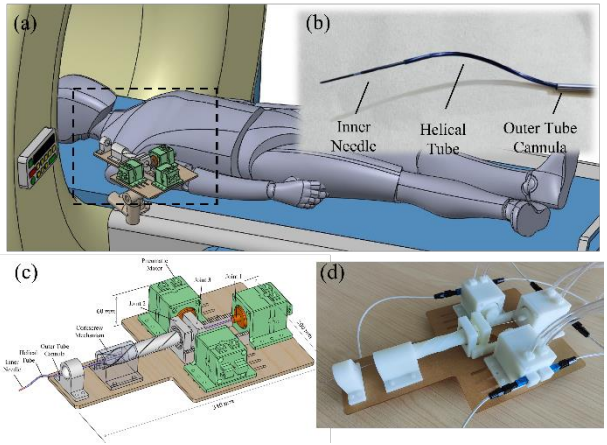

Figure 4 (a) Schematic diagram of an MRI-compatible steerable needle robot actuated by the proposed motor. (b) A minimally invasive concentric steerable needle. (c) Design details of the needle deployment robot. (d) Photo of the first-generation prototype.

3. RESULTS

3.1. Motor Performance Evaluation

An experimental prototype of the proposed MRI compatible motor is designed and fast manufactured to study its working mechanism and performance. The integrated rotary encoder is first tested to evaluate its performance accuracy by comparing the calculated speed with measurements from a commercial handheld laser tachometer (FEITA). Different pressures are supplied to the proposed motor, leading to different rotary speeds. Since a long polyurethane transmission air hose (1 m, I.D. 4mm, O.D. 6mm) is used, pressure delay and hence motor response delay are inevitable, which also occurs in the real MRI compatible pneumatic surgical robots [26]. Here, rotary speed is read once the motor reaches its steady state. Figure 5 plots and compares the rotary speed (without strain wave gear system) measurements from the integrated encoder and the commercial tachometer at various shaft speeds. It can be seen that both signals match well and errors for speeds higher than $300\ [rpm]$ in between falls below 2%. The large error at low speed comes from light pulse miscounting and this affects significantly at lower speeds. Since gear-down component exists and the motor normally operates at middle to high speed, the miscounting would affect less and hence the accuracy of the proposed encoder is sufficient.

Next, the output shaft of the prototype is attached to a magnetic particle brake (SKISIA PMB-0.5, 0.5 Nm max) to simulate various resistive load torques. The input pressure is manually altered by a throttle valve, and pressure level is measured by a pressure transducer (LONTROL, 0-0.6 MPa, 4-20 mA) placed right next to the motor. Under a certain level of

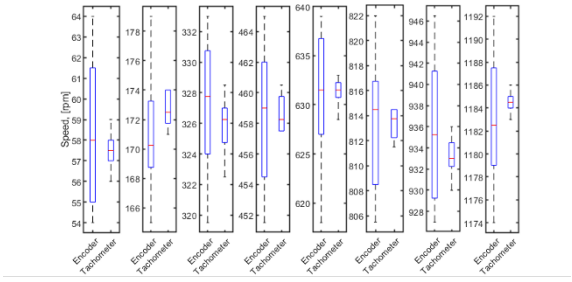

(a)

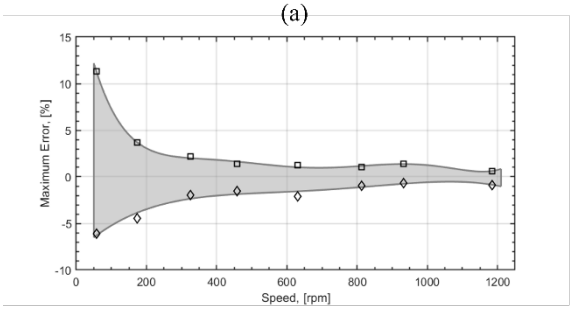

(b)

Figure 5 Encoder accuracy. (a) Encoder measurements vs tachometer measurements [rpm]. (b) Error bounds from 8 trails for each test speed [%].

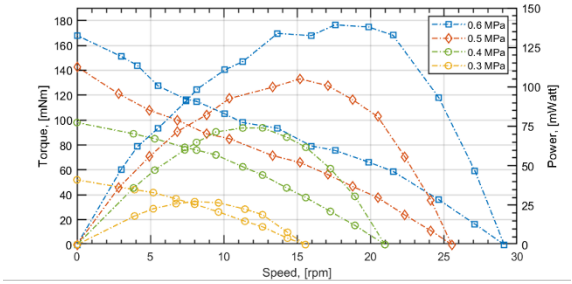

(a)

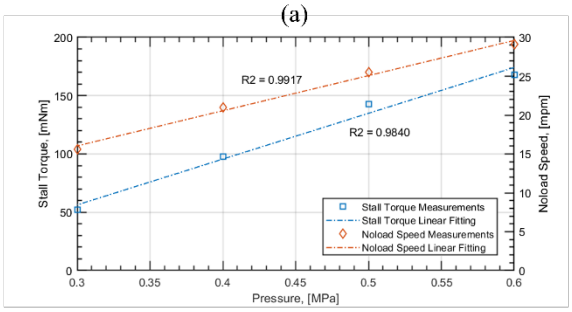

(b)

Figure 6 (a) Left y-axis: Torque vs speed under different pressures. Right y-axis: Corresponding power vs speed under different pressures. (b) Stall torque and no-load speed with respect to various input pressure.

input pneumatic pressure, the resistive load torque is gradually increased from zero until the stall torque. A steady rotary speed is eventually reached under a certain load torque and input pressure, reflecting the speed versus torque characteristics.

The resulting motor performance characteristics are plotted in Figure 6(a). The left y-axis shows different torque versus rotary speed under various supplied pressure, while the right one shows the corresponding output motor power calculated by $P = \omega\tau$. Clear parabolic shapes are noticed in the plot, where maximum power or optimal operation condition lies in the middle-to-high speed region. Dynamic models of the pneumatic motor can be characterized and fitted using the acquired empirical data. However, since surgical operations are slow and steady, only low bandwidth motions (<0.5~1Hz) are needed [26]. Therefore, satisfactory accuracy can still be achieved with model-independent simple PI control using feedback provided by integrated rotary encoder.

Intersections of these characteristic curves with x-axis and y-axis show the stall torque and no-load speed versus different input pressure, which are more straightforwardly plotted in the left and right y-axes of Figure 6(b), respectively. It can be seen that the motor speed and torque have a fairly linear relationships with input pressure (R^2>0.98). The slope also relies on the gear ratios.

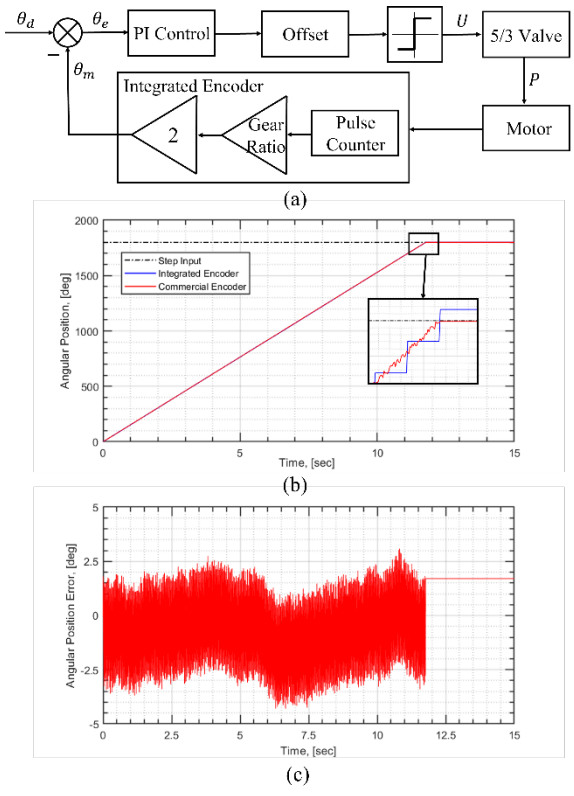

Figure 7 (a) Control diagram. (b) Angular position step response [deg]. (c) Error between the integrated encoder and a commercial rotary encoder [deg].

3.2. Motor Control Performance

A closed-loop control test is conducted to further evaluate the proposed motor with its integrated rotary encoder. A step input of $10\pi\ rad$ (five revolutions, output shaft rotary angle) is sent as a set point to the pneumatic motor. The integrated encoder counts the pulses to acquire the rotated angle. A command voltage is generated by a simple PI controller with angular position error as the input. Since a basin-like relationship between the input electrical signal (it is more obvious for voltage command than current command) and the pneumatic conductance around the center exists for conventional 5/3 directional proportional solenoid pneumatic valves, an offset is established (positive 5 Volts here). The supplied air pressure is set to 0.5 MPa. An absolute optical rotary encoder (HKT32) is used to compare with the integrated encoder and the results are plotted out in Figure 7.

Generally, the two signal matches fairly well except that some discrepancy occurs at the end region. This can be explained by the fact that one input shaft revolution only generates two pulses and 80 pulses for each output shaft revolution, leading to a $4.5\ deg$ resolution. Also, note that this simple control strategy works because a dead band caused by the gear system's frictions can halt the rotor fast enough once the supplied pressured is stopped, which is similar to other turbine or gear-based MRI compatible pneumatic actuators.

3.3. Comparative Study

The proposed motor is compared with some representative MRI compatible pneumatic actuators in the aspects of size, manufacture complexity, dynamic performance, integrated encoder, and bi-directional motion ability, listed in Table 2. A comprehensive comparison among recent MRI compatible actuators including pneumatics, hydraulics, SMA, piezo motor and other novel methods can be found in [4].

Table 2 MRI compatible motor comparison

	Stoianovici et al. [22]	Sajima et al. [20]	Chen et al [21]	Chen et al [16]	Proposed
Mechanism	Pneumatics, gear	Pneumatics, gear	Pneumatics, gear	Pneumatics, turbine	Pneumatics, turbine
Number of parts	~25	~10	~7	~30*	20**
Size [mm]	Φ85×30	Φ30×35	Φ10×60	Φ44×79	60×40×40
Speed [rpm]	166.6	50	60	370	29
Torque [mNm]	640	150	90	460	170
Power [W]	3	0.47	2.4	6	0.14
Encoder	Yes	No	No	Yes	Yes
Bi-directional	No	No	No	Yes	Yes

*Every piece of all the Tamiya® planetary gear boxes is counted.

**Including all screws and nuts.

The proposed MRI compatible pneumatic motor is inspired by the needs of improving the previous design (Chen's Pneumatic Motor [16], developed by the author's former

group). It can be seen that the proposed pneumatic motor consists relatively fewer components due to the usage of the strain wave gear mechanism. Compared with Chen's Motor [16], the proposed pneumatic motor is manufacturable through fast additively manufacture and standard mechanical components, eliminating dependencies on purchasing Tamiya® No. 72001 for the (four) planetary gear box. Though these planetary gear boxes can be 3D printed, it involves more components than the proposed design, leading to higher structure complexity. Also, since it falls into the pneumatic turbine based actuator category, it is capable of generating continuous bi-directional motion, serving as a more flexible surgical robot joint.

Yet, note that the output speed and torque of the proposed pneumatic motor prototype are comparatively low with other actuators. This may be explained by the fact that 1) the friction between the rolling ball bearing case and the inner side of the flex spline is relatively large, and 2) the mesh between the flex spline and the circular spline does not meet quite well since 3D printed TPU shows slightly lower manufacture resolution than ABS.

4. CONCLUSION

A novel design of a MRI compatible pneumatic motor based on strain wave harmonic mechanism is proposed in this paper, which features few as two inputs, continuous and back-drivable motion outputs, and fast additively manufacture ability (22 components in total). An integrated MRI-compatible speed sensor is designed that provides a pre-aligned click-on/off option for easy installation. Detailed design methods and motor performance tests are presented, offering a new actuation method for the community to actuate various surgical robotic platforms.

Future work includes further design optimization as the proposed MRI compatible harmonic driven pneumatic motor prototype is noticed to have slightly large friction torque compared with other turbine/fan based pneumatic motor. Also, motor performance tests covering larger operating conditions, bandwidth tests for various gear-down ratios and with different lengths of air transmission hoses should be tested in the future to meet a range of practical requirements.

5. REFERENCES

[1] T. Peters and K. Cleary, Image-guided interventions: technology and applications. *Springer Science & Business Media*, 2008.

[2] A. Standard, "F2503. standard practice for marking medical devices and other items for safety in the magnetic resonance environment," *ASTM International*, West Conshohocken, PA, 2013.

[3] F. G. Shellock, T. O. Woods, and J. V. Crues III, "Mr labelling information for implants and devices: explanation of terminology," pp. 26–30, 2009.

[4] Q. Xiao, R. Monfaredi, M. Musa, K. Cleary, and Y. Chen, "Mrconditional actuations: A review," *Annals of Biomedical Engineering*, pp. 1–27, 2020.

[5] Z. Dong, Z. Guo, K.-H. Lee, G. Fang, W. L. Tang, H.-C. Chang, D. T. M. Chan, and K.-W. Kwok, "High-performance continuous hydraulic motor for mr safe robotic teleoperation," *IEEE Robotics and Automation Letters*, vol. 4, no. 2, pp. 1964–1971, 2019.

[6] A. Bruyas, F. Geiskopf, L. Meylheuc, and P. Renaud, "Combining multi-material rapid prototyping and pseudo-rigid body modeling for a new compliant mechanism," in *2014 IEEE International Conference on Robotics and Automation (ICRA)*. IEEE, 2014, pp. 3390–3396.

[7] N. Burkhard, S. Frishman, A. Gruebele, J. P. Whitney, R. Goldman, B. Daniel, and M. Cutkosky, "A rolling-diaphragm hydrostatic transmission for remote mr-guided needle insertion," in *2017 IEEE international conference on robotics and automation (ICRA)*. IEEE, 2017, pp. 1148–1153.

[8] M. Ho and J. P. Desai, "Characterization of sma actuator for applications in robotic neurosurgery," in *2009 Annual International Conference of the IEEE Engineering in Medicine and Biology Society*. IEEE, 2009, pp. 6856–6859.

[9] S. Hao, A. Camilo, G. A. Cole, H. Nobuhiko, C. M. Tempany, and G. S. Fischer, "High-field mri-compatible needle placement robot for prostate interventions," *Studies in Health Technology and Informatics*, vol. 163, p. 623, 2011.

[10] R. A. Lathrop, D. C. Rucker, and R. J. Webster, "Guidance of a steerable cannula robot in soft tissue using preoperative imaging and conoscopic surface contour sensing," in *2010 IEEE International Conference on Robotics and Automation*. IEEE, 2010, pp. 5601–5606.

[11] D.Wu, G. Li, N. Patel, J. Yan, R. Monfaredi, K. Cleary, and I. Iordachita, " Remotely actuated needle driving device for mri-guided percutaneous interventions," in *2019 International Symposium on Medical Robotics (ISMR)*. IEEE, 2019, pp. 1–7.

[12] Y. M. Senturk and V. Patoglu, "Design and control of an mri compatible series elastic actuator," in *2016 IEEE international conference on robotics and biomimetics (ROBIO)*. IEEE, 2016, pp. 1473–1479.

[13] Y. Chen, I. Godage, H. Su, A. Song, and H. Yu, "Stereotactic systems for mri-guided neurosurgeries: a state-of-the-art review," *Annals of Biomedical Engineering*, vol. 47, no. 2, pp. 335–353, 2019.

[14] C. Nimsky, O. Ganslandt, B. Von Keller, J. Romstock, and R. Fahlbusch, "Intraoperative high-field-strength mr imaging: implementation and experience in 200 patients," *Radiology*, vol. 233, no. 1, pp. 67–78, 2004.

[15] Y. Chen, S. Xu, A. Squires, R. Seifabadi, I. B. Turkbey, P. A. Pinto, P. Choyke, B. Wood, and Z. T. H. Tse, "Mri-guided robotically assisted focal laser ablation of the prostate using canine cadavers," *IEEE Transactions on Biomedical Engineering*, vol. 65, no. 7, pp. 1434–1442, 2017.

[16] Y. Chen, I. S. Godage, Z. T. H. Tse, R. J. Webster, and E. J. Barth, "Characterization and control of a pneumatic motor for mr-conditional robotic applications," *IEEE/ASME Transactions on Mechatronics*, vol. 22, no. 6, pp. 2780–2789, 2017.

[17] Y. Chen, K.-W. Kwok, and Z. T. H. Tse, "An mr-conditional high-torque pneumatic stepper motor for mri-guided and robot-assisted intervention," *Annals of Biomedical Engineering*, vol. 42, no. 9, pp. 1823–1833, 2014.

[18] G. S. Fischer, I. Iordachita, C. Csoma, J. Tokuda, S. P. DiMaio, C. M. Tempany, N. Hata, and G. Fichtinger, "Mri-compatible pneumatic robot for transperineal prostate needle placement," *IEEE/ASME Transactions on Mechatronics*, vol. 13, no. 3, pp. 295–305, 2008.

[19] F. S. Farimani and S. Misra, "Introducing pneuact: parametricallydesigned mri-compatible pneumatic stepper actuator," in *2018 IEEE International Conference on Robotics and Automation (ICRA)*. IEEE, 2018, pp. 200–205.

[20] H. Sajima, H. Kamiuchi, K. Kuwana, T. Dohi, and K. Masamune, "Mrsafe pneumatic rotation stepping actuator," *Journal of Robotics and Mechatronics*, vol. 24, no. 5, pp. 820–827, 2012.
[21] Y. Chen, C. D. Mershon, and Z. T. H. Tse, "A 10-mm mr-conditional unidirectional pneumatic stepper motor," *IEEE/ASME Transactions on Mechatronics*, vol. 20, no. 2, pp. 782–788, 2014.
[22] D. Stoianovici, A. Patriciu, D. Petrisor, D. Mazilu, and L. Kavoussi, "A new type of motor: pneumatic step motor," *IEEE/ASME Transactions on Mechatronics*, vol. 12, no. 1, pp. 98–106, 2007.
[23] V. Groenhuis, F. J. Siepel, and S. Stramigioli, "Dual-speed mr safe pneumatic stepper motors." in *Robotics: Science and Systems*, 2018.
[24] D. B. Comber, J. E. Slightam, V. R. Gervasi, J. S. Neimat, and E. J. Barth, "Design, additive manufacture, and control of a pneumatic mrcompatible needle driver," *IEEE Transactions on Robotics*, vol. 32, no. 1, pp. 138–149, 2016.
[25] J. Erlach, "Pelton turbine," Aug. 21 1990, US Patent 4,950,130.
[26] M. Turkseven and J. Ueda, "An asymptotically stable pressure observer based on load and displacement sensing for pneumatic actuators with long transmission lines," *IEEE/ASME Transactions on Mechatronics*, vol. 22, no. 2, pp. 681–692, 2016.

Biographies



Mengtang Li received the B.S. degree with honor in Astronautics Engineering from Northwestern Polytechnical University, Xi'an, China, in 2014, the M.S. degree in Electrical Engineering and the Ph.D. degree in Mechanical Engineering from Vanderbilt University, Nashville, TN, USA, in 2016 and 2020, respectively. Dr. Li was a visiting scholar in Sarver Heart Center, School of Medicine, University of Arizona during 2018 to 2020. He is currently an Assistant Professor in School of Intelligent Systems Engineering in Sun Yat-Sen University, Shenzhen, China. His research interests include fluid powered soft robotic system design and control, mechanical circulatory support device (total artificial heart, ventricular assist device) design, mobile unmanned robots/vehicles/aircrafts control.



Jing Zhang is currently pursuing her B.S. degree with School of Intelligent Systems Engineering, Shenzhen Campus of Sun Yat-Sen University, Shenzhen, China. Her research interests include modelling and control of surgical robots.

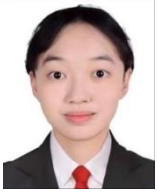

Xiyun Wu is currently pursuing her B.S. degree with School of Intelligent Systems Engineering, Shenzhen Campus of Sun Yat-Sen University, Shenzhen, China. Her research interests include modelling and control of surgical robots.



Jieting Yuan is currently pursuing her B.S. degree with School of Intelligent Systems Engineering, Shenzhen Campus of Sun Yat-Sen University, Shenzhen, China. Her research interests include machine learning and deep learning.



Xiyu Wang is currently pursuing the B.S. degree with School of Intelligent Systems Engineering, Shenzhen Campus of Sun Yat- sen University, Shenzhen, China.
Her research interests are in robotics and machine learning.



Yongyin Ye is currently pursuing the B.S. degree with School of Intelligent Systems Engineering, Shenzhen Campus of Sun Yat-Sen University, Shenzhen, China. Her research interests are related with Neural Network Learning and Applications of parallel robots and Intelligent Control.



Beichen Ding received his Ph.D. in Mechanical Engineering from the University of Bath, UK, in 2019. He is currently an Associate Professor in the School of Intelligent Systems Engineering, Sun Yat-sen University, China.

A Study on a Twin-Screw Pump for Thermal Management Systems by means of CFD using SimericsMP+®: experimental validation and focus on Pressure Pulsation

Pasquale Borriello[1,3], Emma Frosina[2], Pierpaolo Lucchesi[3], Adolfo Senatore[1]

[1]Department of Industrial Engineering University of Naples Federico II - Naples, Italy, pasquale.borriello@unina.it, senatore@unina.it

[2]Department of Engineering University of Sannio - Benevento, Italy, frosina@unisannio.it
[3]Fluid-o-Tech s.r.l.- Milan, Italy, p.lucchesi@fluidotech.it

Abstract.

This research is about an innovative methodology for simulating spindle pumps using a full 3D-CFD transient approach by means of Simerics MP+®. Spindle pumps are known from the literature to be very reliable, efficient, and low-noise emission machines. Latest EU Regulations have been ambitious by pushing the transportation sector increasingly towards the reduction of primary harmful pollutants and CO_2 emissions. In this context, the thermal management of BEVs (Battery Electric Vehicle) is gaining a new technological interest. In this scenario, improvements on pump efficiency are needed to determinately reduce the absorbed energy during real on-the-road operation. Commonly, centrifugal pumps are used for this kind of application, but their efficiency is highly vulnerable to rotational speed, wasting energy in real exercise, even if they are designed to have a very high efficiency at the design point. Thus, adopting an accurately designed spindle pump for thermal management systems could fit the new needs coming, in particular, from the automotive industry. Computational Fluid Dynamic (CFD) allows the real-time monitoring of pressure distribution, velocity field, mass flow rate, rotor torque, and other performance indicators resulting in a very powerful tool to lead design and optimization phases of such kind of machines. In this paper, a new Simerics MP+® template which allows for the simulation of spindle pumps, never presented in literature, has been adopted and validated by comparing the model results with tests coming from an experimental campaign. In the last section, data on pressure-pulsation of a spindle-pump using CFD are shown for the first time: considerations are carried out both in time-domain and frequency-domain.

Keywords. Screw pump, spindle pump, thermal management, automotive, CFD, SimericsMP+, experimental validation, pressure pulsation.

1. INTRODUCTION

During the recent years, primary pollutants and CO_2 emissions caused by on the road transportation sector have been reduced worldwide through increasingly strict regulations. The European Union (EU) with the European Green Deal aims to grab climate neutrality by 2050. Regulation (EU) 2021/1119 of the European Parliament and of the Council of 30 June 2021 place new targets: 55% net greenhouse gas emissions reduction compared to 1990 by 2030, better known as "Fit for 55" package. To face this issue, vehicle manufacturers are expanding the production of hybrid and electric vehicles [1], which may help in cutting down primary pollutants in urban areas [2]. Also, the recent assimilation of different thermal needs in the engine cooling system (charge air cooling [3, 4, 5], air conditioning condenser [6], separated cooling between engine head and block [7], cabin heater, etc.) outcomes an increased complexity, which claims for increased degrees of freedom in designing new cooling strategies [8, 9, 10]. Generally, centrifugal pumps are qualified in engine cooling systems. In traditional Internal Combustion Engine (ICE) cooling system, centrifugal pumps, mechanically coupled with the crankshaft, were used. This technology does not let on to vary the pump speed separately from the engine speed, preventing a high pump efficiency, which highly relies on the impeller speed. Indeed, centrifugal pumps grant the best performances at the design point, known as at Best Efficiency Point (BEP), commonly located at high flow rate and rotational speed, corresponding to the maximum engine mechanical power. However, the pump works far from the BEP in the course of homologation cycles, resulting in a decreased pump efficiency (between 15-20%), and so in a compelling power absorbed compared to the propulsion one [11]. An electrically actuated centrifugal pump would deliver a faster engine warm-up, accountable for around 2/3 of the whole harmful emissions in typical driving cycles [12], but not a pump efficiency increase.

Rather, spindle pumps are rotary, positive displacement pumps that can have one or more spindles to deliver high or low viscosity fluids along an axis. Like all positive displacement pumps, efficiency is essentially independent on rotational speed. Additionally, spindle pumps are known for simplicity, small volume, high ability of self-priming, smooth working, easy disassembly, low vibration, pressure fluctuation and noise emissions [13]. Such features make them a good fit for the new demands coming from automotive sector, as explained already in [14]. Yet, the spindle kinematics and internal flow field of these machines are very complicated, so the number of accessible flow studies on spindle pumps is quite narrow, and the understanding of the internal flow is yet lacking. Consequently, to meet the modern needs coming from the market, the full recognition of the process within the pump is vital. Spindle machines have been extensively investigated in terms of thermodynamic modelling [15, 16, 17], even for multiphase flow [18, 19, 20]. Spindle pump performances can be predicted as well by lumped-parameters models. A triple spindle pump for an aerospace application has been considered in [21], where a parametric analytical model was developed and validated, arranging the boundary-layer theory [22] to get the volumetric capabilities of the pump. The indirect correlation between backflow and wear resistance in triple spindle pumps was studied developing an accurate theoretical model in [23]. That research was later expanded computing the pressure loads acting on the pump rotors in [24], and finally simulated and experimentally validated even considering dynamic effects in [25]. Lumped parameter models have been developed also for multiphase spindle pumps: in [26] is presented an exhaustive thermodynamic model experimentally validated,

model further upgraded considering gas-liquid mixtures with very high gas volume fractions (up to 99 %) [27]. The literature resources credited above give a good understanding of the working process but points out that enhancements are achievable specially for novel applications of multiphase pumps. Recapitulating, most of the current works are based on the thermodynamic chamber, mathematical models which neglect kinetic energy and simplify the analysis on the main and leakage flows. Few published works rely on steady state CFD which considers static mesh of the moving flow domains [13, 28, 29, 30]: by adopting a static grid, however, the transient essence of the working process and the actual velocity field of the main flow are ignored. Breakthrough in employing CFD for the study of positive displacement spindle machines was made by Kovacevic et al. [31] who generated a structured moving mesh for spindle compressor rotor based on a rack generation approach arranged by Stosic et al. [32]. This revolutionary work in grid generation for spindle machines allowed for the CFD simulations and performance prediction of spindle pumps and compressors [33, 34, 35], even catching cavitation phenomena [36, 37].

This paper shows an innovative methodology for simulating spindle pump all-in-one commercial software, never showed before. In fact, differently from what described by the authors in [37], in which the commercial software SCORG® was adopted to mesh the rotors, both the structured moving mesh of rotor fluid domain and the mesh for stationary domains such as ports and pipes are generated using the grid generator built into the commercial software SimericsMP+®. The resolution of the structured moving mesh in the CFD solver is supported by use of the user-defined function and interface, as described in [38] [39]. In particular, the General Gear Template implemented in SimericsMP+® v.5.2.13 has been used to manage the mesh and the movement of the deforming in time field of the rotors. A standard k-ε turbulence model to include turbulent phenomena and a full cavitation model available in SimericsMP+® have been empowered as well to accurately predict the pressure distribution, velocity field, real-time mass flow rate, rotor torque, and other important performance indicators. In the next sections, the 3D-CFD model will be introduced and validated with experimental results. In the end, data on pressure-pulsation of a spindle pump by means of CFD are presented for the first time: results are carried out both in time-domain and frequency-domain.

This research is part of a particular program, established by the Italian government, named PON Research & Innovation where Italian Universities develop Ph.D. programs in collaboration with Italian firms and foreign universities. The parties involved in this program are the University of Naples Federico II, University of Sannio, Fluid-o-Tech, located in Corsico (MI) - Italy, and the Maha Fluid Power Research Center, Purdue University (USA).

2. TWIN-SCREW PUMP MODELLING

2.1. Reference Machine

Spindle pumps transfer the fluid medium in perpetual volume cavities, labelled chambers, from suction to delivery side. Of course, like all positive displacement machines, spindle pumps do not create pressure but rather simply move the medium from one spot to another; the output pressure of the pump is dependent on the back pressure downstream. Due to the helical shape of the spindles, chambers are regularly identified by closely intermeshed

counter-rotating spindles and moved linearly towards the discharge port. The chambers are not perfectly sealed but connected to each other via different small gaps, termed circumferential, radial and flank gaps where a leakage flow results [40], shown in Fig.2.1. The clearance between the tip of one spindle and the shaft of the other spindle coincide to the radial gap, while the clearances between the tip of the spindles and pump housing consist in the circumferential gaps. Differently to radial and circumferential gaps, flank gap exhibits a complex 3D geometry which brings a considerable difficulty regarding the set-up of a CFD model. In this application case, the driving screw consists of a double-start thread trapped 900° around its corresponding shaft. The driven spindle is a three-start thread resulting in a 2/3 transmission ratio. It is qualitatively shown in Fig. 2.1; no more geometrical parameters are reported for confidentiality reason. The screws are just entrained inside a cylindrical support bordered by the pump housing, no bearings are adopted to facilitate the pump manufacture, as ordinarily demanded in automotive applications, but permits axes misalignments, and thus casual dry friction phenomena between rotors and casing may take place during pump operation. But ordinarily, the film of fluid entrained in the circumferential gap hydrodynamically supports the rotating spindles. The flow conditions of this thin film of fluid are determined by pump speed and pressure rise. So, for very low pump speed operation or very high pressure rise the pump may face risk of damages.

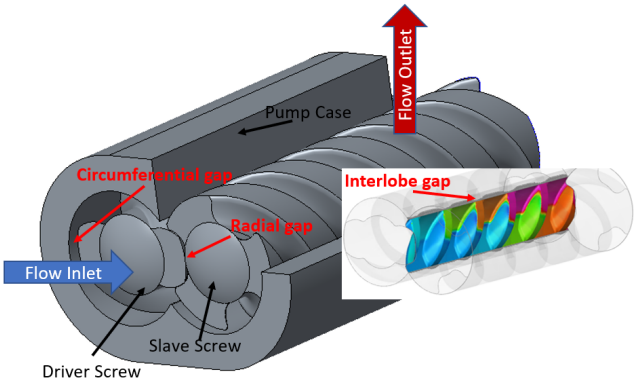

Figure 2.1. Main leakage paths and reference twin-screw pump.

2.2. Experimental Set-Up

The hydraulic schematic of the test rig is presented in Fig.2.2; the medium is a 50:50 mixture of water and glycol (IP Antifreeze Red) at room temperature, with a density of 1070 kg/m3 and viscosity of 0.004 Pa s. A variety of working points are achieved by using a control valve on the discharge side. Rotational speed can be regularly controlled and modified by a dual-range torque meter (Kistler Type 4503A). The pressure at discharge pipe is recorded by an amplified pressure transducer (Unik 5000 pmp). The uncertainty of pressure measurements is estimated to be lower than 0.4 %. The flow rate is measured in the discharge pipe by the means of a Coriolis flowmeters (Sitrans F C Mass 2100 Di 3-40) with an uncertainty below 0.15 % in the involved mass flow range.

The experimental test champaign has been carried out at the Laboratory of Fluid-o-Tech, an Italian company with over 70 years of experience in the engineering and manufacturing of positive displacement pumps and fluidics system.

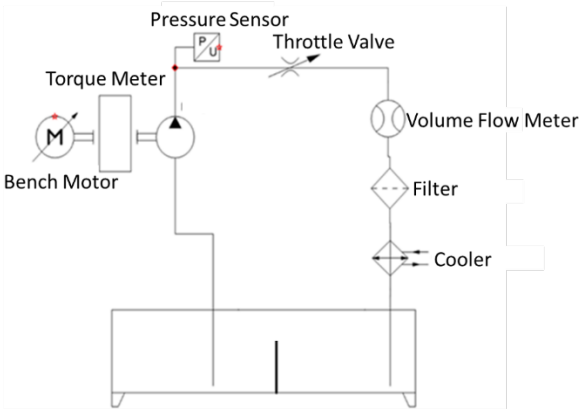

Figure 2.2. Hydraulic schematic of experimental results.

3. SIMULATION METHODOLOGY

Positive displacement spindle pumps act on the basis of changing the size and position of a working domain which therefore causes variation in the pressure of the working domain thereby moving the fluid. To determine performances of a spindle pump, quantities such as mass, momentum, energy, etc. require to be numerically modelled. A closely coupled, time dependent set of partial differential equations (PDEs), based on a finite volume method (FVM) represent the governing equations to be solved. The solution of the governing equations is achieved using the commercial software Simerics MP+®. Technicalities on the solution scheme can be found in [41] and are shortly condensed here. The numerical scheme is based on the Reynolds-averaged Navier-Stokes (RANS) equations, and a standard k - ε model is used to consider turbulence effects. In Simerics MP+®, as in the original Singhal et al model [42], the fluid in cavitating flows is always considered to be a mixture of liquid, vapor, and some non-condensable gases. By default, the cavitation model accounts for both liquid-vapor phase change and the effect of non-condensable gases. Based on the modelling approach for non-condensable gas (NGC) effect, Equilibrium Dissolved Gas Model (EDGM), in which the mass fraction of the non-condensable gas dissolved in the liquid is equivalent to the equilibrium value, was employed. Simulations have been conducted with a reference pressure of 1.01 bar as pump inlet pressure, while the pump outlet pressure has been set at different discharge pressure up to 4.01 bar. By modifying the pressure difference between the inlet and the outlet, the required flow rate is obtained. Rotating speed of the driver rotor ranges from 500 rev/min up to 4000 rev/min. Stagnation inlet and pressure outlet are used correspondingly for the inlet and outlet boundaries. The starting pressure and initial velocity are 1.01 bar and 0 m/s, respectively. The turbulence intensity is 1% and the turbulence viscosity ratio is 10.

3.1. Grid Generation

Generating the mesh consists in discretizing a working domain in control volumes for which a solution of local fluid properties is to be established. In this work, the Grid Generator built in SimericsMP+® permits the discretization of the computational domain. The volume of fluid (VOF) domain, shown in Fig.3.1, has been extracted from the CAD 3D drawing using the commercial software Creo®, and spilt in sub-volumes, which will be interfaced afterward in Simerics MP+®. Finally, the VOF has been imported in the CFD code in STL format and then meshed with appropriate grid sizes.

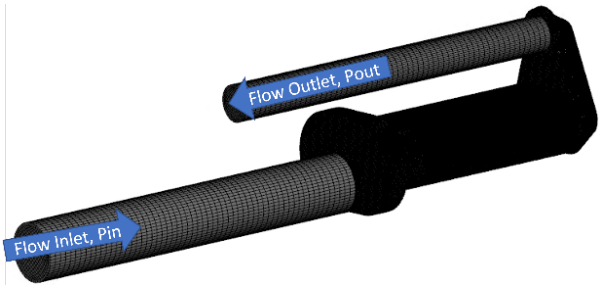

Figure 3.1. VOF domain.

An unstructured body-fitted binary tree approach is employed for the static mesh of the inlet port and outlet port using SimericsMP+® general grid generator. For the spindles, whose working domain has to change and deform time accordingly following the aspect of the operating principle, the new General Gear rotor template mesher for spindle machines have been adopted. A mesh sensitivity analysis has been managed to obtain the outlet volumetric flowrate independence of cell size, as shown in Fig. 3.2. The VOF counts around 2.87 M cells, in particular the rotor mesher for the structured spindle volumes has been set as follows: 120 cells in the circumferential direction, 8 in the radial direction and 600 in the axial direction. Models with finer mesh have been explored, but the results did not sustain the increment in the computational time.

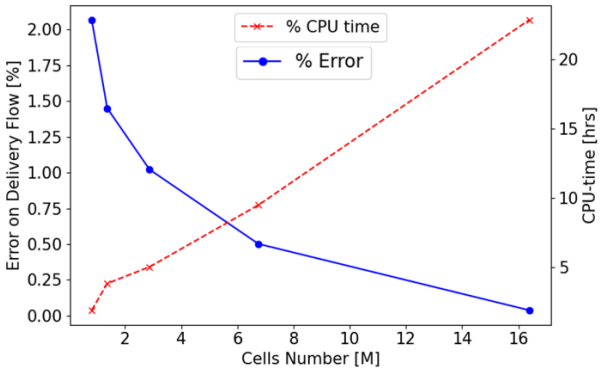

Figure 3.2. Mesh sensitivity analysis.

4. RESULTS

After completing the mesh sensitivity analysis, the CFD model can be validated on experimental data. Simulation have been run on a desktop workstation equipped with a 32 cores Intel® Xeon® Gold 6142 CPU 2.60GHz processor with 128 Gb memory, where each run took about five hours for a pump revolution. Each spindle pump rotation has been simulated by means of 180 time-steps, resulting in 2 degrees main rotor rotation per step, as previously done by the authors [37]. An opportune convergence criterion of four order of magnitude has been chosen to satisfy mass flow conservation between inlet and outlet and achieved in 50 inner iterations at each time step. As regards the flow rate, time averaging is performed for one spindle revolution, after it has been guaranteed that initial transients have been abated.

4.1. Model Validation

In Fig. 4.1 experimental and numerical results are compared on a flow-pressure diagram; comparison among four rotational speeds are showed (500, 1500, 3000, 4000 rev/min). These results show the benefit obtained considering the micro-motion of the spindles due to the unbalanced pressure field in the radial cross because of the helical shape of the spindles, as shown in Fig.4.2. Basically, to recreate the realistic situation of the spindles being pushed by the hydrostatic force [42], both spindles have been shifted from the center of the pump housing, resulting in the spindles eccentric with respect to the pump housing, with the smaller gap set at 5 μm. In fact, in [37], the maximum error in the averaged flow rate was 10%, with a standard deviation of the same order of magnitude. In this study the mean error in the averaged flow rate is 0.3% with a maximum error of 1.2% and a standard deviation of 0.7%. Therefore, a first critical achievement obtained by the fluid-dynamic model developed in the present paper is the considerable reduction of the error with respect to the previous modeling approach.

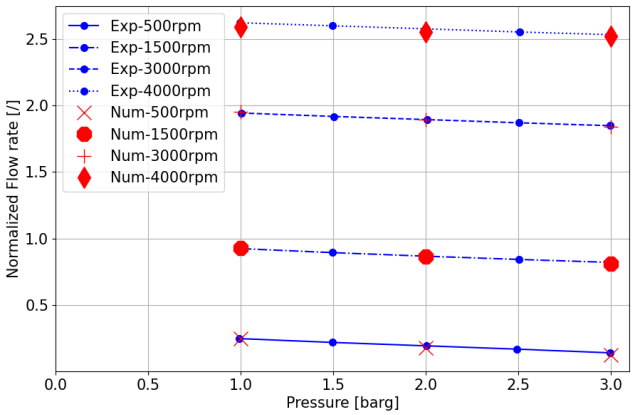

Figure 4.1. Numerical model validation – Normalized Flow rate vs Pressure.

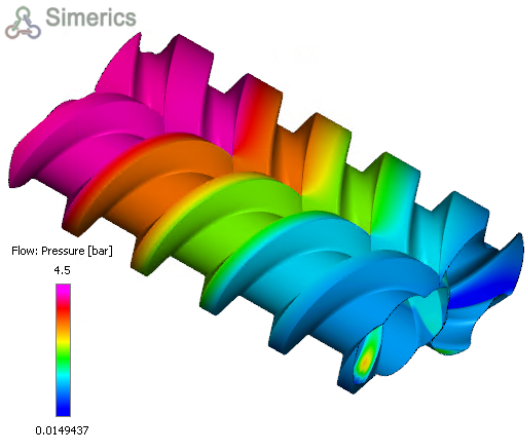

Figure 4.2. Pressure distribution: unbalanced in radial cross section.

Fig.4.3 shows the comparison between the predicted and measured torque at two different pressures rises and over four different pump's speed: excluding 500 rev/min, the maximum error is 11.2% while average error is 4% with a standard deviation of 6.9%.

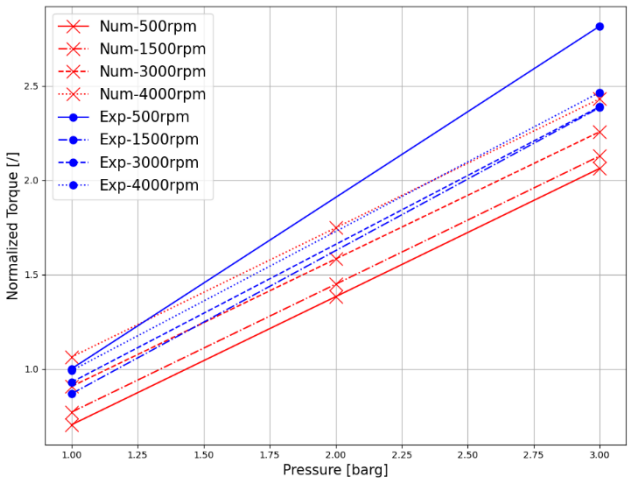

Figure 4.3. Numerical model validation – Torque vs Pressure.

This is an interesting result, meaning that torque due to friction and contact between the spindles is a very small part respect to torque due to pressure and viscous effect that are instead kept into account by the CFD model. From Fig.4.3 is also visible that, while at 1500 and 3000 rev/min torque predicted from CFD tends to underestimate the real torque, as expected, at 4000 rev/min the trend is the opposite. This can be explained looking at Fig.4.4:

in a) six probing points along the axis direction of the spindles have been put; in b) the pressure of each of those points has been plotted. It is evident that the higher the speed the higher the pump's suction capability, resulting in a lower pressure at spindles' inlet side, eventually meaning that the delta pressure the spindles have to overcame at 4000 rev/min results bigger than at 500 rev/min.

At 500 rev/min, instead, higher torque absorptions can be explained due to a not fully developed lubrication regime, as anticipated in Section 2.1.

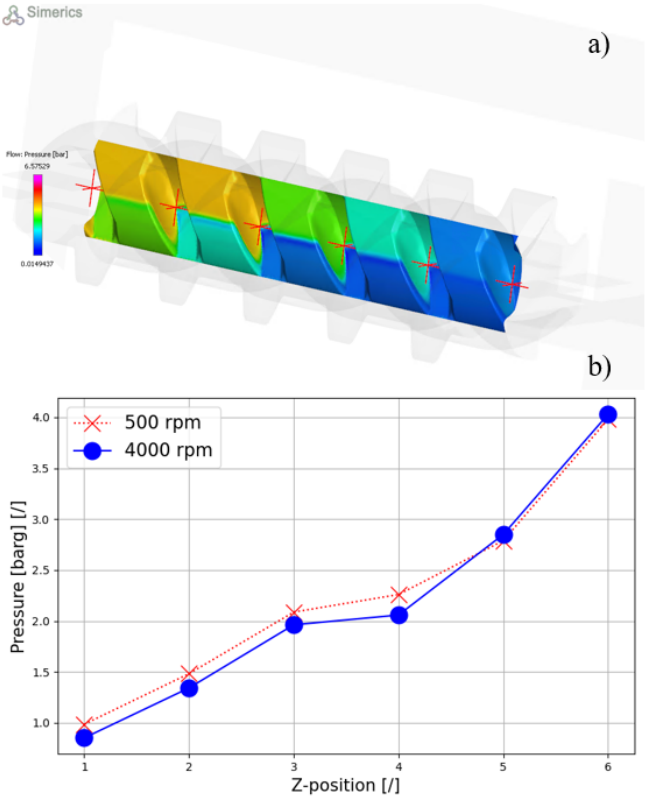

Figure 4.4. Torque analysis: a) six probing points have been put along the axis of the spindle in the CFD model; b) local pressure has been plotted for each point. At 400 rev/min pressure at spindle's inlet side is lower due to higher suction capability resulting in a bigger pressure drop.

4.2. Pressure Pulsation

In this section, for the first time in literature, pressure pulsation of spindle pump by means of CFD are presented. The fluid domain described above has been modified according to [44-45].

As showed in Fig. 4.5, avoiding any discontinuity in the diameter, the system implements a perfect constant diameter duct coupled with a calibrate orifice: this design creates a system load, that can be easily replicated in the numerical model. In future, numerical ripples will be compared with experimental data to be done by modifying the test rig and placing a pressure transducer in the same position of the red probing point visible in Fig. 4.5.

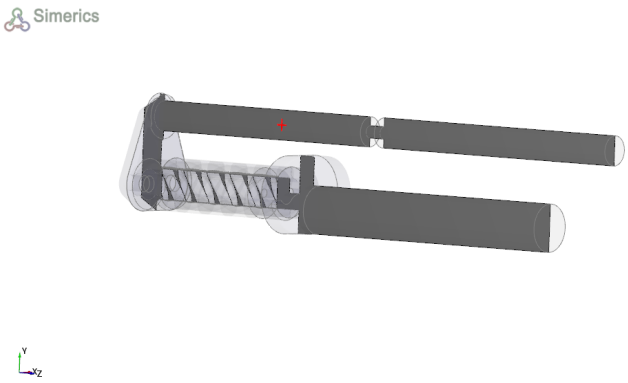

Figure 4.5. VOF on a X-plane – Detail on the delivery line

In Fig.4.6 is reported a numerical comparison of the pressure ripple, both in time domain and frequency domain, for three different imposed circumferential gaps: a) baseline pump, b) double than baseline (later called 2* Baseline), c) four times bigger than baseline (later called 4* Baseline). All the three models have been run at 2641 rev/min. Looking at frequency-domain, main contributes are imputable to geometrical parameters of the spindles. In fact, considering that:

$$f_1 = {}^{2641}/_{60} = 44.02\ Hz \tag{4.1}$$

and recalling that the driver spindle has 2 starts while the driven spindle has 3 starts, frequencies such as:

$$2 * f_1 = 88.03\ Hz \tag{4.1}$$

$${}^{2}/_{3} * f_1 = 29.34\ Hz \tag{4.1}$$

$${}^{3}/_{2} * f_1 = 66.03\ Hz \tag{4.1}$$

and their multiples such as:

$$3 * f_1 = 132.05\ Hz \tag{4.1}$$

$$4 * f_1 = 176.07\ Hz \tag{4.1}$$

$$6 * f_1 = 264.1\ Hz \tag{4.1}$$

$$8 * f_1 = 352.13\ Hz \tag{4.1}$$

can be individuated.

Analyzing in time domain results from Fig. 4.6, it is clear that Baseline and 2*Baseline shapes are very much comparable. Even in frequency domain, the contributions are consistently at the same values, with a much higher component at $2f_1$. Going at much higher circumferential gap, like the 4*Baseline model, contributions on frequency domain are spread across more frequencies, as guessable looking at the shape in time domain. Since the three different models are exposed to a different downstream pressure because they have different volumetric efficiency, the Non-Uniformity Grade (NUG) [46] is reported in Table I for comparison. Thus, the analysis confirms that, as known from literature, fluid born noise in spindle pumps has a very little contribute on the overall noise emission since pressure pulsation are very low.

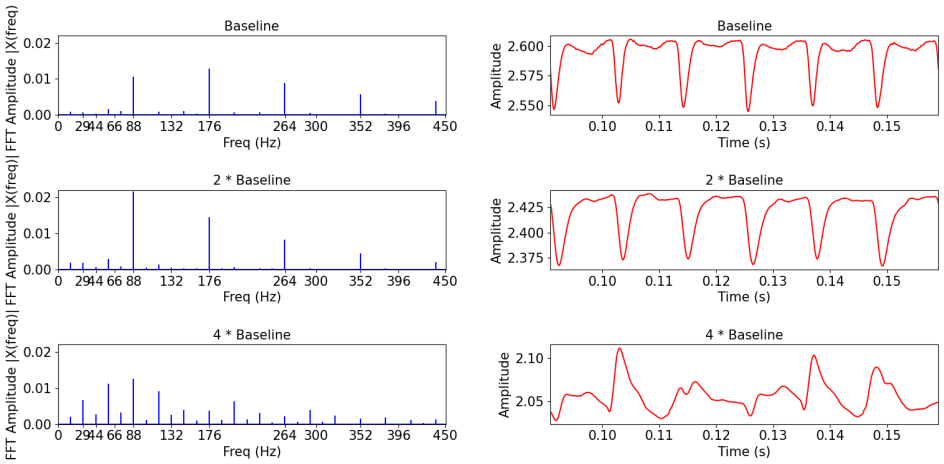

Figure 4.6. Pressure pulsation in time-domain and frequency-domain for three different circumferential gap: a) Baseline; b) 2*Baseline; c) 4*Baseline.

TABLE I. NUG AMONG THREE DIFFERENT CFD MODELS

MODELS	NUG
a) Baseline	0.024
b) 2 Baseline*	0.030
c) 4 Baseline*	0.041

4.3. Cavitation

3D-CFD simulation allows the user to monitor important performance indicators such as pressure distribution, mean velocity distribution, velocity distribution in gap areas, parameters related to turbulence model and many others. In this section considerations related to cavitation phenomena are carried out.

Cavitation may occur at the spindle leading edge, the radial gaps and the flank gaps, as already described in [37]. Over flank gaps, as visible in Fig.4.4.a), high pressure differences lead local velocities to reach high values consequently lowering the local static pressure. Along circumferential gaps, local velocities reach high values because of high rotational speed. That higher circumferential velocity causes higher pressure losses in the lower part of the chamber resulting in a consequent reduction of total pressure, also increasing the dynamic pressure. The reduction of total pressure and the rise of the dynamic pressure on the other hand leads to lower static pressure at the bottom side of any chamber. As showed in Fig.4.7, Gas Volume Fraction in proximity of the 5 μm clearances along circumferential gaps are more important to what showed in [37] since rotors are moved in y-direction accounting for the unbalanced pressure in the radial cross, as discussed in Section 4.1.

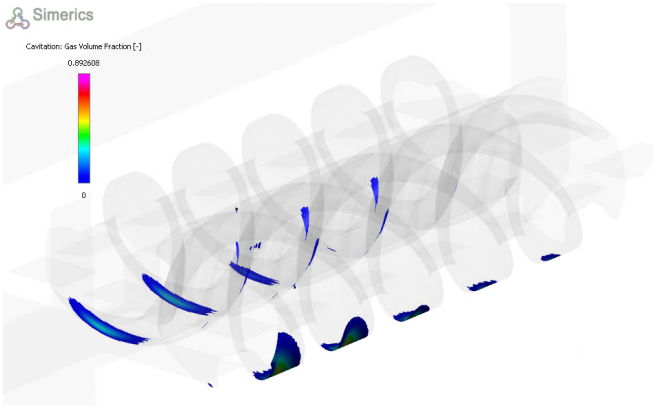

Figure 4.7. Isosurface of the Gas Volume Fraction at 3000 rev/min and ΔP=3 bar.

5. CONCLUSIONS

This paper presented a methodology for simulating spindle pumps by means of 3D-CFD employing the commercial software SimericsMP+®. Turbulence and cavitation have been included in the numerical model to capture any aspect during the real operation. An experimental test campaign was specifically performed with the aim of validating the developed tool. Comparisons between experimental results and numerical predictions were presented as concerns the unit steady-state operating features.

Numerical results were also presented concerning the fluctuations of the outlet pressure for three different circumferential gaps, that is a parameter of primary importance when studying the fluid borne noise for the reduction of the noise emissions in hydraulic machines. The presented comparisons highlight the potentiality of the tool for the prediction of pressure ripple as effects of the operating conditions and to identify the main design. Finally, it is possible to conclude that the presented tool has powerful capability in predicting with a good accuracy the real-time mass flow rate and rotor torque; by also looking at pressure distribution, velocity field, and other important performance indicators, the presented numerical approach can lead design and optimization phase of such kind of machines.

6. ACKNOWLEDGMENTS

The authors would like to thank the support from Giuseppe Ricucci of Fluid-o-Tech, from Federico Monterosso and Micaela Olivetti of OMIQ s.r.l.

7. REFERENCES

[1] IEA, Global EV Outlook 2021.

[2] S.I. Ehrenberger, M. Konrad, F. Philipps, "Pollutant emissions analysis of three plug-in hybrid electric vehicles using different modes of operation and driving conditions", Atmos. Environ. 234, 2020.

[3] R. Cipollone, D. Di Battista, A. Gualtieri, "A novel engine cooling system with two circuits operating at different temperatures", Energy Conversion and Management, 75, pp. 581-592, 2013.

[4] H. Chen et al., FCA US LLC, "Chiller system for an engine with a forced induction system", United States Patent, US10006339B2, 2018.

[5] D. E. Hornback et al., FCA US LLC, "Vehicle thermal system for reduced fuel consumption", United States Patent, US 10216258B1, 2019.

[6] D. Di Battista, R. Cipollone, High efficiency air conditioning model based analysis for the automotive sector, International Journal of Refrigeration, 64, pp. 108-122, 2016.

[7] R. Cipollone, D. Di Battista, A. Gualtieri, "Head and block split cooling in ICE", IFAC Proceedings Volumes (IFAC-PapersOnline), 45 (30), pp. 400-407, 2012.

[8] T. Castiglione, P. Morrone, L. Falbo, D. Perrone, S. Bova, Application of a model-based controller for improving internal combustion engines fuel economy, Energies, 13 (5), art. no. 1148, 2020.

[9] A. K. Haghighat, S. Roumi, N. Madani , D. Bahmanpour, M. G. Olsen, "An intelligent cooling system and control model for improved engine thermal management", Applied Thermal Engineering 128, 253–263, 2018.

[10] H. Mu, Y. Wang, H. Teng, Y. Jin, X. Zhao, X. Zhang, "Cooling system based on double-ball motor control valve", Advances in Mechanical Engineering, Vol. 13(5) 1–12 , 2021.

[11] L. Mariani, M. Di Bartolomeo, D. Di Battista, R. Cipollone, F. Fremondi, R. Roveglia, "Experimental and numerical analyses to improve the design of engine coolant pumps", E3S Web of Conf. 197, 06017, 2020.

[12] J. Gao, G. Tian, A. Sorniotti, A. E. Karci, R. Di Palo, "Review of thermal management of catalytic converters to decrease engine emissions during cold start and warm up", Applied Thermal Engineering 177–187, 2019.

[13] Li, W., Lu, H., Zhang, Y., Zhu, C., Lu, X., & Shuai, Z., "Vibration analysis of three-screw pumps under pressure loads and rotor contact forces", Journal of Sound and Vibration, 360, 74-96, 2016.

[14] G. Di Giovine, L. Mariani, M. Di Bartolomeo, D. Di Battista, R. Cipollone, "Triple-Screw pumps for ICE cooling systems in the transportaction sector", E3S Web of Conferences 312, 07024, 2021.

[15] Li F. Screw pump [M]. Beijing, China: Machine Press, 2010.

[16] Vetter, G., and Wincek, M, "Performance Prediction of Twin-Screw Pumps for Two- Phase Gas/Liquid Flow," Pumping Machinery, Fluid Engineering Conference (FED), ASME, Washington, DC, 154, pp. 331-340, 1993.

[17] Patil A., “Performance evaluation and CFD simulation of multiphase twin-screw pumps”, PhD Thesis, Texas A&M University, College Station, TX, 2013.
[18] Mewes D, Aleksieva G, Scharf A, et all., “Modelling twin screw multiphase pumps – a realistic approach to determine the entire performance behaviour”. [2nd International EMBT Conference, Hannover, April 2008, pp.104–116, 2008].
[19] Rabiger K. “Fluid dynamic and thermodynamic behavior of multiphase screw pumps handling gas-liquid mixtures with very high gas volume fractions”, PhD Thesis, Faculty of Advanced Technology, University of Glamorgan, 2009.
[20] Hu B., Cao F., Yang X. “Theoretical and experimental study on conveying behavior of a twin-screw multiphase pump”, [Proceedings of the Institution of Mechanical Engineers, 230(4), pp. 304-315, 2016].
[21] A. Putira, “Parametrization of Triple Screw Pumps for Aerospace Applications”, https://commons.erau.edu/edt, 2018.
[22] H. Schlichting, K. Gerten, “Boundary-Layer Theory”, Ninth Edit, Springer, 2017.
[23] G.C. Mimmi, P.E. Pennacchi, “Design of three-screw positive displacement rotary pumps”, Trans. Eng. Sci. 7, 1995.
[24] G.C. Mimmi, P.E. Pennacchi, “Computation of pressure loads in three screw pump rotors”, J. Mech. Des. Trans. ASME, 581–588, 1998.
[25] G.C. Mimmi, P.E. Pennacchi, “Dynamic effects of pressure loads in three screw pump rotors”, J. Mech. Des. Trans. ASME, 12, 589–592, 1998.
[26] C. Feng, P. Yueyuan, X. Ziwen, S. Pengcheng, Thermodynamic performance simulation of a twin-screw multiphase pump, Proc. Inst. Mech. Eng. Part E J. Process Mech. Eng. 215, 157–163, 2001.
[27] K. Räbiger, “Fluid dynamic and thermodynamic modelling of multiphase screw pumps, operating on the threshold of an exclusive gas compression”, [7th International Conference on Compressors and their Systems 2011, Pages 385-400, 2011].
[28] R. Ma and K. Wang, “CFD Numerical Simulation and Experimental Study of Effects of Screw-Sleeve Fitting Clearance upon Triangular Thread Labyrinth Screw Pump (LSP) Performance”, Journal of Applied Fluid Mechanics, Vol. 3, No. 1, pp. 75-81, 2010.
[29] Tang Q and Zhang Y, “Screw optimization for performance enhancement of a twin-screw pump”, Proc IMechE. Part E: J Process Mechanical Engineering, 228, pp.73–84, 2014.
[30] Qian Tang, Yuanxun Zhang, Linqing Pei, Jiong Tang, “Optimal design of screw and flow field analysis for twin-screw pump”, [Proceedings of the ASME 2011 International Design Engineering Technical Conferences & Computers and Information in Engineering Conference IDETC/CIE 2011 August 28-31, Washington, DC, USA , 2011]
[31] Kovacevic´ A, Stosic´ N and Smith IK. Screw compressors: three-dimensional computational fluid dynamics and solid fluid interaction. New York, NY: Springer.
[32] Stosic N, Smith IK and Kovacevic A. Screw compressors: mathematical modelling and performance calculation. New York, NY: Springer, 2005.
[33] E. Mujic, A. Kovacevic, N. Stosic, I. Smith, “Advanced Design Environment for Screw Machines”, Int. Compress. Eng. Conf., 2010.
[34] Y. Lu, A. Kovacevic, M. Read, N. Basha, “Numerical Study of Customised Mesh for Twin Screw Vacuum Pumps”, Designs, 3(4), 52, 2019.

[35] Yan D., Kovacevic A., Tang Q, “Numerical modelling of twin-screw pumps based on computational fluid dynamics”, Proceedings of the Institution of Mechanical Engineers, 231(24), pp. 4617-4634, 2017.
[36] D. Yan, A. Kovacevic, Q. Tang, S. Rane, Numerical investigation of cavitation in twin-screw pumps, Institution of Mechanical Engineers Part C, 2017.
[37] P. Borriello, E. Frosina, A. Senatore, F. Monterosso, “Numerical Modelling and Experimental Validation of Twin-Screw Pumps based on Comuputational Flud Dynamics using Scorg® and SimericsMP+®”, E3S Web of Conferences 312, 05007, 2021.
[38] Frosina, E.; Senatore, A.; Rigosi, M, “Study of a High-Pressure External Gear Pump with a Computational Fluid Dynamic Modeling Approach”, Energies 2017, 10, 1113, 2017.
[39] A. Corvaglia, M. Rundo, P. Casoli, A. Lettini, “Evaluation of Tooth Space Pressure and Incomplete Filling in External Gear Pumps by Means of Three-Dimensional CFD Simulations”. Energies 2021, 14, 342, 2021.
[40] Moghaddam, A. H., Kutschelis, B., Holz, F., Börjesson, T., and Skoda, R, "Three-Dimensional Flow Simulation of a Twin-Screw Pump for the Analysis of Gap Flow Characteristics." ASME. J. Fluids Eng, March 2022.
[41] Inc. S. Simerics MP+’s User Manual – v 5.2.13.
[42] A. Singhal, M. Athavale, H. Li and Y. Jiang, “Mathematical basis and validation of the full cavitation model”, J. Fluids Eng., 124, pp. 617-62, 2002.
[43] Vacca A., Guidetti M., “Modelling and Experimental Validation of External Spur Gear Machines for Fluid Power Applications”, Simulation Modelling Practice and Theory, Vol. 19, No.9, pp.2007-2031, 2011.
[44] E. Frosina, G. Marinaro, A. Senatore, Experimental and Numerical Analysis of An Axial Piston Pump: A Comparison Between Lumped Parameter And 3D CFD Approaches, Proceedings of the ASME-JSME-KSME 2019, 8th Joint Fluids Engineering Conference AJKFluids2019, July 28-August 1, San Francisco, CA, USA, 2019.
[45] E. Frosina, G. Marinaro, A. Senatore, M. Pavanetto, “Effects of PCFV and Pre-Compression Groove on the Flow Ripple Reduction in Axial Piston Pumps”, 2018 Global Fluid Power Society PhD Symposium, GFPS 2018.
[46] J. Ivantysyn and M. Ivantysynova, “Hydrostatic Pumps and Motors: Principles, Design, Performance, Modelling, Analysis, Control and Testing”, Tech Books International, 2003.

Biographies



Pasquale Borriello received the bachelor's degree in mechanical engineering from University of Naples Federico II in 2017, the master's degree in mechanical engineering

from University of Naples Federico II in 2019 after a 7 months Visiting Scholar experience at Purdue University. He pursued the philosophy of doctorate degree in Industrial Engineering from University of Naples Federico II in 2024 having as partners Purdue University, where he spent six months as Research Visiting in 2022-2023, and University of Sannio.

Along with his academic career, he developed an industry track starting with a 2-month internship at F-lab in 2019 and working from 2020 as Product Innovation Engineer at Fluid-o-Tech in Milan. He currently works at Fluid-o-Tech as Product Innovation Manager leveraging simulation and computer science knowledges to develop new products and technologies.

An efficient simulation approach to determine the thermal equilibrium of drive systems in mobile machinery

Eric Pohl, Sven Osterland, Jürgen Weber

Chair of Fluid-Mechatronic Systems, TU Dresden, Germany,
eric.pohl2@tu-dresden.de
Chair of Fluid-Mechatronic Systems, TU Dresden, Germany,
sven.osterland@tu-dresden.de
Chair of Fluid-Mechatronic Systems, TU Dresden, Germany,
juergen.weber@tu-dresden.de

Abstract

For the calculation of the thermal behavior of hydraulic systems, network models with lumped parameters have become established in the last decades. Here, the calculation of mass and energy conservation is carried out via time-dependent differential equations with very small time steps. For complex systems, such as the entire drive system of a mobile machine, this leads to very high simulation times, which are not suitable for parameter studies and optimizations. In this paper, an efficient computational approach to determine system temperatures in thermal equilibrium is presented, which significantly reduces the simulation time by up to a factor of 100 while maintaining almost the same accuracy. The new method is validated by a comparison with a classical, i.e. time-dependent, simulation using an elementary hydraulic circuit as an example. An extensive statistical analysis is made by varying the dynamic process conditions by different volume flow curves in order to prove the accuracy and the reduction of the simulation time.

Keywords: mobile machines, thermal simulation, lumped-parameter network model, calculation approach, thermal equilibrium, steady-state.

River Journal, 1–16.
© 2024 *River Publishers. All rights reserved.*

1 Introduction

The thermal balance of mobile machines significantly influences their design, efficiency, operability and reliability. During the development and design of the different machine or drive subsystems, the thermal behavior is only taken into account to a limited extent. Currently, design adaptations are often carried out iteratively via costly prototype measurements. In order to reduce development time and costs, an accurate prediction of the thermal behavior of the entire system within the design process is necessary. Due to the complex thermal interactions within hydraulic drive systems, efficient simulation methods are needed to calculate the thermal equilibrium. In recent decades, thermal lumped-parameter models have been successfully established as the most efficient simulation option for stationary applications [1–3]. However, in the field of mobile machines the highly application- and operation-dependent varying environmental conditions and performance requirements make it difficult to collect comparable and repeatable data for parameterization and validation compared to stationary processes. The basic feasibility of functional thermal modeling based on lumped-parameter network models of a mobile machine has been demonstrated by the research of Zimmerman and Busquets for a displacement-controlled mini-excavator [4–7] and Kwon et al. for the hydraulic drivetrain of a hybrid vehicle [8–10]. The aforementioned works have in common that they calculate the thermal behavior using time-dependent differential equations to solve conservation of mass and energy, which result from lumped-parameter network models. Therefore, the entire heating process must be calculated over countless small-scale time steps in order to finally determine temperatures in thermal equilibrium. For systems of low complexity, results can thus be obtained in a short to moderate time. However, with increasing complexity of the system, this computational approach can lead to simulation times of many hours up to days due to very small time steps. Therefore, for an economically efficient simulation of the thermal equilibrium of the entire machine, it is desirable to develop a calculation approach that significantly reduces the simulation time without losing accuracy. In the following paper, an efficient simulation approach for thermal lumped-parameter network models with dynamic loads is presented, which directly determines the state of thermal equillibrium without calculating the dynamical heating process. Calculation results are discussed and compared to a classical time-dependent simulation. A statistical analysis was made due to the approximations inherent in the method. The results of the analysis and the potential scope of the method are shown and discussed.

2 Modelling Approach

In most cases, the design of mobile machines does not require knowledge of the transient behavior of component and fluid temperatures, especially the heating process. To optimize efficiency, operability and reliability only temperatures at which the machine operates in the thermal equilibrium range are useful. Therefore, a computational approach for lumped-parameter network models has been developed to directly determine the temperatures in thermal equilibrium without time-consuming solution of time-dependent differential equations of energy conservation due to varying temperatures (Fig. 1). For this purpose, the fluidic domain and thermal domain are decoupled.

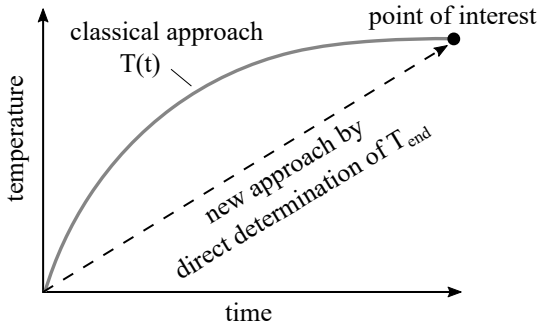

Figure 1 Developed steady-state approach compared to classical approach

For the determination of process parameters and fluid properties, a considered duty cycle (dc) has to be simulated only once instead of several times. The time-dependent characteristics of parameters and properties are then used as boundary conditions for a steady-state calculation to determine thermal equilibrium.

2.1 Derivation of thermal model

Defined by the 1st law of thermodynamics, thermal equilibrium of an arbitrary system is reached when the internal energy U no longer changes over time:

$$\frac{dU}{dt} = \sum_i \dot{Q}_i + \sum_j \dot{W}_j + \sum_k \dot{H}_{in,k} - \sum_l \dot{H}_{out,l} = 0 \qquad (1)$$

with $\dot{Q}$ as external heat flow, $\dot{W}$ as technical power and $\dot{H}$ as enthalpy flow into and out of the system. If U no longer change, all temperatures in the system have to be constant. An established state of equilibrium for an arbitrary

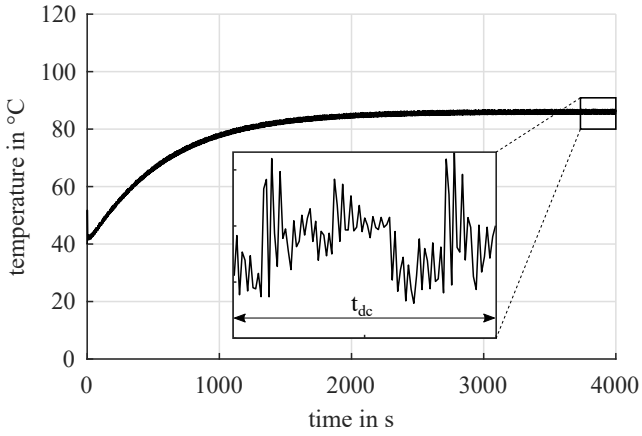

Figure 2 Exemplary dynamic temperature behavior

duty cycle with $t_{dc} = 10s$, which is periodically repeated, is exemplarily shown in Fig. 2. Looking at the behavior of the curve within the thermal equilibrium ($t > 3800s$) it can be seen that temperatures are still varying within the duty cycle. This is due to the fact that the state of equilibrium in (1) is never reached at any time t within the cycle, if the considered timestep in (1) is $dt < t_{dc}$:

$$\frac{dU}{dt} \neq 0 \tag{2}$$

Thus, thermal equilibrium does not establish locally within the cycle, but is an averaged consideration of temperatures and energy over several cycles ($dt = t_{dc}$):

$$\frac{d\bar{U}}{dt_{dc}} = 0 \tag{3}$$

This consideration leads to the assumption that the state of equilibrium can be described by process-averaged quantities:

$$\frac{d\bar{U}}{dt} = \sum_i \bar{\dot{Q}}_i + \sum_j \bar{\dot{W}}_j + \sum_k \bar{\dot{H}}_{in,k} - \sum_l \bar{\dot{H}}_{out,l} = 0 \tag{4}$$

Related to an arbitrary duty cycle, this means that the cycle is considered as a steady-state and not as a transient calculation case. Since conservation of energy applies, the energy E of a process is determined by integrating the

power P over time.

$$E = \int_{t_0}^{t_{dc}} P(t)\,\mathrm{d}t \tag{5}$$

Due to the applicable laws of physics, only conservation quantities, i.e. extensive quantities, may be averaged over time. In terms of energy this leads to the time-averaged power $\bar{P}$.

$$\bar{P} = \frac{E}{t_{dc} - t_0} = \frac{1}{t_{dc} - t_0} \cdot \int_{t_0}^{t_{dc}} P(t)\,\mathrm{d}t \tag{6}$$

This averaging is allowed for heat Q, technical work W and enthalpy H, since they are all forms of energy. This means that it is technically possible to reduce any duty cycle to a steady state case via energy or average power.

In case of technical work W the technical power $\dot{W}$ can be obtained by the functional process behavior of the considered system via volume flow rate $\dot{V}$, differential pressure Δp and total efficiency η_{tot}.

$$\bar{\dot{W}} = \frac{1}{t_{dc} - t_0} \cdot \int_{t_0}^{t_{dc}} \dot{V}(t) \cdot \Delta p(t) \cdot \eta_{tot}\,\mathrm{d}t \tag{7}$$

The map of total efficiency $\eta_{tot} = f(\dot{V}(t), \Delta p(t))$ is considered to be known.

Besides $\dot{V}$ and p enthalpy H additionally directly depends on fluid temperature T_f. Since temperature is an intensive quantity, the average value does not necessarily correspond to the time-averaged temperature of the cycle. To determine the extensive quantity H, the fluid temperature is related to the extensive quantity mass m or, in case of enthalpy flow $\dot{H}$, to the mass flow $\dot{m}$.

$$\begin{aligned} \bar{\dot{H}} = {} & \frac{1}{t_{dc} - t_0} \cdot \int_{t_0}^{t_{dc}} c_p \cdot \dot{m}(t) \cdot T_f(t)\,\mathrm{d}t \\ + & \frac{1}{t_{dc} - t_0} \cdot \int_{t_0}^{t_{dc}} \frac{\dot{m}(t)}{\rho(t)} \cdot (1 - \gamma(t) \cdot T_f(t)) \cdot p(t)\,\mathrm{d}t \end{aligned} \tag{8}$$

The specific heat capacity for constant pressure c_p is considered constant and the coefficient of thermal expansion γ is time-dependent. The assumption that the state of equilibrium can be described by process-averaged quantities implies that there have to be process-averaged temperatures belonging to those quantities. This leads to the fact that there exists a process-averaged

fluid temperature $\tilde{T}_f$, which is constant, so (8) can therefore be expressed as follows:

$$\begin{aligned}\bar{\dot{H}} = \frac{\tilde{T}_f}{t_{dc}-t_0} \cdot \int_{t_0}^{t_{dc}} \overbrace{c_p \cdot \dot{m}(t) \cdot -\frac{\dot{m}(t)}{\rho(t)} \cdot \gamma(t) \cdot p(t)}^{P_{H1}(t)} \, \mathrm{d}t \\ + \frac{1}{t_{dc}-t_0} \cdot \int_{t_0}^{t_{dc}} \underbrace{\frac{\dot{m}(t)}{\rho(t)} \cdot p(t)}_{P_{H2}(t)} \, \mathrm{d}t\end{aligned} \tag{9}$$

Because of the time dependence of $\dot{m}$ and the relationship between intensive and extensive quantities, $\tilde{T}_f$ is not equal to the time-averaged fluid temperature $\bar{T}_f$. As in (7) mass flow and pressure are known from the process. To determine ρ and γ, these are interpolated via $\tilde{T}_f$ and p using the known property map of the fluid. With all known quantities the average over time of the introduced auxiliary variables P_{H1} and P_{H2} can be build, which leads to

$$\bar{\dot{H}} = \tilde{T}_f \cdot \bar{P}_{H1} + \bar{P}_{H2} \tag{10}$$

With (10) the thermodynamic state of the fluid is describeable for any point in the system.

In general, heat extraction at a given point is determined by four heat flows: mainly convective transfer from fluid into the mechanical structure (fs), conduction through the mechanical structure (c), heating of the mechanical capacity (cap) and transfer from wall into the environment (s∞). The latter is divided into radiation (rad) and convection (conv). During the heating process, a part of the heat flow from the fluid into the wall is used to heat the mechanical structure until thermal equilibrium is reached.

$$\dot{Q}_{fs}(t) = \dot{Q}_c(t) + \dot{Q}_{cap}(t) \tag{11}$$

$$\dot{Q}_c(t) = \dot{Q}_{s\infty}(t) = \dot{Q}_{s\infty,conv}(t) + \dot{Q}_{s\infty,rad}(t) \tag{12}$$

with

$$\dot{Q}_{fs}(t) = \alpha_{fs}(t) \cdot A_i \cdot (T_f(t) - T_{w1}(t)), \tag{13}$$

$$\dot{Q}_c(t) = \lambda \cdot \frac{A}{d} \cdot (T_{w1}(t) - T_{w2}(t)), \tag{14}$$

$$\dot{Q}_{s\infty,conv}(t) = \alpha_{s\infty}(t) \cdot A_o \cdot (T_{w2}(t) - T_\infty), \tag{15}$$

and

$$\dot{Q}_{s\infty,rad}(t) = \sigma \cdot \epsilon \cdot A_o \cdot (T_{w2}^4(t) - T_\infty^4), \tag{16}$$

where A_i is the inner transfer surface with corresponding wall temperature T_{w1} and A_o is the outer transfer surface, i.e. to the environment, with corresponding wall temperature T_{w2}. λ is the heat conduction coefficient of the mechanical structure and the term $\frac{A}{d}$ depends on the considered geometry. Furthermore, the radiation is defined by Stefan-Boltzmann constant σ and the emission coefficient ϵ. As with the fluid temperature, it is assumed that there also exist process-averaged wall temperatures $\tilde{T}_{w1}$ and $\tilde{T}_{w2}$. Since λ, σ and ϵ are constants, the avegared heat conduction and radiation is defined by

$$\bar{\dot{Q}}_c = \lambda \cdot \frac{A}{d} \cdot (\tilde{T}_{w1} - \tilde{T}_{w2}) \tag{17}$$

$$\bar{\dot{Q}}_{s\infty,rad} = \sigma \cdot \epsilon \cdot A_o \cdot (\tilde{T}_{w2}^4 - T_\infty^4), \tag{18}$$

Following the rule of averaging as in (9) and substituting the time-dependent temperatures in (13) and (15), the averaged convective heat flow is given by

$$\bar{\dot{Q}}_{fs} = \bar{\alpha}_{fs} \cdot A_i \cdot (\tilde{T}_f - \tilde{T}_{w1}), \tag{19}$$

$$\bar{\dot{Q}}_{s\infty,conv} = \bar{\alpha}_{s\infty} \cdot A_o \cdot (\tilde{T}_{w2} - T_\infty), \tag{20}$$

2.2 Boundary conditions

Since $\tilde{T}_f$, $\tilde{T}_{w1}$ and $\tilde{T}_{w2}$ are the process-averaged temperatures to be calculated, all other variables within the thermal model must be known. To determine the time-dependent process variables within a duty cycle a functional-energetic simulation of the cycle has to be made by using a lumped-parameter network model. In contrast to previous procedures, which simulate the considered duty cycle many times solving the time-dependent differential equations of mass and energy conservation untill thermal equilibrium is reached, only one duty cycle has to be calculated. In addition, this functional-energetic simulation of the single duty cycle is calculated with a constant fluid temperature, which makes it even faster because it greatly simplifies the calculation of energy conservation. Thus, the time-dependent process variables $\dot{m}$ and p are given. Pressure p und an initial fluid temperature $\tilde{T}_f$ are used to interpolate fluid properties ρ and γ using the known property map of the fluid.

The thermal equilibrium of any system is a state which is defined by the 1st law of thermodynamics. If this state is reached the inner energy U is not changing anymore. This means that all temperatures within the system have to be considered as constant. This leads to the fact that the heat flow into the mechanical structure $\bar{\dot{Q}}_{cap}$, described in (11), gets zero. Thus, all the heat flow from the fluid into the mechanical structure is also emitted from the outer wall to the environment. Hence, it follows that $\bar{\dot{Q}}_{fs}$, $\bar{\dot{Q}}_{c}$ and $\bar{\dot{Q}}_{s\infty}$ are equal.

$$\bar{\dot{Q}}_{fs} = \bar{\dot{Q}}_{c} = \bar{\dot{Q}}_{s\infty} \tag{21}$$

At this point, two of three necessary equations to solve the three unknown process-averaged temperatures are given. However, the information about the causal correlations is still unknown, i.e. the energy supply and removal within the system which determine the local state of fluid and structure.

In order to be able to calculate the causal correlations required to determine the correct thermal state of any point in the system, the enthalpy flow (10) is used. This is uniquely determined by the current state of the system and, considered in isolation, is independent of the system's previous history. Thus, in order to derive the causal relationship, the change of state from a defined point to the point under consideration must be considered.

$$\Delta \bar{\dot{H}}_{ab} = \bar{\dot{H}}_{a} - \bar{\dot{H}}_{b} \tag{22}$$

The change of enthalpy flow $\Delta \bar{\dot{H}}_{ab}$ is caused by the increase or decrease of technical work and by heat flows supplied and removed across the system boundary between state a and b. One of the possible heat flows must be the emitted heat flow in the point to be calculated (in this case point b). Losses within the system boundary do not lead to a change in enthalpy flow. The change in enthalpy flow can be expressed as follows:

$$\Delta \bar{\dot{H}}_{ab} = \bar{\dot{H}}_{a} - \bar{\dot{H}}_{b} = \sum_{i} \bar{\dot{W}}_{ab,i} + \sum_{j} \bar{\dot{Q}}_{ab,j} - \bar{\dot{Q}}_{fs,b} \tag{23}$$

Now, (21) and (23) form a system of equations, which can be solved by using (10), (17), (18), (19) and (20) to determine $\tilde{T}_{f}$, $\tilde{T}_{w1}$ and $\tilde{T}_{w2}$ at point b. If the state $\bar{\dot{H}}_{a}$ is known, for example by constant inflow conditions in an open hydraulic system, the state $\bar{\dot{H}}_{b}$, i.e. the temperatures at this point, can be calculated analytically. If the state $\bar{\dot{H}}_{a}$ is unknown, as in a closed hydraulic system, the temperatures must be calculated iteratively using an additional set

of (21) and (23) for state a. Therefore, all missing informations in terms of energy within the closed system have to be considered. This means that any number of points within the system, i.e. states, can be determined as long as all energy inputs and outputs within the system are taken into account.

2.3 Correction loop

As already mentioned, process quantities and fluid properties are determined by a functional-energetic simulation of a single duty cycle with constant fluid temperature. For this, an initial fluid temperature must be specified. Since this temperature can be arbitrary, it is obvious that the determined properties and quantities do not match those in the state of thermal equilibirum. This leads to incorrect power values and power losses in the system and thus to incorrect temperatures calculated by the thermal model. Therefore, a correction loop must be done. Thereby, the calculated fluid temperature calculated by the thermal model is set as the new initial temperature for next step, i.e. the following functional-energetic simulation of the single duty cycle. The loop ends when a certain relative deviation δ between the initial and newly determined fluid temperature is fallen short of, for example $\delta < 0.1\%$. In summary, the developed calculation approach works as shown in Fig. 3. The thermohydraulic system behavior is decoupled in a functional-energetic, i.e. only hydraulic, and a thermal lumped-parameter network model. The first mentioned model, which includes all mandatory power sources and sinks, is simulated over only one considered duty cycle, for example an y-cycle of a wheel loader ($t_{sim} = t_{cycle}$). This is done with an arbitrary initial fluid temperature. Since the functional-energetic model shall not take into account

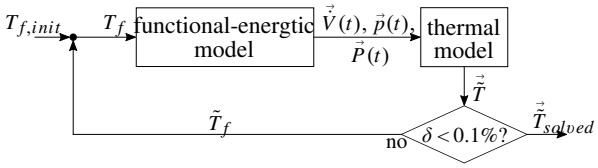

Figure 3 Correction loop within developed approach

the thermodynamic bevahior, the fluid temperature is constant over the whole cycle. The obtained process parameters are forwarded to the script based thermal model, where the averaged quantities are calculated in the first step. These are then used to iterate the temperatures within thermal equilibrium. Since the simulated power quantities belong to the initial fluid temperature, the determined fluid temperature $\tilde{T}_f$ is used as the new initial value. This

correction loop is performed until termination criterium is reached, i.e. the determined relative deviation is undercut.

3 Comparison with classical approach

3.1 Elementary hydraulic circuit

To validate the developed calculation approach, a comparison with the classical, i.e. time-dependent, approach is made. Therefore, an elementary hydraulic circuit was built. As mentioned above, the calculation of an open hydraulic system with known inflow conditions is just an analytical solution, since one state is defined by boundary conditions. Thus, the focus of the comparison is on a closed hydraulic system. The elementary circuit consists of a hydraulic pump with constant displacement, which is controlled by rotational speed via preset curves. Furthermore, a hydraulic motor with a constant moment is used to drain technical work from the system, which ensures same load conditions for varying volume flow curves. Pump and motor are connected by hoses, which are simplified modeled as a flow resistance and corresponding volume. On the low-pressure side, a pressure source is used to define a constant pressure of 10 bar and ensure robust calculation of initial values for any setting of initial conditions. To simplify the model, the behavior of the pump and motor is considered to be lossless. Nevertheless, a total loss is determined via a constant total efficiency and inserted as heat flow behind the pump and the motor, respectively. The resulting elementary circuit with external heat flows is shown in Fig. 4. The thermodynamical states, i.e. fluid and wall temperatures, are determined for the hoses. The heat transfer is modeled by convective heat flow from fluid into the mechanical structure, conduction within the structure and convection and radiation from the mechanical structure to the environment. The heat transfer coefficients required for convective heat transfer are determined using Nusselt correlations. Since these depend not only on geometric and fluidic parameters but also on the mass flow, they can be calculated time-dependently for arbitrary volume flow curves, which is necessary for correct averaging. For simplicity, the emitted heat flows of the mechanical structure of pump and motor are not included in this model, but can easily be added. There are no limits to the complexity of thermal discretization. In contrast to the developed calculation approach, in the classical calculation method all the above-mentioned functional and thermal aspects must be modeled in one simulation model in order to solve the mass and energy conservation correctly.

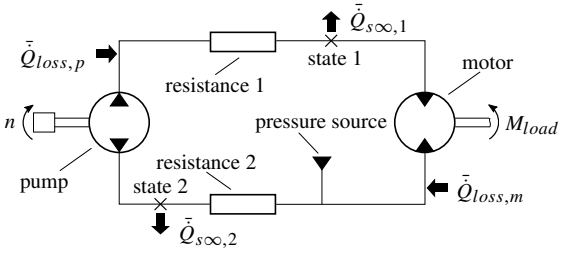

Figure 4 Elementary hydraulic circuit used for comparison

4 Statistical test cases

Due to the aforementioned assumptions, the uncertainty based on the averaged quantities and the non-linear dependence of the heat transfer coefficients on the volume flow rate, a deviation from the results of the classical calculation approach is to be expected. Therefore, test cases were generated using statistical methods in order to be able to provide a statement on the possible scope of the developed calculation approach. To cover a wide range of possible curve shapes within a process, a statistically representative number of 10^6 volume flow curves were randomly generated within a range of $0 - 400\frac{l}{min}$ and a process duration of $10s$, where a random volume flow rate value is assigned for each second. Since simulating 10^6 cases is too costly, a careful selection of 100 curves was made. Since these curves are intended to cover

Table 1 Volume flow rate related measures

measure	**description**	**equation**
D_1	mean value	$\frac{1}{t_{dc}-t_0} \cdot \int_{t_0}^{t_{dc}} \dot{V}(t)\,\mathrm{d}t$
D_2	maximum value / mean value	$\frac{\dot{m}_{max}}{D_1}$
D_3	dynamics	$\int_{t_0}^{t_{dc}} \lvert \frac{d}{dt}\dot{V}(t) \rvert\,\mathrm{d}t$
D_4	dynamics / mean value	$\frac{D_3}{D_1}$
D_5	mean absolute deviation	$\frac{1}{n} \cdot \sum_{i=1}^{n} \lvert \dot{V}_i - \bar{\dot{V}} \rvert$
D_6	mean abs. deviation / mean value	$\frac{D_5}{D_1}$

the entire spectrum of all curves, it is not expedient to randomly select 100 curves. Therefore, in a first step, six different measures related to the volume flow rate are introduced to define certain characteristics of the curves (Tab. 1). If the values of the measures are related to each other, they form a complex six-dimensional structure representing the entire spectrum of all curves. In order to achieve the best possible distribution within this structure, the latin hypercube sampling method is used in multiple steps. Therefore, measures are normalized to ensure equal weighting despite different magnitudes. This made it possible to select 100 curves that both cover the extrema in the boundary regions and have a good distribution within the entire spectrum. Fig. 5 shows exemplary volume flow curves with the maximum and minimum values of D_3 and D_5, respectively. The 100 volumetric flow curves, representing

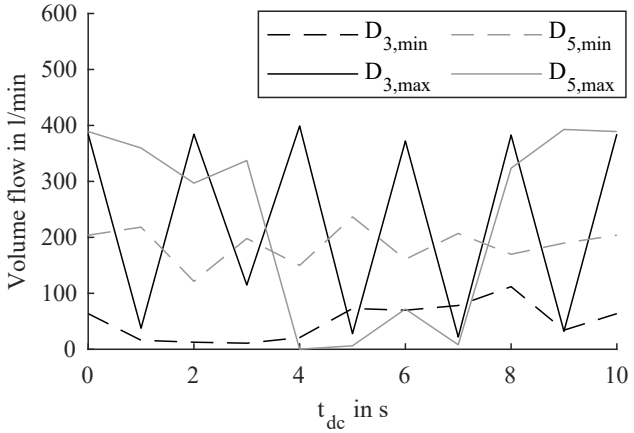

Figure 5 Exemplary volume flow curves for D_3 and D_5

the full spectrum of all randomly generated curves, are now used to compare the developed approach with the classical approach, allowing the potential scope to be estimated.

5 Results and validation

For the classical calculation of the elementary circuit and for the simulation of the functional-energetic model of the developed approach the multi-domain software SimulationX® is used. The thermal model of the presented approach is scripted and calculated in MATLAB® . The objective of the presented cal-

culation method is a significantly faster determination of temperatures within the thermal equilibirum of the complex system of a mobile machine. In the left graph of Fig. 6 the percentage of the computation time of the developed method from the simulation time of the classical method is shown versus absolute computation time of the classical method. It can be seen that the

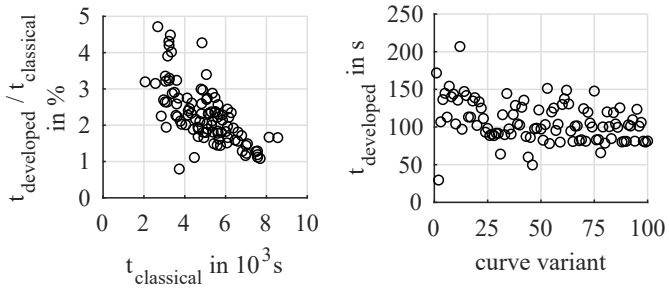

Figure 6 Simulation time of developed approach compared to classical approach

maximum proportion of simulation time is about 4.7% and minimum is about 0.8%, respectively. That means that the method calculates the state of thermal equilibrium 20 times up to 100 times faster for the elementary circuit. Furthermore, it can be seen that the proportion decreases with increased classical simulation time, i.e. with volume flow curves with higher dynamics and mean absolute deviations. Looking at the right graph of Fig. 6, where the simulation times of the developed method show a constant behavior across all simulated cases, it can be concluded that with an increase of the model complexity the proportion will behave similarly. To prove the potential scope of the developed calculation approach, the difference of simulated final temperatures to the classical approach are compared. Fig. 7 shows the absolute temperature

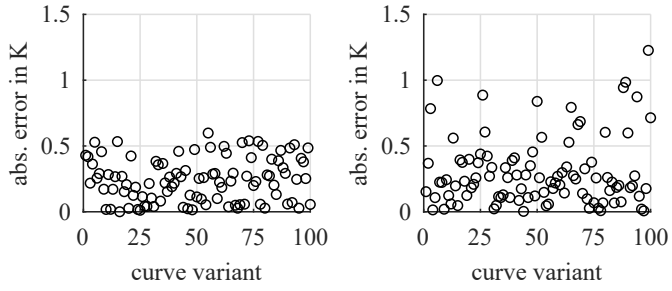

Figure 7 Abs. error compared to class. approach for state 1 (l.) and state 2 (r.)

differences for fluid temperatures of states 1 and 2 (range of absolute values is from approx. $30 - 130^{\circ}C$). It can be seen that the deviation of fluid temperatures across all analyzed curves is less then $0.6K$ in state 1 and less then $1.3K$ in state 2, respectively. In order to be able to interpret these differences correctly, they are shown as relative values in relation to the ambient temperature in Fig 8. The maximum relative deviation in both states across all curves is less then 2.2%. Hence, it can be said that the presented method

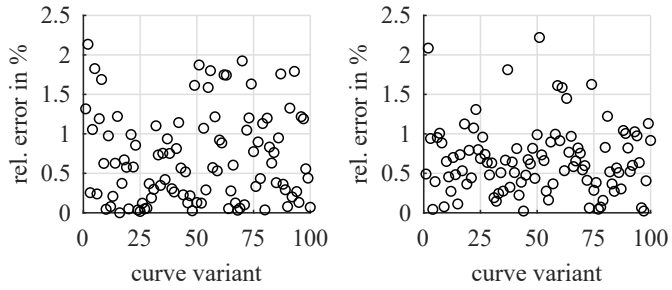

Figure 8 Rel. error compared to class. approach for state 1 (l.) and state 2 (r.)

not only significantly reduces the simulation time but also, in the case of the elementary circuit shown, can be used for arbitrary processes considering the small deviations of the final temperatures.

6 Conclusion

In this paper a calculation approach is presented, which reduces the dynamic heating process of any system to the computation of the steady-state final state using functional dynamic quantities as boundary conditions. This is based on the approach that the state of thermal equilibrium is a process-averaged consideration. Using the well known equations of heat transfer together with state changes of enthalpy flow and functional dynamic process quantities allows an iterative calculation of process-averaged temperatures within the state of thermal equilibrium. A comparison with the classical approach, i.e. using time-dependent differential equations to solve mass and energy conservation, showed a significant reduction of simulation time by up to 100 times. Moreover, the small deviations from the classically calculated temperatures of maximum 2.2% using a carefully selected set of volume flow curves covering a wide range of process conditions showed that the method can be used for any processes, related to the considered elementary hydraulic circuit. Thus,

it can be assumed that the developed approach is applicable to any hydraulic system and, for systems with high complexity, such as the entire drive system of a mobile machine, it far outperforms the classical approach in terms of computational time, making it much more suitable for parameter studies and optimization.

Acknowledgment

The project "Analysis, modeling and consideration of thermal interactions in the design and optimization of drive systems for mobile machinery" (Ref. No. AiF 20993 BR/1) was financed and supervised by the Forschungskuratorium Maschinenbau e.V. FKM, Lyoner Straße 18, 60528 Frankfurt am Main. In the scope of the Programme to promote Industrial Collective Research it was funded by the German Federation of Industrial Research Associations (AiF) with means of the Federal Ministry for Economic Affairs and Climate Action on the basis of a decision by the German Bundestag.

References

[1] J. A. Sidders, D. G. Tilley and P. J. Chapple, "Thermal-hydraulic performance prediction in fluid power systems," in Proceedings of the Institution of Mechanical Engineers, Part I: Journal of Systems and Control Engineering. vol. 49, pp. 231-242, 1996.

[2] B. Johansson, J. Ölvander and P. Krus, "Thermal Modelling of an electrohydrostatic actuation system," in Proceedings of Recent advances in aerospace actuation systems and components. Toulouse, France, pp. 49–54, 2001.

[3] S. Michel, T. Schulze and J. Weber, "Energy-efficiency and thermo energetic behaviour of electrohydraulic compact drives," in Proceedings of the 9th International Fluid Power Conference (IFK). Aachen, Germany, pp. 162–177, 2014.

[4] J. Zimmerman and M. Ivantysynova, "Reduction of Engine and Cooling Power by Displacement Control," in Proceedings of the 6th FPNI PhD Symposium. West Lafayette, USA, pp. 339–352, 2010.

[5] J. Zimmerman and M. Ivantysynova, "40% Fuel Savings by Displacement Control leads to lower Working Temperatures – A Simulation Study and Measurements," in Proceedings of the 52nd National Conference on Fluid Power. 2011.

[6] E. Busquets and M. Ivantysynova, "Cooling power reduction of displacement controlled multi-actuator machines," in Proceedings of the 7th FPNI PhD Symposium on Fluid Power. Regio Emilia, Italy, pp. 453–465, 2012.

[7] E. Busquets and M. Ivantysynova, "Temperature Prediction of Displacement Controlled Multi-Actuator Machines," International Journal of Fluid Power. vol. 14, pp. 25–36, 2013.

[8] H. Kwon and M. Ivantysynova, “System and Thermal Modeling for a Novel On-Road Hydraulic Hybrid Vehicle by Comparison With Measurements in the Vehicle,” in ASME/BATH 2017 Symposium on Fluid Power and Motion Control. Bath, UK, 2017.

[9] H. Kwon, N. Keller and M. Ivantysynova, “Thermal Management of Open and Closed Circuit Hydraulic Hybrids,” in Proceedings of the 11. IFK. Aachen, Germany, 2018.

[10] H. Kwon, M. Sprengel and M. Ivantysynova, “Thermal modeling of a hydraulic hybrid vehicle transmission based on thermodynamic analysis,” Energy. vol. 116, pp. 650–660, 2016.

Digital Electro Hydrostatic Actuator with Variable Speed Digital Hydraulic Pump: A Design Overview

Dimitri Oliveira e Silva[1]*, Marcos Paulo Nostrani[1], Rodrigo Simões Lopes Junior[1], Gierri Waltrich[1], Petter Krus[2], Victor Juliano De Negri[1]

[1] Department of Mechanical Engineering, Federal university of Santa Catarina,

[2] Division of Fluid and Mechatronic Systems, Linköping University.

** Corresponding author: dimitri.oliveira@unifesspa.edu.br*

Abstract.

The electric drive technology has achieved significant maturity and established a new global trend focused on the development of more electric and efficient systems. In the field of hydraulic systems, works on digital hydraulics have shown that it is an attractive solution to improve the energy efficiency. In this context, this paper presents a new approach design of a digital hydraulic actuator comprising a symmetrical cylinder controlled by a digital hydraulic pump driven by a variable rotational speed source in order to maximize the hydraulic energy savings and the controllability of the system. The simulated results show that the non-dissipative control strategy implemented by this system topology can reduce significantly the energy losses. Moreover, the use of a variable rotational speed source makes it possible to obtain a continuous flow rate for each pump unit combination, which increases the digital hydraulic pump flow rate range. A servo-hydraulic actuator was used as a baseline to compare the behaviour and the energy savings. The analysis shows that the baseline system has consumed about ten times more energy than the proposed digital hydraulic solution.

Keywords. Digital Hydraulics, Digital Hydraulic Pump, Variable-Speed Digital Electro Hydrostatic Actuator.

1. INTRODUCTION

In recent decades, new environmental regulations have led researchers to develop energy-optimized systems to improve energy savings. Latest studies have presented the digital hydraulic as a promising alternative to improve the energy efficiency of hydraulic systems. In the digital hydraulic concept, the servo valve is replaced by a set of on/off valves in order to avoid the energy dissipation of the throttling control, commonly used on typical hydraulic position control systems. Additionally, it is possible to implement different control strategies

to control the opening and closing movements of the on/off valves, which brings some flexibility to the system [1 – 4].

The technological advances in electric drives have started a new global trend based on the use of electricity as a major power source. This tendency presents some benefits such as high efficiency, weight reduction, and reduced maintenance costs [5]. In the aviation industry, the More Electric Aircraft – MEA concept aims to replace the typical servo valve controlled hydraulic actuators (SHA) and its centralized power unit by the use of decentralized and power-by-wire systems [6].

Considering the global electrification tendency and recent research in digital hydraulics, this study proposes a new hydraulic actuator design, which comprises a symmetrical multi-chamber cylinder, a digital hydraulic pump controlled by a variable rotational speed motor, and a set of free leakage on/off seat valves. The objective of this paper is to describe the main aspects of the preliminary design of the proposed solution by evaluating its dynamic model, which was sized according to typical flight control surface requirements. A servo hydraulic actuator model is used as a baseline to compare the dynamic response and the hydraulic energy consumed.

2. DIGITAL HYDRAULICS

Digital Hydraulics emerged as a solution to improve the energy efficiency of hydraulic systems, reducing the throttling losses and internal leakages presented in servo valves, using simple components like on/off valves and flexible control strategies to better manage the hydraulic energy [1]. Digital hydraulics is divided into two main branches, called fast switched commutation and parallel connection [1]. In [2], a review of digital hydraulics was presented, where some characteristics of different digital hydraulic systems were discussed. It is shown that the parallel connection is becoming the commonly used approach since fast switching hydraulic still requires specific components due to their high switching frequency.

In [3], the digital parallel connection approach is used to combine the flow rate with the cylinder areas to provide velocity control. In [7], the parallel connection is used to combine different pressure levels with the cylinder areas to obtain force control. In both cases, a multi-chamber cylinder with different areas is used to increase the number of output combinations.

In [7] a strategy for defining the cylinder areas and the constant pressure sources in a secondary control digital actuator is presented. The authors point out that is important to predict linear distributions with evenly spaced output values when designing digital hydraulic systems, since this simplifies the control system and promotes smooth actuator movements with an adequate dynamic response.

However, due to design constraints, the number of discrete outputs of the digital hydraulic system is limited, which means that is not possible to meet intermediary values between two consecutive discrete output levels. If an intermediary value is demanded, the control strategy must be able to manage this lack of required output by choosing the best available output e.g. by using a cost function [3]. In this case, the cost function implies that the output can be higher or lower than requested.

3. DIGITAL HYDRAULIC ACTUATOR PROPOSED

In this study, the use of the variable rotational speed source coupled to a digital hydraulic pump to supply a symmetric cylinder is proposed, denominated as Variable Speed Digital Electro Hydrostatic Actuator (VSDEHA) (Fig. 3.1). In this configuration, the variable rotational speed digital hydraulic pump is not limited to discrete output flow, the pump is able to provide continuous values of flow rate for each pump unit combination, which increases the number of output flow available to the hydraulic system.

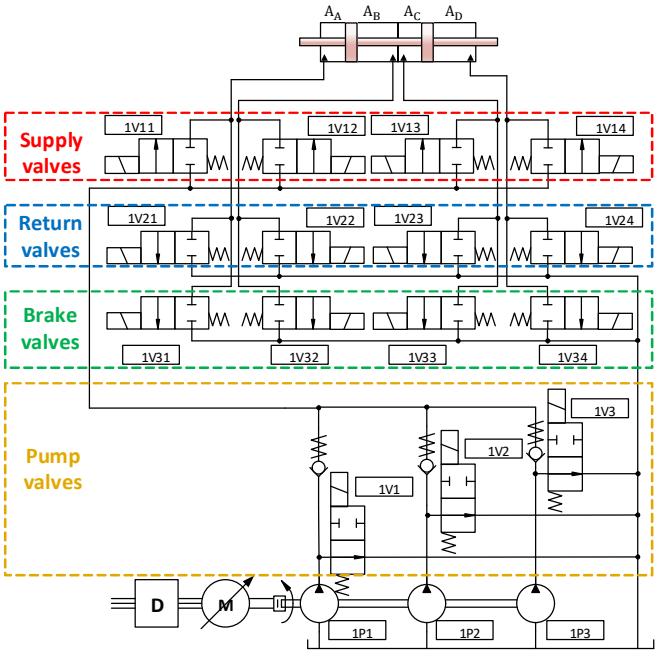

Figure 3.1. Variable Speed Digital Electro Hydrostatic Actuator.

The proposed digital hydraulic pump is composed of three pump units with different volumetric displacement sizes distributed and related to each other by a numerical sequence of power of two ($2^n, n = 1, 2, 3, \dots$), which increases the number of different flow rates available for each rotational speed **Error! Reference source not found.**. The pumps are controlled by the on/off valves 1V1, 1V2, and 1V3, which direct the flow rate to the system or to the reservoir, independently. The pump combination is defined by the number of pumps connected to the system. In this case, there are seven combinations available for the system. When using a variable rotational speed source there is no need to use a multi-chamber cylinder to obtain different velocities. Nevertheless, the multi-chamber cylinder strategy can be adopted to manage the size constraints and the work pressure levels. The cylinder movement is controlled by on/off valves, where the valves 1V11, 1V12, 1V13, and 1V14 connect the pump with each cylinder chamber A_A, A_B, A_C and A_D, respectively. The valves 1V21, 1V22, 1V23, and 1V24 connect the cylinder chambers with the return line according to the cylinder movement direction.

The third set of valves, called brake valve (BV), is used to connect the cylinder chambers to the reservoir line (1V31, 1V32, 1V33, 1V34). During the development of the solution it was

noticed that, in the presence of assistive external loads, the cylinder velocity was reaching values over the maximum designed, compromising the controllability of the system. The brake valves are designed to restrict the flow rate and to limit the maximum cylinder velocity when an assistive load condition is detected. In this case, under normal conditions, the return and brake valves are used to connect the cylinder chambers to the return line. However, when the assistive load is detected, only the brake valves are used.

4. SYSTEMS DESIGN MODELLING

The method proposed by [8] was used to design the system for position control. The system parameters are the cylinder stroke of 0.1 m, a mass of 200 kg, viscous friction of 20 kNm/s, and maximum working pressure of 20 MPa. As system requirements, a step response of 0.05 m, a settling time of 1 s, and a maximum force of 76 kN were used based on **Error! Reference source not found.**. In this context, the results obtained according to the design method were: the maximum cylinder velocity of 0.11 m/s, the maximum flow rate of 6.7×10^{-4} m³/s (40.2 L/min), and the total cylinder area of 0.006 m², which was divided to obtain a four-chamber cylinder with equal areas of 0.003 m².

To supply the maximum flow rate, the volumetric displacement of the pump units was distributed in a power of two sequence with the pump sizes of 6.36×10^{-7}, 1.27×10^{-6}, and 2.54×10^{-6} m³/rad (4, 8, 16 cm³/rev). The maximum rotational speed is 178.02 rad/s (1700 rpm), which is based on a generic four poles induction machine. At this rotational speed, the digital pump theoretically supplies a maximum flow rate of 7.9×10^{-4} m³/s (47.6 l/min). The equation of motion was used to model the symmetrical cylinder as

$$p_A A_A - p_B A_B + p_C A_C - p_D A_D - F_{fri} - F_{load} = M\ddot{x}, \tag{4.1}$$

where p_A, p_B, p_C, and p_D are the pressures in each cylinder chamber [Pa], A_A, A_B, A_C, and A_D are the cylinder chamber areas [m²], F_{fri} is the friction force [N], F_{load} is the load force [N], M is the total mass moved [kg], and $\ddot{x}$ is the acceleration [m/s²].

The dynamic friction force was modeled using the LuGre friction model. The parameters were adapted from [9] and are presented in Table I, where σ_0, σ_1, and σ_2 are the average stiffness coefficient of bristles [N/m], the average damping coefficient of bristles [kg/s], and the viscous coefficient [kg/s], respectively; f_c, f_s, and $v_s$are the Coulomb friction force [N], the stiction friction force [N], and the Stribeck velocity [m/s], respectively. The cylinder chambers were modeled using the Continuity Equation applied to each cylinder chamber, that is

$$q_{v_{in}} - q_{v_{out}} = q_{v_{leak}} + Av + \frac{V}{\beta}\frac{dp}{dt}, \tag{4.2}$$

where $q_{v_{in}}, q_{v_{out}}$, and $q_{v_{leak}}$ are the inlet, outlet and leakage flow in each chamber [m³/s], respectively. A is the cylinder area [m²], v is the cylinder velocity [m/s], V is the chamber volume [m³], β is the effective Bulk modulus [Pa], and p is the pressure in the chamber [Pa].

The on/off valves were modeled using the orifice flow equation, being

$$q_v = c_d f \pi d x_{max} \sqrt{\frac{2\Delta p}{\rho}}, \tag{4.3}$$

where c_d is the discharge coefficient, f is the fraction of the perimeter of the spool, d is the spool diameter [m], x_{max} [m] is the maximum spool displacement, Δp is the valve pressure differential [Pa], and ρ is the fluid specific mass [kg/m³].

TABLE I. LuGre friction model parameters adapted from [9].

Parameters	Value
σ_0 [N/m]	5×10^7
σ_1 [kg/s]	0.1
σ_2 [kg/s]	5×10^4
f_c [N]	1510
f_s [N]	1600
v_s [m/s]	0.02

The valve dynamics for the opening and closing movements were modeled by a second-order transfer function [10]. The dynamic parameters of the valve were obtained from [9] and are described in Table II, where ω_{on} and ω_{off} are the valve bandwidths [rad/s] to open and close, respectively; the time delays on and off are the times to charge and discharge the valve solenoids, and ξ is the damping coefficient. The sizes of the valves were adjusted to achieve a better balance between the energy efficiency and controllability.

TABLE III. Valve parameters adapted from [9].

Parameters	Valves			
	Supply	Return	Brake	Pump
ω_{on} and ω_{off} [rad/s]	2000	2000	2000	1000/1500
ξ [-]	0.7	0.7	0.7	0.7
Time delay on [s]	0.01	0.005	0.001	0.01
Time delay off [s]	0.01	0.005	0.001	0.01
x_{max} [m]	0.003	0.0017	0.001	0.001
c_d [-]	0.67	0.67	0.67	0.67
d [m]	0.0014	0.0006	0.00033	0.0046
f [-]	1	1	1	1
ρ [kg/m³]	890	890	890	890

In the digital hydraulic pump, the internal leakages were modeled by a laminar orifice connecting the pump outlet with its inlet. The output flow rate for each pump is determined by

$$q_{vp} = D\omega - k_{vin}\Delta p, \tag{4.4}$$

where D is the pump volumetric displacement [m³/rad], ω the pump rotational frequency [rad/s], and Δp is the differential pressure [Pa]. A variable leakage coefficient (k_{vin}) [m³/(sPa)] is calculated in real-time using a lookup table from the manufacturer's datasheet, which calculates the difference between the theoretical and the datasheet flow rate.

The manufacturer datasheet used was the Bosch Rexroth – External gear pump standard performance AZPW [11]. The external gear pump is used due to the ease of mounting several pumps on the same shaft and relative cost-benefit.

In this work, the dynamic behavior of the rotational speed source was considered as a second-order transfer function, where the dynamic parameters based on the typical response of electric motors presented in [12] were used, being the natural frequency of 10.47 rad/s and the damping coefficient of 1. The component models and lines of the hydraulic circuit were implemented using the software Hopsan 2.14.2 [13]. The supply and return lines have a total volume of 0.0015 m³.

4.1. Controller

The system control was developed in the MatLab/Simulink. Fig. 4.1 shows the system block diagram, where the position of the actuator is controlled by a PI controller. The output of the controller is converted to a required flow information into the pumps and valves selector block, which have the flow, torque and overall efficiency maps of the pumps calculated from the manufacturer's datasheet. The selector block chooses the valves, the pump combination, and the rotational frequency necessary to supply the flow demanded to achieve the position. Since the same flow rate is possible to be achieved by different combinations of active pumps and rotational frequency, the selection is based on the overall efficiency of the pump combination [4].

The valve delay control block is used to synchronize the opening and closing of the valves [10]. In the selector block, a time interval of 0.05 seconds is used by the selector to calculate and send a new command to the system. This time is to ensure that the valves complete their movement before receiving a new command. The rotational frequency command is sent to the rotational speed source. The valve synchronized command and the rotational frequency are the inputs to the digital hydraulic system block, which comprises the hydraulic system implemented in Hopsan.

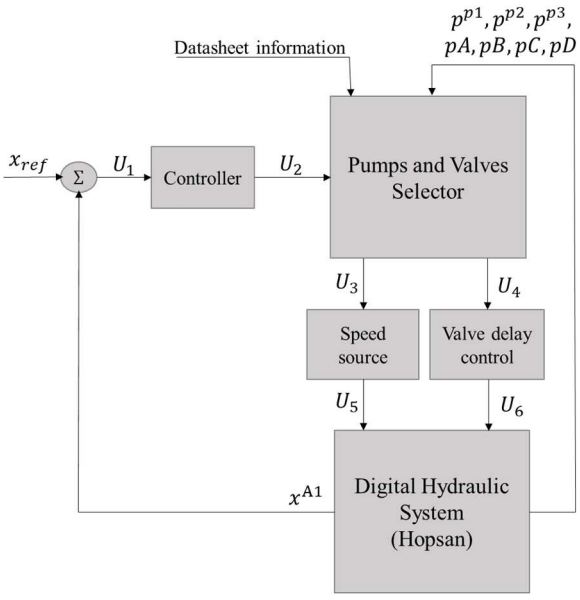

Figure 4.1. System block diagram.

4.2. Servo Hydraulic Actuator

The Servo Hydraulic Actuator (SHA) or Hydraulic Servo Actuator (HSA) is a typical name used on aircraft area to describe systems that have servo valve controlled actuators [14, 15]. The SHA model described in [9] was used and adapted to the same design parameters of the VSDEHA, in order to be used as base line to compare with the proposed solution. The parameters adopted for the servo valve were: flow coefficient k_v of $1.2 \times 10^{-7} \mathrm{m}^3/\mathrm{sPa}^{1/2}$, bandwidth ω_n of $1256.6\ \mathrm{rad/s}$ and dapping factor of 0.9. The servo valve is supplied by a constant pressure source of 20 MPa.

4.3. Energy Evaluation

For the energy analysis, the hydraulic power provided by the sources was considered as input and the hydraulic power consumed by the cylinder as output. The energy input of the SHA and VSDEHA are described, respectively, by

$$E_{in}^{SHA} = \int (q_v^{sv_1} p^{sv_1} + q_v^{sv_2} p^{sv_2})\, dt \tag{4.5}$$

$$E_{in}^{VSDEHA} = \int (q_v^{p_1} \Delta p^{p_1} + q_v^{p_2} \Delta p^{p_2} + q_v^{p_3} \Delta p^{p_3}) dt \tag{4.6}$$

where q_v^{sv} is the flow rate $[\mathrm{m}^3/\mathrm{s}]$ supplied by the pressure source, p^{sv} is the supplied pressure [Pa] at servo valve, q_v^p is the flow rate supplied for each pump unit $[\mathrm{m}^3/\mathrm{s}]$, and Δp^p is the pressure differential in each pump unit [Pa].

The hydraulic energy consumed by the cylinder in both systems is described by

$$E_{out}^{A_1} = \int (p_A A_A - p_B A_B + p_C A_C - p_D A_D) v^{A_1}\, dt, \tag{4.7}$$

where v^{A_1} is the cylinder velocity [m/s].

5. SIMULATION RESULTS

In order to evaluate the system behavior and the energy consumption, a workload profile was proposed using a spring load with a stiffness coefficient of 156 kN/m, which produces a load of 76 kN with a cylinder displacement of 0.05 m. This load profile is used to simulate the aerodynamic load into an aircraft control surface, which increases with the displacement as noticed in [9].

Figure 5.1 shows the reference profile and the simulation responses. The VSDEHA using brake valve was able to follow the reference within the predetermined settling time as the SHA, although subtle differences in behavior were observed in the return movement with assistive load. The first difference occurs between the time of 15 and 20 seconds on the negative step reference, where the SHA shows a better response.

The second difference was observed in the ramp reference between 35 and 36 seconds, where the VSDEHA follows the reference moving in a stair trajectory, effect of the successive switching of the valves to track the reference, with overshooting at some points. In both cases, SHA model has the advantage to manage the movement with assistive load, since it is possible to proportionally graduate the valve orifices, while the VSDEHA, with the proposed brake valve, has a fixed orifice size to control the maximum cylinder velocity.

The control strategy considers a minimum time interval for consecutive opening and closing of the valve. When a change is required within this time interval the system response may be delayed, the overshoot can be considered the result of this delay to close the valves.

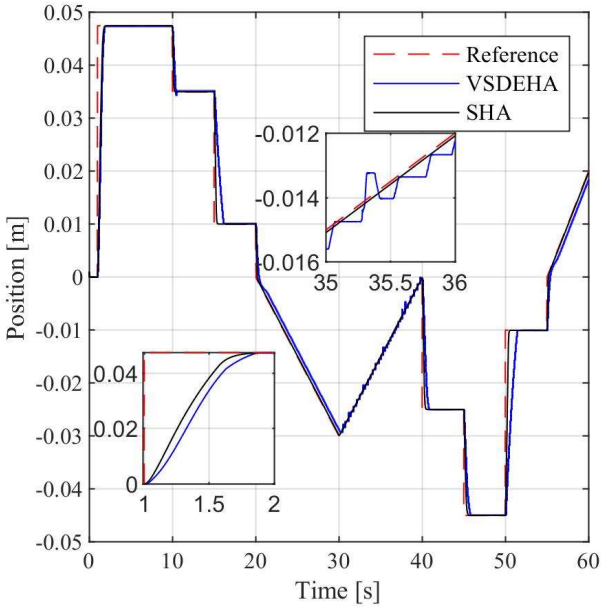

Figure 5.1. Position profile and system response.

Figure 5.2 shows the cylinder velocity behavior for both systems. The cylinder velocity is kept inside the range of maximum velocity (0.11 m/s). The largest difference between the models is noticed in the time interval of 30 and 40 seconds, where the external load effect quickly increases the cylinder velocity making the valve be activated to close and to open it consecutively, tracking the position reference.

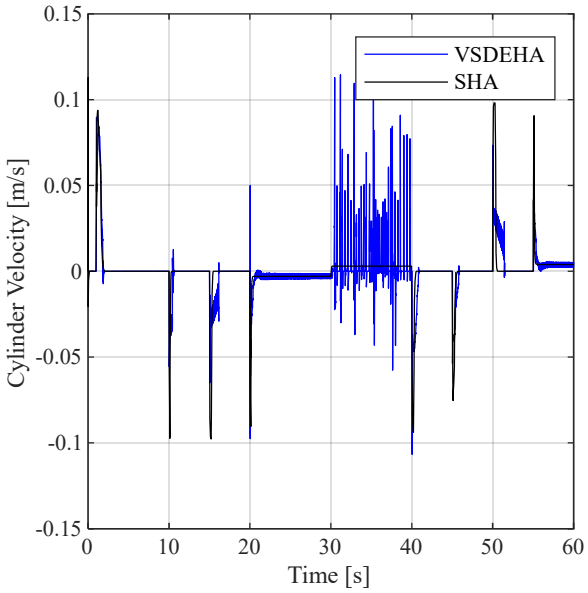

Figure 5.2. Cylinder velocity using SHA and VSDEHA.

Figure 5.3 shows the electric motor speed command and its dynamic response. In the time 1s, for the cylinder to reach the reference position, the pump requires a high rotational speed, which decreases according to the cylinder position error is reduced. At the same time, the pump combination is changed following the strategy to choose the best combination for the required flow rate. In the stand-by condition, the electric motor is kept running at 500 rpm to reduce the system time response and to keep the pump lubrication.

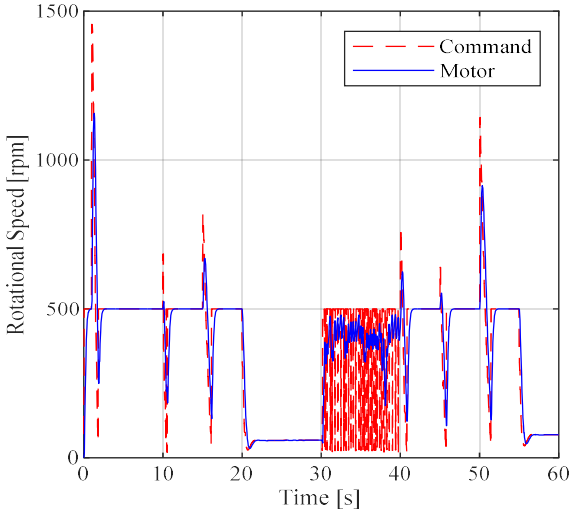

Figure 5.3. Electric motor speed behaviour.

From the electric motor perspective, the peaks presented are a point of attention for the power consumption and the dynamics necessary to perform the rapid variation of rotation speed. Moreover, the efficiency of the electric motor at low rotational frequency and high load have to be observed. In this work, the aspects related to the electric motor are not addressed.

The hydraulic energy of the system was monitored during the work profile and the results are shown in Fig. 5.4**Error! Reference source not found.**, where is presented the input and output energy accumulated.

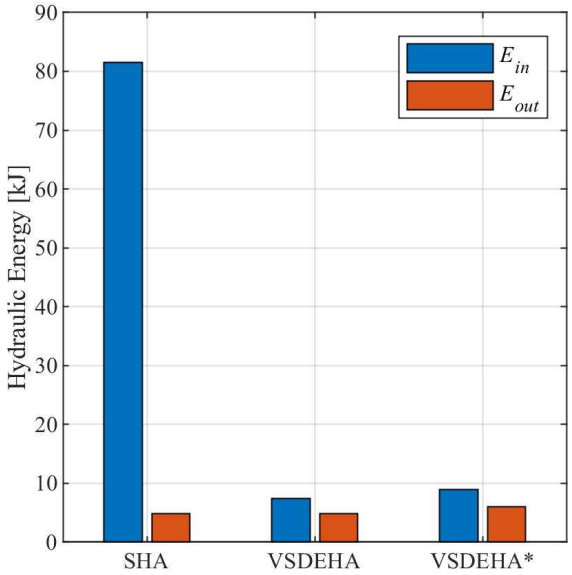

Figure 5.4. Energy input and output. *Without brake valve.

The total input energy of the SHA model was about 80 kJ and its output energy was about 5 kJ, which means that 75 kJ were lost, mainly due to the throttling control of the servo valve. When the system is on standby, the servo valve internal leakage needs to be supplied by the power source. The VSDEHA follows the power-on-demand concept and presented a total input energy of 7 kJ and an output energy of 5 kJ, approximately, which means that the energy dissipated during the work is related to hydraulic losses in the hydraulic circuit. When the cylinder is moving against the external load, there is no throttling control. In standby mode, the digital pump is connected to the reservoir at low pressure differential, avoiding high energy dissipation and the rotational speed is reduced.

A comparative analysis of the system with and without the use of the brake valves is presented in Fig.5.5. The brake valves are used to dissipate part of the external energy in order to limit the maximum cylinder speed and mitigate the overshoots. Without the brake valves, the cylinder exceeds the designed maximum speed, and compromise the controllability of the system, as highlighted in the time interval 9 to 11 and 35 to 36 seconds, where the valves are not able to close fast enough to follow the position reference and the overshoots are more frequent.

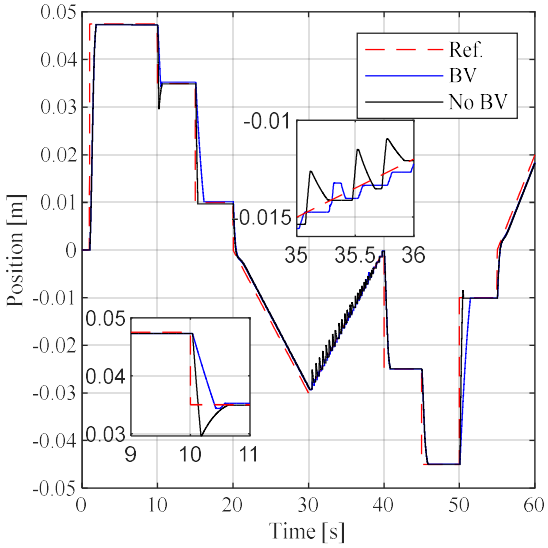

Figure 5.5. Position analysis with and without valve brake.

The total energy input of the system with and without brake valve was 7.3 kJ and 8.9 kJ, respectively (Figure 5.4). This means that, without the brake valves, the system spends 1.6 kJ more energy to follow the position reference.

6. CONCLUSIONS

This study presented a design of a digital hydraulic actuator comprising a symmetrical cylinder controlled by a digital hydraulic pump driven by a variable rotational speed source. The use of a digital hydraulic pump with variable rotational speed is justified due to the possibility to choose the best operational point for each pump combination to maximize the pump energy efficiency and to supply power on demand to the system.

The model is the first approach to evaluate the needs of the proposed topology and some parameters were based on previous studies developed by the authors on the aircraft area. The model presented a high energy-saving potential and a good compromise with the dynamic response of the system.

In digital hydraulics, one of the objectives is to avoid the use of throttling control. Although, it was demonstrated that the use of the brake valves, to dissipate the extra external energy, has improved the controllability without increasing the energy consumption of the system. However, the concept still requires future work evaluations to better manage the external energy and to improve the system controllability.

7. ACKNOWLEDGMENT

This work was carried out with the support of CNPq, National Council for Scientific and Technological Development; CISB, Swedish-Brazilian Research and Innovation Center, Saab AB, (grant number CNPq 201325/20209) and CAPES the Coordination of Superior Level Staff Improvement. The authors are grateful for all the support offered by the entities CISB, CAPES, CNPq, Saab AB, Linköping University, Federal University of Southern and Southeastern Pará and Federal University of Santa Catarina.

8. REFERENCES

[1] M. Linjama. “Digital Fluid Power – State of Art. Proceedings of the 12th Scandinavian International Fluid Power Conference Vol3, p.331-xx, 2011.

[2] V. H., Donkov,T. O. Andersen, M. Linjama, M. K. Ebbesen, “Digital Hydraulic Technology for Linear Actuation: A State of the Art Review”. Vol 21, p.263-304,2020

[3] M. P. Nostrani, H. Raduenz, A. Dell’Amico, V. J. De Negri, P. Krus, “Multi-Chamber Actuator Using Digital Pump for Position and Velocity Control Applied in Aircraft”. Global Fluid Power Society – GFPS 2020 PhD Symposium, 2020.

[4] D.O. Silva, L.A.B,Carvalho, V.J. De Negri, G. Waltrich, “Digital Hydraulic Pump: na energy efficiency study”. Proceedings of the 26th International Congress of Mechanical Engineering. ABCM, 2021. https://doi.org/10.26678/ABCM.COBEM2021.COB2021-1613.

[5] S.Bozhko, C. I. Hill, T. Yang, “More-Electric Aircraft: Systems and Modeling, 2018.

[6] J. C. Maré, J. Fu, “Review on signal-by-wire and power-by-wire actuation for more electric aircraft”. Chinese Journal of Aeronautics, vol.30, no..3, p. 857-870, 2017.

[7] H. C. Belan, C. C. Locateli, B. Lantto, P. Krus, V. J. De Negri, “Digital Secondary Control Architecture for Aircraft Application”. The Seventh Workshop on Digital Fluid Power, P.21-39, 2015.

[8] V. J. De Negri, J. R. B. Ramos Filho, A. D. C Souza, “A design method for hydraulic positioning systems”. Proceedings of USA: NFPA, p.669-679, Las Vegas, 2008.

[9] R. S. Lopes, M. P. Nostrani, L. A. Carvalho, A. Dell’Amico, P. Krus, and V. J. De Negri, “Modeling and Analysis of a Digital Hydraulic Actuator for Flight Control Surfaces,” Proceedings of the BATH/ASME 2021 Symposium on Fluid Power and Motion Control. Virtual, Online. October, 2021, doi: 10.1115/FPMC2021-68923

[10] I. J. Mantovani, H. A. Kagueiama, A. T. Gama, A. Dell' Amico, P. Krus, V. J. De Negri, “On/Off Valves Synchronization and Reliability Evaluation of a Digital Hydraulic Actuator.” Proceedings of the BATH/ASME 2020 Symposium on Fluid Power and Motion Control. Virtual, Online. September 9–11, 2020. V001T01A041. ASME. https://doi.org/10.1115/FPMC2020-2778.

[11] Rexroth Bosch Group. “External gear pump standard performance AZPW.” Edition 06. 2016, p.36, 2016. Online, Available in https://www.boschrexroth.com/pt/br/produtos/grupos-de-produtos/hidraulica-mobil/pumps/external-gear-pumps/azpw

[12] P. C. Krause, O. Wasynczuk, S. Sudhof, S. Pekarek, “Analysis of Electric Machinery and Drive Systems.”, Third Edition. vol. 75. John Wiley & Sons, 2013.

[13] R. Braum, P. Krus "Tool-independent distributed simulations using transmission line elements and the functional mock-up interface.”, 54rd SIMS conference on Simulation and Modelling, Bergen, Norway, 2013.

[14] J. C. Maré. “Aerospace actuators 1: Needs, reliability and hydraulic power solutions.”, John Wiley & Sons, 2016.

[15] I. Moir; A. Seabrige. “Aircraft Systems: Mechanical, electrical, and avionics subsystems integration.”, John Wiley & Sons, 2011.

Biographies



Dimitri Oliveira e Silva is an Associate Professor at the Institute of Geosciences and Engineering at the Federal University of the South and Southeast of Pará. He holds bachelor's and master's, and doctoral degrees in Mechanical Engineering. Currently, his research interests lie in mechanical systems design, with a particular focus on hydraulic and pneumatic systems, researching digital hydraulic actuator applications.



Marcos Paulo Nostrani is an Associate Professor in the Department of Mechanical Engineering at the Technological Center of the Federal University of Santa Catarina. He holds bachelor's, master's, and doctoral degrees in Mechanical Engineering. His research interests focus on the modeling and control of hydraulic and pneumatic systems, as well as the development of digital hydraulic actuators.



Rodrigo Simões Lopes Junior is a Mechanical Engineer from the Federal University of Ouro Preto - UFOP and Master's student in Mechanical Engineering in the area of Mechanical Systems Projects - Machine Automation from the Federal University of Santa Catarina - UFCS, where he develops research in the area of digital hydraulic actuators for aircraft primary surfaces in the Laboratory of Hydraulic and Pneumatic Systems - LASHIP.



Gierri Waltrich is an Associate Professor in the Department of Mechanical Engineering at the Technological Center of the Federal University of Santa Catarina. He holds bachelor's, master's, and doctoral degrees in Electrical Engineering. His research interests encompass multilevel inverters, multiport converters, and electric vehicles.



Petter Krus has a background from fluid and mechanical systems technology, specifically focusing on system dynamics, control and system simulation and optimization. He is professor and head of the division for Fluid and Mechatronic Systems, Flumes, of Linköping University. His research has been more on mobile hydraulic systems and components with emphasize on energy efficient systems, aircraft systems, design methods, and modelling and simulation, leading to the development of the all new version of the HOPSAN simulation package.



Victor Juliano De Negri is a Professor in the Department of Mechanical Engineering at the Technological Center of the Federal University of Santa Catarina. He is head of the Laboratory of Hydraulic and Pneumatic Systems (LASHIP) and also of the SC2C.Aero Santa Catarina's Center of Convergence for Aerospace Technologies. His research areas encompass the analysis and design of hydraulic and pneumatic systems and components, methodologies for automation and control of equipment and processes, and the design of Mechatronic systems.

A piezo-electrically actuated valve for hydraulic exoskeleton drives — modelling and measurement of a prototype

Philipp Albrecht-Zagar*, Rudolf Scheidl

Johannes Kepler University Linz, Institute of Machine Design and Hydraulic Drives, philipp.albrecht-zagar@jku.at

Abstract

This paper deals with the development of a prototype for a piezo-electrically actuated hydraulic spool valve which shall be used as a low-power, miniaturized hydraulic valve for e.g. exoskeleton applications where size, weight and efficiency plays a crucial role. The two main ideas of the hydraulic valve are (i) using a buckling beam as an element which amplifies the displacement of the piezo stack and provides bistable behavior and (ii) introducing a resonant mechanical system consisting of the valve's spool and two springs which is excited by the coupling to the piezo stack. The resulting valve is a bistable, piezo-electrically switched hydraulic 4/2-valve. The paper first explains the valve concept and the design of the valve prototype. A mathematical model for the piezoelectric actuator is derived by using higher order beam theory. A Ritz-Ansatz is introduced to get approximate expressions for the beam displacement and which proves to predict measurements very well. In a next step, the model is extended to describe the complete system. This system consists of a lumped, quasi-static piezo stack model which is coupled to the approximated beam solution, equations of motion of the spool and hydraulics. Numerical simulations prove the working principle of the valve and give insights of how parameters such as the spring stiffness affect the switching time and the pressure built-up at the output of the valve.

River Journal, 1–19.
© 2024 *River Publishers. All rights reserved.*

Keywords: piezo electric actuator, hydraulic valve design, bistable, mathematic modelling.

1 Introduction

Modern applications of hydraulics such as exoskeleton drives for medical or military use demand for small and light-weight hydraulic valves [1]. Typically, valves for such applications are switched electromagnetically which is not only bulky but also costly and inefficient in terms of energy demand. The last point is especially relevant for battery-driven applications. To overcome these disadvantages of magnetically actuated valves the use of piezoelectric [3] or magnetostrictive [2] materials can increase the power density and pave the way to miniaturized hydraulic components. Besides these advantages, using smart materials for valve actuation also introduces some downsides. Simic et al. highlighted the advantages and disadvantages of the use of piezo-electric materials for valve actuation [4].
Within the last two decades several different approaches for valves using piezo-electric actuators where investigated. Especially, a lot of research was done on the actuation of servo valves with different types of actuator designs such as piezo stack actuators, bimorph benders, ring benders and amplified piezo stacks. A detailed review for such piezo-actuated servo-valves can be seen in e.g. Tamburrano et al. [5]. Other papers deal with the performance evaluation and control of direct actuated servo valves using piezos [6–8]. In the dissertation of Reichert the complete developement of two piezo-actuated servo-valves was systematically investigated [9]. The mentioned papers mainly focus on servo valves which are directly actuated via a piezo actuator. However, in this paper a piezo switching valve is analyzed which uses an amplification mechanism based on a buckled beam as introduced in [10]. Meanwhile, several works on valve switching using such a buckling mechanism where published in the field of hydraulics, such as [11–13]. A prototype for an 4/2-valve is introduced with the aim to analyze two concepts using a piezo-electrically actuated buckling beam as a switching element. Fig. 1 shows a schematic of the prototype. The piezo actuator consists of the piezo stack which is mounted on a spring element. At the end of the spring element a buckling beam is attached which is connected to the spool of a hydraulic 4/2-valve. Two springs on the left and right hand side of the spool together with the spool mass

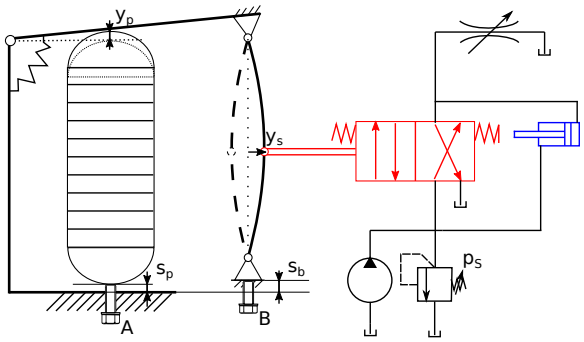

Figure 1 Schematic of a hydraulic valve prototype.

create a mass-spring system which is held in either the left or right position depending on the buckled beam's stationary point. When the beam swings from one end-position to the other by actuating the piezo stack the valve is switched. Fig. 2 shows the two concepts (*a* and *b*):

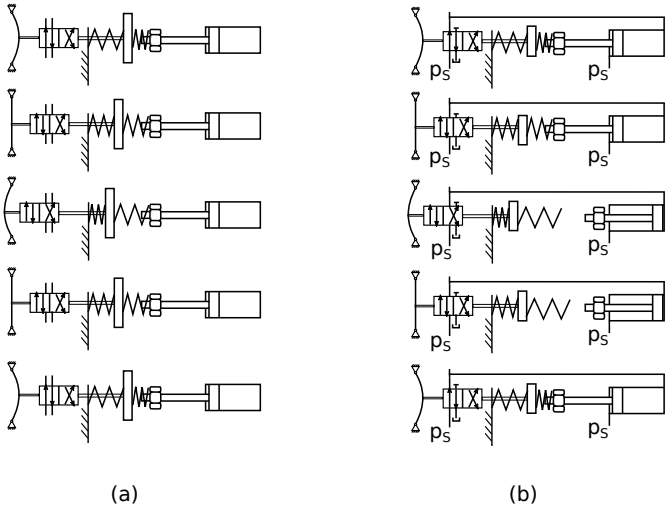

Figure 2 Schematic of a different switching phases of hydraulic valve prototype for concept *a* and *b*.

Direct actuation of spool In this concept in order to switch the valve the piezo actuator directly affects the spool's position. If the beam initially is buckled towards the right and the spool shall be moved from

right to left, the piezo actuator opens the spring element to straighten the beam. This accelerates the spool until it reaches a dead point where the beam is straight and no lateral force can be applied through the actuator anymore. Due to the spool's inertia this dead zone is passed and the piezo actuator starts closing the spring element again which leads to a buckling of the beam in the direction of movement. The spool ends up at a position which corresponds to the left buckled beam's stationary point when the piezo stack is closed.
This concept demands for a large piezo actuator. By assuming the spool displacement to be in the range of one mm and that a displacement amplification mechanism amplifies the piezo stack displacement by a factor of 50, the piezo stack must have a nominal travel range of $20\mu m$ and therefore a stack length of $\approx 20mm$. The fact that the moving parts (spool and manipulator of actuator) have to travel through the dead zone without actuation only due to inertia, low friction is necessary in the bearings of the beam as well as in the sealing gaps of the valve. In particular this becomes crucial for miniaturized valves such as needed for exoskeleton applications where masses should be very low. In contrast to magnetically switched valves the actuation happens electrostatically by loading the piezo's capacitance, so only the resistive and hysteretic losses during the switching process are degrading efficiency.

Hydraulic feedback actuation and snap-through mechanism
In this concept the buckled beam has the function of a piezo-electrically adjustable snap-through element. When the spool position is on the right hand side a small hydraulic cylinder is fed by the valve's output which applies a force via a spring on the spool in the direction that would drive the spool to the left position. This force is compensated by the buckled beam as long as it is smaller than the minimum needed lateral force for snap-through. For switching the valve, the piezo stack is expanded for a short period of time which slightly straightens the buckled beam. This decreases the needed lateral force for snap-through and the valve switches. Doing so, the beam buckles to the left, thereby, compressing the spring on the left which acts on the spool. The valve's output is fed back to the hydraulic cylinder which moves the cylinder to the right. At this state the force of the left spring and the lateral force of the buckling beam are compensating each other and the spool is at rest on the left hand side. Switching back also happens by

expanding the piezo stack for a short period of time. The force on the spool which is applied from the left spring then exceeds the lateral force for snap-through and the spool swings to the right position. This lets the hydraulic cylinder move to the left which applies a force on the right spring of the spool. A critical design parameter is the delay with which the hydraulic cylinder feeds back the output signal.

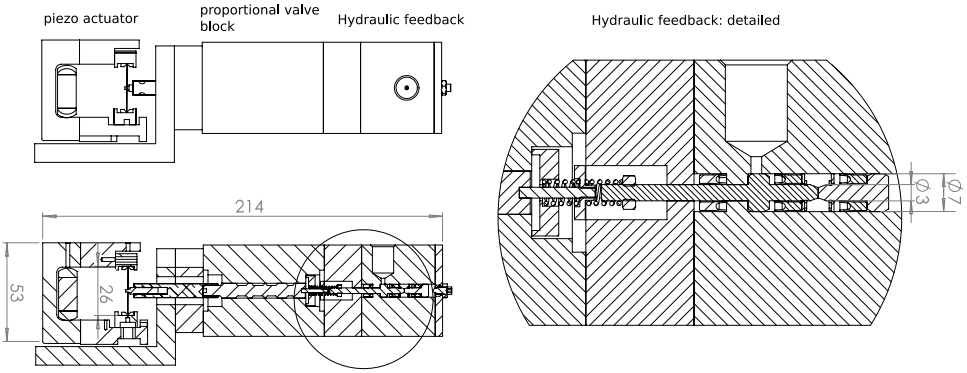

Figure 3 Technical drawing of valve prototype.

Fig. 3 shows the design of both, the piezo actuator and the hydraulic module which includes two springs attached at the valve's spool as well as the small hydraulic cylinder which establishes a feedback loop to the spool. For the prototype the valve block and the spool of a closed loop proportional valve (NG6 from Bosch Rexroth) was used as such valves exhibit zero overlap which is preferred in this applications with low spool displacement. The spool is connected to the buckling beam via a rivet on the left hand side and to a spring suspension consisting of two springs via a $M2$ screw thread on the right hand side. This allows the spool to be axially adjusted to the zero position of the valve when the beam is not buckled by rotation around its axis. The spring suspension's left side sits on the proportional valve block. The right side can be either free or in contact with the hydraulic feedback element depending on the switching state of the valve and hence the fed back pressure in the hydraulic feedback cylinder.

2 Modeling

2.1 Buckling Beam

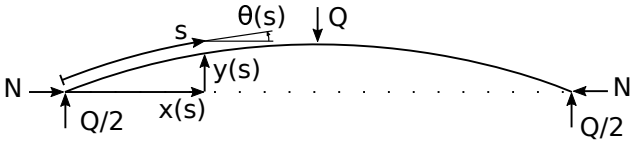

Figure 4 Schematic of the valve prototype.

Fig. 4 shows the free body diagram of a pin ended buckling beam with a normal force N at the end joints and a transversal force Q applied in the middle of the beam. s is the coordinate along the beam and $x(s)$ and $y(s)$ is the horizontal and transversal displacement of the point at s respectively. Due to symmetry only one half of the beam must be considered and the governing equation of the static buckling beam becomes

$$yN - xQ/2 = EI\frac{\mathrm{d}\theta}{\mathrm{d}s} \qquad \forall s \in (0, L/2) \tag{1}$$

where E is the elastic modulus of the beam's material, I is the area moment of inertia and $\theta(s)$ is the tangent angle at position s on the beam. The right hand side of equation (1) describes the bending moment in the beam which is proportional to the beam's curvature $\mathrm{d}\theta/\,\mathrm{d}s$. By using the relation $\mathrm{d}y = \mathrm{d}s\sin(\theta)$ this expression expands to $\mathrm{d}\theta/\,\mathrm{d}s = \mathrm{d}^2y/\,\mathrm{d}s^2/\sqrt{1-(\mathrm{d}y/\,\mathrm{d}s)^2}$. Inserting this expression and $x(s) = \int\sqrt{1-(\mathrm{d}y/\,\mathrm{d}s)^2}$ into (1) with subsequent approximation to the fourth order terms of $\mathrm{d}y/\,\mathrm{d}s$ this leads to the equation

$$D(y, y', y'') = -\frac{yN}{EI} + \frac{Q\int_0^s 1 - {y'}^2/2\,\mathrm{d}s}{2EI} - y''\left(1 + {y'}^2/2\right) = 0. \tag{2}$$

Using the ansatz function $\hat{y}(s) = A\sin(\omega s)$ and inserting it into the differential operator $D(y, y', y'')$ in (2) results in a non-zero residual. To calculate the parameter A via the method of Galerkin, the ansatz function itself is utilized as a weighting function. This results in the orthogonality condition

$$\left\langle D(\hat{y}, \hat{y}', \hat{y}''), \hat{y}\right\rangle = 0. \tag{3}$$

Inserting the relations

$$q = Q/N_{cr}, \quad n = N/N_{cr}, \quad a = A/L$$

with the beam length L and the critical buckling load $N_{cr} = EI\omega^2$ equation (3) solves to

$$n = \frac{3\pi^4 a^3 - 16\pi^2 a^2 q + 24\pi^2 a + 48q}{24\pi^2 a}. \tag{4}$$

The variable a is the beam's deflection related to the beam length L which is the same as the related spool displacement when the beam is connected as shown in Fig. 3. Hence, Eq. (4) approximates the relation between the applied vertical and lateral forces and the elastic deformation of the beam considering the first buckling mode. The distance between both clamped points is

$$\Delta L = 2\int_0^{L/2} \sqrt{1 - y'} ds - L = \frac{a^2\pi^2}{4}. \tag{5}$$

2.2 Piezo stack actuator

In the next step a static model for the piezo actuator is derived. Starting point is the IEEE standard model [14] for piezoelectric materials Std 176-1987 with its governing equations

$$D = \varepsilon E + c_P \sigma \tag{6a}$$

$$S = c_P E + c_E \sigma \tag{6b}$$

with the electric flux density field D, the electric field E, the strain tensor of the piezo material S and the mechanical stress tensor σ. The tensor c_P is the piezoelectric coefficient, c_E the elastic compliance and ε the permittivity of the piezo electric material. Eqs. (6) describe the predominant conditions at an arbitrary point in the piezo material. This can be simplified to get lumped system parameters by considering only uniaxial field quantities. Using basic piezo stack parameters such as the area A, the number for piezo slices for the stack N and the height of

one slice h the fields in (6) can be written as

$$D = \frac{Q}{NA} \qquad E = \frac{U_p}{h} \tag{7a}$$

$$\sigma = \frac{F_p}{A} \qquad S = \frac{Y_p}{Nh} - 1. \tag{7b}$$

Inserting in (6) results in a displacement $Y_p(U_p, F_p)$ can be written as

$$Y_p = U_p k_p - k_e F_p \tag{8}$$

with the piezo voltage U_p, the piezo force F_p and two constants k_e and k_p which consider the piezo effect and the mechanical stiffness of the piezo material respectively.

Momentum balance for the upper part of the U-form in the static case

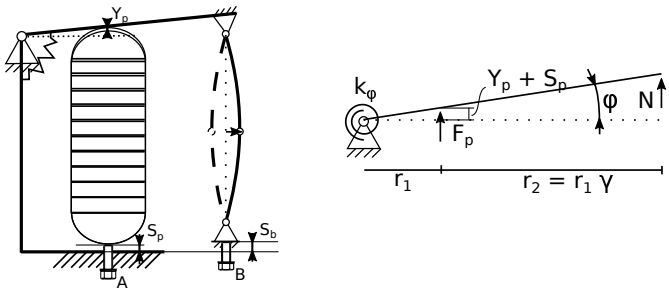

Figure 5 Schematic of the piezo actuator and the free body diagram of the piezo actuator's upper part.

(see Fig. 5) results for small angles $\varphi \approx (Y_p + S_p)/r_1$ in

$$F_p + N\gamma = C_u(Y_p + S_p) \tag{9}$$

with the transmission ratio $\gamma = r_1/r_2$ and the equivalent linear spring constant at the piezo position $C_u = k_\varphi/r_1^2$. The length S_p is adjusted through screw A (Fig. 5) and is needed to preload the piezo stack. To adjust the buckled equilibrium position of the beam screw B (Fig. 5) is used. The displacement via screw B basically acts on two serially connected spring systems: the buckled beam in normal direction and the U-form spring element. Hence, the displacement of the upper clamping position of the buckling beam $S_b - \gamma(Y_p(U_p) - Y_p(0))$ is the sum of the change of the buckling beam's vertical length ΔL (Eq. (5))

and the displacement of the U-form spring element:

$$S_b - \gamma(Y_p(U_p) - Y_p(0)) = \frac{a^2\pi^2}{4} + \gamma^2 N/C_u. \tag{10}$$

Inserting (8) in (9), solving for the piezo displacement $Y_p(U_p)$ and converting the result into non-dimensionless form by relating every length to the beam length L and substituting $u = U_p/U_{max}$ expression (10) becomes

$$s_b - u\frac{\gamma\kappa_p}{c_U\kappa_e + 1} = \frac{\gamma^2 n}{c_U} + \frac{a^2\pi^2}{4}. \tag{11}$$

This equation together with Eq. (4) describes the static model behavior of the piezo actuator. It relates the non-dimensional voltage u, the non-dimensional lateral force q and the non-dimensional lateral buckling displacement a in an algebraic expression which is evaluated by measurements in the next section.

2.3 Spool valve and hydraulics

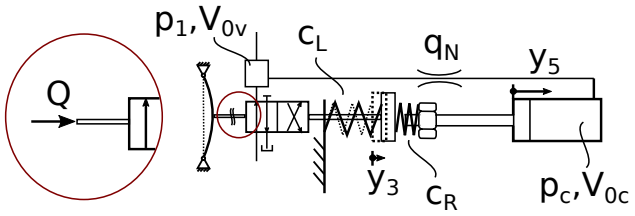

Figure 6 Technical sketch for spool and hydraulics modeling.

The state space representation of the system which is sketched in Fig. 6 considers six states, i.e. the pressures p_1 and p_c at the output of the valve and the chamber of the feedback cylinder as well as displacement and velocity for the spool mass (y_3,$\dot{y_3}$) and the feedback cylinder (y_5,$\dot{y_5}$).
First, the equation of motion for the spool is derived: Fig. 6 shows the spool element which is connected to the buckling beam on the left side and which is fixed between two spring elements with constants c_L and c_R. When the feedback cylinder is at position $y_5 = 0$ the spring elements are preloaded since the screw nut on the cylinder rod presses the right spring element to the left. The reaction force from the spring to the cylinder depends on the current position of the spool (or

the buckling beam). Since compression springs which can only act in positive direction, forces from the left and right spring element are

$$F_L = -c_L(y_3 - y_{3,0}),\ F_R = -c_R(y_3 - y_5 + y_{5,0})$$

as long as these values are greater than zero and zeros otherwise. y_3 describes the position of the spool which is the same as the buckling amplitude A (see previous section). Besides F_R and F_L, the lateral force of the buckling beam Q as well as a viscous damping force F_d is acting on the spool. The lateral force Q is as a function of piezo voltage U and displacement y_3.
Together with the equation of motion for the cylinder and the pressure build-up equations for p_1 and p_c the state space model reads as

$$\dot{p_1} = \frac{E}{V_{0,v}} \left(q_L + \frac{y_3}{\hat{y}_3} \frac{q_{N,v}}{\sqrt{p_N}} \sqrt{p_S - p_1} \right) \tag{12a}$$

$$\dot{y_3} = v_3 \tag{12b}$$

$$\dot{v_3} = \frac{1}{m_s}(F_L + F_R + Q(y_3, U) - d_f v_3) \tag{12c}$$

$$\dot{p_c} = \frac{E}{V_{0,c} - A_A(y_5 - s_c)} \left(v_5 A_A + \frac{q_{N,t}}{\sqrt{p_N}} \sqrt{p_1 - p_c} \right) \tag{12d}$$

$$\dot{y_5} = v_5 \tag{12e}$$

$$\dot{v_5} = \frac{1}{m_c}(-p_c A_A + p_S A_B - F_R + F_c) \tag{12f}$$

where q_L is the load at the output of the valve, m_s is the spool mass, m_c is the cylinder mass, $q_{N,v}$ and $q_{N,t}$ are the nominal flow rate of the valve when opened with $\hat{y}_3$ and the nominal flow of the throttle in the feedback loop, respectively, d_f is a factor which includes dissipation through velocity proportional friction. Eqs. (12) considers the feedback cylinder and hence models valve concept b which was explained in section 1. For simulation of the concept a this model reduces to

$$\dot{p_1} = \frac{E}{V_{0,v}} \left(q_L + \frac{y_3}{\hat{y}_3} \frac{q_{N,v}}{\sqrt{p_N}} \sqrt{p_S - p_1} \right) \tag{13a}$$

$$\dot{y_3} = v_3 \tag{13b}$$

$$\dot{v_3} = \frac{1}{m_s}(F_L + F_R + Q(y_3, U) - d_f v_3) \tag{13c}$$

and the force $F_R = F_R(y_3, y_5)$ evaluated at $y_5 = 0$.

3 Measurements and Simulations

Table 1 Values for simulation model of valve prototype

valve and hydraulics			
p_S	100 bar	p_T	1 bar
E	14000 bar	V_{0v}	1.0 l
V_{0c}	2.0 l	q_{Nv}	40 l/min
$q_N t$	8 l/min	A_A	38.5 mm^2
A_B	31.4 mm^2	$\hat{y}_5$	0.3 mm
m_s	5 g	c_L, c_R	16 N/mm
piezo actuator			
κ_e	5.7×10^{-6}	κ_p	3.7×10^{-4}
c_U	9.7×10^{-3}	γ	4.5
beam			
B	10 mm	H	0.3 mm
E_{steel}	180 kN/mm^2	l_0	26.9 mm
s_b	270 µm		

3.1 Piezo actuator

The model for the piezo stack actuator was verified through measurements of lateral displacement of the buckling beam, normal force N at the clamping points of the beam and lateral force Q. Fig. 7 shows some results for those quantities for a piezo actuator with a linear spring constant of $C_U = 2N/m$ that was discussed in [15]. In the upper diagram on the left the lateral displacement as a function of the normal force N is shown. Theory suggests that the beam remains straight until the buckling force N_{cr} is reached. At this bifurcation the beam can buckle towards both sides. Due to imperfections of the beam measurements (red, blue) show that the beam already starts buckling at lower normal forces, that it buckles always on a preferred side and that theory represents the asymptotic behavior to which the measurement converges for high and low normal forces. Also, severe hysteresis can be seen which is due to friction in the beam's joints. In the upper diagram of the right hand side graphs show the lateral force Q as a function of beam displacement for theoretical piezo actuators with different linear spring constants c_U. A measurement for an actuator with $c_U = 2$ N/µm proofs the theory to fit well. On the left hand side

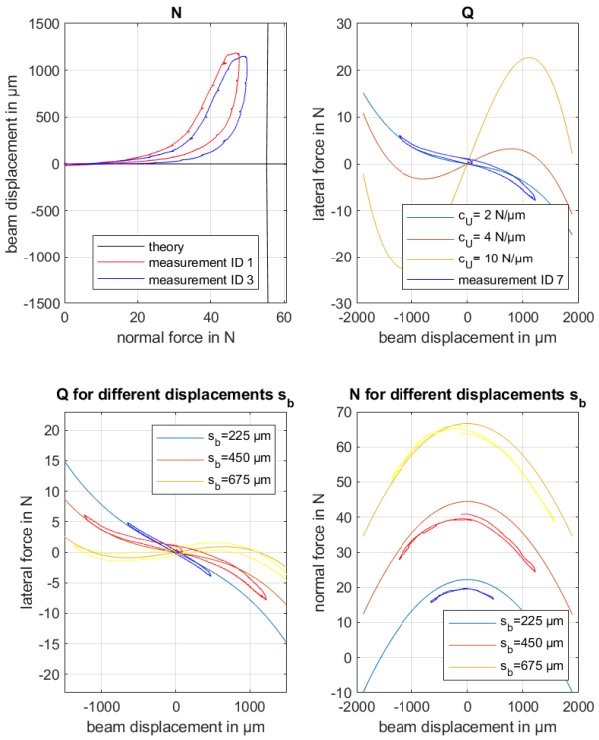

Figure 7 Measurements of a piezo actuator with linear spring constant of $C_U = 2N/m$.

on the bottom graphs show theoretical and real relationships between the lateral force and the beam displacement for an actuator with $c_U = 2$ N/µm and different values for the displacement of the beam screw s_b. For the same values of s_b the bottom right diagram shows theory and measurements of the normal force N as function of beam displacement. These measurements proof that the theory derived in section 2 works very well and is suitable for prototype design as well as for simulation of the prototype valve. One disadvantage when using piezo materials is the severe hysteresis (see [4, 5]). Such effects can be modelled by using e.g. a Preisach-model [17], however, the reader should be aware of, that

within this paper such type of nonlinearity was not consindered in the simulation.

3.2 Piezo valve

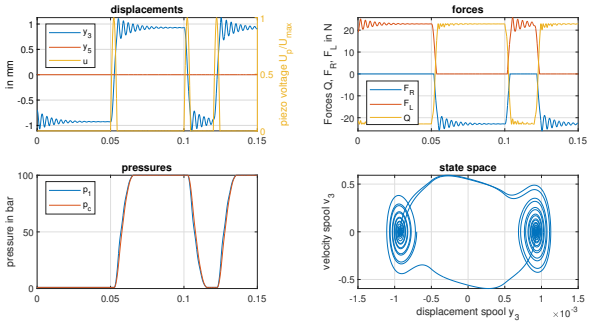

Figure 8 Simulation of valve concept *a*: optimal switching behavior

Valve concept *a* Fig. 8 shows a simulation of the valve concept *a*. The upper left diagram shows that the switching time of the valve in both directions is approximately $t_s = t_{10\%} - t_{90\%} \approx 3.1$ ms and the same due to symmetry for both directions. After reaching the opened or closed state the spool oscillates with a frequency of $f \approx 303$ Hz which corresponds to the approximate beams natural frequency of

$$f_0 = \frac{1}{2\pi}\sqrt{c/m} = 310\text{Hz}$$

with $c = EI\pi^4/(2L^3)$ and $m = m_s + \rho BHL/2$ which is derived by a Ritz-Ansatz in [16]. In the upper right diagram the interplay of the spring forces F_L and F_R as well as the lateral force Q applied from the beam is shown. On the bottom right hand side the phase space representation of the spool's motion is shown. One can see the two attracting local minima which exist if the nondimensional piezo voltage u is low enough. This concept demands for a piezo actuator which can fully open such that the beam can swing from one side to the other almost freely without the need to snap-through. Therefore, the disadvantage to concept *b* is the need for a big piezo stack which makes the actuator less useful for miniaturization and expensive. The graphs in Fig. 9 on the top show how different nondimensional switching

voltages ($u_1 = 1.0$, $u_2 = 0.6$, $u_3 = 0.8$) affect the swichting behavior. For a small value of $u_2 = 0.8$ the switching process is not successful. The two diagrams on the bottom show an approximated behavior of the valve with an imperfect beam which is plastically deformed in the lateral direction by $\Delta a = 50$ µm. Fig. 9 shows that an actuator with such a beam is not able to switch the valve anymore, even though the spool displacement is already getting positive for some time.

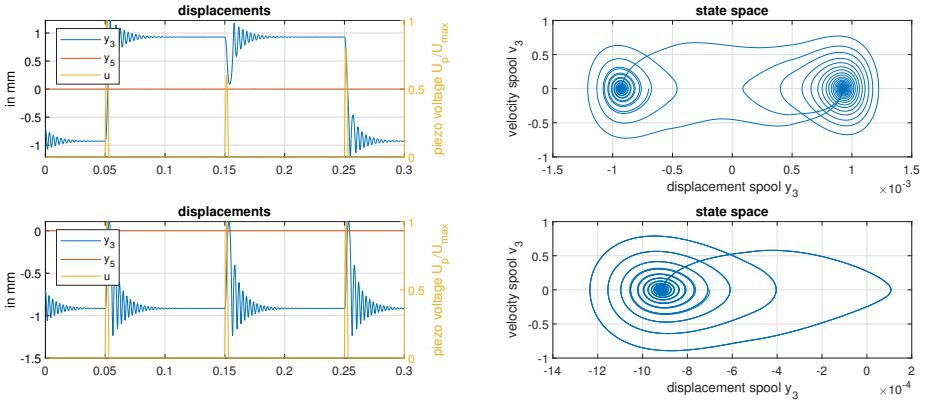

Figure 9 Simulation of valve concept a: switching errors due to small voltages and beam imperfections

valve concept b Fig. 10 shows the simulation results for the valve concept b which uses hydraulic feedback to ease the switching process. This relaxes the demand for big piezo stacks as needed in concept a. The top left diagram shows three successful switching processes. Notice that a nondimensional voltage of $u = 0.6$ is applied which already led to malfunction of concept a. In Fig. 10 one can realize an unequal behavior for different switching directions which is caused by an asymmetric design: If no buckling beam was there, the spool together with the two spring elements act as a mass-spring system. The equilibrium point is defined by the preload of the springs. The function of the feedback cylinder is to switch between two preload forces, hence, change the equilibrium point towards the right or left. The rod side chamber of the cylinder is always pressurized with system pressure. At the other side the output pressure, which is either $p_A = p_S$ or $p_A = 0$ bar, is

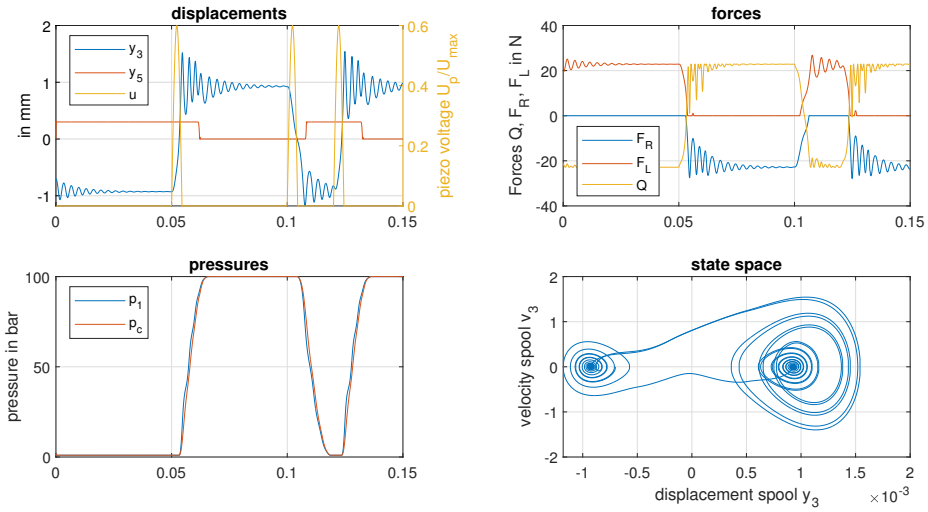

Figure 10 Simulation of valve concept *b*.

applied which makes the cylinder starts moving at

$$p_c = p_S A_B / A_A.$$

For parameters listed in table 1 $p_c \approx 81$ bar. This asymmetric (not at $(p_{v,max} - p_{v,min})/2 = 50$ bar) switching condition is the reason for the seen switching behavior. For the first and third switching process (at $t_1 = 0.05$ s and $t_3 = 0.12$ s) the spool shoots. During this phase the hydraulic cylinder position is still $y_5 = 0.3$ mm, the output pressure is fed back towards the piston and the pressure p_c grows. When the pressure hits $p_c \approx 81$ bar the piston moves in the negative direction, hits against the spring system and applies a higher preload to it. This makes the equilibrium point of the spool move towards the negative direction where the spool finally settles. In the phase space portrait on the bottom right in Fig. 10 this can be seen by two overlaying spirals on the right which converge to two different equilibrium positions. When switching of the spool from $y_3 > 0$ to $y_3 < 0$ which can be seen at $t_1 = 0.1$ s the shift of the equilibrium position happens earlier and during the switching process because the condition $p_c < 81$ bar is met very fast.

4 Conclusion

Two concepts for a piezo-actuated valve are presented in this paper. First a static model of the piezo actuator is presented and verified by measurements. Using the derived models simulations show that concept *a* exhibits symmetric switching behavior but is more sensitive to e.g. imperfections of the buckling beam. Concept *a* also demands for an actuator which exhibits high displacements. This can be seen, as the switching process fails when lower voltage is applied. This necessity raises the costs of the piezo stack and makes the concept unsuitable for miniaturization. Concept *b* overcomes these problems by using an additional hydraulic feedback cylinder which results in successful switching for low voltages which is not possible with concept *a*.

Acknowledgment

This work has been supported by the COMET-K2 Center of the Linz Center of Mechatronics (LCM) funded by the Austrian federal government and the federal state of Upper Austria.

References

[1] R. Scheidl, Digital fluid power for exoskeleton actuation - guidelines, opportunities, challenges ,The Ninth Workshop on Digital Fluid Power, September 7-8, 2017, Aalborg, Denmark.

[2] V. Apicella C. S. Clemente, D. Davino, D. Leone and C. Visone, Review of Modeling and Control of Magnetostrictive Actuators, Actuators 2019, 8(2), 45

[3] S. Yokota, K. Akutu, A Fast-Acting Electro-Hydraulic Digital Transducer (A Poppet-Type On-Off Valve using a Multilayered Piezoelectric Device, JSME International Journal, Series II, Vol. 34, No. 4, 1991.

[4] Simic, M.; Herakovic, N. Piezo actuators for the use in hydraulic and pneumatic valves. In Proceedings of the International Conference Fluid Power 2017, Maribor, Slovenia, 14–15 September 2017; University of Maribor Press: Maribor, Slovenia, 2017

[5] Tamburrano P, Sciatti F, Plummer AR, Distaso E, De Palma P, Amirante R. A Review of Novel Architectures of Servovalves Driven by Piezoelectric Actuators. Energies. 2021; 14(16):4858. .

[6] Lindler, J. E., & Anderson, E. H. (2002). Piezoelectric direct drive servovalve. In Smart Structures and Materials 2002: Industrial and Commercial Applications of Smart Structures Technologies (Vol. 4698, pp. 488-496). International Society for Optics and Photonics.

[7] Jeon, J.; Nguyen, Q.H.; Han, Y.M.; Choi, S.B. Design and evaluation of a direct drive valve actuated by piezostack actuator. Adv. Mech. Eng. 2013, 5, 986812.
[8] Han, C.; Hwang, Y.H.; Choi, S.B. Tracking control of a spool displacement in a direct piezoactuator-driven servo valve system. Front. Mater. 2017, 4, 9.
[9] Reichert, M., & Murrenhoff, H. (2010). Development of high-response piezo servovalves for improved performance of electrohydraulic cylinder drives. PhD thesis. Aachen university
[10] Garstenauer, M. (2001). Theoretical and experimental investigations of a novel concept for hydraulic, high-speed, switching valves. PhD thesis. Johannes Kepler University Linz
[11] Scheidl, R., Scherrer, M. & Zagar, P. The buckling beam as actuator element for on-off hydraulic micro valves. International Journal of Hydromechatronics, Vol. 4, No. 1, pp 55-68, 2021.
[12] Scherrer, M., Scheidl, R., & Manhartsgruber, B. Optimization of a Snap Through Spring for a Hydraulic Valve With Hysteresis Response Behavior. Proceedings of the ASME/BATH 2019 Symposium on Fluid Power and Motion Control. ASME/BATH 2019 Symposium on Fluid Power and Motion Control. Longboat Key, Florida, USA. October 7–9, 2019. V001T01A038. ASME.
[13] Scheidl, R, & Mittlböck, S. A Hydraulic Piloting Concept of a Digital Cylinder Drive for Exoskeletons. Proceedings of the BATH/ASME 2018 Symposium on Fluid Power and Motion Control. BATH/ASME 2018 Symposium on Fluid Power and Motion Control. Bath, UK. September 12–14, 2018. V001T01A040. ASME.
[14] An American National Standard — IEEE Standard on Piezoelectricity, ANSI/IEEE Std 176-1987.
[15] Zagar P., Scheidl R., "A piezo-electric valve actuator for hydraulic exoskeleton drives Part I: design": Proceedings of the 2020 IEEE Global Fluid Power Society PhD Symposium (GFPS), October 19-21, 2020, Guilin, CHINA, 2020.
[16] F. Ziegler, "Mechanics of Solids and fluids." Springer-Verlag, New York, Vienna, 1991.
[17] F. Preisach: Über die magnetische Nachwirkung. In: Zeitschrift für Physik. Band 94, 1935, S. 277–302.

Biography



Philipp Albrecht-Zagar. Born May 29th 1989 in Graz (Austria). MSc of Electrical Engineering at Vienna University of Technology in 2014. Industrial research and development experience in Electronics (E+E Elektronik, 2014-2018). Since Sept. 2018 employed at the Johannes Kepler University Linz as junior researcher, university assistant and PhD candidate.



Rudolf Scheidl. Born November 11th 1953 in Scheibbs (Austria). MSc of Mechanical Engineering and Doctorate of Engineering Sciences at Vienna University of Technology. Industrial research and development experience in agricultural machinery (Epple Buxbaum Werke), continuous casting technology (Voest Alpine

Industrieanlagenbau) , and paper mills (Voith). Since Dec. 1990 Full Professor for Mechanical Engineering at the Johannes Kepler University Linz. Research topics: hydraulic drive technology with emphasis on digital fluid power and mechatronic design.

Different Solutions for the Achievement of Variable Margin Load Sensing Systems: Energy Saving and Increased Performance

Davide Mesturini[1], Mattia Scolari[1], Francesco De Martino[1], Ulderico Busani[1]

[1]*Walvoil SpA (Interpump Group), Reggio Emilia (RE), Italy*

Abstract

Load Sensing system is one of the most common types of hydraulic circuit; its relative simplicity, the high level of controllability and the energy savings achievable in combination with a variable pump have made it commercially successful over the last few decades. However, in order to ensure good control, a certain amount of energy is usually dissipated in the so-called "LS-margin".
A greater opportunity for improvement is now guaranteed by electronic integration; in particular, the management of a variable LS-margin allows further savings, also guaranteeing interesting control strategies that can increase productivity, precision and working comfort in the off-highway machineries.
The paper presents two different solutions for the management of variable stand-by margin.
The first one, known under the commercial name ALS (Adaptive Load Sensing) is an electrohydraulic device integrated in the directional control valve and provided with an ECU that defines its control strategy. The system has been simulated and tested on a telehandler with significant improvements in terms of consumption and performance.
The second one consists of an electronically controlled variable piston pump, where the displacement is defined by a closed loop control. In this case as well, an external ECU is providing the best logic to match with the directional control valve actuation.
The paper provides the results of the simulations, the case studies and the experimental data, comparing benefits and drawbacks of both solutions.
A specific focus is provided on the management software developed in Codesys environment and on the specific implemented working functions. A complete system approach in the work allows for the definition of a complete system, provided with Piston Pump, Directional Control Valve, ECU and HMI devices.

Keywords. Load Sensing, Electronic Control, Variable Margin, Energy saving.

1. INTRODUCTION

Load Sensing (LS) systems are still today one of the most widespread and most appreciated solutions on the Non-Road Mobile Machinery (NRMM) market, despite the fact that the solution is now several decades old and has not significantly changed over time [1].
The strengths of the LS systems are the relative simplicity of the components, the good controllability achieved and the reasonable energy consumption resulting from the use of a Variable Displacement Pump (VDP) in combination with an LS Directional Control Valve (DCV).
One of the limits of traditional LS system is represented by the LS-margin, that is the additional pressure drop needed by the system to perform the control, as illustrated by Bedotti [2].
Already many years ago an upgraded version of LS concept integrating electronic control was theorized [3, 4]. In this system, the physical connection between the DCV and the VDP is not present, as the LS pressure is read by a pressure transducer on the DCV and elaborated by the Electronic Controls Unit (ECU) to pilot the VDP. The concept was developed and improved by various researchers [5, 6], especially regarding the software control stability [7, 8] and showing some specific machineries application cases [9, 10], but it took many years to find a widespread application on the market.
Only in the last decade, the larger availability of electro-hydraulic components and the spread of ECUs have opened up new possibilities for improvement both in terms of efficiency and in terms of functionality, giving rise to Electronic Load Sensing (ELS) systems.
The potential of ELS systems lies in the ability to optimize the interaction of multiple components, providing a holistic approach and the optimal whole system logic.
This paper presents two different configurations of an ELS system and their practical application in two different types of machines:

- the Adaptive Load Sensing (ALS): an additional electro-hydraulic device interposed between the DCV and the pump and its application to a 79.5 kW Telehandler;
- the electro-hydraulic operated VDP and its application to a 5t Mini-excavator.

2. ADAPTIVE LOAD SENSING DEVICE

Under the name of ALS, Walvoil SpA introduces a new electro-hydraulic device that can be interposed between the VDP and the DCV to realize specific system logic and allow an energy saving.
The electro-hydraulic device can be a stand-alone manifold or can be integrated into a traditional LS DCV to create an ELS in combination with a traditional VDP equipped with a common hydromechanical LS controller: this feature makes it particularly interesting for the after-sales market, since it can be easily installed to upgrade machines, introducing an important benefit even on already operational fleets.
A very interesting aspect of the ALS device is the possibility of creating an ELS also in fixed displacement systems; there are still many applications on the market that, for cost or simplicity reasons, require the use of a fixed displacement pump, although much less efficient than a variable

displacement pump. Thanks to the ALS system interfaced to the DCV main compensator, it is possible to anyway increase the efficiency, as well as benefit from the functional advantages of ELS systems.

2.1. Adaptive Load Sensing System Description

Figure 2.1.1 shows the ISO1219 scheme of the ALS manifold. The system receives as input the LS signal from the DCV and outputs a modified LS signal (LSC) that is supplied to the VDP or to the inlet compensator of the DCV in case of fixed pump systems. The main stage of the device is represented by a 3/2 spool valve, which, feeding from the high-pressure line P and discharging any overpressures in the exhaust line T, adjusts the modified pressure LSC by reference to the LS signal itself and a pair of proportional signals pil1 and pil2 generated by a couple of electrically operated proportional pressure reducing valves. When no control is provided at the pilot stages, the device copies the LS signal in LSC without any modification; increasing the current I1 or I2 to the pilot stages, the value of LSC is consequently modified comparing to the original LS value.

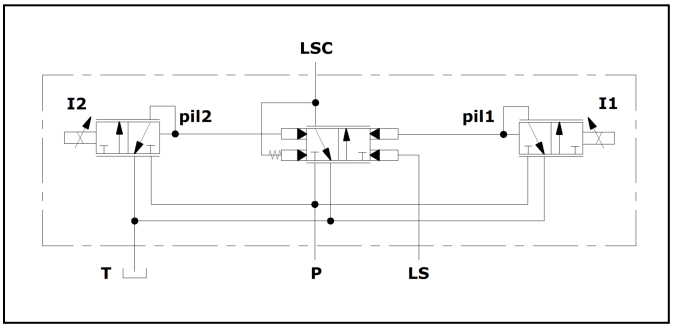

Figure 2.1.1. Adaptive Load Sensing manifold ISO1219 scheme

It is clear that the modification of the LS signal through the pressures imposed by the pilot stages allows to vary the pressure margin (PM) across the metering areas of the DCV. In the following equation, PPM is the mechanical pressure margin set by the standard Load Sensing pump regulator (or by the DCV main compensator in case of fixed displacement pumps): it imposes a constant margin between LS and P. In case we provide LSC as reference instead of LS, the value of PM is consequently modified:

$$\mathrm{PM} = \mathrm{P} - \mathrm{LS} = \mathrm{LSC} + \mathrm{PPM} - \mathrm{LS} = \mathrm{PPM} + (\mathrm{LSC} - \mathrm{LS}) \qquad (2.1.1)$$

Referring to Figure 2.1.1, the pil1 signal acts in the direction of increasing the pressure margin, while the pil2 signal in the direction of reducing it. As a final result, the following operative conditions are possible:

- I1 = I2: LS = LSC: PM = PPM (2.1.2)
- I1 < I2: LSC < LS: PM < PPM (2.1.3)

- I1 > I2: LSC > LS: PM > PPM (2.1.4)

Figure 2.1.2 shows a cut view of the 3/2 spool, main stage of the ALS. The spool is realized by means of internal coupled pins that allows the influence of four different pressures (LS, LSC, pil1, pil2) on the two piloting faces.

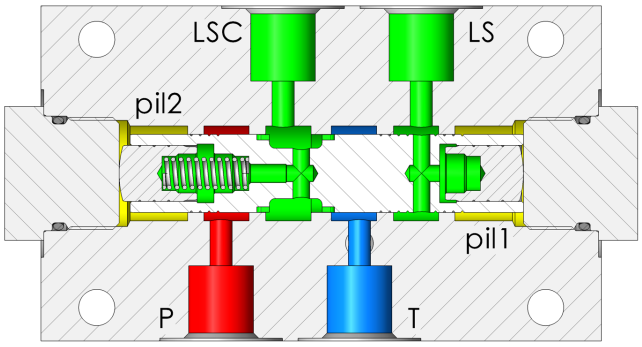

Figure 2.1.2. ALS 3/2 main stage spool design

Other versions of the ALS are available, including alternatively only the pil1 or only the pil2 pilot stage; in these specific versions the device is built to only increase or only reducing the PM from an original value imposed by the spring. The design and the different possible configurations are described in [11].

2.2. ALS Software Structure and the Implemented Functions

Various types of logic implemented in the ECU, allow to realize various modes of operation; the most simple and intuitive gives the operator the possibility of selecting different working modes: typically, a fast/dynamic mode (using a high PM) and a high-precision/efficient mode (using a low PM).
For all the tests described in this paper, a different logic has been used, varying the LS pressure margin according and proportionally to the control signals of the DCV. The flow demand required by the operator is detected directly through the signals generated in the human-machine interfaces (HMIs) and defines an increasing PM, proportionally to the DCV spools displacement: this allows to modify and shape the flow delivery characteristic, improving the fine control at low speed and minimizing the consumption, while maintaining the actuator maximum speed. In case of simultaneous actuations, a specific priority logic is applied, in order to set a common and appropriate PM.
The software has been developed in the Walvoil PHC Studio® environment, with a combination of Structure Texts and Function Block Diagrams. The ECU communicates through SAEJ1939 protocol with the HMIs and directly generates the PWM control of the DCV.

The PM control has been tested in both open and closed loop logic; in the second case the P and LS pressure feedback allows a more precise and responsive control.
An additional feature of the ALS software is the capability of the torque/power limitation. The function can be implemented by adding a pressure sensor on the pump delivery and an angle sensor on the pump swash plate, to evaluate the actual torque. A dedicated logic block has been developed to reduce the PM when a specific torque level (given as the product of pump displacement and pump pressure) is reached. The function has been successfully tested on the bench, but it has not been implemented in the application yet.

2.3. 3D Map-based ALS Control Logic

As a final stage of the development, a further logic has been tested: it consists in a 3D map-based algorithm that autonomously selects, depending on the flow required by the operator, the best and most energy-efficient combination of PM and DCV metering area. Compared to the linear logic applied during the tests, there is no more a direct proportionality between HMIs signals and the spools displacement: the DCV meter-in areas are adjusted by the ECU, depending on the actual PM. Figure 2.3.1 shows the different PM strategies compared to the standard LS: in the 3D map-based case the choice of larger metering areas in the spools allows to reach the target iso-flow curve at a lower PM, giving an additional efficiency improvement. The results of this control strategy have been investigated in a dedicated work [12].

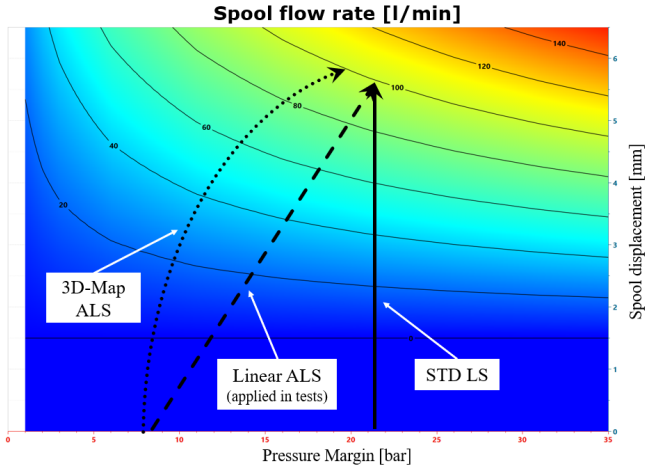

Figure 2.3.1. Linear and 3D map-based algorythms compared to standard LS system

2.4. Application of Adaptive Load Sensing to a Telehandler

The development of the ALS system went through a detailed simulation analysis by means of a lumped parameters model in AMESim© software; [13] and [14] illustrate some use modes and applications of the system and estimate a good consumption save, especially interesting on

electrified agricultural tractors. After a performance test activity on the hydraulic bench, the ALS system has been installed on a Dieci Agri Farmer 34.7 GD® Telehandler, shown in Figure 2.4.1.



Figure 2.4.1. Dieci Agri Farmer 34.7 GD® Telehandler

The Dieci Agri Farmer has a tandem gear pump and represents a significant example of use of ALS in combination with fixed displacement pump. The machine has been equipped with the following components:

- Electronic joysticks DJW®, with electronic multifunction MTH® grips;
- CED400® ECU dedicated to ALS management and interfaced to the machine system with SAEJ1939 protocol;
- Tandem Gear Pump (43cc/rev+17cc/rev);
- ALS Manifold;
- Flow Sharing DPX100® DCV, 4 working sections, with electro-hydraulic control.

2.5. Test on the Dieci Agri Farmer® Telehandler

The tests of the machine were performed at Dieci R&D Center and were based on a combination of functional and efficiency checks.
The direct feedback from the operators made it possible to optimize some aspects relating to the controllability and driving comfort; additionally, four tests were carried out on the track to assess the consumption of a vehicle equipped with the original system compared to one equipped with ALS system:

- Positioning test: loading and unloading two different loads at a defined distance;

- Fine positioning test: precision loading and unloading of a load in narrow and critical space;
- On road test: vehicle drive in various conditions;
- Track test: constant speed vehicle driving with load.

The following table summarizes the results of the tests.

	Consumption reduction with ALS [%]
Positioning test	6,3
Fine positioning test	5,9
On road test	5,0
Track test	5,4

Table 2.5.1. Dieci Agri Farmer Tests Results

Beyond the excellent energy results, with the use of ALS, the vehicle also reported numerous additional advantages; a series of augmented functionalities have allowed the drivers to carry out more operating cycles in the same time, especially in precision movements, experiencing a greater productivity of the machine.
Some instabilities and jerking present in the system have been eliminated by introducing dynamic effects in the control of the PM, significantly improving the driver comfort.

3. ELECTRONIC CONTROL PUMP-BASED ELS SYSTEM

The second practical application applies the ELS to a 5t mini-excavator (Figure 3.1) and involves the use of a variable displacement axial piston pump equipped with an electro-proportional controller, according to the most usual way of building an ELS system.



Figure 3.1. 5t mini-excavator equipped with Walvoil ALS

3.1. Variable Pump Eletromechanical Control

According to the peculiarities of each application, different layouts and control strategies are needed to maximize the working cycle and minimize the energy consumption. Various types of electro-proportional regulators have been developed and studied by the research team, aiming to reduce the number of components on the system, while maintaining a comfortable feeling by the operator and a high level of safety.
For this test a Walvoil PWLS53® axial piston variable displacement pump has been used, with an electro-hydraulic controller including pressure control and flow control capabilities. It incorporates a 3/2 spool proportionally operated by a coil and an electro-proportional relief valve, according to Figure 3.1.1 ISO1219 scheme; it also comprehends an angle Hall effect-sensor, to detect the swash plate position.
An in-depth experimental activity was preliminarily carried out to optimize the pump regulator performance and to finalize the control software. This substantial part of the development has retraced many of the theories and solutions illustrated in past works [15, 16] regarding both physical layout and control algorithms. The mechanical-hydraulic tuning mainly focused on the definition of the 3/2 spool metering areas and its overlaps. Both the pressure and the flow stages control have been improved in terms of hysteresis, thanks to an accurate proportional electric control.

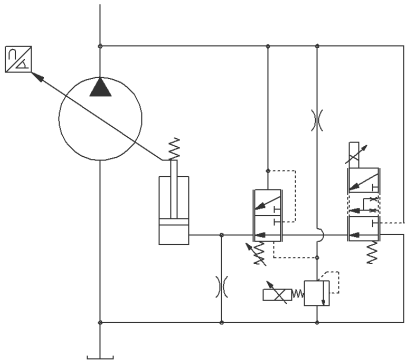

Figure 3.1.1. Electro-hydraulic control for the pump displacement

In order to keep a direct comparability with previous experiences on ALS system, a simple pressure control mode has been chosen, mainly operating on the proportional relief valve to achieve the PM target imposed by the ECU. The PM logic applied is the linear one described in § *2.2*: PM increase from 8 to 16 bar is directly proportional to the spool displacement, defined by the HMIs signals.
Figure 3.1.2 shows the synoptic layout of the excavator system, including the HMIs, the pump and the LS pressure transducers to provide a closed loop controlled PM.

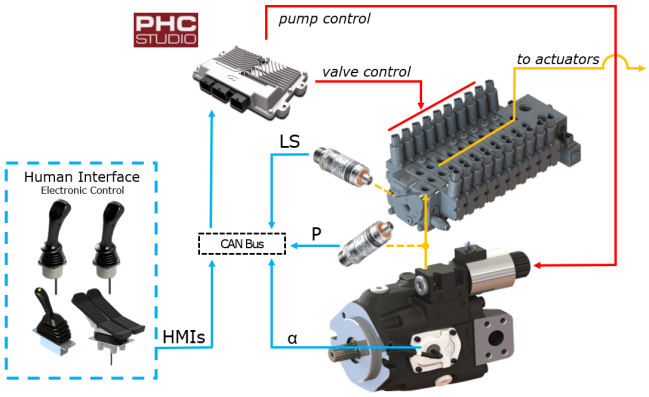

Figure 3.1.2. Mini-excavator components layout

3.2. Excavator System Simulation in AMESim©

Before approaching the experimental activity, the system has been simulated by means of the AMESim© software. A typical "digging and unloading" cycle has been performed on the excavator by an average expert operator; pressures and flows of all actuators' ports have been logged and used as input parameters for the model.

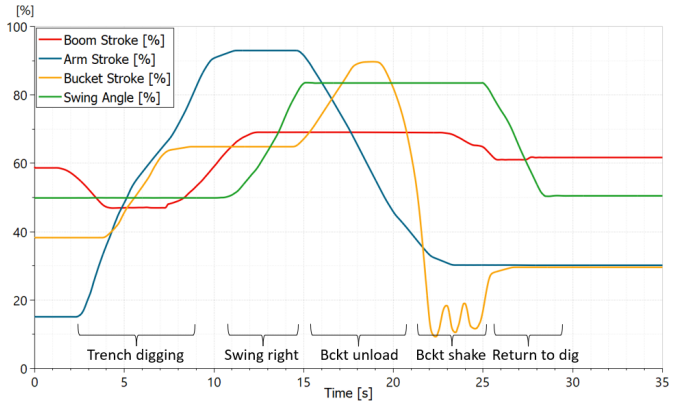

Figure 3.2.1. Main actuators' displacement performed in the simulation cycle

The cycle involves boom, arm, bucket and swing functions, whose actuator displacement is shown in Figure 3.2.1.
The spools' displacement is calculated backward from the input flows and the input pressures are superimposed to the actuators' ports. The variable PM is consequently defined.

Figure 3.2.2 shows the value of the PM imposed by the control during the whole simulated cycle, expressed as a percentage of the regulation range (8-16 bar). Figure 3.2.3 shows the developed AMESim© model with special focus on DCV block.
The total consumed energy along the cycle at pump level is calculated:

- Traditional LS (constant 15 bar PM): 140,1 kJ;
- ELS (variable PM): 132,4 kJ.

The reduction in hydraulic energy consumption settles on 5,5%; it is reasonable to expect that a similar reduction is also present at fuel level.
This outcome is very similar to the one obtained with the application of ALS to the telehandler: the contribution of the variable margin seems to settle indicatively in the same range, regardless of the application case and the method of use. As a confirmation, analogous results have been found also in previous works [12, 13, 14].

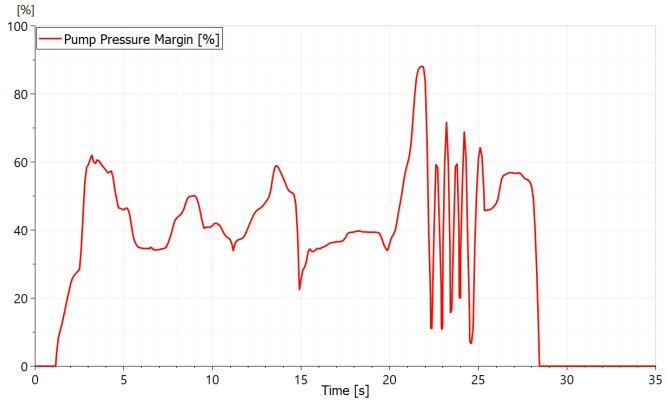

Figure 3.2.2. Variable pump pressure margin during the simulated cycle

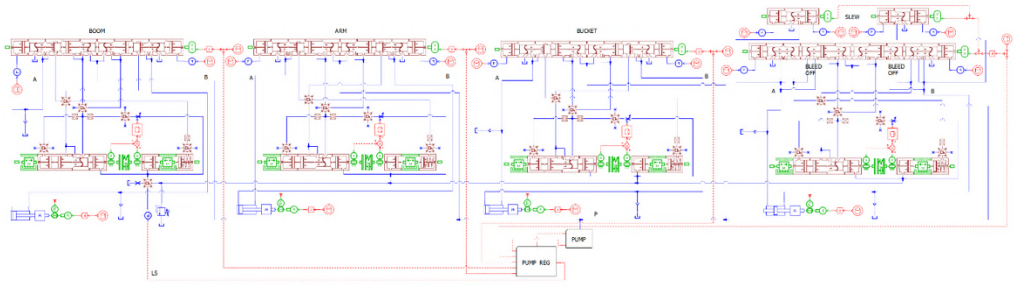

Figure 3.2.3. AMESim© model of the excavator's DCV block

3.3. Experimental Layout built on the 5t Mini-excavator

The ELS system simulated in AMESim© has been eventually installed on the mini-excavator. The system is composed by following components:

- Electronic joysticks HJW®, with electronic multifunction XMH® grips;
- Electronic pedals CPW® for tracks control;
- N°5 CED400® ECUs interconnected with SAEJ1939 protocol and dedicated to the system logic, to the PWM outputs and to the various sensors log for a complete analysis of the machine performance;
- Variable axial piston pump PWLS53® with electro-hydraulic controller;
- Flow Sharing DPX100® DCV, 10 working sections, with electro-hydraulic control;
- Fan Drive system.

As a first stage, an accurate tuning of the DCV has been made in order to guarantee the best machine controllability. Secondarily the ELS control has been applied and checked in its performance in the machine operating cycle. In this case as well, as already experienced in the telehandler, the adjustable PM over the spool displacement helps significantly to smooth the operations and to make the machine dynamic more sensitive.
An additional development phase has integrated the electronic torque/power control, that was previously realised in the mini-excavator by means of a mechanical torque limiter in the VDP.
The linear PM logic described in § 2.2 has been eventually applied and verified to work properly. Figure 3.3.1 shows a log of the digging cycle performed on the mini-excavator with the ELS system working. The red line is the actual modified PM applied to the system, while the black dotted line represents the dimensionless PID controller output.

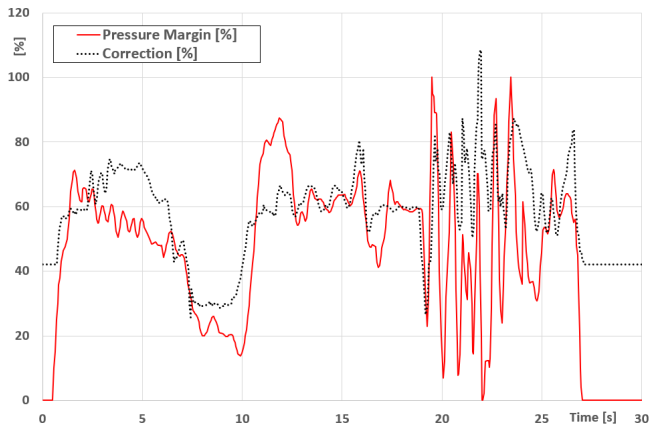

Figure 3.3.1. PM and PID correction gain data acquired during the mini-excavator test

The simulation model has been compared and optimised according to the experimental results by means of simple and directly comparable operations (as for example single movement step response).
Regarding the whole cycle, diagram in Figure 3.3.1 is not perfectly comparable to the simulation diagram in Figure 3.2.2, due to the unavoidable differences in the time scale and in the actuation sequence; nevertheless, the two diagrams are similar on a qualitative base and show analogous dynamic and behaviour. The PM is continuously varying according to the joystick actuation and to the power limiting control. The PM is dynamically adjusted between 8 and 16 bar and the PID controller correction gain is monitored.
A first approximate evaluation of the consumption is confirming the saving values estimated in the simulation, but the machine will be soon equipped with a more accurate fuel consumption measurement system for a more reliable data collection.

4. CONCLUSIONS AND OUTLOOK

Two different configurations of ELS have been studied and compared; the unprecedented Adaptive Load Sensing system has been practically applied on a Dieci telehandler in a fixed displacement circuit, while the classical solution using an electro-hydraulic pump regulator has been studied on the bench, simulated and eventually applied to a 5t mini-excavator.
Both technologies have proven the capability to perform a variable pressure margin logic, allowing an average 5% reduction in fuel consumption. The practical application on the Dieci telehandler and on the mini-excavator has furthermore shown some augmented control capabilities and improved drive comfort. The direct comparison of the two possible approaches has highlighted the following aspects:

- The ALS system integrated in the DCV, represents an immediate and easy solution to benefit of the ELS opportunities. The simple and stand-alone installation makes it an interesting way for the retrofit market and for the enhancement of existing machine models;
- The ALS system integrated in the DCV makes it possible to benefit of ELS opportunities even on fixed displacement circuits that still represents a significant percentage of the market applications;
- The ALS system integrated in the DCV results to be more stable and easier to set comparing to the ELS realized by means of the pump electronic control. The proportional control of the ALS guarantees a higher definition and resolution of the electronic proportional control;
- The electronic control pump-based ELS, offers a multitude of additional opportunities thanks to a more sophisticated software. Especially the capability to switch from flow control to pressure control, opens to various strategies of coordinated control of the DCV and of the VDP.

Next activities will be focused on the development of mixed control strategies to improve the match of DCV and VDP, exploiting especially the beneficial effect of flow control on the pump-based ELS, capable of significantly reducing the oscillations and instabilities typical of pressure controls.

5. ACKNOWLEDGMENT

We thank the company Dieci for the continuous collaboration and the shared effort in applying the ALS system. We also thank Prof. Casoli from University of Parma and prof. Zardin from the University of Modena and Reggio Emilia for the supportive activities within the TASC project.

6. REFERENCES

[1] H.C. Pedersen, T.O. Andersen, M. Hansen, "Load sensing systems - A review of the research contributions throughout the last decades", Proceedings of the 4th IFK Workshop, Dresden, Germany, 24–26 March 2004.

[2] A. Bedotti, F. Campanini, M. Pastori. L. Riccò, P. Casoli, "Energy saving solutions for a hydraulic excavator", 72nd Conference of the Italian Thermal Machines Engineering Association, ATI 2017, Lecce, Italy.

[3] B. Zähe, R. Schmidt, M. Eschweiler, "Elektrohydraulisches Loadsensing", Ölhydraulik und Pneumatik, 34, 1990.

[4] W. Backé, B. Zähe, "Electrohydraulic load-sensing", SAE Technical Paper Series, nr. 911814, 1991.

[5] H. Esders, "Elektrohydraulisches Load Sensing für mobile Anwendungen", PhD thesis, Technischen Universität Braunschweig, Germany, 1995.

[6] M. Hansen, T.O. Andersen, H.C. Pedersen, F. Conrad, "Feasibility study of electronic load sensing concept for hydraulic variable", Proceedings of the 7th International Conference in Education and Mechatronics (REM06).

[7] A. Langen, "Experimentelle und analytische Untersuchungen an vergesteuerten hydraulisch-mechanischen und elektro-hydraulischen pumpenregulungen", PhD thesis, Rheinisch-Westfälischen Technischen Hochschule Aachen, Germany.

[8] G. Tewes, H.H. Harms, "Fuzzy control for an electrohydraulic load-sensing system", Proc. 9th Bath International Fluid Power Workshop, September 1996.

[9] T.O. Andersen, M. Hansen, H.C. Pedersen, "Experimenting with electrical load sensing on a backhoe loader", Proceedings of the 6th International Conference on Fluid Power Transmission and Control (ICFP 2005).

[10] R.H. Hansen, A.M. Iversen, M.S. Jensen, T.O. Andersen, H.C. Pedersen, "Modeling and control of a teletruck using electronic load sensing", Proceedings of the ASME 2010 10th Conference on Engineering System Design and Analysis, ESDA 2010, July 12-14, 2010, Istanbul, Turkey.

[11] Patent application EP3667103 Applicant Walvoil s.p.a.

[12] P. Casoli, F. Scolari, C.M. Vescovini, D. Mesturini, F. Zannoni, “Excavator hydraulic circuit solution to reduce dissipations and fuel consumption”, 76th Conference of the Italian Thermal Machines Engineering Association, ATI 2021, Roma, Italy.

[13] A. Gaiola, B. Zardin, P. Casoli, M. Borghi, F. Mazzali, F. Pintore, S. Fiorati, “The hydraulic power generation and transmission on agricultural tractors: feasible architectures to reduce dissipation and fuel consumption - Part 1”, 75th Conference of the Italian Thermal Machines Engineering Association, ATI 2020, Roma, Italy.

[14] P. Casoli, B. Zardin, S. Ardizio, M. Borghi, F. Pintore, D. Mesturini, “The hydraulic power generation and transmission on agricultural tractors: feasible architectures to reduce dissipation and fuel consumption - Part 2”, 75th Conference of the Italian Thermal Machines Engineering Association, ATI 2020, Roma, Italy.

[15] M. Scherer, M. Geimer, B. Weiss, “Contribution on Control Strategies of Flow-On-Demand Hydraulic Circuits”, The 13th Scandinavian International Conference on Fluid Power, SICFP2013.

[16] M. Axin, “Mobile Working Hydraulic System Dynamics”, Linköping Studies in Science and Technology, Dissertations No. 1697, 20.

Numerical Simulations of a High Frequency Switching 4/2 ON/OFF Valve for Pulse Modulation Switching Digital Circuits

Francesco Sciatti[1*], Paolo Tamburrano[1], Andrew R. Plummer[2], Elia Distaso[1], Pietro De Palma[1] and Riccardo Amirante[1]

[1] *Department of Mechanics, Mathematics and Management (DMMM), Polytechnic University of Bari, 70121 Bari, Italy;*

[2]*Centre for Power Transmission and Motion control (PTMC), University of Bath, Bath BA2 7AY, UK;*

**Corresponding author: francesco.sciatti@poliba.it*

Abstract.

Proportional valves and servovalves are employed in several industrial and aeronautical applications. However, both employ sliding spools, which cause high power consumption, essentially due to the large pressure drops across the metering orifices. A recent research field aims to substitute spool valves with ON/OFF valves that have high switching frequency and produce low pressure drops, in order to drastically reduce such high-energy dissipations. The aim of this paper is to evaluate the performance of a novel high frequency switching four-way two-position (4/2) ON/OFF valve actuated directly by a commercially available multilayer piezoelectric actuator, called ring stack. To this end, well-established equations, implemented in Simulink by means of the libraries of Simscape Fluids, are used. The proposed architecture shows simplicity of construction; in addition, very effective flow modulation along with low pressure drops and high flow rates are predicted by the simulations.

Keywords. Piezoelectric Actuators, Spool Valves, Digital Hydraulics, ON/OFF Valves, Simulink.

1. INTRODUCTION

Analog hydraulic valves, both proportional valves and servovalves, have extensively been used in lots of industrial and aeronautical applications for several decades [1], [2], [3]. The basic function of these valves is to control the oil flow delivered to an actuator by changing the opening of the valve metering orifices by means of the main spool displacement [4], [5], [6]. Additionally, these control components are crucial in pneumatic systems, such as in vital biomedical equipment like lung ventilators for intensive care units, regulating patient gas

inhalation and exhalation [7]. However, the use of proportional and servovalves is not energy efficient since both employ sliding spools, which cause high throttling losses in the system [8], [9]. In a previous study by the authors of this paper, a power dissipation equal to 7 kW was evaluated for a medium size spool valve considering a pressure drop of 60 bar and a flow rate of 60 L/min [10]. In addition, the correct operation of spool valves can easily be hindered by oil contamination [4], [5].

A recent research field aims to substitute commercially available spool valves, both proportional and servovalves, with the digital hydraulic technology by means of the use of low-cost ON/OFF valves in order to reduce the energy consumption and increase the efficiency of the system [11], [12], [13]. Higher reliability, lower energy consumption, more precision in machine motions, fewer shutdowns, less loss of production, lower original investment and spare parts carrying costs are among the benefits [14], [15]. Moreover, the digital hydraulic technology directly adopts digital signals to control valves without D/A conversion, which simplifies the control mode and removes the noise sensitivity typical of servovalves [16].

A standard definition of digital hydraulics is provided in [16], namely, “a system which controls a discrete fluid with a modulated, discrete, digital signal directly to realize active and intelligent control of the system output”.

The digital hydraulic technology can be divided into two main categories; in the first type, the hydraulic circuit is composed of a large number of parallel – connected on/off valves; in the second type, the hydraulic circuit is based on high frequency switching technologies [16]. The two types of digital hydraulic circuits are shown in Figure 1 and Figure 2.

The circuit shown in Figure 1 is called Digital Flow Control Unit (DFCU). In this system, the Pulse Code Modulation (PCM) approach is used. In particular, a precise flow control can be obtained through the encoding control of several robust ON/OFF valves connected in parallel. Thus, if more precise flow rates are required, more ON/OFF valves need to be used. In the DFCU circuit, the ON/OFF valve is normally a closed two-way two-position valve, which blocks flow when it is in the unactuated position and passes flow when actuated. If there are N switching valves in the circuit, there will be 2^N possible combinations, thus, by turning the valves on and off, the individual valve flows are combined to form a total flow using a binary table. The main issue of this approach is that numerous ON/OFF valves are needed and must be actuated at the same time, necessitating a precise timing of each individual valve.

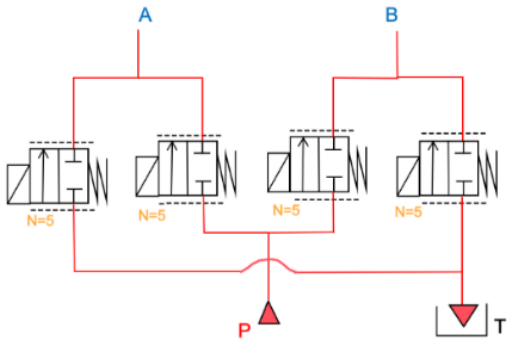

Figure 1. Digital Flow Control Unit (DFCU) circuit with simplified drawing symbol, where N represents the number of ON/OFF valves.

Because these valves are ON/OFF, they do not require a spool adjusting flow and can have the same architecture as that of poppet valves. A poppet valve is capable of performing several working cycles with lower pressure drops than proportional valves because the flow area can be designed larger [14].

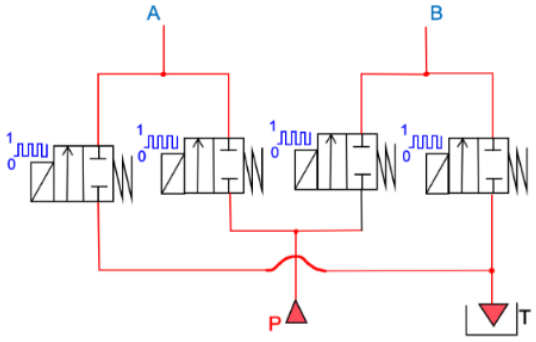

Figure 2. Pulse Modulation Switching (PMS) digital circuit using four 2/2 ON/OFF valves.

The circuit depicted in Figure 2 is called Pulse Modulation Switching (PMS) digital circuit. The ON/OFF valves used in this circuit are the same as those used in the DFCU circuit, apart from being larger. High frequency switching controlled valves allow the average flow area to be adjusted by the Pulse Width Modulation (PWM) technique. In particular, a pulse signal (from 0 to 1) is delivered to the digital valve and flow modulation is obtained by changing the frequency of the pulse signal. The switching frequency has an impact on the controllability: the lower the frequency, the higher the controllability obtained. However, a low frequency increases the pressure pulsation. Accumulators and inertance tubes are normally used to suppress noise and smooth the flow rate obtained [17], [18]. A PMS digital circuit can be considered the better solution since it requires fewer valves than those employed in a DFCU circuit.

Considerable research has been done in the past decades into the development of digital valves. The basis for the design of such devices is to create a rapid switch from fully open to fully closed position in less than 5 ms with very small pressure losses.

Regarding the PCM approach, Bower's invention, issued in 1961, is the first to use real PCM control with a dual-acting actuator [19]. However, the most general PCM valve system was presented by Murphy and Weil in 1962 [20]. In this system, each flow line has its own ON/OFF valve series, allowing for meter-in and meter-out flow control. Despite the fact that the PCM method and its modifications have actively been patented in the field of hydraulics, only few articles appear in the literature [21], [22].

Regarding the PWM approach, various high frequency switching digital valves were studied and developed by several researchers [23], [24], [25]. These valves presented very fast response, but the flow rates were limited to low flow applications. Because of this, apart from very small circuits, digital hydraulics has yet to find practical applications.

In this scenario, this paper proposes a novel high frequency switching 4/2 ON/OFF valve architecture that can be manufactured and used in the digital hydraulic circuit shown in Figure 3, in order to replace proportional and servovalves in aeronautical and industrial applications. PMS digital circuits are usually proposed to be equipped with 2/2 ON/OFF valves. In the present paper, it is proposed to use 4/2 ON/OFF valves in order to reduce the number of the components, as shown in Figure 3.

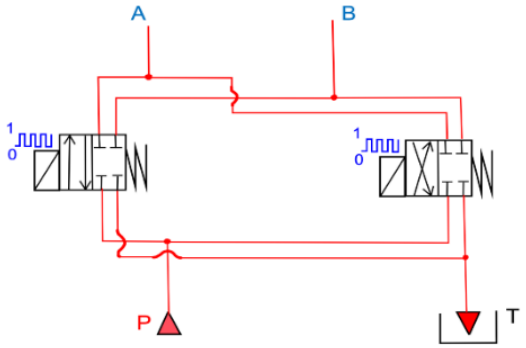

Figure 3. Pulse Modulation Switching (PMS) digital circuit using two 4/2 ON/OFF valves.

The idea here investigated thoroughly consists in using a commercially available multilayer piezoelectric actuator, called ring stack, to move two inner poppets in the 4/2 poppet valve. This idea was partially presented in [10], where a feasibility study of a high frequency switching 2/2 ON/OFF valve was performed using a simplified Simulink model in order to predict simple open-loop step tests. In this paper, the investigation regards the 4/2 valve, and a more complete assessment is performed using a more detailed Simulink model, which is now able to simulate closed loop control.

The PWM technique is proposed to be used. In particular, by changing the duty cycle of the input pulse voltage (V_c), different values of the average flow rate (Q_{mean}) can be obtained. The duty cycle, denoted by *%DC*, is the ratio of the pulse duration (Δt_{on}) to the overall period of the input signal (τ). The latter is kept constant; therefore, the duty cycle ($\%DC = \Delta t_{on}/\tau$) is changed from 0 to 1 and is expressed as a percentage, i.e. from 0% to 100%.

Firstly, the valve architecture is presented. Then, the improved Simulink model is described. After that, the simulation results obtained through open and closed loop control are presented and discussed. The findings allow one to understand the benefits and drawbacks, which are finally summarised in the conclusions.

2. VALVE LAYOUT

In this section, the valve layout is analysed. The main component of this architecture is the ring stack actuator. It consists of a series of piezoelectric ring elements stacked one on top of the other and enclosed between two electrodes. The thickness of the layers is of the order of 25–100 μm. Various combinations of maximum free stroke and blocking force can be obtained depending on the height of the stack. The blocking force is the maximum actuation force and is obtained when the actuator is blocked from moving and when the maximum operating voltage is applied; the maximum free stroke is the maximum displacement ideally achievable for a null actuation force, i.e., when the actuator experiences no resistance to movement, and when the maximum voltage is applied. The ring stack with the maximum height (200 mm) produced by Noliac is adopted in the numerical simulations, namely, model NAC2125-HXX [26]. In Table 1, its main characteristics are shown.

Table 1. NAC2125-HXX RING STACK: Specifications [26].

Parameter	Symbol	Unit	Value
Length/outer diameter	d_o	mm	20
Width/ inner diameter	d_i	mm	12
Height	H	mm	200
Max. operating voltage	V_{max}	V	200
Max. free stroke	x_{max}	μm	325
Max. blocking force	$F_{b,max}$	N	8450
Capacitance	C_{ap}	nF	79300
Stiffness	k_p	N/m	$26 \cdot 10^6$

A feasibility study of a 2/2 poppet-type valve based on the use of the same piezo actuator was performed in [10]. In order to reduce the number of valves from four to two and, thus reducing the complexity of the system, a novel 4/2 poppet-type valve architecture, shown in Figure 4, is now presented. The valve, in order to be employed in the digital circuit shown in Figure 3, must meet the following targets:

- it must switch between open and closed in a very short time interval, i.e., less than 5 ms;
- it must generate low pressure drops even for high flow rates. A real goal is to achieve a maximum pressure drop of 20 bar at 60 L/min;
- it must be robust, since it must switch numerous times a day.

In the novel 4/2 valve architecture, shown in Figure 4, the ring stack actuator (1) allows the poppets (2) to be moved. The latter, which are inserted through the hole of the stack (3), are kept in contact with the piezo actuator by means of a spring (4) which in turn ensures a correct pre-compression (δ_0) to the ring stack. Indeed, since the piezo stack actuator cannot withstand large pulling forces, a preload must be applied to avoid damage. It has widely been proved that a correct value of preload grants a longer lifetime for this type of piezoelectric actuator [27]. In particular, the values for the optimum preload range from 20 to 50 percent of the blocking force [28]. When a differential voltage is applied to the ring-stack, the poppets are moved from their seat and flow is allowed from Port P to Port A, and from Port B to Port T. Taking advantage of the rapid response of the piezoelectric actuator

as well as the simplicity of the valve architecture, this valve has the potential to satisfy the previously specified targets.

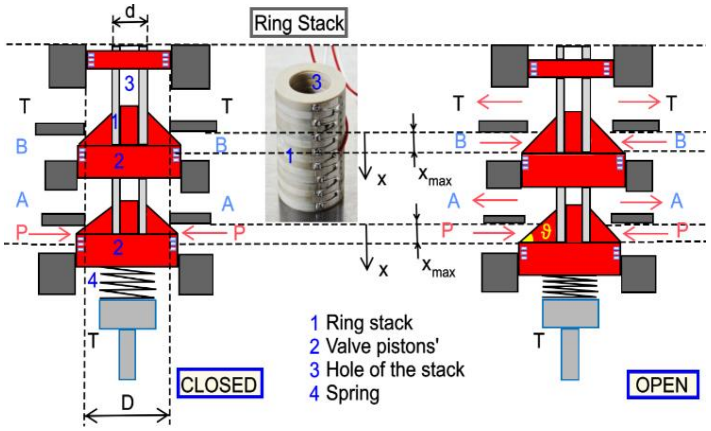

Figure 4. Proposed 4/2 poppet-type valve architecture: closed position (left), open position (right).

3. SIMULINK MODEL

A numerical model simulating the performance of the valve concept, shown in Figure 4, has been developed. The equations of the numerical model, which have been implemented into the Simscape Fluids environment [29], are described in the following.

An amplifier is needed to transform a low input pulse voltage V_c (from 0 to 5 V) into a high output voltage V_{amp} (from 0 to 200 V). A second order transfer function $G(s)$ is used to model the relation between V_{amp} and V_c, as already done in previous studies [10]:

$$G(s) = \frac{V_{amp}}{V_c} = \frac{k_a \omega_n^2}{s^2 + 2\xi\omega_n s + \omega_n^2}, \tag{1}$$

where s is the complex variable, while k_a, ω_n, and ξ are the gain, natural frequency and damping ratio of the amplifier, respectively. In the code, it is possible to model the current limit I_{max}, thus the rate of change of voltage can be limited according to Equation (2):

$$\left(\frac{dV_{amp}}{dt}\right)_{max} = \frac{I_{max}}{C_{ap}}, \tag{2}$$

where C_{ap} is the capacitance of the ring-stack.

The blocking force F_b depends on the amplified voltage V_{amp} as follows:

$$F_b = K_{VF} V_{amp}, \tag{3}$$

where K_{VF} is a conversion factor (from voltage to newton). The blocking force F_b determines the actuation force F_{act}, which can be calculated as follows [26]:

$$F_{act} = F_b - k_p x, \tag{4}$$

where k_p is the stiffness of the actuator and x is the displacement of the poppets.

The equilibrium of the forces acting on the poppets, when the valve is actuated, can be written as follows [10]:

$$F_{act} - k_s(x + \delta_0) - F_{flow} - C\dot{x} - m\ddot{x} = 0, \tag{5}$$

where k_s is the stiffness of the additional spring, which ensures a correct pre-compression δ_0 to the ring stack; F_{flow} is the flow force acting on the poppets'; C and m are the damping factor (accounting for fluid viscosity) and the mass of the moving parts, respectively.

To evaluate the damping factor of the moving parts, which is due to the frictional forces acting on it, the following relation can be used [10]:

$$C = \frac{\mu\pi D_p l_p}{c\sqrt{1 - \left(\frac{\varepsilon}{c}\right)^2}}, \tag{6}$$

where μ is the dynamic viscosity of the oil, D_p and l_p are the diameter and length of the part in contact with the case; c is the radial clearance and ε is the radial eccentricity.

For each metering chamber, the flow forces F_{flow} and the restriction area A_r can be estimated by the following equations [10]:

$$F_{flow} = \rho\frac{Q^2}{A_r}cos\vartheta, \tag{7}$$

$$A_r = \pi D x sin\vartheta, \tag{8}$$

where ρ is the oil density, θ is the poppets' angle equal to the flow angle, D is its effective diameter and Q is the flow rate, which can be calculated as follows [10]:

$$Q = C_D A_r\sqrt{\frac{\Delta p}{\rho}}, \tag{9}$$

where C_D is the discharge coefficient and Δp is the overall pressure drop across the valve. In the model, Port A and Port B are hydraulically connected and the pressure drop $p_A - p_B$ is neglected. Therefore, the pressure drop in Equation (9) becomes:

$$\Delta p = p_P - p_T = 2(p_B - p_T) = 2(p_P - p_A), \tag{10}$$

The values of p_P and p_T are constant input in the model.

The poppets' stroke is confined by two stops which restrict its motion between an upper and a lower bound. Each stop is represented as a spring combined with a damper. When the maximum or minimum displacement is reached, a force F_{stop} which acts on the ring stack can be calculated as [10]:

$$F_{stop} = K_{stop}(x_{max} - x) + C_{stop}\frac{d}{dt}(x_{max} - x), \quad \text{for } x \geq x_{max} \tag{11}$$

$$F_{stop} = K_{stop}(x_{min} - x) + C_{stop}\frac{d}{dt}(x_{min} - x), \quad \text{for } x \leq x_{min}, \tag{12}$$

where K_{stop} and C_{stop} are the spring stiffness and damping of the stop, respectively, with x_{max} and ($x_{min} = 0$) denoting the maximum and minimum displacement of the ring stack.

A block called "Constant Volume Hydraulic Chamber" is used to simulate the volume of oil contained between (P) and (A), and between (B) and (T). This block simulates a fixed-volume chamber with rigid walls while also accounting for fluid compressibility. The following equations are applied [10]:

$$V_{cham} = V_0 + \frac{V_0 p}{E}, \tag{13}$$

$$q_c = \frac{dV_{chamb}}{dt} = \frac{V_0}{E}\frac{dp}{dt}, \tag{14}$$

where V_0 represents the geometrical volume of the chamber (equivalent to the product of an internal diameter D_0 and an overall internal length L_0), V_{cham} represents the oil volume in the chamber at pressure p, and q_c represents the volumetric flow rate through the chamber. The actual bulk modulus E is calculated as follows [10]:

$$E = E_0 \frac{1 + \sigma(\frac{p_a}{p})^{1/\gamma}}{1 + \sigma \frac{{p_a}^{1/\gamma}}{\gamma\, p^{(\gamma+1)/\gamma}} E_o}, \tag{15}$$

where E_0 is the pure liquid bulk modulus, γ is the gas-specific heat ratio (γ = 1.4), σ is the relative gas content at atmospheric pressure and is p_a the atmospheric pressure.

An open-loop control can be simulated in which the duty cycle (*%DC*) of the input pulse voltage V_c can be set, and the output is the mean flow rate Q_{mean}. Alternatively, a closed-loop control can be simulated, in which a proportional–integral (PI) controller adjusts the duty cycle (*%DC*) to obtain the desired mean flow rate according to the calculated error $e(t)$:

$$(\%DC) = K_P e(t) + K_I \int_0^t e(t)dt. \tag{16}$$

where K_P and K_I denote the proportional and integral gain, respectively. The derivative action is not considered in the controller since it is highly sensitive to noise in the process variable signal.

The hysteresis of the ring stack is not simulated. The Simulink solver (Ode 14x) computes the dynamic system's states at successive time steps (0.01 ms) over a specified time span (25 ms), using information provided by the model [29].

4. NUMERICAL RESULTS

The results of the numerical simulations, which concerned both metering chambers of the same valve, i.e., P → A and B → T, are now presented and discussed. The values of the operating parameters are reported in Table 1 (regarding the ring stack actuator) and Table 2 (the system).

Table 2. System parameters assumed for the simulations.

Component	Parameter	Value	Unit
Oil (ISO VG 32)	Temperature (T)	50	[°C]
	Density (ρ)	851	[kg/m^3]
	Viscosity (μ)	0.0187	[kg/(ms)]
Discharge line	Discharge Pressure (p_T)	1	[bar]
Oil chamber volume	Equivalent Diameter (D_0)	60	[mm]
	Equivalent length (L_0)	50	[mm]
	Volume chamber (V_0)	$2 \cdot 10^{-4}$	[m^3]
PiezoValve	Effective poppets' diameter (D)	60	[mm]
	Piston angle (ϑ)	45	[°]
	Length parts contact case (l_p)	50	[mm]
	Eccentricity (ε)	0	[mm]
	Clearance (c)	1	[μm]
	Poppets' damping factor (C)	60	[Ns/m]
	Discharge coefficient (C_D)	0.7	-
	Conversion factor (K_{VF})	42.25	[N/V]
	Stiffness of add. Spring (k_s)	190000	[N/m]
	Pre-compression (δ_0)	8.90	[mm]
	Stop stiffness (K_{stop})	10^8	[N/m]
	Stop Damping (C_{stop})	5000	[Ns/m]
Amplifier	Natural frequency (ω_n)	10000	[rad/s]
	Damping factor (ξ)	1.5	-
	Gain of the amplifier (k_a)	40	-

The proposed setting was used in order to obtain switching times of 5 ms; the average flow rate was modulated by acting on the pulse width of the input signal V_c. Thus, V_c was simulated as a pulse signal from 0 to 5V with a frequency of 200 Hz (overall period τ =5 ms) with variable duty cycle (*%DC*). No current limit was set in the program.

Firstly, the effects of the mass of the moving parts on the system was evaluated. Figure 5 shows open-loop predictions obtained for *%DC*=80% of the input pulse voltage V_c and different values of the mass, namely, *m*=100 g, 150 g and 200 g. In addition to V_c, the time history of the amplified voltage (V_{amp}), of the poppets' position (x), of the flow rate (Q) and of the mean flow rate (Q_{mean}) are plotted. For clarity, the input voltage is multiplied by 20. The graph reveals that the greater the mass, the larger the oscillations of the poppets' position. Since the trend of the flow rate is similar to the trend of the poppets' position, it is important that the mass of the moving parts of the ring stack actuator is taken not too large. In addition, accumulators and an inertance tubes can be used to smooth these oscillations [17], [18]. However, in all the three cases, the average flow rate computed by the program is the same and equal to $Q_{mean} = 53.7$ L/min.

The open loop predictions obtained for Δp=20 bar and *m*=100 g, while considering *%DC*=40%, and *%DC*=70% are shown in Figure 6a and Figure 6b, respectively. Along with the previous quantities, the blocking force (F_b), the actuation force (F_{act}), the current (I) and the mean current (I_{mean}) are plotted. As shown by the graphs, the input pulse voltage (V_c) is converted into a high pulse voltage by the amplifier (V_{amp}) in about 1.5 ms, which in turn is converted into the blocking force (F_b) by means the conversion factor (K_{VF}). The actuation

force (F_{act}), calculated as the difference between the blocking force (F_b) and the internal spring force ($k_p x$), allows the poppets to move and reach a certain position. The poppets oscillate around the achieved position which, however, is not equal to the maximum free stroke (x_{max}) due to the resistance forces, i.e., the force of the additional spring and the flow force. The varying duty cycle results in different values of the mean flow rate: the greater the duty cycle (*%DC*), the greater the average flow rate obtained. In particular, a mean flow rate of 26 L/min and 46 L/min is obtained for a duty cycle equal to 40% and 70%, respectively. In addition, given the rapid response of the high-performance amplifier simulated, the regulation is very effective in all two different scenarios. The simulations also show a large peak of current equal to I =43.5 A, because no current limitation was set in these simulations. However, the peak current only occurs for a brief time, while the mean current is not high ($I_{mean} \approx 6A$).

In Figure 5 and 6, the overall pressure drop across the valve was set to Δp=20 bar, because, as previously explained, the objective is to design a valve which can produce high flow rate with low pressure drops, thus a pressure drop of 10 bar for each metering chamber (P → A and B → T) can be regarded as a right choice, as previously explained.

To evaluate the effects of the flow forces, Figure 7 shows open-loop predictions obtained for different values of Δp (10, 20, 30 bar), while keeping *%DC*=80% and *m*=100 g. As shown in the graph, the higher the overall pressure drop, the greater the mean flow rate obtained. In addition, as the pressure drop across the valve increases, the generated flow forces increase. However, the increased flow forces do not affect the actuation capability of the ring stack actuator since the flow forces (expressed in N in the graph) are much lower than the actuation force (expressed in hN in the graph) in all the three cases examined, as shown in Figure 7b. Thus, the three curves of the actuation forces are coincident (the same occurs with the position *x* (Figure 7a)).

All the results presented up to this point were obtained through an open-loop control system. However, closed loop control is mandatory in real applications. Thus, closed-loop control was also simulated using a simple PI controller which changes the duty cycle (%DC) of the input control signal (V_c) according to Equation (15) to reach the target average flow rate (set point). The parameters of the PI controller, which were determined with the use of the Ziegler–Nichols method, are K_P = 0.01125 and K_I = 3.6. The back calculation anti-windup method was used.

In order to evaluate the effectiveness of the piezo-valve, step tests have been simulated by imposing different values for the set point. The controlled variable is the average flow rate, whereas the control variable is the duty cycle of the input pulse voltage applied to the ring stack. In these simulated closed-loop step tests, the parameters assumed for the simulations were again those presented in Table 1 (regarding the ring stack) and Table 2 (the system). In addition, the mass of the moving parts and the overall pressure drop across the valve were set equal to Δp=20 bar and *m*=100g, respectively.

Figure 8a and Figure 8b show the time history of the simulated mean flow rate obtained during two step tests, i.e., Q_{mean} =40 L/min and Q_{mean} =55 L/min. As visible in the graphs, the time necessary to reach 90% of the set point (i.e., 90% rise time) is very short, specifically a value lower than 10 ms is registered for Q_{mean} = 40 L/min and for Q_{mean} = 55 L/min.

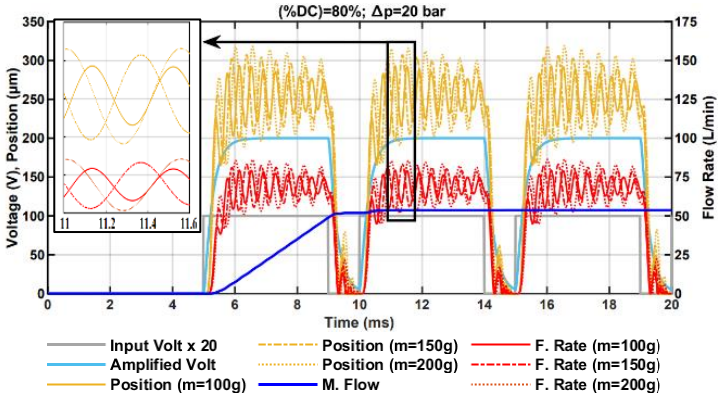

Figure 5. Open loop predictions simulated for (%DC)=80% of the input pulse voltage V_c (from 0 to 5 V) and different values of m (Δp=20 bar): Amplified Voltage (V_{amp}), Poppets' Position (x) , Mean Flow (Q_{mean}) and Flow Rate (Q).

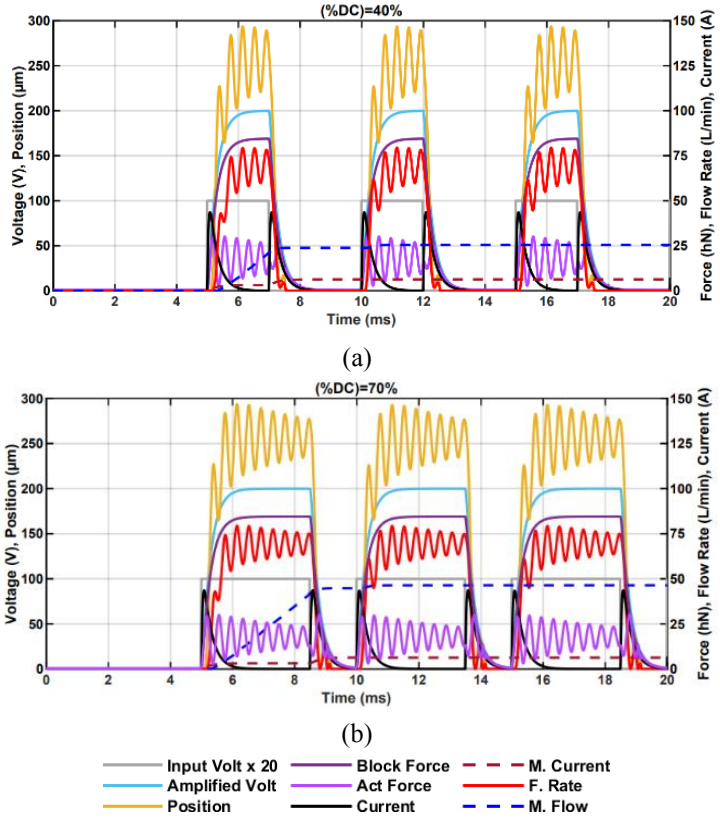

Figure 6. Open loop predictions simulated for two different duty cycles of the input pulse voltage V_c (from 0 to 5 V) (m=100g, Δp=20 bar): (a) (*%DC*)=40%; (b) (*%DC*)=70%.

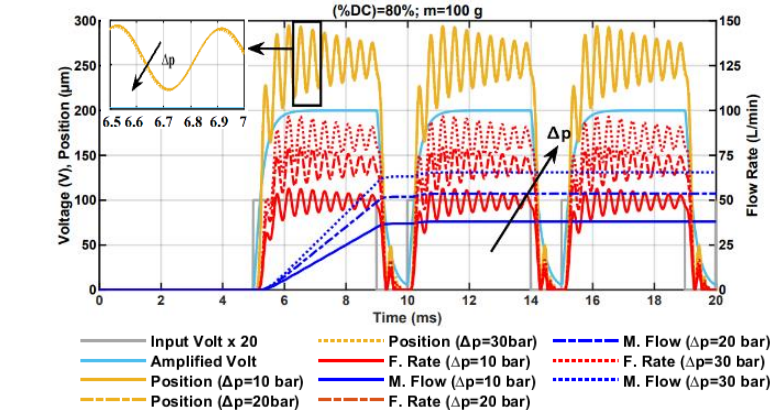

(a)

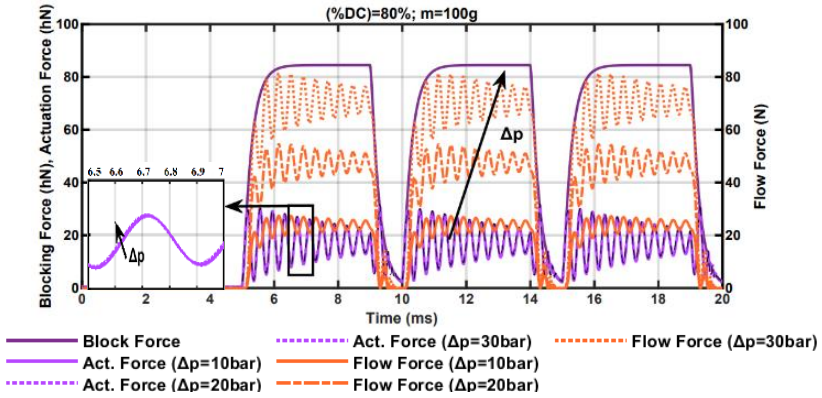

(b)

Figure 7. Open loop predictions simulated for (%DC)=80% of the input pulse voltage V_c (from 0 to 5 V) and different values of Δp (m=100g): (a) Amplified Voltage (V_{amp}), Poppets'Position (x), Flow Rate (Q), Mean Flow (Q_{mean}); (b) Blocking Force (F_b), Actuation Force (F_{act}), Flow Force (F_{flow}).

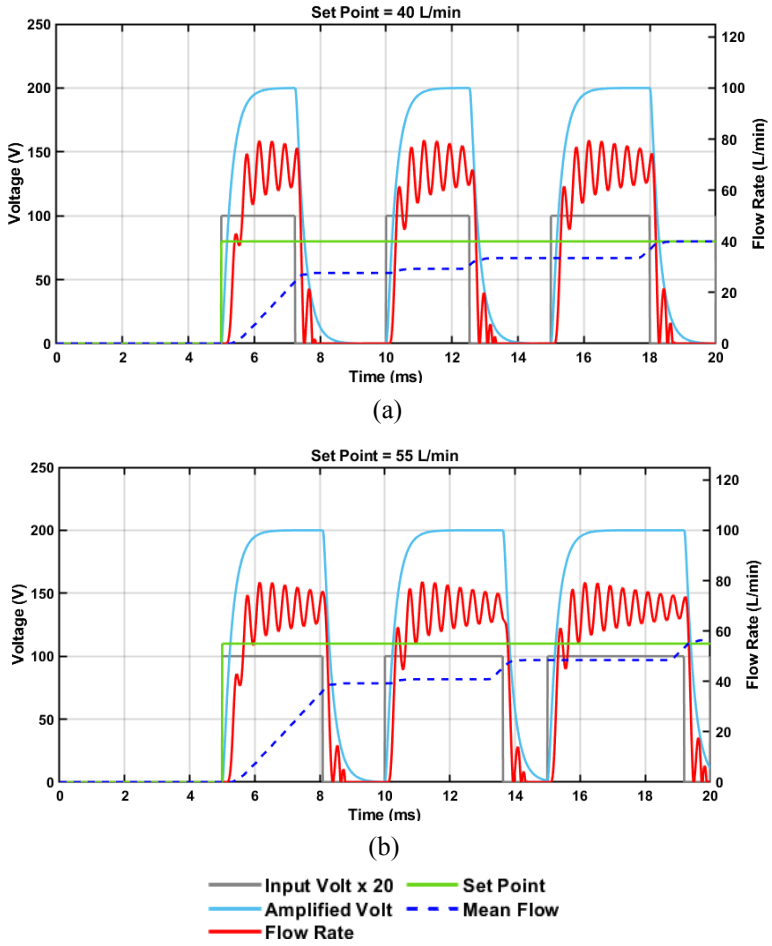

Figure 8. Closed loop results (m=100 g, Δp=20 bar): (a) Q_{mean}=40 L/min; (b) Q_{mean}=55 L/min.

5. CONCLUSIONS

A new fast switching 4/2 ON/OFF valve based on the use of a piezo ring stack was proposed. The piezovalve has characteristics comparable to proportional and servovalves, thus it offers new possibilities for utilizing digital hydraulics in different industrial and aeronautical implementations.

The performance of the new valve architecture was evaluated using detailed and well-established equations implemented in a Simulink code. Firstly, the results obtained with an open-loop control system were presented: by changing the duty cycle of the input pulse voltage, it was possible to change the average flow obtained through the valve. The simulations showed that the control strategy is very effective: an average flow rate of 53.7 L/min was obtained for (*%DC*)=80%, an overall pressure drop across the valve equal to 20 bar and a mass of the moving parts equal to 100 g.

Afterwards, in order to evaluate the effectiveness of the piezo-valve, the results, obtained with a closed-loop average flow rate, were discussed. The parameters of the closed-loop controller were determined by the Ziegler–Nichols method. It was shown that the interval time necessary to reach 90% of the set point is very short, i.e. lower than 10 ms for 40 L/min and for 55 L/min.

Through both the analysis of the characteristics of the ring stack and the simulation results, it is possible to define the advantages and disadvantages aspects of the proposed architecture. The negative aspects are the large size and the high cost of the ring stack, and the need for a high-performance amplifier. The positive aspects are the simplicity of the architecture, the low pressure drops and the very fast response time.

In conclusion, this paper showed that the use of digital hydraulics in industrial and aeronautical applications is feasible and interesting features can be obtained, such as the low energy consumption.

REFERENCES

[1] Moog, "Proportional and Servo Valve Technology," 2003.

[2] F. Sciatti, P. Tamburrano, P. De Palma, E. Distaso, and R. Amirante, "Detailed simulations of an aircraft fuel system by means of Simulink," in *Journal of Physics: Conference Series*, IOP Publishing, 2022, p. 012033.

[3] P. Tamburrano *et al.*, "Fuels systems and components for future airliners fuelled with liquid hydrogen," in *Journal of Physics: Conference Series*, IOP Publishing, 2022, p. 012041.

[4] P. Tamburrano, A. R. Plummer, E. Distaso, and R. Amirante, "A Review of Electro-Hydraulic Servovalve Research and Development," *International Journal of Fluid Power*, Apr. 2019, doi: 10.13052/ijfp1439-9776.2013.

[5] P. Tamburrano, A. R. Plummer, E. Distaso, and R. Amirante, "A review of direct drive proportional electrohydraulic spool valves: Industrial state-of-the-art and research advancements," *Journal of Dynamic Systems, Measurement and Control, Transactions of the ASME*, vol. 141, no. 2, Feb. 2019, doi: 10.1115/1.4041063.

[6] A. Plummer, "Electrohydraulic servovalves – past, present, and future.," in *Proc 10th International Fluid Power Conference*, 2016.

[7] P. Tamburrano, F. Sciatti, E. Distaso, L. Di Lorenzo, and R. Amirante, "Validation of a simulink model for simulating the two typical controlled ventilation modes of intensive care units mechanical ventilators," *Applied Sciences*, vol. 12, no. 4, p. 2057, 2022.

[8] P. Tamburrano, F. Sciatti, A. R. Plummer, E. Distaso, P. De Palma, and R. Amirante, "A review of novel architectures of servovalves driven by piezoelectric actuators," *Energies (Basel)*, vol. 14, no. 16, p. 4858, 2021.

[9] P. Tamburrano, E. Distaso, A. R. Plummer, F. Sciatti, P. De Palma, and R. Amirante, "Direct drive servovalves actuated by amplified piezo-stacks: Assessment through a detailed numerical analysis," *Actuators*, vol. 10, no. 7, Jul. 2021, doi: 10.3390/act10070156.

[10] P. Tamburrano, P. De Palma, A. R. Plummer, E. Distaso, F. Sciatti, and R. Amirante, "Simulation of a high frequency on/off valve actuated by a piezo-ring stack for digital hydraulics," in *E3S Web of Conferences*, EDP Sciences, 2021, p. 05008.

[11] R. Scheidl, M. Linjama, and S. Schmidt, "Is the future of fluid power digital?," *Proceedings of the Institution of Mechanical Engineers, Part I: Journal of Systems and Control Engineering*, vol. 226, no. 6, pp. 721–723, 2012.

[12] P. Achten, M. Linjama, R. Scheidl, and S. Schmidt, “Discussion: Is the future of fluid power digital?,” *Proceedings of the Institution of Mechanical Engineers, Part I: Journal of Systems and Control Engineering*, vol. 226, no. 6, pp. 724–727, 2012.

[13] M. S. A. Laamanen and M. Vilenius, “Is it time for digital hydraulics,” in *The eighth Scandinavian international conference on fluid power*, 2003.

[14] Vemet forward, “https://www.valmet.com/media/articles/up-andrunning/ newtechnology/FPDigHydr/.”

[15] M. Linjama, “DIGITAL FLUID POWER-STATE OF THE ART,” 2011.

[16] Q. Zhang, X. Kong, B. Yu, K. Ba, Z. Jin, and Y. Kang, “Review and development trend of digital hydraulic technology,” *Applied Sciences (Switzerland)*, vol. 10, no. 2. MDPI AG, Jan. 01, 2020. doi: 10.3390/app10020579.

[17] M. Pan, N. Johnston, A. Plummer, S. Kudzma, and A. Hillis, “Theoretical and experimental studies of a switched inertance hydraulic system,” *Proceedings of the Institution of Mechanical Engineers, Part I: Journal of Systems and Control Engineering*, vol. 228, no. 1, pp. 12–25, 2014.

[18] C. Yuan, M. Pan, and A. Plummer, “A review of switched inertance hydraulic converter technology,” *J Dyn Syst Meas Control*, vol. 142, no. 5, p. 050801, 2020.

[19] J. L. Bower, “Digital fluid control system.” Google Patents, Sep. 12, 1961.

[20] R. Murphy and J. Weil, “Hydraulic Control System. ,” US Patent No. 3038449., 1962

[21] T. K. Virvalo, “Cylinder speed synchronization,” *Hydraulics & Pneumatics*, vol. 31, no. 12, pp. 55–57, 1978.

[22] A. Laamanen, M. Linjama, J. Tammisto, K. T. Koskinen, and M. Vilenius, “Velocity control of water hydraulic motor,” in *Proceedings of the JFPS International Symposium on Fluid Power*, The Japan Fluid Power System Society, 2002, pp. 167–172.

[23] P. Cui, R. T. Burton, and P. R. Ukrainetz, “Development of a high speed on/off valve,” *SAE transactions*, pp. 312–316, 1991.

[24] J. Yu, X. Han, and Y. Zhang, “Application of high speed digital control solenoid valves in the electronic control of diesel engines,” *Journal of Beijing Institute of Technology*, vol. 14, no. 1, pp. 91–95, 1994.

[25] J. Zhang, M. Yang, and B. Xu, “Design and experimental research of a miniature digital hydraulic valve,” *Micromachines (Basel)*, vol. 9, no. 6, p. 283, 2018.

[26] Noliac. Available online: http://www.noliac.com/products/actuators/ (accessed on 1 March 2022).

[27] M. Fouaidy, M. Saki, N. Hammoudi, and L. Simonet, “Electromechanical characterization of piezoelectric actuators subjected to a variable pre-loading force at cryogenic temperature,” IPN, 2007.

[28] Y. K. Yong, “Preloading piezoelectric stack actuators in high-speed nanopositioning systems,” *Front Mech Eng*, vol. 2, p. 8, 2016.

[29] Guide, Mathworks. Matlab & Simulink. In SimscapeTM User’s R2018a; Mathworks. Natick, MA, USA, 2018.

Design for Structural Durability of an Hydraulic Main Valve for Mobile Applications

Filippo Ciardo[1], Giovanni Meneghetti[1], Edoardo Caldesi[2], Cesare Dolcin[3], Alessandro Cervi[3], Davide Mesturini[3]

[1]*Department of Industrial Engineering University of Padova, Padova (PD), Italy*

[2]*C2MacGroup Research & Development, Crevalcore (BO), Italy*

[3]*Research & Development, Walvoil SpA (Interpump Group), Reggio Emilia (RE), Italy*

Abstract

A fatigue analysis has been conducted to assess the structural durability of a valve component made of cast iron. A well-known local approach based on the linear elastic strain energy density as fatigue damage parameter has been used to account for geometrical stress concentration effects. The fatigue design curve has been calibrated on fatigue test results obtained from laboratory specimens. The theoretical estimations of the fatigue strength have been compared with results of fatigue tests on real valve components subjected to pulsating hydraulic pressure and a satisfactory level of accuracy has been obtained.

Keywords. Fatigue design, structural durability, strain energy density, finite element analysis.

1. INTRODUCTION

Hydraulic valves for mobile applications are subjected to in-service fatigue loadings owing to the time-variant pressure regimes. Given the general tendency of extending the operating pressure range, fatigue issues may become of primary concern. Therefore, this paper aims at assessing the fatigue strength of a hydraulic main valve by using a local approach based linear elastic finite element (FE) analyses and appropriate fatigue testing of laboratory specimens.

2. THEORETICAL BACKGROUND

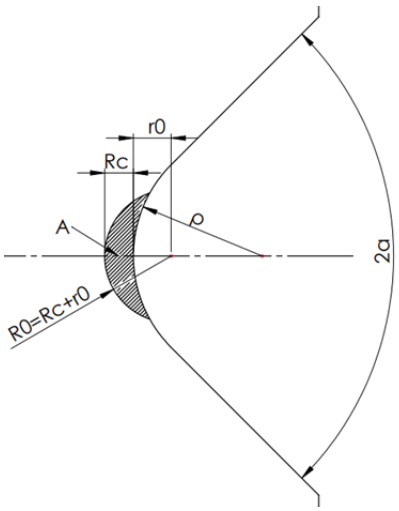

Figure 2.1. The SED approach to notch fatigue [1-3]

The linear elastic Strain Energy Density averaged in a properly defined material structural volume (i.e. the SED approach) has been selected among the local approaches available in the technical literature.
According to the approach sketched in Figure 2.1, the material fatigue strength is made to depend on the averaged SED parameter inside a structural volume having size R_c [1-3].
The SED parameter is evaluated from a linear elastic FE analysis and is compared with the fatigue design curve determined by means of fatigue tests on laboratory specimens. The size R_c of the structural volume, where the SED parameter is to be averaged, is thought of as a material property and results from the material fatigue characterisation. More precisely, R_c is found by equating the averaged SED for two different specimen's geometries at the endurance limit [1-2]. The geometrical parameter r_0 depends on the notch geometry [3].

3. MATERIAL CHARACTERISATION

Plain and notched specimens made of EN-GJS 500-7 have been prepared from separately cast Y-blocks as well as from real main valve components for evaluating the influence of the manufacturing process, as shown in Figure 3.1.

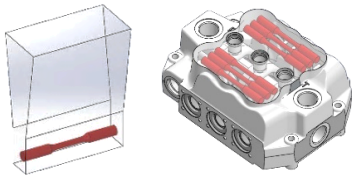

Figure 3.1. Specimens location in separately cast Y-blocks (on the left) and in real main valve components (on the right)

Results of static tensile tests are reported in Table 1. Brinell hardness resulted 224 HB and 208 HB for the Y-block and component materials, respectively.

Material	E [MPa]	$\sigma_{p,02}$ [MPa]	σ_R [MPa]	$\varepsilon_{\%,R}$ [%]
EN-GJS500-7 (Y-block)	169000	401	749	6.7
EN-GJS500-7 (component)	169000	358	593	2.7

Table 3.1. Results of static tensile tests

Fatigue tests have been performed under a nominal load ratio (i.e. the ratio between the minimum and maximum applied loads) approximately equal to zero by using a standard servo-hydraulic axial testing machine MTS Minibionix II equipped with a 15 kN load cell and a digital controller MTS Testar IIm. Load test frequencies were kept in the range 10-40 Hz. The adopted specimens' geometry included plain (Figure 3.2), bluntly notched (Fig. 3.3) and sharply notched (Fig. 3.4) specimens.

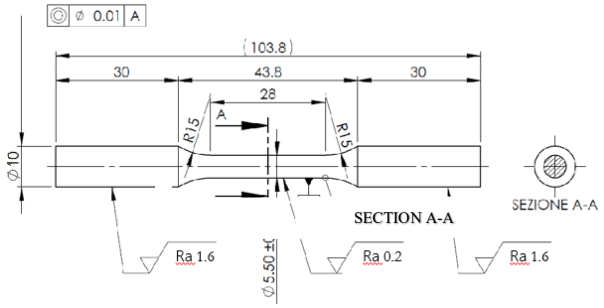

Figure 3.2. Geometry of plain specimens

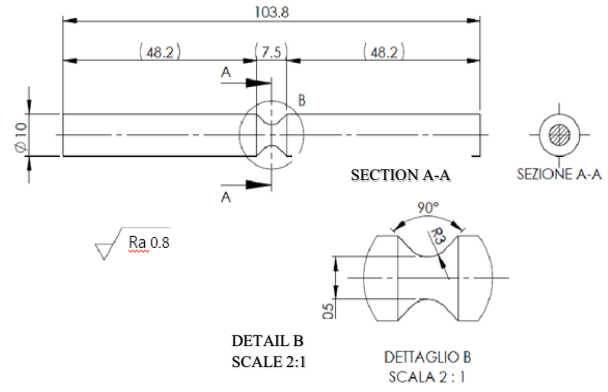

Figure 3.3. Geometry of bluntly notched specimens

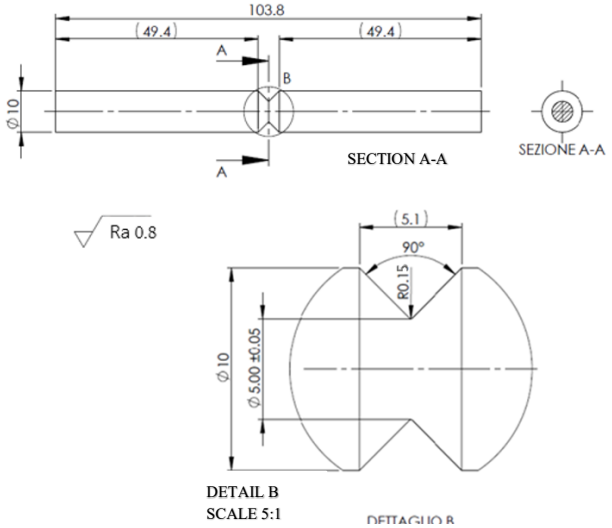

Figure 3.4. Geometry of sharply notched specimens

Short stair-case procedures were run to evaluate the endurance limit at 10 million cycles. The fatigue test results are reported in Figures 3.5-3.8 in terms of number of fatigue cycles to failure as a function of the applied nominal stress amplitude. The specimens used in the short stair-case procedure are reported with red markers, where circle markers (o) indicate the run-out test, while star markers (*) indicate the broken specimens. The microstructures are reported in Figures 3.9 and 3.10, which highlight the high pearlite content in the range 95%-97%. It was assumed that the microstructure of the specimens taken from the main valve according to figure 3.1 is also applicable to the crack initiation location, which will be commented later on.

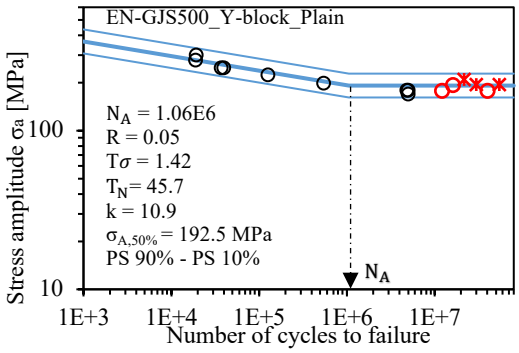

Figure 3.5. Fatigue test results of plain specimens taken from Y-block. The nominal stress is evaluated at the net-section

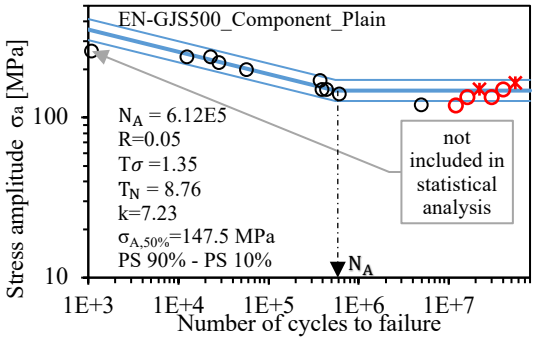

Figure 3.6. Fatigue test results of plain specimens taken from components. The nominal stress is evaluated at the net-section

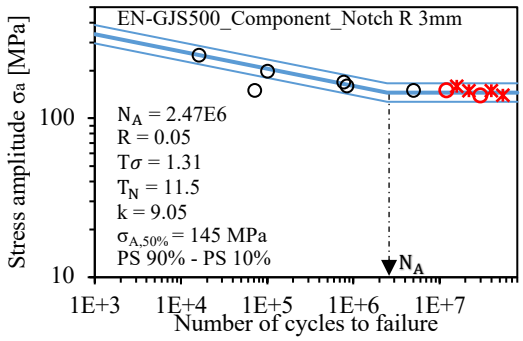

Figure 3.7. Fatigue test results of notched specimens (R=3 mm) taken from components. The nominal stress is evaluated at the net-section

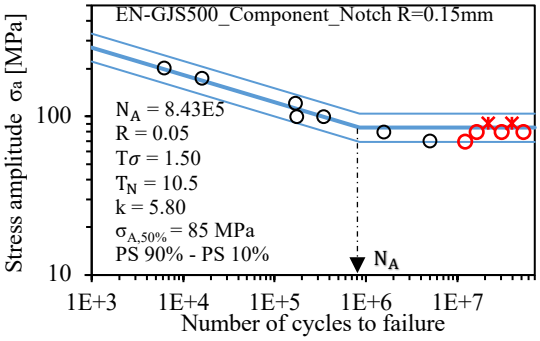

Figure 3.8. Fatigue test results of notched specimens (R=0.15 mm) taken from components. The nominal stress is evaluated at the net-section

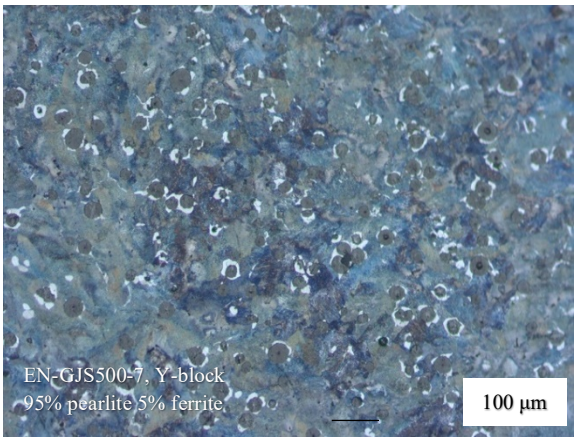

Figure 3.9. Microstructure of the cast iron material from the Y-block

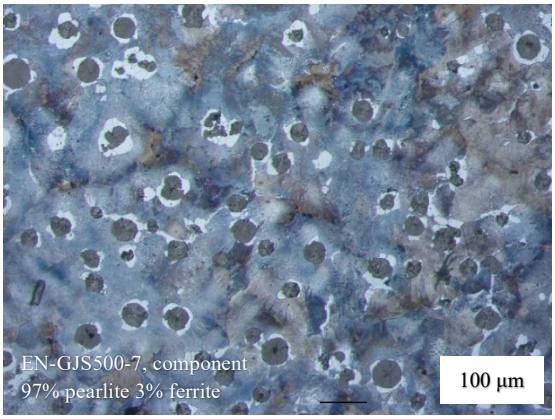

Figure 3.10. Microstructure of the cast iron material from the component

4. FE ANALYSIS OF THE VALVE COMPONENT

Linear elastic finite element analyses have been performed in parallel to evaluate the local stresses and assess the fatigue strength. Figure 4.1 reports the geometry of the GJS 500-7 cast component investigated.



Figure 4.1. Geometry of the cast component investigated

The applied boundary conditions included the internal hydraulic pressure, the force applied by the caps (Figure 4.2) and the tightening forces applied in the threaded connections along with the fixed holes through which the component was constrained to the test bench (Figure 4.3).
The CAD model of the valve component was imported in Ansys Mechanical environment and meshed by running the free mesh generation algorithm using 10-node, second order tetrahedral finite elements. The element size of 1.5 mm was properly selected after a convergence analysis and a picture of the adopted mesh is reported in Figure 4.4.

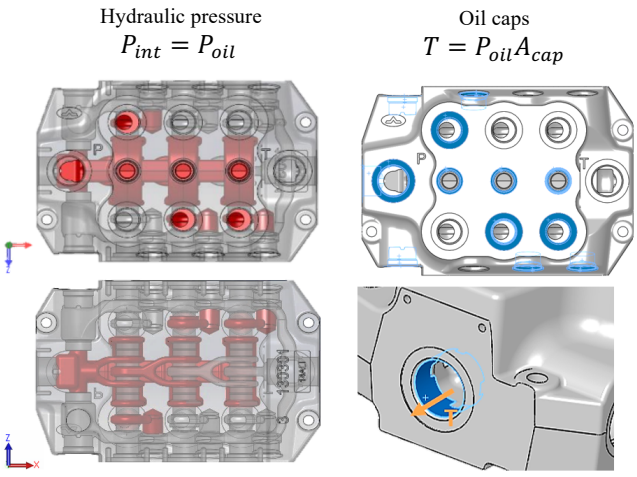

Figure 4.2. Boundary conditions applied to the valve component (hydraulic pressure and caps)

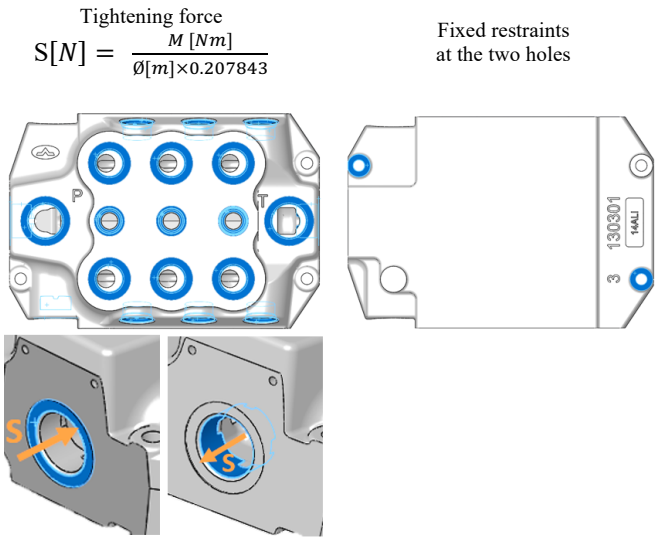

Figure 4.3. Boundary conditions applied to the valve component (tightening forces and constraints)

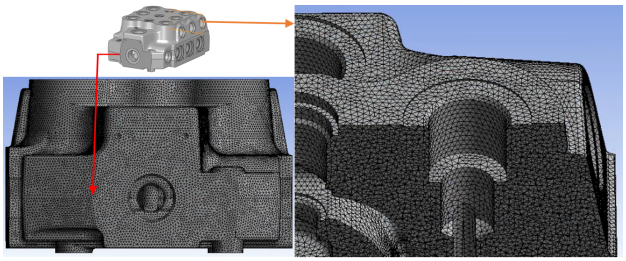

Figure 4.4. Adopted FE mesh of 10-node tetrahedral finite element in Ansys Mechanical environment (22 million degrees of freedom)

Linear elastic FE analyses were performed and a general view of the Von Mises stress distribution evaluated by applying an hydraulic pressure of 500 bar is reported in Figure 4.5.

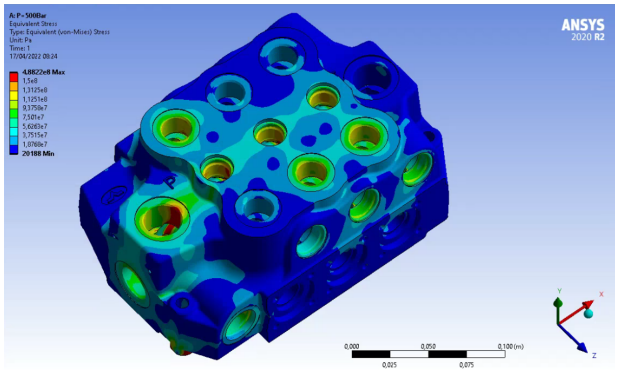

Figure 4.5. Von Mises stress distribution with 500 bar internal hydraulic pressure

5. FATIGUE TESTS OF REAL VALVE COMPONENTS

With the task to carry out fatigue tests in parallel with standard material specimens, 20 samples of a main valve block were manufactured. Walvoil's commercial product SDM140/3 was chosen: a GJS500 cast block weighing 16,5 kg. The complicated internal circuit was only partially pressurised (Fig. 5.1 and 5.2), in order to maximise the deformation and to replicate the worst stress typologies and distribution that the product can face in field applications.

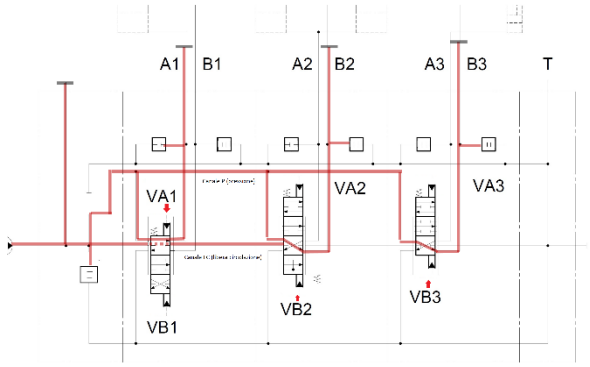

Figure 5.1. Hydraulic test schematic

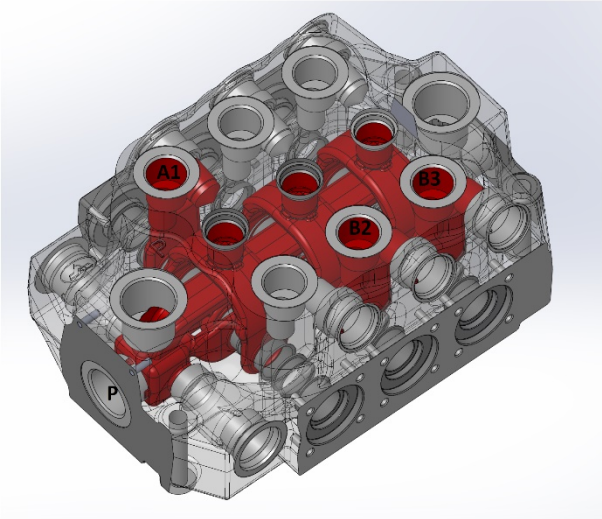

Figure 5.2. Pressurised circuit in cast samples

Up to five different test rigs have been used in parallel, with over 9 months of total bench time to apply altogether more than 50 million pressure cycles to the samples. A meaningful test set up is shown in Figure 5.3, while pressure variation during a test is represented in Figure 5.4.

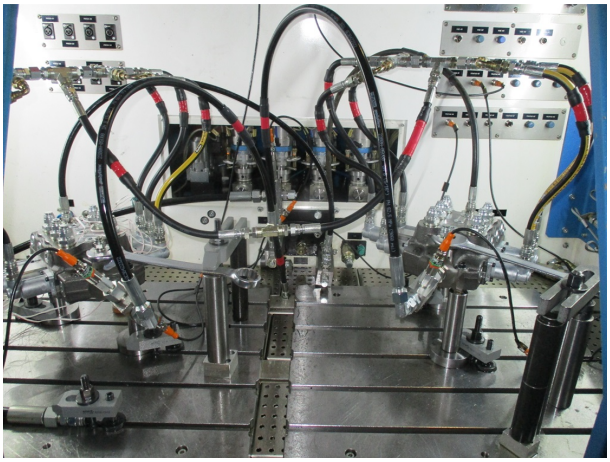

Figure 5.3. Set up of one of the tests

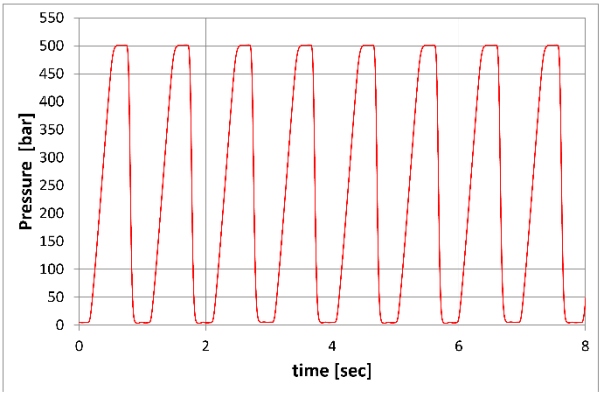

Figure 5.4. Pressure variation during a 500 bar test

Due to high tensile strength of cast material, the breaking of the samples occurred at higher than expected number of cycles. The earliest rupture happened after 1,2 million pulses at 500 bar, while both samples tested at 380 bar broke just after passing 8,6 million cycles. With the aim to shorten the test time, the lower side of 12 samples was milled for a depth of 12 mm, leaving wall thicknesses ranging between 0,90 and 1,95 mm (measured after their breakage). The geometry of the modified component is reported in Figure 5.5.

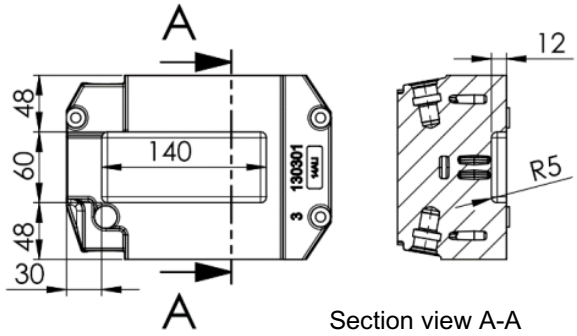

Figure 5.5. Geometry of the modified valve component

These modified samples showed much shorter fatigue lives, ranging from a minimum of 1.556 cycles of the earliest rupture at 500 bar to the latest happening at 235.000 cycles at 260 bar, while both samples tested at 220 bar were considered run-out after surviving over 9 million cycles. All results are summarized within the semi-logarithmic graph of Figure 5.6, where the blue dots represent the fatigue lives of whole casting and the red dots regard the samples with milled surface (labelled with material residual thickness).

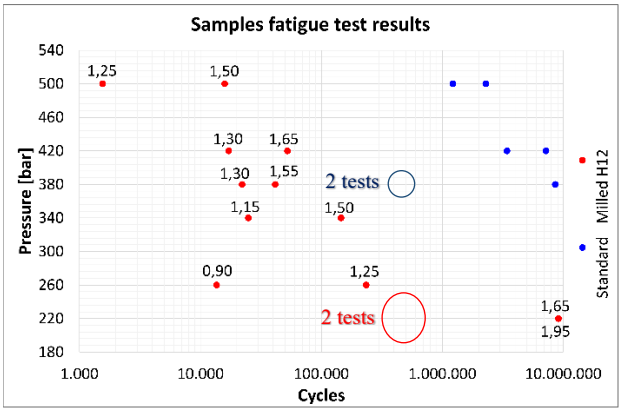

Figure 5.6. Fatigue test results on cast samples

In the six standard castings the fatigue crack always propagated from bottom part of section ports (A1 in one case, between B2 and B3 in the other five cases, Figures 5.2 and 5.7), while in the twelve samples with lowered thickness the crack always initiated at the "Y" duct of the P line near to the machined surface (Fig. 5.8).

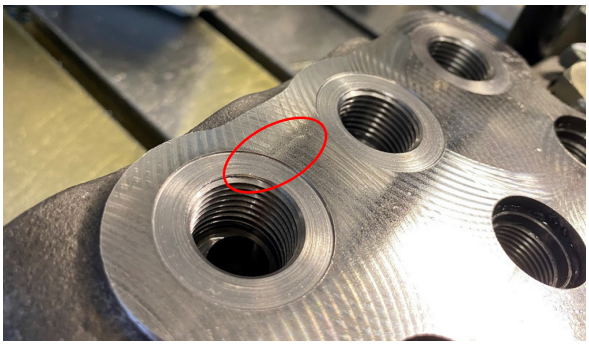

Figure 5.7. Crack on sample 002, between ports B2 and B3, after 8.613.179 cycles at 380 bar

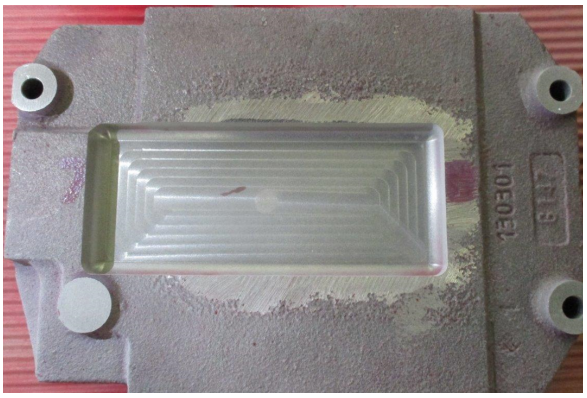

Figure 5.8. Crack on sample 010 with reduced thickness, after 15.888 cycles at 500 bar

6. FATIGUE LIFE ESTIMATIONS AND COMPARISON WITH EXPERIMENTAL RESULTS

The control volume of the EN-GJS500-7 material from cast component was determined by equating the SED values at the endurance limit relevant to the two notched specimens (R=3 mm and R=0.15 mm, respectively) [1-3]. The resulting structural control volume R_c was 0.121 mm. The size of the structural volume takes into account the material microstructure [1, 2, 4]. After calibrating the structural volume, the notched specimens' results could be plotted in the same fatigue scatter band, as reported in Figure 6.1.

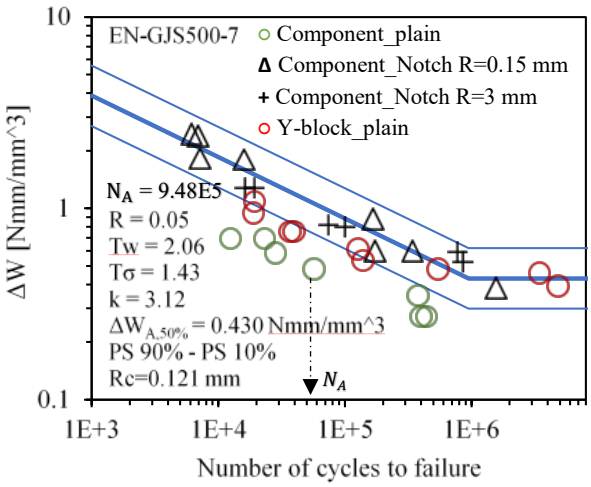

Figure 6.1. Summary of notched fatigue results in terms of averaged SED

According to the SED approach, all geometrical effects are included in the fatigue design curve reported in Figure 6.1. Therefore, the SED was evaluated in the structural volumes located at the crack initiation locations, which led to fatigue failures according to previous Figures 5.7 and 5.8. Figures 6.2 and 6.3 report the control volume at the crack initiation

location of the original valve component (Figure 5.7), where the adopted element size is 0.015 mm, and of the component with milled surface (Figure 5.8), where the element size is 0.035 mm, in order to increase the mesh density inside the control volume and guarantee convergence. A transition zone having size approximately equal to 5 mm was created around the control volume and outside this zone the element size was 1.5mm as shown in the previous analysis.

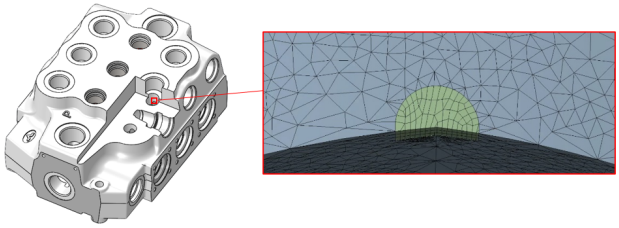

Figure 6.2. Control volume for the averaged SED evaluation at the crack initiation point between ports B2 and B3 (Figures 5.2 and 5.7) of the original valve component.

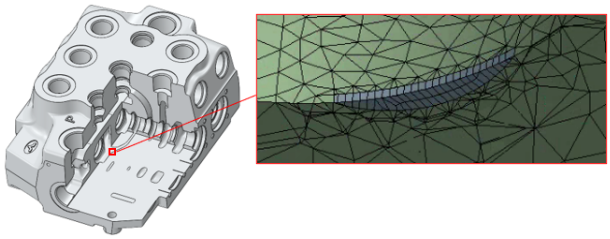

Figure 6.3. Control volume for the averaged SED evaluation at the crack initiation point of the valve component with milled surface (Figure 5.8).

Finally Figure 6.4 reports the comparison between the fatigue design scatter band calibrated on laboratory specimens (Figure 6.1) and the experimental test results on valve components (previously reported in Figure 5.6).

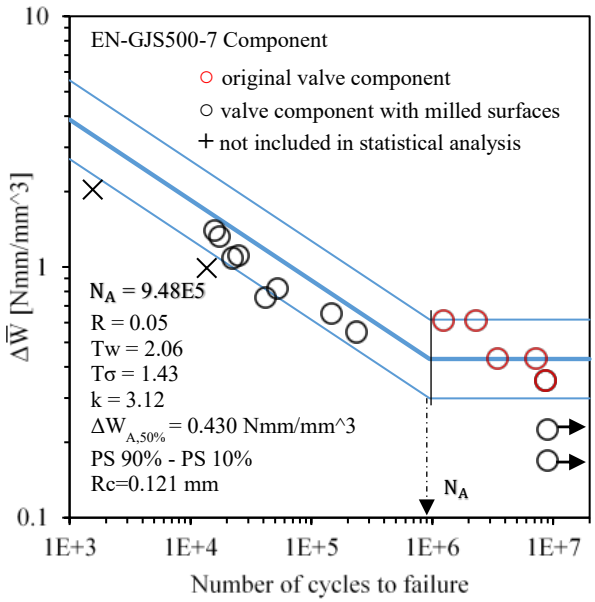

Figure 6.4. Comparison between the fatigue design scatter band calibrated on laboratory specimens (Figure 6.1) and the experimental test results on valve components

It is worth mentioning that failure initiated from an as-cast surface both in the original valve component and in component with milled surface. Conversely, the design scatter band calibrated on specimens (Figure 6.1) accounts only for geometrical effects in fatigue with machined surfaces. Therefore, the scatter band reported in Figures 6.1 and 6.4 should be downgraded to include the surface roughness effect. In a previous investigation, a downgrading factor of 1.4 was found on plain specimens tested in push-pull fatigue [5]. However, it is expected that the downgrading effect found on plain specimens is not fully effective when notched components are considered, as it is the present case.

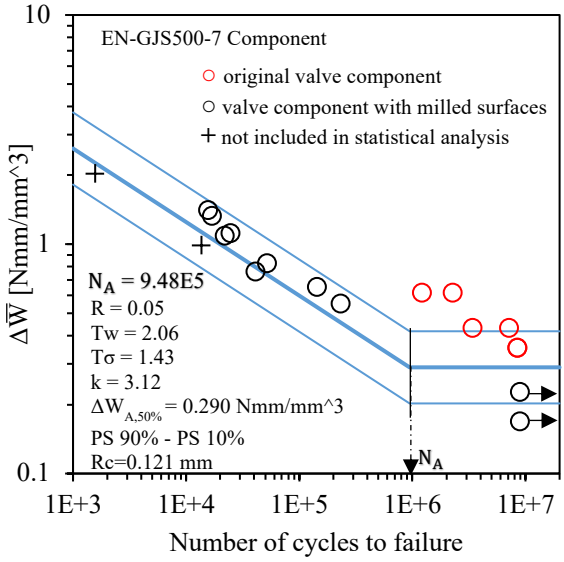

Figure 6.5. Comparison between the fatigue design scatter band calibrated on laboratory specimens (Figure 6.1) and the experimental test results on valve components with surface roughness effect

Due to the lack of knowledge regarding the partial surface roughness effect, the downgrading factor 1.4 valid for push-pull fatigue has been updated for the case of tension-tension (R=0.05) fatigue in terms of energy ($K^2_{L,R0.05} = 1.22^2$=1.48) and has been fully applied to the fatigue design scatter band reported in Figures 6.1 and 6.4. Results are reported in Figure 6.5. The design fatigue curves reported in Figure 6.5 can be used to assess the fatigue life of valve components, all geometrical effects being included in the evaluation of the averaged SED.

7. CONCLUSIONS

Fatigue strength assessment of a valve component made of EN-GJS500-7 spheroidal cast iron have been performed. The local approach based on the linear elastic strain energy density has been applied to synthesize the fatigue strength of notched specimens taken from the component itself. By so doing a fatigue design curve able to unify the geometrical stress concentration effects has been determined and subsequently it has been used to assess the fatigue strength of the real valve components, which have been tested under pulsating pressure in dedicated test benches. The comparison between the estimated and the experimental fatigue strength was satisfactory.

8. ACKNOWLEDGMENT

C2MacGroup is gratefully acknowledged for financial support.

9. REFERENCES

[1] P. Lazzarin, R. Zambardi, “A finite-volume-energy based approach to predict the static and fatigue behavior of components with sharp V-shaped notches”, Int. J. Fract., Vol. 112, pp. 275–298, 2001.

[2] P. Lazzarin, C.M. Sonsino, R. Zambardi, “A notch stress intensity approach to assess the multiaxial fatigue strength of welded tube-to-flange joints subjected to combined loadings”, Fatigue Fract. Eng. Mater. Struct., vol. 27, pp. 127–140, 2004.

[3] P. Lazzarin-F. Berto, Some expressions for the strain energy in a finite volume surrounding the root of blunt V-notches, International Journal of Fracture, 2005

[4] B. Atzori, P. Lazzarin, G. Meneghetti, “Unified treatment of the mode I fatigue limit of components containing notches or defects”, Int. J. Fracture, vol. 133, pp. 61-87, 2005.

[5] F. Scacco, A. Campagnolo, M. Franceschi and G. Meneghetti, “Strain-Controlled Fatigue Behavior of a Nodular Cast Iron in Real Off-Highway Axles: Effects of Casting Skin and Strain Ratio”, Metals, vol. 12, p. 426, 2022.

Generation and validation of a real time multibody model for off-highway vehicles, aiming at the design of suspension systems

Andrea Fornaciari[1], Barbara Zardin[1] and Massimo Borghi[1]

[1] *Enzo Ferrari Engineering Department, University of Modena and Reggio Emilia, Modena, Italy*

E-mail: andrea.fornaciari@unimore.it; barbara.zardin@unimore.it; massimo.borghi@unimore.it

Abstract.

This study presents the logical process followed to develop a multibody model of an off-highway vehicle with independent suspension that can run in real-time regardless of the imposed maneuver. This multibody model has been developed to support in the next future the study, design, and optimization process of different hydro-pneumatic suspension systems for the vehicle.
The starting point was the development of the complete 3D multibody model of the vehicle of interest in Simcenter Amesim®, with particular focus on the suspension mechanism. This model was used as the reference for the real-time one. The final real-time model was developed step by step in the same simulation environment and validated by comparing the complete 3D multibody model dynamic response referring to standard maneuvers (ISO 5008, moose test, lateral bumps test) after the introduction of inertial contributions, tires model, and road profiles.
Lastly, it was possible to adjust some parameters to make the model able to run with a fixed step solver to support model-in-the-loop simulations. The main result obtained is a significant reduction of simulation time from several minutes to a few seconds. This is a clear benefit that can be further emphasized in the optimization processes of hydro-pneumatic suspension systems.

Keywords. Independent suspension, off-highway, real-time model, multibody model.

NOMENCLATURE

m_{sp}	vehicle sprung mass
$m_{wheel_{f/r}}$	front/rear wheel mass
$m_{strut_{f/r}}$	front/rear wheel structure mass
m_{axle}	front axle mass

$m_{wishbone_{low/up}}$	lower/upper wishbone mass
$m_{steer_{link}}$	steering link mass
$m_{steer_{cyl}}$	steering cylinder mass
w	vehicle wheelbase
w_f	distance between vehicle CoG and front axle
$F_{z_{susp_{f/r}}}$	vertical load on front/rear axle
$F_{z_{tire_{f/r}}}$	vertical load on front/rear tire
$R_{w_{f/r}}$	free radius of front/rear wheel
$R_{w_{load_{f/r}}}$	loaded radius of front/rear wheel
$k_{z_{tire_{f/r}}}$	vertical stiffness of front/rear tire
$perc_{sprung}$	sprung percentage for intermediate masses
$x_{axle_{CoG}}$	x coordinate of axle CoG
g	gravitational acceleration

1. INTRODUCTION

To study the dynamic behavior of a vehicle and the interaction with the vehicle subsystems, primarily suspension, steering or braking systems, the multibody representation of the vehicle is one of the most effective approaches, and it is adopted always more often by researchers and engineers. Nevertheless, the multibody modeling approach presents some issues, for example the modeling and the parametrization of the tire-soil contact or the general parametrization of some unknown information, as the friction contributions, and the computational time needed for the simulation. In this work, the multibody modeling approach is applied to an agricultural tractor, a very complex vehicle per se, with the aim to create a virtual platform where it will be possible to integrate very detailed models of several architectures of hydro-pneumatic suspensions system, in order to compare and optimize different design.

Modern agricultural tractors are sophisticated vehicles, and are always more often, even the smaller ones, equipped with a hydro-pneumatic suspension at the front axle. Hydro-pneumatic suspension is undoubtedly the best solution for this vehicle [1], where integration of the suspension system in the already present hydraulic circuit, which controls several functions of the tractor, seems the more efficient solution. With the freedom given by the chance to adopt different architectures, damping, and stiffness characteristics for the suspension system, comes the responsibility to choose the best solution (a compromise between comfort and safety) and tuning. That is a real challenge and often involves long and exhausting experimental tests on ISO tracks and fields, to test several dynamic conditions [2]. It is recognized in the literature that, though extensive knowledge exists on suspension systems different layouts, and tuning, there are topics where improved understanding is needed. In particular, the comparison between alternative concepts on the architectures of the suspension and guidelines on the process of the suspension “tuning”, because generic tuning strategies have not been widely developed [3]. In this context, a virtual tool, able to simulate the system and perform the requested tests would be very helpful, not only to compare different architectures or to carry out the tuning, but also to reach a better insight

of the suspension and vehicle behavior. In fact, considering that the achievement of an optimal behavior is a very challenging task, a full understanding of underlying system dynamics would be very useful. To do this, the virtual model must give a detailed description of both the suspension system and the vehicle. The integration of the hydraulic model of the suspension with the kinematic multibody model of the vehicle, though numerically challenging, seems the right way to approach the problem. An example of a detailed multibody model of a tractor may be found in [4] and [5]; great attention has been focused here on the description of the tire-terrain contact characteristics and the correlation with experimental data. Biral et al. in [6] and [7] analyzed a semi active hydro-pneumatic suspension system for a tractor with the focus of optimizing the control logic of the system. Here the experimental and numerical analysis is developed by referring to a quarter car model of the vehicle. In this work, the focus was the design of opportune control logic for the suspension and the analysis of the main limits of the different semi-active control strategies, that were found to be due to the damper dynamics and the non-linear behavior of the hydraulic suspension, in particular due to the friction forces acting on the piston-cylinder assembly. However, recognizing the importance of considering the pitching motion of the tractor in the suspension analysis to develop an optimized control strategy, the authors proposed in [8] a half car model of the vehicle coupled also with a more detailed thermo-hydraulic model of the hydraulic suspension system.

It is doubtless difficult to develop a detailed model of the hydro-pneumatic suspension interacting with a full car model of an agricultural tractor but, at the same time, only with this approach all the dynamic motions of the tractor are considered. Another challenging aspect is that once the virtual tool is ready, simulation time may be discouraging in utilizing it, especially in the industry daily work, and particularly if the idea is to apply an optimization process to guide the design and choice of the suspension characteristics. For this reason, this work focuses on developing a simplified off-highway vehicle model able to reduce simulation time, while keeping the same steady-state and dynamic behavior of a more complex and detailed model.

A tractor multibody model was developed in Simcenter Amesim® starting from an MSC Adams® multibody reference one, which was previously validated with experimental tests. We chose Simcenter Amesim® because it allows both a multibody modeling and a more simplified one leveraging the multi-environmental libraries within the software, which is suitable for the creation of a Real Time (RT) model. Once the multibody model was aligned with the reference one, an embedded Amesim® tool has been exploited to create several look-up tables that replicate the kinematic behavior of the suspended axle. Some intermediate models were then used to consider the inertial effects even in the simplified model. We subsequently employed another software tool to analyze the system stability and modify some parameters to match the frequency range of interest of a fixed step solver. This is a fundamental step to make the system stable with this kind of integration and so with RT simulation.

Lastly, some standard maneuvers have been simulated with both the multibody model and the Real Time one. In this way, it was possible to compare the results and validate the entire methodology presented.

2. OFF-HIGHWAY VEHICLE MODEL IN SIMCENTER AMESIM®

The off-highway vehicle taken as reference for the present study is shown in Figure 2.1. It is a 116 kW tractor with independent suspension on the front axle, while the rear one is not suspended.

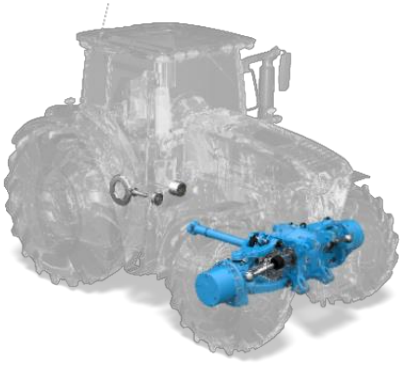

Figure 2.1. Tractor with a suspended axle used as reference

These vehicles, or the tractors in general, are specifically designed to deliver a high tractive effort (or torque) at slow speeds, to haul a trailer or machinery such as that used in agriculture, mining, and/or construction. Usually, a ballast is used so that the load is not too unbalanced on one axle concerning the other when machinery is coupled with the vehicle. Vehicles with an independent suspension on the front axle have both a more comfortable and safer driving on-road and performance optimization on the field.

The presented activity focuses on the realization of the RT model having as a starting point the detailed lumped parameter multibody model of the examined vehicle. The model has been developed with Simcenter Amesim®. The multibody model was used not only as a starting point for the development of the RT simplified one, but also as a benchmark for the RT model validation. Several main components of the vehicle have been identified to facilitate both the multibody model development and comprehension.

These components are indeed easily distinguishable and have been interfaced to obtain the detailed vehicle model. These main components are:

- the vehicle sprung mass;
- the steering cylinder;
- the wheel upright and hub (unsprung mass);
- the detailed model of the front axle with the examined independent suspension;
- the Pacejka tire and road model;
- the capability of considering the connection with the hydraulic circuit of a hydro-pneumatic suspension.

These elements are highlighted in Figure 2.2, where the block diagram of the multibody model is reported.

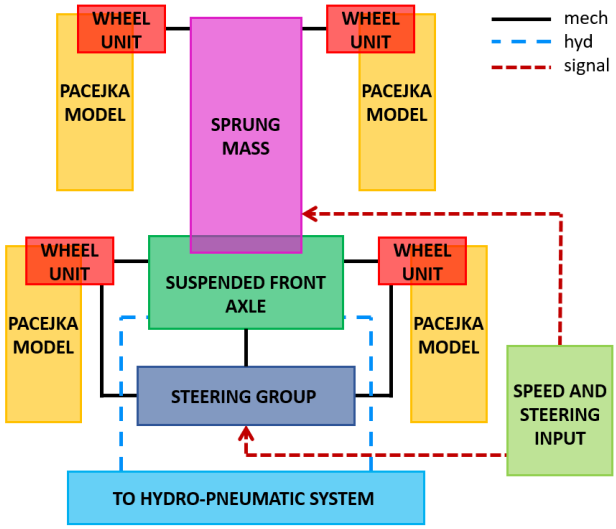

Figure 2.2. Scheme of the Simcenter Amesim® multibody model

As anticipated, the model has been developed in a modular way so that it is easy to modify or replace one or more components. The modification of the suspension geometry or even the replacement of the whole suspension type could be very interesting to compare the different suspension performances.

The study reported in this paper presents the case of a double-wishbone suspension. Nevertheless, it would be sufficient to replace the 3D model of the suspension kinematics to evaluate the performance of another type of suspension on the same vehicle.

Moreover, the parametric characteristic of the model allows to vary all the vehicle parameters as masses, inertias, and/or geometries in a very easy way.

In this way, the numerical model is adjustable to both the substitution of the examined suspension and the modification of the whole vehicle size.

This lumped parameter multibody model developed in Simcenter Amesim® was then compared with another multibody model, previously developed in MSC Adams®. This reference model was created and experimentally validated thanks to on-road and on-field tests by the off-highway engineering department of Dana Italia. The impossibility of simplifying the MSC Adams® model to make it able to run in real time and the lack of capability of including the detailed model of the hydraulic circuit led to the need for developing the present Simcenter Amesim® model.

The results comparison was carried out considering several simulations to validate both the kinematic and dynamic aspects of the vehicle model.

While the suspension kinematics turned out to be perfectly aligned between the two models, some differences have been noticed in the vehicle dynamic simulations, which were the ISO 5008 test [9] and the asymmetric bump test.

In particular, the latter highlighted different dynamic responses of the wheels mainly due to the usage of different wheel-soil contact models in the two software. In fact, while MSC

Adams® uses a contact surface, the Simcenter Amesim® limits the choice between a single contact point and a model called “tandem egg”, where two contact points are considered.

Despite the possible difficulty of aligning two different contact models, a further investigation on this particular topic has been started with Siemens (i.e., the developer of Simcenter Amesim®) support. This activity is still ongoing and may be the subject of future work.

Anyway, the presented methodology in this work to develop a RT vehicle model is valuable, regardless of the differences in the contact model.

3. DEVELOPMENT OF THE SIMCENTER AMESIM® REAL TIME MODEL

3.1. Kinematic Tables generation and validation

The first logical step of the proposed methodology is the creation of several kinematics lookup tables of the suspension and their subsequent numerical validation. These lookup tables are necessary to replace the 3D suspension kinematics model, while ensuring the correct response to pure bounce, pure roll, or pure steer input.
A Simcenter Amesim® tool named K&C (Kinematics and Compliance) Data Generator was used for these lookup tables creation. This tool works as a virtual test bench for the examined suspended axle. The inputs for the K&C Data Generator are thus the suspension type and the hardpoints coordinates. This tool already provides a hardpoints template for McPherson and Double Wishbone suspensions (Figure 3.1), as the examined one, but it is also possible to create a template for other types.

The hardpoints coordinates must refer to the left wheel and must be expressed in the chassis reference frame. With particular reference to Figure 3.1, the hardpoints to be defined for a Double Wishbone suspension are the following:

- A: wheel center
- B: center of tire contact patch
- C1: upper wishbone link with chassis (external)
- C2: upper wishbone link with chassis (internal)
- D: spindle link with lower wishbone
- E1: lower wishbone link with chassis (external)
- E2: lower wishbone link with chassis (internal)
- M: spindle link with tie rod of steering system
- N: tie rod link with steering rack body or cylinder
- K: spindle link with upper wishbone
- R1: damper lower link with spindle
- R2: dumper upper link with chassis
- W: external point defining the wheel rotation axis

Once the information regarding the suspension geometry is entered, it is necessary to set the variation range for vertical wheel displacement and steering rack displacement and the intermediate steps to analyze the suspension behavior.

This step defines the total number of combinations of vertical displacement and steering displacement to consider, so that is the total number of batch runs for the virtual bench. The total number of runs is thus $n \cdot m$ where m is the dimension of the vertical displacement vector and n is the dimension of the steering rack displacement vector.

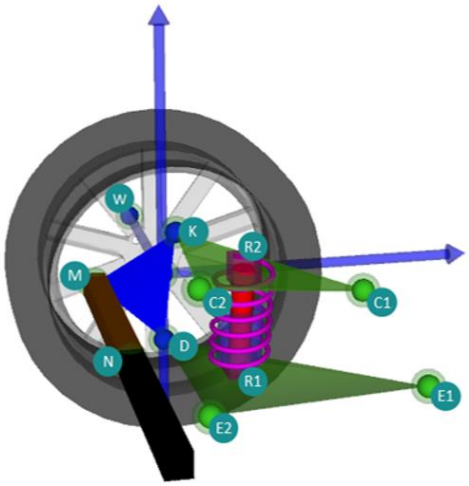

Figure 3.1. K&C template for double-wishbone suspension

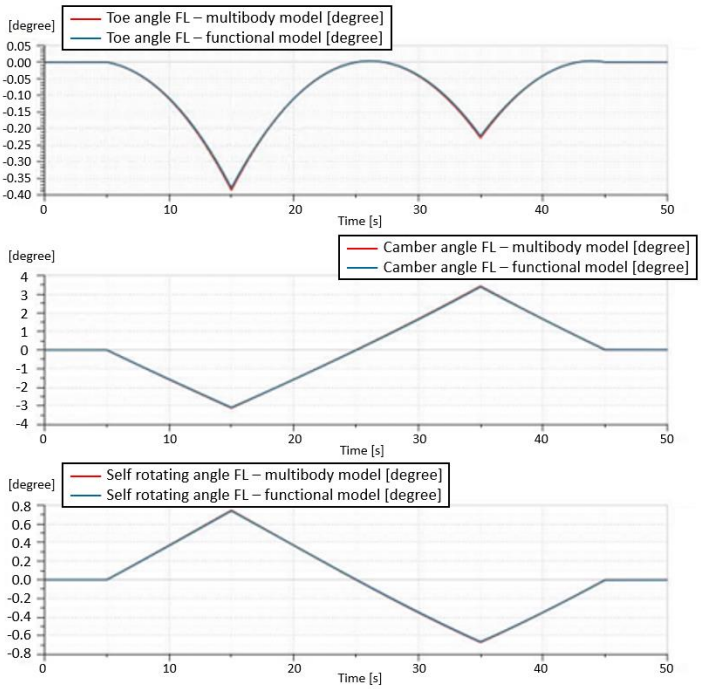

Figure 3.2. Kinematics comparison between multibody (red) and functional model (blue)

The outputs of this tool are the 3D lookup table for the suspension kinematics parameters as a function of the vertical wheel displacement and the steering rack displacement.
These kinematics parameters are the toe angle, the camber angle, the dive angle, X and Y displacement, the damper length, and the damper length variation.
There are 14 lookup tables, 7 for the left wheel and 7 for the right one. As anticipated, the subsequent step is the numerical validation of the newly created kinematic lookup tables.

Both the starting multibody model of the vehicle and the simplified functional model where the kinematics lookup tables are entered were considered in the same Simcenter Amesim® sketch to facilitate the comparison.

This functional model is based on a specific sub-model (VDCAR15DOF1 [10]) available in the Vehicle Dynamics library of the software. The input elements and sensors of the K&C demo are replicated for both models. This allows considering the same combination of pure bounce, pure roll, and pure steer for both of them. Furthermore, both the models are clamped.

The comparison of some suspension kinematics parameters of the two models with a pure bounce input is depicted in Figure 3.2, where toe, camber, and caster angles are reported for the left wheel. The results for the right wheel are obviously similar, so they were not reported in figure.
It is easy to note that the graphs are almost perfectly aligned. Similar results were obtained with a pure roll input, a pure steer, and with a combined input.

The kinematics lookup tables are thus validated, and the kinematics behavior of the functional model is aligned with the multibody model one.

3.2. Vehicle Dynamics integration

The following steps regard the introduction of the dynamic aspects in the functional model, like gravity, masses, inertias, and the tire model.

Firstly, all the information related to masses and inertias was introduced into the Global Parameter. This passage was repeated for the following main system components:

- sprung mass m_{sp}
- tire and wheel structure m_{wheel_f}, m_{wheel_r}, m_{strut_f}, m_{strut_r}
- front axle m_{axle}
- suspension wishbones $m_{wishbone_{low}}$, $m_{wishbone_{up}}$
- steering cylinder and links $m_{steer_{cyl}}$, $m_{steer_{link}}$

The first model considered for the vehicle dynamics validation was a Comfort Bench Model, which was used only for the analysis of the vertical dynamics. Both the multibody model and the functional one are subjected to a frequency sweep displacement of the front wheels to evaluate the frequency response.

In addition to the entering of masses and inertias into the VDCAR15DOF1 element of the functional model, it was necessary to also include the tire vertical stiffness, the tire lateral and longitudinal stiffness, the road vertical excitation and its connection to the vehicle. The tire parameters were entered in the model from the datasheet or the correspondent **.tir* file.

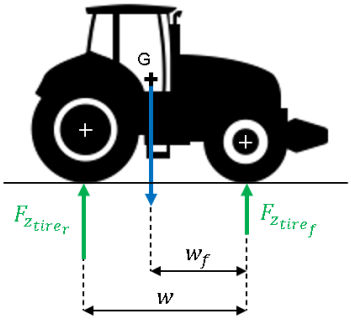

Figure 3.3. Calculation of vertical tire forces

Moreover, the equilibrium for the functional model was calculated. The vehicle front and rear vertical load were evaluated using the vehicle wheelbase (Figure 3.3).

$$F_{z_{susp_f}} = (w - w_f)/w \cdot m_{sp} \cdot g \tag{3.1}$$

$$F_{z_{susp_r}} = w_f/w \cdot m_{sp} \cdot g \tag{3.2}$$

From these, the vertical tire forces were obtained by adding the weight of the tire and wheel assembly. These forces and the tire vertical stiffness were thus used to evaluate an estimate of tire loaded radius.
Note that at first not all masses were considered in this calculation for simplicity.

$$F_{z_{tire_f}} = \frac{F_{z_{susp_f}}}{2} + \left(m_{wheel_f} + m_{strut_f}\right) \cdot g \tag{3.3}$$

$$F_{z_{tire_r}} = \frac{F_{z_{susp_r}}}{2} + \left(m_{wheel_r} + m_{strut_r}\right) \cdot g \tag{3.4}$$

$$R_{w_{load_f}} = R_{w_f} - \frac{F_{z_{tire_f}}}{k_{z_{tire_f}}} \tag{3.5}$$

$$R_{w_{load_r}} = R_{w_r} - \frac{F_{z_{tire_r}}}{k_{z_{tire_r}}} \tag{3.6}$$

Some of the results obtained from the Comfort Bench model are depicted in Figure 3.4, where there is a comparison between the functional model (in blue) and the multibody one (in red). The alignment is acceptable but not perfect, probably because of the simplification in the calculation above.

The following step provides for the substitution of the longitudinal and lateral stiffness values with the Pacejka 2002 model for both the front and rear axle and the subsequent driving on road. The vertical excitation was replaced with the 3D road model and a properly calibrated velocity controller (PID) was integrated. The Pacejka model parameters were taken from the *.*tir* tire files.

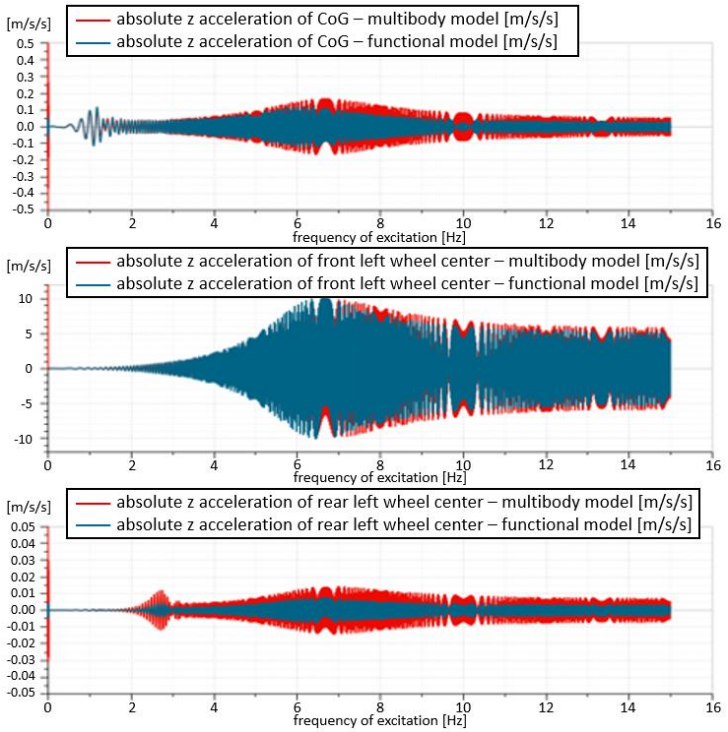

Figure 3.4. Comfort bench comparison between multibody (red) and functional model (blue)

The standard maneuver considered for this further model comparison was the asymmetric bump. This because this test is short but at the same time quite demanding for the model.

A refinement of equilibrium calculation for the functional model with the inclusion of the other masses was considered necessary before continuing. Firstly, the new position of the system center of gravity was evaluated considering, as said, not only the vehicle sprung mass, but also the front axle, the suspension wishbones, and the steering links. All the added masses were considered as centered in the center of gravity of the front axle for simplicity. The system was thus simplified to a system of two particles (Figure 3.5) where the center of gravity is defined by (3.7).

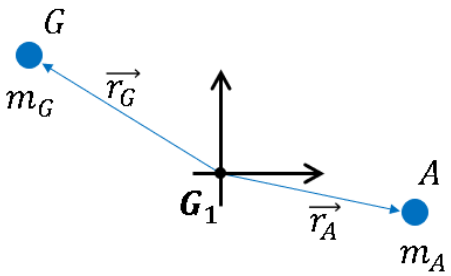

Figure 3.5. Two particles system

$$\begin{pmatrix} x_{G1} \\ y_{G1} \\ z_{G1} \end{pmatrix} = \begin{pmatrix} 0 \\ 0 \\ 0 \end{pmatrix} = \frac{\sum m_i \vec{r_i}}{\sum m_i} = \frac{m_G \vec{r_G} + m_A \vec{r_A}}{m_G + m_A} \tag{3.7}$$

The terms m_G and m_A are defined in (3.8)-(3.9).

$$m_G = m_{sp} \tag{3.8}$$

$$m_A = m_{axle} + perc_{sprung} \cdot (m_{wishbone_{up}} + m_{wishbone_{low}} + m_{steer_{link}}) \tag{3.9}$$

The term $perc_{sprung}$ was introduced to consider only the sprung percentage of the wishbone and link masses. In fact, these components are not completely sprung or unsprung due to their intermediate position, but the percentage value is not known. However, this percentage was set to 50% after a brief sensitivity analysis. Equations (3.10)-(3.11) show the modification of the front and rear axle loads.

$$F_{z_{susp_f}} = \left((w - w_f) \cdot m_{sp} + \left(w - x_{axle_{CoG}}\right) \cdot \left(m_{axle} + 2 \cdot perc_{sprung} \cdot \left(m_{wishbone_{up}} + m_{wishbone_{low}} + m_{steer_{link}} \right) \right) \right) \cdot \frac{g}{w} \tag{3.10}$$

$$F_{z_{susp_r}} = \left(w_f \cdot m_{sp} + x_{axle_{CoG}} \cdot \left(m_{axle} + 2 \cdot perc_{sprung} \cdot \left(m_{wishbone_{up}} + m_{wishbone_{low}} + m_{steer_{link}} \right) \right) \right) \cdot \frac{g}{w} \tag{3.11}$$

Similarly, (3.12) shows the modification of the vertical tire force.

$$F_{z_{tire_f}} = \frac{F_{z_{susp_f}}}{2} + \left(m_{wheel_f} + m_{strut_f} + \left(1 - perc_{sprung}\right) \cdot \left(m_{wishbone_{up}} + m_{wishbone_{low}} + m_{steer_{link}} \right) \right) \cdot g \tag{3.12}$$

Finally, all the inertias were modified using the Huygens–Steiner theorem by referring to the new center-of-mass frame.

After entering all these modifications into the Global Parameter and into the VDCAR15DOF1 element, it was possible to analyze the simulation results of the asymmetric bump test.
The comparison between the functional model behavior (in red) and the multibody model one (in blue) regarding the most interesting results is depicted in Figure 3.6. These results are the front wheel center positions and the vehicle Euler angles (i.e. roll, pitch and yaw).
The results qualitative comparison turned out to be satisfying. Note that this was only a qualitative comparison, while a quantitative one will be presented for the final RT model.

The Amesim® functional model was thus considered validated concerning the Amesim® multibody one.

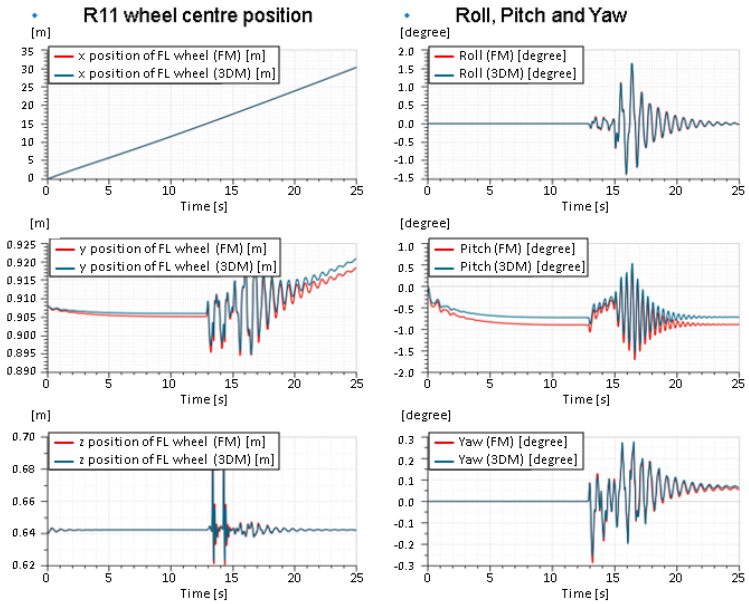

Figure 3.6. Drive on road comparison between multibody (blue) and functional model (red)

3.3. Model modifications for fixed step simulations

As said, the last step regards the modification necessary to make the functional model able to run in real time. In fact, some quantities must be adapted to match the frequency range of interest of a fixed step solver. The Performance Analyzer tool of Simcenter Amesim® was used to do so. The tool template is reported in Figure 3.7.

Switching from a variable time step solver to a fixed time step solver is a pre-requisite for using a model for Real-Time study. To ensure numerical stability and real-time target limitation, the value of the fixed time step must be in a dedicated range that depends on the model.

This tool allows visualizing all the information regarding the numerical stability region of the system and the critical modes for the selected integration method. Firstly, it is necessary to set an appropriate number of linearizations during the run (in orange in Figure 3.7). After selecting a guestimate of the fixed step solver (in blue), the tool shows the stability region for the eigenmodes (in pink). After the simulation has run, the user has access to the modes for each linearization time, to the maximum time step for the given solver method (in light blue), and to the time and contributors causing the maximum problem (in green and red) [10].

This information is necessary to modify these contributors of the modes causing troubles and then to choose the maximum fixed time step. Once the parameters have been appropriately modified, it is possible to test the Real Time model.

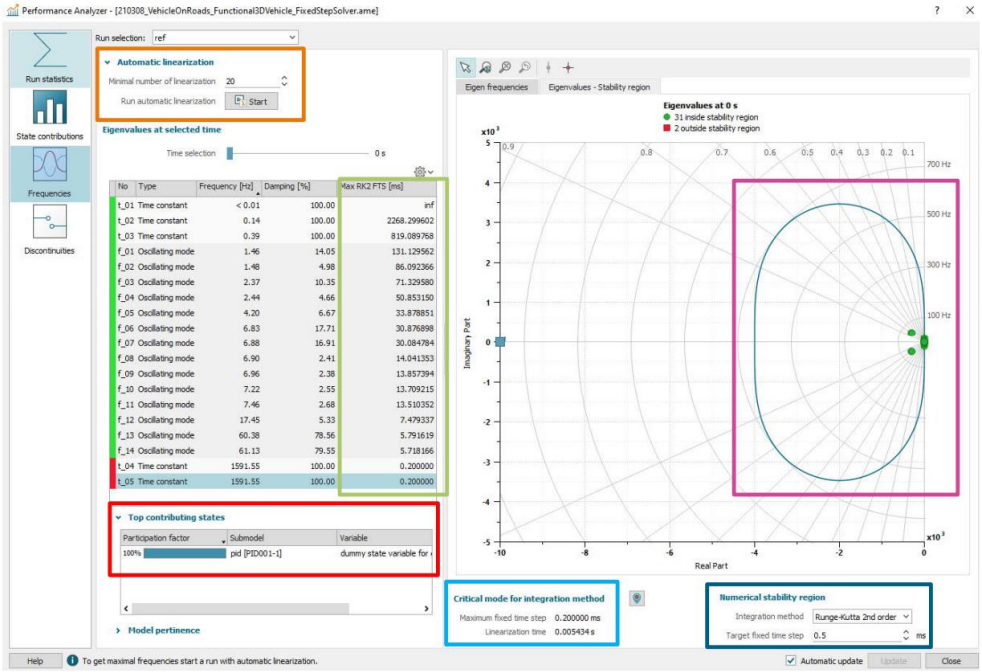

Figure 3.7. Simcenter Amesim® Performance Analyzer

4. REAL TIME VEHICLE MODEL

The vehicle Real Time model created following the previous steps was used to simulate three standard maneuvers, which are:

- Asymmetric bump test
- ISO5008
- Moose Test (Double line change)

The RT model results were then compared with the starting multibody model ones.

The figures below depict the comparison between these two models' general behavior with the asymmetric bump test. Figure 4.1 shows the positions of the front left wheel center in the RT model compared to the 3D model ones. It is easy to note that the results are quite well aligned. The small differences in the y position graph can be considered negligible, since the lateral shift is in the order of millimeters after tens of meters of longitudinal drive.

Figure 4.1 shows also the comparison of the three Euler angles in the two considered models. As before, the results are generally well aligned. The small offset in the pitch graph can be explained by a remaining small inaccuracy in the system mass identification or balancing. Nevertheless, the results remain satisfactory.

To confirm that, Fig. 4.2 depicts a histogram of the percentage errors of some of the most interesting results of the RT model concerning the multibody one.

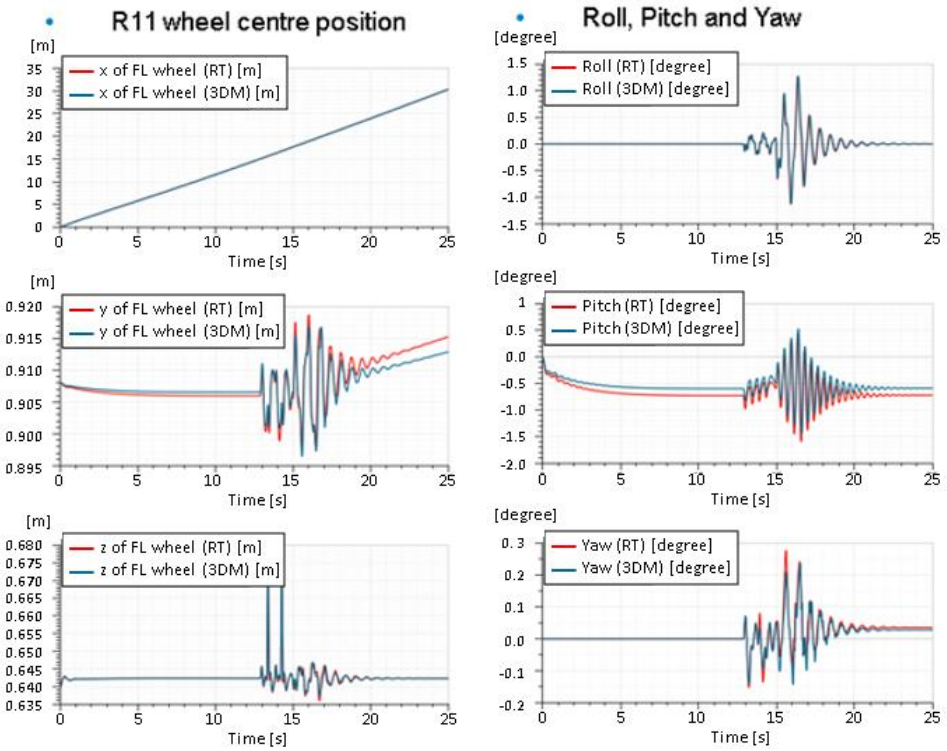

Figure 4.1. Comparison between multibody (blue) and RT model (red) for asymmetric bump test – position of front left wheel center and vehicle Euler angles

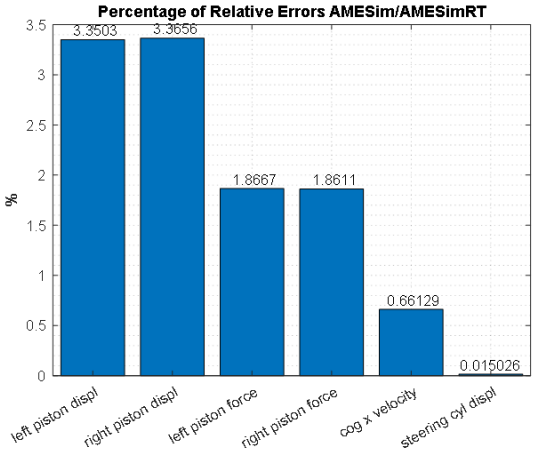

Figure 4.2. Percentage errors for asymmetric bump test

Similar results alignments were obtained also for the ISO 5008 and the moose test. The histograms of the main percentage errors regarding the ISO 5008 and the moose test are reported in Figure 4.3 and 4.4.

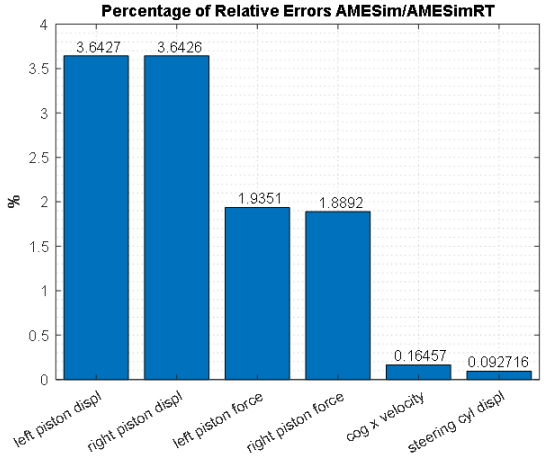

Figure 4.3. Percentage errors for ISO 5008

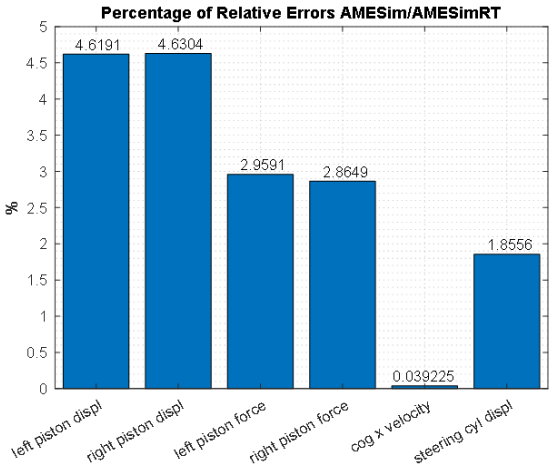

Figure 4.4. Percentage errors for moose test

In summary, the results are quite well aligned for all three considered tests. This aspect is highlighted by the percentage error values, which are all below the 5% threshold. The RT model could thus be considered validated with respect to its multibody counterpart.

Another aspect to highlight is the remarkable improvement in CPU time to run these simulations. In fact, the CPU time is reduced to few seconds for all three considered tests, while the multibody model needs minutes or tens of minutes depending on the simulation.

5. CONCLUSIONS

5.1. Achievements

The development of the presented methodology in Simcenter Amesim® enabled the creation of a tractor simplified model with independent suspension which can run in Real Time. The followed steps allowed us to consider both the kinematics and dynamics aspects of the starting multibody model. Thanks to this, the results of the RT model turned out to be well aligned with the multibody reference ones. The key aspect of this work is the improvements in terms of computational time to run the simulations. In fact, while both the Amesim® multibody model and the Adams® reference one has computational times in the range of minutes (depending on the simulated maneuver), the RT model can simulate all the tested maneuvers in just a few seconds.

5.2. Real Time future usage

The possibility to have a vehicle model that can run in Real Time and provide reliable results is already a benefit. However, this aspect is highlighted if this model can be used within an optimization workflow for the whole independent suspension system where it is necessary to evaluate the performances of a high number of consecutive designs. Passing from minutes to seconds of computational time for a single simulation, it is easy to imagine that the total time-saving during the entire optimization can easily be tens of hours. If we instead consider the same amount of time, this model ensures to evaluate more designs and so a more robust and accurate optimization.

5.3. Future work

As anticipated, the alignment between the Amesim® multibody model and the reference Adams® one is not perfect due to the different wheel-soil contact models used. This open point is already under investigation, and it is the first we would like to clarify to validate the RT model completely.

The next activity will concern the analysis and modeling of the hydro-pneumatic system of the suspension, which was not considered in this work, that had the aim to generate and validate the dynamic model of the vehicle. Despite it is not easy to make a hydraulics system model capable of running in Real Time due to its high-frequency features, the usage of a neural network could solve this problem. The creation and the appropriate training of a neural network could thus be the subject of future work.

6. REFERENCES

[1] W. Bauer, “Hydropneumatic Suspension Systems”, Springer, Berlin, Heidelberg, 2011.

[2] G. Panetta, F. Mancarella, M. Borghi, B. Zardin, F. Pintore,” Dynamic Modelling of an off-road vehicle for the design of a semi-active, hydropneumatic spring-damper system”, Proceedings of the ASME 2015 International Mechanical Engineering Congress and Exposition. Volume 4B: Dynamics, Vibration, and Control. Houston, Texas, USA. November 13–19, 2015.

[3] D. J. Cole (2001), Fundamental Issues in Suspension Design for Heavy Road Vehicles, Vehicle System Dynamics, 35:4-5, 319-360, DOI: 10.1076/vesd.35.4.319.2045

[4] G. Previati, M. Gobbi, G. Mastinu, “Farm tractor models for research and development purposes”, Vehicle System Dynamics: International Journal of Vehicle Mechanics and Mobility, Volume 45, Issue 1, pp. 37-60, 2007.
[5] M. Gobbi, G. Mastinu, G. Previati, “Farm tractors with suspended front axle: anti-dive and anti-lift characteristics”, Journal of Terramechanics, Volume 56, Pages 157-172, December 2014.
[6] F. Biral, M. Grott, R. Oboe, C. Maffei, E. Vincenti, "Modelling, control and design of heavy duty suspension systems”, AMC’08 The 10th IEEE International Workshop on Advanced Motion Control, 2008.
[7] M. Grott, F. Biral, R. Oboe, A. Cis, E. Vincenti, “Semi-active suspension systems for heavy-duty vehicles: multibody model development, identification and control algorithm evaluation”, Proceedings of the ASME 2009 International Mechanical Engineering Congress and Exposition, Lake Buena Vista, Florida, USA, November 13–19, 2009.
[8] M. Grott, F. Biral, A. Sorniotti, R. Oboe, et al., "Vehicle simulation for the development of an active suspension system for an agricultural tractor", SAE International Journal of Commercial Vehicles, 2010.
[9] ISO 5008:2002, Agricultural wheeled tractors and field machinery - Measurement of whole-body vibration of the operator.
[10] Simcenter Amesim Help Manual.

Biographies



Andrea Fornaciari received the bachelor’s degree in mechanical engineering from University of Modena and Reggio Emilia in 2016, the master's degree in mechanical engineering from University of Modena and Reggio Emilia in 2019, and the philosophy of doctorate degree in industrial and environmental engineering from University of Modena and Reggio Emilia in 2023, respectively. He is currently working as research fellow at the Fluid Power Lab of the “Enzo Ferrari” Department of Engineering, University of Modena and Reggio Emilia. His main research areas are hydraulic and fluid power for both mobile and industrial application.

A Parametric Study on Architectures Using Common-Pressure Rail Systems and Multi-Chamber Cylinders.

Mateus Bertolin, Andrea Vacca

Purdue University/Maha Fluid Power Research Center, matbertolin@hotmail.com
Purdue University/Maha Fluid Power Research Center, avacca@purdue.edu

Abstract.

Amidst the increasing need to improve efficiency of fluid power systems in off-road vehicles, different architectures have been proposed in literature to reduce system throttling losses. Among the most cited ones, are architectures based on the use of common-pressure rails (CPRs), which in some cases have been combined with multi-chamber cylinders to further reduce power loss. This kind of solution appears to be particularly attractive in systems with several actuators with many instances of overrunning loads, such as in earthmoving machines. In this scenario, a basic question arises concerning the maximum amount of energy that can be saved by adding extra pressure rails and/or cylinder chambers. Answering this question can be challenging given that many parameters such as cylinder areas and pressure levels can affect the results for a given application. This paper proposes an extended parametric analysis that compares different architectures considering an optimized design for each solution considered. While ensuring design feasibility, the proposed algorithm finds the optimal system parameters (e.g., cylinder areas and pressure levels) for each architecture. The particular case of reference is an excavator, for which an instantaneous-optimization controller is used to ensure near-optimal control and cycle tracking for each design. Results show that even when compared to the already efficient architectures available in literature, a reduction of up to 29.3% power consumption can still be achieved with the most efficient solution. Obviously, the most suitable solution results from a compromise between implementation cost and energy efficiency. The paper qualitatively addresses these aspects.

Keywords. Common Pressure Rails, Multi-chamber cylinders, Multi-pressure rails, Off-road vehicles, Excavators.

1. INTRODUCTION

Increasing environmental awareness and governmental push towards lower carbon emissions has led the mobile machinery industry towards the development of more efficient systems. When it comes to off-road vehicles, there is an increasing trend towards the electrification of small, compact construction and agricultural machines. Nevertheless, in the case of larger and high-productivity machines, replacing the engine with an electric prime mover still imposes challenges, and many OEMs are also considering alternatives such as electric hybrids, hydraulic hybrids and hydrogen powered machines.

Regardless of the technology of choice for the prime mover, it is agreed among the technical community that the transmission efficiency of the hydraulic actuation system must increase to reduce environmental impact, machine autonomy, and operational costs.

1.1. Common Pressure Rails Systems

In the above scenario, many solutions have been proposed to improve the efficiency of fluid power systems in multi-actuators off-road vehicles, commonly aiming at reducing throttling losses. An approach that has gained interest in recent years is based on the Common Pressure Rails (CPRs) concept. In these architectures, multiple actuators share common supply lines, kept at different pressure levels. The hydraulic circuit is designed such that all actuator chambers can be connected to any of these supply lines. The concept was first introduced by Lumkes and Andruch [1]. The idea was further improved by the STEAM architecture which added accumulators to at least two of these pressure rails. Adding these accumulators opened the possibility for energy storage within the system and for advanced secondary control like strategies for the cylinders. The concept was presented by Vukovic, Sgro and Murrenhoff [2], with a prototype 18 ton. excavator being presented in [3]. This machine achieved up to 55% improvement in efficiency for an air grading cycle with a circuit that achieved the same functionality as the one showed in Figure 1.1 (a).

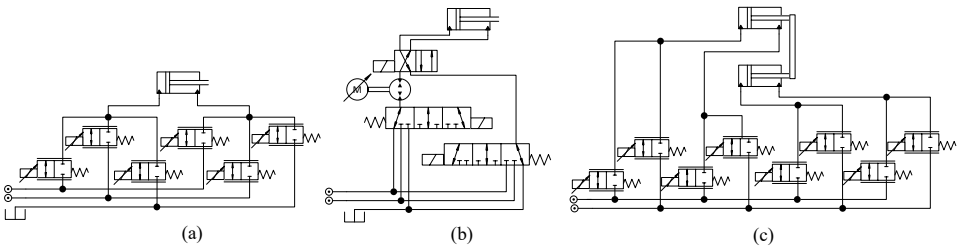

Figure 1.1. Conceptual schematics of architectures proposed byVukovic, Sgro and Murrenhoff (a), Li, Siefert and Bigelow (b) and Heybroek and Sahlman (c).

In a similar fashion, Li, Siefert and Bigelow [4] proposed an architecture with hydraulic accumulators and three pressure rails. However, in their case, it was proposed to substitute the valves - which can only waste power in throttling losses - with a pump/motor that is driving/being driven by an electric machine. This architecture is shown in Figure 1.1 (b). More recently, Guo et al [5]. proposed to use CPRs for agricultural machines, achieving an average efficiency improvement of 45%.

1.2. Multi-Chamber Cylinders and CPRs

Another approach to CPRs is based on the principle of digital hydraulics. By using linear actuators with more than 2 chambers, it is possible to increase even further the efficiency of CPRs systems. This is because the efficiency of such system increases with a larger number of achievable force levels, which is given by

$$n_{FL} = n_{PR}^{n_{CC}} \quad (1)$$

where n_{FL} is the number of available force levels, n_{PR} is the number of pressure rails and n_{CC} is the number of cylinder chambers. The idea was initially proposed by Linjama et al. [6]. Many studies have been carried out for multi-chamber cylinders, but the most successful is the implementation in a 30 ton. excavator by Heybroek and Sahlman [7] which achieved fuel efficiency gains in the range of 34-60%. This architecture is presented in Figure 1.1 (c). In a similar fashion, Dell'Amico et al. proposed using a 4-chamber cylinder with 3 pressure rails, but the architecture has only been implemented in a lab experimental set-up [8].

With respect to the design of multi-chamber cylinders, Huova and Linjama [9] showed that system efficiency can be improved by proper area selection. Nevertheless, no specific selection procedure was described. Belan et al. [10] proposed a method for designing multi-chamber cylinders in aircraft applications. In their work, the goal was to extend the number of available forces in retraction direction and a serial linkage design was used. Although no specific consideration was made with respect to the efficiency of the selected areas, the authors limited the maximum gap between force levels.

1.3. Paper Scope

Although intuition based on (1) can qualitatively give an idea of how different architectures would be ranked in terms of efficiency, to the authors' knowledge no formal analysis has been carried to quantify efficiency differences between these systems.

Admittedly, a more significant comparison would be in terms of cost-convenience for each architecture, based on parameters like return of investment time. However, such analysis still requires an estimation of the operational costs and, therefore, efficiency comparison becomes a crucial point of such analysis.

In this context, it is interesting to understand how the design of a multi-chamber cylinder, with its internal areas, affects the system efficiency. Past multi-chamber cylinder design approaches attempted keeping a constant gap between the force levels inherently realizable by the cylinder. However, it is important to understand if a different design approach for the cylinder areas could bring to further energy efficiency benefits.

As classified by Kolks and Weber [11] multi-chamber cylinders can be divided into three different arrangements: serial linkage, parallel linkage and convolution. While the series linkage design may be the simpler choice from the manufacturing point of view, the fact that it requires at least twice the length of a usual cylinder makes its application to off-road vehicles prohibitive. Parallel linkage design on the other hand results in bulkier solutions. For these reasons, industry and academia have shifted their attention mostly towards the convolution design, especially for off-road vehicle applications. A conceptual drawing of this design is shown in Figure 1.2.

The proposed study focuses on cylinders with at most 4 chambers. This is because previous works do not show practical implementations for cylinders with larger number of chambers. In addition, architectures with at most 3 pressure rails are analyzed. Intuitively, the higher is

the number of rails the more is the potential for energy saving. Nonetheless, the cost is higher. A study performed by Guo et. al [5] shows that the efficiency gains per pressure rail added significantly decrease after 3 rails. Despite that work considered a different application, also this work limits the analysis to 3 rails. Nonetheless, the methodology proposed here could also be extended to architectures with a larger number of rails.

Taking a convolution design as the arrangement of choice, this paper undertakes a full factorial search to find the optimal cylinder areas, given different levels of pressure in the supply lines. The cylinder control method and the effect of the controller gain in the energy efficiency are also briefly discussed. The result is a step-by-step cylinder design procedure that maximizes efficiency for a given duty cycle. The paper will also perform a comparison between optimal solutions for different architectures.

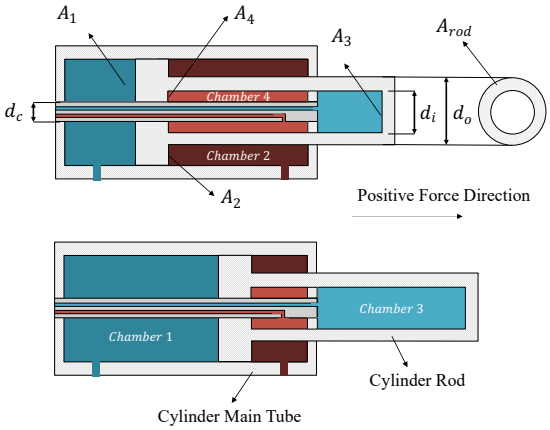

Figure 1.2. Convolution Design Conceptual Drawing

The paper structure is as follows: first, the reference machine and duty cycle are introduced in section 2. Then, a parametrization procedure is discussed, and the design constraints of the convolution arrangement are analyzed (section 3). Section 4 considers the effects of the valves actual size and the variability of the rails pressure levels. Then, a supervisory controller for managing the local cylinder control is described, followed by a description of the cylinder area optimization approach. Next, area optimization results for the arm cylinder of the reference machine are presented, followed by a comparison with other established design methods. An architecture comparison that includes all the actuators of the reference machine is discussed in section 9. Lastly, the main conclusions of this work are discussed and summarized.

2. REFERENCE MACHINE AND DUTY CYCLE

This work takes as reference machine a 20 ton. excavator. Considering that the energy efficiency of off-road machines is heavily dependent on the specific duty-cycle, this paper proposes a cycle-dependent optimization. It takes as reference a 90° truck loading cycle, which is typically used to evaluate the efficiency of excavators. Examples include [7] and

[12]. In these working conditions, the machine digs into the ground, rotates 90° while lifting the boom actuator. It then dumps the bucket content into a truck with the boom fully extended. Real-world data coming from expert operator measurements were available to the authors and were used as input to the proposed optimization algorithm. The data included measured actuator pressures as well as cylinder positions.

3. MULTI-CHAMBER CYLINDER DESIGN PARAMETRIZATION AND DESIGN SPACE GENERATION

The following paragraphs formalize the space domain of the feasible multi-chamber cylinder designs that can be suitable for a given application. In this analysis, it is assumed that the required maximum and minimum forces are previously known based on the baseline machine specifications. The system design starts with a selection of the minimum pressure allowed in the rail with the highest pressure, as well as the maximum pressure allowed in the pressure rail with the lowest pressure level. This is done to ensure maximum force availability, regardless of the pressure levels in the rails, which can vary over time despite the large capacitance added by accumulators. Then, the total areas in the positive and negative directions are obtained by solving the following system of equations

$$\begin{aligned} p_{HP,min}\, A_{pos} - p_{LP,max} A_{neg} &= F_{max} \\ p_{LP,max}\, A_{pos} - p_{HP,min} A_{neg} &= F_{min} \end{aligned} \tag{2}$$

where A_{pos} is the total area in the positive direction and A_{neg} is the total area in the negative direction. Considering a general case, it is possible to define

$$\begin{aligned} A_{pos} &= A_1 + A_3 + A_5 + \cdots + A_{2n-1} \\ A_{neg} &= A_2 + A_4 + A_6 + \cdots + A_{2m} \end{aligned} \tag{3}$$

where n is the total number of chambers acting in the positive direction, and m is the total number of chambers acting in the negative direction. The cylinder design can then be parametrized by $P = (n + m - 2)$ parameters given by

$$\begin{aligned} r_{2i-1} &= A_{2i+1}/A_1, \; i = 1,2,\dots,n \\ r_{2j} &= A_{2j+2}/A_2, \;\; j = 1,2,\dots,m \end{aligned} \tag{4}$$

Considering the case of a cylinder with at most 2 chambers acting in each direction:

$$\begin{aligned} A_{pos} &= A_1 + A_3 = A_1(1 + r_1), \quad r_1 = A_3/A_1 \\ A_{neg} &= A_2 + A_4 = A_2(1 + r_2), \quad r_2 = A_4/A_2 \end{aligned} \tag{5}$$

In this way, the number of design parameters is reduced to only two: r_1, the ratio of areas in the positive direction and r_2 the ratio of areas in the negative direction. Note that, even though the case of a 4-chamber cylinder is considered, cylinders with 2 and 3 chambers can be considered in this analysis by making r_1 and/or r_2 = 0.

To establish a clear relationship between the parameters r_1 and r_2 and the actual cylinder design specifications, a few diameters are defined according to Figure 1.2. They are the cylinder central diameter (d_c), the rod inner diameter (d_i), and the rod outer diameter (d_o). By inspection of the geometry, the following design constraints can be derived:

A. $A_1 = A_2 + A_4 + A_{rod}$

B. $A_{1,min} = \frac{\pi}{4}(d_o^2 - d_i^2)$

C. $A_{3,min} = \frac{\pi}{4} \cdot d_c^2$

D. $A_4 = \frac{\pi}{4}(d_i^2 - d_c^2) = \frac{\pi}{4}\left(\frac{4}{\pi} \cdot \frac{A_{pos}}{(1+r_1)} \cdot r_1 - d_c^2\right)$

With the constraints A-D defined, the cylinder rod area can be obtained by

$$A_{rod} = \frac{\pi}{4}(d_0^2 - d_i^2) \tag{6}$$

In addition,

$$A_3 = \frac{\pi}{4} \cdot d_i^2 \tag{7}$$

Manipulating (6) and (7) and substituting in the physical constraint A, it is possible to show that

$$d_o = \sqrt{(A_{pos} - A_{neg})\, 4/\pi} \tag{8}$$

3.1. Inner Rod Diameter Minimum Value

Although other solutions are possible, this work considers that the hydraulic connection to chambers 3 and 4 is done through an inner connection inside the main cylinder tube. This

means that, in practice, it is necessary to ensure that there is enough space for the hydraulic connection. Therefore, a fifth constraint is obtained

E. $d_{c,min} \leq d_c \leq d_i$

It is worth mentioning that this requirement for a minimum central diameter also imposes a constraint on the minimum value of the rod inner diameter (d_i). Consequently, it also imposes a constraint on the minimum value of A_3, as highlighted by constraint C and E.

3.2. Buckling Analysis and r_1 Maximum Value

The design space should exclude the cylinders that do not satisfy the Euler's critical load for buckling. It is worth mentioning that for the proposed design, only the load bared by chamber one can cause the rod buckling. Therefore,

$$F_{max,buck} = p_{HP,max} \cdot A_1 = p_{HP,max} \cdot \frac{A_{pos}}{1 + r_1} \tag{9}$$

The cylinder safety coefficient is then defined as

$$S_c = \frac{F_{cri}}{F_{max,buck}}, \quad F_{cri} = \frac{\pi^2 E\, I_{min}}{(KL)^2}, \quad I_{min} = \frac{\pi}{64}(d_o^4 - d_i^4) \tag{10}$$

By re-writing (10) in terms of A_{pos}, A_{neg} and r_1, it can be shown that there is a direct relationship between the safety factor and the parameter r_1. This is shown in Figure 3.1, which points out that there is a limit to the maximum value of r_1 ($r_{1,max}$). This ultimately leads to a limitation on the maximum value of A_3, and, based on (7), to the maximum value of the rod inner diameter (d_i). Therefore, a sixth constraint is added:

F. $d_c \leq d_i \leq d_{i,max}$

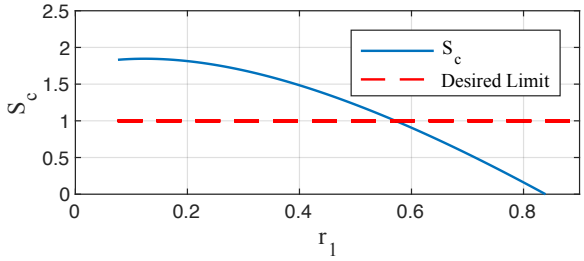

Figure 3.1. Normalized S_c vs r_1 for one of the actuators of the reference machine.

3.3. Cylinder Design Space

With all the constraints determined, the complete design space can be generated. Different designs are created by varying the diameters d_i and d_c, within pre-determined ranges obtained with constraints E and F. The design space generation procedure is summarized as follows:

1. Define $p_{HP,min}$ and $p_{LP,max}$.
2. Solve (2) to determine A_{pos} and A_{neg} given F_{max} and F_{min}.
3. Evaluate d_o with (8).
4. Define $d_{c,min}$ and evaluate $r_{1,min}$.
5. Discretize r_1 within the range $r_{1,min} \leq r_1 \leq 1$. Evaluate S_c for each r_1 and determine $r_{1,max}$ based on buckling analysis.
6. Re-discretize r_1 within the range $r_{1,min} \leq r_1 \leq r_{1,max}$. For each value of r_1, determine d_i.
7. For each value of r_1, discretize values of d_c within the range $d_{c,min} \leq d_c \leq d_i$.

Because of the physical constraint D, there is a clear relationship between r_1 and A_4. Consequently, there is also a relationship between r_1 and the achievable r_2. By manipulating the definition in eq. (5), and using constraints D and E, it can be shown that the feasible range of r_2 will be limited with this limitation being a function of r_1. In this way, once $r_{1,min}$ and $r_{1,max}$ are defined, a feasible range for r_2 can be found for each value of r_1. Such result is clearly seen in the final design space presented in Figure 3.2.

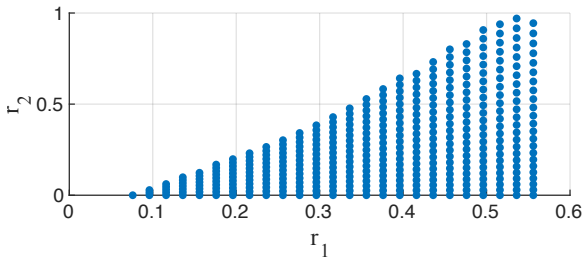

Figure 3.2. Final feasible design space for the boom cylinder of the reference machine.

4. CONSIDERATIONS ON VALVE SIZE AND MEDIUM PRESSURE RAIL LEVEL

Considering that the focus of the proposed optimization is to improve efficiency, two important factors beyond the cylinder design can impact the results. They are valve size and

medium pressure level (in architectures with 3 pressure rails). With respect to the first one, this study assumes that each valve is sized for a user defined maximum pressure drop (Δp_v) at its maximum flowrate. Since different chambers will have different maximum flowrates, this means that valves are sized accordingly to the chamber they are connected to.

Another relevant factor is the pressure level used in the medium pressure rail, p_{MP}. Intuitively, the average between maximum and minimum pressure can be a good choice. However, this work evaluates each cylinder design considering different possibilities for the p_{MP} value. This is done by adding a third variable parameter to define the overall design architecture. Besides varying r_1 and r_2, which define the cylinder areas, a third parameter r_3 defines the pressure in the intermediate pressure level according to

$$p_{MP} = (p_{HP} - p_{LP}) \cdot r_3 + p_{LP}, \qquad 0 \leq r_3 \leq 0.9 \tag{11}$$

In the proposed analysis, supply pressures are assumed constant. It is important to observe that the case of systems with two pressure rails are included in the analysis. In fact, in Eq. (11) when $r_3 = 0$, p_{MP} becomes equal to p_{LP}, which corresponds to the case of a system with 2 pressure rails.

5. CYLINDER CONTROL

One of the main advantages of architectures using CPRs and multi-chamber cylinders is the opportunity to configure the cylinder connections to the pressure rails so that throttling losses are reduced. This means that, for an efficient operation, each actuator requires a supervisory controller that selects the best connections between different rails and chambers based on the current cylinder load.

This work uses an approach similar to the Force Index Controller (FIC) proposed by Sjoberg and Heybroek [13], but with modifications in the cost evaluation as expressed by the cost function (12), (13) and (14). In this way, all terms in the cost function have energy units. The instantaneous optimization controller selects the configuration id that minimizes the losses in the cylinder at the time step k according to

$$J_{k,k-1}(id) = E_{th,k}(id) + W_{sw} \cdot E_{sw,k,k-1}(id) \tag{12}$$

where the first term evaluates the throttling losses

$$E_{th,k}(id) = \left|\dot{x}_{meas,k} \cdot t_s \cdot \left[F_{meas,k} - F(id)\right]\right| \tag{13}$$

and the second term accounts for the compressibility losses, according to

$$E_{sw,k,k-1}(id) = \sum_{i=1}^{4} \frac{V_{i,k}}{B} p_{i,k}(id) \cdot (p_{i,k}(id) - p_{i,k-1}) \tag{14}$$

where $V_{i,k}$ is instantaneous volume of chamber i, at time step k. More information on the derivation of eq. (14) can be found in [14]. The gain W_{sw} was proposed in [13] and is used to give more or less importance to the switching losses. Its impact on cylinder efficiency is discussed in the results section. The reference force $F_{meas,k}$ in this work is a simulation input obtained from the measured actuator pressures in the reference machine.

6. PROPOSED AREA OPTIMIZATION METHOD

A full factorial analysis of the design space (variations of the parameters r_1, r_2 and r_3) is performed to obtain a thorough comparison between different cylinder designs and system architectures. To reduce the impact of the controller switching gain W_{sw} in the results, a fourth parameter is added to the analysis

$$W_{sw} = r_4, \quad 0 \leq r_4 \leq 2 \tag{15}$$

The duty cycle measured data for a reference actuator is fed into a cylinder control block, which determines the optimal configuration for the cylinder connections between rails at that given time step. A simplified schematic is shown in Figure 6.1.

Once these connections are found, both throttling and switching losses are evaluated at the given time-step. The total losses for each design over the reference duty cycle are obtained by summing up the throttling and the compressibility losses of each time-step:

$$J_{cyl} = \sum_{k=1}^{N} E_{th,k}(id_k^*) + E_{sw,k,k-1}(id_k^*) \tag{16}$$

It is important to remark some of the key assumptions of the proposed method. First, the rails pressures are assumed constant and the valve opening dynamics are neglected. Consequently, any possible cross-leakage between rails during chamber pressure level transitions are not considered.

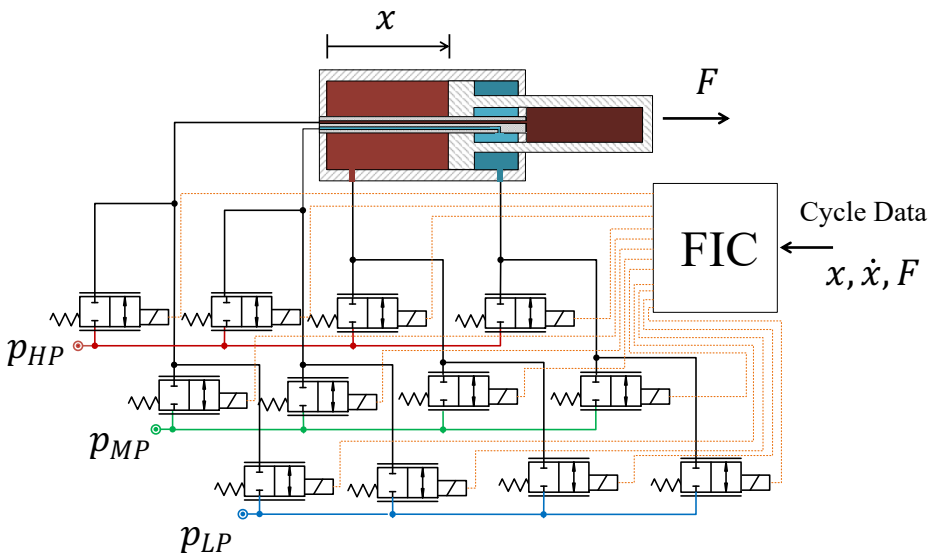

Figure 6.1. Conceptual schematic of control and hydraulic system considering the most general case in this study, with 3 pressure rails and a 4-chamber cylinder.

7. AREA OPTIMIZATION RESULTS

This section presents the area optimization results for the arm cylinder of the reference machine. Section 9 will summarize the results considering all the machine actuators. The main parameters used in the optimization are presented in Table 7.1.

Table 7.1: Main Optimization Parameters

Parameter	***Values***
$p_{HP} = p_{HP,min}$	330 bar
$p_{LP} = p_{LP,max}$	30 bar
$r_{1,arm}$	[0.076:0.02:0.576]
d_c	$[d_{c,min}: 0.002: d_{c,max}(r_1)]$
$d_{c,min}$	40 mm
r_3	[0 0.25 0.5 0.6 0.7 0.8 0.9]
r_4	[0:0.1:1.2 1.5 2]
p_{MP}	[30 105 180 210 240 270 300] bar
t_s	0.1 s
B	$1.5 \cdot 10^9$ Pa
Δp_v	10 bar

7.1. Four-Chamber Cylinders

Figure 7.1 shows the results for the entire design space (combinations of r_1 and r_2) at different levels of medium pressure rail (r_3) pressure. In each case, only the results with the most efficient controller gain ($r_4 = W_{sw}$) are shown.

First, it is clear from the comparison of the colors in Figure 7.1 (a) and (b) that losses can be considerably reduced when a third rail is added to the circuit ($r_3 \neq 0$). Although this was expected, the plot quantifies this difference reduction to be as significant as 69% when comparing systems with 81 (4 chambers and 3 rails) and 16 (4 chambers and 2 rails) force levels. In practice, this value may be lower due to cross-leakage losses during switching and due to dynamic challenges imposed by frequent switching. Nevertheless, it represents a significant margin for improvement.

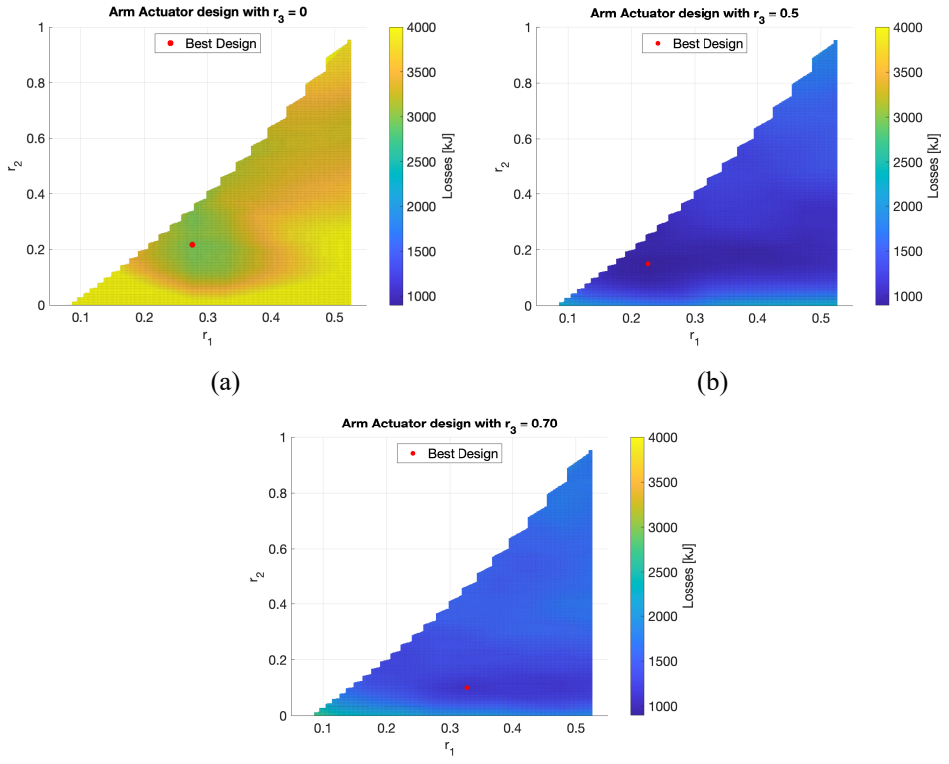

Figure 7.1. Area optimization results considering arm cylinder of reference machine with $r_3 = 0$ (a), $r_3 = 0.5$ (b) and $r_3 = 0.7$ (c).

It is also interesting to comment on the optimal areas found in each case. When only two pressure rails are used, the optimal areas differ from the typical multi-chamber cylinder design approach seen in literature [6], [7] which uses ($r_1 = r_2 = 0.25$). The rationale for such is twofold: first, this optimization is cycle dependent and therefore a finer discretization

in certain operating areas may be beneficial, while the typical design approach simply achieves an even force distribution. In addition, this approach accounts for compressibility losses, which are not considered in the typical design.

When a third pressure rail is added, the optimal areas are dependent on the pressure level selected for the medium rail. This is clear by comparing the plots (b) and (c) in Figure 7.1 which show that for a higher pressure level in the medium rail, different values of r_1 and r_2 are recommended. Nonetheless, different cylinder designs can achieve a similar level of efficiency, as it is clear from Figure 7.1(b), which allows the designer to select the parameters r_1 and r_2 based on other requirements such as safety factor.

A summary of the optimal area ratios and controller gain for each value of r_3 is shown in Table 7.2. These results confirm that the medium pressure level should be placed at the average value between high and low pressure levels. Even a small difference of 30 bar in this pressure level, can lead to an increase of more than 10% in losses when compared to the optimal solution. In addition, it is noticed that both optimal r_1 and r_2 values are always below 0.44, with r_1 always being below 0.38. This is important since higher safety factors are obtained with lower values of r_1.

Another interesting observation is that the optimal controller gain W_{sw} is always less than one. This means that the switching losses have less importance in the cost function (12) when compared to the throttling losses. Nonetheless, none of the optimal solutions resulted in $r_4 = 0$. Therefore, switching losses may have lower importance when compared to the throttling losses, but optimizing the cylinder operation only for throttling losses will lead to suboptimal results.

Table 7.2. Main Optimization Results: 4-chamber Cylinder Case

r_1	r_2	r_3	W_{sw}	p_{MP} *(bar)*	J_{cyl} *(kJ)*
0.296	0.173	0	0.2	-	2,935
0.356	0.434	0.25	0.3	105	1,035
0.216	**0.147**	**0.5**	**0.2**	**180**	**896**
0.216	0.126	0.6	0.3	210	1,008
0.336	0.102	0.7	0.2	240	1,137
0.376	0.079	0.8	0.3	270	1,367
0.296	0.173	0.9	0.3	300	1,754

This can be explained by the fact that a true instantaneous optimization of the losses ($r_4 = w_{sw} = 1$) does not guarantee globally optimal control decisions. This is because (14) shows that any decision made at time step k-1, will affect the decision in the following time step. Therefore, values too high of r_4 may prevent a switch, that will occur in the near future anyways, increasing the throttling losses in the current time step. Nevertheless, it is true that cross-leakage between rails during force level switch is neglected in this analysis, while in practice slow valve dynamics can lead to a higher importance of switching losses.

7.2. Three-Chamber Cylinders

This section discusses the special case of cylinders with 3-chambers ($r_2 = 0$). A summary of the optimal solutions found for each pressure level is shown in Table 7.3. As in the case of the 4-chamber cylinders, the optimal solution is found with $r_3 = 0.5$.

When compared to the results of the more general case shown in Figure 7.1, the losses of this configuration fall somewhere between the levels of Figure 7.1(a) and Figure 7.1(b). As shown in Table 7.3, the optimal solution considering the three-chamber cylinder case has losses of 1739 kJ, which is 94% higher when compared to a system with 4-chambers and 3 rails, but 41% lower when compared to a system with 4-chambers and only 2 rails.

Table 7.3. Main Optimization Results: 3-chamber Cylinder Case

r_1	r_3	W_{sw}	p_{MP} *(bar)*	J_{cyl} *(kJ)*
0.296	0	0.2	-	4,190
0.456	0.25	0.2	105	1,907
0.256	**0.5**	**0.3**	**180**	**1,739**
0.216	0.6	0.3	210	1,860
0.476	0.7	0.2	240	1,835
0.396	0.8	0.2	270	1,923
0.336	0.9	0.2	300	2,555

Figure 7.2 (left) shows the losses for different combinations of W_{sw} and r_1 considering optimal medium pressure level, r_3 for each case. It is seen that neglecting compressibility losses ($r_4 = W_{sw} = 0$) can significantly increase losses. This figure also confirms that values of W_{sw} around 0.3 lead to a minimum in cylinder losses. With respect to the cylinder design parameter r_1, a global minimum exists around 0.25, although similar efficiency levels can be also found with larger r_1 values around 0.47.

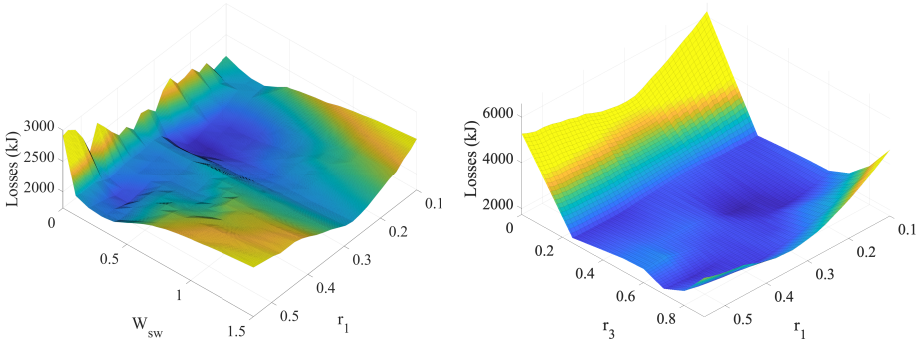

Figure 7.2. Losses as function of r_1 and W_{sw}, considering optimal r_3 and $r_2 = 0$ (left). Losses as function of r_1 and r_3, considering optimal W_{sw} and $r_2 = 0$ (rigth).

Figure 7.2 (right) shows the cylinder losses for each combination of r_1 and r_3, considering optimal controller gain selection. It is evident that there is a significant increase in losses as the value of r_3 approaches zero. In addition, a relatively small difference in losses for values of r_3 between 0.4 and 0.6 is observed, especially near the optimal cylinder design parameter ($r_1 \approx 0.25$). This means that when sizing the accumulator for the medium pressure line, a pressure variation between 150 and 210 bar can be allowed without significant increase in cylinder losses. The figure also shows that not all designs benefit from the medium pressure level at the average of the highest and lowest pressure. For example, at larger values of r_1, the system may benefit from a higher pressure in the medium pressure rail.

7.3. Two-Chamber Cylinder

To complete the analysis, a study was run forcing $r_1 = r_2 = 0$ corresponding to a 2-chamber cylinders. The results are shown in Figure 7.3. It can be seen that a minimum in losses exist at $r_3 \approx 0.25$, which differs from the cases with multi-chamber cylinders.

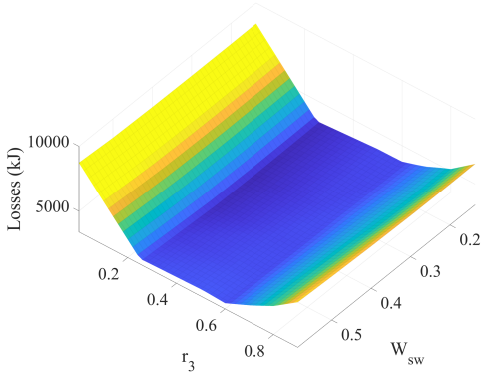

Figure 7.3. Cylinder losses for combinations of r_3 and W_{sw}, with $r_1 = r_2 = 0$

8. COMPARISON WITH ESTABLISHED DESIGN METHOD

Past work such as [6] and [8] have designed multi-chamber cylinders with an even force distribution. This means that the steps between force levels are equal. The main drawback of this solution is that it requires a given ratio α between maximum forces in the retraction and extension directions. For example, systems designed with 2 pressure rails should have the areas following the ratio 8:4:2:1, which means

$$r_1 = r_2 = 0.25, \qquad \alpha = A_{neg}/A_{pos} = 0.5 \tag{17}$$

The proposed cylinder design method, on the other hand, finds the optimal ratios r_1 and r_2 assuming that α is defined by the cylinder application[1].

Although the force ratios are different in each case, it can be interesting to discuss the force discretization obtained with the proposed optimization results with that of the established design method in literature. This comparison is shown in Figure 8.1 for the case of cylinders with 4 chambers and 2 pressure rails. The optimal solution obtained with the proposed procedure converges to a final design that achieves a force distribution very close to that of the traditional design, despite having a different force ratio, α. The drawback of setting $\alpha \neq 0.5$ is that two force levels end up being almost equal, as highlighted in Figure 8.1

However, results are different if 3 pressure rails are considered. In this case, to achieve an even force distribution the area ratios should be modified to 27:9:3:1, which results in

$$r_1 = r_2 = 0.11, \qquad \alpha = 0.33 \tag{18}$$

Additionally, the medium pressure rail level should be placed in the average of the two extreme rails. Therefore, $r_3 = 0.5$. In this scenario, the total force availability in one direction is much greater than the other, which may not be practical for some applications since it would require increasing the actuator size. This is shown in Figure 8.2.

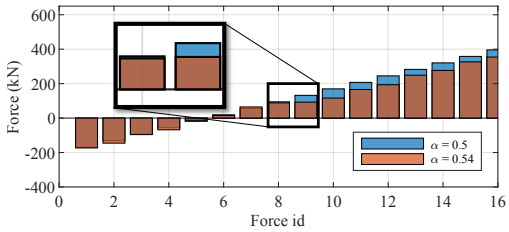

Figure 8.1. Force discretization comparison with established design method for the case of two pressure rails. Note two almost identical force levels in the design w/ α = 0.54.

Although one could argue that it is possible to adjust the force levels by reducing the highest pressure level in the system, that can be a challenging task in highly dynamic applications such as excavators that use large accumulators in their supply line. Should the maximum retraction force be needed, a large flow supply would be required to quickly increase the pressure level in a line with a large capacitance. Considering these, the optimized design results in a force discretization much more appropriate to the given application, with smaller gaps between force levels in most cases and all 81 force levels within a usable range with high pressure in one of the supply lines.

[1]It is worth noticing that it is possible to include the area ratio α in the proposed optimization procedure by solving (2) for different force ratios and repeating the optimization process for discrete values of α.

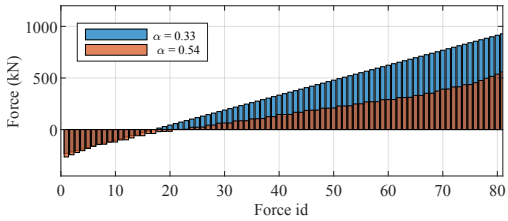

Figure 8.2. Force discretization comparison with established design for the case of three pressure rails

9. OVERALL SYSTEM ARCHITECTURE COMPARISON

The previous section considered only the arm cylinder of the reference machine. Obviously, the medium pressure rail level should not be optimized considering only a single actuator, since it can negatively impact the efficiency of the others. To have a better picture of the efficiency of each architecture, the following procedure was used: the total energy consumption, e.g., useful energy plus losses, was evaluated considering the optimal cylinder designs for Boom, Arm and Bucket for each discrete value of p_{MP}. The process is repeated forcing $r_2 = 0$ (3-chamber cylinders case) and forcing both $r_1 = r_2 = 0$ (2-chamber cylinder case).

Table 9.1 presents the percent difference in energy consumption between different architectures taking the system with 2-cylinder chambers and 3 pressure rails as baseline (like the STEAM system [3]). These results show that keeping the medium pressure level at the average between high and low levels is the best alternative, regardless of the number of cylinder chambers used. It also demonstrates that by adding two extra chambers to cylinders in a system with 3 pressure rails, it is possible to reduce the losses of the linear actuators by 72.4%, resulting in energy consumption reduction of 29.3%.

Table 9.1. Architecture Comparison. Energy Consumption Percent Difference when compared to baseline system.

		# Cylinder Chambers		
r_3	p_{MP} ***(bar)***	**2**	**3**	**4**
0	-	+57.6%	+ 9.9%	-8.0%
0.25	105	+5.7%	-18.9%	-28.1%
0.5	180	**baseline**	**-21.5%**	**-29.3%**
0.6	210	+3.9%	-19.5%	-28.1%
0.7	240	+5.1 %	-18.6%	-26.5%
0.8	270	+14.8%	-16.5%	-24.3%

On the other hand, results also show that efficiency gains are not as significant when adding extra chambers to the cylinders when compared to the addition of extra pressure rails.

Considering the best medium pressure level, the energy consumption reduction with respect to the baseline is of 21.5% when adding a third chamber, and 29.3% when adding a fourth.

10. CONCLUSIONS

This paper proposed a parametrization method for multi-chamber cylinders as well as a procedure to find the optimal design parameters for a given machine and duty cycle. The advantage of such approach with respect to previous works is that it allows the designer to freely select the area ratio α, and optimizes the remaining cylinder parameters. This allows for a more compact design, which can be used in wider range of applications.

The intuitive idea that adding pressure rails and cylinder chambers improves efficiency was confirmed. Nonetheless, this work quantifies that difference by showing that a reduction of up to 29.3% in cylinder power consumption is possible when comparing systems that use cylinders with 2 (baseline) and 4 chambers. In general, efficiency gains are higher when adding an extra pressure rail when compared to adding an extra cylinder chamber. It is worth mentioning that different architecture configurations will require a different number of components, e.g., valves and accumulators. Ultimately, what will lead to the success of one or another configuration is its cost-effectiveness. Although a cost evaluation is out of the scope of this work, the proposed method should provide interested companies with a clear map of how much each concept can achieve in terms of efficiency.

11. REFERENCES

[1] J. H. Lumkes Jr. and J. Andruch III, “Hydraulic Circuit for Reconfigurable and Efficient Fluid Power Systems,” presented at The Twelfth Scandinavian International Conference on Fluid Power, Tampere, Finland, May, 18-20, 2011.

[2] M. Vukovic, S. Sgro, and H. Murrenhoff, “Steam - A mobile hydraulic system with engine integration,” presented at The ASME/BATH 2013 Symposium on Fluid Power and Motion Control, Sarasota, Fl, Oct. 6-9, 2013, FPMC2013-4408, 2013.

[3] M. Vukovic, R. Leifeld, and H. Murrenhoff, “STEAM – a hydraulic hybrid architecture for excavators,” Proceedings of the 10th International Fluid Power Conference, pp. 151–162, 2016.

[4] P. Y. Li, J. Siefert, and D. Bigelow, “A Hybrid Hydraulic-Electric Architecture (HHEA) for High Power Off-Road Mobile Machines,” presented at the ASME/BATH 2019 Symposium on Fluid Power and Motion Control, Longboat Key, FL, Oct. 7-9,2019, FPMC2019-1628, 2019.

[5] X. Guo, R. Madau, J. Lengacher, A. Vacca, and R. Cardoso, “Multi-Pressure Rail System Design with Variable Pressure Control Strategy,” presented at the 13th International Fluid Power Conference, Aachen, Germany, June 13-15, 2022.

[6] M. Linjama, H.-P. Vihtanen, A. Sipola, and M. Vilenius, “Secondary Controlled Multi-Chamber Hydraulic Cylinder,” presented at The 11th Scandinavian

International Conference on Fluid Power SICFP'09, Linköping, Sweden, June 2-4, 2009.

[7] K. Heybroek and M. Sahlman, "A hydraulic hybrid excavator based on multi-chamber cylinders and secondary control – design and experimental validation," *International Journal of Fluid Power*, vol. 19, no. 2, pp. 1–15, 2018.

[8] A. Dell'Amico, M. Carlsson, E. Norlin, and M. Sethson, "Investigation of a Digital Hydraulic Actuation System on an Excavator Arm," in *Proceedings from the 13th Scandinavian International Conference on Fluid Power*, Linköping, Sweden, June 3-5, 2013, vol. 92, pp. 505–511, 2013, doi: 10.3384/ecp1392a50.

[9] M. Huova, A. Laamanen, and M. Linjama, "Energy efficiency of three-chamber cylinder with digital valve system," *International Journal of Fluid Power*, vol. 11, no. 3, pp. 15–22, 2010, doi: 10.1080/14399776.2010.10781011.

[10] H. C. Belan, C. C. Locateli, B. Lantto, K. Petter, and V. J. de Negri, "Digital Secondary Control Architecture for Aircraft Application," in *The Seventh Workshop on Digital Fluid Power*,Linz, Austria, Feb. 26-27,2015, pp. 21–39.

[11] G. Kolks and J. Weber, "Symmetric single rod cylinders with variable piston area? A comprehensive approach to the right solution," presented at the BATH/ASME 2018 Symposium on Fluid Power and Motion Control, Bath, UK, Sept. 12-14, 2018, doi: 10.1115/FPMC2018-8810.

[12] J. Zimmerman, E. Busquets, and M. Ivantysynova, "40% Fuel Savings By Displacement Control Leads To Lower Working Temperatures - a Simulation Study and Measurements," presented at The 52nd National Conference on Fluid Power, Las Vegas, NV, USA, 2011.

[13] K. Heybroek and J. Sjoberg, "Model Predictive Control of a Hydraulic Multichamber Actuator: A Feasibility Study," *IEEE/ASME Transactions on Mechatronics*, vol. 23, no. 3, pp. 1393–1403, 2018, doi: 10.1109/TMECH.2018.2823695.

[14] R. H. Hansen, T. O. Andersen, and H. C. Perdersen, "Analysis of discrete pressure level systems for Wave Energy Converters," in *Proceedings of 2011 International Conference on Fluid Power and Mechatronics*, 2011, pp. 552–558. doi: 10.1109/FPM.2011.6045825.

Biographies



Mateus Bertolin received his bachelor's degree in mechanical engineering from Federal University of Santa Catarina (Brazil), and the Doctorate degree in Engineering from Purdue University (USA) in 2023. Main areas of interest include optimization methods, hybrid vehicles, fluid power systems design and controls.



Andrea Vacca is a fellow of the American Society of Mechanical Engineers (ASME) and he received his Master's degree in Mechanical Engineering from the University of Parma (Italy) and his Doctoral degree in Energy Systems from the University of Florence (Italy). Currently is the director of the Maha Fluid Power Research Center, the largest academic research center dedicated to fluid power research in the United States. His research focuses on several aspects of hydraulic control technology including new concepts to perform hydraulic actuations, new designs and modeling of positive displacement machines, electrification of fluid power systems, modeling of the properties of hydraulic fluids, reduction of noise emissions from hydraulic components. His research has been funded by the U.S. Department of Energy, the U.S. Department of Agriculture, the National Science Foundation, and several industry partners

Challenges in the designing process of hydraulic cylinders made of plastics

Piotr Stryczek

Wroclaw University of Science and Technology, piotr.stryczek@pwr.edu.pl

Abstract.

The use of plastics in the designing of hydraulic components is becoming a new direction in the development of hydraulics. An important example of these course are hydraulic cylinders made of plastics. Previous works of the author presents the process of designing as well as manufacturing and tests of such actuators.
This process was carried out in the following stages: developing of a concept; developing of a design solution and a technological solution; execution of a prototype; computer and experimental research.
On each stage of this process there are challenges, which results from the use of plastics. These challenges differ from those, which are known for the cylinders made of traditional metal materials. Within the article these challenges are stated, propositions of solving them are discussed and some corresponding examples are presented.
Respectively for the stage of concept developing, the rules for selecting the initial technical parameters of the plastic cylinder where set, as well as the rules for selecting the design material and for determining the overall structure of the cylinder. In the stage of developing of the structural solution, special detailed solutions of individual elements are considered. In parallel to the design process, possibilities of the execution of actuator's manufacturing process should be analysed, which aims to obtain the best solution in terms of cost, manufacturing technology and design solution. In the stage of manufacturing of the cylinder, it is of particular importance to obtaining the design features responsible for the technical parameters of the cylinder. Tests of plastic cylinders performed in expanded range are seemed justified, due to the design material which is used. As a preliminary verification, FEM simulation tests are performed. The final verification is carried out through experimental tests, the course of which was determined on the basis of the ISO standard (evaluation of operation correctness and leakages appearance) and extended to tests of efficiency.
The formulation of the challenges is the basis for an effective process of designing hydraulic cylinders made of plastics. As a result, this led to receiving a type of series of such cylinders..

Keywords. hydraulic cylinders, plastics, methodology of design

1. INTRODUCTION

The use of plastics and plastic composites in design of hydraulic components and systems is becoming a new direction on the fluid power. The analysis of the literature shows that a lot of attention is paid to composite cylinders. In works [1, 2] the issue of design and experimental tests of composite cylinders built of carbon fiber and epoxy resin is discussed. In [3] on the other hand, composite cylinder with a multilayer coating is shown, which is characterized by increased strength in relation to the single layer cylinder. The problem of winding and forming of layers on a metal tube is presented in [4]. This knowledge was applied to the design of the composite cylinder [5]. Composite cylinders have lower mass than metal cylinders, they are also durable and can operate under working pressure up to p=20 MPa.

An alternative for composite materials is using of pure plastic materials without composite additives [6]. Prototypes of basic hydraulic elements made of Polyoxymethylene (POM) were presented, which are: gear pump [7], gerotor pump [8], maximum valve and on-off valve [9] as well as cylinder. It was shown that these elements arranged in a hydraulic system are able to operate with the working pressure p = 5 MPa. Particular attention was paid to cylinders made of plastics, for which the design principles and experimental research are presented in [10, 11]. The benefits of using cylinders made of plastics are following:

- cylinders made of plastics, same as composite ones, have lower mass than metal cylinders;
- plastic materials used in their production are cheap and can be recycled;
- cheap manufacturing methods (injection molding) can be used;
- cylinders made of plastics can operate with various working fluids (oil, water) and in aggressive environments.

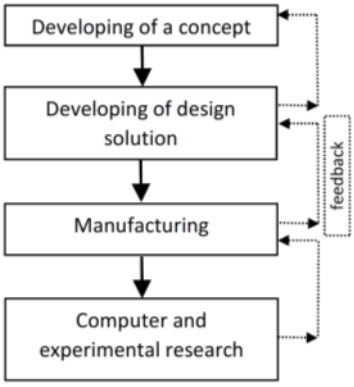

Figure 1.1. Scheme of the process of designing cylinders made of plastics.

After carrying out the process of designing cylinders made of plastics according to scheme shown on fig.1.1, it was found that at each of its stages (concept, design, manufacturing, testing) new challenges arise, which are different from those that occur in case of designing of metal cylinders.

2. CONCEPT

The main challenge that must be met is determination of the general structure of the cylinder and its basic parameters as well as its area of application and operating conditions.

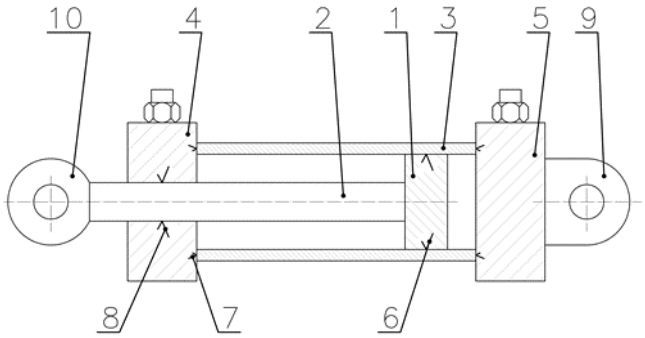

Figure 2.1. Scheme of the basic design concept of cylinder made of plastics.

The general structure of the cylinder is already determined and results from the necessity to implement the principle of reciprocating motion. As shown in Fig. 2.1, it must include a piston (1) with a piston rod (2) that slide inside the cylinder tube (3) to reciprocate. The tube is closed on both sides with cups (4; 5). Because these elements are planned to be made of plastic, which is much more deformable than metal, sealing of individual cylinder nodes becomes a challenge. This applies to the piston seal (6), that cooperates with the cylinder tube (3) which is deforming, the seal between the piston rod and the gland cup (8) and the seal between the tube and the cups (7).

Although plastics are planned to be main materials used in design of cylinders, it should be allowed to use metal for the design material of selected parts that are exposed to the highest loads (stresses). Such approval intends to extend the scope of the cylinders operating parameters, which would be significantly narrowed if only plastics elements would be allowed in design. For example, because of the buckling force, it is advantageous to use metal for the piston rod, thanks to what the entire structure can be loaded with a greater working force. Another example are hydraulic connectors or standard-based mounting parts, which allows the cylinder to be easily installed. However, the share of metal elements should be limited, to enable obtaining biggest advantages of using plastic materials in the structure. To talk about a cylinder made of plastic, it must be the dominant material. Therefore, the share of metal in the structure of the cylinder should not exceed 50% its volume, and the mass of metal parts should not exceed 50% of the mass of its structure. The method of joining metal parts with plastic parts should also be considered.

At the present stage of development, the use of plastic materials, which are less durable than metal, forces limitations for the parameters of cylinders. It is assumed that the cylinders should operate in the range of lower nominal pressures $p_n \leq 6.3$ MPa and maximum (overload) pressures $p_{max} \leq 10$ MPa. The geometrical parameters of cylinders made of plastics should also be narrowed. Plastic cylinder diameters should be less than $d \leq 63$ mm. The possible stroke of plastic cylinders is strongly related to the method of their mounting. It is estimated that the typical method of assembly allows for safe use of cylinders with a stroke $L \leq 250$ mm.

For cylinders made of plastics with a greater stroke, special mounting methods should be provided to increase the stiffness of their structure.

It is also assumed that requirements about life of cylinders made of plastics should be less stringent than for metal cylinders.

It is assumed that cylinders made of plastics could be intended for general applications in low-pressure hydraulic oil systems, where working conditions are not harsh, in particular temperatures are below 50°C.

Plastic cylinders can also be used in water hydraulic systems, which is particularly beneficial for the food, pharmaceutical and medical industries as well for environmental reasons. Cylinders made of plastics can also work in chemically aggressive and corrosive environments as well as environments with electrical voltage.

Finally, the economic and environmental challenges are different. Cylinders made of plastics should be cheap in order to be competitive with metal cylinders. This can be achieved by using cheap, easy available plastics and by adapting methods of manufacturing. An additional positive effect of the use of plastics is that some of them can be recycled and processed many times. As a result of recycling, the same material can therefore be used many times, which reduces costs and environmental pollution.

3. TECHNICAL DESIGN

3.1 Material selection

The fundamental challenge for developing of the technical design is selection of plastic material. The material intended for the design material of the cylinder should meet following criteria:

- mechanical strength (yield point R_e, Young's modulus E) possibly high stability of dimensions which is independent of temperature change (small shrinkage S, small thermal elongation W, low water absorption A);
- possibility to process material by machining and injection molding;
- high availability on the market in form of semi-finished products at the lowest possible price;
- low friction coefficient η in cooperation with seals.

To carry out design work, it is necessary to determine the allowable stresses in the plastic martial. As shown in the strain -stress diagram on fig.3.1, plastic does not have a clear yield point. At the same time, the figure shows that plastics subjected to alternate loading and unloading may not return to its original dimensions, which results from its hysteresis and residual strain. Moreover, fig.3.1 shows that the material strength is connected with the temperature T. Its increase $T_2>T_1$ reduces the strength properties of the material [12, 13]. The mentioned factors should be taken into account while determining the allowable stress level σ_{allow} for plastic material. The easiest way is to assume that the allowable stress σ_{allow} should be equal to the yield stress R_e given by the manufacturer, i.e. $\sigma_{allow}= R_e$.

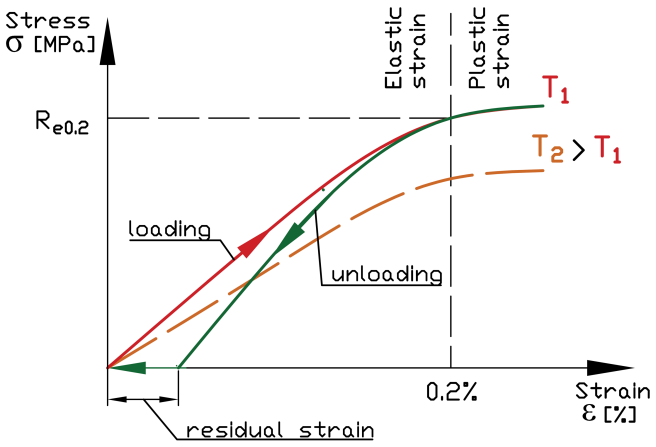

Figure 3.2. Schematic diagram of strain-stress dependences in plastic materials.

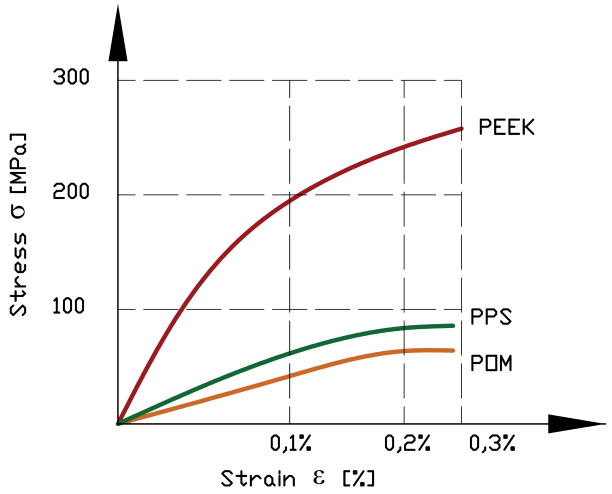

Figure 3.2. Stress-strain diagram for chosen plastic materials: Polyetheretherketone (PEEK), Polyphenylsulfide (PPS) and Polyoxymethylene (POM).

The yield point can also be determined on the basis of own experimental research. The results of such tests for three chosen plastic materials Polyoxymethylene (POM), Polyphenylsulfide (PPS) and Polyetheretherketone (PEEK), are shown in fig. 3.2 in the form of a strain-stress diagram $\sigma=f(\varepsilon)$ [14]. The figure shows that PEEK has the highest strength, then PPS follows, and both are ahead POM in this matter. Own material research confirmed that these plastics do not have a clear yield point. Therefore, the concept of proof stress $R_{0.2}$ was introduced, which is marked with a vertical line in Fig. 3.1. It separates the elastic range of deformations (left side of the diagram) from the plastic one (right side of the diagram). Below proof strength deformations are proportional to loads and it is assumed that after unloading the material does not show significant residual strains. The diagram shows that the strength of the tested plastics does not decrease immediately after exceeding the proof

strength. It can be concluded, that under certain conditions, plastics are able to withstand loads that cause stresses higher than those determined by the proof strength. However, above the proof strength behaviour of the material is difficult to predict, because deformations are not proportional to loads. A positive aspect of these observations is that, when allowable stresses are equated with the proof strength, there remain some safety range, within which the material will not be overloaded.

In order to increase the scope of safe use of plastic materials as design materials, it is possible to reduce allowable stress σ_{allow} by applying safety factors according to the dependence $\sigma_{allow}=R_{e0.2}/x$. In this way, the influence of alternate loading and unloading, as well as influence of temperature can also be taken into account.

The determination of allowable stress σ_{allow} is very important for strength calculations and verifying of plastic cylinders by simulations. The method of determining the permissible stresses should be adapted to the operating conditions and the purpose of developing a design solution. For example, if the cylinder is to operate in single work cycles with very long intermissions, and the material is not in contact with high temperatures, then $\sigma_{allow}= R_{e0.2}$ can be applied. In the same way it is recommended to set allowable stresses for prototypes or research models, where determining of the place and nature of possible changes in the structures are one of the reasons of their development. Then, such models and prototypes will better expose these phenomena during operation. If the priority is to develop a structure which is capable to work under high loads in frequently repeated cycles, as well as in contact with temperatures close to 50°C, it is proposed to use safety factors in the range x> 1

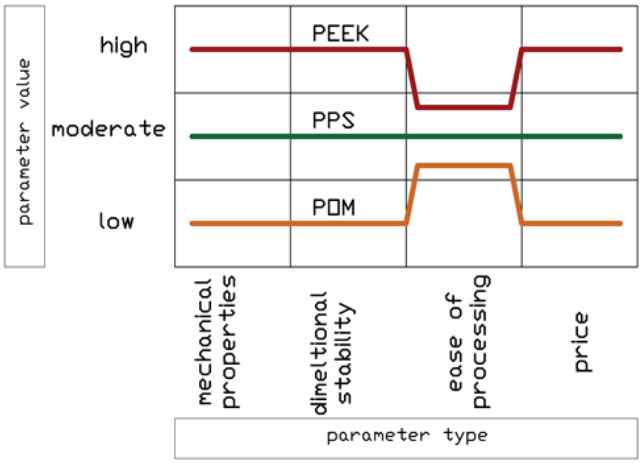

Figure 3.3. Comparison of chosen plastic materials properties: Polyetheretherketone (PEEK), Polyphenylsulfide (PPS) and Polyoxymethylene (POM)

Apart from the strength properties, other properties, which had been signaled at the beginning of this chapter, are considered on fig.3.3. for the selected plastics. Analyzing this scheme it can be noticed again, that PEEK has the best properties, then PPS follows, and both are ahead POM.

However, contrary to these assessments, it is recommended to use POM with sufficient strength and meeting the basic criteria. At the same time POM is easy available and cheap,

which is of great importance according to concept assumptions. It is proposed to treat POM as a base material, and any changes for material with higher strength parameters should be made as a development and improvement of verified structures.

3.2 Development of structural design

TABLE 3.1. TABLE OF EXEMPLARY PARTIAL SOLUTIONS CONCEPTS FOR ELABORATION OF STRUCTURAL DESIGNS FOR HYDRAULIC CYLINDERS MADE OF PLASTICS

Name of the part or design node	**Traditional design solutions**	**Progressive (innovative) solutions**
Tube	1.1 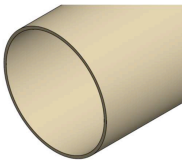	1.2 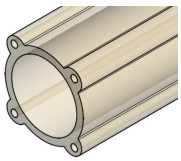
Piston	2.1 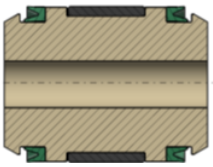	2.2 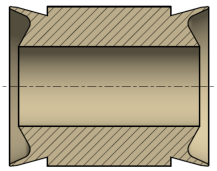
Piston rod	3.1 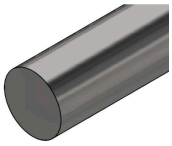	3.2 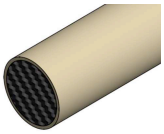
Cups	4.1 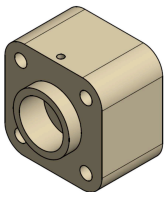	4.2 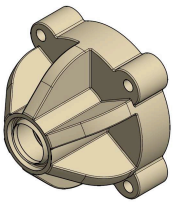
Mounting	5.1 	5.2 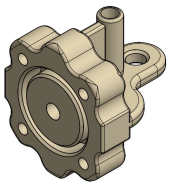

The general concept of the plastic cylinder formulated in chapter 2 should be transformed into a detailed structural concepts. This is done using table of generating design concepts for cylinder components, table 1. In the table two groups of partial solutions are presented, which are significantly different from each other. These groups have been given names of traditional solutions and progressive (innovative) solutions. In the group of traditional solutions there are:

- cylinder tube made of POM;
- divided piston made of POM assembled with U-shape sealing rings and guide ring;
- piston rod made of a steel rod;
- gland cup and bottom cup made of POM;
- mounting parts, tie rods, hydraulic connectors made of steel and assembled to the plastic cups.

In the group of progressive (innovative) solutions there are:

- cylinder tube with ribs, in which there are bores for tie rods;
- single- solid piston with built-in seals;
- piston rod in the form of a tube filled with a composite material;
- cups with a shape corresponding to the cylinder tube and integrated with the mounting elements.

Of course, it is possible to formulate many solutions of the entire structure through different combinations of presented traditional and progressive solutions, as well as generating completely new concepts of solutions. In summary, the process of developing a structural concepts should be carried out in the following steps: generating partial solutions, synthesis of partial solutions (concerning parts, design nodes and subassemblies) into concepts of entire structures, evaluation of the generated structural concepts and selection of one design for the entire cylinder.

Looking at design presented within traditional solutions, it can be noticed, that they are similar to those used in already proven structures of metal cylinders. However, progressive solutions (1.2- 4.2) are noticeably changed in relation to the metal cylinders. Progressive solutions provide new possibilities, but before their final implementation, additional design and research affords should be made to ensure their appropriate, high technical level, it concerns i.e. of piston integrated with built-in seals (2.2)

Technological and economic reasons do not clearly stand on the side of any solution. Traditional solutions can be realized with the use of prefabricated elements (pipes, rods) or ready seals. Conventional machining can be used to achieve such solutions. It is advantageous in the case of designing of model, prototype or unit production, because using traditional processing methods and universal machines, such as lathes or milling machines, allows for maintaining production costs at a level similar to typical metal elements. Some benefits are possible in terms of machining time, energy requirements and wear rate of the cutting tools because of significantly lower hardness and better machinability of the plastics.

On the other hand, in the case of progressive (innovative) solutions, due to the complex geometric shapes, it would be advisable to manufacture them by injection molding, with use of materials suited to this method. This creates the need to design and manufacture injection molds and high investment costs. Such solutions can be considered competitive when the investment costs are spread over many copies made with the use of the above-mentioned expensive injection molds.

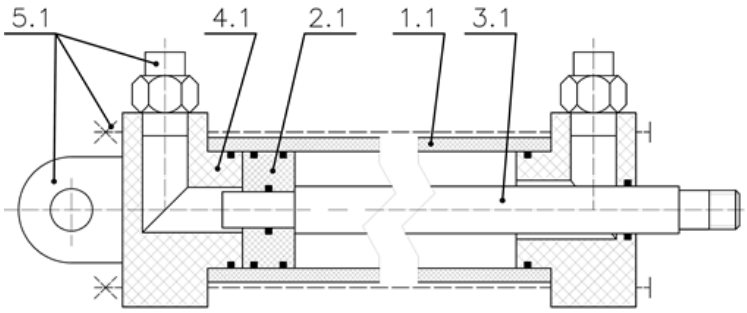

Figure 3.4. Synthesis of partial design solution into one structure of cylinder.

Taking into account presented criteria, a traditional solution was selected for a verification process of design methods of hydraulic cylinders made of plastics, by their implementation through practical application. The reason for such decision was the prototype production scale. Therefore, the subassemblies 1.1- 5.1 were synthesized into one plastic cylinder structure shown in Fig. 3.4.

In the next step, detailed structural design is developed. For this purpose, functional and strength calculations are carried out. Functional calculations concern internal diameter of tube *D*, piston rod diameter *d*, speed of piston (rod) movement, force at the end of the rod, etc. Strength calculations concern thickness of tubes wall *g*, strength of the connections between elements and buckling. The nature of these calculations is considered as quite typical. As a significant innovation may be recognized the use of previously specified allowable stress, which is determined according to the guidelines presented in chapter 3 section 3.1.

As a result of meeting design challenges and synthesizing partial solutions into design solution of whole structure, a plastic cylinder is created.

4. MANUFACTURING

The production of plastic elements of hydraulic cylinders is a serious challenge in the design process and an important stage in the verification of the adopted design assumptions. Thanks to the obtaining of the real object, verification can be carried out in relation to:

- design process correctness
- correctness of standardized parts selection
- manufacturing technology adopted for non-standard parts
- manufacturing quality of parts

There are two basic methods of manufacturing cylinders made of plastics, which are the machining method and the injection molding method.

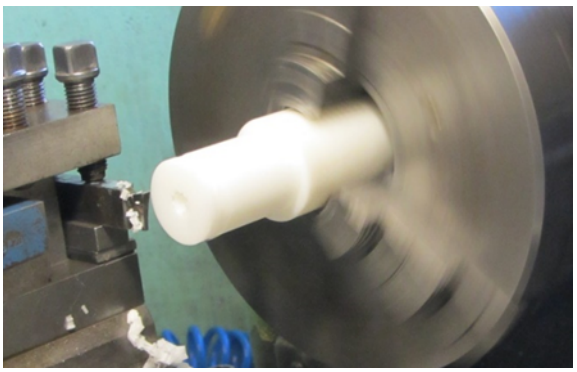

Figure 4.1. Manufacturing of the piston made of plastic (POM) by machining on lathe.

The machining method is more advantageous in the case of small-scale, unit or even prototype production. Cheap and easily available semi-finished products can be used in these method, offered in various dimensional versions in the form of pipes, plates, blocks or rods. The semi-products are machined to obtain the final part geometry. The selection of the appropriate dimensional version and the correct shape of the semi-products for specific parts, allows for reducing of the number of machining operations and shortening of the production time. Example of manufacturing of the piston from plastic (POM) rod by machining on lathe is shown in fig. 4.1. With the use of machining, technological challenges arise. Plastic materials behave slightly different than metals when machined. Typical is a slight deformation (deflection) of the material under the pressure of the tool, as well as change in the dimensions of the material under the influence of heat generated during machining. Due to these phenomena, the manufacturer may not be able to obtain the correct precision on the first attempt. Therefore, it is good practice to perform trial machining operations and adjust the machining parameters to the behavior of the material during its course. Material samples for such trial operations should be provided.

In case of the injection molding method, the plastic elements of the cylinders are shaped in the molds by pressing into them plastic in a liquid form and then solidifying. Therefore, precision of the manufactured elements depends on precision of the molds, the shape of which plastic material acquires. In the process of designing molds, many factors must be taken into account, such as the way the material flow, the speed of solidification of the material, etc. The production of precise injection molds is time-consuming and costly. This makes it a separate issue that requires a lot of specialized knowledge and experience. The injection molded parts themselves should also be designed specifically for this method, e.g. walls of the parts should have low thickness. Thanks to this method, however, any shape can be relatively obtained, which allows to gain large design advantages, which cannot be achieved in cylinders made of metal or some composites.

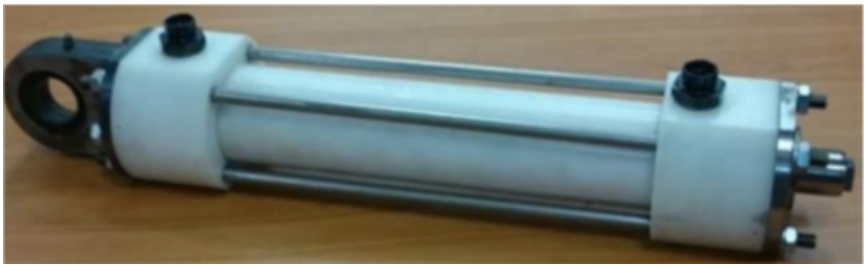

Figure 4.2. Manufacturing of the piston made of plastic (POM) by machining on lathe.

Using the first method, a prototype cylinder of internal diameter Ø=50 mm was made of POM.. Prototype is shown in Fig.4.2. A very important stage of the process is precise machining of the inner surface of the cylinders tube. The process should ensure the precision of the diameter dimension +0.075mm; circularity of the hole up to 0.05 mm; straightness along the tube axis 0.1 mm and surface roughness as specified by the manufacturer of the seals, usually within the limits R_a<0.3. In addition, to ensure the long life of the seal, the key is to obtain right direction of the machining marks, which should be arranged along the axis of the cylinder. It is recommended to do this by preparing special tools, which allows for material cutting in the axial direction, as well as positioning the tube vertically during machining.

5. VERIFICATION- COMPUTER AND EXPERIMENTAL RESEARCH

5.1 Computer Finith Element Method simulations

Because cylinder is made of plastic materials, the strength of which is lower than that of metals, the nature and values of stresses and strains in its structure should be examined.

This challenge is realized with the use of Finite Element Method. Because of the fact, that a computer is used for the FEM simulation, it can be carried out in parallel or before the cylinder manufacturing stage. In the algorithm, however, the simulation stage has been placed in the way that clearly indicate the connection between this stage and the verification of a specific structure developed at the design stage. The geometrical model is therefore developed on the basis of the adopted structural design solution (cylinder Ø50 in Fig. 3.4).

It is assumed that the selected plastic material will work in the range of elastic stresses, below the allowable values set by the constructor on the basis of the guidelines discussed in chapter 3 section 3.1.

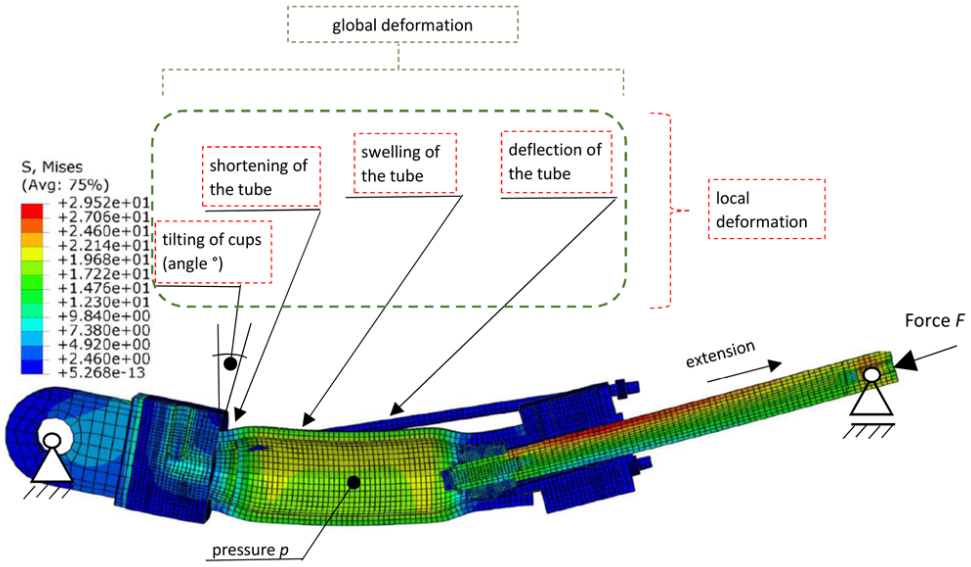

Figure 5.1. Schematic description of deformation in the structure of cylinder made of plastics, which is fixed in the bottom cup and at the end of piston rod.

On fig.5.1 the mechanism of the formation of plastic cylinder deformations is analyzed. The cylinder is fixed in the bottom cover and at the end of the piston rod, which corresponds to the often used method of mounting in machines and devices. At the same time, it is the most unfavorable way of fixing the cylinder. During the extension, under the load of pressure p and force F, the so-called local deformation of the cylinder subassemblies appears, i.e. tilting of the cups as well as swelling, shortening and deflection of the tube. The combination of local deformations results in global deformations of the actuator, in which the deflection and swelling of the actuator are decisive. Their value depends on the material, geometry (e.g. length, diameter, wall thickness) and loads (pressure p and force F).

By analyzing local deformations, behavior of the cylinder during operating can be predicted. Swelling of the cylinder tube walls and a change of its internal diameter can cause internal leakage and decrease of efficiency. This can be prevented by selecting seals which are able to adapt and compensate for changes in inside diameter. Strains analysis allow for prediction of the risk of cylinder buckling. The image of cylinder deformation with the extended piston rod indicates on a clear buckling. Such interpretation supplement the classic buckling calculations.

Apart strain maps, also stress maps in the cylinders elements are obtained. As a standard, their result and values are analyzed and compared with the allowable stresses, which are set by the constructor for the selected plastic material used to for the cylinder. Exceeding the allowable stress is a signal to redesign the overloaded cylinders subassembly or cylinders element.

5.2 Experimental research

The final challenge in the process of designing hydraulic cylinders made of plastics is experimental research, which determines definite judgement about the correctness of structural design of the cylinder and its work.

In the case of metal cylinders, tests according to the ISO 10100:2001 standard are carried out, which cylinder must pass in order to be allow to use. They consist of test for leakage at low pressure p_{min}, piston seal leakage test at p_{nom}, and proof/external leakage test at overload pressure p_{max}. These tests are also performed for plastic cylinders, but in the case of such significant differences in design materials, there is a need for verification in a wider scope. Therefore, additional trails are recommended, where tested are:

- piston rod movement speed during extension and retraction, without and under load
- influence of using plastic material on achieved technical parameters
- ability to long-term operating
- behavior of structures of cylinders made of plastics under load (global deformations)

The constant speed of extension and retraction as well as high efficiency, prove the correct cooperation of the piston with the tube and the piston rod with the gland cup. It also indicates that movement resistances in these design nodes are low. Low resistances of motion are also information that the structure remains stable and there are no significant transverse forces that could lead to increase of such resistances. At the same time, the high efficiency of the cylinder indicates that there is no internal leakage between bottom chamber (under-piston chamber) and gland chamber (over-piston chamber).

Tests of long-term operation, depending on the research capabilities and assumptions on working conditions of the cylinder, may cover the range from 1000 to 1000,000 cycles under load. As a result of its condition, it is possible to determine the life of plastic cylinders, but most of all, it confirms the ability to repeat the cycle of work many times, therefore, eventual suitability for actual use in mechanical systems. It should be taken into account, that plastic cylinders will not be able to last the same long period of operation as metal cylinders. However, this does not disqualify plastic cylinders, as it is assumed that they should operate in a shorter life period and with less work intensity.

A special challenge is experimental research of deformation of cylinders made of plastics. Various test methods can be used to determine deformation, such as strain gauge method, tests with displacement transducers or optical research based on image analysis. The accuracy of the obtained results may depend of the chosen method. However, neither method should be negated because hydraulic cylinders made of plastics are new technical objects. Characteristic aspect of such new technical objects is small amount of information about behavior of their structures. Moreover, the hysteresis of the strength parameters of plastic materials is the reason why their behavior as design materials remains unexplored. Research on the behavior of structures of cylinders made of plastics is therefore of great importance, both in relation to the methods of designing such objects, and the plastics themselves as design materials. Even examining the very nature of deformations without establishing precise values may be important in the context of optimization.

Examples of test results for cylinder deformation are shown in Fig. 5.2. Fig. 5.2. a shows the global displacements measured on the surface of the cylinders tube along its length. Fig. 5.2. b shows schematically the deformed tube superposed on the background of the non-deformed tube. Both figures show that the displacement along the entire length of the tube has positive values. This means that deformation of the tube walls caused by its swelling is greater than its deflection, and consequently the global displacements are positive.

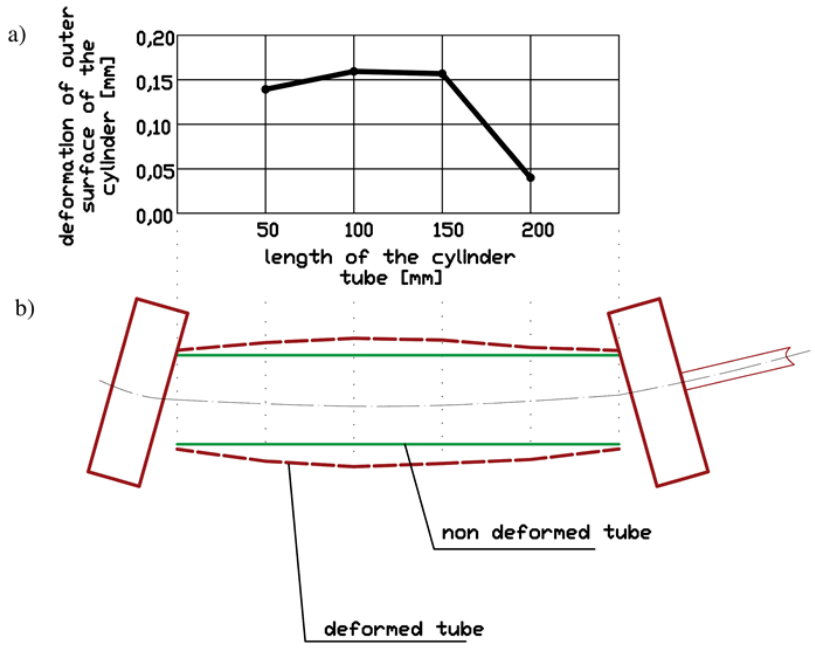

Figure 5.2. Results of tests of deformation performed for prototype of hydraulic cylinder made of plastic: a) values of deformation (displacement) of the other surface of tube; b) schematic representation of global deformation of the prototype.

6. CONCLUSIONS

The use of plastic in the designing of hydraulic cylinders creates new challenges at every stage of the process.

The fundamental challenge is selection of material which has an impact on design, technology, operation and application area. Plastic has lower strength and dimensional stability than metal. Pulsation of loads and an increase of temperature causes decrease of strength, as well as dimensions changes of the plastic parts of the cylinder. Therefore, plastic hydraulic cylinders should have a narrowed range of geometric dimensions (diameter d <63 mm and stroke S <250) and work with lower nominal operating pressure values (p <6.3 MPa) compared to metal cylinders. It is likely that these limitations will decrease, and recommended ranges will become wider with development of cylinders made of plastics. Therefore, the issue of the selection of plastic for design material should not remain a closed area, but it should be updated and supplemented.

The choice of plastic for design material cause arising of design challenges, which are also opportunities for new, innovative design solutions. This applies, among others, to pistons and cups with built-in seals, cups integrated with mounting elements (reducing the number of parts), ribbing of cups and cylinder tubes (increasing the stiffness of the structure).

The use of plastic creates challenges connected with manufacturing. In case of machining, the challenge is to determine machining parameters and adapt machining methods. An example could be a cylinder tube. For the correct cooperation of the sleeve with the piston

seal, it is crucial to obtain a high-quality inner surface of tube and an appropriate orientation of the machining marks. The greater is stroke of the cylinder, the greater is length of the sleeve and the more difficult it is to ensure accuracy. From the other hand, the injection molding method can be expensive due to the need to making the molds

The life of cylinders made of plastics is also a serious challenge. This life may be shorter than that of metal cylinders. At the same time, however, there are aspects encouraging the development of plastic cylinders, such as: lower mass, resistance to aggressive conditions or the ability to work with various working media, including water and chemical liquids, as well as the chance to achieve low costs in production on large-scale .

Finally, many plastics can be recycled, which is very beneficial given the increasing importance of environmental protection.

7. REFERENCES

[1] L. Solazzi, "Design and experimental tests on hydraulic actuator made of composite material", Composite Structures, Volume 232, 2020

[2] S. Mantovani, "Feasibility Analysis of a Double-Acting Composite Cylinder in High-Pressure Loading Conditions for Fluid Power Applications", Applied Sciences, 2020

[3] L. Solazzi, "Stress variability in multilayer composite hydraulic cylinder", Composite Structures, Volume 259, 2021

[4] W. Błażejewski, Composite pressure vessels reinforced with fibers according to mosaic patterns, Oficyna Wydawnicza Politechniki Wrocławskiej, Wrocław 2013

[5] Lubecki, M., Stosiak, M., Gazińska, M, "Numerical and Experimental Analysis of the Base of a Composite Hydraulic Cylinder Made of PET", Lecture Notes in Mechanical Engineering, Volume 24, Springer, cop. 2021, p. 396-405

[6] J. Stryczek "Plastics- a new trend in design of fluid power elements and systems." Lecture Notes in Mechanical Engineering, Volume 24, Springer, cop. 2021, p 440-452.

[7] L.Rodionov, J. Stryczek, P. Rekadze, P. Stryczek, S. Gafurov, A.V. Prokofiev, E. Shakhmatov, "Challenges in design process of gear micropump from plastics", Archives of Civil and Mechanical Engineering, vol. 21, art. 34, 2021, p.1-14

[8] J. Krawczyk, J. Stryczek, "Design and Experimental Research of a Plastic Gerotor Pump", 2018 Global Fluid Power Society PhD Symposium (GFPS), 18-20 July 2018, Samara, Russia, [Piscataway, NJ] : IEEE, 2018

[9] M. Banaś, P. Antoniak, L. Marciniak, J. Stryczek," Visualization of flow phenomena in hydraulic throttle valves of plastics". W: The 14th International Conference on Vibration Engineering and Technology of Machinery (VETOMAC XIV), Lisbon, Portugal, September 10-13, 2018 / eds. N. Maia and Z. Dimitrovová. [Les Ulis : EDP Sciences], 2018. art. 19001, s. 1-6.

[10] P. Stryczek, F. W. Przystupa, M. Banaś, „Design and research on a hydraulic cylinder with plastic components.", Proceedings of ASME 2016 9th FPNI Ph.D. Symposium on Fluid Power, Florianópolis, SC, Brazil, October 26-28, 2016. [New York] : ASME, cop. 2016.

[11] P. Stryczek, F. W. Przystupa, M. Banaś, "Research on series of hydraulic cylinders made of plastics", 2018 Global Fluid Power Society PhD Symposium (GFPS), 18-20 July 2018, Samara, Russia, [Piscataway, NJ] : IEEE, 2018

[12] A. Ptak, P. Tarciak, W. Wieleba, ”Effect of Temperature on the Tribological Properties of Selected Thermoplastic Materials Cooperating with Aluminium Alloy”, Materials. 2021, vol. 14, nr 23, art. 7318, p. 1-14, 2021
[13] M. H. Kujawa, P. Kowalewski, W. Wieleba The influence of deformation under tension on some mechanical and tribological properties of high-density polyethylene. Polymers. 2019, vol. 11, nr 9, art. 1429, p. 1-17.
[14] K. Biernacki, “New construction of cycloidal gear unit made of plastics”, Proceedings of the Institution of Mechanical Engineers. Part C, Journal of Mechanical Engineering Science. 2021, vol. 235, nr 5, p. 800-811

Biographies

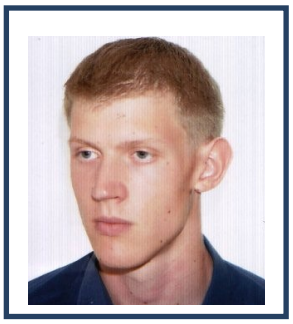

Piotr Stryczek is bound with Wroclaw University of Science and Technology, where he received engineering degree in 2012, master degree in 2014, doctorate degree in 2022, and he continues he's professional work as a lecturer and researcher. His research areas include methodology of designing, fluid power and especially use of plastics for designing fluid power elements. He is an author or co-author of 21 scientific works and he had opportunity to serve as a reviewer for journals and conferences.

Identifying The Future Research Trend for Using Speed-Controlled Hydraulic Cylinders in Offshore Applications through Literature Survey

1st Wei Zhao, 2nd Morten Kjeld Ebbesen, 3rd Torben Ole Andersen

University of Agder, Grimstad, Norway, wei.zhao@uia.no

University of Agder, Grimstad, Norway, morten.k.ebbesen@uia.no

Aalborg University, Aalborg, Denmark, toa@energy.aau.dk

Abstract.

The speed-controlled hydraulic cylinder enhances energy efficiency by removing the control valve throttling, lone pipeline, and HPU losses. Furthermore, it offers energy recovery capability, enables plug-and-play installation, and reduces maintenance. Therefore, it is a promising alternative to the valve-controlled cylinder. This paper surveys the challenges and issues of using the speed-controlled cylinder in offshore applications from the literature and suggests future research trends.

Firstly, the commercial solutions and research done on speed- controlled cylinders are reviewed. The review covers both circuit designs and control algorithms. Speed-controlled cylinders found in the literature are sorted into several classes. Secondly, the research target is selected, and selection criteria are described. Thirdly, the future research trend is discussed. Finally, it is concluded that more research that focuses on high power output levels and system-level (multi-cylinder systems) is needed to show if the technology is feasible for the offshore industry.

Keywords. pump-controlled cylinders, speed-controlled cylinders, linear hydraulic actuation, offshore cranes.

1. INTRODUCTION

As a heavy industry, offshore activities usually involve many high-force operations, such as heavy lifting and pushing, which inevitably require hydraulic cylinders. The valve-controlled hydraulic cylinder (VCC), developed for almost 170 years [1], is still dominating the market and the industry. However, the VCC has a significant shortcoming: poor energy efficiency due to control valve throttling, e.g., a study on the energy analysis of a load-sensing (LS) compact excavator has shown that 35 % of the total system energy is consumed

in control valves [2]. Furthermore, the VCC cannot offer energy recuperation capability under overrunning load. Although new designs, such as the independent metering technology, can significantly increase the system's energy efficiency, they cannot fundamentally remove the throttling losses from the system. In addition to throttling losses, offshore VCC systems experience the downside of a central HPU and long pipelines increasing energy losses and the risk of environmental pollution. Therefore, new user-friendly and environment-friendly technologies are needed to remove the throttle loss, offer energy recovery, and keep a similar dynamic performance as the VCC. The speed-controlled hydraulic cylinder (SCC) is one of these technologies.

As a promising technology to replace the VCC, the SCC enhances energy efficiency by removing the control valve throttling, lone pipeline, and HPU losses. Furthermore, it offers energy recovery capability, enables plug-and-play installation, and reduces maintenance. The SCC is a sub-branch of the pump-controlled cylinder (PCC). A simplified diagram of the PCC is shown in Fig. 1. In a PCC, One or two ports of the cylinder are connected to hydraulic pump(s) and the reservoir through auxiliary valves; auxiliaries valves are used for safety reasons, compensating for the differential flow rates, and changing flow directions; an accumulator or an open tank works as the reservoir.

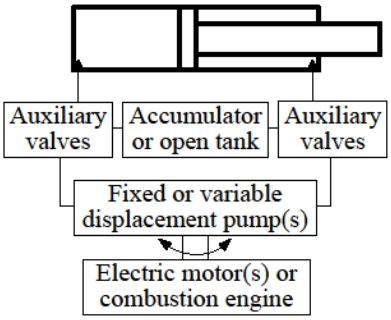

Figure 1. Structure of a PCC.

In a PCC, when the oil in the rod side of the cylinder can flow to the piston side without passing through the reservoir, it is called a closed-circuit PCC. Otherwise, it is called an open-circuit PCC. In PCCs, controlling the cylinder motion is equivalent to controlling the pump's flow rate. There are two ways to control the pump's flow rate in a PCC: using the variable-displacement pump(s) driven by the constant-speed prime mover(s), which can be called the displacement-controlled cylinder (DCC); using the fixed-displacement pump(s) driven by the variable-speed prime mover(s), which can be called the speed-controlled cylinder (SCC).

The pump-controlled technology initially started from displacement-controlled symmetrical actuators. It was firstly used for controlling super high power hydraulic motors in the early times [3]. Then it was used to control a double rod cylinder [4]. The single-rod DCC was intensively researched and developed around the 2000s but almost exclusively for non-road mobile machinery because an internal combustion engine is often used as the only prime mover [5]. However, DCCs have some shortcomings compared with SCCs, such as variable-displacement pumps are more expensive and less efficient than fixed-displacement pumps under partial load [6], [11], [25]; the prime mover in idling mode causes energy losses, noise,

and extra heat [6]; the swashplate control systems and external low-pressure source undermine the system compactness and increase the energy losses. Therefore, academia and industry are paying less and less attention to DCCs and putting more weight on SCCs [7].

The electrification trend of hydraulic systems and the development of electric servo motors enhanced the development of SCC. Historically, SCCs emerged in the aircraft industry for primary flight control in the early 1990s driven by the concept of power-by-wire [8], [9]. Nowadays, SCCs are widely used in different industries due to their high energy efficiency, compact structure, plug-and-play installation, reduced maintenance, low noise level, and control by frequency converters instead of control valves [7], [8], [10], [11].

Electro-mechanical cylinders (EMCs), another drive technology encouraged by electrification, have some advantages similar to SCCs, such as a similar efficiency range, high degree of user-friendliness and compact design [12]. However, SCCs are still superior to EMCs in several features. SCCs generate higher forces, have better acceleration performance, absorb more impacts, and can be operated at higher speeds [12]. For heavy operations, SCCs are more energy-efficient, have lower weight and cost, and are easier to complete with security features [11]. SCCs have higher continuous power capability, less installed electric power, longer expected service life, and less overall mass [13].

2. STATE OF THE ART OF SCC

In this section, the state of the art of SCCs is categorized into five parts: SCC architectures, SCC controls, SCC thermal analysis, other SCC topics, and identified research gaps.

2.1. SCC Architectures

In terms of the number of electric motors and hydraulic pumps used, SCC architectures can be classified into four groups: one-motor-one-pump (1M1P), one-motor-two-pumps (1M2P), one-motor-three-pumps (1M3P), and two-motors-two-pumps (2M2P) SCCs. Simplified SCC diagrams within these four groups are shown in Fig. 2.

2.1.1. 1M1P SCC

The 1M1P SCC was initially developed for driving double-rod cylinders used in the aerospace industry [9] but has since then expanded into many other industries [7]. The advantage of double-rod SCCs is that there are no differential flow rates in the circuit. Therefore, the hydraulic circuit is simpler. Other research works on double-rod SCCs can be found: In [14], a double-rod SCC was tested and evaluated on the F-18 research aircraft; In [15], the deadband issue of a double-rod SCC was investigated; In [16], double-rod SCCs were implemented on a train as tilt actuators; In [17], A double-rod SCC with a power regulator was proposed.

80 % of cylinders used in the industry are single-rod cylinders, especially in heavy industries [18]. Therefore, most works on SCCs are about single-rod SCCs. An in-depth numerical and experimental comparison between a SCC and a load-sensing VCC in motion control and energy efficiency aspects was presented in [19], [20]. The SCC has significantly better control performance, such as 75 % shorter settling time, 61 % less overshoot, 66 % better position tracking, reduction of pressure oscillations, and remarkably consumed 62 % less energy.

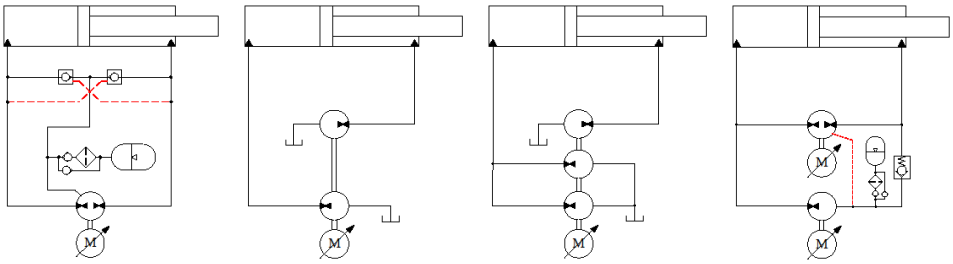

(a) Open 1M1P SCC. (b) Open 1M2P SCC. (c) Open 1M2P SCC. (d) Open 2M2P SCC.

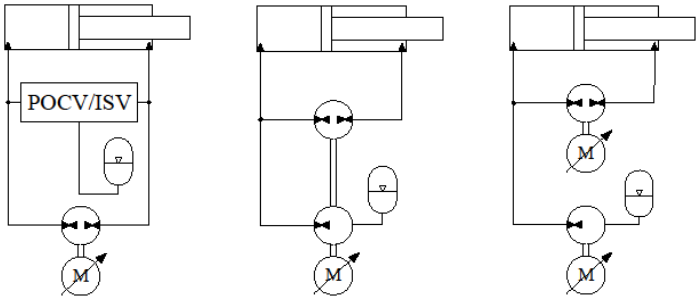

(e) Close 1M1P SCC. (f) Close 1M2P SCC. (g) Close 2M2P SCC.

Figure 2. SCC structures

System-level implementation is important for investigating the all-around performance of SCCs. A system-level simulation study of implementing three 1M1P SCCs on a pipe racking machine was shown in [21]. Simulation results demonstrated that the new SCC system consumed 83.4 % less energy than the VCC system if the energy recuperation function was considered. Another system-level comparative research of implementing six 1M1P SCCs on an excavator was presented in [22]. The simulation showed maximum 75.1 % energy saved by SCCs, and experimental results showed 47.8 % energy saved by SCCs compared with VCCs.

An inverse shuttle valve (ISV) or two pilot-operated check valves (POCV) are often used to compensate for the differential flow rates in single-rod SCCs. However, these two methods suffer from mode oscillation under certain operating conditions. Mode oscillation in an SCC using an ISV was analysed in [10]. The author presented a new approach to describe the dependence between the inertial load (the acceleration rate) and the occurrence of mode oscillation. In the study [23], it was revealed that a partially open ISV is required in an unstable load pressure region during actuator retracting to prevent mode oscillation. Therefore, an elaborate underlapped ISV was proposed and validated by numerical and experimental tests. Instead of using two POCVs, two digital on/off valves were proposed to suppress mode oscillation when compensating for the differential flow rates in an SCC [24].

Standard hydraulic pumps are designed to run above a minimum speed because it is difficult to provide a durable lubrication film between the working parts inside the pump [6], [9]. However, hydraulic pumps used in SCCs may be operated at high pressure and low or nearly zero speed. A closed- circuit SCC using a 2/2 proportional valve as a bypass valve (BPV) was proposed to address the low-speed challenge and compared with its open-circuit

counterpart in [25]. The BPV connects two ports of the differential cylinder and increases the pump speed when the cylinder is moving slowly. Simulation results showed that the BPV undermined the two systems' energy efficiency in low-speed working modes. The open-circuit SCC has higher energy efficiency than the closed- circuit counterpart because the two-quadrant pump used in the open-circuit SCC has higher efficiencies than the four-quadrant pump used in the closed-circuit SCC. Furthermore, both architectures could regenerate up to 81.8 % of the actuator energy under overrunning load and achieve an energy efficiency level of 84.7 % [25].

2.1.2. 1M2P SCC

A closed-circuit 1M2P SCC with an accumulator on each side of the cylinder was implemented on a modern flight training simulator [26]. The calculation results and experimental measurements showed that the power consumption was significantly reduced from 45 kW to 5 kW while retaining the same dynamic performance as the VCC. This circuit design requires the displacement volume ratio of the pumps to match the piston area ratio of the cylinder [26].

An open-circuit 1M2P SCC design was proposed and analysed in [27]. Experiment results revealed that the retracting efficiency is low due to no energy recuperation function and the mismatch between pumps' size and the cylinder area ratio. To investigate the energy efficiency of this 1M2P SCC at the system level, a simulation study of implementing three 1M2P SCCs on an excavator with digital on/off valves for load-holding was presented in [28]. Simulation results showed that the overall efficiency of this SCC excavator could achieve 73.3 %, which is much higher than the VCC excavator [28].

An open-circuit 1M2P SCC, which incorporates an anti- cavitation system and two proportional valves used for bleeding off the excessive pressure was modelled, analysed, and experimentally verified in [29]. Experimental results demonstrated that the proposed SCC could maintain a non-load carrying pressure of 25 bar which can secure a satisfactory dynamic performance. The simulation study [30] proposed six different SCCs (four 1M2P and two 1M1P) with self- locking functions. The pressure levels could also be controlled in these new architectures but introduced a delay-like issue and excessive power consumption in static load carrying situations. Furthermore, the proposed SCCs cannot recuperate energy. Low speed and high load working conditions of SCCs were considered in [31], where a proportional bleed-off was introduced to increase the shaft speed when the cylinder speed is running low.

Implementing one isolated 1M2P SCC to every cylinder is not the most feasible idea concerning efficiency and the system flexibility [32]. Three SCC networks were designed and numerically implemented on a knuckle boom crane. Simulations showed that proposed drive networks may improve the energy efficiency and control performance compared with isolated 1M2P SCCs [32].

2.1.3. 1M3P SCC

Based on the 1M2P SCC in [29], a redesigned 1M3P SCC was proposed in [33]. In this 1M3P SCC, the cylinder area and pump displacement ratios were deliberately mismatched to cause pressure build-up or cavitation in the return chamber. The third gear pump supplies

one- way flow to avoid the caused cavitation. Simulation results showed that this redesigned 1M3P SCC has a similar tracking performance as a VCC, but much higher energy efficiency [33]. Later, an in-depth controller design of this over-actuated 1M3P SCC was proposed in [34].

2.1.4. 2M2P SCC

The investigation of applying closed- circuit 2M2P SCCs on plastic injection moulding machines can be found in [6], [35]. Furthermore, the study [35] reported two advantages of the closed-circuit 2M2P SCCs: the insensitivity of cylinder velocity to load pressure change and the capability of amplifying the load pressure by pump revolution. A VCC, a closed-circuit 2M2P SCC, and an open-circuit 2M2P SCC were numerically compared in energy efficiency in [36]. Simulation results demonstrated that the two proposed SCCs have much higher energy efficiency than the VCC. Moreover, the closed-circuit 2M2P SCC is more efficient, more cost- effective, and requires a smaller reservoir than the open-circuit one. A 2M2P SCC with load-holding functions was proposed and investigated in [37]. Simulation results demonstrated good performances in motion control, pressure level control, and load-holding.

2.2. SCC Controls

SCCs are characterized by low system damping, leading to mechanical structure oscillations. This shortcoming can be addressed by adding active damping via either pressure or acceleration feedback. These two approaches were implemented in a 1M1P SCC driving robotic manipulators [38]. Simulation results demonstrated that both approaches could greatly improve the system damping. Research on pressure feedback can also be found in [39].

When introducing more control elements into SCCs, such as extra electric motors and hydraulic pumps, the system output power is increased, and the pressure level can be controlled. However, it involves complicated multi-input-multi-out (MIMO) controls. A novel MIMO controller used for controlling the cylinder motion and pressure level in an over- actuated 1M3P SCC was proposed in [34], and the relative gain array (RGA) method was used for the state coupling analysis. The RGA method was also adopted to develop a MIMO controller for controlling the motion, backpressure, and temperature in a 1M2P SCC [40]. The experimental verification showed that another control input is needed for a cooler, and the decoupled pressure control needs to be improved [40]. Furthermore, the RGA method was used in the MIMO controller design for a 2M2P SCC with a load-holding function [37] and a 2M2P SCC using a bootstrap reservoir [41], [42].

2.3. SCC Thermal Analysis

Based on a heat resistance network, a thermo-hydraulic model of a 1M1P SCC was developed to predict the thermal energetic behaviour and secure a stable temperature operation [43]. The influence of temperature in the range of 910 to +22 ◦C to a 1M2P SCC prototype was investigated in [44]. Experiments with the thermal camera showed that the change of the outside temperature influenced the system's energy efficiency. Furthermore, a thermo-hydraulic model of a 1M2P SCC was developed in SimulationX and validated against experimental measurements utilizing thermocouples and the thermal camera [45]. A lumped thermo-hydraulic model of a 1M1P SCC was derived and verified against

experimental measurements [46]. It was revealed that the dynamic pressure- temperature coupling could be neglected; an elaborate thermal resistance network offers better temperature predictions than a simple model [46].

2.4. Other SCC Topics

Self-contained SCCs often use a gas accumulator as the reservoir. However, for high power level SCCs, the size and mass of the gas accumulator are significant, which may affect the system. Using a bootstrap reservoir instead of a gas accumulator can greatly downsize the reservoir [47]. However, strong state couplings were found when the bootstrap was introduced in 2M2P SCCs [41], [42].

In a self-contained SCC, all components are often mounted together, leading to the electric motor, hydraulic pumps, and accumulators being extra weights to the cylinder, which may affect the machine structure and the system's performance. This issue was investigated in [48] via finite element analysis and simulations of an excavator. Simulation results demonstrated that the extra weights do not significantly affect the excavator structure. If the energy recuperation was assumed, the increased energy consumption related to the increased mass was about 12 %. A study on the mass effects of self- contained SCCs used on a knuckle boom crane was presented in [49]. This paper concluded that the chosen SCCs only reduce the payload capacity in the range from 0.8 % to 2.1 % according to different work scenarios.

Prime movers in high-power SCCs are usually oversized to meet the peak power requirement. A hybrid system, consisting of an SCC and an energy storage system, was proposed in [50] to shave the power peak and downsize the prime mover. Compared with the nonhybrid system, the hybrid system only requires a prime mover with 70 % less installed power with- out degrading the control performance; however, the system compactness and cost are compromised [50].

SCCs are usually self-contained systems using an accumulator as the reservoir, leading to wear and contamination sensitivity. Endurance tests of a 1M2P SCC were presented in [51], where oil samples were periodically taken, and visual inspections evaluated the pump wear. Test results demonstrated that although the hydraulic pump was robust against the high particle load, SCCs could not be driven without a filter. In [31], the wear rate of the journal bearing of the gear pump used in a 1M2P SCC was analysed based on the Ocvirk Number and Archard's Wear Law, and a wear-reducing control was proposed, which, however, induces extra losses.

2.5. Identified Research Gaps

Most of the research on SCCs is done at a single drive level and low power level. High power level (over 200 kW) and system-level research, where the hydraulic power can be shared and exchanged among multiple drives and recyclable, have not been identified.

3. IDENTIFY THE RESEARCH TARGET

According to the research gaps identified in II-E, the research target should have high power output and power consumption and comprise multiple cylinders. Furthermore, it should involve control challenges, e.g., automation and four-quadrant operations. In an offshore hydraulic machine survey conducted by the author, the Pipe Handling Crane (PHC) is the only one that meets all the conditions above. In a PHC, as shown in Fig. 3, there are one or

two cylinders in parallel driving the main boom, one cylinder driving the knuckle boom, one cylinder driving the telescope, and two hydraulic motors driving the slew motion.



Figure 3. A PHC from National Oilwell Varco. ©

The knuckle boom cylinder's piston velocity and load force vary independently between negative and positive during operation. Therefore, the knuckle boom cylinder is operated in four quadrants. The main boom and telescope cylinders are operated in two quadrants because their load forces never change directions. The PHC is used to lift and move heavy tubular loads on drilling ships and platforms, such as drill pipe, drill collar, and casing. A PHC from *National Oilwell Varco* with product number PC1891K is chosen as the research target. Its maximum load capacity is 12 t, and its maximum input power is 259.6 kW. It has long working hours because it continuously delivers drill pipe between the pipe deck and the catwalk machine during the entire offshore drilling operation.

4. DISCUSSION

Compensating for the differential flow rates is still one of the main challenges for closed-circuit 1M1P single-rod SCCs. POCVs or an ISV can be used to compensate for the differential flow. However, they suffer from mode oscillation under certain loads and working conditions. Mode oscillation is unacceptable to large offshore cranes due to safety requirements. Most approaches in the literature preventing mode oscillation are control approaches. Therefore, the future research trend of closed-circuit 1M1P single-rod SCCs used offshore could focus on new architectures that can compensate for the differential flow without triggering mode oscillation under all load conditions and at the same time consider circuit simplicity. Although the low operating speed issue in 1M1P SCCs can be addressed by adopting a bypass valve [25], the system energy efficiency is compromised. Therefore, there is a need to explore more efficient designs in this regard.

1M2P SCCs can compensate for the differential flow rates without triggering mode oscillation. However, the two pumps' displacement ratio must match the cylinder area ratio, limiting universal availability. The open-circuit 1M2P SCC has a lower power transmission ratio, leading to oversized prime movers. Low drive stiffness is common for one prime mover SCCs, mainly due to the system's low damping ratio and the low backpressure. Adopting extra control valves [30] or pumps [34] improves the drive stiffness. Nevertheless, these methods are rather complicated and costly for broadly offshore use. Future research

on one prime mover SCCs used offshore should focus on control methods, such as adding active damping [38], and new architectures that can realize the backpressure control without increasing the circuit complexity and cost.

The closed-circuit 2M2P SCC is the best SCC architecture for offshore applications. It offers the best scalability, the insensitivity of cylinder velocity to load pressure change, a relatively simple circuit structure, and system pressure level control. Its future circuit designs should consider coping with high power output at low operation speeds, common for offshore high-power cranes. Furthermore, the 2M2P SCC re- quires sophisticated MIMO control. However, only the MIMO control design with the RGA method has been identified. Other methods should be explored in future research.

The electric motor, pump, and accumulator are often mounted together with the cylinder when implementing SCCs on applications. It might be an issue for offshore applications. For example, the PHC has long cylinders driving long beams, and the cylinders are far from the deck and operation room, which is inconvenient for maintenance. When cylinders are retracted, there might not be enough space for components attached to cylinders. Moreover, the weight of the electric motor, pump, and accumulator causes extra energy consumption, especially when the energy recovery device is not in place. Therefore, future research on offshore SCCs should explore alternative layouts and compare the differences.

Implementing isolated SCCs on a large system is not always practical and energy efficient. SCC networks [32] can improve the energy efficiency and control performance and might shave the power peak for a single SCC due to the hydraulic power can be shared among SCCs. Therefore, future research on offshore SCCs should also explore and implement more possible SCC networks.

5. CONCLUSION

This paper presented a literature review of speed-controlled cylinders, a description of a chosen research target, and a discussion about future research on using speed-controlled cylinders in offshore applications. It is concluded that more research that focuses on high power output levels and system- level (multi-cylinder systems) is needed to show if the technology is feasible for the offshore industry.

6. REFERENCES

[1] Finotek, “Hydraulic valve history,” [EB/OL]. https://www.finotek.com/hydraulic-valve-history/ (Accessed November 14, 2020).

[2] J. D. Zimmerman, M. Pelosi, C. A. Williamson, and M. Ivantysynova, “Energy consumption of an LS excavator hydraulic system,” Proceedings of the ASME 2007 International Mechanical Engineering Congress and Exposition. Volume 4: Design, Analysis, Control and Diagnosis of Fluid Power Systems. Seattle, Washington, USA. November 11–15, 2007. pp. 117-126. ASME.

[3] H. E. Merritt. Hydraulic Control Systems. New York, Wiley, 1967.

[4] W. Hahmann. “The dynamic behavior of hydrostatic drives with servo pump and its use in control circuits,” PhD thesis, RWTH, Aachen, Germany, 1973.

[5] M. Ivantysynova. “The swash plate machine for displacement control unit with great development potentiality,” In First IFK Aachen, Germany, 1998.

[6] S. Helduser, “Electric-hydrostatic drive—an innovative energy-saving power and motion control system,” Proceedings of the Institution of Mechanical Engineers, Part I: Journal of Systems and Control Engineering, vol. 213, no. 5, Aug. 1999, pp. 427–437.

[7] S. Ketelsen, D. Padovani, T. Andersen, M. Ebbesen, and L. Schmidt, “Classification and review of pump-controlled differential cylinder drives,” Energies, vol. 12, no. 7, p. 1293, Apr. 2019.

[8] J. Weber, B.S. Beck, E.H. Fischer, R. Ivantysyn, G. Kolks, M. Kunkis, H. Lohse, J. L¨ubbert, S. Michel, M. Schneider, L. Shabi, A. Sitte, J. Weber, and J. Willkomm, “Novel system architectures by individual drives,” (2016).

[9] S. Frischemeier, “Electrohydrostatic actuators for aircraft primary flight control-types, modelling and evaluation,” Proceedings of the Fifth Scandinavian International Conference on Fluid Power, 1997, pp. 1–16.

[10] S. Michel and J. Weber. “Electrohydraulic compact-drives for Low Power applications considering energy-efficiency and high inertial loads,” The 7th FPNI PhD Symposium on Fluid Power, Reggio Emilia, 2012.

[11] K. Rydberg, “Energy efficient hydraulics – system solutions for loss minimization,” National Conference on Fluid Power,” Hydraulikdagar’15”, Link¨oping University, Link¨oping, Sweden, 2015.

[12] S. Michel and J. Weber, “Energy-efficient electrohydraulic compact drives for low power applications,” Fluid Power and Motion Control - FPMC, Bath, 2012, pp. 93–107.

[13] D. Hagen, D. Padovani and M. Choux, “Guidelines to Select Between Self-Contained Electro-Hydraulic and Electro-Mechanical Cylinders,” 2020 15th IEEE Conference on Industrial Electronics and Applications (ICIEA), 2020, pp. 547-554.

[14] R. Navarro. “Performance of an electro-hydrostatic actuator on the F-18 systems research aircraft,” NASA Technical Memorandum, (206224), 1997.

[15] J. Li, “Design and analysis of novel airborne integrated electro hydro- static actuator,” 2003.

[16] M. Enomoto, S. Kamoshita, M. Kamiyama, K. Sasaki, T. Hamada, and A. Kazato, “Development of tilt control system using electro-hydraulic actuators,” Quarterly Report of Rtri, 46, 2005, pp. 219-224.

[17] R. Kang, Z. Jiao, S. Wang, and L. Chen, “Design and simulation of electro-hydrostatic actuator with a built-in power regulator,” Chinese Journal of Aeronautics, Volume 22, Issue 6, 2009, pp. 700-706.

[18] Z. Quan, L. Quan, and J. Zhang, “Review of energy efficient direct pump controlled cylinder electro-hydraulic technology, Renewable and Sustainable Energy Reviews,” Volume 35, 2014, pp. 336-346.

[19] D. Hagen, D. Padovani, and M. Choux, “A comparison study of a novel self-contained electro-hydraulic cylinder versus a conventional valve-controlled actuator—part 1: motion control,” Actuators, vol. 8, no. 4, p. 79, Dec. 2019.

[20] D. Hagen, D. Padovani, and M. Choux, “A comparison study of a novel self-contained electro-hydraulic cylinder versus a conventional valve-controlled actuator—part 2: energy efficiency,” Actuators, vol. 8, no. 4, p. 78, Dec. 2019.

[21] D. Hagen, D. Padovani, and M. Choux, “Enabling energy savings in offshore mechatronic systems by using self-contained cylinders,” Modelling, Identification and Control, vol. 40, no. 2, pp. 89-108, 2019.

[22] K. K. Ahn, J. I. Yoon, and D. Q. Truong, “Design and verification of a new energy saving electric excavator,” Proceedings of the 28th International Symposium on Automation and Robotics in Construction, ISARC 2011, pp. 259–264.

[23] H. Çalışkan, T. Balkan, and B. E. Platin, “A complete analysis and a novel solution for instability in pump controlled asymmetric actuators,” ASME. J. Dyn. Sys., Meas., Control. September 2015; 137(9): 091008.

[24] P. H. Gøytil, D. Padovani, and M. R. Hansen, “A novel solution for the elimination of mode switching in pump-controlled single-rod cylinders,” Actuators, vol. 9, no. 1, p. 20, Mar. 2020.

[25] S. Qu, D. Fassbender, A. Vacca, and E. Busquets, “A high-efficient solution for electro-hydraulic actuators with energy regeneration capability, Energy,” Volume 216, 2021.

[26] K. G. Cleasby, A. R. Plummer, and Thales Company, “A novel high efficiency electro-hydrostatic flight simulator motion system,” ASME/BATH 2008 Symposium on Fluid Power and Motion Control, 2008, pp. 437–449.

[27] C. Bonato, T. Minav, M. Pietola, and P. Sainio, “Position control of direct driven hydraulic drive,” the 8th FPNI Ph.D Symposium on Fluid Power, FPNI, (March), 2014.

[28] S. Zhang, T. Minav, and M. Pietola, “Decentralized hydraulics for micro excavator,” Proceedings of 15:th Scandinavian International Conference on Fluid Power, Fluid Power in the Digital Age, SICFP’17, June 7-9, 2017 - Linköping, Sweden, 144(June), pp. 187–195.

[29] H. C. Pedersen, L. Schmidt, T. O. Andersen, and M. H. Brask, “Investigation of new servo drive concept utilizing two fixed displacement units,” JFPS International Journal of Fluid Power System, 2015, Volume 8, Issue 1, Pages 1-9.

[30] L. Schmidt, S. Ketelsen, M. H. Brask, and K. A. Mortensen, “A class of energy efficient self-contained electro-hydraulic drives with self-locking capability,” Energies, vol. 12, no. 10, p. 1866, May 2019.

[31] N. Grønkær, P. Johansen, K. V. Hansen, and L. Schmidt, “Tribotronics in electro-hydraulic actuator technology: improving durability by control,” Proceedings of the BATH/ASME 2020 Symposium on Fluid Power and Motion Control. Virtual, Online. September 9–11, 2020. V001T01A008. ASME.

[32] L. Schmidt and K. V. Hansen, “Electro-hydraulic variable-speed drive networks—idea, perspectives, and energy saving potentials,” Energies, vol. 15, no. 3, p. 1228, Feb. 2022.,

[33] L. Schmidt, D. B. Roemer, H. C. Pedersen, and T. O. Andersen, “Speed-variable switched differential pump system for direct operation of hydraulic cylinders,” Proceedings of the ASME/BATH 2015 Symposium on Fluid Power and Motion Control. Chicago, Illinois, USA. October 12–14, 2015. V001T01A042. ASME.

[34] L. Schmidt, M. Groenkjaer, H. C. Pedersen, and T. O. Andersen, “Position control of an over-actuated direct hydraulic cylinder drive,” Control Engineering Practice, 64(March), 2017, pp. 1–14.

[35] S. H. Cho, S. Räcklebe, and S. Helduser, “Position tracking control of a clamp-cylinder for energy-saving injection moulding machines with electric-hydrostatic drives,” Proceedings of the Institution of Mechanical Engineers, Part I: Journal of Systems and Control Engineering. 2009;223(4):479-491.

[36] P. H. Gøytil, D. Padovani, and M. R. Hansen, “On the energy efficiency of dual prime mover pump-controlled hydraulic cylinders,” ASME/BATH 2019 Symposium on Fluid Power and Motion Control, FPMC 2019, (c):1–10, 2020.

[37] S. Ketelsen, T. O. Andersen, M. K. Ebbesen, and L. Schmidt, “A self-contained cylinder drive with indirectly controlled hydraulic lock,” Modeling, Identification and Control: A Norwegian Research Bulletin, 2020, 41(3):185–205.

[38] D. Padovani, “Adding Active Damping to Energy-Efficient Electro- Hydraulic Systems for Robotic Manipulators — Comparing Pressure and Acceleration Feedback,” 2020 the 5th International Conference on Robotics and Automation Engineering (ICRAE), 2020, pp. 175-181.

[39] D. Hagen, D. Padovani, and M. Choux, “Design and implementation of pressure feedback for load-carrying applications with position control,” n Proceedings of The Sixteenth Scandinavian International Conference on Fluid Power, May 22-24, 2019, Tampere, Finland.

[40] N. Grønkær, L.N. Nielsen, F.Ø. Nielsen, S. Ketelsen, and L. Schmidt, “Multi-objective control of a self-locking compact electro-hydraulic cylinder drive,” In Fluid Power, Hydraulics, Pneumatics, 12th International Fluid Power Conference. Vol. 1. Dresden: Dresdner Verein zur Förderung der Fluidtechnik e.V. Dresden. 2020. p. 241-252.

[41] V. Donkov, S. Ketelsen, T. Andersen, M. K. Ebbesen, and L. Schmidt, “Improving the performance of self-contained cylinder drives with load- holding capabilities,” Proceedings of the 17:th Scandinavian International Conference on Fluid Power, SICFP’21, June 1-2, 2021, Link¨oping, Sweden.

[42] S. Ketelsen, D. Padovani, M. K. Ebbesen, T. Andersen, and L. Schmidt, “A gasless reservoir solution for electro-hydraulic compact drives with two prime movers.” Proceedings of the BATH/ASME 2020 Symposium on Fluid Power and Motion Control. BATH/ASME 2020 Symposium on Fluid Power and Motion Control. Virtual, Online. September 9–11, 2020. V001T01A038. ASME.,

[43] S. Michel, T. Schulze, and J. Weber, “Energy-efficiency and thermo energetic behaviour of electrohydraulic compact drives,” 9th International Fluid Power Conference (IFK), (October 2020):162–177, 2014.

[44] T. Minav, P. Sainio, and M. Pietola, “Efficiency of direct driven hydraulic setup in arctic conditions,” In Proceedings of the Fourteenth Scandinavian International Conference on Fluid Power, Tampere, Finland, May 20 - 22, (May), 2015.

[45] N. Karlén, T. Minav, and M. Pietola, “Investigation of thermal effects in direct driven hydraulic system for off-road machinery,” In Proceedings of the 9th FPNI Ph.D. Symposium on Fluid Power, pages 1–8, 2016.

[46] S. Ketelsen, S. Michel, T. O. Andersen, M. K. Ebbesen, J. Weber, and L. Schmidt, “Thermo-Hydraulic Modelling and Experimental Validation of an Electro-Hydraulic Compact Drive,” Energies, vol. 14, no. 9, p. 2375, Apr. 2021.

[47] S. Ketelsen, G. Kolks, T. Andersen, L. Schmidt, and J. Weber, “Boot- strap reservoir concept for electro-hydraulic compact drives,” In 12th International Fluid Power Conference. Dresden Technische Universität. 2020. p. 201-215.

[48] A. Niraula, S. Zhang, T. Minav, and M. Pietola, “Effect of zonal hydraulics on energy consumption and boom structure of a micro- excavator,” Energies, vol. 11, no. 8, p. 2088, Aug. 2018.

[49] S. Ketelsen, T. O. Andersen, M. K. Ebbesen, and L. Schmidt, “Mass estimation of self-contained linear electro-hydraulic actuators and evaluation of the influence on payload capacity of a knuckle boom crane,” Proceedings of the ASME/BATH 2019 Symposium on Fluid Power and Motion Control. Longboat Key, Florida, USA. October 7–9, 2019.

[50] D. Padovani, S. Ketelsen, and L. Schmidt, “Downsizing the Electric Motors of Energy-Efficient Self-Contained Electro-Hydraulic Systems by Using Hybrid Technologies.” Proceedings of the BATH/ASME 2020 Symposium on Fluid Power and Motion Control. Virtual, Online. September 9–11, 2020.

[51] S. Michel and J. Weber, “Investigation of Self-Contamination of Electrohydraulic Compact Drives,” 10th JFPS International Symposium on Fluid Power, no. June 2018, pp. 1–7, 2017.

Loading system for wind turbine drivetrain test bench with model-based compensation control strategy

Danyang Li [a], Yajing Gu*[a, b], Yonggang Lin [a, b], Jiajun Song [a], Xiangheng Feng [a], Hongwei Liu [a, b]

a. The State Key Laboratory of Fluid Power and Mechatronic Systems, Zhejiang University, Hangzhou, China

b. Ocean Academy, Zhejiang University, Zhoushan, China

danyang.li@zju.edu.cn, guyj90@zju.edu.cn, yglin@zju.edu.cn, jjsong07@zju.edu.cn, Xiangheng_f97@zju.edu.cn, lhwei@zju.edu.cn

Abstract.

The dramatic expansion of wind turbines sets higher demands on the drivetrain test bench. The loading system of the drivetrain test bench should accurately reproduce real wind loads on the ground to evaluate the reliability of turbine components. In this paper, the multi-cylinder electrohydraulic digital-servo loading technology is applied to the non-torque loading system. The hydraulic cylinders groups are designed to substitute the original loading points. The loading center of each cylinders group is deviated due to the installation distance and the changed force distribution. Thus, a novel loading principle is proposed to compensate for the eccentric moment. The loading formula should be recalculated in real-time to ensure the implementation of accurate reproduction of 5-DOF loads based on the integration of multiple hydraulic cylinders groups. In addition, there are reverse sudden changes caused by the asynchronous opening and closing characteristics of the servo valve and the onoff valve. An advanced model-based sliding mode controller compensation strategy is proposed to achieve smooth switching. A mathematical analytical model is derived to deal with the parametric uncertainties and nonlinearities. Moreover, the extensive AMESim-Simulink co-simulations under various signals that represent the real wind loads have been conducted to investigate the performance of the proposed control strategy. By comparing the advanced controller to a traditional PID controller, the simulation results showed that the switching error was greatly reduced and the total loading process was smoother for the model-based sliding mode controller compensation strategy. The excellent tracking performance proved the feasibility and effectiveness of the proposed strategy.

Keywords. Loading system, drivetrain test bench, model-based compensation control strategy, co-simulation.

1. INTRODUCTION

The development of large scale wind turbines has expanded dramatically during the past few decades with the global cumulative wind power capacity reaching 743 gigawatts (GW) by the end of 2020 **Errore. L'origine riferimento non è stata trovata.**. The research trend for the further development of wind power technology has been generalized to large offshore wind turbines above 15 megawatts (MW). The rapid growth of wind turbine capacity sets higher demands for the ground test and evaluation of components, including hardware components-structural, mechanical, electrical, thermal, hydraulic and software components **Errore. L'origine riferimento non è stata trovata.**. Unexpected failures of the drivetrain system, as the fundamental type of failure, require long waiting periods and higher maintenance costs **Errore. L'origine riferimento non è stata trovata.**. Thus, it is inevitable to implement a loading system for the wind turbine drivetrain test bench to identify evaluation issues and assess component performances.

The wind turbine is usually subjected to various loads, consisting of gravitational loads, aerodynamic loads and centrifugal loads **Errore. L'origine riferimento non è stata trovata.**. These loads compose of six-degree-of-freedom (6-DOF) loading elements including three moment elements and three force elements **Errore. L'origine riferimento non è stata trovata.**. The loading system should accurately reproduce real wind loads on the ground to evaluate the reliability of turbine components. There are several utility-scale drivetrain test benches worldwide. Fig. 1.1(a) shows the 4MW wind turbine system test bench at the Center for Wind Power Drives of RWTH Aachen University **Errore. L'origine riferimento non è stata trovata.**. Fig. 1.1(b) represents the 7.5 MW mechanical test benches conducted at the Wind Turbine Drivetrain Testing Facility at Clemson University **Errore. L'origine riferimento non è stata trovata.**. Fig. 1.1(c) depicts the 15 MW wind turbine nacelle test facility in Offshore Renewable Energy (ORE) Catapult **Errore. L'origine riferimento non è stata trovata.**. Fig. 1.1(d) illustrates the 25 MW test facility model which is the wind industry's largest and most advanced test bench in LORC **Errore. L'origine riferimento non è stata trovata.**.

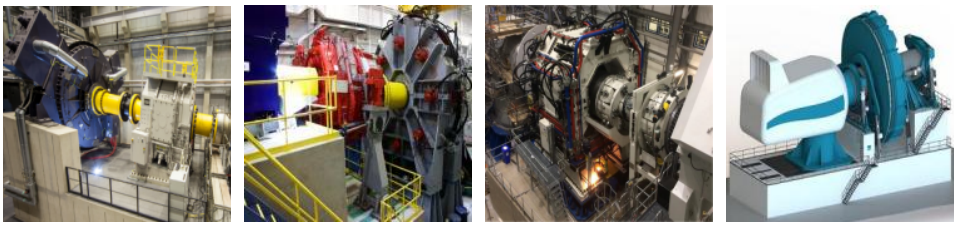

(a) (b) (c) (d)

Fig. 1.1 Photographs of wind turbine drivetrain test bench. (a) 4 MW test bench in RWTH Aachen University, (b)7.5 MW test bench in Clemson University, (c)15 MW test facility in ORE Catapult, (d) 25 MW test facility illustration in LORC.

The drivetrain test bench consists of the drive motor, the non-torque load unit and the device under test. The drive motor is able to emulate the wind torque loads. The other 5-DOF loads are reproduced by the non-torque load unit. A grid emulator can be mounted with the device under test and applied to a typical grid faults test. The critical research lies in the reproduction technology of non-torque loads. The non-torque loading system is composed of multiple

electrohydraulic actuators in various arrangements. The basic loading unit is an electrohydraulic servo valve and a hydraulic cylinder. However, with the dramatically increasing capacity of wind turbines, the loading force exerted by each servo-valve controlled (SVC) cylinder is growing. A novel multi-cylinder electrohydraulic digital-servo loading (MEDSL) is proposed to solve the inaccuracy loading problem for large load reproduction. A traditional single cylinder is replaced by a new hydraulic cylinders group that includes N hydraulic cylinders at each point, in which one is controlled by the electrohydraulic servo valve and the others (N-1) are controlled by the onoff valve **Errore. L'origine riferimento non è stata trovata.**. The loading accuracy is substantially increased. However, there are reverse sudden changes caused by the asynchronous opening and closing of the servo valve and the onoff valve. At the same time, the loading center of each cylinders group is deviated due to the installation distance and the changed force distribution. The above matters require an advanced controller to achieve the accurate reproduction of real wind loads.

As the increment of hydraulic cylinders, the control strategy turns to be more complex with more variables induced in the loading system. Many nonlinear controllers have been proposed for the multi-input multi-output (MIMO) system. The model-based control techniques can be employed to deal with the parametric uncertainties and nonlinearities of electrohydraulic systems. The necessary conditions for the feasibility of the MIMO sliding mode controller (SMC) were investigated **Errore. L'origine riferimento non è stata trovata.**. A nonlinear MIMO SMC was designed for tracking the pitch angle and the plunge of the wind turbine blade tip **Errore. L'origine riferimento non è stata trovata.**. The continuous SMC was proposed to ensure arbitrarily small errors as desired for a class of nonlinear MIMO systems **Errore. L'origine riferimento non è stata trovata.**. Samir Zeghlache *et al.* proposed an observer-based robust controller for two twin-rotor MIMO systems **Errore. L'origine riferimento non è stata trovata.**. Farzaneh Bagheri *et al.* proposes a MIMO SMC synchronizing the control of all state variables for the quasi-Z-source inverter feeding a load **Errore. L'origine riferimento non è stata trovata.**. The model-based control strategy can effectively deal with the nonlinear issues and realize precise control effects based on adaptive and robust control theory. Therefore, in this paper, a model-based compensation control strategy was proposed for the MEDSL system. The loading performance was investigated by the AMESim and Simulink co-simulation. The results showed the advantages of the controller. It builds a foundation for the non-torque loading system of MW-class wind turbines.

This paper is organized as follows. The modified loading scheme of MEDSL is constructed considering the eccentric moment of hydraulic cylinders in Section II. The mathematical analytical model of MEDSL is derived and the model-based compensation controller is designed in Section III. In Section IV, the effect of the proposed control strategy is studied based on the co-simulation platform. Section V discusses the conclusion and future work.

2. LOADING SCHEMES

The real rotor and blades are substituted by a rotating loading disc. The mass and inertia moment is designed as the equivalent of the real wind turbine components. The distribution of hydraulic cylinders employs symmetrical loading scheme. Eight axial electrohydraulic loading points are symmetrically positioned on each left and right side of the disc. Eight radial

loading points are evenly distributed on the circumferential surface of the disc. Each loading point is composed of a digital-servo hydraulic cylinders group, including an SVC cylinder and (N-1) onoff valve controlled (OVC) cylinder. The loading force of each cylinders group can be defined as

$$F_{Li} = F_{Li0} + \sum_{n=1}^{N-1} F_{Lin} \tag{2.1}$$

$$F_{Ri} = F_{Ri0} + \sum_{n=1}^{N-1} F_{Rin} \tag{2.2}$$

$$F_{di} = F_{di0} + \sum_{n=1}^{N-1} F_{din} \tag{2.3}$$

$$F_{d'i} = F_{d'i0} + \sum_{n=1}^{N-1} F_{d'in} \tag{2.4}$$

where F_{Li} (i=1~8) denotes the loading force of the left side of the loading disc; F_{Li0} is the loading force of the SVC cylinder; F_{Lin} represents the loading force of the OVC cylinder; N is the number of cylinders in a group; F_{Ri} (i=1~8)denotes the loading force of the right side of the loading disc; F_{di} and $F_{d'i}$ (i=1~4) are the loading force of radial surface of the disc, as shown in Fig. 2.1, which illustrates the N=4 case.

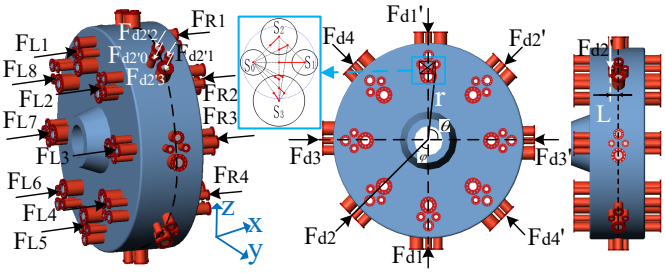

Figure 2.1. Loading diagram and the distribution of the loading vectors

The force of one loading point and its symmetrical counterpart can be considered as a loading force unit. The axial loading force F_{Ai} and the radial loading force F_{ri} can be expressed as

$$F_{Ai} = F_{Li} - F_{Ri} \quad (i = 1 \sim 8) \tag{2.5}$$

$$F_{ri} = F_{di} - F_{di'} \quad (i = 1 \sim 4) \tag{2.6}$$

However, there exists an eccentric moment due to the installation distance and the changed force distribution of the cylinders group. As can be seen from the blue box in Fig. 2.1, the central loading point of each hydraulic cylinders group is a factor varying with the change of the loading force. Thus, the loading radius, the eccentricity and the angle with the coordinate axis are all variables. Hence, the loading force vectors and the load vectors can be defined as

$$\mathbf{F} = \left[F_{A1}, F_{A2}, F_{A3}, F_{A4}, F_{A5}, F_{A6}, F_{A7}, F_{A8}, F_{R1}, F_{R2}, F_{R3}, F_{R4}\right]^{\mathrm{T}} \tag{2.7}$$

$$\mathbf{W} = \left[F_x, F_y, F_z, M_y, M_z\right]^{\mathrm{T}} \tag{2.8}$$

The balance equation between the force vectors and the load vectors is governed as

$$\begin{bmatrix} F_x \\ F_y \\ F_z \\ M_y \\ M_z \end{bmatrix} = \begin{bmatrix} 1 & 1 & 1 & 1 & 1 & 1 & 1 & 1 & 0 & 0 & 0 & 0 \\ 0 & 0 & 0 & 0 & 0 & 0 & 0 & 0 & \sin\phi_1 & \sin\phi_2 & \sin\phi_3 & \sin\phi_4 \\ 0 & 0 & 0 & 0 & 0 & 0 & 0 & 0 & \cos\phi_1 & \cos\phi_2 & \cos\phi_3 & \cos\phi_4 \\ r_1\sin\theta_1 & r_2\sin\theta_2 & r_3\sin\theta_3 & r_4\sin\theta_4 & r_5\sin\theta_5 & r_6\sin\theta_6 & r_7\sin\theta_7 & r_8\sin\theta_8 & L_1\cos\phi_1 & L_2\cos\phi_2 & L_3\cos\phi_3 & L_4\cos\phi_4 \\ r_1\cos\theta_1 & r_2\cos\theta_2 & r_3\cos\theta_3 & r_4\cos\theta_4 & r_5\cos\theta_5 & r_6\cos\theta_6 & r_7\cos\theta_7 & r_8\cos\theta_8 & L_1\sin\phi_1 & L_2\sin\phi_2 & L_3\sin\phi_3 & L_4\sin\phi_4 \end{bmatrix} \bullet \begin{bmatrix} F_{A1} \\ F_{A2} \\ F_{A3} \\ F_{A4} \\ F_{A5} \\ F_{A6} \\ F_{A7} \\ F_{A8} \\ F_{R1} \\ F_{R2} \\ F_{R3} \\ F_{R4} \end{bmatrix} \tag{2.9}$$

where r_i (i=1~8) is the distance between the actual loading point of each cylinders group and the center of the loading disk; θ_i (i=1~8)denotes the angle between the actual loading point of each axial cylinders group and the positive direction of the y-axis; L_i (i=1~4) represents the distance between the actual loading point of each radial cylinders group and the radial centerline of the circumferential surface of the loading disc; φ_i (i=1~4) is the angle between the actual loading point of each radial cylinders group and the negative direction of the z-axis.

Equation (2.9) can be solved as

$$\mathbf{W} = \mathbf{P} \bullet \mathbf{F} \Leftrightarrow \mathbf{F} = \mathbf{P}^{-1} \bullet \mathbf{W} \tag{2.10}$$

where **W** denotes the load vectors; **F** is the loading force vectors; **P** is the transformation matrix between the total load vectors and the loading force vectors; $\mathbf{p}^{-1}$ is the inverse transformation matrix of **P**. The matrix **P** can be written as

$$\mathbf{p} = \begin{bmatrix} 1 & 1 & 1 & 1 & 1 & 1 & 1 & 1 & 0 & 0 & 0 & 0 \\ 0 & 0 & 0 & 0 & 0 & 0 & 0 & 0 & \sin\phi_1 & \sin\phi_2 & \sin\phi_3 & \sin\phi_4 \\ 0 & 0 & 0 & 0 & 0 & 0 & 0 & 0 & \cos\phi_1 & \cos\phi_2 & \cos\phi_3 & \cos\phi_4 \\ r_1\sin\theta_1 & r_2\sin\theta_2 & r_3\sin\theta_3 & r_4\sin\theta_4 & r_5\sin\theta_5 & r_6\sin\theta_6 & r_7\sin\theta_7 & r_8\sin\theta_8 & L_1\cos\phi_1 & L_2\cos\phi_2 & L_3\cos\phi_3 & L_4\cos\phi_4 \\ r_1\cos\theta_1 & r_2\cos\theta_2 & r_3\cos\theta_3 & r_4\cos\theta_4 & r_5\cos\theta_5 & r_6\cos\theta_6 & r_7\cos\theta_7 & r_8\cos\theta_8 & L_1\sin\phi_1 & L_2\sin\phi_2 & L_3\sin\phi_3 & L_4\sin\phi_4 \end{bmatrix} \tag{2.11}$$

Therefore, the loading force vector **F** can be solved using (2.7)-(2.11). The loading formula should be recalculated in real-time to ensure the implementation of accurate reproduction of 5-DOF loads based on the integration of multiple hydraulic cylinders groups.

3. CONTROLLER DEVELOPMENT

The accuracy of the loading system with MEDSL depends on each cylinders group. However, the response speed of the SVC cylinder is faster than the OVC cylinder. Thus, there are reverse sudden changes in each switching process. To compensate for this loading error, a model-based SMC control strategy is proposed. The condition of an SVC cylinder and an OVC cylinder is investigated.

3.1. State-space Modelling

The load flow rate model of SVC and OVC cylinders can be depicted as **Errore. L'origine riferimento non è stata trovata.**

$$Q_{Ls} = A_s \frac{dx_s}{dt} + C_{tps} p_{Ls} + \frac{V_s}{4\beta_{es}} \frac{dp_{Ls}}{dt} \tag{3.1}$$

$$Q_{Lo} = A_o \frac{dx_o}{dt} + C_{tpo} p_{Lo} + \frac{V_o}{4\beta_{eo}} \frac{dp_{Lo}}{dt} \tag{3.2}$$

where Q_{Ls} and Q_{Lo} are the flow of the servo-valve and the onoff valve; A_s and A_o are the effective area of the piston for SVC and OVC cylinder; x_s and x_o are defined as the spool displacement of the servo-valve and the onoff valve; C_{tps} and C_{tpo} are the total leakage coefficient of the SVC and OVC cylinder; p_{Ls} and p_{Lo} are the load pressure of the SVC and OVC cylinder; β_{es} and β_{eo} are the oil effective bulk modulus; V_s and V_o are the total volume of the SVC and OVC cylinder. The force balance equation of the hydraulic cylinder is

$$A_s p_{Ls} = m_s \frac{d^2 x_s}{dt^2} + B_s \frac{dx_s}{dt} + K_s x_s \tag{3.3}$$

$$A_o p_{Lo} = m_o \frac{d^2 x_o}{dt^2} + B_o \frac{dx_o}{dt} + K_o x_o \tag{3.4}$$

where m_s and m_o are the equivalent mass; B_s and B_o are the equivalent viscous damping coefficient; K_s and K_o are the load spring stiffness of SVC and OVC cylinder, respectively. The relationship between the input control signal and the spool displacement can be described as

$$x_s = \frac{k_s}{\tau_s + 1} u_s \tag{3.5}$$

$$x_o = \frac{k_o}{\tau_o + 1} u_o \tag{3.6}$$

where k_s and τ_s denotes the gain and the time constant of the first-order inertia element for the servo valve; k_o and τ_o denotes the gain and the time constant of the first-order inertia element for the onoff valve; u_s and u_o are the input signal of servo valve and the onoff valve, respectively. The pressure-flow characteristic equation of the servo valve and the onoff valve can be written as

$$Q_{Ls} = \frac{k_{sz}}{\tau_s + 1} g(u_s) u_s \quad g(u_s) = \sqrt{p_s - \mathrm{sgn}(u_s) p_{Ls}} \tag{3.7}$$

$$Q_{Lo} = \frac{k_{oz}}{\tau_o + 1} g(u_o) u_o \quad g(u_o) = \sqrt{p_s - \mathrm{sgn}(u_o) p_{Lo}} \tag{3.8}$$

where k_{sz} and k_{oz} are the coefficient of servo-valve and onoff valve, and p_s denotes the pressure of the system. Define a set of state variables as

$$x=\left[x_1,x_2,x_3,x_4,x_5,x_6,x_7,x_8,y\right]^T=\left[x_s,\dot{x}_s,p_{Ls},\dot{p}_{Ls},x_o,\dot{x}_o,p_{Lo},\dot{p}_{Lo},y\right]^T \tag{3.9}$$

where y is the total loading force of the system. The state-space model can be described as

$$\begin{aligned}
&\dot{x}_1=x_2\\
&\dot{x}_2=-a_1x_1-a_2x_2+a_3x_3\\
&\dot{x}_3=x_4\\
&\dot{x}_4=\frac{1}{\tau_s}\left[-a_6x_1-a_7x_2-a_8x_3-a_9x_4+b_1k_{sz}g(u_s)u_s\right]\\
&\dot{x}_5=x_6\\
&\dot{x}_6=-a_{11}x_5-a_{12}x_6+a_{13}x_7\\
&\dot{x}_7=x_8\\
&\dot{x}_8=\frac{1}{\tau_{o1}}\left[-a_{16}x_5-a_{17}x_6-a_{18}x_7-a_{19}x_8+b_2k_{oz}g(u_o)u_o\right]\\
&y=x_3A_s+x_7A_o
\end{aligned} \tag{3.10}$$

where $a_1=k_s/m_s$, $a_2=B_s/m_s$, $a_3=A_s/m_s$, $a_4=4\beta_{es}A_s/V_s$, $a_5=4\beta_{es}C_{tps}/V_s$, $b_1=4\beta_{es}/V_s$, $a_6=-a_1a_4\tau_s$, $a_7=a_4-a_2a_4\tau_s$, $a_8=a_5+a_3a_4\tau_s$, $a_9=a_5\tau_s+1$, $a_{11}=k_o/m_o$, $a_{12}=B_o/m_o$, $a_{13}=A_o/m_o$, $a_{14}=4\beta_{eo}A_o/V_o$, $a_{15}=4\beta_{eo}C_{tpo}/V_o$, $b_2=4\beta_{eo}/V_o$, $a_{16}=-a_{11}a_{14}\tau_o$, $a_{17}=a_{14}-a_{12}a_{14}\tau_o$, $a_{18}=a_{15}+a_{13}a_{14}\tau_o$, $a_{19}=a_{15}\tau_o+1$.

3.2. Model-based SMC Design

Set y_d as the expected total loading force of the system, and the tracking error and its derivatives are given by

$$\begin{cases}e_1=y_d-y\\ e_2=\dot{y}_d-\dot{y}\\ e_3=\ddot{y}_d-\ddot{y}\end{cases} \tag{3.11}$$

Design the sliding mode switching function of the system as

$$s=c_1e_1+c_2e_2 \tag{3.12}$$

where c_1 and c_2 are the positive coefficients of the switching function. The derivative of the switching function is given by

$$\dot{s}=c_1e_2+c_2e_3 \tag{3.13}$$

The reaching law is chosen as depicted to obtain SMC

$$\dot{s}=-\varepsilon\mathrm{sat}(\frac{s}{\phi})-ks \tag{3.14}$$

where ε, k are both positive real parameters, ϕ is the thickness of the boundary layer. And the saturation function is defined as follows to eliminate the chattering problem

$$\mathrm{sat}(\frac{s}{\phi})=\begin{cases}\dfrac{s}{\phi} & \text{if}\left|\dfrac{s}{\phi}\right|<1,\\ \mathrm{sgn}(\dfrac{s}{\phi}) & \text{if}\left|\dfrac{s}{\phi}\right|\geq 1,\end{cases} \tag{3.15}$$

The expression of the model-based SMC strategy can be obtained

$$a_{10}g(u_s)u_s + a_{20}g(u_o)u_o = (c_1e_2 + \varepsilon sat(\frac{s}{\varphi}) + ks) / c_2 + \ddot{y}d - \left(A_s f_s(x) + A_o f_o(x)\right) \quad (3.16)$$

where $a_{10} = A_s b_1 k_{sz} / \tau_s, a_{20} = A_o b_2 k_{oz} / \tau_o, f_s(x) = (-a_6 x_1 - a_7 x_2 - a_8 x_3 - a_9 x_4) / \tau_s,$ $f_o(x) = \left(-a_{16} x_5 - a_{17} x_6 - a_{18} x_7 - a_{19} x_8\right) / \tau_o.$

4. SIMULATION RESEARCH

A co-simulation model of the one SVC cylinder and one OVC cylinder case has been built in AMESim and Simulink to validate the effect of the model-based SMC compensation control strategy. The details of the simulation are listed in Table I. The other related parameters are set as the default values in AMESim. As shown in Fig. 3.1(a), the hydraulic model consists of the motor, the relief valve, the three-position four-way servo valve, the two-position four-way solenoid directional valve, two identical hydraulic cylinders, the equivalent load and the co-simulation interface. The model-based SMC compensation strategy is calculated in Simulink as illustrated in Fig. 3.1(b). The simulation step is 1e-4 s, and the total simulation time is 10 s.

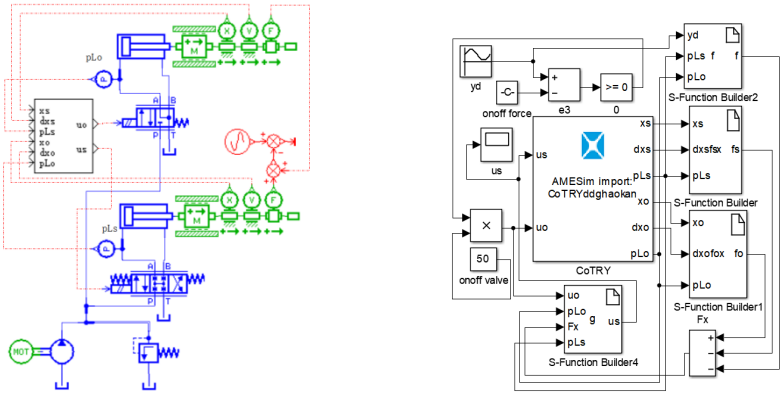

(a) (b)

Fig. 3.1 Co-simulation model in AMESim and Simulink.

To investigate the performance of the model-based SMC compensation method, the traditional proportional-integral-derivative (PID) controller was used to be compared under various sinusoidal signals. The first simulation was carried out using 0.2 Hz sinusoidal total loading wave. As illustrated in Fig. 3.2(a), the total loading force of the system is the sum of loading forces from the SVC cylinder and OVC cylinders. The maximum force that can be exerted by the SVC cylinder was about 10 kN. Thus, the force was increasing stably before 1.25 s. The input signal of the OVC cylinder was a series of digital values. Then the OVC cylinder was open to offer the maximum force while the force of the SVC cylinder is 0 at this time.

TABLE 3.1 SIMULATION PARAMETERS

Component	Parameter	Value	Component	Parameter	Value

hydraulic cylinder	Piston diameter /mm	50	Hydraulic source	Pressure source /MPa	5
	Rod diameter /mm	32		Pump displacement (cc /rev)	100
	Cylinder stroke /mm	50		Typical speed of pump (rev/min)	1500
	Bulk modulus /MPa	800	SMC	c_1	5e3
				c_2	10
	Leakage coefficient	2e-13	SMC	ε	1e4
				k	500
	τ_s	1.25e-3		ϕ	1e-3
	τ_o	8e-3	PID	P	0.9
	k_{sz}	1.36e-10		I	0.5
	k_{oz}	2.46e-10		D	0.008

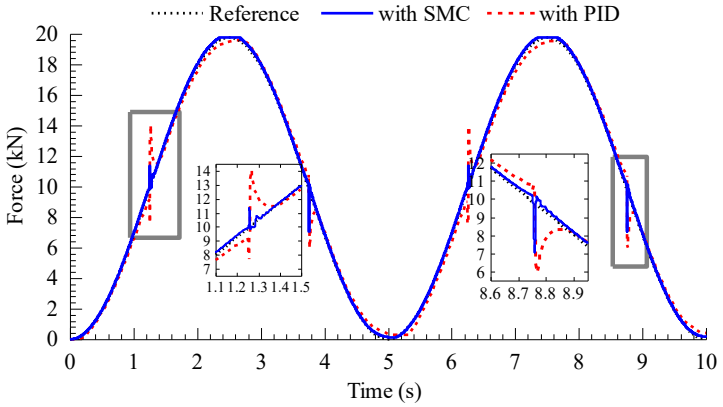

(a)

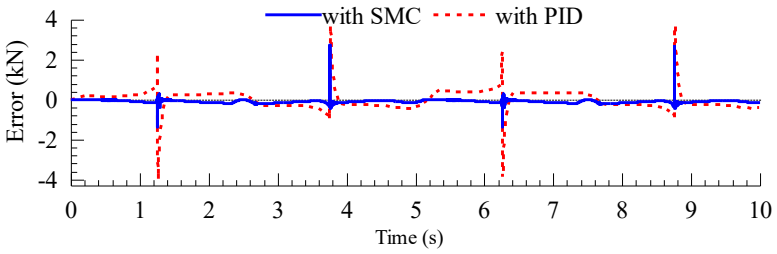

(b)

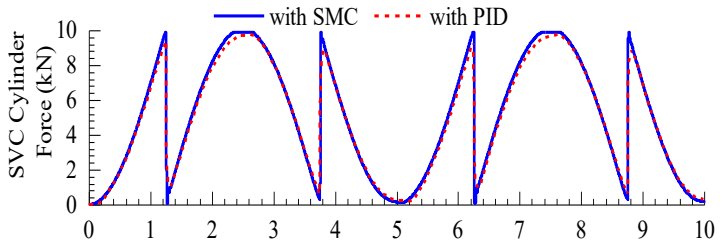

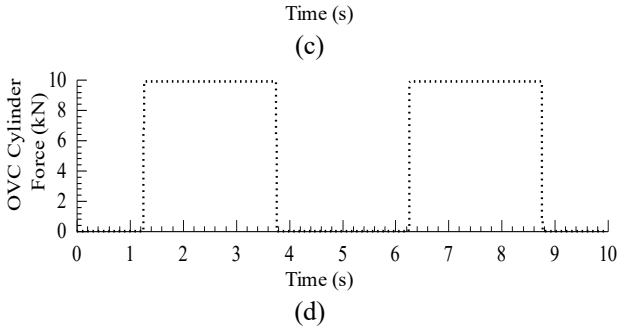

Fig. 3.2 Simulation results for 0.2 Hz loads. (a) Tracking performance. (b) Tracking error. (c) Tracking force of SVC cylinder. (d) Tracking force of OVC cylinder.

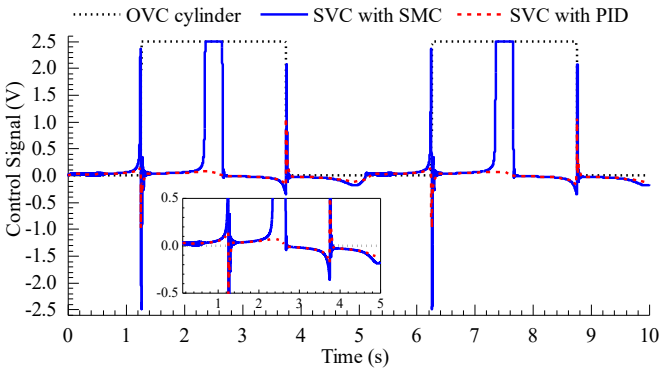

Fig. 3.3 Simulation results for control signal of 0.2 Hz loading.

As can be seen from Fig. 3.2(a), the total loading force had an obvious trend of increasing first and then reducing for the PID controller. A similar phenomenon appeared in the decreasing process. However, the model-based SMC compensation strategy exhibited better tracking performance by considering the asynchronous opening and closing characteristics of the servo valve and the onoff valve. The control signals was shown in Fig. 3.3, the input signal of OVC cylinder was a series of square wave, the input signal of SVC cylinder had impulse response at switching.

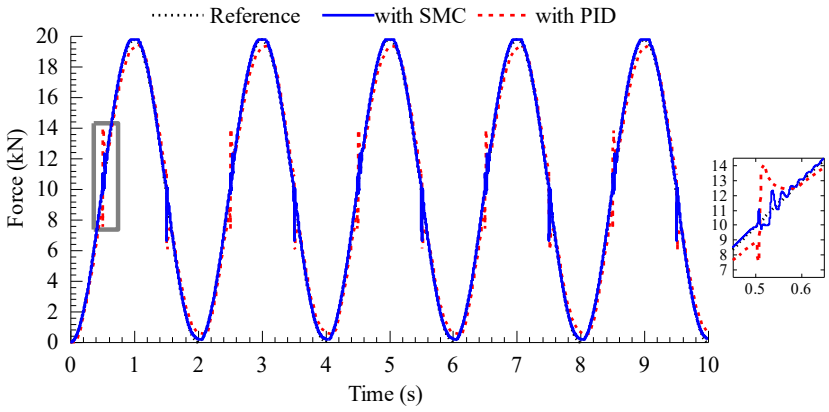

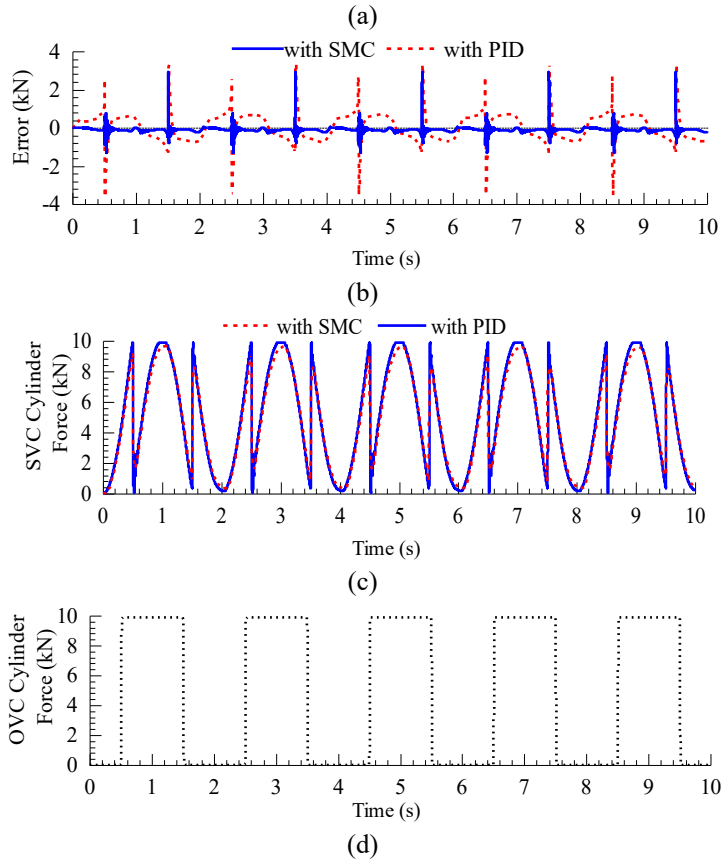

Fig. 3.4 Simulation results for 0.5 Hz loads. (a) Tracking performance. (b) Tracking error. (c) Tracking force of the SVC cylinder. (d) Tracking force of the OVC cylinder.

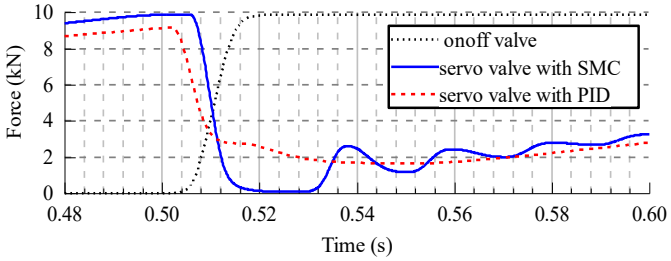

Fig. 3.5 Simulation results for the 0.5 s switching time of the servo valve and onoff valve.

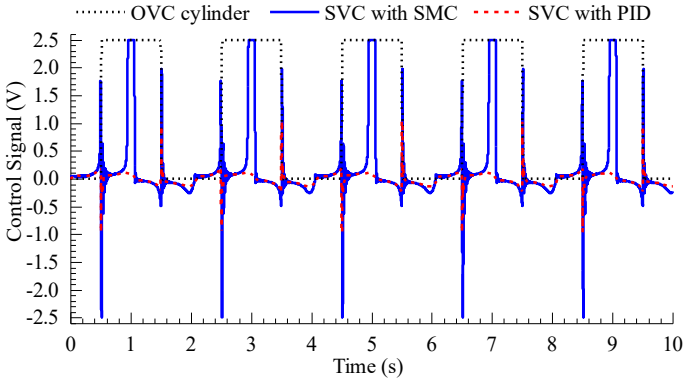

Fig. 3.6 Simulation results for the control signal of 0.5 Hz loading.

Moreover, the effect of the model-based SMC compensation strategy was also tested for 0.5 Hz and 1 Hz sinusoidal loads, as shown in Fig. 3.4 and Fig. 3.7, respectively. And the control signals for 0.5 Hz and 1 Hz sinusoidal loads of the servo valve and the onoff valve were shown in Fig. 3.6 and Fig. 3.8, respectively. It can be seen from the enlarged figure of Fig. 3.4(a), the switching error is reduced from about 6.3 kN to 2.4 kN at 0.5 s switching time. By expanding the simulation result of the switching process as plotted in Fig. 3.5, the response time of the onoff valve was about 20 ms while the servo valve began to respond in 3 ms under the PID controller. Thus, the total loading force declined rapidly and then rebounded with the onoff valve gradually opening. In contrast, the servo valve under model-based SMC actively slowed down the response speed. It began to respond in 9 ms. Therefore, the total loading force was relatively increasing smoothly. Besides, the tracking error except for the switching error was within 0.4 kN for SMC while the tracking error was about 1.4 kN for PID control as shown in Fig. 3.7(b). It can be concluded that the switching error is greatly reduced and the tracking performance is better for the model-based SMC compensation strategy.

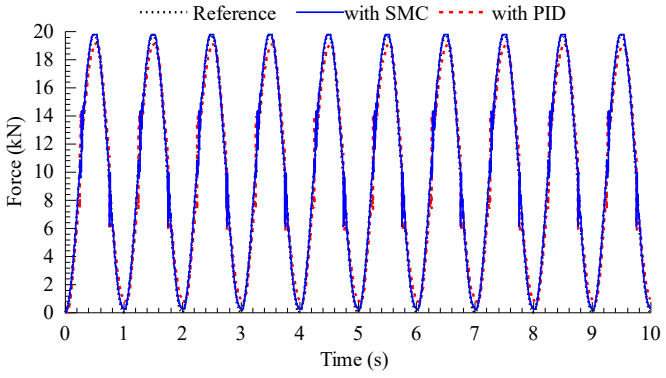

(a)

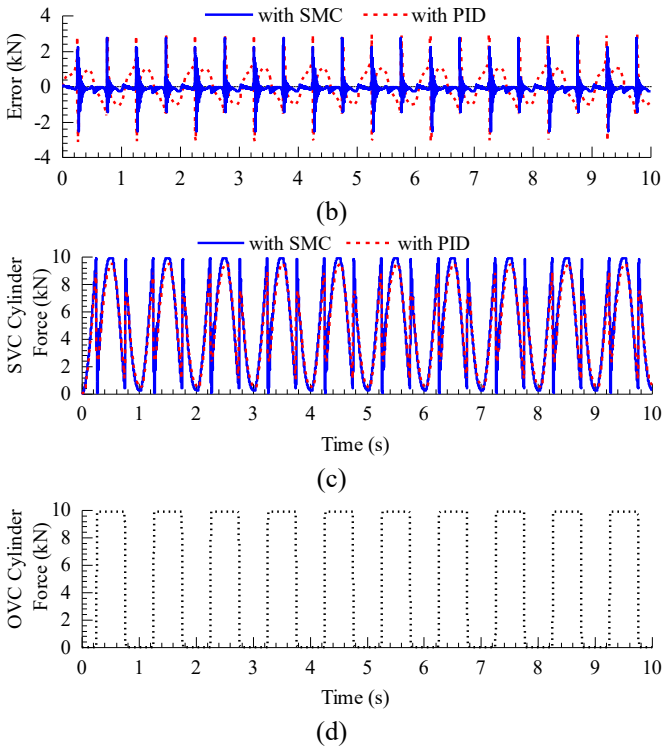

Fig. 3.7 Simulation results for 1.0 Hz loads. (a) Tracking performance. (b) Tracking error. (c) Tracking force of the SVC cylinder. (d) Tracking force of the OVC cylinder.

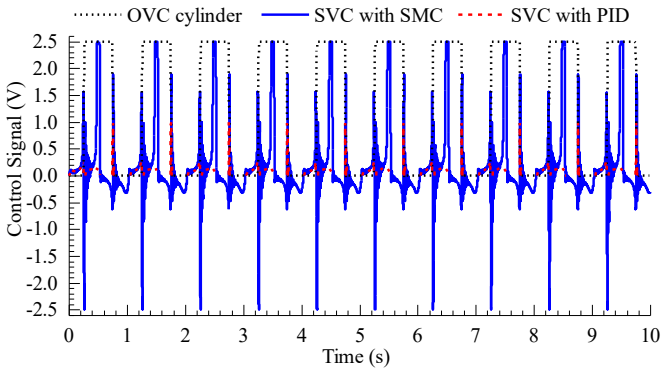

Fig. 3.8 Simulation results for the control signal of 1 Hz loading.

5. CONCLUSION

In this paper, the method of applying MEDSL to the non-torque hydraulic loading system is proposed. To solve the eccentric moment caused by the installation distance and the changed force distribution, the whole loading principle is designed. The loading formula is set up to ensure the implementation of accurate reproduction of 5 DOF loads. In addition, a model-based SMC compensation control strategy is proposed aiming at the asynchronous switching

characteristic of the servo valve and the onoff valve. The loading performance is investigated by the AMESim and Simulink co-simulation. The results show that the switching error is reduced and the total loading process is smoother by using the advanced controller.

Furthermore, for the total loading force, the switching error of the descending process is larger than that of the ascending process. This is mainly due to the difference between opening and closing characteristics, which should be solved in further research. Besides, this paper shows the control strategy of one servo valve and one onoff valve condition, which is the foundation theory of the MEDSL system. The extended cases for more OVC cylinder are not considered and illustrated which can be explored in further studies. Moreover, the research of twelve force application points, involving additional disturbances and accurate calculation of loading matrix, will be the focus research of the next stage for the author's work.

6. ACKNOWLEDGMENT

This study was supported in part by the National Key R&D Program of China under Grant 2018YFB1501900, in part by the Science Fund for Creative Research Groups of National Natural Science Foundation of China under Grant 51821093, in part by the Youth Foundation of National Natural Science Foundation of China under Grant 51905472, and in part by Zhejiang Provincial Natural Science Foundation of China under Grant LZ19E050001.

7. REFERENCES

[1] Global Wind Energy Council, Global Wind Report 2021 [Online]. Available: https://gwec.net/global-wind-report-2021/.

[2] J. M. P. Pérez, F. P. G. Márquez, A. Tobias, M. Papaelias, "Wind turbine reliability analysis," Renewable Sustain. Energy Rev., vol. 23, pp. 463-472, 2013.

[3] K. Y. Oh, J. K. Lee, H. J. Bang, J.Y. Park, J. S. Lee, B. I. Epureanu, "Development of a 20 kW wind turbine simulator with similarities to a 3 MW wind turbine," Renewable Energy, vol. 62, pp. 379-387, 2014.

[4] X. Yin, Y. Lin, W. Li, H. Ye, "Loading system and control strategy for simulating wind turbine loads," J. Vib. Control, vol. 23, no. 11, pp. 1739-1752, 2015.

[5] X. Yin, Y. Lin, W. Li, H. Ye, Y. Gu, and H. Liu, "Reproduction of five degree-of-freedom loads for wind turbine using equispaced electro-hydraulic actuators," Renewable Energy, vol. 83, pp. 626-637, 2015.

[6] N. Averous, M. Stieneker, S. Kock, C. Andrei, A. Helmedag, R. De Doncker, et al., "Development of a 4 MW full-Size wind-turbine test bench," IEEE Trans. Emerg. Sel. Topics Power Electron., vol. 5, no. 2, pp. 600-609, 2017.

[7] R. F. Schkoda, "Sliding mode control of a hydraulically actuated load application unit with application to wind turbine drivetrain testing," IEEE Trans. Control Syst. Technol., vol. 23, no. 6, pp. 2203-2215, 2015.

[8] Offshorre Renewable Energy, Powertrain Testing Services [Online]. Available: https://ore.catapult.org.uk/what-we-do/testing-validation%e2%80%a8/powertrain-facilities/.

[9] R&D, R&D Test Systems is developing the world's largest test bench for LORC [Online]. Available: https://www.rd-as.com/insights/worlds-largest-test-bench-lorc/.

[10] Y. Lin, D. Li, Y. Gu, H. Liu, X. Feng, J. Ding, "Multi-cylinder electrohydraulic digital loading technology for reproduction of large load," Mechatronics, vol. 76, pp. 1-10, 2021.
[11] A. Palmieri, R. Procopio, A. Bonfiglio, M. Brignone, M. Invernizzi, A. Morini, B. Veselic, "Tuning and Feasibility Analysis of Classical First-Order MIMO Non-Linear Sliding Mode Control Design for Industrial Applications." Machines, vol. 7, no. 10, 2019.
[12] R. Agarwala, R. A. Chin, P. Malali, "Design of a nonlinear multi-input–multi-output sliding mode pitch angle and plunge controller for a 5MW wind turbine blade tip," Energy Sources, Part A: Recovery, Utilization, and Environmental Effects, 2019.
[13] H. Cho, T. Wanichanon, F.E. Udwadia, "Continuous sliding mode controllers for multi-input multi-output systems," Nonlinear Dyn., 2018.
[14] S. Zeghlache, N. Amardjia, "Real time implementation of nonlinear observer-based fuzzy sliding mode controller for a twin rotor multi-input multi-output system (TRMS)," Optik, vol. 156, pp. 391-407, 2018.
[15] F. Bagheri, H. Komurcugil, O. Kukrer, N. Guler, S. Bayhan, "Multi-Input Multi-Output-Based Sliding-Mode Controller for Single-Phase Quasi-Z-Source Inverters," IEEE Trans. Ind. Electron., vol. 67, no. 8, pp. 6439-6449, 2020.
[16] Y. Gu, Y. Lin, Q. Xu, H. Liu, W. Li, "Blade-pitch system for tidal current turbines with reduced variation pitch control strategy based on tidal current velocity preview," Renewable Energy, vol. 115, pp. 149-158, 2018.

Biographies

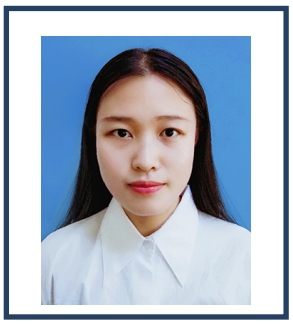

Danyang Li received the B.Eng degree from Yanshan University, Qinhuangdao, China, in 2019. She is currently working toward the Ph.D. degree in mechatronic engineering at Zhejiang University. Her research interests include the test system of wind turbine and electro-hydraulic system control.



Yajing Gu received the B.S. degree and the Ph.D. degree both in mechatronics from Zhejiang University, Hangzhou, China, in 2013 and 2018, respectively. He is currently a research associate at Zhejiang University. His research interests include ocean energy system, intelligent control, and multi-turbine array design.



Yonggang Lin received the M.Eng. degree from Jilin University, Changchun, China, in 2001, and the Ph.D. degree from Zhejiang University, Hangzhou, China, in 2005, both in mechatronic engineering.

In 2016, he was promoted to the rank of Professor at Zhejiang University. His research interests include machinery and electrohydraulic control of wind turbines, wave energy converters, and marine current turbines.



Jiajun Song received the B.S. degree from Beijing Institute of Technology, Beijing, China, in 2012, the M.Sc. and the Ph.D. degree from Michigan Technological University, Michigan, US, in 2020, all in Mechanical Engineering. In 2021, he started working as a post-doc in Zhejiang University. His research interests include wave energy converters, optimization algorithm, and optimal control.



Xiangheng Feng received B.Eng. Degree from Nanjing University of Aero-nautics and Astronautics, Nanjing, China, in 2019. He is currently working toward the Ph.D. degree in mechatronic engineering at Zhejiang University. His research interests include floating offshore wind turbine and load control system.



Hongwei Liu received the M.Eng. degree from the Taiyuan University of Technology, Taiyuan, China, in 2004, and the Ph.D. degree from Zhejiang University, Hangzhou, China, in 2009, both in mechatronic engineering. In 2011, he became a Faculty Member with Zhejiang University, where he was promoted to the rank of Associate Professor, in 2013. He is the Reviewer of Renewable and Sustainable Energy Reviews and Automation of Electric Power Systems. His research interests include ocean energy, hydraulic transmission system, and mechatronic system.

Global Fluid Power Society PhD Symposium 2022| Naples, Italy - 2022

Cartesian Damping Controller with Nonlinear Control for a Floating-Base Hydraulic Manipulator

Pauli Mustalahti and Jouni Mattila

Faculty of Engineering and Natural Sciences, Tampere University, Finland,
pauli.mustalahti@tuni.fi
Faculty of Engineering and Natural Sciences, Tampere University, Finland,
jouni.mattila@tuni.fi

Abstract

Hydraulic manipulators are widely used to move loads to the desired position in many industrial sectors. Specifically, in the forestry, mining, and construction industries, a rigid hydraulic manipulator is mounted on a moving wheeled or tracked platform. These mobile manipulators extend the working envelope of the manipulator due to the mobility of the platform. Common to these industrial applications is that the uneven terrain conditions of the environment cause the manipulator to float. Considering the coupled and nonlinear dynamics behavior of the mobile platform and the rigid manipulator, designing a high-performance closed-loop controller is challenging. In this paper, our main focus is to define the control equations of the model-based Virtual Decomposition Control (VDC) approach to handle mobile manipulator platform movements during the manipulator end-effector motions. As a novel feature, VDC allows control design locally at the subsystem level without imposing additional approximations. The simulation results with a 3-Degrees-of-freedom (DOF) hydraulic manipulator mounted on a floating base are used to demonstrate the effectiveness of the proposed controller.

1 Introduction

Heavy-duty articulated hydraulic manipulators are widely used in industrial applications to transfer heavy loads to desired locations. For industrial applications, it is typical that a rigid hydraulic manipulator is mounted on a moving platform. A non-fixed manipulator base enables extension of the work envelope and the functionality of the manipulator compared to the fixed-base system. Therefore, the combined manipulator and the moving platform are operated as a mobile manipulator. Considering mobile manipulator operations, the working envelope typically consists of uneven terrain conditions (e.g., in the forest, mining and ship industries). Due to the mobile manipulator's complex dynamics and the strong coupling between the mobile platform and the manipulator, designing a closed-loop control and operating these systems are difficult tasks [2, 4].

Decreased human operator workload, energy efficiency, and manipulator safety can be improved by using semi-automated operations. For these reasons, hydraulic manipulator robotic closed-loop control and more automatic operations are currently an important research topic [1, 13]. The first commercial resolved-rated controlled hydraulic manipulators are already available [3, 18] for forest log loading and harvesting applications. However, these commercial solutions typically do not consider the manipulator floating-base movements during the operations. For this reason, manipulator end-effector control is sensitive to platform movements. The majority of the proposed anti-sway control methods for hydraulic heavy-duty manipulators in the literature [5, 14, 17, 19] demonstrates control methods for handling oscillation of the passive unactuated joints. However, in these methods the manipulator is assumed to be in a fixed position. This paper assumes that the motion of the floating base is known, and the uncertainty of the motion of the base can be further considered.

As reported in [13], nonlinear model-based (NMB) control designs have been shown to provide superior control performance for hydraulic manipulators versus the state-of-the-art methods presented. Due to the highly nonlinear dynamics behavior [20] of hydraulic systems, NMB control methods are needed. The Virtual Decomposition Control (VDC) approach, introduced in [21, 22], was reported to provide state-of-the-art control performance with hydraulically driven manipulators in [8, 10, 12]. The VDC controller for the 3-degrees-of-freedom (DOF) manipulator arm was presented in [15], and the VDC controller for the 6-DOF hydraulic manipulator was given in [16].

The main focus of this study is to extend the VDC approach to handle a control design for a floating-base hydraulic manipulator. In this study, it is assumed that the manipulator is placed on the floating-base. Considering the uneven terrain conditions for the mobile manipulator, the floating-base movements follow from the mobile manipulator platform movements. Therefore, it is also assumed that there are no actuators to compensate for the effects of the platform movements on the to manipulator base. The proposed control method effectiveness is verified by using simulation results with a 3-DOF hydraulic manipulator with a 6-DOF floating-base platform.

This paper is organized as follows. Section 2 briefly introduces the mathematical notations of the VDC approach. In Section 3, the virtual decomposition for the entire system is expressed. In addition, the kinematics modeling for the examined entire system is presented in Section 3. The control equations for the examined system are presented in Section 4. Finally, the experimental results are presented in Section 5, and conclusions are drawn in Section 6.

2 Mathematical Foundation

The mathematical notations of the VDC approach are defined as follows. Let us assume that successive orthogonal three-dimensional coordinate frames $\{\mathbf{A}\}$ and $\{\mathbf{B}\}$ are fixed to a rigid body. Then, restrictions [22] for these coordinate frames can be defined as

$$^{\mathbf{B}}V = {}^{\mathbf{A}}\mathbf{U}_{\mathbf{B}}^{T}\,{}^{\mathbf{A}}V \tag{1}$$

$$^{\mathbf{A}}F = {}^{\mathbf{A}}\mathbf{U}_{\mathbf{B}}\,{}^{\mathbf{B}}F, \tag{2}$$

where ${}^{\mathbf{A}}\mathbf{U}_{\mathbf{B}} \in \mathbb{R}^{6\times 6}$ is the force/moment transformation between two fixed coordinate frames. In Eq. (1), the linear/angular velocity vector ${}^{\mathbf{A}}V = [{}^{\mathbf{A}}\mathbf{v}\ \ {}^{\mathbf{A}}\boldsymbol{\omega}]^T$ in coordinate frame $\{\mathbf{A}\}$ can be defined as a combination of the linear velocity vector and $\mathbf{v} \in \mathbb{R}^3$ and the angular velocity vector ${}^{\mathbf{A}}\boldsymbol{\omega} \in \mathbb{R}^3$. Furthermore, the force/moment vector ${}^{\mathbf{A}}F = [{}^{\mathbf{A}}\mathbf{f}\ \ {}^{\mathbf{A}}\mathbf{m}]^T$ can be defined as a combination of the force vector ${}^{\mathbf{A}}\mathbf{f} \in \mathbb{R}^3$ and the moment vector ${}^{\mathbf{A}}\mathbf{m} \in \mathbb{R}^3$.

Furthermore, the dynamics of the rigid links described in coordinate frame $\{\mathbf{A}\}$ can be defined [22] as

$${}^{\mathbf{A}}F^{*} = \mathbf{M}_{\mathbf{A}}\frac{d}{dt}({}^{\mathbf{A}}V) + \mathbf{C}_{\mathbf{A}}({}^{\mathbf{A}}\boldsymbol{\omega})\,{}^{\mathbf{A}}V + \mathbf{G}_{\mathbf{A}}, \tag{3}$$

where $\mathbf{M_A} \in \mathbb{R}^{6\times6}$ denotes the mass matrix, $\mathbf{C_A}({}^{\mathbf{A}}\omega) \in \mathbb{R}^{6\times6}$ denotes the Coriolis and centrifugal terms, ${}^{\mathbf{A}}F^* \in \mathbb{R}^6$ denotes the net force/moment vector, and $\mathbf{G_A} \in \mathbb{R}^6$ denotes the gravity vector.

In a control design, the required rigid body dynamics can be defined with the linear parameterization expression as

$$\mathbf{Y_A}\theta_\mathbf{A} \stackrel{\text{def}}{=} \mathbf{M_A}\frac{d}{dt}({}^{\mathbf{A}}V_\mathrm{r}) + \mathbf{C_A}({}^{\mathbf{A}}\omega){}^{\mathbf{A}}V_\mathrm{r} + \mathbf{G_A}. \tag{4}$$

In Eq. (4), the regressor matrix $\mathbf{Y}_A \in \mathbb{R}^{6\times13}$ and the parameter vector $\theta_\mathbf{A} \in \mathbb{R}^{13}$ are specified in [22].

The required net force/moment vector for the *rigid links* is defined as

$${}^{\mathbf{A}}F_r^* = \mathbf{Y_A}\theta_\mathbf{A} + K_\mathbf{A}({}^{\mathbf{A}}V_r - {}^{\mathbf{A}}V), \tag{5}$$

where $K_\mathbf{A}$ is the velocity feedback control gain.

3 Virtual Decomposition and Kinematics Modeling for the 3-DOF Manipulator

In many industrial applications, it is typical that a mobile working machine with a rigid heavy-duty manipulator is operated in uneven terrain conditions. Varying terrain conditions affect operations, because the orientation of the working machine platform and displacement movements cause a floating-base for the manipulator. Our main focus is to use the VDC approach as a framework to investigate a control design for a hydraulic manipulator with a floating-base. In this paper, it is assumed that the platform movements follow from varying terrain conditions. Further, it is assumed that platform actuators cannot be used to compensate for the floating-base movements of the manipulator base. Considering that the platform movements follow from the environment, it is assumed that there are no constraints on these movements.

As reported in [13], the VDC framework has been used to achieve high control performance for hydraulic manipulators. The VDC the control equations for the complex robot system to be designed locally at the subsystem level [21]. However, in previous studies [8, 10], a 2-DOF manipulator with a fixed-base was examined and a 3-DOF manipulator with a fixed-base was examined in [15].

Next, the three main steps of the VDC framework control design are presented as follows: 1) the coordinate frame attachment to subsystems, 2) virtual decomposition of the entire manipulator system, and 3) presentation

of the simple oriented graph (SOG). Finally, the kinematic equations of the 3-DOF manipulator are presented for the control design.

3.1 Virtual Decomposition of the 3-DOF Manipulator

To describe the kinematics and dynamics relations of the subsystems, fixed coordinate frames need to be attached to the rigid bodies. The coordinate frames for 3-DOF manipulator are presented in Fig. 1(a). Then, the entire system needs to be virtually decomposed into subsystems, which are called open chains and objects, by placing conceptual virtual cutting points (VCPs) in the examined system. VCPs comprise directed separation points between successive subsystems for the six-dimensional force/moment related to these subsystems. A VCP is simultaneously interpreted as driving one subsystem and being driven for another. The driven VCP is the point to which the force/moment is exerted, and the driving VCP is the point from which the force/moment vector is exerted. Virtual decomposition for the manipulator is presented in Fig. 1(b).

The dynamics between successive subsystems in a virtual decomposition system can be represented as a SOG (see definition 2.14 in [22]). The SOG describes force/moment directions as directed edges, and the rigid links are described as nodes. The SOG for the manipulator is presented in Fig. 1(c). In view of [22], the platform's relation to a fixed-inertial frame is described with a massless virtual manipulator, which has one VCP with the platform. The virtual manipulator is used to describe the interaction force from the environment to the platform.

The VDC enables modular control design on subsystem level; thus, subsystems can be connected in a plug-and-play manner to other designed subsystems. The VDC control design for the 2-DOF manipulator is presented detail in [6], and the control design for a 3-DOF manipulator with a base rotation is given in [15]. The dynamics model for the hydraulic cylinder is specified in [11, 22], with the corresponding modular control equation. Considering the control design for the manipulator in Fig. 1(b), the floating-base does not affect the control equations for manipulator subsystems.

3.2 Kinematics Modeling for the 3-DOF Manipulator

In robotics applications, the desired manipulator end-effector motions are typically provided as a reference trajectory to the control system. In the VDC approach, the control objective is to make the controlled actual veloc-

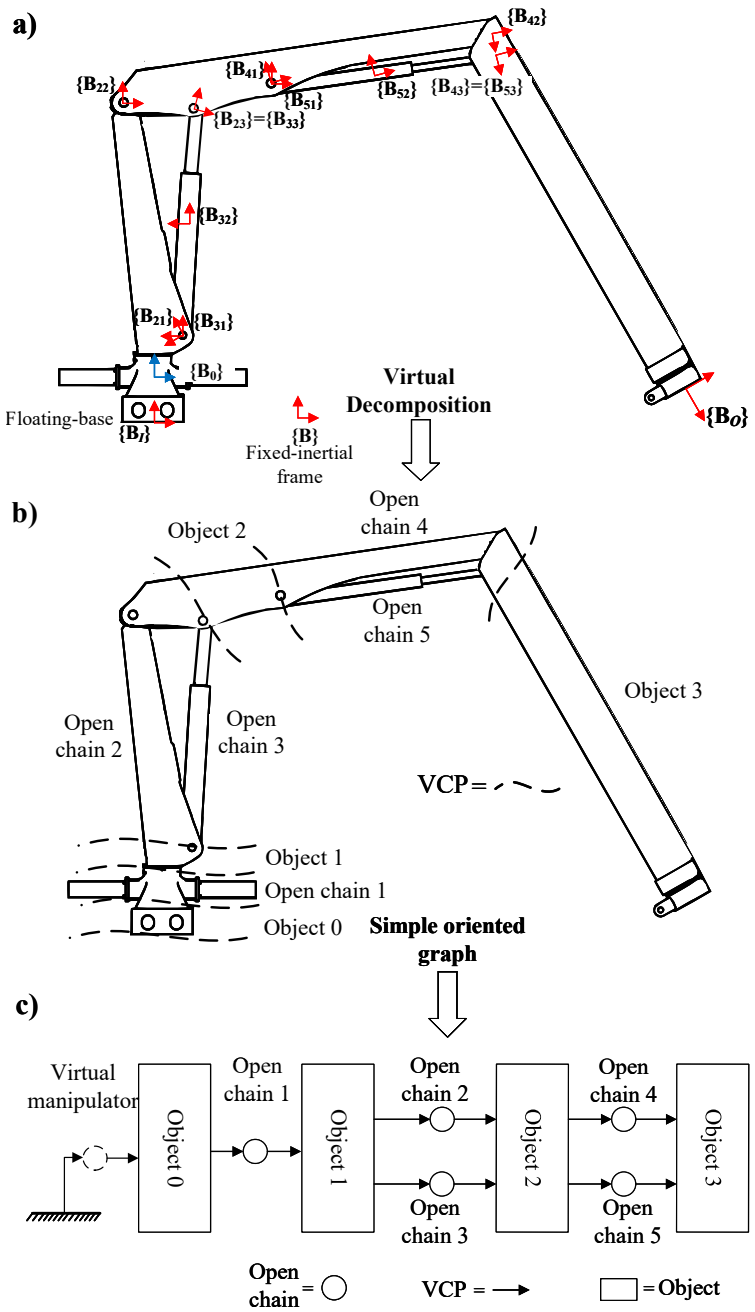

Figure 1 Virtual decomposition for the entire manipulator.

Table 1 DH-parameters for a Three-Bar Manipulator

a	d	α	θ
0	L_0	$-\pi/2$	0
L_{11}	L_{12}	$\pi/2$	θ_1
L_1	0	0	θ_2
L_2	0	0	θ_3

ities track with the required velocities, which consist of the desired velocity and one or more terms that are related to control errors [22]. This can be performed either in the Cartesian space or in joint space. As demonstrated in [7], the VDC approach provides high control performance in the Cartesian space. By considering the manipulator with the floating-base in Fig. 1(a), the platform movements need to incorporate to in the Cartesian space reference design.

The kinematic chain of spatially rigid links in a mechanical system can be modeled using Denavit–Hartenberg (DH) parameters to describe the convention between coordinate frames as a function of the joint angles. The coordinate frames required to describe the kinematics in joint space are given in Fig. 2. These frames are set according to the right-hand rule, so that in blue frames, the y-axis points through the paper, and in other frames, the z-axis points out from the paper. Thus, the kinematics of the manipulator in Fig. 2 can be defined with the DH-parameters in Table 1. The parameters L_{11}, L_{12}, L_0, L_1, and L_2 describe the constant lengths of the rigid links and the joint angles θ_1, θ_2, and θ_3, which are assumed to the measured. In addition, a linear/angular velocity vector in the floating-base coordinate frame $\{\mathbf{B}_I\}$ is assumed to be measured related to the fixed-inertial frame $\{\mathbf{B}\}$.

Comparing the coordinate frames in Fig. 1(a) and Fig. 2, in the latter figure, frames are defined according to DH-parameters. This enables more compact kinematic equations. However, as shown in [9], the rotations for the coordinate frames in Fig. 1(a) can be written according to the joint angles.

The manipulator kinematics can be analyzed by defining the linear/angular velocities in the defined coordinate frames in Fig. 2. Now, by using the DH-parameters in Table 1 and by reusing Eq. (1), the kinematics

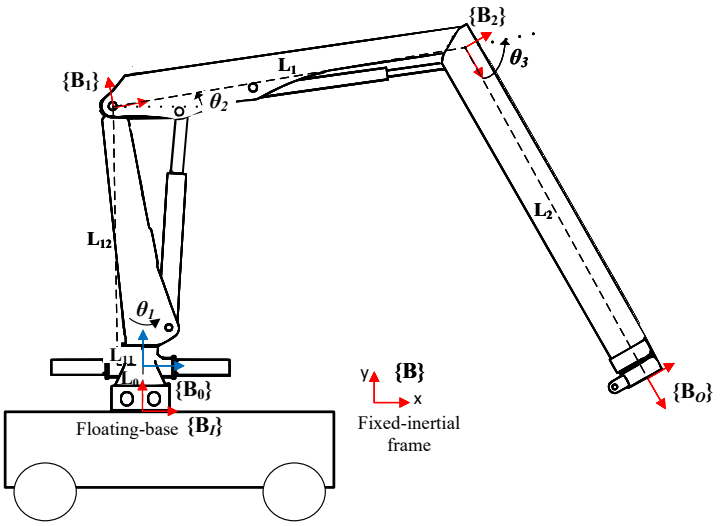

Figure 2 A floating-base mobile manipulator.

for the manipulator can be written as

$$
\begin{aligned}
{}^{\mathbf{B}_0}V &= {}^{\mathbf{B}_I}\mathbf{U}_{\mathbf{B}_0}^{T}\,{}^{\mathbf{B}_I}V + \mathbf{z}\dot{\theta}_1 && (6)\\
{}^{\mathbf{B}_1}V &= {}^{\mathbf{B}_0}\mathbf{U}_{\mathbf{B}_1}^{T}\,{}^{\mathbf{B}_0}V + \mathbf{z}\dot{\theta}_2 && (7)\\
{}^{\mathbf{B}_2}V &= {}^{\mathbf{B}_1}\mathbf{U}_{\mathbf{B}_2}^{T}\,{}^{\mathbf{B}_1}V + \mathbf{z}\dot{\theta}_3 && (8)\\
{}^{\mathbf{B}_O}V &= {}^{\mathbf{B}_2}\mathbf{U}_{\mathbf{B}_O}^{T}\,{}^{\mathbf{B}_2}V, && (9)
\end{aligned}
$$

where $\dot{\theta}_1$, $\dot{\theta}_2$, and $\dot{\theta}_3$ are the angular velocities of the manipulator joints and $\mathbf{z} = [0\ 0\ 0\ 0\ 0\ 1]^T$. In Eq. (6), ${}^{\mathbf{B}_I}V$ is the linear/angular velocity vector for the platform. In this study, it is assumed that the platform velocities can be measured.

3.3 Required Kinematics of the 3-DOF Manipulator

The corresponding equations for the control design can be written by reusing Eqs. (6)–(9), as

$$
\begin{aligned}
{}^{\mathbf{B}_0}V_r &= {}^{\mathbf{B}_I}\mathbf{U}_{\mathbf{B}_0}^{T}\,{}^{\mathbf{B}_I}V_r + \mathbf{z}\dot{\theta}_{1r} && (10)\\
{}^{\mathbf{B}_1}V_r &= {}^{\mathbf{B}_0}\mathbf{U}_{\mathbf{B}_1}^{T}\,{}^{\mathbf{B}_0}V_r + \mathbf{z}\dot{\theta}_{2r} && (11)\\
{}^{\mathbf{B}_2}V_r &= {}^{\mathbf{B}_1}\mathbf{U}_{\mathbf{B}_2}^{T}\,{}^{\mathbf{B}_1}V_r + \mathbf{z}\dot{\theta}_{3r} && (12)\\
{}^{\mathbf{B}_O}V_r &= {}^{\mathbf{B}_2}\mathbf{U}_{\mathbf{B}_O}^{T}\,{}^{\mathbf{B}_2}V_r, && (13)
\end{aligned}
$$

where $\dot{\theta}_{1r}$, $\dot{\theta}_{2r}$, and $\dot{\theta}_{3r}$ are the required joint velocities, and $\mathbf{z} = [0\ 0\ 0\ 0\ 0\ 1]^T$. In the VDC approach, the required actuator dynamics are used to define a feedforward control term for actuators. As Eqs. (4)–(5) show, the required dynamics of the rigid objects in Fig. 2 can be calculated by defining the required velocities, which is a unique property of the VDC. The required angles for the closed-chain subsystem in lift and elbow joints can be written as a function of manipulator joint angles $\dot{\theta}_{1r}$, $\dot{\theta}_{2r}$, and $\dot{\theta}_{3r}$, which are defined in the following section.

4 Cartesian Control for the Floating-Base Manipulator

Considering the mobile working machine with a heavy-duty manipulator, the platform movements during the operation of manipulators affect control design. It is assumed that the automation level of the hydraulic manipulators will rise [13] due to the robotic control of these manipulators. Nowadays, many commercial solutions for these kinds of hydraulic manipulators are available. However, these commercial solutions typically do not consider the effects of platform movements on the end-effector position.

In robotics, it is typical that the desired end-effector motions are investigated in the Cartesian space. However, in hydraulic manipulators, joint space motions are used in the control (see Fig. 2). In view of [23], the forward differential kinematics relation between the Cartesian space and the joint space for the entire examined system can be defined by reusing Eqs. (6)–(9), as

$$\mathbf{J}_q = \begin{bmatrix} {}^{\mathbf{B}_0}\mathbf{U}_{\mathbf{B}_O}^T\mathbf{z} & {}^{\mathbf{B}_1}\mathbf{U}_{\mathbf{B}_O}^T\mathbf{z} & {}^{\mathbf{B}_2}\mathbf{U}_{\mathbf{B}_O}^T\mathbf{z} \end{bmatrix}, \tag{14}$$

where $\mathbf{z} = [0\ 0\ 0\ 0\ 0\ 1]^T$, and $\mathbf{J}_q \in \mathbb{R}^{6\times 3}$ is the Jacobian matrix for the manipulator. In Eq. (14), only the forward differential kinematics for the manipulator is presented. Now, by considering the floating-base movements, the forward kinematics of the entire system can be written in a matrix form, as

$$\begin{bmatrix} {}^{\mathbf{B}_O}V \\ {}^{\mathbf{B}_I}V \end{bmatrix} = \begin{bmatrix} \mathbf{J}_q & {}^{\mathbf{B}_I}\mathbf{U}_{\mathbf{B}_O}^T \\ 0 & I_6 \end{bmatrix} \begin{bmatrix} \dot{\mathbf{q}} \\ {}^{\mathbf{B}_I}V \end{bmatrix}, \tag{15}$$

where $\dot{\mathbf{q}} = \begin{bmatrix} \dot{\theta}_1\ \dot{\theta}_2\ \dot{\theta}_3 \end{bmatrix}^T$ is the joint velocity vector, ${}^{\mathbf{B}_I}V \in \mathbb{R}^6$ is the platform linear/angular velocity vector, and ${}^{\mathbf{B}_O}V \in \mathbb{R}^6$ is the linear/angular velocity vector of the manipulator end-effector.

In Eq. (10)–(13), the forward kinematics describes the relation from the joint space to the Cartesian space. However, in robotics, it is typical that references for the manipulator are defined in Cartesian space. For this reason,

the relation between the Cartesin space and the joint space can be defined as inverse kinematics. Considering the 3-DOF manipulator in Fig. 2, only the desired reference values for linear velocities in the coordinate frame $\{\mathbf{B}_O\}$ can be designed in the Cartesian space, and the angular velocities of the end-effector cannot be designed. Therefore, the manipulator end-effector velocity needs to be rewritten, as

$$V_{Or} = \begin{bmatrix} v_{Or} \\ \omega_{Or} \end{bmatrix}, \tag{16}$$

where $v_{Or} \in \mathbb{R}^3$ is the required linear velocity vector, and $\omega_{Or} \in \mathbb{R}^3$ is the required angular velocity in coordinate frame $\{\mathbf{B}_O\}$. Moreover, the Jacobian matrix in Eq. (14) can be rewritten as

$$\mathbf{J}_q = \begin{bmatrix} \mathbf{J}_x \\ \mathbf{J}_\omega \end{bmatrix}, \tag{17}$$

where $\mathbf{J}_x \in \mathbb{R}^{3\times3}$ is the displacement Jacobian and $\mathbf{J}_\omega \in \mathbb{R}^{3\times3}$ is the rotational Jacobian. Now, the inverse solution for manipulator kinematics in the joint space can be written as

$$\dot{\mathbf{q}}_r = \mathbf{J}_x^{-1} v_{Or} - \mathbf{J}_q^{*\,{}^{\mathbf{B}_I}V_r}, \tag{18}$$

where ${}^{\mathbf{B}_I}V_r$ is the required platform velocity, and $\dot{\mathbf{q}}_r$ is the required joint velocity vector. In this paper, it is assumed that platform velocities follow directly from environmental changes and are not controllable. Therefore, it can be assumed that ${}^{\mathbf{B}_I}V_r = {}^{\mathbf{B}_I}V$. In Eq. (18), $\mathbf{J}_q^* \in \mathbb{R}^{3\times6}$ is the weighted pseudoinverse solution for the Jacobian inverse. In this study, the inverse solution is calculated by using Moore-Penrose pseudoinverse solution.

In the Cartesian space, the required linear velocity v_{Or} in Eq. (18) can be defined by using the desired linear velocity and the desired end-effector position, as

$$v_{Or} = v_{Od} + \lambda(X_d - X), \tag{19}$$

where $\lambda \in \mathbb{R}^{3\times3}$ is the position feedback gain matrix with diagonal [λ_x λ_y λ_z] for the Cartesian position, $X_d \in \mathbb{R}^3$ and $X \in \mathbb{R}^3$ are the desired and measured Cartesian position values for the manipulator end-effector, and v_{Od} is the desired linear velocity in frame $\{\mathbf{B}_O\}$. Typically, the desired positions and linear velocities are provided as a reference trajectory. In this paper, the measured value for Cartesian position is calculated by using measured joint angles and manipulator kinematics equations.

Table 2 Manipulator main links parameters for simulation

Link	Length	Mass
L_0	0.25 m	20 kg
L_1	1.30 m	50 kg
L_2	2.00 m	50 kg
L_{11}	-0.12 m	0 kg
L_{12}	1.30 m	90 kg

5 Simulation Results

In this section, we discuss how the control equations in Sections 3 and 4 are verified by simulation results. The proposed control equations are simulated in three different test cases. In the first case, it is demonstrated that the proposed control equations can be used to compensate for the effects of the platform angular velocities on the end-effector position. The second simulation results show that the proposed control equations enable the desired velocity of the manipulator end-effector to be designed despite platform movements. In the final case, the effectiveness of the proposed control equations is demonstrated when the platform has linear and angular velocities.

The mechanical model for the floating-base mobile manipulator in Fig. 2 is constructed in the MATLAB Simscape Multibody software environment. This simulation environment provides a multi-body simulation for 3D-mechanical systems, including rigid body inertial parameters, joints, and constraints. In Table 2, the main dimensions and the mass parameters for the manipulator's rigid links are presented. The dimensions for the manipulator's cylinders (see Fig. 2) are $80/60-380$ for the rotation cylinder, $80/60-600$ for the lift cylinder and $80/60-600$ for the elbow cylinder. In simulations, all system measurements are defined to correspond the real-time experimental setup in [15]. The feedback gains in the Cartesian space (see Eq. (19)) are set for each direction as $\lambda_x = \lambda_y = 8$ and $\lambda_z = 14$ are used in all simulation cases.

In the first case, it is assumed that the platform orientation in coordinate frame $\{\mathbf{B}_I\}$ (see Fig. 2) can be changed related to fixed frame $\{\mathbf{B}\}$. The desired linear velocity for the end-effector in frame $\{\mathbf{B}_O\}$ is defined as zero and the reference position is set as fixed to point $[2.92\ 0.97\ 0.1858]^T$. The angular velocities in the floating-base coordinate frame $\{\mathbf{B}_I\}$ are shown in Fig. 3. The corresponding Cartesian space position for the manipulator end-effector is presented in Fig. 4. As the Fig 4 shows, the proposed control equations

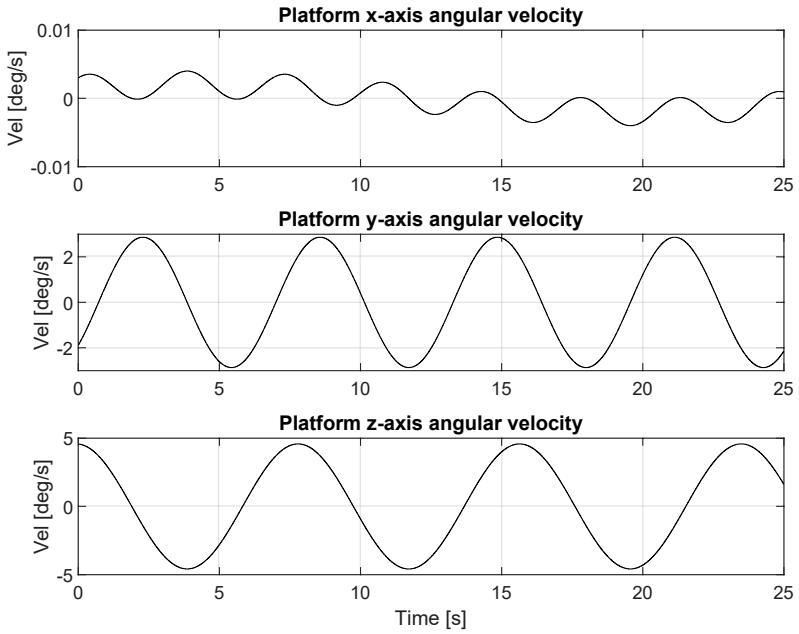

Figure 3 Manipulator floating-base angular velocities.

enable efficiently compensate the floating-base movements by end-effector Cartesian space control.

In the second case, a point-to-point quintic reference trajectory is used to the define desired linear velocity for the end-effector. The end-effector x-axis desired linear velocity in frame $\{\mathbf{B}_O\}$ is designed so that the end-effector moves from point 3.0 m to 2.8 m in a 2 s period, while the other directions are set to constant. The floating-base angular velocities in this case are similarly to the first test case. The corresponding end-effector position is presented in Fig. 5. The results show that the proposed control equations allow us to design an end-effector Cartesian position reference separate from the platform movements. Comparing the simulation the results in Fig. 5 to results in Fig. 4, the manipulator movements does not effect significantly to position tracking errors.

In the final case, it is assumed that the platform also has the linear velocity along the x-axle in coordinate frame $\{\mathbf{B}_O\}$. The platform velocities in this case are presented in Fig. 6, where the angular velocities are the same as in Fig. 3. Similar to the first case, the desired linear velocity for the end-effector

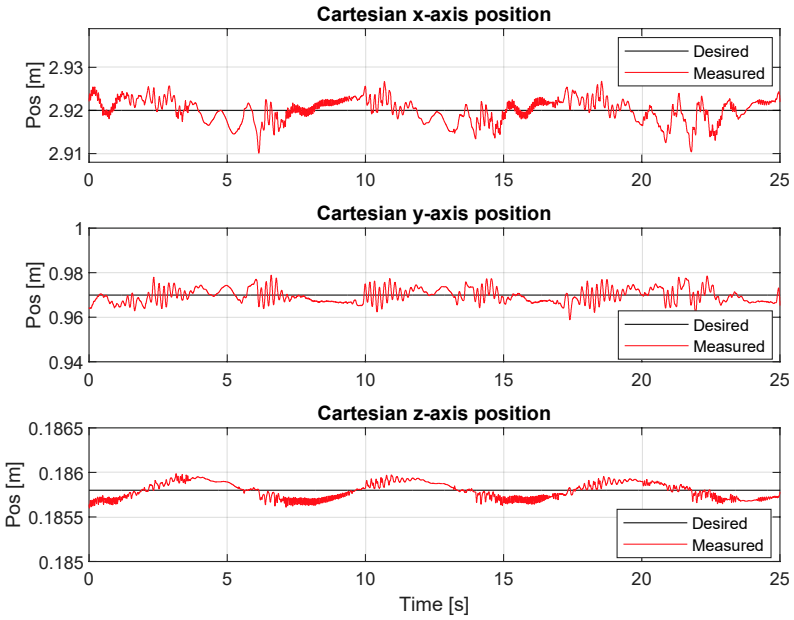

Figure 4 Manipulator end-effector position with a constant reference.

is zero, and the end-effector position is set to $[2.92\ 0.97\ 0.1858]^T$. Now, the end-effector positions with the platform velocities in Fig. 6 are presented in Fig. 7. Comparing the simulation results in Fig. 4 to the results in Fig. 7, also in this case, the proposed control equations enable compensation for platform movements. Considering the tracking errors in Fig. 4 and Fig. 7, the platform linear velocity does not affect the tracking error of the end-effector position.

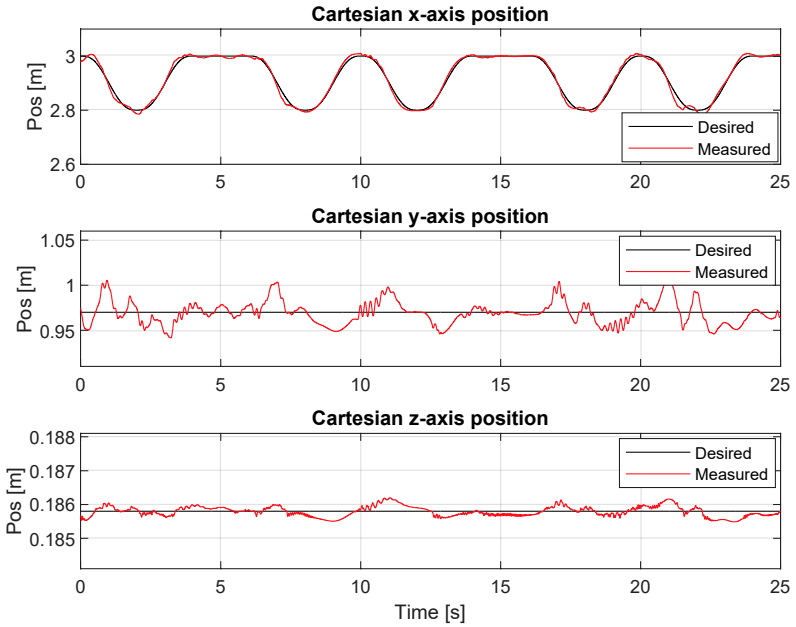

Figure 5 Manipulator end-effector position with motion.

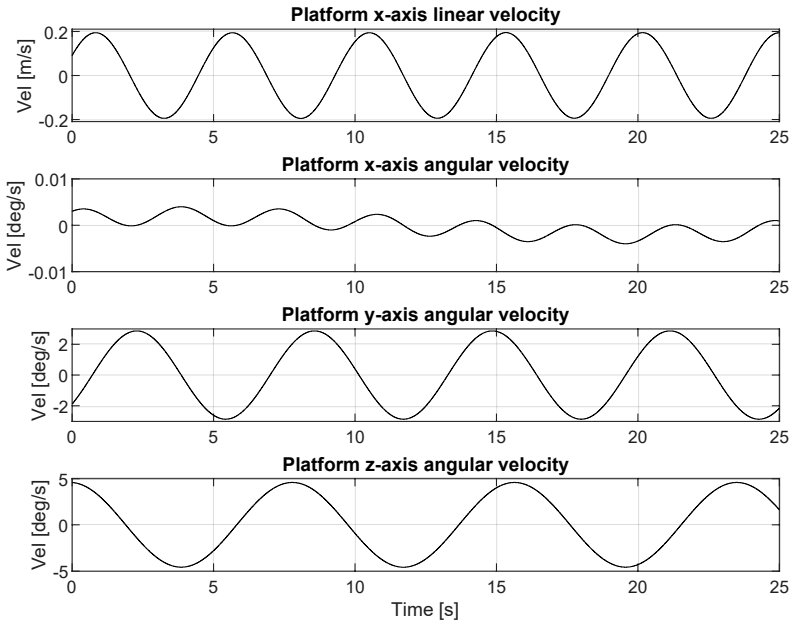

Figure 6 Floating-base linear and angular velocities.

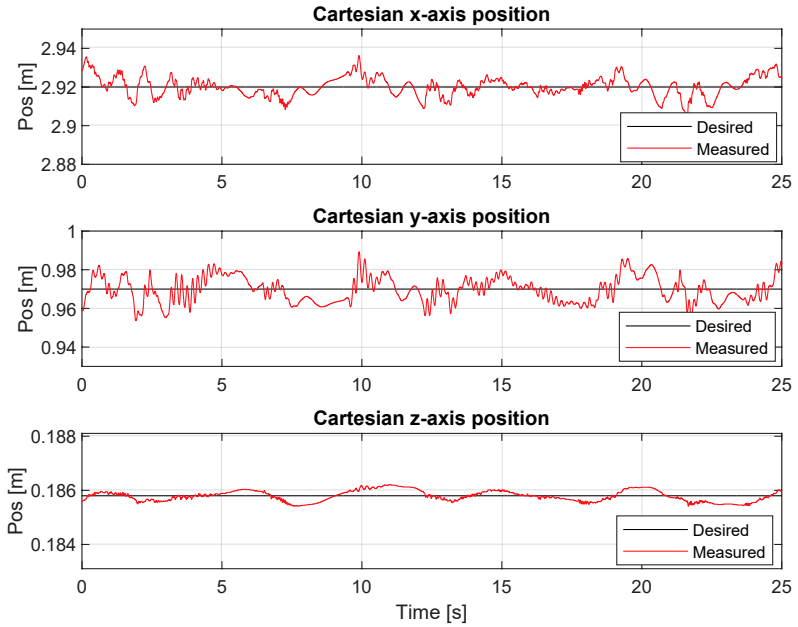

Figure 7 Manipulator end-effector position with a constant reference.

6 Conclusion

This paper's main focus was proposing an NMB controller for a heavy-duty manipulator mounted with a floating-base-like mobile platform. The proposed control equations enables mobile manipulator movements to be handled during end-effector movements. As the simulation results demonstrated, the proposed control equations can be used to compensate for the effects of the platform movements from the manipulator end-effector control design.

The results of this study provided a baseline controller for our future studies, where the proposed controller will be implemented to full-size commercial manipulators, and the experimental results will be presented to verify the effectiveness of the proposed controller.

References

[1] EU. *EU Robotics*. 2018. [online], accessed 23.6.2022, available: Strategic research agenda for robotics in europe 2014–2020.

[2] Raouf Fareh, Mohamad R. Saad, Maarouf Saad, Abdelkrim Brahmi, and Maamar Bettayeb. Trajectory tracking and stability analysis for mobile manipulators based on decentralized control. *Robotica*, 37(10):1732–1749, 2019.

[3] HIAB. *Crane Tip Control*. 2021. [online], accessed 24.6.2022, available: https://www.hiab.com/en/media/news/hiab-crane-tip-control.

[4] Rongyu Jin, Paolo Rocco, and Yunhai Geng. Cartesian trajectory planning of space robots using a multi-objective optimization. *Aerospace Science and Technology*, 108:106360, 2021.

[5] Jouko Kalmari, Juha Backman, and Arto Visala. Nonlinear model predictive control of hydraulic forestry crane with automatic sway damping. *Computers and Electronics in Agriculture*, 109:36–45, 2014.

[6] Janne Koivumäki and Jouni Mattila. High performance nonlinear motion/force controller design for redundant hydraulic construction crane automation. *Automation in Construction*, 51:59–77, 2015.

[7] Janne Koivumäki and Jouni Mattila. Stability-guaranteed force-sensorless contact force/motion control of heavy-duty hydraulic manipulators. *IEEE Trans. Robotics*, 31(4):918–935, 2015.

[8] Janne Koivumäki and Jouni Mattila. Stability-guaranteed impedance control of hydraulic robotic manipulators. *IEEE/ASME Trans. Mechatronics*, 22(2):601–612, 2017.

[9] Janne Koivumäki, Wen-Hong Zhu, and Jouni Mattila. Addressing closed-chain dynamics for high-precision control of hydraulic cylinder actuated manipulators. In *BATH/ASME 2018 Symposium on Fluid Power and Motion Control*, pages V001T01A018–V001T01A018. ASME, 2018.

[10] Janne Koivumäki, Wen-Hong Zhu, and Jouni Mattila. Energy-efficient and high-precision control of hydraulic robots. *Control Engineering Practice*, 85:176–193, 2019.

[11] Santeri Lampinen, Janne Koivumäki, and Jouni Mattila. Improved hydraulic cylinder model for the virtual decomposition control approach. In *2019 IEEE International Conference on Cybernetics and Intelligent Systems (CIS) and IEEE Conference on Robotics, Automation and Mechatronics (RAM)*, pages 113–118. IEEE, 2019.

[12] Santeri Lampinen, Janne Koivumäki, Wen-Hong Zhu, and Jouni Mattila. Force-sensorless bilateral teleoperation control of dissimilar master-slave system with arbitrary scaling. *IEEE Transactions on Control Systems Technology*, pages 1–15, 2021.

[13] Jouni Mattila, Janne Koivumäki, Darwin G Caldwell, and Claudio Semini. A survey on control of hydraulic robotic manipulators with projection to future trends. *IEEE/ASME Trans. on Mechatronics*, 22(2):669–680, 2017.

[14] Pauli Mustalahti, Janne Koivumäki, and Jouni Mattila. Stability-guaranteed anti-sway controller design for a redundant articulated hydraulic manipulator in the vertical plane. In *ASME/BATH Symp. on Fluid Power and Motion Control*, pages V001T01A031–V001T01A031. ASME, 2017.

[15] Pauli Mustalahti and Jouni Mattila. Nonlinear model-based controller design for a hydraulic rack and pinion gear actuator. In *BATH/ASME 2018 Symp. on Fluid Power and Motion Control*, pages V001T01A020–V001T01A020. ASME, 2018.

[16] Pauli Mustalahti and Jouni Mattila. Nonlinear model-based control design for a hydraulically actuated spherical wrist. In *Fluid Power Systems Technology*, volume 59339, page V001T01A027. American Society of Mechanical Engineers, 2019.

[17] Jörg Neupert, Eckhard Arnold, Klaus Schneider, and Oliver Sawodny. Tracking and anti-sway control for boom cranes. *Control Engineering Practice*, 18(1):31–44, 2010.

[18] Ponsse. *Active Crane*. 2021. [online], accessed 24.6.2022, available: https://www.ponsse.com/en/web/guest/products/tailored-solutions/product/-/p/activecranebisonbuffaloelephant.

[19] Geir Ole Tysse, Andrej Cibicik, Lars Tingelstad, and Olav Egeland. Lyapunov-based damping controller with nonlinear mpc control of payload position for a knuckle boom crane. *Automatica*, 140:110219, 2022.

[20] J. Watton. *Fluid Power Systems: modelling, simulation, analog and microcomputer control*. Prentice Hall, New York, 1989.

[21] W.-H. Zhu, Y.-G. Xi, Z.-J. Zhang, Z. Bien, and J. De Schutter. Virtual decomposition based control for generalized high dimensional robotic systems with complicated structure. *IEEE Trans. Robot. Autom.*, 13(3):411–436, 1997.

[22] Wen-Hong Zhu. *Virtual decomposition control: toward hyper degrees of freedom robots*, volume 60. Springer Science & Business Media, 2010.

[23] Wen-Hong Zhu and Joris De Schutter. Adaptive control of electrically driven space robots based on virtual decomposition. *Journal of guidance, control, and dynamics*, 22(2):329–339, 1999.

Biography



Pauli Mustalahti received the M.Sc. degree in engineering from the Tampere University of Technology in 2016 and the D.Sc. (Tech.) in Automation Science and Engineering from the Tampere University in 2023. He is a researcher in the Automation Technology and Mechanical Engineering, Tampere University, Tampere, Finland. His research interests include nonlinear model-based control of robotic manipulators.



Jouni Mattila received his M.Sc. in 1995 and Dr. Tech in 2000, both from Tampere University of Technology (TUT), Tampere, Finland. He is currently a professor of machine automation with the unit of Automation Technology and Mechanical Engineering, Tampere University. His research interests include machine automation, nonlinear model-based control of robotic manipulators and energy-efficient control of heavy-duty mobile manipulators.

Real-time trajectory scaling algorithm for hydraulic manipulators subject to limited on-board power

Lionel Hulttinen, Jouni Mattila

Tampere University, Faculty of Engineering and Natural Sciences, lionel.hulttinen@tuni.fi

Abstract.

Online trajectory generation is a practical necessity when implementing semi-autonomous control functionality for hydraulic working machines, such as earthmoving excavators or forestry loader cranes. In these human-in-the-loop systems, smooth and consistent trajectories need to be generated from hand-lever commands provided by the user, while considering the various local and global constraints of the actuation and power delivery system. For hydraulic manipulators, many velocity-level scaling algorithms have been presented in the last years, which take into account the inherent limitations of the hydraulic power unit by considering the sum of demanded volumetric flows compared to the pump capacity. However, there is a need to generate consistent trajectories that include continuous and bounded acceleration references, and additionally also respect the limitation set by the maximum rated power of the prime mover, which the previous velocity-level approaches are not able to satisfy. In this paper, a power-limited on-line trajectory generation method for load-sensing hydraulic systems is formulated, and simulation results with a 2-DOF manipulator are provided to demonstrate the proposed algorithm.

Keywords. Motion planning, hydraulic manipulator, on-line trajectory scaling.

1. Introduction

Online trajectory generation is an important consideration when developing high-performance motion control systems for hydraulic working machines, such as excavators or various types of loader cranes. When retrofitting these machines into semi-autonomous robotic systems, where the human operator is controlling the tip of the crane instead of commanding each hydraulic cylinder separately, a remarkable effort is required to take into account the different constraints imposed by the actuators and their power transmission.

General methods to generate consistent and smooth motion trajectories for hydraulic cranes from hand-lever/joystick commands have been presented in [1, 2]. However, these schemes consider the actuation bounds of the system by defining velocity and acceleration limits for every degree of freedom separately, which can become cumbersome to tune so that global constraints, such as limits on the sum of actuator velocities or power consumption, are not violated. Performance limits for coordinated motion control of these manipulators are affected by the net gross power provided by the prime mover carried on-board, which drives a common pump supplying multiple functions at the same time.

The most obvious implication of the power constraint is the limited net velocity of the actuators [3]. Unless equipped with a flow-sharing type of hydraulic system (also known as LUDV or 'social flow distribution') preventing fluid from taking the path of least resistance, pump flow saturation leads to lagging of the most loaded actuator. This can often be witnessed as a sudden deceleration of the lift cylinder mechanism and a consequent dipping of the tool center point, typically when fast motions are demanded from multiple actuators simultanenously. This is detrimental to controller performance, since the feedback controllers are not capable of handling control input saturations appropriately unless the reference generation knows the system's inherent limitations.

In the context of hydraulic manipulators, trajectory scaling algorithms that take account the volumetric flow limitations imposed by the hydraulic power unit have been presented in the last years [4, 5]. The firstly mentioned work solved this problem by formulating it as a quadratic program subject to an ℓ_1-norm constraint, while the latter work relied on path-velocity decomposition to uniformly scale down velocity references when the sum of demanded volumetric flows exceeded the pump capacity. While trajectory generation under pump saturation has been succesfully treated in these papers, for advanced motion control of hydraulic machinery, there is a need generate dynamically consistent trajectories that also include continuous acceleration profiles, which the previous velocity-level approaches are not able to provide.

Many works consider constrained motion planning for automated earthmoving excavators, in order to achieve minimum time solutions that respect, e.g., actuator force constraints [6, 7]. In this paper, we develop an online trajectory generation method that generates consistent, continuous trajectories while considering the limited on-board power. The main contribution is to combine an existing real-time trajectory scaling filter [8] and the pump saturation handlers [4, 5], and extend them to varying loading/velocity conditions by additionally considering the power-limiting (anti-stall) valve of the load-sensing hydraulic system. The functionality of the proposed power-limited on-line trajectory generator is verified by simulation experiments.

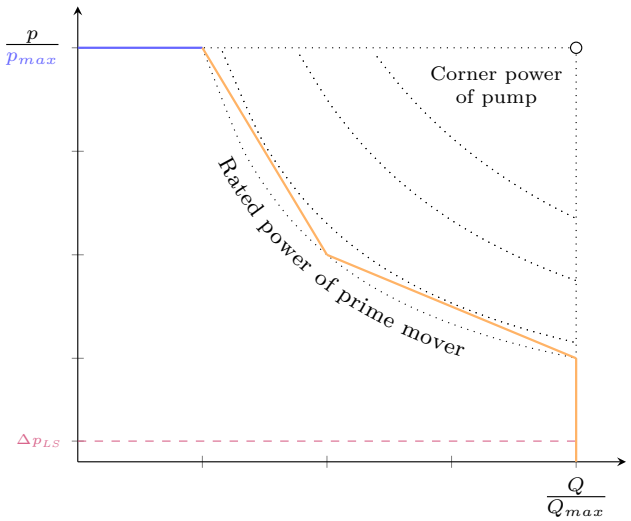

Figure 1. Ideal constant power hyperbola, and its discrete approximation by the power-limiting valve of the load-sensing pump controller.

2. BACKGROUND

Load-sensing (LS) hydraulic systems with variable displacement pumps and pressure-compensated valves are an industry standard for mobile hydraulic working machines, such as excavators. In these systems, the highest load signal determines the pressure level at the pump, and the delivered flow is adjusted according to demand. However, prime movers cannot always fully match the power that could demanded by the pump in some conditions. Often, the power required during standard operation is used as a dimensioning criteria for the rated power of the prime mover, which might only be a third of the corner power of the pump (see Fig. 1). This leads to a system where full actuator speed can only be maintained at a low loading condition, but in high loading condition, a power-limiting valve in the pump's LS controller starts to limit system performance in order to prevent the prime mover from stalling [10].

An LS controlled variable-displacement pump with power limiting is illustrated in Fig. 2. The pump displacement is controlled by a control piston, whose stroke is determined by the load-sensing (FR) and pressure-limiting (DR) spools, so that pump displacement is adjusted according to the required pressure and volumetric flow. If the combination of required pressure and flow exceeds the maximum power setting of the power-limiting (LR) valve, this relief valve reduces the load-sensing pressure signal acting on the FR spool, which in turn decreases the pump displacement in order to meet the power constraint.

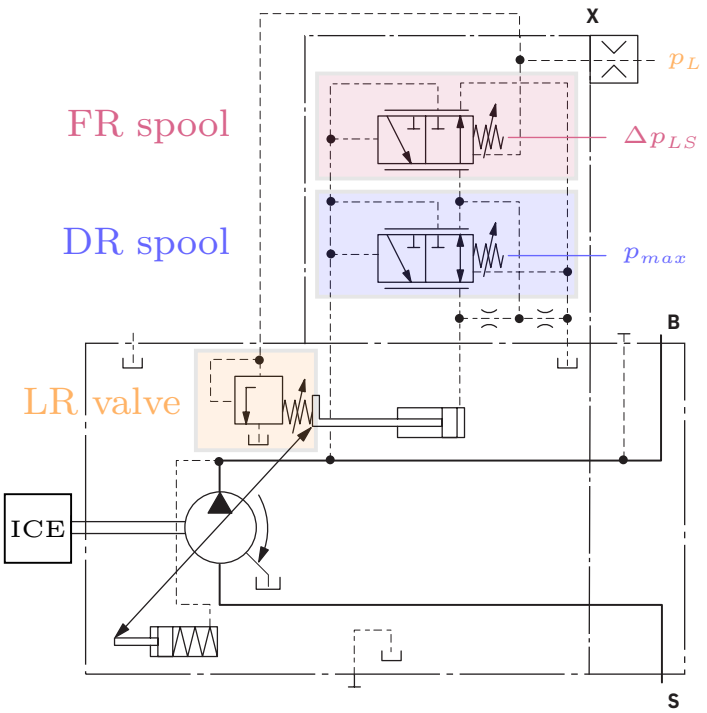

Figure 2. Hydraulic diagram of variable displacement axial piston pump Bosch Rexroth A10VSO with load-sensing controller [9]; the power-limiting (LR) valve is marked in yellow.

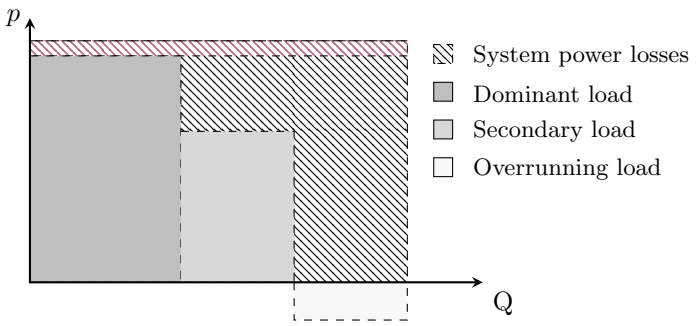

Figure 3. Example of power draw in a load-sensing hydraulic system.

Thus, the LR valve ensures that the hydraulic power at the pump does not exceed the rated power of the prime mover and cause stalling, while allowing the pump to be used at any operating point below the power hyperbola (e.g., to conduct fast movements under low loading conditions). This power-limiting mechanism used alongside an LS system is merely a relief valve and should be distinguished from actual closed-loop power controllers, which maintain the pump power constant and do not allow flow control below the power hyperbola.

This power limiting function in the LS system can be considered an additional global saturation nonlinearity of the hydraulic system, in addition to the flow/velocity and pressure/force limitations of the individual actuators. This power saturation in high loading conditions due to mismatch between the setting of the LR valve (rated power of the prime mover) and the corner power the pump should be considered in the trajectory generation of these machines, in order to prevent biasing and accumulation of controller tracking errors due to unrealizable motion references.

2.1. Power consumption in a load-sensing system

The load flow consumed by an actuator is calculated as

$$Q_L = |\dot{x}|A_c \tag{1}$$

where $\dot{x}$ is linear velocity of the piston and A_c is the effective pressurized area depending on the direction of motion. To take into account overrunning loads, the load pressure of each actuator is defined as

$$p_L = -\operatorname{sign}(f\dot{x})\frac{|f|}{A_c} \tag{2}$$

where f is the cylinder piston force. Here $f\dot{x} < 0$ signifies a resistive load (positive load pressure), while $f\dot{x} > 0$ signifies an overrunning load (negative load pressure) [11].

In a load-sensing hydraulic system, the power draw of the pump is determined by the highest load pressure p_L and the sum of load flows ΣQ_L (see Fig. 3) as

$$P = (\max(p_L) + \Delta p_{LS})\Sigma Q_L \tag{3}$$

where Δp_{LS} denotes the standby pressure at zero stroke, which is generally about 20 bar. The pump power draw is kept below a specified maximum power P_{max}, which is set by the pump manufacturer based on customer orders.

3. Proposed Scaling Algorithm

Using path-time decomposition, a desired trajectory can be expressed as a function of an n-times differentiable path $\mathbf{f}(\cdot)$, and a path coordinate s and its n time-derivatives as

$$\mathbf{q}_d = \mathbf{f}(s) \tag{4a}$$

$$\dot{\mathbf{q}}_d = \mathbf{f}'(s)\dot{s} \tag{4b}$$

$$\ddot{\mathbf{q}}_d = \mathbf{f}'(s)\ddot{s} + \mathbf{f}''(s)\dot{s}^2 \tag{4c}$$

The objective of a trajectory scaling system is to generate a value for the highest time derivative of s, the path coordinate, so that any physical constraints of the system are not violated. As a classic example, trajectory scaling systems use the dynamic model of the manipulator to determine in real-time the maximum feasible accelerations, given bounded actuation torques [12], or maximum feasible jerk by additionally considering the actuator dynamics [13].

For the purpose of trajectory scaling, we can simplify the dynamic equations by neglecting any closed-chain structures. In this case, we can express the inverse dynamic equation for a serial manipulator in joint-space as

$$\tau = \mathbf{H}(\mathbf{q})\ddot{\mathbf{q}} + \mathbf{C}(\mathbf{q}, \dot{\mathbf{q}})\dot{\mathbf{q}} + \mathbf{g}(\mathbf{q}) + \tau_{ext} \tag{5}$$

where $\mathbf{H}(\mathbf{q})$ is the joint-space mass matrix, $\mathbf{C}(\mathbf{q}, \dot{\mathbf{q}})$ is the matrix of centrifugal and Coriolis forces, $\mathbf{g}(\mathbf{q})$ is a vector of gravitational torques, and τ_{ext} is a vector of external disturbance forces due to friction, payload and/or contact with the environment. Equation (5) can then be parametrized as

$$\tau(\ddot{s}, \dot{s}, s) = \mathbf{m}(s)\ddot{s} + \mathbf{b}(\dot{s}, s) \tag{6}$$

where

$$\mathbf{m}(s) = \mathbf{H}(\mathbf{q}_d)\mathbf{f}'(s) \tag{7}$$

$$\mathbf{b}(\dot{s}, s) = \mathbf{H}(\mathbf{q}_d)\mathbf{f}''(s) + \mathbf{C}(\mathbf{q}_d, \dot{\mathbf{q}}_d)\dot{\mathbf{q}}_d + \mathbf{g}(\mathbf{q}_d) + \tau_{ext} \tag{8}$$

From Eq. (6) upper and lower bounds for the path acceleration coordinate $\ddot{s}$ can be solved, which can be used as a part of a trajectory scaling algorithm to generate feasible motion references.

3.1. *Power limit of the system*

Analogously to the pump flow limit or actuator torque bounds, there exists a sum-power limit restricting the curvilinear accelerations of the system. In [14], the power limit was defined as the sum power of the actuators

$$\left|\mathbf{f}'(s)\dot{s}^\top\left(\mathbf{m}(s)\ddot{s} + \mathbf{b}(\dot{s}, s)\right)\right| \leq P_{max} \tag{9}$$

from which the upper and lower bounds for the path acceleration can be solved as

$$\bar{\ddot{s}} = \begin{cases} \dfrac{P_{max} - \mathbf{f}'(s)\dot{s}^\top\mathbf{b}(\dot{s}, s)}{\mathbf{f}'(s)\dot{s}^\top\mathbf{m}(s)} & \text{if } \dot{s} \geq 0 \\ \dfrac{-P_{max} - \mathbf{f}'(s)\dot{s}^\top\mathbf{b}(\dot{s}, s)}{\mathbf{f}'(s)\dot{s}^\top\mathbf{m}(s)} & \text{if } \dot{s} < 0 \end{cases} \tag{10a}$$

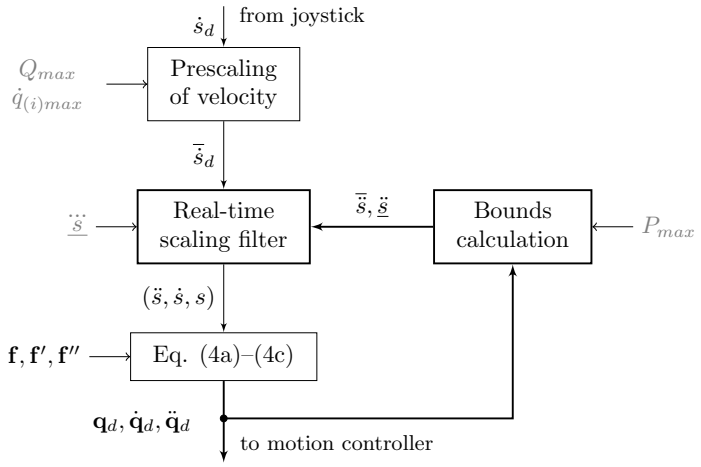

Figure 4. Block diagram of the proposed power-constrained trajectory scaling algorithm. $\dot{s}_d$ denotes user-requested velocity generated by joystick.

$$\underline{\ddot{s}} = \begin{cases} \dfrac{-P_{max} - \mathbf{f}'(s)\dot{s}^\top \mathbf{b}(\dot{s},s)}{\mathbf{f}'(s)\dot{s}^\top \mathbf{m}(s)} & \text{if } \dot{s} \geq 0 \\ \dfrac{P_{max} - \mathbf{f}'(s)\dot{s}^\top \mathbf{b}(\dot{s},s)}{\mathbf{f}'(s)\dot{s}^\top \mathbf{m}(s)} & \text{if } \dot{s} < 0 \end{cases} \tag{10b}$$

This formulation has the downside that it is not in line with the working principle of the load-sensing hydraulic system; for example, it models negative/assistive loads as generating power into the system, and does not consider the highest load pressure as the determining factor for pump power draw.

A correct definition of the power constraint for load-sensing systems would be defined as

$$\Sigma \left| \mathbf{f}'(s)\dot{s} \right| \max \left(\mathbf{m}(s)\ddot{s} + \mathbf{b}(\dot{s},s) \right) \leq P_{max} \tag{11}$$

which leads to constraints in the form

$$\bar{\ddot{s}} = \frac{P_{max} - \Sigma |\mathbf{f}'(s)\dot{s}| \mathbf{b}_i(\dot{s},s)}{\Sigma |\mathbf{f}'(s)\dot{s}| \mathbf{m}_i(s)} \tag{12a}$$

$$\underline{\ddot{s}} = \frac{-P_{max} - \Sigma |\mathbf{f}'(s)\dot{s}| \mathbf{b}_i(\dot{s},s)}{\Sigma |\mathbf{f}'(s)\dot{s}| \mathbf{m}_i(s)} \tag{12b}$$

where $\mathbf{m}_i(s)$ and $\mathbf{b}_i(\dot{s},s)$ denote the torque components corresponding to the highest load torque.

3.2. Real-time trajectory scaling filter

The block diagram of presented trajectory scaling method is illustrated in Fig. 4. As an input, the operator provides a desired path velocity command $\dot{s}_d$ by the hand-lever/joystick. This reference velocity is prescaled within admissible values $\bar{\dot{s}}_d$ determined by the capacity of the

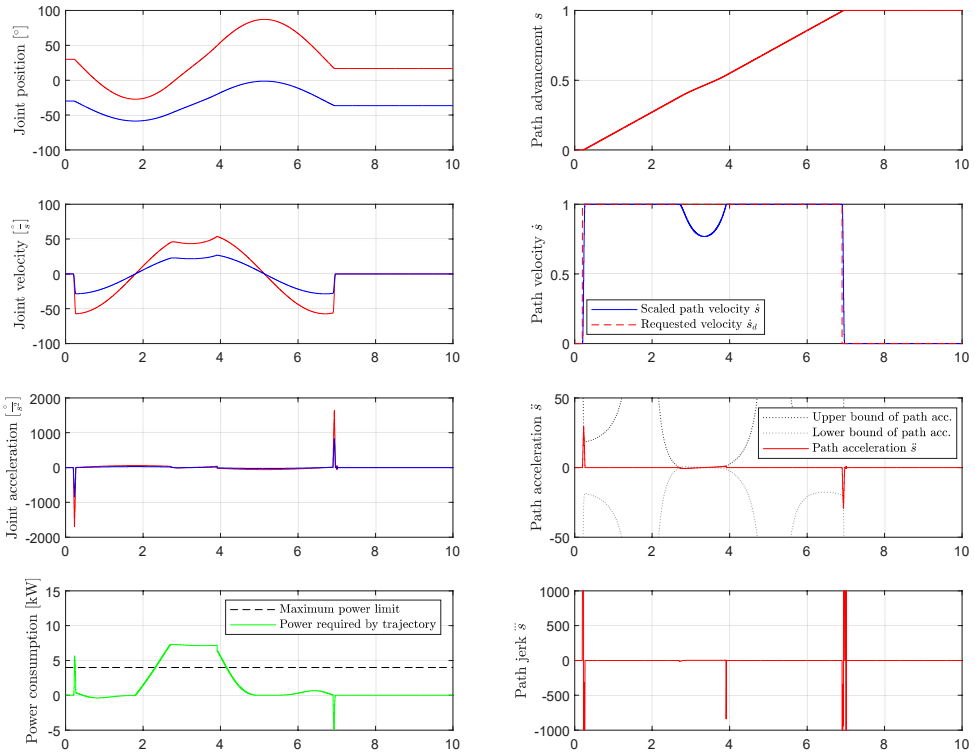

Figure 5. Results with constraints from [14].

pump Q_{max} and/or the maximum velocities $\dot{q}_{(i)max}$ of the individual actuators, determined by the flow saturation of the pressure-compensated valves.

Next, after prescaling of the user-provided velocity command, the desired velocity command $\bar{\dot{s}}_d$ is fed to a real-time suitable trajectory scaling filter. The previously calculated bounds $(\bar{\ddot{s}}, \underline{\ddot{s}})$ on the path acceleration, derived from the power limit, are fed as inputs to a trajectory scaling filter adopted from [8] (presented in detail in Appendix). In [8], this scaling filter was used to enforce bounds on robot control torques and their time derivatives. The same real-time scaling filter has also been recently employed in teleoperation systems to prevent inconsistencies between the master device and a hydraulic slave manipulator [15].

The working principle of the trajectory scaling filter is to generate $\dddot{s}$ so that $(\ddot{s}, \dot{s}, s)$ do not cause constraint violations. The $\dddot{s}$ generated by the filter passes through a chain of three integrators to yield $\ddot{s}$, $\dot{s}$ and s, from which the reference trajectory is computed according to (4a)–(4c). If a constraint violation is about to occur (e.g., if the power constraint cannot be maintained), the trajectory scaling filter is to temporarily gives up tracking the desired velocity path coordinate $\dot{s}_d$, leading into a deviation between $\dot{s}$ and $\dot{s}_d$.

4. Simulation Experiments

In order to demonstrate the effectiveness of the proposed method, a simulation study considering a planar 2R manipulator is carried out. Sinusoidal trajectories were applied for both joints, the path geometry being defined by

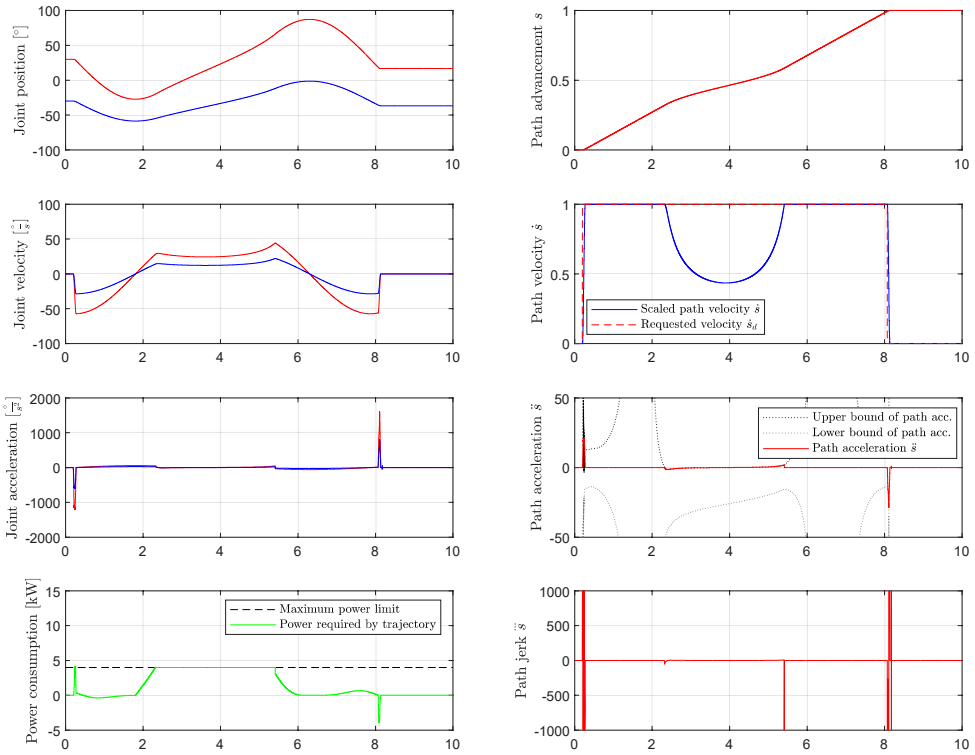

Figure 6. Results with proposed method.

$$\mathbf{f}(s) = \begin{bmatrix} \frac{\pi}{6} - \sin(s) \\ -\frac{\pi}{6} - 0.5\sin(s) \end{bmatrix} \tag{13a}$$

$$\mathbf{f}'(s) = \begin{bmatrix} -\cos(s) \\ -0.5\cos(s) \end{bmatrix} \tag{13b}$$

$$\mathbf{f}''(s) = \begin{bmatrix} \sin(s) \\ 0.5\sin(s) \end{bmatrix} \tag{13c}$$

In this study, a symmetric upper/lower bound for the path jerk coordinate $\dddot{s}$ is adopted and used as a tuning parameter representing the response dynamics of the load-sensing controller of the pump. The path jerk limit was set to $\underline{\dddot{s}} = -1000$, i.e., $|\dddot{s}| < 1000$.

4.1. Shortcomings of existing approach

We first employ the constraint (10a)–(10b) from [14] for the path geometry described by (13a)–(13c), using the trajectory scaling filter described in the previous section and illustrated in Fig. 4. The left side of Fig. 5 shows the generated motion trajectory $(\mathbf{q}_d, \dot{\mathbf{q}}_d, \ddot{\mathbf{q}}_d)$ and the power consumption of this trajectory. The right side of Fig. 5 shows the path variable and its

time derivatives $(s, \dot{s}, \ddot{s}, \dddot{s})$, together with the upper/lower bounds for path acceleration $(\overline{\ddot{s}}, \underline{\ddot{s}})$ calculated from the power constraint.

When operating below the power hyperbola (i.e., at low loading conditions), only the prescaling according volumetric flow bound of the pump to takes place. In this case, the scaling filter is able to create continuous acceleration trajectories from the user-requested path velocity (compared to velocity-level trajectories in [5]).

On the other hand, if the power limit is about to be exceeded, the filter scales down path velocity until the power consumption of the trajectory is below the limitation set by the power hyperbola. As seen in Fig. 5, when violating the power limit, the trajectory filter gives up tracking the user-commanded path velocity $\dot{s}_d$. Thus, the net velocity of the manipulator, and consequently the sum of volumetric flows demanded from the pump, is always adjusted to the level determined by the LR valve setting.

However, when the trajectory is scaled using constraints (10a) and (10b), the definition of power consumption (shown in green in Fig. 5) does not correspond to the actual power draw on the pump in the load-sensing system. Thus, the definition of power consumption used in [14] could actually lead to violation of the power constraint in a load-sensing system, leading to biasing of the trajectory due to the mismatch between the filter constraint and the realizable control effort, affected by the constrained pump outflow determined by the LR valve setting.

4.2. Proposed approach

Next, for comparison, we employ the constraint (12a)–(12b) for the same path geometry. The resulting motion trajectory together with system power consumption, and the evolution of the path variable and its time derivatives, are illustrated in Fig. 6.

As can be seen from plot in the lower left corner, the bounds on system acceleration defined in the real-time scaling algorithm are capable to keep the power consumption of the trajectory within the specified upper limit P_{max}. Consequently, since meeting the power limit requires slowing down the net velocity of the trajectory in order to decrease volumetric flow demand from the pump, the trajectory duration is longer compared to the previous experiment.

As a summary, the proposed trajectory generator allows fast load lowering when needed, but prevents exceeding the system power limit during load lifting operations. Consequently, the trajectory scaling system prevents biasing of the reference trajectories and excessively increased controller tracking errors due to unfeasible motion commands due to limited power. If a sudden direction change of the load occurs (e.g., a shift from load lowering to lifting motion) and causes a drastic change in the highest load pressure, this might lead to temporary situtation where the commanded trajectory exceeds the power limit for short period of time before adapting to meet the power constraint.

5. CONCLUSION

An algorithm for online time scaling of motion trajectories for single-pump, multi-actuator load-sensing hydraulic systems subject to limited prime mover power was presented. The method takes advantage of an existing real-time suitable trajectory scaling filter, and extends it to handle the global saturation effects relevant for hydraulic mobile machinery, namely pump volumetric flow and prime mover power constraints. The method was shown to be able to generate consistent, continuous trajectories while satisfying the power limit.

If the power limit can not defined due to lack of an accurate dynamic model, the presented method can still be used to generate to acquire continuous acceleration references from flow-bounded velocity trajectories generated using the approach described in [5]. Integration of the proposed trajectory scaling algorithm to a momentum-based disturbance observer [16] or other means of real-time external force estimation to create a payload-aware/force-adaptive trajectory generator is left for future studies.

6. References

[1] K. L. Knierim and O. Sawodny, "Real-time trajectory generation for three-times continuous trajectories," in *2012 7th IEEE Conf. on Industrial Electronics and Applications (ICIEA)*, 2012, pp. 1462–1467.

[2] S. Fodor, C. Vazquez, and L. Freidovich, "Interactive on-line trajectories for semi-automation: Case study of a forwarder crane," in *2016 IEEE Int. Conf. on Automation Science and Engineering (CASE)*, pp. 928–933.

[3] A. R. Enes and W. J. Book, "Optimizing point to point motion of net velocity constrained manipulators," in *49th IEEE Conference on Decision and Control (CDC)*, 2010, pp. 6415–6420.

[4] J. Wanner and O. Sawodny, "Tool-center-point control of a concrete pump using constrained quadratic optimization," *IEEE Transactions on Automation Science and Engineering*, vol. 18, no. 1, pp. 382–396, 2021.

[5] S. Lampinen, J. Niemi, and J. Mattila, "Flow-bounded trajectory-scaling algorithm for hydraulic robotic manipulators," in *2020 IEEE/ASME Int. Conf. on Advanced Intelligent Mechatronics (AIM)*, 2020, pp. 619–624.

[6] S. Yoo, C.-G. Park, S.-H. You, and B. Lim, "A dynamics-based optimal trajectory generation for controlling an automated excavator," *Proceedings of the Institution of Mechanical Engineers, Part C: Journal of Mechanical Engineering Science*, vol. 224, no. 10, pp. 2109–2119, 2010.

[7] Y. Yang, J. Pan, P. Long, X. Song, and L. Zhang, "Time variable minimum torque trajectory optimization for autonomous excavator," *ArXiv*, vol. abs/2006.00811, 2020.

[8] C. Guarino Lo Bianco and O. Gerelli, "Trajectory scaling for a manipulator inverse dynamics control subject to generalized force derivative constraints," in *2009 IEEE/RSJ Int. Conf. on Intelligent Robots and Systems*, 2009, pp. 5749–5754.

[9] Bosch Rexroth AG, "Axial piston variable pump A10VSO," [Online] Accessed January 24, 2022.

[10] M. Vukovic, R. Leifeld, and H. Murrenhoff, "Reducing fuel consumption in hydraulic excavators – a comprehensive analysis," *Energies*, vol. 10, no. 5, 2017.

[11] A. Bonavolonta, C. Dolcin, P. Marani, E. Frosina, and A. Senatore, "Comparison of energy saving and recovery systems for hydraulic mobile machines," *AIP Conference Proceedings*, vol. 2191, 2019.

[12] O. Dahl and L. Nielsen, "Torque-limited path following by online trajectory time scaling," *IEEE Transactions on Robotics and Automation*, vol. 6, no. 5, pp. 554–561, 1990.

[13] M. Tarkiainen and Z. Shiller, "Time optimal motions of manipulators with actuator dynamics," in *1993 Proceedings IEEE Int. Conf. on Robotics and Automation (ICRA)*, 1993.

[14] F. G. Flores and A. Kecskeméthy, "Time-optimal path planning along specified trajectories," in *Multibody System Dynamics, Robotics and Control*, H. Gattringer and J. Gerstmayr, Eds. Springer, 2013.

[15] F. Zhang, J. Zhang, M. Cheng, and B. Xu, "A flow-limited rate control scheme for the master-slave hydraulic manipulator," *IEEE Transactions on Industrial Electronics*, vol. 69, no. 5, pp. 4988–4998, 2022.

[16] B. Son, C. Kim, C. Kim, and D. Lee, "Expert-emulating excavation trajectory planning for autonomous robotic industrial excavator," in *2020 IEEE/RSJ Int. Conf. Intelligent Robots and Systems*, pp. 2656–2662.

Appendix: Trajectory scaling filter

The adopted trajectory scaling filter is a modified version of the original filter presented in [8]; the modified filter equations are provided below. The filter was modified in two ways; firstly, to allow the upper and lower bounds of $\ddot{s}$ both to be negative, and secondly, to enforce motion to stop when the user-provided velocity command is zero.

$$z^+ = \operatorname{sign}(\bar{\ddot{s}})\frac{\bar{\ddot{s}} - \ddot{s}_d}{T\,\underline{\dddot{s}}} \tag{14}$$

$$z^- = \frac{\underline{\ddot{s}} - \ddot{s}_d}{T\,\underline{\dddot{s}}} \tag{15}$$

$$\dot{z}^+ = -\operatorname{sign}(\bar{\ddot{s}})\operatorname{ceil}(z^+)\left(z^+ - \frac{\operatorname{ceil}(z^+)-1}{2}\right) \tag{16}$$

$$\dot{z}^- = \operatorname{ceil}(-z^-)\left(-z^- - \frac{\operatorname{ceil}(-z^-)-1}{2}\right) \tag{17}$$

In this paper $\dot{s}_d$ is generated by the user from the joystick, while $\ddot{s}_d$ is set to zero.

$$z = \frac{1}{T\alpha}\left|\frac{\dot{s}-\dot{s}_d}{T} + \frac{\ddot{s}-\ddot{s}_d}{2}\right| \tag{18}$$

$$\gamma = \begin{cases} z^+ & \text{if } z < z^+ \\ z^- & \text{if } z > z^- \\ z & \text{otherwise} \end{cases} \tag{19}$$

$$m = \operatorname{floor}\left(\frac{1+\sqrt{1+8|\gamma|}}{2}\right) \tag{20}$$

$$\dot{\tilde{z}} = -\frac{\gamma}{m} - \frac{m-1}{2}\operatorname{sign}(\gamma) \tag{21}$$

$$\dot{z} = \begin{cases} \frac{\ddot{s}-\ddot{s}_d}{T|\alpha|} & \text{if } z \geq 0 \text{ and } \frac{\ddot{s}-\ddot{s}_d}{T|\alpha|} \leq \dot{\tilde{z}} \\ \frac{\ddot{s}-\ddot{s}_d}{T|\alpha|} & \text{if } z < 0 \text{ and } \frac{\ddot{s}-\ddot{s}_d}{T|\alpha|} \geq \dot{\tilde{z}} \\ \frac{\ddot{s}-\ddot{s}_d}{T|\beta|} + \frac{\alpha+\beta}{|\beta|}\left(\frac{m-1}{2} + \frac{|\gamma|}{m}\right) & \text{otherwise} \end{cases} \tag{22}$$

We can define

$$\sigma = \begin{cases} 0 & \text{if } \dot{s}_d = 0 \text{ and } \dot{s} = 0 \\ \dot{z} - \dot{\tilde{z}} & \text{otherwise} \end{cases} \tag{23}$$

A switching control law for the path jerk is then defined as

$$\dddot{s} = \begin{cases} \bar{\dddot{s}}\min(1,\sigma) & \text{if } \sigma \geq 0 \\ \underline{\dddot{s}}\max(-1,\sigma) & \text{if } \sigma < 0 \end{cases} \tag{24}$$

where $\underline{\dddot{s}} < 0$ defines the lower bound for the jerk coordinate.

Acknowledgment

This work was supported in part by the STREAM project funded by Shift2Rail Joint Undertaking (JU), established under the European Union's Horizon 2020 Framework Programme for Research and Innovation, under Grant Agreement No. 101015418. The content of this work reflects only the author's view, and that the Shift2Rail JU is not responsible for any use that may be made of the information it contains.

Biographies

Lionel Hulttinen received B.Sc. (Tech.) and M.Sc. (Tech.) degrees in Automation Engineering from Tampere University of Technology (TUT) in 2017 and 2018, respectively. His research interests include system identification and model-based control of hydraulic robotic manipulators.

Jouni Mattila. received the M.Sc. (Eng.) and Dr. Tech. degrees from Tampere University of Technology (TUT), Tampere, Finland, in 1995 and 2000, respectively. He is currently a Professor of machine automation with the unit of Automation Technology and Mechanical Engineering, Tampere University. His current research interests include machine automation, nonlinear model-based control of robotic manipulators, and energy-efficient control of heavy-duty mobile manipulators.

Compliance Motion Control of the Hydraulic Dual-Arm Manipulator Based on Virtual Decomposition Control

Bolin Sun[1], Min Cheng[1,*], Ruqi Ding[2], Bing Xu[3], Jouni Mattila[4]

1. State Key Laboratory of Mechanical Transmissions, Chongqing University, Chongqing, China, 20220701019@stu.cqu.edu.cn & chengmin@cqu.edu.cn

2. Key Laboratory of Conveyance and Equipment, Ministry of Education, East China Jiaotong University, Nanchang, China, dingruqi0791@sina.com

3. State Key Laboratory of Fluid Power and Mechatronic Systems, Zhejiang University, Hangzhou, China, bxu@zju.edu.cn

4. Faculty of Engineering and Natural Sciences, Tampere University, Tampere, Finland, jouni.mattila@tuni.fi

Abstract.

With the limitation of the single robotic arm's operating capacity, dual-arm collaborative operation has become increasingly prominent. Compared with electrically driven dual-arm manipulator, the closed-chain object transportation task of the hydraulic dual-arm manipulator is more difficult to accurately track the desired motion trajectory, which may cause object deformation or even breakage. To overcome this problem, a compliance motion control method based on virtual decomposition control (VDC) is proposed for the hydraulic dual-arm manipulator in this paper. First of all, for each manipulator of the hydraulic dual-arm system, the VDC method is used to enable its end-effector to accurately track the desired motion trajectory. Then, for the held object, a compliance motion controller is designed to realize the motion control of the object and the internal force control between the object and the manipulator with the aim of minimizing the contact forces between the manipulators and the object. Finally, considering the uncertainty of the object, an adaptive parameter updating method is designed to estimate the inertial parameters and obtain the required net force of the object. Through a simulation study, the advantages of this control method are proved. Compared with the separate position control method of two manipulators, the position and orientation errors of the object are reduced 79.8% and 54.1% by the proposed method, and the internal force and internal moment between the manipulators and the object are also correspondingly reduced 63.9% and 89.4%. In addition, the inertial parameters of the unknown object can be accurately estimated through the adaptive law.

Keywords. Virtual decomposition control, hydraulic dual-arm, compliance motion control, unknown load.

1. INTRODUCTION

With the benefit of high-power density and environmental adaptability [1], hydraulic manipulator has been the main operating mechanism of excavators, cranes and other heavy-duty equipment for undertaking strategic security tasks such as demolition and obstacle

removal, material transfer [2, 3]. Due to complexity of working environment and diversity of task demands, the problem of low working efficiency and high safety risk for single hydraulic manipulator is being more and more serious, and the necessity and superiority of heavy-duty dual-arm cooperative manipulation is more and more apparent. However, compared with electrically-driven cooperative dual-arm, the hydraulic dual-arm manipulator has the features of flow/pressure coupling, low damping and oscillation tendency just like the hydraulic single manipulator [4-6], leading to control difficulty of the fine internal force and remarkable error of coordinated motion.

Great progress has been made for the research of electrically-driven dual-arm in recent years, e.g., hybrid force/position control, impedance control [7]. However, none of these methods take into account the uncertainty of hydraulic manipulator system parameters. The existing research results of the electrically-driven dual-arm are difficult to be fully applicable for the hydraulic dual-arm, and still cannot meet its closed-chain operation requirements. The above defects limit the operational efficiency and safety performance of the hydraulic dual-arm. In this paper, a compliance motion control method based on VDC [8] method is proposed for the hydraulic dual-arm manipulator. The aim of the proposed hydraulic dual-arm compliance motion control method is to reduce the position and orientation error when the hydraulic dual-arm manipulator performs the closed-chain collaborative task, and to reduce the internal force and internal moment between the end-effectors of the hydraulic dual-arm manipulator and the held object.

This paper is organized as follows. In Section 2, the VDC approach for the single hydraulic manipulator is briefly introduced. The compliance motion control method of the hydraulic dual-arm manipulator based on VDC method is presented in detail, and the parameter adaptive method for the unknown object is given. In Section 3, the comparison of the simulation results of the proposed method with the individual position control and the results of parameter adaption for the unknown object are given. Finally, the conclusion is given in Section 4.

2. COMPLIANCE MOTION CONTROL OF THE HYDRAULIC DUAL-ARM MANIPULATOR

In this section, the hydraulic dual-arm coordination system can be decomposed into the held object and two individual hydraulic manipulators. The control problem of the whole system can be transformed into the control sub-problem of the held object, and the control sub-problem of each manipulator by the concept of virtual stability [8]. Firstly, the VDC method of the individual hydraulic manipulator is briefly introduced. Then, this section is focused on the motion and internal force control of the object held by the hydraulic dual-arm manipulator.

2.1. Virtual Decomposition

The hydraulic manipulator is a nonlinear system with a high degree-of-freedom, which has a complex structure and many parameter uncertainties. Traditional control methods are more difficult to obtain the desired performance. The VDC controller has the features of easy expansion and low computational complexity. The VDC approach is a model-based control method, which can decompose the whole system of hydraulic manipulator with high complexity into subsystems. The controller can be designed at the subsystem level to obtain

good control performance, and the stability of the whole system can be ensured through the concept of virtual power flow [8]. For the VDC method, the purpose is to realize the accurate position control of the hydraulic cylinders and then the end-effector of the manipulator. The individual hydraulic manipulator model of the dual-arm manipulator studied in this paper is shown in Figure 1.

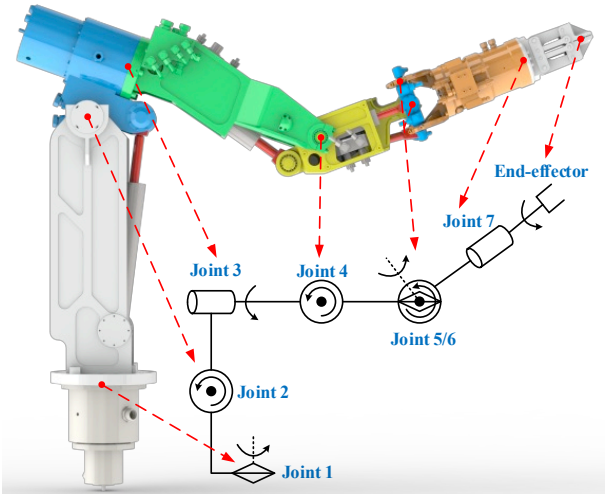

Figure 1. Model of the Single Hydraulic Manipulator

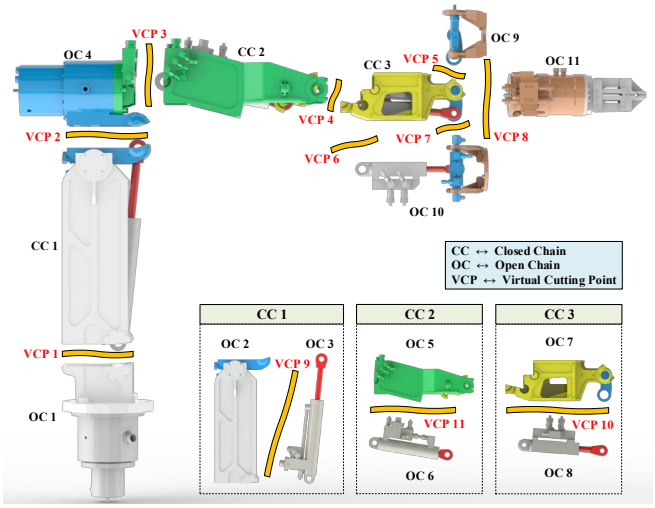

Figure 2. Schematic diagram of Virtual Decomposition for the Hydraulic Manipulator

The schematic diagram of virtual decomposition for the hydraulic manipulator is shown in Figure 2. And the decomposition method is described as follows. First, the hydraulic manipulator is decomposed into open chain, closed chain and object by placing virtual cutting points. Each open chain (OC1, OC4, OC9, OC10 and OC11 in Figure 2) contains one joint and two rigid bodies. The closed chain (CC1, CC2 and CC3 in Figure 2) generally contains

two joints (i.e., the prismatic joint of the hydraulic cylinder and its driven revolute joint) and four rigid bodies (two representing the links and the other two representing the hydraulic cylinder). After that, the closed chain can be decomposed into two open chains, i.e., CC1 is decomposed into OC2 and OC3, CC2 is decomposed into OC5 and OC6, and CC3 is decomposed into OC7 and OC8. And the objects are all zero-mass objects, and no motion control specification is assigned to the zero-mass objects.

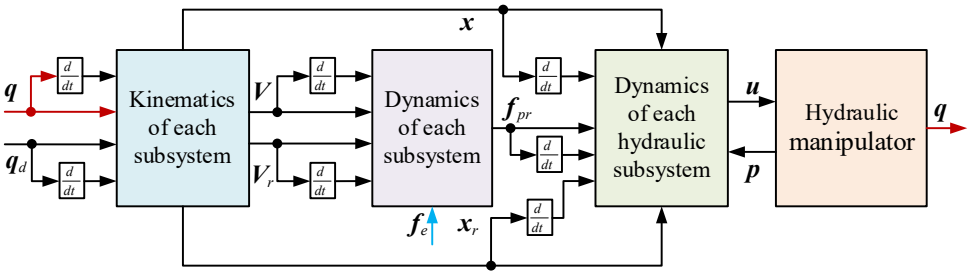

Figure 3. Control Block Diagram for the Single Hydraulic Manipulator

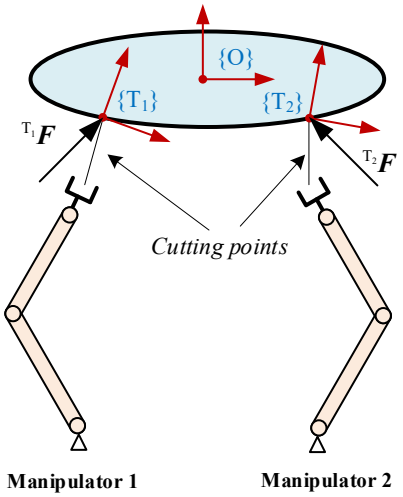

Figure 4. Virtual Decomposition of Dual-Arm Robot

After the hydraulic manipulator is virtually decomposed, each subsystem needs to be modeled mathematically separately to realize the motion control of the hydraulic manipulator [2]. The control block diagram is shown in Figure 3. In Figure 3, $\boldsymbol{q}$ and $\boldsymbol{q}_d$ are the actual joint angle and desired joint angle of the manipulator, respectively, $\boldsymbol{V}$ and $\boldsymbol{V}_r$ are the actual velocity vector and required velocity vector for each subsystem, respectively, $\boldsymbol{f}_e$ is the contact force/moment vector between the end-effector and the environment, $\boldsymbol{p}$ is the pressure vector of the hydraulic system, $\boldsymbol{f}_{pr}$ is the required chamber pressure-induced force, $\boldsymbol{x}$ is the cylinder displacement, $\boldsymbol{x}_r$ is the required cylinder displacement, $\boldsymbol{u}$ is the valve control signal.

In this control method for the individual hydraulic manipulator, the basic idea is to realize control through model feedforward and error feedback. In addition, the adaptive method is

used to estimate the uncertain parameters of the hydraulic manipulator in real time online (i.e., the inertia parameters of the manipulator, the friction force of the hydraulic cylinder, the flow coefficient of valves, and the oil volume elastic modulus in the hydraulic system, etc.). So as to realize the high-precision motion control.

To make the VDC applicable, two cutting points are also placed between the end-effectors of the hydraulic dual-arm and the object, as shown in Figure 4. The original system is decomposed into one held object and two separate hydraulic manipulators. In total, there are three frames fixed to the object. The frames $\{T_1\}$ and $\{T_2\}$ are located at the cutting points. The frame $\{O\}$ which attached to the object is used for motion and internal force control.

2.2. Kinematics and Dynamics of the Held Object

1) Kinematics of the Held Object

When the held object is under free motion, the velocity of the frame $\{O\}$ can be expressed as

$$ {}^{O}\boldsymbol{V} = \begin{bmatrix} {}^{O}\mathbf{R}_{W}\dot{\boldsymbol{x}} \\ {}^{O}\mathbf{R}_{W}\boldsymbol{\omega} \end{bmatrix} = \begin{bmatrix} {}^{O}\boldsymbol{v} \\ {}^{O}\boldsymbol{\omega} \end{bmatrix} \tag{1} $$

where $\boldsymbol{x} \in \mathbb{R}^3$ denotes the position vector of the origin of frame $\{O\}$ expressed in the world frame $\{W\}$, $\boldsymbol{\omega} \in \mathbb{R}^3$ denotes the angular velocity vector of the origin of frame $\{O\}$ expressed in the world frame $\{W\}$, ${}^{O}\mathbf{R}_{W} \in \mathbb{R}^{3\times3}$ denotes the rotation matrix from the object frame $\{O\}$ to the world frame $\{W\}$, ${}^{O}\boldsymbol{v}$ and ${}^{O}\boldsymbol{\omega}$ denote the linear and angular vectors of the origin of frame $\{O\}$ expressed in the frame $\{O\}$, respectively.
Since the frame $\{O\}$, $\{T_1\}$ and $\{T_2\}$ are all attached to the same object, it follows that

$$ \mathbf{V}_{T} = \begin{bmatrix} {}^{T_1}\boldsymbol{V} \\ {}^{T_2}\boldsymbol{V} \end{bmatrix} = {}^{O}\mathbf{U}_{T}{}^{T}\mathbf{H}^{T}\,{}^{O}\boldsymbol{V} \tag{2} $$

with

$$ {}^{O}\mathbf{U}_{T} = \mathrm{diag}\left({}^{O}\mathbf{U}_{T_1}, {}^{O}\mathbf{U}_{T_2} \right) \tag{3} $$

$$ \mathbf{H} = \left[\mathbf{I}_6 \;\; \mathbf{I}_6 \right] \tag{4} $$

where ${}^{T_1}\boldsymbol{V}$ and ${}^{T_2}\boldsymbol{V}$ denote the linear/angular velocity vectors at the cutting points, ${}^{O}\mathbf{U}_{T_1} \in \mathbb{R}^{6\times6}$ and ${}^{O}\mathbf{U}_{T_2} \in \mathbb{R}^{6\times6}$ denote the force/moment transformation matrices, and the detailed expression of $\mathbf{U}$ is given in [8], $\mathbf{I}_6 \in \mathbb{R}^{6\times6}$ denotes an identity matrix.

2) Dynamics of the Held Object

According to rigid body dynamics, the dynamics of object can be expressed as

$$ \mathbf{M}_{O}\frac{d}{dt}\left({}^{O}\boldsymbol{V} \right) + \mathbf{C}_{O}\left({}^{O}\boldsymbol{\omega} \right){}^{O}\boldsymbol{V} + \mathbf{G}_{O} = {}^{O}\boldsymbol{F}^{*} \tag{5} $$

where $\mathbf{M}_{O} \in \mathbb{R}^{6\times6}$ is the inertial matrix, $\mathbf{C}_{O} \in \mathbb{R}^{6\times6}$ is the Coriolis and centrifugal matrix, and $\mathbf{G}_{O} \in \mathbb{R}^{6}$ is the gravity vector. The detailed expressions of $\mathbf{M}_{O}$, $\mathbf{C}_{O}({}^{O}\boldsymbol{\omega})$ and $\mathbf{G}_{O}$ are given in [8]. The net force/moment vector ${}^{O}\boldsymbol{F}^{*} \in \mathbb{R}^{6}$ can also be expressed as

$$ {}^{O}\boldsymbol{F}^{*} = {}^{O}\mathbf{U}_{T_1}{}^{T_1}\boldsymbol{F} + {}^{O}\mathbf{U}_{T_2}{}^{T_2}\boldsymbol{F} \tag{6} $$

where ${}^{T_1}\boldsymbol{F} \in {}^{\sim}6$ and ${}^{T_2}\boldsymbol{F} \in {}^{\sim}6$ denote the force/moment vectors in frame $\{T_1\}$ and $\{T_2\}$ at the cutting points. By introducing an internal force vector, the force/moment vectors at the cutting points can be resolved from (6) as

$$\mathbf{F}_T = \begin{bmatrix} {}^{T_1}\boldsymbol{F} \\ {}^{T_2}\boldsymbol{F} \end{bmatrix} = {}^{T}\mathbf{U}_O \begin{bmatrix} \boldsymbol{\Omega}_m & \boldsymbol{\Omega}_f \end{bmatrix} \begin{bmatrix} {}^{O}\boldsymbol{F}^* \\ \boldsymbol{\eta} \end{bmatrix} \tag{7}$$

where ${}^{T}\mathbf{U}_O = {}^{O}\mathbf{U}_T{}^{-1}$ is defined by (3). A possible way to define the internal forces is to let the internal forces characterize the squeeze force/moment vectors among the end-effectors. As in [9], the matrix $\boldsymbol{\Omega}_m \in {}^{\sim}12\times6$ and the matrix $\boldsymbol{\Omega}_f \in {}^{\sim}12\times6$ are governed by

$$\boldsymbol{\Omega}_m = \frac{1}{2}\begin{bmatrix} \mathbf{I}_6 & \mathbf{I}_6 \end{bmatrix}^T \tag{8}$$

$$\boldsymbol{\Omega}_f = \begin{bmatrix} \mathbf{I}_6 & -\mathbf{I}_6 \end{bmatrix}^T \tag{9}$$

Then, the internal force vector can be defined as

$$\boldsymbol{\eta} = \boldsymbol{\eta}_{1,2} \tag{10}$$

where $\boldsymbol{\eta}_{1,2} \in {}^{\sim}6$ denotes the internal force/moment vector exerted from the 1st end-effector to the 2nd end-effector, expressed in frame $\{O\}$. Because the matrix $\begin{bmatrix} \boldsymbol{\Omega}_m & \boldsymbol{\Omega}_f \end{bmatrix} \in {}^{\sim}12\times12$ is of full rank, there must exist a matrix $\boldsymbol{\Phi} \in {}^{\sim}6\times12$ such that

$$\boldsymbol{\Phi} = \frac{1}{2}\begin{bmatrix} \mathbf{I}_6 & -\mathbf{I}_6 \end{bmatrix} \tag{11}$$

Thus, the internal force/moment vector can be obtained from (7) by using the force/moment measurements at the end-effectors as

$$\boldsymbol{\eta} = \boldsymbol{\Phi}\,{}^{O}\mathbf{U}_T\mathbf{F}_T \tag{12}$$

2.3. Motion and Internal Force Control of the Held Object

1) Motion and Internal Force Control Specifications

Define a frame $\{D\}$, whose origin and orientation represent the desired position and orientation of the frame $\{O\}$. The motion control objective is to make frame $\{O\}$ track frame $\{D\}$. Meanwhile, let $\boldsymbol{\eta}_d \in {}^{\sim}6$ be the desired internal force coordinate vector. The internal force control objective is

$$\boldsymbol{\eta}_d - \boldsymbol{\eta} \to \mathbf{0} \tag{13}$$

2) Required Velocity and Force/Moment Vectors

The required velocity vector of frame $\{O\}$ is designed as

$${}^{O}\boldsymbol{V}_r = {}^{O}\boldsymbol{V}_d + \mathbf{E} \tag{14}$$

$${}^{O}\boldsymbol{V}_d = \begin{bmatrix} {}^{O}\mathbf{R}_W\dot{\boldsymbol{x}}_d \\ {}^{O}\mathbf{R}_W\boldsymbol{\omega}_d \end{bmatrix} \tag{15}$$

$$\mathbf{E}=\begin{bmatrix} k_x\,{}^{\mathrm{O}}\mathbf{R}_{\mathrm{W}}\left(\boldsymbol{x}_d-\boldsymbol{x}\right) \\ k_\omega\,{}^{\mathrm{O}}\boldsymbol{\mu} \end{bmatrix} \tag{16}$$

where $k_x>0$ and $k_\omega>0$ are two constants, $\boldsymbol{x}_d\in{}^{\sim}{}^{3}$ denotes the desired position (the origin of frame {D}) vector, $\boldsymbol{\omega}_d\in{}^{\sim}{}^{3}$ denotes the desired angular velocity vector, and ${}^{\mathrm{O}}\boldsymbol{\mu}\in SO^3$ denotes the vector part of a quaternion representing the rotation from frame {O} to frame {D}.

According to (2), the required linear/angular velocity vectors of the end-effectors can be designed as

$$\mathbf{V}_{Tr}=\begin{bmatrix} {}^{\mathrm{T}_1}\boldsymbol{V}_r \\ {}^{\mathrm{T}_2}\boldsymbol{V}_r \end{bmatrix}={}^{\mathrm{O}}\mathbf{U}_{\mathrm{T}}{}^{T}\left[\mathbf{H}^{T}\,{}^{\mathrm{O}}\boldsymbol{V}_r+\boldsymbol{\Phi}^{T}\mathbf{A}_{f\eta}\left(\tilde{\boldsymbol{\eta}}_d-\tilde{\boldsymbol{\eta}}\right)\right] \tag{17}$$

where $\mathbf{A}_{f\eta}\in{}^{\sim}{}^{6\times6}$ is a diagonal positive-definite matrix, $\tilde{\boldsymbol{\eta}}_d$ and $\tilde{\boldsymbol{\eta}}$ can be obtained by

$$\dot{\tilde{\boldsymbol{\eta}}}_d=\mathbf{C}_{f\eta}\left(\boldsymbol{\eta}_d-\tilde{\boldsymbol{\eta}}_d\right) \tag{18}$$

$$\dot{\tilde{\boldsymbol{\eta}}}=\mathbf{C}_{f\eta}\left(\boldsymbol{\eta}-\tilde{\boldsymbol{\eta}}\right) \tag{19}$$

where $\mathbf{C}_{f\eta}\in{}^{\sim}{}^{6\times6}$ is a diagonal positive-definite matrix.

Note that the second term on the right hand side of (17) contains the filtered internal force error vector that is added to the complementary motion configuration space spanned by $\boldsymbol{\Phi}^{T}$. This term is used to achieve the filtered internal force control characterized by $\tilde{\boldsymbol{\eta}}_d-\tilde{\boldsymbol{\eta}}\to\mathbf{0}$. Equations (18) and (19) define two low-pass filters to be used to filter out the desired and actual internal forces, respectively. The cut-off frequency of the two filters is determined by matrix $\mathbf{C}_{f\eta}$.

Based on the unknown inertial parameters of the held object in the real situation, an adaptive parameter updating approach is used to estimate the dynamics of the unknown object in this paper. The linear parametrization expression of (5) can be written as

$$\mathbf{M}_{\mathrm{O}}\frac{d}{dt}\left({}^{\mathrm{O}}\boldsymbol{V}_r\right)+\mathbf{C}_{\mathrm{O}}\left({}^{\mathrm{O}}\boldsymbol{\omega}\right){}^{\mathrm{O}}\boldsymbol{V}_r+\mathbf{G}_{\mathrm{O}}=\mathbf{Y}_{\mathrm{O}}\boldsymbol{\theta}_{\mathrm{O}} \tag{20}$$

where $\mathbf{Y}_{\mathrm{O}}\in{}^{\sim}{}^{6\times13}$ is a regression matrix, $\boldsymbol{\theta}_{\mathrm{O}}\in{}^{\sim}{}^{13}$ is a parameter vector. For the unknown object, $\boldsymbol{\theta}_{\mathrm{O}}$ is generally uncertain [10, 11].

So, the required net force/moment vector of the held object is written as

$${}^{\mathrm{O}}\boldsymbol{F}_r^{*}=\mathbf{Y}_{\mathrm{O}}\hat{\boldsymbol{\theta}}_{\mathrm{O}}+\mathbf{K}_{\mathrm{O}}\left({}^{\mathrm{O}}\boldsymbol{V}_r-{}^{\mathrm{O}}\boldsymbol{V}\right) \tag{21}$$

where $\mathbf{K}_{\mathrm{O}}\in{}^{\sim}{}^{6\times6}$ is a positive-definite gain matrix, $\hat{\boldsymbol{\theta}}_{\mathrm{O}}\in{}^{\sim}{}^{13}$ denotes the estimate of $\boldsymbol{\theta}_{\mathrm{O}}\in{}^{\sim}{}^{13}$.The specific parameter adaptive function and adaptive process can be referred to [8].

After ${}^{\mathrm{O}}\boldsymbol{F}_r^{*}\in{}^{\sim}{}^{6}$ is obtained from (21) and $\boldsymbol{\eta}_d\in{}^{\sim}{}^{6}$ is obtained from the internal force control specification which mentioned below, the required force/moment vectors at the end-effectors are designed from (7) as

$$\mathbf{F}_{Tr} = \begin{bmatrix} {}^{\mathrm{T}_1}\boldsymbol{F}_r \\ {}^{\mathrm{T}_2}\boldsymbol{F}_r \end{bmatrix} = {}^{\mathrm{T}}\mathbf{U}_{\mathrm{O}} \begin{bmatrix} \boldsymbol{\Omega}_m & \boldsymbol{\Omega}_f \end{bmatrix} \begin{bmatrix} {}^{\mathrm{O}}\boldsymbol{F}_r^* \\ \boldsymbol{\eta}_d \end{bmatrix} \tag{22}$$

3) Internal Force Optimization

The desired internal force vector $\boldsymbol{\eta}_d \in {}^{\sim 6}$ can be designed in different ways. Most commonly, it can be used to minimize the contact forces/moments at the end-effectors, that is, find $\boldsymbol{\eta}_d$ to minimize $\mathbf{F}_T{}^T \mathbf{W}_\eta \mathbf{F}_T$ under (13), where $\mathbf{W}_\eta$ is a weighting matrix and $\mathbf{F}_T$ is being defined by (7). For this purpose, equation (7) can be re-written as

$$\mathbf{F}_T = \mathbf{A}_\eta \boldsymbol{\eta} + \mathbf{B}_\eta \tag{23}$$

with

$$\mathbf{A}_\eta = {}^{\mathrm{T}}\mathbf{U}_{\mathrm{O}} \boldsymbol{\Omega}_f \tag{24}$$

$$\mathbf{B}_\eta = {}^{\mathrm{T}}\mathbf{U}_{\mathrm{O}} \boldsymbol{\Omega}_m {}^{\mathrm{O}}\boldsymbol{F}^* \tag{25}$$

In the sense of minimizing $\mathbf{F}_T{}^T \mathbf{W}_\eta \mathbf{F}_T$, the least-square solution for $\boldsymbol{\eta}$ is

$$\boldsymbol{\eta} = -\left(\mathbf{A}_\eta{}^T \mathbf{W}_\eta \mathbf{A}_\eta\right)^{-1} \mathbf{A}_\eta{}^T \mathbf{W}_\eta \mathbf{B}_\eta \tag{26}$$

In line with (26), the desired internal force coordinate vector $\boldsymbol{\eta}_d$ is designed as

$$\boldsymbol{\eta}_d = -\left(\mathbf{A}_\eta{}^T \mathbf{W}_\eta \mathbf{A}_\eta\right)^{-1} \mathbf{A}_\eta{}^T \mathbf{W}_\eta \mathbf{B}_{\eta r} \tag{27}$$

$$\mathbf{B}_{\eta r} = {}^{\mathrm{T}}\mathbf{U}_{\mathrm{O}} \boldsymbol{\Omega}_m {}^{\mathrm{O}}\boldsymbol{F}_r^* \tag{28}$$

4) Dual-arm motion/force control frame

The block diagram of the hydraulic dual-arm compliance motion control based on VDC is shown in Figure 5. For the held object, the desired velocity of the object is given, the object required velocity is obtained from the compliance motion controller. The actual velocity of the object is obtained according to the coordination constraint relationship between the dual-arm and the object and fed back to the compliance motion controller [12]. In addition, the required velocity of the dual-arm end-effectors can be obtained from the coordination constraint relationship based on the required velocity of the object. Then, the desired joint angle and angular velocity of the dual-arm are obtained by inverse kinematics, and the actual joint angle and angular velocity of the dual-arm are obtained by the dual-arm environment. The inverse kinematics solution method for the hydraulic manipulator which studied in this paper can be obtained from [13].

And then, the two hydraulic manipulators are controlled separately by VDC method, and the valve control voltage signal of each hydraulic cylinder of the manipulators are input to the dual-arm environment. The actual joint angles of the dual-arm are output from the dual-arm environment to the forward kinematics of the manipulators to obtain the end-effectors motion trajectory, and the output contact force is fed back to the compliance motion controller for the object. And, the forward kinematics can also be obtained from [13]. Finally, the whole closed-loop control is formed to realize the compliance motion control of the hydraulic dual-arm cooperative manipulation.

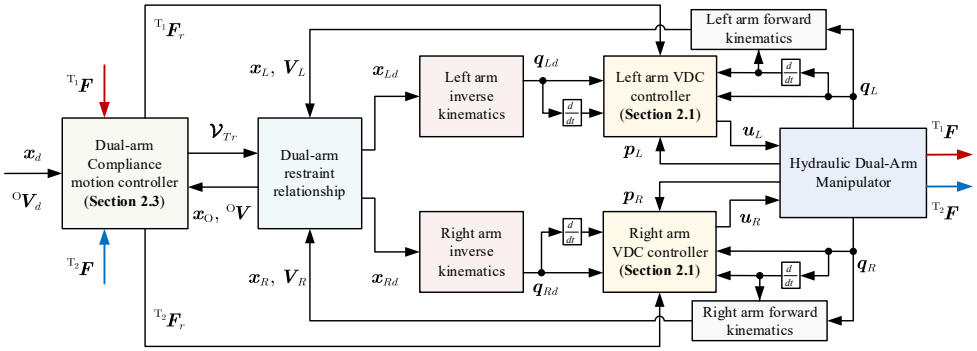

Figure 5. Block Diagram of the Dual-Arm Compliance Motion Control

3. SIMULATION STUDY

3.1. Simulation Model and Settings

In this section, the feasibility of the proposed control method is verified for hydraulic dual-arm to complete the task of closed chain collaboration. To verify the advantage of the proposed method, the end-effector position control (PC) method is used for comparison with it, i.e., the desired trajectory of the end-effector of each hydraulic manipulator is obtained by constraint relation according to the desired motion trajectory of the object, and then each arm is controlled by VDC method to track this trajectory.

The MATLAB/Simulink is used to build the simulation platform for hydraulic dual-arm manipulator and carry out a real-time simulation, which is composed of two hydraulic manipulators from Section II. The simulation model and frame configuration are shown in Figure 6, and all the system parameters settings of the simulation model are based on the experimental prototype from the [13]. In the simulation, the desired motion trajectory of the frame {O} on the object which set in the Cartesian coordinates is a circular trajectory with a center of [1.5m, 1.3m] (located in the yOz plane) and a radius of 0.25m, which can be expressed as

$$\boldsymbol{x}_d \Rightarrow \begin{cases} x = 0 \quad y = 1.5 \quad z = 1.05 \quad if \ t < 2 \\ x = 0 \\ y = 0.25\sin\left(2\pi(t-2)/T\right) + 1.5 \quad if \ 2 \le t < 12 \\ z = -0.25\cos\left(2\pi(t-2)/T\right) + 1.3 \end{cases} \tag{29}$$

where t is the simulation time , $T = 10$ s is the motion period.

The total simulation time is set to 12 s, using a fixed step solver, and the simulation step is set to 0.001 s. The simulation is divided into two stages. In the first stage (0~2 s), as shown in the yellow area in Figure 7-9 below, the object is held still by dual-arm manipulator. And in the second stage (2~12 s), as shown in the green area in Figure 7-9 below, the object is held by dual-arm manipulator to do the above circular motion. And the main parameters used in the simulation model are listed in Table I.

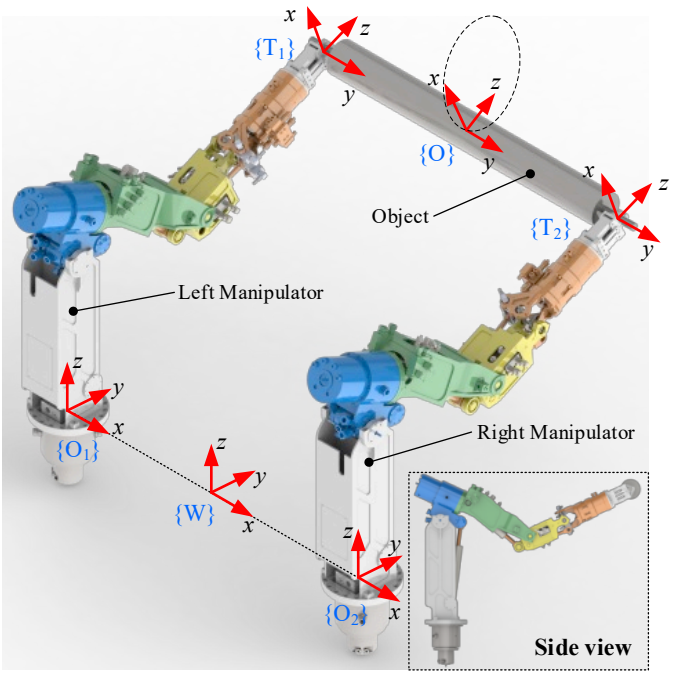

Figure 6. Simulation model of the Hydraulic Dual-Arm Manipulator

Table I. Main parameters used in the simulation model

Parameter	Symbol	Value
Gain of position error	k_x	0.6
Gain of orientation error	k_ω	0.6
Gain matrix of filtered internal force error vector	$\mathbf{A}_{f\eta}$	$10^{-5}\cdot\mathbf{I}_6$
Cut-off frequency matrix of the filter	$\mathbf{C}_{f\eta}$	$30\cdot\mathbf{I}_6$
Gain matrix of velocity error vector	$\mathbf{K}_O$	$100\cdot\mathbf{I}_6$
Weighting matrix for internal force optimization	$\mathbf{W}_\eta$	$\mathbf{I}_{12}$

3.2. Simulation results

Note that the solid lines in Figures 7 and 8 represent the position error, orientation error, internal force and internal moment of the object in the three directions of xyz under the PC method, respectively, while the dotted lines in Figures 7 and 8 represent the CMC method.

A comparison of the object position and orientation errors for separate position control (PC) and compliance motion control (CMC) is shown in Figure 7. During the period when the object is held still (0~2 s) by the arms, the position and orientation errors of the object do not change much, but the CMC method is significantly better than the PC method. The position and orientation errors of the object using the CMC method are basically zero. In the subsequent process, the position and orientation errors of the object for circular motion (2~12 s) is also similar. It always has a large error in the z direction by the PC method, mainly because the inertial parameters of the unknown object cannot be accurately estimated.

Compared with the PC method, the position and orientation errors of the object are reduced 79.8% and 54.1% by the proposed method (CMC method). As a whole, the accuracy of coordinated motion of dual-arm is improved.

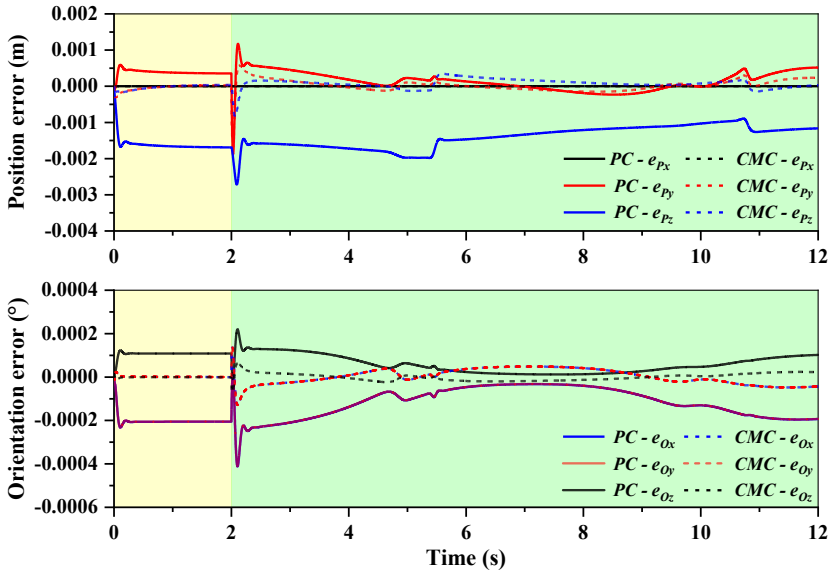

Figure 7. Position and orientation errors

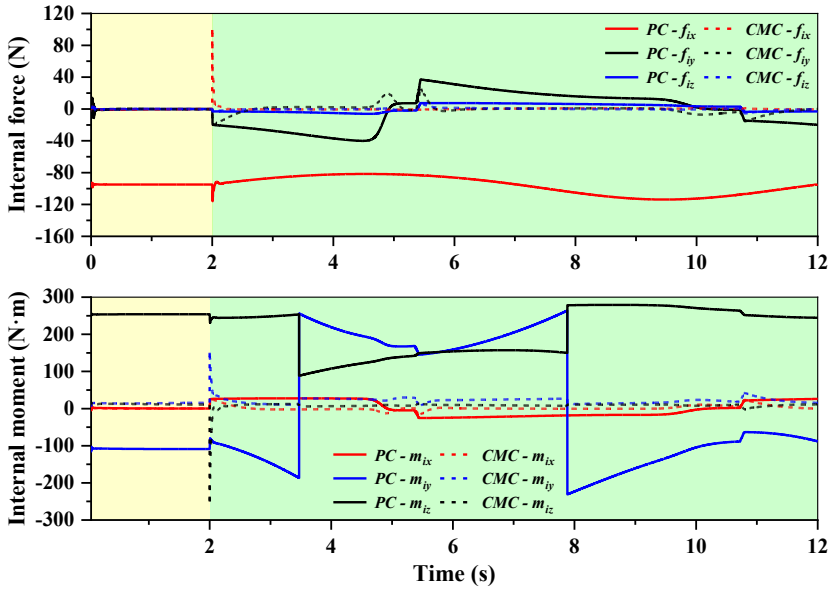

Figure 8. Internal force and moment

Then, a comparison of the internal force/moment results is shown in Figure 8. From the perspective of the overall control effect, compared with the PC method, the control effects of the internal force and the internal moment of the CMC method are maintained at a small

value. Compared with the PC method, the internal force and moment between the arms and the object are also correspondingly reduced 63.9% and 89.4% by the CMC method.

The control effects of different control methods are shown in Table II. Note that the error reduction ratio here refers to the reduction of their maximum values in the three directions of xyz, and the reduction ratio of internal force and internal moment here also refers to the reduction of their maximum values in the three directions of xyz.

Since the inertia parameters of the held object are difficult to obtain in advance in real situations, the parameter adaptation method is used to estimate inertial parameters of the unknown object in the simulation experiment. Among all inertial parameters, the mass has a great influence on the accuracy of the motion. Therefore, only the results of object mass adaptation are presented here, as shown in Figure 9.

As shown in the dashed line, the real mass of the object model in the simulation is 402.726 kg, and the adaptive value of the object mass rises rapidly after the motion starts and gradually stabilizes around the real value. It can also be seen that the error between the adaptive value and the real value is small which below ±1.5%.

Table II. Comparison of the different control methods

Parameter	PC	CMC
Position error (m)	2.71×10^{-3}	0.547×10^{-4}
Orientation error (°)	4.11×10^{-4}	1.89×10^{-4}
Internal force (N)	115.81	41.81
Internal moment (N·m)	279.28	29.60

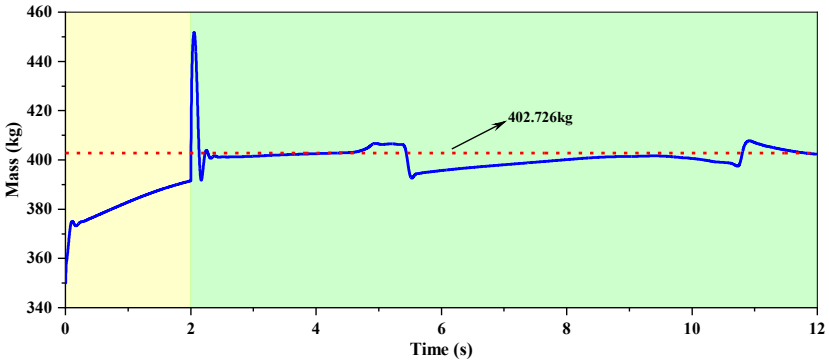

Figure 9. Adaptive Results of Object Mass

4. CONCLUSION

In this paper, we propose a compliance motion control method of hydraulic dual-arm based on virtual decomposition control for the closed-chain collaborative task, and verify the effectiveness of the method by simulation. The simulation results show that the compliance motion control method of hydraulic dual-arm can effectively reduce the position and orientation errors by 79.8% and 54.1% of the end-effectors of the dual-arm, and also reduce the internal force/moment by 63.9% and 89.4% between the end-effectors and the object. In

addition, the method can make a more accurate estimation of the inertia parameters of the unknown object such as mass, and the error can be as low as ±1.5%.

In the future, the research will focus on the study of the hydraulic dual-arm system under the constrained motion.

5. ACKNOWLEDGMENT

This work is supported by the National Natural Science Foundation of China under Grant 52075055 and 52111530069, the Natural Science Foundation of Chongqing, China under Grant cstc2020jcyjmsxmX0780m.

6. REFERENCES

[1] R. Ding, M. Cheng, L. Jiang, and G. Hu, "Active Fault-Tolerant Control for Electro-Hydraulic Systems With an Independent Metering Valve Against Valve Faults," *IEEE Trans. Ind. Electron.*, vol. 68, no. 8, pp. 7221-7232, 2021.

[2] J. Koivumäki and J. Mattila, "High performance nonlinear motion/force controller design for redundant hydraulic construction crane automation," *Autom. Constr.*, vol. 51, pp. 59-77, 2015.

[3] X. Rong, Y. Li, J. Ruan, and B. Li, "Design and simulation for a hydraulic actuated quadruped robot," *J. Mech. Sci. Technol.*, vol. 26, no. 4, pp. 1171-1177, 2012.

[4] J. Koivumaki and J. Mattila, "Stability-Guaranteed Force-Sensorless Contact Force/Motion Control of Heavy-Duty Hydraulic Manipulators," *IEEE Trans. Rob.*, vol. 31, no. 4, pp. 918-935, 2015.

[5] M. Cheng, J. Zhang, B. Xu, R. Ding, and J. Wei, "Decoupling Compensation for Damping Improvement of the Electrohydraulic Control System With Multiple Actuators," *IEEE/ASME Trans. Mechatron.*, vol. 23, no. 3, pp. 1383-1392, 2018.

[6] S. H. Hyon, D. Suewaka, Y. Torii, N. Oku, and H. Ishida, "Development of a fast torque-controlled hydraulic humanoid robot that can balance compliantly," in *2015 IEEE-RAS 15th International Conference on Humanoid Robots (Humanoids)*, 2015, pp. 576-581.

[7] C. Smith *et al.*, "Dual arm manipulation—A survey," *Rob. Auton. Syst.*, vol. 60, no. 10, pp. 1340-1353, 2012.

[8] W. H. Zhu, *Virtual decomposition control: Toward hyper degrees of freedom robots*, 1st ed. (Springer Tracts in Advanced Robotics). Berlin: Springer Berlin, Heidelberg, 2010.

[9] W. H. Zhu, "On adaptive synchronization control of coordinated multirobots with flexible/rigid constraints," *IEEE Trans. Rob.*, vol. 21, no. 3, pp. 520-525, 2005.

[10] Z. Wen-Hong and J. D. Schutter, "Adaptive control of mixed rigid/flexible joint robot manipulators based on virtual decomposition," *IEEE Transactions on Robotics and Automation*, vol. 15, no. 2, pp. 310-317, 1999.

[11] W.-H. Zhu and J.-C. Piedboeuf, "Adaptive Output Force Tracking Control of Hydraulic Cylinders With Applications to Robot Manipulators," *J. Dyn. Syst. Meas. Contr.*, vol. 127, no. 2, pp. 206-217, 2004.

[12] J. J. Duan, Y. H. Gan, M. Chen, and X. Z. Dai, "Symmetrical adaptive variable admittance control for position/force tracking of dual-arm cooperative manipulators with unknown trajectory deviations," *Rob. Comput. Integr. Manuf.*, vol. 57, pp. 357-369, 2019.

[13] M. Cheng, Z. N. Han, R. Q. Ding, J. H. Zhang, and B. Xu, “Development of a redundant anthropomorphic hydraulically actuated manipulator with a roll-pitch-yaw spherical wrist,” *Frontiers of Mechanical Engineering*, vol. 16, no. 4, pp. 698-710, Dec 2021.

Biographies



Bolin Sun received the B.S. degree in mechanical engineering from Shandong University of Science and Technology, Qingdao, China, in 2020. Since 2022, he has been working toward the Ph.D. degree in mechanical engineering with the State Key Laboratory of Mechanical Transmission, Chongqing University, Chongqing, China. His research interests include electrohydraulic control systems of mobile machinery and motion control of hydraulic systems.



Min Cheng received the B.S. and Ph.D. degrees in mechatronics from Zhejiang University, Hangzhou, China, in 2009 and 2015, respectively. He is currently a Professor with the State Key Laboratory of Mechanical Transmissions, Chongqing University, Chongqing, China. His research interests include electrohydraulic control systems of mobile machinery, energy saving and motion control of hydraulic systems, and mechatronic systems design.



Ruqi Ding received the B.S. degree in mechatronics engineering from Nanchang University, Nanchang, China in 2009, and the Ph.D. degree in fluid power transmission and control from Zhejiang University, Hangzhou, China, in 2015. He is currently a Professor with the Key Laboratory of Conveyance and Equipment, Ministry of Education, East China Jiaotong University. His research interests include electrohydraulic control systems, as well as the motion control of hydraulic manipulators.



Bing Xu received the Ph.D. degree in fluid power transmission and control from Zhejiang University, Hangzhou, China, in 2001. He is currently a Professor and a Doctoral Tutor in the Institute of Mechatronic Control Engineering, and the Deputy Director of the State Key Laboratory of Fluid Power Transmission and Control, Zhejiang University. He has authored or co-authored more than 200 journal and conference papers and authorized 49 patents. Professor Xu is a Chair Professor of the Yangtze River Scholars Programme, and a science and technology innovation leader of the Ten Thousand Talent Programme.



Jouni Mattila received the M.S. and Ph.D. degrees in automation engineering from the Tampere University of Technology, Tampere, Finland, in 1995 and 2000, respectively. He is currently a Professor with the Unit of Automation Technology and Mechanical Engineering, Tampere University, Tampere, Finland. His research interests include machine automation, nonlinear model-based control of hydraulic robotic manipulators, and energy-efficiency of fluid power systems.

Pressure Feedback Control Of Electro-Hydraulic Actuators Using Fixed Displacement Hydraulic Machines

Shaoyang Qu[1], Hassan Assaf[1], Andrea Vacca[1], Enrique Busquets[2]

[1]*Maha Fluid Power Research Center, Purdue University*

[2]*Engineering Department of North America, Bosch Rexroth in US*

Abstract.

This paper presents the development of a control strategy for Electro-Hydraulic Actuator (EHA) systems based on fixed displacement hydraulic machines. Although some previous studies on EHAs show benefits in terms of energy efficiency and regeneration capability compared to conventional hydraulic systems, few studies focus on the dynamic performance of EHAs. Unlike traditional valve-controlled systems, an EHA based on a fixed displacement pump typically relies on variation of the electric motor shaft speed to control the actuator velocity. This study shows that pressure feedback can be used to control the speed of the electric machine, thus achieving the required actuator machine dynamic response. A simulation model is developed by including the EM, the hydraulic system, and the actuation system, which can give a realistic prediction of the EHA performance for a typical duty cycle. An open-circuit EHA previously proposed by the authors is used to validate the control strategy, and the simulation results show superior dynamic performance, exhibiting a reduction in response time and oscillatory behavior, compared to a feedforward EHA controller. Following the method presented in this study, it is possible to design a controller with a pressure feedback strategy for EHA systems with different size and actuation requirements.

Keywords. EHA, Dynamic performance, Pressure feedback control.

1. INTRODUCTION

The electrification trend affecting the off-highway vehicle market has increased the interest in high-efficiency electro-hydraulic actuator (EHA), which can address the limitation of efficiency of traditional valve-controlled actuator systems. Particularly attractive are solutions that combine a variable speed electric machine with a fixed displacement hydraulic machine due to considerations of cost and efficiency [1, 2]. Compared to the traditional valve-controlled system, an EHA based on a fixed displacement pump typically controls the actuation velocity by varying the pump flow through the electric machine (EM) speed. Therefore, it is arguable that such an EHA can adopt the same control as a conventional hydraulic system to achieve the same dynamic performance, such as limiting the oscillations of the actuator.

The project is funded by the Department of Energy, USA (DOE project DEEE0008334, 'Individual Electro-Hydraulic Drives for Off-Road Vehicles')

With the purpose of reducing the actuator oscillations, pressure feedback control is proved to be effective for traditional valve-controlled systems and for displacement-controlled systems. The pressure feedback is implemented with high-pass filter to eliminate the faster dynamic from the pulsations, while using the information from the velocity response in the control loop. This method has been proved effective to improve dynamic performance of hydraulic system, such as adaptive damping. This is documented in several studies: for example, [3, 4] describe the use of the pressure feedback strategy in a pump-controlled actuator to achieve active damping and to eliminate unstable switching between pumping and motoring that can occur in a closed-circuit system. [5] applies an active oscillation damping strategy in a displacement-controlled actuator to increase the productivity of the machine and comfort of the operator. Ding et al. [6] discuss the case of vibration reduction of an excavator with an independent metering system. Pressure feedback can also be used for the so-called ride control, to reduce cabin vibrations based on the commanded motion of the loader function [7]. Pedersen and Andersen well explained the principle of pressure feedback in hydraulic control systems through detailed mathematical analysis, and provided guidelines to tune the control parameters using the root-locus method, and on the selection between high and low pass filter [8].

Nevertheless, all the mentioned examples are based on valve control, where the idea is to control the flow rate by adjusting the opening of the valves. In this study, a novel method is studied by pump control, i.e., controlling the pump speed to adjust flow rate with pressure feedback strategy. In fact, instantaneous pump displacement control was achieved using a servo valve in [3], while in the other cases, the control action was performed directly by a metering control element. Therefore, for an EHA system, the main question arises on the opportunity to utilize a pressure feedback strategy to increase the damping of the system. The dynamics of an electric machine (EM) is very different from that of hydraulic valves. Taking the permanent magnet synchronous machine (PMSM) as an instance, in speed control mode, the torque command is converted to speed via a PI control structure. The motor speed response depends on the control parameters, as well as the machine parameters such as inertia and torque limit [9]. The EM usually cannot respond as fast as hydraulic control valves unless the maximum torque available is very high with respect to the system torque requirements. This means an EM rotor and shaft inertia much higher than a valve spool, which limits the acceleration.

This study aims to address the challenges mentioned above and provides the development of a pressure feedback controller for the EHA system. The pressure feedback signal from the actuator is processed via a high-pass filter with a feedback gain, and then summed with the speed command to the EM before its torque-speed PI controller. A simulation model validated with experimental results that integrate the EM control, hydraulic system, and the mechanism of the actuator is used to validate the pressure feedback controller effectiveness. On the basis of the simulation results, the damping vibration is reduced with the closed-loop pressure feedback control compared to a feedforward-controlled EHA.

The structure of the paper is as follows: in Section 2 the reference system will be introduced, focusing on the control structure; Section 3 gives the method to formulate the controller; finally, the simulation model and results will be shown in Section 4 before concluding the work in Section 5.

2. REFERENCE SYSTEM

2.1. Hydraulic layout

The architecture of the studied system along with the reference machine is shown in Figure 1. It is considered as a throttle-less circuit with a hydraulic energy efficiency that can reach 84.7\%, as well documented in previous work [12]. A two quadrant hydraulic pump (HP) driven by a variable electrical machine (EM) controls the speed of the cylinder based on an open circuit configuration. The directional valve (4/3 DV) is only used to switch among the working modes to allow for a four-quadrant operation of the system. A BPV valve is used to allow for slow actuation velocity whenever the speed demand is lower than the minimum recommended pump speed operating region, and for fast actuation velocities in overrunning loads. Although the circuit studied in this paper includes a BPV that can be used for active damping, this might not be the case in other circuits that can achieve low speed modes without the need of a throttling element, for this reason the authors conceived the idea examining the potential of using an electrical motor to increase the damping of the system. The detailed working principle, control logic [10,11] and the performance of this EHA layout [11] are explained in previous studies by the authors.

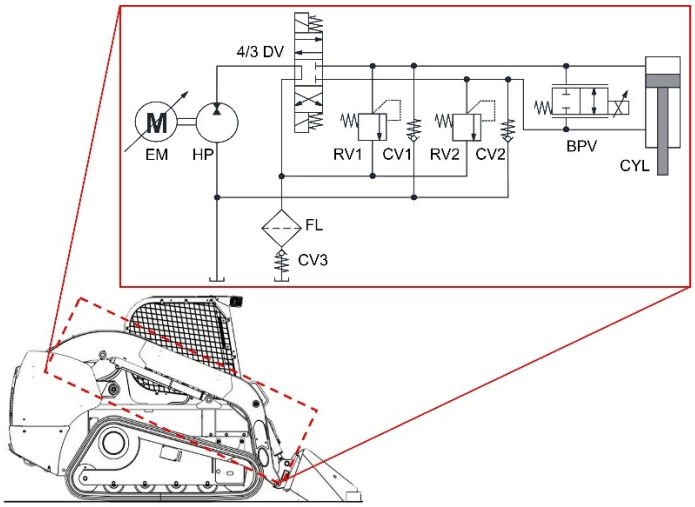

Figure 1. Hydraulic circuit of the reference machine

2.2. Control structure

Figure 2 represents the control flow of the studied EHA system. The operator sets the desired actuator speed by a joystick command. This speed command is properly converted to an equivalent EM shaft speed command. The details of this process are given in [10]. The speed command is an input to the EM inverter (power electronics), which is converted to a torque command with a PI controller that uses speed feedback. With the torque command, the EM and the HP can reach the desired speed and supply flow to the hydraulic system [13].

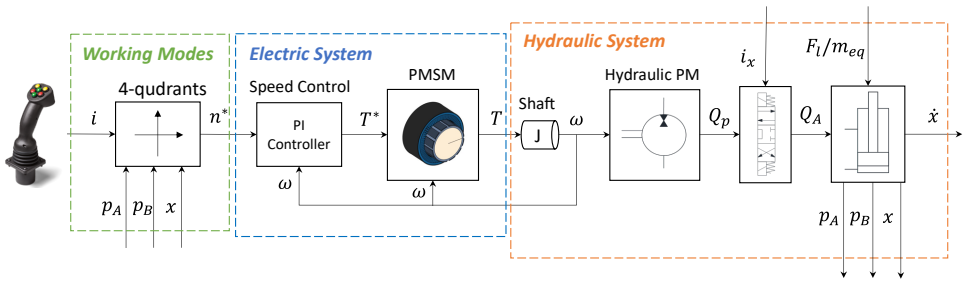

Figure 2. Hydraulic circuit of the reference machine

The working modes block includes the control logic for 4-quadrant operation, such as commanding speed to the electric machine accordingly (e.g., reverse speed for energy regeneration", and use the bypass valve for extreme low-speed operation. For brevity, more details can be found in other work of the authors [10-13].

This control logic requires the use of position and pressure sensors to identify the working modes of the EHA. The pressure sensors also allow one to implement the pressure feedback controller.

3. FORMULATION OF THE CONTROLLER

3.1. System linearization

The linear model can be viewed as two separate parts: First, the boom actuation that includes the hydraulic system and the boom mechanism; Second, the electrical machine control.

3.1.1. Hydraulic boom actuation

For control design and analysis, a linearized model of the system is developed, starting from the boom mechanism highlighted in Figure 1. For the development of the linear model, the boom mechanism is simplified to a mass-spring-damper system. Figure 3 shows the scheme of the linear model that includes a hydraulic cylinder and the boom mechanism.

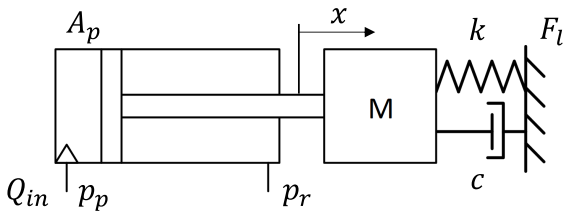

Figure 3. Linearized model of the boom cylinder mechanism

Based on the linear model, applying Newton's second law, the equation of motion of the cylinder is described as in equation (1), derived from the force balance of the hydraulic

cylinder. The spring stiffness can be assumed as zero (i.e., $k \approx 0$), and the equivalent mass is calculated numerically from the kinematic model.

$$\ddot{x} = \frac{1}{M_{eq}}\left(A_p p_p - A_r p_r - c\dot{x} - kx - F_L\right) \tag{1}$$

The pressure build-up inside the cylinder chambers is given in equation (2) and equation (3), for piston side and rod side, respectively. Internal cylinder leakage is neglected for this analysis (i.e., $K_l = 0$).

$$\dot{p}_p = \frac{K_{oil}}{V_p}\left[Q_p - A_p\dot{x} - K_L\left(p_p - p_r\right)\right] \tag{2}$$

$$\dot{p}_r = \frac{K_{oil}}{V_r}\left[-Q_r + A_r\dot{x} + K_L\left(p_p - p_r\right)\right] \tag{3}$$

The hydraulic capacitance C_h can be defined as in equation (4)

$$C_h = \frac{V}{K} \tag{4}$$

The hydraulic capacitance of the piston and rod chamber side is defined in equation (5) and (6), respectively.

$$C_{h,p} = \frac{V_p}{K_{oil}} = \frac{V_{line,p} + A_p \cdot x}{K_{oil}} \tag{5}$$

$$C_{h,r} = \frac{V_r}{K_{oil}} = \frac{V_{line,r} + A_r \cdot (l - x)}{K_{oil}} \tag{6}$$

For a concise expression, the pressure differential across the cylinder is defined in equation (7), so that the force can be obtained as equation (8).

$$\Delta p^* = p_p - \frac{A_r}{A_p} \cdot p_r = p_p - \frac{1}{\lambda} \cdot p_r \tag{7}$$

$$F_{cyl} = A_p \Delta p^* = A_p p_p - A_r p_r \tag{8}$$

As a result, the mechanical system can be simplified to two equations in terms of force balance and pressure build-up. First, by combining equation (1) and (8) to form (9). Second, by substituting equation (4), (7) into equation (2) and (3) to form (10).

$$\ddot{x} = \frac{1}{M_{eq}}\left(A_p \Delta p^* - c\dot{x} - F_L\right) \tag{9}$$

$$\Delta\dot{p}^* = \frac{Q_{in}}{C_{h,eq}} - \frac{A_p\dot{x}}{C_{h,eq}} \tag{10}$$

Based on these two equations, a state-space representation of the linearized mechanism can be represented as in equation (11) and (12).

$$\begin{bmatrix} \Delta\dot{p}^* \\ \ddot{x} \end{bmatrix} = \begin{bmatrix} 0 & -\frac{A_p}{C_{h,eq}} \\ \frac{A_p}{M_{eq}} & -\frac{c}{M_{eq}} \end{bmatrix} \begin{bmatrix} \Delta p^* \\ \dot{x} \end{bmatrix} + \begin{bmatrix} \frac{1}{C_{h,eq}} & 0 \\ 0 & -\frac{1}{m_{eq}} \end{bmatrix} \begin{bmatrix} Q_{in} \\ F_l \end{bmatrix} \tag{11}$$

$$\begin{bmatrix} F_l \\ \dot{x} \end{bmatrix} = \begin{bmatrix} A_p & 0 \\ 0 & 1 \end{bmatrix} \begin{bmatrix} \Delta p^* \\ \dot{x} \end{bmatrix} \tag{12}$$

The equivalent hydraulic capacitance $C_{h,eq}$ is defined as equation (13).

$$C_{h,eq} = \left(\frac{1}{C_{h,p}} + \frac{1}{\lambda^2 C_{h,r}} \right)^{-1} \tag{13}$$

Based on the equations above, the actuation velocity $\dot{x}$ can be represented as an s-function shown in equation (14), with the inlet flow rate Q_{in} and the load force F_l as the input.

$$\dot{x}(s) = \frac{1}{\left(s^2 + \frac{c}{M_{eq}} s + \frac{A_p^2}{M_{eq} C_{h,eq}} \right)} \left(\frac{A_p}{M_{eq} C_{h,eq}} Q_{in} - \frac{s}{M_{eq}} F_l \right) \tag{14}$$

The actuation velocity follows a second-order response, and the natural frequency and damping ratio can be obtained as in equation (15) and (16).

$$\omega_n = \sqrt{\frac{A_p^2}{M_{eq} C_{h,eq}}} \tag{15}$$

$$\zeta = \frac{c}{2} \sqrt{\frac{C_{h,eq}}{A^2 M_{eq}}} \tag{16}$$

In this hydraulic model, the losses of the pump (e.g., leakage) and throttles losses are also included. However, this information is more about the efficiency performance of the system, while the dynamic behavior is mainly determined by the mechanism with low natural frequency.

3.1.2. Electrical machine control

Regarding the EM control, the PI controller with the speed feedback shown in Figure 2 can be further detailed in Figure 4. To achieve a fast response of the EHU, whenever the user sends a command to the EM, the maximum torque is commanded to accelerate the shaft to the desired speed, before it goes back down to the steady state torque required by the pump. This maximum torque is limited based on the EM size, and is used to protect the EM from overheating. Thus, a saturation block is added to the PI output to protect the EM from overheating. The anti-windup strategy can be added to this control flow for better performance.

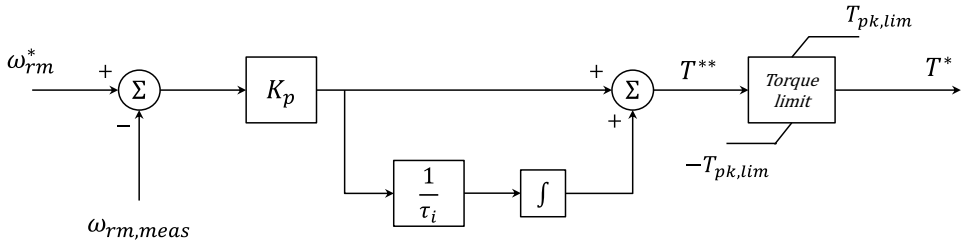

Figure 4. PI controller of the electric machine

Given a mechanical load on the EM, the dynamics of the EM mechanical parts is governed by equation (17). T_l computes as in equation (18). Considering the mechanical losses based on an efficiency map and assuming the inlet pressure to be equal to the tank pressure, we have $\Delta p^* \approx \Delta p$. The coefficient B is usually neglected and set at zero in this study. It may be possible to measure this value in the future study.

$$\dot{\omega} = \frac{1}{J}(T_e - B\omega - T_l) \tag{17}$$

$$T_l = \frac{\Delta p^* V_d}{2\pi} \tag{18}$$

The flow supplied by the EHU is represented in equation (19).

$$Q_p = n \cdot V_d \cdot \eta_{vol} \tag{19}$$

Combined with the linearized model given in equation (11) and (12), the linearized EHA system can be described as in equation (20) and (21), where the inputs are the torque T and the load force F_l.

$$\begin{bmatrix} \ddot{x} \\ \Delta\dot{p}^* \\ \dot{\omega} \end{bmatrix} = \begin{bmatrix} -\frac{c}{m_{eq}} & \frac{A_A}{m_{eq}} & 0 \\ -\frac{A_A}{C_{eq}} & 0 & C_0/C_{eq} \\ 0 & -C_0/J & -B/J \end{bmatrix} \begin{bmatrix} \dot{x} \\ \Delta p^* \\ \omega \end{bmatrix} + \begin{bmatrix} 0 & -\frac{1}{m_{eq}} \\ 0 & 0 \\ 1/J & 0 \end{bmatrix} \tag{20}$$

$$\begin{bmatrix} \dot{x} \\ F_l \\ \omega \end{bmatrix} = \begin{bmatrix} 1 & 0 & 0 \\ 0 & A_p & 0 \\ 0 & 0 & 1 \end{bmatrix} \begin{bmatrix} \dot{x} \\ \Delta p^* \\ \omega \end{bmatrix} \tag{21}$$

Based on the linearized EHA model, the poles of the system can be calculated for stability analysis. Figure 5 graphically represents the system poles. The shaft inertia was estimated using the available CAD designs of the HP and the EM. The real pole represents the impact of the EHU speed response to a torque command. Two complex conjugate poles have a small damping ratio, corresponding to the behavior of the boom mechanism. The real pole is closer to the imaginary axis, thus dominating the response time. When increasing the inertia of the EHU shaft, the response time can increase. The PI controller described in Figure 4 addresses the real pole and maintains the fast response. Therefore, to reduce vibration, the feedback controller should focus on the complex conjugate poles.

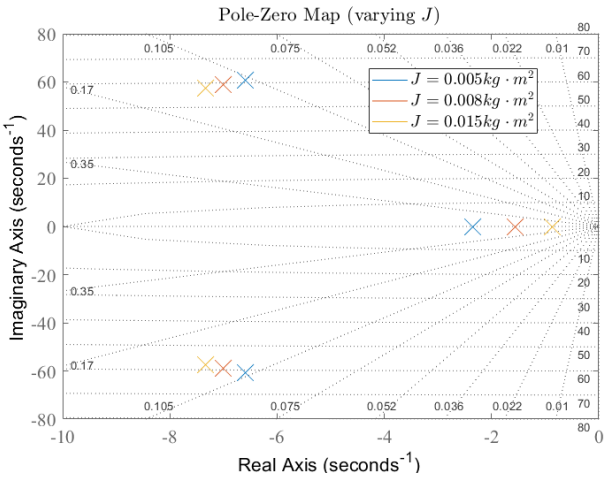

Figure 5. Pole position of the linearized EHA model with different rotational inertia

3.2. Pressure feedback

Figure 6 shows the controller with the pressure feedback controlling the EM speed. The pressure feedback controller includes a high-pass filter and a gain K_f which can be represented as in equation (22). The oscillation with the frequency lower than $1/\tau$ can be roughly excluded, thus the controller is effective for a certain bandwidth. The feedback control block between the working modes and electric system works as a summation point when the pressure feedback is activated. It also includes basic logic control so that the operator can disable the feedback function or adjust the control parameters, which is not the focus of the current study. Therefore, in the following sections, this block simply represents a summation point.

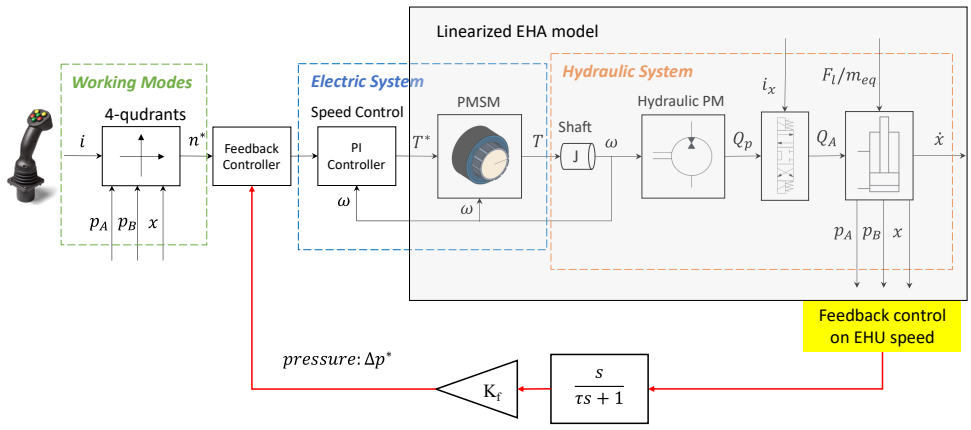

Figure 6. Controller with pressure feedback of the EHA system

$$H(s) = K_f \frac{s}{\tau s + 1} \tag{22}$$

Focusing on the damping vibration, the complex conjugate poles are from the state-space representation given in equation (11). By setting the EM speed ω as input (i.e., replacing the flow input Q_{in}), the state-space representation can be rewritten as in equation (23). By comparing (11) and (23), it can be found the updated model is about the definition of the input.

$$\begin{bmatrix} \Delta\dot{p}^* \\ \ddot{x} \end{bmatrix} = \begin{bmatrix} 0 & -\frac{A_p}{C_{h,eq}} \\ \frac{A_p}{m_{eq}} & -\frac{c}{M_{eq}} \end{bmatrix} \begin{bmatrix} \Delta p^* \\ \dot{x} \end{bmatrix} + \begin{bmatrix} \frac{V_d}{2\pi C_{h,eq}} & 0 \\ 0 & -\frac{1}{M_{eq}} \end{bmatrix} \begin{bmatrix} \omega \\ F_l \end{bmatrix} \tag{23}$$

The plant described in (23) denotes as $G(s)$ With the pressure feedback controller, $H(s)$ given in (22), the transfer function can be stated in equation (24).

$$\frac{y}{u} = \frac{G(s)}{1+G(s)H(s)} \tag{24}$$

Setting the time constant within a reasonable range (e.g., $t \in (\frac{1.8}{\omega_n}, \frac{2.6}{\omega_n})$) according to [8], a root-locus plot can be obtained by varying the value of the feedback gain K_f. Figure 7 shows the root-locus plot.

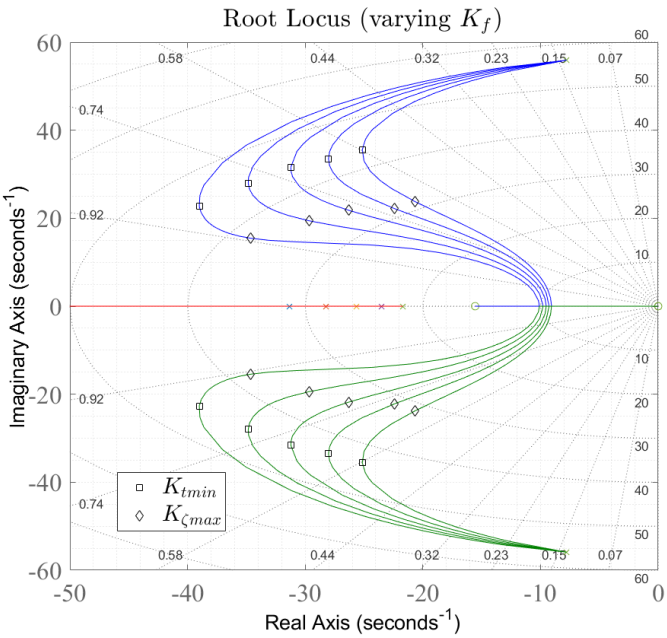

Figure 7. Root locus plot of the EHA system with pressure feedback controller

In the figure, the value between K_{tmin} (i.e., minimum response time) and $K_{\zeta max}$ (i.e., maximum damping ratio with relative high frequency) is suggested for K_f. However, because the dynamic behavior is estimated at the beginning, when tuning K_f a greater range deserves attempt. This root locus plot includes the motor model,

but the PI-control is simplified as shown in equation (23). The input of the model, flow rate Q is translated to motor speed ω in a directly way. The derivation assumes: the speed response of electric machine is much faster than that of boom mechanism. In this study, the assumption is effective and the system performance is stable.

4. SIMULATION

4.1. Simulation model

An integrated EHA model that includes all the electrical-hydraulic-mechanical (EHM) domains in a single simulation platform is developed in Amesim environment. The coupling between the EHM parts of the model along with the control logic allows to simulate the system dynamics in a realistic way.The data for the valve dynamics were selected based on the valve data sheet, while the EM maximum torque is based on a prototype of the unit built at the authors lab at Purdue University. Figure 8 shows the scheme of the integrated EHA model. The details to develop such a lumped parameter model are explained in previous work by the authors [11], where the model is validated in terms of functionality and energy performance.

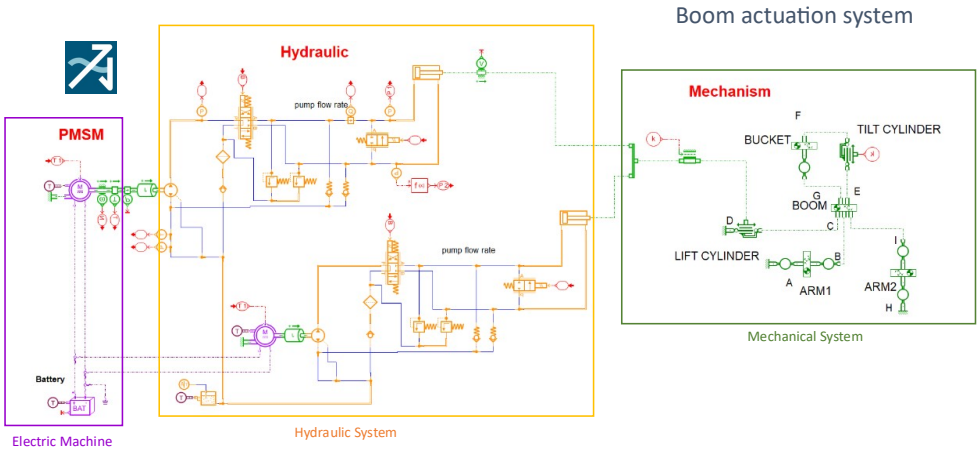

Figure 8. Integrated simulation model of the proposed EHA

The main parameters of the simulation model are listed in Table 1 for the EHU, while Table 2 gives the control parameters. The simulation will vary the feedback gain K_f to determine the optimal controller setup.

Parameters of components		Value [unit]
Hydraulic pump	Nominal displacement V_d	10.69 [cc/rev]
	Maximum speed n_{max}	4300 [rpm]

	Minimum speed n_{min}	500 [rpm]
	Maximum pressure p_{max}	200 [bar]
Electric machine	Nominal speed n_{nom}	4300 [rpm]
	Nominal torque T_{nom}	20.87 [Nm]
	Nominal current I_{nom}	24.22 [A]
	Number of poles P	10 [-]
	Shaft inertial J	0.008 [kgm^2]
	Rated voltage U_n	244 [V_{rmx}]
	Rated current I_n	7.32 [A_{rmx}]

Table 1 Parameters of the hydraulic pump and electric machine.

Parameters	Value [unit]
Natural frequency ω_n	56.45 [rad/s]
Feedback high-pass time constant τ	0.055 [1/s]
EM proportional gain K_p	10 [rpm]
EM integral gain K_i	2000 [-]
EM anti-windup gain K_{aw}	1000 [-]

Table 2 Control parameters in the simulation model.

4.2. Linear model parameters

The parameters used in the linear mechanism model are tuned based on the actual system size described in [11]. The optimal parameters are listed in Table 3.

Parameters	Value [unit]
Equivalent mass M_{eq}	4500 [kg]
Damping constant c	70000 [N/(m/s)]
Load force F_l	16000 [N]

Length of cylinder stroke l	0.8865 [m]
Cylinder piston side area A_p	3.837e-3 [m^2]
Cylinder rod side area A_r	2.828e-3 [m^2]
Oil bulk modulus K	1.4815e3 [MPa]

Table 3 Parameters used in the linearized model.

4.3. Results

First, the model is used to test the system response based on a feed-forward controller. Then, the proposed pressure feedback controller is compared with the open-loop control strategy.

Figure 9 shows the simulated step response of the actuator velocity and the corresponding displacement with feed-forward control relevant to Figure 2. The response has three phases as highlighted in the plot. In phase 1, an undershoot occurs due to the transition of the on/off valve. A 3mm undershoot of actuator displacement can be noticed. Nevertheless, for a machine with hydraulic cylinders which have a 900 mm length of stroke, it is negligible. This problem is addressed in [14] by using a pressure control, but it is not in the scopes of this study. The ramp in phase 2 represents the response of the EM, in terms of speed. Phase 3 is the focus of this study, which shows the damping oscillation of the actuator.

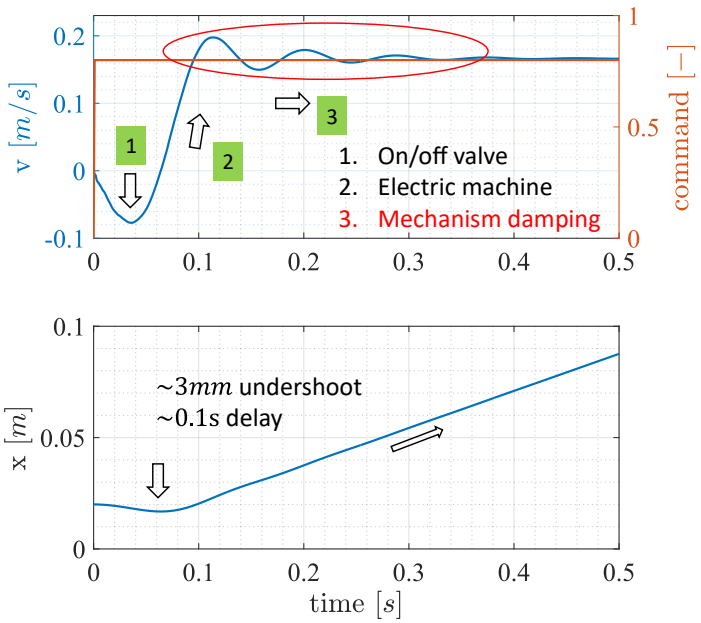

Figure 9. Step response of the EHA with feedforward control

Figure 10 shows a comparison of the velocity response of the hydraulic cylinder with a pressure feedback control (using different gains K_f), and without feedback. The red curve is the baseline response without feedback. The black line represents the optimal result, which

effectively reduces the oscillation of the system. The blue and green dotted lines give results with different feedback gain values.

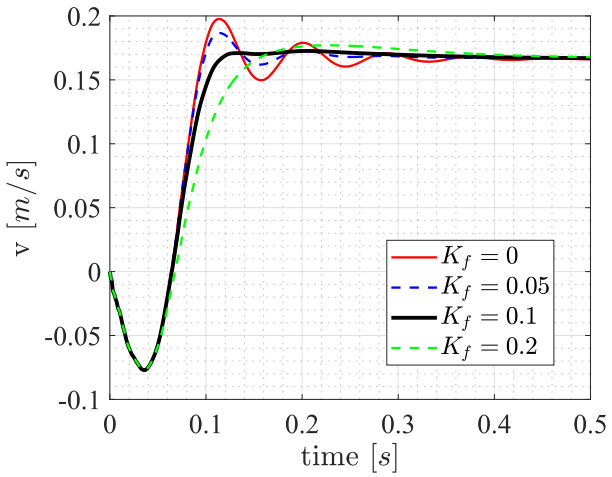

Figure 10. Step response of the EHA with pressure feedback

Focusing on the prime mover, Figure 11 shows a comparison of the torque and speed response with or without feedback control. In the feed-forward case (baseline), given a speed command, the maximum torque command is given to the EM to achieve the fastest response. However, this results in a low damping ratio in the actuator. With pressure feedback, the torque command of the EM is adjusted, leading to the change in the acceleration slope. The EM speed response in the rising time region also changes and can be seen in Figure 11 between 0.05 seconds and 0.14 seconds. This change in EM speed increases the damping ratio of the actuator and results in better dynamic performance of the actuator as shown in Figure 10.

The torque response appears not natural compared to original open-loop controller. This is due to the need of slowing down the motor speed for better dynamic performance with feedback controller. As a result, the torque does not need to keep the maximum in the motor acceleration phase. This is a novel method studied based on simulation model, so such torque performance still results in smooth speed control. For future work, experimental validation can be significant to investigate more about torque control and speed response.

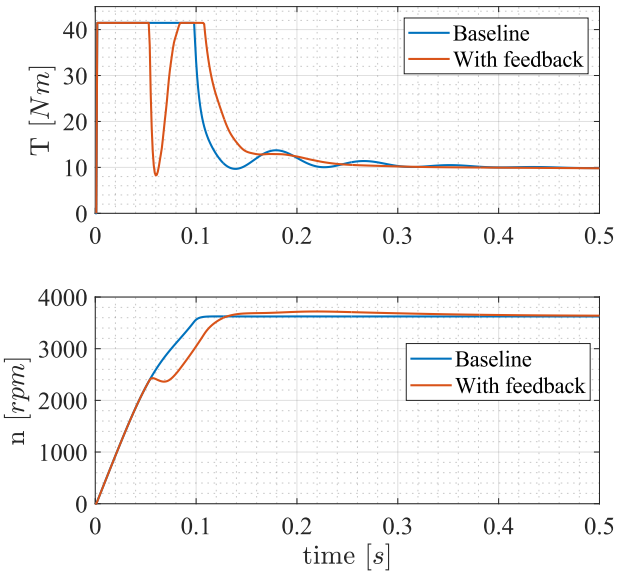

Figure 11. Step response of the EHA with pressure feedback

5. CONCLUSION

This paper investigates the implementation of a pressure feedback strategy that acts on the prime mover of an EHA, aiming to reduce the damping oscillation and thus improve the dynamic performance. The paper derives the controller on the basis of a system linearization. After that, a lumped-parameter simulation model is developed to validate the controller design. Based on the simulation results, the damping oscillation of the actuation velocity response is effectively reduced with pressure feedback. The response time to steady state is much less (from 0.4s to 0.1s), and the overshoot due to the oscillation of about 15\% is eliminated via the pressure feedback controller. Experimental validation of the study may be a focus of future work. Since this architecture is implemented with a bypass valve, it would be used to compare the effectiveness of both methods.

6. NOMENCLATURE

$\ddot{x}$	Acceleration
Δp	Pressure differential
η_{vol}	Volumetric efficiency
λ	Area ratio
ω	Angular velocity
ω_n	Natural frequency
ζ	Damping ratio

A	Area
B	Viscous coefficient of the machine bearings
C_h	Hydraulic capacitance
c	Viscous friction
F	Force
I	Current
J	EM and pump inertia
K	Oil bulk modulus
k	Spring stiffness
K_f	Feedback gain
l	Length of cylinder
M_{eq}	Equivalent mass
n	Motor speed
p	Pressure
Q	Flow rate
T	Torque
U	Voltage
V	Volume
V_d	Pump displacement
x	Cylinder position

7. ACKNOWLEDGMENT

The authors wish to thank CNH Industrial for providing the information of the mechanism to develop the model. The authors would also like to thanks Siemens for the use of the Simcenter Amesim software. The project is funded by the Department of Energy, USA (DE-EE0008334, 'Individual Electro-Hydraulic Drives for Off-Road Vehicles').

8. REFERENCES

[1] S. Ketelsen, D. Padovani, T. O. Andersen, M. K. Ebbesen, and L. Schmidt, "Classification and review of pump-controlled differential cylinder drives," Energies, vol. 12, no. 7, pp. 1–26, 2019, issn: 19961073. doi: 10.3390/en12071293.

[2] H. Liu, X. Zhang, L. Quan, and H. Zhang, "Research on energy consumption of injection molding machine driven by five different types of electro-hydraulic power

units," Journal of Cleaner Production, vol. 242, p. 118 355, 2020, issn: 09596526. doi: 10.1016/j.jclepro.2019.118355.

[3] C. Williamson, S. Lee, and M. Ivantysynova, "Active vibration damping for an off-road vehicle with displacement controlled actuators," International Journal of Fluid Power, vol. 10, no. 3, pp. 5–16, 2009, issn: 14399776. doi: 10.1080/14399776.2009.10780984.

[4] C. Williamson, and M. Ivantysynova, "Stability and motion control of Inertial loads with displacement controlled hydraulic actuators," 6th FPNI-PhD Symposium, pp. 499-514, 2010.

[5] R. Rahmfeld, M. Ivantysynova, and B. Eggers, "Active Vibration Damping for Off-Road Vehicles Using Valveless Linear Actuators," SAE Technical Papers, pp. 724, 2004.

[6] R. Ding, B. Xu, J. Zhang, and M. Cheng, "Self-tuning pressure-feedback control by pole placement for vibration reduction of excavator with independent metering fluid power system," Mechanical Systems and Signal Processing, vol. 92, no. 38, pp. 86–106, 2017, issn: 10961216. doi: 10.1016/j.ymssp.2017.01.012.

[7] R. Madau, A. Vacca. "Active Ride Control for Construction Machines Based on Pressure Feedback". ASME/BATH 2019 Symposium on Fluid Power and Motion Control.

[8] H. C. Pedersen and T. O. Andersen, "Pressure Feedback in Fluid Power Systems - Active Damping Explained and Exemplified," IEEE Transactions on Control Systems Technology, vol. 26, no. 1, pp. 102–113, 2018, issn: 10636536. doi: 10.1109/TCST. 2017.2650680.

[9] P. C. Krause, O. Wasynczuk, S. D. Sudhoff, and S. Pekarek, Analysis of electric machinery and drive systems. Wiley Online Library, 2002, vol. 2.

[10] S. Qu, D. Fassbender, A. Vacca, and E. Busquets, "Formulation, Design and Experimental Verification of an Open Circuit Electro-Hydraulic Actuator," in 2020 IEEE Global Fluid Power Society PhD Symposium (GFPS), 2020, pp. 129–136.

[11] S. Qu, D. Fassbender, A. Vacca, and E. Busquets, "A Cost-Effective Electro-Hydraulic Actuator Solution with Open Circuit Architecture," International Journal of Fluid Power, vol.22, no.2, pp.233–258, 2021. doi:10.13052/ijfp1439-9776.2224

[12] S. Qu, D. Fassbender, A. Vacca, and E. Busquets, "A high-efficient solution for electro-hydraulic actuators with energy regeneration capability," Energy, vol.216, p.119291, 2020. doi:10.1016/j.energy.2020.119291

[13] S. Qu, F. Zappaterra, A. Vacca, Z, Liu, and E. Busquets, "Design and verification of an electro-hydraulic actuator system with an integrated electro-hydraulic unit," in The 13th International Fluid Power Conference (13. IFK), 2022.

[14] D. Hagen, D. Padovani, "A Method for Smoothly Disengaging the Load-Holding Valves of Energy-Efficient Electro-Hydraulic Systems," Proceedings. 2020; 64(1):36. https://doi.org/10.3390/IeCAT2020-08478.

Biographies

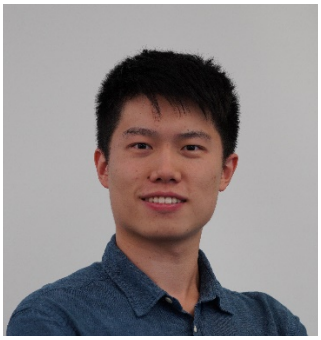

Dr. Shaoyang Qu is currently a electrified systems engineer in Bosch Rexroth US. His work mainly focuses on the R&D work on electrified solutions of the state-of-the-art hydraulic systems and the development of next generation electrification platforms. He is also responsible for the customer commissioning, system solutions, and engineering support of eLION products in North America. He got the Ph.D. degree in the School of Mechanical Engineering at Purdue University, where he worked in Maha Fluid Power Research Center on electrification of mobile hydraulics since 2018. Before that, he attended Tsinghua University in Beijing, China, where he received his B.E. in Mechanical Engineering and B.S. in Business administration in 2018.



Dr. Hassan Assaf is currently a control systems senior engineer at Caterpillar with the focus in the development of electro-hydraulic systems for motor graders and medium wheel loaders. He got his PhD degree in Agricultural Engineering at Purdue University, where he worked at the Maha Fluid Power Research Center. Hassan has a Master of Science in Mechatronics Engineering from Politecnico di Torino in Italy, and a Bachelor of Science in Mechanical Engineering from the same university. Hassan has worked on numerous projects involving the modeling and optimization of hydraulic systems, and the development of Electro-hydraulic Actuators. He has also designed and built novel hydraulic trainers and has

implemented a virtual trainer in Purdue fluid power classes. In addition to his technical skills, Hassan is fluent in Arabic and proficient in Italian.



Dr. Andrea Vacca is the director of the Maha Fluid Power Research Center, the largest academic research center dedicated to fluid power research in the United States. His research focuses on several aspects of hydraulic control technology including new concepts to perform hydraulic actuations, new designs and modeling of positive displacement machines, electrification of fluid power systems, modeling of the properties of hydraulic fluids, reduction of noise emissions from hydraulic components.

Dr. Vacca holds about 20 patents/patent applications and he is author of about 200 technical papers, and of the textbook “Hydraulic Fluid Power”. He is the Editor in Chief of the International Journal of Fluid Power, one of the directors of the Global Fluid Power Society (GFPS) and a former chair of the Society of Automotive Engineers (SAE) - Fluid Power Division and of the American Society of Mechanical Engineers (ASME) - Fluid Power System and Technology Division. In 2019, Andrea Vacca was awarded the 2019 Joseph Bramah Medal from the Institution of Mechanical Engineers for his contributions to global fluid power research, particularly related to gear pumps.

Andrea Vacca is a fellow of the American Society of Mechanical Engineers (ASME) and he received his master’s degree in mechanical engineering from the University of Parma (Italy) and his Doctoral degree in Energy Systems from the University of Florence (Italy).).



Dr. Enrique Busquets is currently responsible for the service and aftermarket business in North America. In addition, his current role in engineering has been the engineering director with regional product and business development responsibility on electronics, software, telematics, and electrification at Bosch Rexroth North America since April 2021. Additionally, Enrique has been responsible for the testing and validation infrastructure in North America since 2018 and innovations since 2016.

Previously, Enrique Busquets was the engineering manager responsible for systems and software development at Bosch Rexroth North America from 2018 to 2021. The technology focus was on mobile applications with electronified hydraulics and electrified systems.

Enrique holds a bachelor's degree from the University of Texas at El Paso and a master's, and doctorate degree in mechanical engineering from Purdue University with emphasis on hydraulics and electronic controls.

In addition to his professional activities, Dr. Enrique Busquets is the Bosch Rexroth industry sponsor and representative at the Maha research center and the National Fluid Power association.

Energy Saving Enhancement through 3 way Downstream Compensator Main Valve, a Viable Option for Efficient Off Highway Applications

Cesare Dolcin[1], Gianluca Ganassi[2], Ulderico Busani[2], Francesco Ferdinando De Martino[2]

[1]*Test Department, Walvoil SpA (Interpump Group), Reggio Emilia (RE), Italy*

[2]*Hydraulic R&D Dept., Walvoil SpA (Interpump Group), Reggio Emilia (RE), Italy*

Abstract

In the last decade, the high percentage of energy wasted on the control of movements by pressure throttling on mobile machines has been the subject of increasingly detailed studies, which drove to the proposal of revolutionary hydraulic architectures as Valveless and Zonal Hydraulics. Despite of higher efficiency, those proposals found poor application by OEMs, due to their higher complexity and cost, and to mind-set change required to all people involved, from design to aftersales.
As an intermediate solution, Walvoil has developed the evolution of a LS Flow-Sharing Main Valve, introducing a 3-way compensator downstream of the spool meter-out notches, in which the third way opens an energy recovery line, with an enthalpy flow available for storage or conversion into electricity.
This work presents the results of the experimental comparison of the energy consumption measured on repeated cycles of lifting and lowering loads carried out with two different architectures (standard LS flow-sharing valve and evolved LS flow-sharing valve with downstream 3-way compensator) applied to a front-loader with double actuation on boom and tilt. Both configurations were tested simulating the application to a hybrid vehicle, where the main power is supplied by a test bench (in place of the prime mover), while a battery pack combined with an asynchronous motor equipped with a gear pump acts as both complementary energy supplier and energy recovery line and converter. In order to properly compare the efficiency, the same number of cycles is performed, computing the whole energy consumption given by both the prime mover and the battery (monitoring its "State of Charge").
Electrical, hydraulic and control parameters were monitored throughout the duration of the tests, to evaluate the efficiency of the sub-components too.

Keywords. Energy saving, Energy recovery, Downstream compensation, Hybrid vehicles.

1. INTRODUCTION

In recent years, the high fraction of energy wasted on the control of movements by pressure throttling on earthmoving and agricultural machines has attracted growing attention and has been the subject of increasingly detailed studies, in order to investigate the energy leakage from prime mover shaft to final users, throughout the whole hydraulic system.
If pumps account generally for 15 to 31% of losses (on excavators, e.g.), the directional flow control valve (DFCV) has been proven to be the main culprit of the energy waste, with percentages ranging from 40 to 62% of the total energy that the prime mover makes available at the shaft [1, 2, 3, 4, 5].
The global trend of reducing the consumption of fossil fuels and their conversion into harmful emissions has also forced the Fluid Power sector to devise innovative solutions to perform the same tasks requiring less energy to the prime mover ("energy saving"), and perhaps even succeeding to recover from inertial or overrunning loads, or through less dissipative controls of the movement ("energy recovery") [18, 32].
Several applications have been studied in order to evaluate where to recover energy on machines [6, 7, 8], how and where to store or use it [9, 10], and how to integrate the Energy Recovery System within the hydraulic circuit [8, 11, 12].
To avoid energy losses due to the compensation of the different resistant loads applied to users simultaneously activated and powered by the same source, the logically most promising method is to make the flow rate supplied to coincide, for each movement, with that one strictly necessary to reach the speed of required actuation, with the minimum pressure sufficient to overcome the load opposing the movement.
This finding led to the proposal of very efficient architectures (attributable to the concepts of "Valveless Hydraulics" [13, 14] and "Zonal Hydraulics" [15, 16, 17]), but quite more complicated and expensive than those currently consolidated on the market, thus finding poor application by OEMs to date.
Despite of difficulties that these architectures implied, due to significant circuit changes at the level of design, production, after-sale service, and due to benefits to communicate to final users in order to justify the vehicle's price remarkable increase, both academic and industrial players have been further investigating an holistic approach to optimize the overall energy efficiency of the vehicle, including prime mover, transmission and users [4, 19, 20, 21].
Consistent efforts have also been done to develop innovative components, potentially useful for energy recovery and storage or direct drive of single user, as digital accumulators [22], hydraulic transformers [23, 24], special displacement controlled implements, close-circuit electro-hydraulic actuators [25, 26], or dedicated lines for energy recovery [33, 34].
Among these efforts, Walvoil (together with National Research Council of Italy and University of Naples Federico II) is developing a Load Sensing Flow Sharing (LSFS) DFCV with new circuit solutions: a 3-way compensator downstream of the spool meter-out notch, in which the third way opens an energy recovery line (references [27, 28, 29, 30, 31 and especially 37], that details evolution from existing LSFS DFCV).
On this line, an enthalpy flow is available for storage in a hydraulic accumulator or for conversion into electricity (useful in coming hybrid vehicles).

2. AIM OF PRESENT WORK



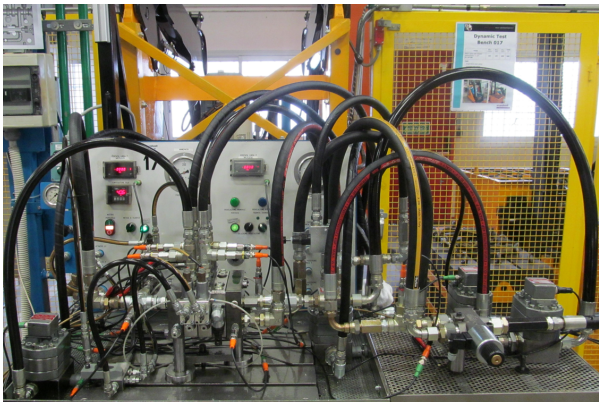

Figures 2.1, 2.2. Test rig configuration and hydraulics *set-up*

In consideration of worldwide increasing diffusion of hybrid on-road vehicles, also off-road mobile machines OEMs are manufacturing prototypes of hybrid vehicles and engines ([35, 36], e.g. Caterpillar 336E excavator, Carraro SRX Hybrid tractor, Kohler K-HEM hybrid engine, etc.). This opens new chances on energy management of vehicles, due to the availability on the vehicle of devices for electricity conversion, management and storage (motor, inverter, batteries, etc.). By convoying the energy flow recovered from the DFCV "third line" to a hydraulic volumetric device (hydraulic pump/motor) connected to an electric motor, it is possible both to convert recovered oil enthalpy into electricity to be stored into batteries and to assist the motor that can compress oil via the volumetric device. This device can work in parallel to the main pump installed on the prime mover in order to generate the required flow, so creating a hybrid vehicle.
This work presents the results of the experimental comparison of the energy consumption measured on repeated cycles of lifting and lowering loads carried out with two different circuit solutions applied to a front loader, connected to an experimental test bench available at Walvoil Test Department.

The two hydraulic solutions are:

- standard load sensing flow sharing DFCV (here following called DPX);
- evolved load sensing flow sharing DFCV with downstream 3-way compensator (here following called EPX).

The application consists in the lifting, lowering and tilting of a load by double simultaneous actuation of front loader boom and bucket cylinders (with the first having differential areas with ratio of 1,39, while the second is a double rod cylinder).
The purpose is to physically simulate a hybrid vehicle with a prime mover giving about 85% of energy required to accomplish the task, while the remaining 15% is given by an electric booster, a motor coupled with a volumetric hydraulic device used to convert oil internal energy into electricity and vice versa.

3. Simplifications Introduced in the Test and Methods of Comparison and Analysis

3.1. Prime Mover

On the test rig it has been substituted by a 37 kW asynchronous motor, running at constant speed of 1.450 rpm and equipped with a 71 cm^3 variable displacement Load Sensing (LS) axial piston pump.

3.2. Electrical Hybrid Booster

Electrical power is supplied by a 48 V Li-MH 16 kWh battery pack, combined with a 12 kW asynchronous motor, coupled to a Group 2 11,0 cm^3 external gear pump. Its speed is controlled by a programmable inverter that communicates with an external ECU via CAN protocol (a Walvoil CED400X programmed with proprietary Integrated Development Environment "PHC Studio"). It can work as both "electrical motor + hydraulic pump" and "hydraulic motor + electrical generator".

3.3. Load

The front loader has been loaded with a steel basket containing seven "200kg-weights", for a total payload of 1.750 kg, plus the weight of the loader itself.

3.4. Cycle

A general cycle has been chosen, in order to have combinations of simultaneous resistant and overrunning loads: a first "boom-up + bucket-down" phase was followed by a "boom-down + bucket-up" second phase.

3.5. Actuation and Control

The spools of both sections were automatically activated by the same ECU that communicates with the inverter in order to set the electrical booster motor angular speed. Both the positions of the spools and the angular speed were set-up in "open-loop" mode, with values chosen after careful tuning.

3.6. Repetition and Duration

In each configuration the cycle was automatically repeated 10 times under control of the same ECU, setting same flow rates, spool positions and motor's revolution per minute, and checking time and cylinder position. Repeatability in different configurations was within ±0,3 s out of the 368,6 s of time required to run the 10 cycles.

3.7. Hydraulic Main Valve

A provisional casting has been used, in order to be able to switch rapidly from DPX to EPX configuration and vice versa; the internal circuits are not optimized in neither DPX, nor EPX configurations, due to the different castings that would have been necessary. The two different circuits are realized by changing spools, compensators, notches, etc. Due to prototype internal constraints, it was chosen to do not include regeneration in DPX mode, meanwhile it was in EPX mode. Anyway, pressure levels re-entering from cylinders are lower in DPX than EPX, so implying higher benefits from regeneration for this last one configuration. Since this is due to test set-up and not to state-of-the-art limits, its energetic contribution will be carefully evaluated in comparison and conclusions.

3.8. Energy Consumption

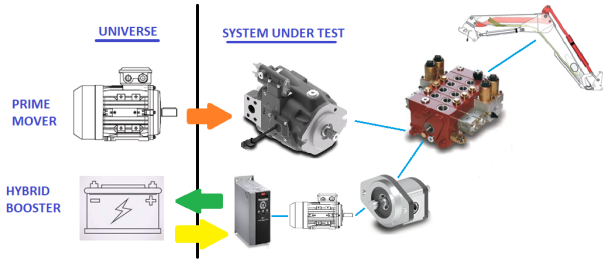

Figure 3.8.1. System border and energy exchange with environment

The "border" of the system (Figure 3.8.1) on which to evaluate the consumed energy was placed at the prime mover shaft and at the cables connecting the inverter to the battery pack of the electrical booster. The prime mover pump total efficiency $\eta_{T,p}$ was characterized on a dedicated test bench, while the delivered flow rate (QP, in liter per minute) and pressure (pP, in bar) were measured throughout the test. The power absorbed at the prime mover shaft (W_{PM}, in Watts) was hence calculated with the following formula (where the "0,6" coefficient at denominator is due to a mix of units of measure taken from both SI and the still widespread industrial practice):

$$W_{PM} = \frac{QP \cdot pP}{0{,}6 \cdot \eta_{T,p}} \qquad (3.8.1)$$

Similarly, the power exchanged with the batteries (W_{EL} when discharging and W_R when recharging, i.e. recovering energy), was calculated through the following formulas:

$$W_{EL} = V \cdot I_d \qquad (3.8.2)$$

$$W_R = V \cdot I_c \qquad (3.8.3)$$

where V is the battery voltage (in Volt), I_d and I_c are the discharge and charge currents (in Ampere) respectively.

3.9. Datalogging and Sensors

25 physical variables (including 10 pressures, 7 flow rates, 4 strokes, 2 currents, 1 voltage and 1 angular speed) were monitored during each test, and logged with a sampling interval of 9 ms during each whole test. Several virtual sensors where then implemented upon the signals of these real sensors.
The pressure sensors used have 60 MPa full scale (FS), except the Tank line and the Stand-by differential pressure, having 6 MPa and 5,2 MPa FS respectively, and total error of ±0,3% of FS. Gear flow counters used can detect a 2 cm^3 flow rate pulse and have an accuracy of ±0,3% of the read value, up to a FS of 120 lpm.
Cylinder strokes have been measured through optical laser sensors (600 mm FS and 0,25% FS total error), while compensator strokes relied on LVDT sensors, calibrated prior the test and compensated in post-processing to a residual error of less than 0,1 mm.
Voltage was measured with a precision of ±0,02 V.
Current was measured with an accuracy of ±1% of 300 A FS.
Electronics of datalogger channels have an accuracy of 0,10% of FS.
Overall precision in datalogging is within ±1% for each physical variable, and within ±0,5% for most of them.
Hydraulic mineral oil used during the test is VG46 class; its temperature was regulated within a range of ±2 °C from the 40 °C temperature target.

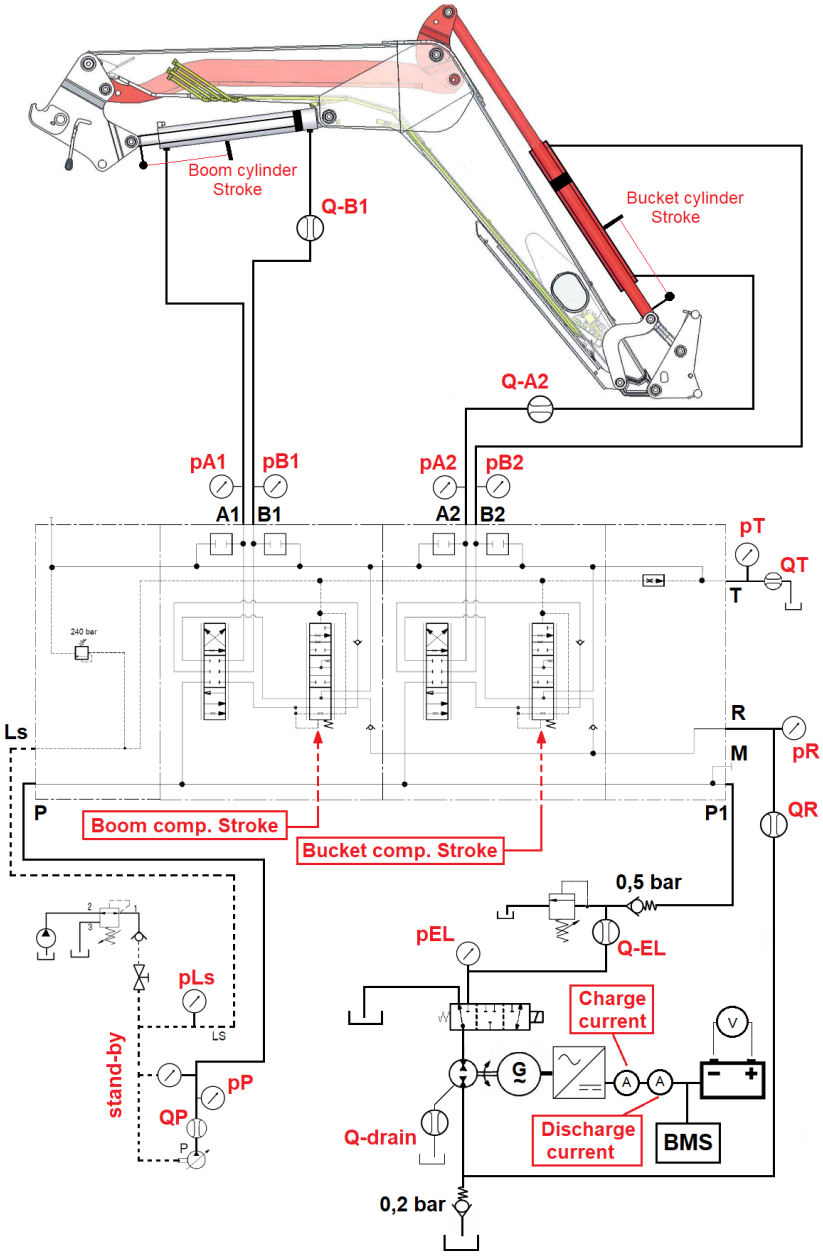

Figure 3.9.1. Hydraulic schematic and sensors position, EPX mode

4. CIRCUIT SET-UP AND TEST DEFINITION

During the set-up phase of the test, some difficulties emerged about the commutation of the hydraulic volumetric device of the electric booster from "pump" operation to "motor" operation and vice versa. To overcome these problems and other minor issues about stability of the system, the two phases in each configuration were simplified as follows.

4.1. DPX Configuration, "Boom-up + Bucket-down" Phase

Prime mover's pump delivers 32 lpm, while the electrical booster's one delivers 6 lpm in parallel. Both pumps have suction side at Tank pressure and P side at about 170 bar, due to pump margin of 20 bar and LS pressure given by boom cylinder pressure, base side, of 150 bar. Bucket compensator throttles inlet pressure to the required 20 bar to avoid cavitation, while the meter-out spool notch throttles the reentry pressure from 85 bar (due to overrunning load) to Tank pressure. Recovery line plugged.

4.2. DPX Configuration, "Boom-down + Bucket-up" Phase

Electrical booster switched off. Prime mover's pump delivers all the required 38 lpm at about 140 bar, necessary to push-up the bucket cylinder. Boom compensator throttles inlet pressure to the required 30 bar to avoid cavitation, while the meter-out spool notch throttles the reentry pressure from 120 bar (due to overrunning load) to Tank pressure. Recovery line plugged.

4.3. EPX Configuration, "Boom-up + Bucket-down" Phase

Recovery line opened to electrical booster pump suction side; regenerative line through bleed-off hole opened inside the bucket spool. The Recovery line takes energy from the bucket-down overrunning load, rising suction pressure side at 110 bar, so the current required from the electrical booster decreases from the 70 A necessary in DPX configuration to the present 25 A, in order to accomplish the same task of delivering 6 lpm at 170 bar. Due to regeneration inside bucket spool, prime mover's pump has to deliver just 26 lpm, instead of the 32 lpm of DPX configuration.

4.4. EPX Configuration, "Boom-down + Bucket-up" Phase

Recovery line opened to electrical booster pump suction side; regenerative line through bleed-off hole opened inside the boom spool. The Recovery line takes energy from the boom-down overrunning load, collecting 24 lpm flow rate at an average pressure of 140 bar during the movement; flow diverted to Tank after generating an average current of 70 A in the hybrid device. Due to regeneration inside boom spool, prime mover's pump has to deliver just 29 lpm, instead of the 38 lpm of DPX configuration.

5. TEST RESULTS

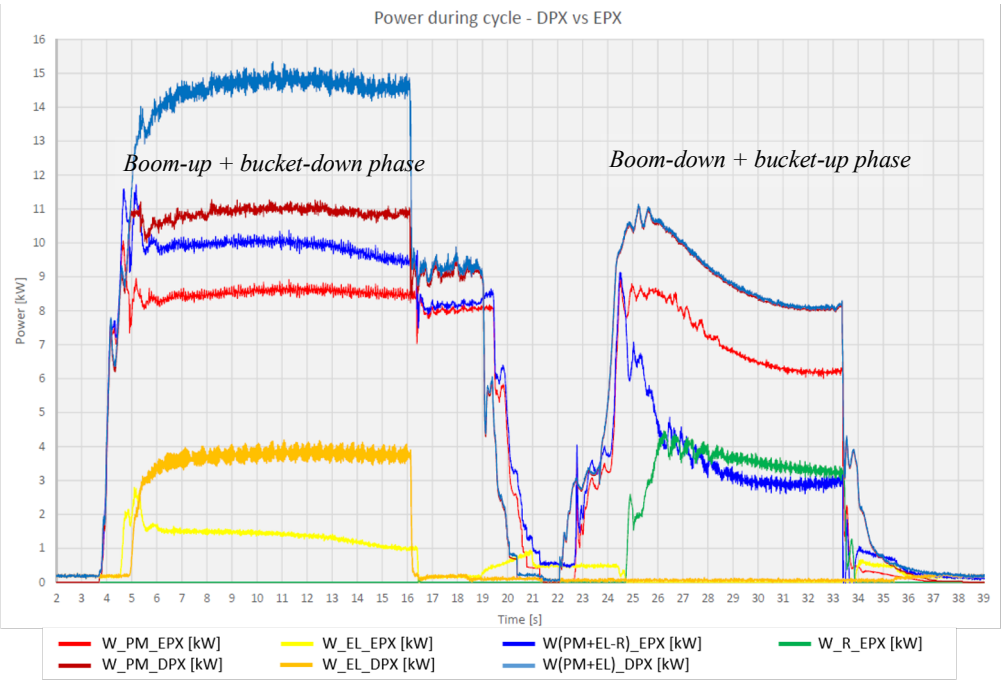

Figure 5.1. Power demanded and produced in both DPX and EPX configurations during a cycle

As depicted in Figure 5.1, the power demanded by the prime mover during "boom-up + bucket-down" phase (I) decreased from 11 kW to 8,5 kW passing from DPX to EPX mode (dark and bright red lines respectively). Similarly, the power demanded by the hybrid booster decreased from 4 to 1,5 kW (golden and yellow lines respectively).
The total power demanded was hence reduced from almost 15 kW in DPX configuration to about 10 kW with EPX (dark and bright blue lines respectively).
During the "boom-down + bucket-up" phase (II) the electrical hybrid unit was switched off in DPX mode, while it was used to generate current to be stored into batteries (without supporting the inlet flow to the main valve) in EPX mode. So in this phase prime mover power required by DPX coincides with total required power, at an average value of almost 9 kW (the value is not stable during this phase due to the kinematics of the bucket during cylinder extension). Meanwhile in EPX mode the prime mover delivers an average power of about 7 kW, but (after an initial transient) almost 4 kW are generated, thanks to the recovery line, and sent back to the battery (green line), so halving the net energy demand during this phase, to an average value of about 3,5 kW.

6. ENERGY CONSUMPTION COMPARISON

By integrating over time the power values previously calculated, it was possible to evaluate the total energy consumed to carry out the planned ten-cycle-test in both cases of DPX and EPX configurations.

As depicted in the pie charts of Figure 6.1 and in the histogram of Figure 6.2, the ten cycles carried out in DPX configuration needed a total amount of 2.988 kJ given by both the prime mover (2.535 kJ, 85%) and the hybrid electrical booster (453 kJ, 15%).

To accomplish the same task with EPX configuration just 2.277 kJ were required to prime mover (2.058 kJ, 90%) and hybrid electrical booster (219 kJ, 10%), but during phase II of each cycle the hybrid system had actually charged the battery through conversion into electricity of the fluid power flowing in the recovery line. A total amount of 302 kJ was stored back into the battery, bringing down to 1.975 kJ the net value of energy used, with battery receiving back in charging phase II 83 kJ of energy more than the amount supplied in discharging phase I.

By comparing DPX and EPX working modes and respective energy flows, it is possible to analyse where and how the energy consumption was reduced switching from DPX to EPX circuit.

About 478 kJ (16% of what required by DPX configuration) were saved by asking lower flow rate at the prime mover's pump, thanks to the bleed-off holes giving flow regeneration through bucket-down movement in phase I and through boom-down movement in phase II.

A further 233 kJ (8% of the total) were saved by using EPX R-line to overcharge the hybrid booster's pump suction side, thanks to bucket-down movement during phase I.

Moreover, there are the 302 kJ (10% of the DPX mode total) recovered and sent back to the battery, by using the EPX R-line to supply the hybrid unit in order to convert it into an electrical generator, thanks to boom-down movement during phase II.

With EPX mode was saved 24% of energy used in DPX mode, and further 10% was recovered.

Regarding the net value of energy used, so including the recovered energy within the balance, it's possible to evaluate in Figure 6.2 as EPX cycle ran using only 66% of energy used by DPX configuration.

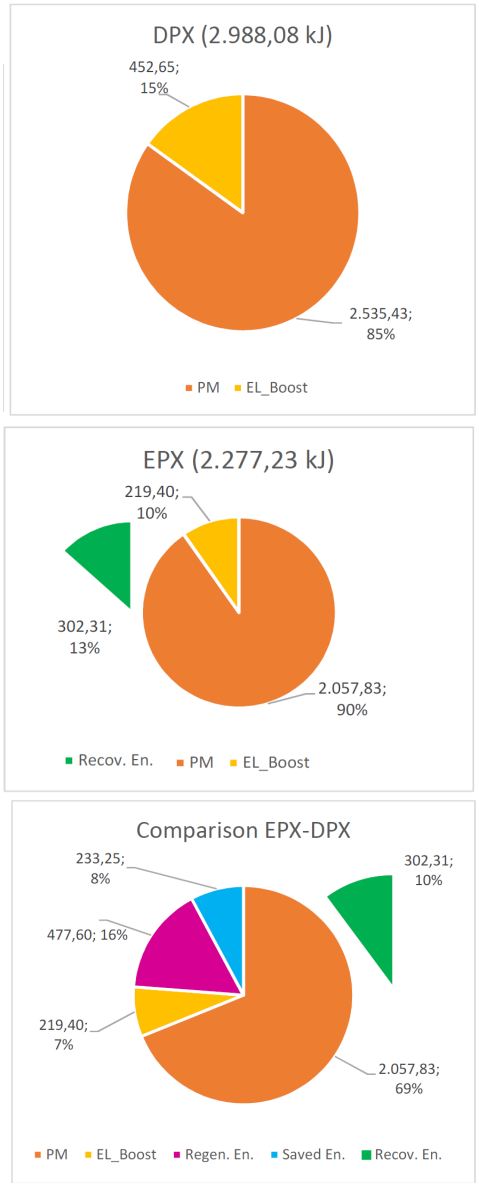

Figure 6.1. Total energy exchanged during the 10-cycle-test

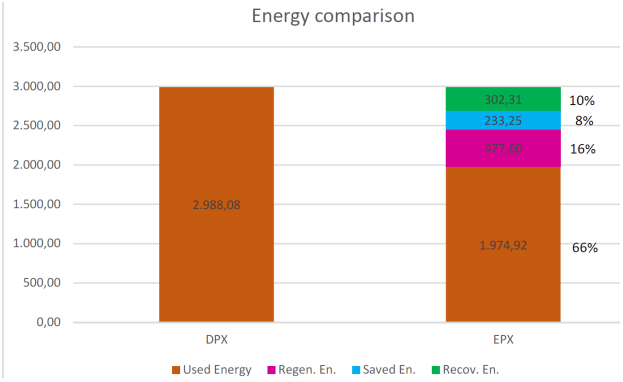

Figure 6.2. Comparison of net values of total energy used carrying-out the 10-cycle-test in DPX and EPX modes

7. CONCLUSIONS, LESSONS LEARNT, NEXT STEPS

Overall savings of 34% went beyond expectations. Even if almost half of the total came from regeneration inside spools (that wasn't possible to use in DPX mode with this provisional casting), the result of 18% reached by savings and recovery through the R-line is quite good.

Introducing bleed-off and regeneration in DPX mode would similarly decrease the amount of energy required by this configuration, and this would bring the energy saved and recovered through R-line in EPX mode at a very satisfactory percentage value ranging around 20-21%.

Wider total savings are expected in different applications, eventually ranging up to 35% in forklift and cranes, while complex circuits as those of excavators and backhoe loaders have to be carefully investigated through simulation and testing, in order to fully exploit their potential.

It is correct to point out that even if this experiment benefited from presence of overrunning loads in each phase, EPX mode can generate a flow in R-line also exploiting the pressure compensations happening during multiple sections actuation in LS DFCV.

Beside satisfactory results regarding the amount of energy saved and recovered, several further goals were achieved carrying out the test, sketching the path for the following steps of the research activity.

The prototype external gear pump emerged to be critical in phases with rapid switch between the conditions of working as pump and as motor: with suction and delivery sides having similar pressure values, the drain flow rate can increase significantly, jeopardising the energy efficiency. Different volumetric device typologies are to be tested.

Further efficiency benefits can arrive from the introduction of closed loop control strategies: models with feed-back on compensator positions and recovery line pressure are under development.

Further benefits from EPX introduction can come from prime mover downsizing: after hybridization premises, with the 15 kW maximum demand split to 11 kW from prime mover and 4 kW from hybrid system, EPX reduced the required amount to 10 kW. Last but not least, lower use of oil throttling to control movements can drive to lower oil aging and downsizing of oil cooling system, with further indirect benefits in energy saving.

8. REFERENCES

[1] J. Lodewyks, P. Zurbrügg – *Decentralized energy-saving hydraulic concepts for mobile working machines* – Proceedings of the 10th International Fluid Power Conference (IFK), 8-10 March 2016, Dresden, Germany.

[2] M. Vukovic, J. Schmitz, J. Zhou – *Systematic Data Analysis for Optimal System Design* – Proceedings of the 11th International Fluid Power Conference (IFK), 19-21 March, 2018, Aachen, Germany.

[3] A. Bedotti, F. Campanini, M. Pastori, L. Riccò, P. Casoli – *Energy saving solutions for a hydraulic excavator* – Energy Procedia 126 (2017) 1099-1106.

[4] M. Inderelst, F. Weidner, N. Dongdong, C. Stammen – *Quantification of Energy Saving Influencers in a 21t Excavator Hydraulic System – A Holistic Investigation?* – Proceedings of the 11th International Fluid Power Conference (IFK), 19-21 March, 2018, Aachen, Germany.

[5] V. Salomaa, T. Minav, J. Mattila, M. Pietola – *Efficiency Study of an Electro-Hydraulic Excavator* – Proceedings of the 11th International Fluid Power Conference (IFK), 19-21 March, 2018, Aachen, Germany.

[6] M. Vukovic, J. Schmitz, J. Zhou – *Systematic Data Analysis for Optimal System Design* – Proceedings of the 11th International Fluid Power Conference (IFK), 19-21 March, 2018, Aachen, Germany.

[7] P. Casoli, L. Riccò, F. Campanini, A. Lettini, C. Dolcin – *Mathematical model of a hydraulic excavator for fuel consumption predictions* – ASME/Bath Symposium on Fluid Power and Motion Control, 12-14 October, 2015, Chicago, USA.

[8] J. Choonshik, M. Stangl – *Application of Power Regenerative Boom system to excavator* – Proceedings of the 10th International Fluid Power Conference (IFK), 8-10 March 2016, Dresden, Germany.

[9] M. Erkkilä, F. Bauer, D Feld – *Universal Energy Storage and Recovery System – A Novel Approach for Hydraulic Hybrid* – 13th Scandinavian International Conference on Fluid Power (SICFP2013), June 3-5, 2013, linköping, Sweden.

[10] Thiebes, P., Geimer, M. – *Energy storage devices for industrial vehicles with hybrid drivetrains* – VDI Fachkonferenz "Getriebe in mobilen Arbeitsmaschinen", 07-08 June, 2011, Friedrichshafen, Germany.

[11] P. Casoli, L. Riccò, F. Campanini, C. Dolcin, A. Lettini – *Hydraulic Hybrid Excavator: Layout Definition, Experimental Activity, Mathematical Model Validation and Fuel Consumption Evaluation* – Proceedings of the 10th International Fluid Power Conference (IFK), 8-10 March, 2016, Dresden, Germany.

[12] M. Ochiai, S. Ryu – *Hybrid in construction machinery* – Proceedings of the 7th International Symposium on fluid Power (JFPS), 15-18 September 2008, Toyama, Japan

[13] E. Busquets, M. Ivantysynova – *Toward Supervisory-Level Control for the Energy Consumption and Performance Optimization of Displacement-Controlled Hydraulic Hybrid Machines* – Proceedings of the 10th International Fluid Power Conference (IFK), 8-10 March, 2016, Dresden, Germany.

[14] N. Daher, M. Ivantysynova – *Electro-hydraulic energy-saving power steering systems of the future* – Proceedings of the 7th FPNI PhD Symposium on Fluid Power, 27-30 June, 2012, Reggio Emilia, Italy.

[15] T. Minav, T. Lehmuspelto, P. Sainio, M. Pietola – *Series Hybrid Mining Loader with Zonal Hydraulics* – Proceedings of the 10th International Fluid Power Conference (IFK), 8-10 March, 2016, Dresden, Germany.

[16] D. Filatov, T. Minav, J. Heikkinen – *Adaptive Control for Direct-Driven Hydraulic Drive* – Proceedings of the 11th International Fluid Power Conference (IFK), 19-21 March, 2018, Aachen, Germany.

[17] S. Morselli, P. Marani, C. Dolcin, M. Scolari, C. Ferrari – *Efficiency analysis of an electro-hydraulic drive for mobile lifting machines* – Proceedings of Bath/ASME Symposium on Fluid Power and Motion Control (FMCP2020), 9-11 September, 2020, Bath, UK.

[18] H. Murrenhoff, S. Sgro, M. Vukovic – *An Overview of Energy Saving Architectures for Mobile Applications* – Proceedings of the 9th International Fluid Power conference (IFK), 24-26 March, 2014, Aachen, Germany.

[19] M. Vukovic, S. Sgro, H. Murrenhoff, – *STEAM: a mobile hydraulic system with engine integration* – Proceedings of the ASME/BATH Symposium on Fluid Power & Motion Control (FMCP2013), 6-9 October, 2013, Sarasota, USA.

[20] M. Vukovic, S. Sgro, H. Murrenhoff – *STEAM: a holistic approach to designing excavator systems* – Proceedings of the 9th International Fluid Power conference (IFK), 24-26 March, 2014, Aachen, Germany.

[21] M. Schneider, O. Koch, J. Weber, M. Bach, G. Jacobs – *Green Wheel Loader: Development of an energy efficient drive and control system* – Proceedings of the 9th International Fluid Power conference (IFK), 24-26 March, 2014, Aachen, Germany.

[22] F. Bauer, D. Feld, C. Stauch – Increased energy efficiency of hydraulic hybrid drives by means of a multi-chamber accumulator – Proceedings of the 10th International Fluid Power Conference (IFK), 8-10 March, 2016, Dresden, Germany.

[23] P. Achten, T. van den Brink, J. van den Oever, J. Potma, M. Schellekens, G. Vael, M. van Walwijk – Dedicated design of the Hydraulic Transformer – Proceedings of the 3rd International Fluid Power Conference (IFK), 5-6 March, 2002, Aachen, Germany.

[24] M. Wang, P. Danzl, C. Larish, V. Mahulkar, D. Piyabongkarn, P. Brenner – A hydraulic test stand for demonstrating the operation of Eaton's energy recovery system (ERS) – Proceedings of the 10th International Fluid Power Conference (IFK), 8-10 March, 2016, Dresden, Germany.

[25] A. Elbig, C. Boes – Electric Hydrostatic Actuation: modular building blocks for industrial applications – Proceedings of the 10th International Fluid Power Conference (IFK), 8-10 March, 2016, Dresden, Germany.

[26] S. Qu, D. Fassbender, A. Vacca, E. Busquets, U. Neumann – A closed circuit electro-hydraulic actuator with energy recuperation capability – Proceedings of the 13th International Fluid Power conference (IFK), 12-14 October, 2020, Dresden, Germany.

[27] P. Marani, M. Martelli – Energy and control characteristics of a novel meter out hydraulic system – Proceedings of the 2017 Bath/ASME Symposium on Fluid Power and Motion Control (FPMC2017) – 16-19 October, 2017, Sarasota, USA.

[28] P. Marani, M. Milani – Operating principles and simulation of a novel meter out control system for mobile machines – Proceedings of the 10th JFPS International Symposium on Fluid Power, 24-27 October, 2017, Fukuoka, Japan.

[29] P. Marani, M. Milani, D. Mesturini, U. Busani – Experimental Evaluation of the New Meter Out Sensing Architecture – Proceedings of the 11th International Fluid Power Conference (IFK), 19-21 March, 2018, Aachen, Germany.

[30] D. Mesturini, C. Dolcin, U. Busani, P. Marani, A. Bonavolontà, E. Frosina – *Optimization of directional control valves through downstream compensation approach* – Proceedings of the 13th International Fluid Power conference (IFK), 12-14 October, 2020, Dresden, Germany.

[31] A. Bonavolontà, D. Mesturini, E. Frosina, C. Dolcin, P. Marani, U. Busani – *Experimental and Modelling Analysis of a Downstream Compensation system: Energy Optimization of the Directional Control Valves* – Proceedings of the 2020 IEEE *Global Fluid Power Society PhD Symposium*, 19-21 October, 2020, Guilin, China.

[32] A. Bonavolontà, C. Dolcin, P. Marani, E. Frosina, A. Senatore – *Comparison of energy saving and recovery systems for hydraulic mobile machines* – 74th Congresso Nazionale ATI, 11-13 September, 2019, Modena, Italy.

[33] J. Siebert, M. Geimer – *Reduction of System Inherent Pressure Losses at Pressure Compensators of Hydraulic Load Sensing Systems* – Proceedings of the 10th International Fluid Power Conference (IFK), 8-10 March, 2016, Dresden, Germany.

[34] J. Amrhein, U. Neumann – *PRB: Regeneration of potential energy while boom-down* – Proceedings of the 8th International Fluid Power Conference (IFK), 26-28 March, 2012, Dresden, Germany.

[35] T. Lin, Q. Wang, B. Hu, W. Gong – *Development of hybrid powered hydraulic construction machinery*. Automation in Construction 19 (2010) 11-19.

[36] L. Guzzella, A. Sciarretta – *Vehicle Propulsion Systems* – 2007, Springer-Verlag Berlin Heidelberg, Germany.

[37] G. Ganassi, D. Mesturini, C. Dolcin, A. Bonavolontà; E. Frosina, P. Marani - *Viable Energy Recovery Strategies through advanced Directional Control Valve* – Proceedings of the 13th International Fluid Power Conference (IFK), June 13-15, 2022, Aachen, Germany

System for recovering energy in hydraulic circuit by using a small Pelton turbine

Marco Rizzoli[1], Giovanni Cillo[2], Barbara Zardin[1], Danilo Manfredi[3] and Massimo Borghi[1]

[1] Enzo Ferrari Engineering Department, University of Modena and Reggio Emilia, Modena, Italy
[2] SmartFluidPower, https://smart.fluidpower.it, Modena, Italy
[3] ELT FLUID, www.eltfluid.com, Castelnovo ne' Monti, Reggio Emilia, Italy
E-mail: marco.rizzoli@unimore.it; smartfluidpower@gmail.com; barbara.zardin@unimore.it; info@eltfluid.com; massimo.borghi@unimore.it

Abstract.

Energy recovery and energy dissipation reduction are nowadays very important topics of academic and industrial research in the field of fluid power systems. In this paper, the authors wanted to study the possibility to recover the hydraulic energy that would be otherwise wasted through a pressure relief valve in a typical industrial hydraulic system, using a Pelton turbine connected to the shaft of the pump. The hydraulic system is a power transmission application in which a fixed displacement pump is applied. The energy usage on the actuator side is discontinuous and thus creates high energy waste through the pressure relief valve. For this application, the use of a variable displacement pump is considered to increase too much the cost of the system, so an alternative solution is proposed, which is based to the recovery of the wasted energy. The operating conditions considered are in the range of high pressure and low flow rate, so the hydraulic system here examined has been compared to small hydraulic power plant that uses Pelton turbines, where the installation faces watercourses for energy transformation. In this article the design of a Pelton turbine is then examined for the application previously introduced, by means of standard design methods; the goal of the design is to obtain the best efficiency by appropriate sizing. Successively, a lumped parameter model of the entire system, created to validate the concept when working in the real operating conditions, is presented and discussed.

Keywords. Hydraulic system, energy recovery, Pelton turbine, design.

1. INTRODUCTION

Fluid power systems are widely used in industrial and mobile applications thanks to some clear advantages in the power transmission, which are: the high power-to-weight ratio, capability of being integrated in complex systems – in relatively small spaces–, the

capability to be quickly reversed, or operated intermittently, the fast response and acceleration, and the reliable operation and long service life. However, as well known, they are characterized for having some critical issues, one of the more concerning nowadays is the low efficiency. Since the sensibility to the energy waste and pollution is now increasing more than ever, forcing each technology to improve, also in the fluid power field different solutions have been introduced to compensate the gaps, in some cases with installation of electrical equipment, in other with different solutions that comprise the recovery/regeneration of otherwise wasted energy. Researchers, for example, address this topic with some alternative solutions for standard fluid power architectures [1, 2]. An entire special issue has been dedicated recently to energy efficiency in fluid power systems [3].

In this paper an industrial fluid power system is considered and a possible way to recover some energy is studied, with reference to the use of the system for a specific characteristic working cycle. As it is typical for some industrial applications, a single fluid power generator group, made of a fixed displacement pump driven by an electric motor and a pressure relief valve, is used for multiple purposes, and hence it's not optimized for a specific application. Here, this generator group is used to replicate a working cycle characterized by the use of the fluid power for a short time and then during the rest of the time the hydraulic power produced is wasted through the pressure relief valve.

Several possible more efficient alternatives to this simple system already exist, which may be more suitable for the working cycle, i.e. variable displacement pumps with different displacement controls. However, with the idea of improving an existing system that already employs a fixed displacement pump which, for various reasons, the user doesn't want to modify, an alternative idea is to recover the energy that would otherwise be wasted. The reasons for not replacing the fixed displacement pump with a variable one can be different, for example: initial cost, issue in choosing a more delicate pump in case the system is working with an average level of contamination of the fluid, critical response time of the pump to possible rapid requests of flow rate by the actuation.

The concept explored in this paper is to re-transform in mechanical energy that fraction of hydraulic energy that would be wasted by the system through the pressure relief valve. In this way, we can generate a closed loop of power transformation that would help to decrease the absorption at the source. Because of the discontinuous working phase – that leads to drag losses during inactivity – and the atypical configuration, it was decided to explore the chance to use a Pelton turbine instead of using a positive displacement motor to recover the energy. If a hydraulic motor is used, which would be operated frequently without receiving flow rate from the system, the two main concerns are the losses and hence the power adsorption at the pump shaft and the rotation of the motor without enough flow rate even to lubricate the gaps, resulting in overheating and possible wear. Of course, the first point concern also the use of the Pelton turbine and was taken into account in the analysis. To minimize resistances and losses in this closed loop of energy recovery the initial intention was to design the machine to be directly connected to the pump shaft, but after first calculations (discussed in chapter III) it was evident that this solution was not possible. Anyhow the loss introduced by the presence of a reduction drive is quite low and the solution of a Pelton turbine plus reducer may be appealing. In the next sections we describe the modified layout of the system, discuss the Pelton turbine design according to two practical methods and present the

modelling of the complete system, to simulate the duty cycle and verify if the solution is convenient from the energy recovery point of view.

2. BRIEF DESCRIPTION OF THE CONCEPT

As announced in the introduction, we want to explore a design solution where the recovery of energy is performed by using a Pelton turbine, that should collect the high-pressure fluid otherwise wasted through the relief valve of the system during passive intervals of the duty cycle considered. For the practical application, we are referring to a test rig that is replicating the duty cycle of interest: the Pelton turbine will be coupled to the pump-motor shaft via a reduction drive, (the design of the Pelton turbine excludes the chance to connect the turbine directly to the pump as it is explained later), the fluid sent to the turbine is first collected in an accumulator with a chosen pre-charged pressure. This was a mandatory choice due to the discontinuous characteristics of the flow rate discharged by the relief valve. The accumulator allows to reduce the irregularities in the flow rate and pressure. An opportune control logic, based on the accumulator pressure, decides when opening the on/off valve that faces the turbine runner. The working position of this valve is the nozzle of the turbine. A layout of the test rig is shown in Figure 2.1.

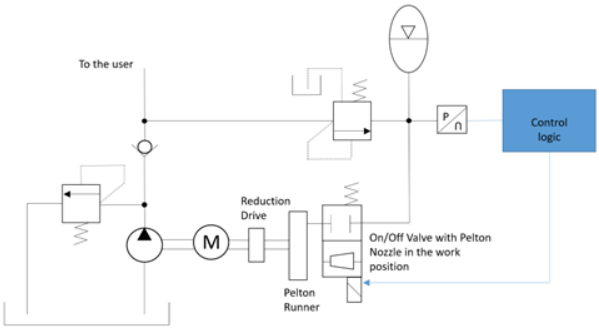

Figure 2.1. Hydraulic diagram of the fluid power generator group of the test rig with the integration of the Pelton turbine

The next step is to design a Pelton turbine that can be used in the application referring to the target operating conditions. The size of the turbine starts from the estimation of the mean value of power lost that is around some kW.

3. DESIGN OF THE PELTON TURBINE: DISCUSSION

3.1. Preliminary observations

In turbomachinery different dimensionless parameters classify the operative conditions and are used, thanks to the Similitude Theory, to choose the type of turbine, as a function of the machine size and target flow [4, 5]. In this study these parameters are also used to estimate how far the actual operating condition is from the standard ones.

A turbine preliminary design is being considered with some input parameters that circumscribe the boundary condition of the design [6, 7, 8]:

- the net head available H, a characteristic of the system, equivalent to $\frac{p}{g\rho}$ where g is the gravitational acceleration, p the fluid pressure and ρ is the fluid density;
- volumetric flow rate $\dot{Q}_{jet}$, another characteristic of the system, even if sometimes it is substituted by the power at the shaft P;
- the rotational speed N, a mechanical characteristic of the system; in the first step of the design process we are considering that the turbine is directly jointed to the pump-motor shaft that rotates at 1500 [rpm].

The first important design factor for turbines is the *specific speed* N_s, that is derived from the previous parameters listed. The value of this factor is a guideline that helps to select the type of turbine that is more efficient at the nominal operating conditions considered for the design. In this work the definition of the specific speed considered is expressed by (1):

$$N_s = N\frac{\sqrt{\dot{Q}_{jet}}}{H^{3/4}} \tag{1}$$

In Eqiation (1) N is expressed in revolution per unit of time, so N_s is not dimensionless; it can be transformed in a dimensionless parameter (the speed number) using the angular speed instead of N and dividing for $g^{3/4}$, but it is often used as shown in (1) in diagrams and tables. Alternatively, the *power specific speed* can be defined as in (2):

$$\Omega_{sp} = \Omega\frac{\sqrt{P/\rho}}{H^{5/4}} \tag{2}$$

In (2) Ω is the *angular speed* expressed in rad/s, P is the power and ρ is the fluid density. In general, low specific speed machines correspond to low volumetric flow rates and high heads, whereas high specific speed machines correspond to high volumetric flow rates and low heads [9].

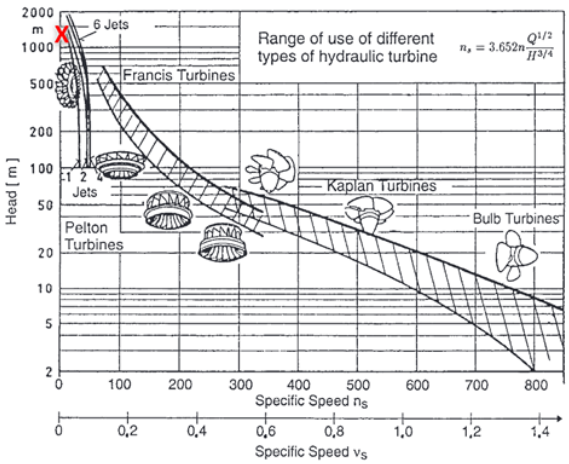

Figure 3.1.2. Operative setting point of the discussed system, red cross, with application ranges of various types of turbines [10]

In Figure 3.1.1 it is possible to compare the operative conditions of the considered system (red cross in figure) to the most common operating range of hydraulic turbines. The common values for Ω_s are also shown in Table I.

TABLE I. OPERATING RANGES OF HYDRAULIC TURBINES [9]

	Pelton turbine	Francis turbine	Kaplan turbine
Specific speed Ω_s [rad]	0.05 – 0.4	0.4 – 2.2	1.8 – 5.0
Head H [m]	100 – 1770	20 – 900	6 – 70
Optimum efficiency [%]	90	95	94

The high delivery pressure value on the delivery line of the test rig is the high and the volumetric flow rate is the small, leading to a critic low value of *specific speed* and *power specific speed* (3):

$$\Omega_s = 2\pi \cdot N_s = 0.01 \tag{3}$$

To have an idea of the *rotational speed* that should be used as reference operating condition for the turbine we can refer to diagrams such as the one in Figure 3.1.2, where *typical efficiencies* of turbines are related to the *specific speed value*. Again, we can see that our operating condition is at the limit also for a Pelton turbine and that, even if it may be possible to design the turbine, the efficiency would be too low. The idea to directly connect the turbine to the pump-motor shaft that rotates at 1500 rpm failed since this would lead totally out of good efficiency range, hence a reduction drive between the turbine and the pump is necessary.

To obtain a total energy transformation, diameter and velocity of jet flow through the nozzle that faces the turbine runner are defined: the velocity is function of the pressure – defined by the equation of energy transformation – and following, the diameter depends on the volumetric flow rate value (at given pressure). In this paper the transformation efficiency of the nozzle is not considered for simplicity. It is also considered to insert an anti-shock relief valve on the pump delivery line for discharging undesired peaks of pressure and for safety reason. Finally placing an accumulator just before the logic element, allow to control the on-off valve with a simple logic: when the accumulator is full and the pressure reaches the maximum value, an electrical signal opens the logic valve and the flow starts to reach the turbine; the valve remains open till the minimum pressure set is reached, under the minimum pressure the electrical signal is off, the valve closes and the accumulator restarts to fill. These modifications of the standard fluid power generator group allow to overcome the problem of the small and irregular flow coming from the circuit. Without these actions, the behaviour of the turbine would be too irregular and, as shown in Figure 3.1.2, the efficiency of the Pelton turbines drops to low values when working far from the nominal condition.

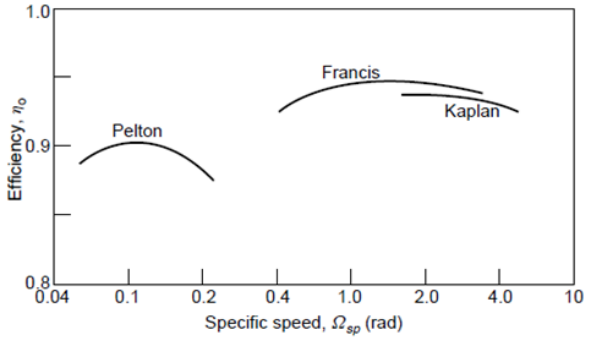

Figure 3.1.2. Typical design point efficiencies of Pelton, Francis and Kaplan [9]

3.2. Design of the Pelton turbine

It is decided to proceed with the design of a Pelton turbine with 1 jet (usually more than 1 jet is applied when the net head is medium-small and the flow is high – the opposite situation of the actual operating condition in our system). Two different theories are used for the machine design: the design A is taken from The Micro-hydro Pelton Turbine Manual by J. Thake [11] and the design B from Pelton Turbines by Z. Zhang [12]. The design A approach [11] is thought for small Pelton turbine applications and it uses some simplified equations based on the specified installation case. Encountering some difficulties in adapting the present case to standard procedures, it is decided to explore a second method [12], which is more recent and theoretically more adaptable to general cases. The two different theories of design are briefly described in the following.

The Thake's theory [11] dimensions the entire turbine on the jet diameter that, as explained before, is depending on the inlet flow rate. The entire geometry is hence determined by this value and the designer has only to scale the design to the application. Equation (4) is used to calculate the *pitch circle diameter* PCD of the turbine, an extremely important characteristic. A parameter δ for the scaling is suggested by common practices and it is normally taken between 0.1 and 0.12 even if in some cases of high head it can reach lower values, such as 0.06÷0.07 [13].

$$\delta = \frac{d_{jet}}{PCD} \tag{4}$$

The common approach of reducing the δ value in cases of high head is justified by the need to avoid high stresses, fatigue problems and cavitation damage caused by too small runner diameter [13, 14]. As already explained, the present application is characterized by an important disproportion between the diameter and velocity of the fluid jet (caused by high pressure and low flow rate operating conditions). Applying a standard value of δ would generate a very small runner diameter that rotates at very high speed. After some investigation, it is decided to proceed assuming a value of $\delta = 0.02$. Once decided the value of the PCD, the minimum number of buckets and all the other dimensions are determined consequently [11]. The output from this theory is a Pelton turbine with a diameter designed on the value of flow rate, but the geometry obtained is less suitable to manage the velocity vector that, in the present case, is extremely high. In Figure 3.2.1 the output turbine CAD model from the first design is shown on the left.

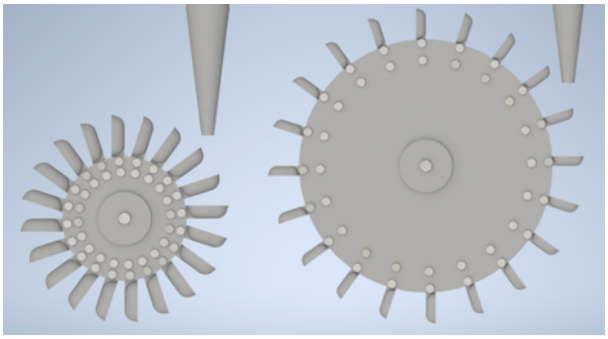

Figure 3.2.1. Design A (left) and design B (right)

The Zhang's method [12] uses both jet velocity and jet diameter to design the turbine. The procedure starts with the definition of coefficients that describe the turbine and correlate the jet properties to it. They are the *peripheral speed coefficient* k_m, which defines the ratio of the peripheral speed of the Pelton wheel on the jet speed (5) and the *bucket volumetric load* φ_B, that correlates the flow rate to the bucket dimension (the flow rate is proportional to the square of the jet diameter) (6), where h is the bucket width.

$$k_m = \frac{PCD \cdot \Omega}{2 \cdot v_{jet}} \tag{5}$$

$$\varphi_B = \left(\frac{d_{jet}}{h}\right)^2 \tag{6}$$

Practical applications establish the range in which these coefficients can vary. Then the wheel size, the number of injectors and the rotational speed of the turbine can be chosen respecting these constraints. The standard ranges that normally are adopted are (7) and (8)

$$\varphi_B \cong 0.11 \tag{7}$$

$$k_m \cong 0.45 \div 0.48 \tag{8}$$

This study does not analyse the effect of the oil viscosity in the bucket and therefore (7) is accepted. Instead (8) must be analysed widely. The range derives from the theoretical efficiency equation of the energy conversion between the jet and a straight-moving bucket expressed in (9) where β_2 is the angle of the outgoing flow from the bucket [12].

$$\eta_{th} = 2k_m(1 - k_m)(1 - cos\,\beta_2) \tag{9}$$

From (9) the highest value of efficiency corresponds to $k_m = 0.5$, then the real value considered is lower, (8), because of the losses in the transformation process. Different contributions of losses must be estimated:

- Missing flow interception: when the velocity of the fluid and the velocity of the bucket differs too much from the theoretical ideal value of 0.5, it can happen that part of the flow is not intercepted by the bucket for the conversion of energy. In this case a coefficient R_Q is introduced to consider the percentage of fluid reaching the bucket, the rest of the fluid – and respectively its energy – is considered wasted [12].

- Windage and friction: the resistance of the rotation in mixture of air and liquid and the mechanical resistances are estimated on the base of simplified models [12, 13]. The shape of the Pelton wheel, together with air that particularly resists against the buckets, complicates the estimation of this friction. Considering the high specific density of the air-oil mixture that is present due to the very high-speed of the wheel, the number of buckets and the orientation of the runner – horizontal or vertical – it is possible to estimate the losses with an accuracy of ±50% [12]. To have higher precision it is suggested to perform a comparison with experimental data, when available. This loss term is addressed as $\eta_{f\&w}$ in the following.

Normally these total losses represent a small percentage on the total efficiency of the turbine (< 1% [12]). Unluckily, in our case the rotational velocity of the wheel, due to the high speed of the fluid, reaches high values, consequently the amount of these losses may have an important impact on the output efficiency. It is decided to proceed as explained in the following: the dimension of the PCD is taken the biggest possible (deemed acceptable for this application) to reduce as much as possible the rotational velocity; then the losses are estimated as function of k_m to realize a new efficiency curve, which will be different from the theoretical efficiency defined in (9). From it, a new value for k_m is taken considering the best condition on the curve of the real efficiency and finally the *rotational speed velocity* and the *reduction drive ratio* are calculated. Differently to design A in this methodology the number of buckets is a variable value that depends on k_m and Ω_s [12]. The calculations suggest a very high number of buckets. By practice this value is limited to 20÷22 due to the narrow space between adjacent buckets. In this application the big PCD and the small bucket would allow more space to adjust more elements, but the cutout edge shape machined at the bucket tips would result deformed by the velocity vectors applied in the shape definition. To avoid an upset of the entire geometry it is decided to accept more space between elements and the limit of 20 buckets is kept.

In Figure 3.2.2 is possible to see the calculation of the new efficiency curve referred to design B. The final curve of η_r is obtained from the theoretical η_{th} multiplied by the missing flow factor R_Q and the friction and windage efficiency $\eta_{f\&w}$. Grey bars represent the inaccuracy in the estimation of $\eta_{f\&w}$. Higher resistances of the model moved the ideal *peripheral speed coefficient* from the ideal value of 0.5 to 0.42. After choosing the number of buckets, it was verified that the full factor R_Q begins decreasing once the maximum efficiency has been reached.

The output of the second design approach is shown on the right in Figure 3.2.1. Finally, a re-calculation of the real efficiency as function of the rotational speed has been performed for both designs A and B and the nominal operative velocity of each turbine can be estimated referring to the point of maximum efficiency, as shown in Figure 3.2.3.

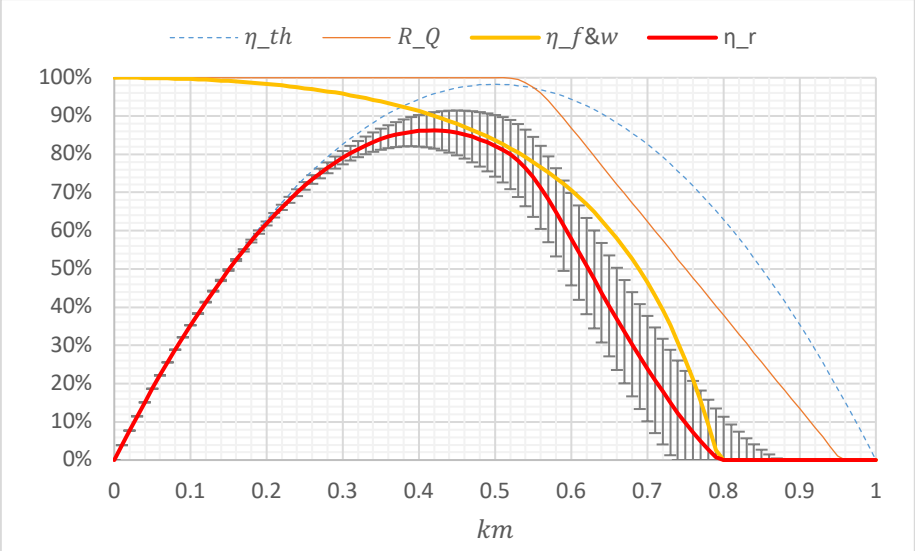

Figure 3.2.2. Contribution of loss in efficiency curve of design B. Black bars represent the effect of resistances inaccuracy

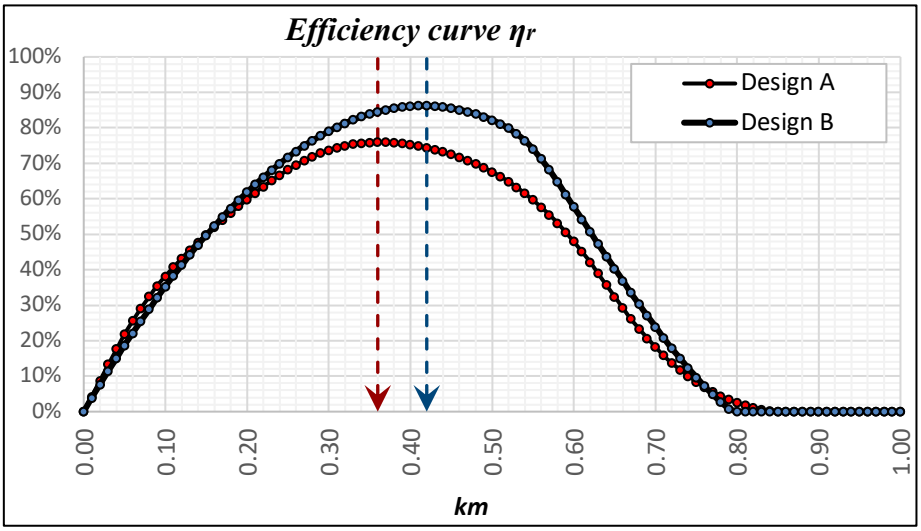

Figure 3.2.3. Characteristic curves of the turbines

4. SYSTEM SIMULATION

The entire system is then modelled with a lumped parameter approach developed in OpenModelica Environment [15] making use of the elements of the hydraulic library developed by SmartFluidPower [16] and presented in Figure 4.1.

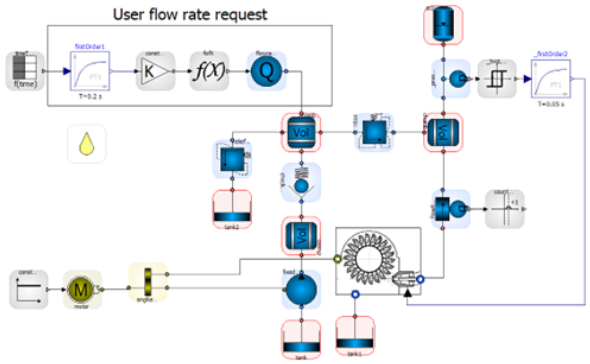

Figure 4.3. Lumped parameter model in OpenModelica environment [15]

In the model it is possible to identify:

- the generation of power composed by pump and electrical motor connected with the reduction drive to the turbine;
- the user flow rate request, numerically controlled by an external table in the model;
- the system of accumulator and activation valve already discussed in Chapter 3. Here the pressure sensor directly controls the opening of the nozzle.

The pump generates a constant amount of volumetric flow rate and, when the user is satisfied or not asking for flow rate, the pressure in the system will rise until the opening of the sequence valve that is filling the accumulator with the oil in excess. The maximum and minimum trigger pressures and accumulator capacity are designed to guarantee as much as possible regular and constant injections of flow to the turbine. The model of the turbine is built using the efficiency Equation (9) and considering an estimation of the losses already discussed inside the machine. The geometrical parameters calculated during the design are the inputs of this model in a way to perform different simulations. The estimations of friction and windage losses are calculated apart from the fluid jet velocity since they are the resistive part of the machine that is present also when the turbine is not collecting fluid from the nozzle (k_m value tending toward infinity). When opened, the pin at the nozzle lets the fluid flow towards the Pelton turbine model that elaborates it and calculates the mechanical power. The mechanical speed velocity is set constant; in the reality the system requires a sort of regulation to compensate the variation of load to the electrical motor when the turbine is switching on/off. Below the results of the turbine of design B are shown.

The simulation is performed with the user request power shown in yellow in Figure 4.2 and the excessed power produced by the pump is directed to the accumulator that opens to the

turbine at the reaching of the maximum pressure value, set on the control logic. It is possible to identify the intervals in which the turbine starts to work and feed power to drive the pump.

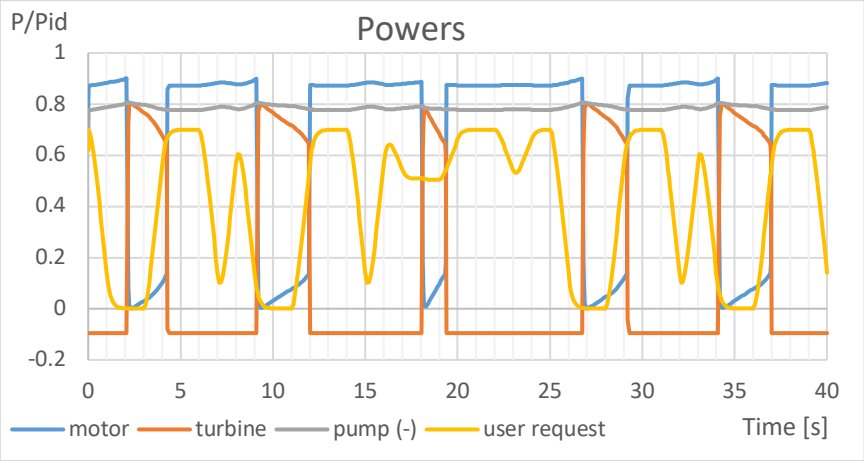

Figure 4.2. Power exchange in model simulation

During the 40 sec of simulated time, 5 injections at the turbine of different durations happen in total. In the remaining time the turbine acts as a dissipator due to frictions and windage resistance. At the accumulator ports, in Figure 4.3, it is possible to notice the action of regularization of the fluid jet properties at the turbine inlet. The fluid arrives at very irregular intensity; it is stored and lately delivered at almost constant value.

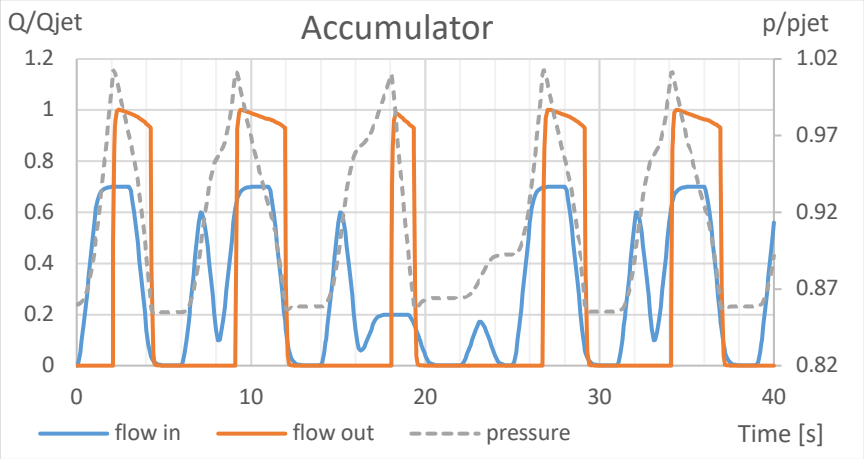

Figure 4.3. Power exchange in model simulation

The variation of volumetric flow rate at the output is due to the accumulator pressure decrease during its emptying (i.e. to the difference between min and max pressure set). Extending these trending to a long-term simulation, it is possible to estimate the recovery of energy shown in Figure 4.4. The model estimates that between the mechanical power at the shaft and the effective hydraulic power collected there is a 53% of overall efficiency, all the rest is lost. Of course, this value strongly depends on the user request. The 23% of energy is

lost due to the power transmission line and the remaining 24% is the potential discharged by the relief valve. The introduction of the Pelton turbine allowed the system to collect this potential. Considering the efficiency in the collection (Figure 3.2.3) and the absorption during passive intervals the net recovery is about 11%. Even this value is user-dependent obviously, different duty cycles should be tested to have more a general idea.

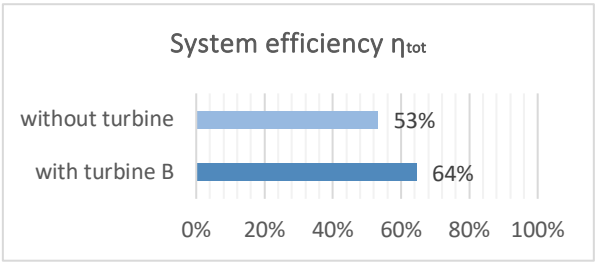

Figure 4.4. Final recover of the system efficiency loss

5. CONCLUSIONS

In this paper, the idea to use a Pelton turbine in a hydraulic industrial system to recover part of the wasted energy during a specific duty cycle has been explored. Two different Pelton turbines have been designed for the application, both requiring to introduce a reduction drive at the shaft between the pump and the turbine, introducing an additional, but typically small, loss of efficiency. The high-speed rotation of the turbine runners is a necessary condition in order to maintain the dimensions of the turbine bounded to remain under certain values. The design process of the Pelton turbine is a mixture of empirical and physical formulas and here has been developed making reference mainly to [11] and [12]. This study is done with the purpose to apply these processes in an un-experienced range of operation and verify the possibility to recover energy in the system. The two designs here experimented led to different turbine designs, with different operative points in terms of speed. It is extremely important to compare the application of these methods and the output efficiency estimations to experimental data. The two turbines have been prototyped and will be tested in the next future by ELT FLUID on the test rig taken as reference for the analysis and, successively, the experimental results will be compared to the simulation. The possibility to obtain some result from a prototype would validate the theory but, most important, it would give the possibility to focus on weak points of the application. The simulation of the lumped parameter model shows that, despite the amount of losses and resistance caused by the high rotational speed of the turbine, energy recovery is possible. Also mechanical resistance of the turbine components has been analysed, in particular the resistance of the buckets to centrifugal forces and to fatigue stress, but not reported here for brevity. A critical issue on this field may be the erosion of the edge of the bucket due to the fluid jet action. In case of splitter edge erosion, the flow detachment from the bucket surface would be more prone to happen leading to significant drop of efficiency [13, 14]. According to formulas from [12], with small jet diameters the decrease of efficiency is more influenced by the splitter rounding. Even an erosion of few decimal points of millimetre can be critic for the interface between bucket and fluid. Another point to be analysed is the air added/mixed with oil during the passage through the turbine, for which an opportune settling time in the tank should be considered.

6. REFERENCES

[1] Love, L.J.; Lanke, E.; Alles, P. Estimating the Impact (Energy Emissions and Economics) of US Fluid Power Industry; Oak Ridge National Laboratory (ORNL): Oak Ridge, TN, USA, 2012.

[2] Milos Vukovic, Hubertus Murrenhoff, The Next Generation of Fluid Power Systems, Procedia Engineering, Volume 106, 2015, Pages 2-7, ISSN 1877-7058, https://doi.org/10.1016/j.proeng.2015.06.002

[3] Vacca, A. Energy Efficiency and Controllability of Fluid Power Systems. Energies 2018, 11, 1169. https://doi.org/10.3390/en11051169

[4] C.Pfleiderer, H.Petermann, "Turbomacchine", Tecniche Nuove, Milano, 1985, ISBN: 8870811301.

[5] A. Santolin, Procedure per la progettazione standardizzata delle turbine delle piccole centrali idroelettriche. PhD thesis 2009, 32, Scuola Di Dottorato Di Ricerca In Ingegneria Industriale, Indirizzo Energetica, Ciclo: XXI, Università degli Studi di Padova. http://hdl.handle.net/11577/3426010

[6] Kenneth E. Nichols P.E, How to Select Turbomachinery For Your Application, technical report, https://www.barber-nichols.com/media/technical-papers, 2019.

[7] O. E. Balje, A Study on Design Criteria and Matching of Turbomachines: Part A "Similarity Relatives and Design Criteria of Turbines", Trans. ASME Series A, January 1962. 4.

[8] O. E. Balje, A Study on Design Criteria and Matching of Turbomachines Part B "Compressor and Pump Performance and Matching of Turbocomponents". Trans. ASME, Series A, January 1962.

[9] Dixon, S. L. Fluid Mechanics-Thermodynamics of Turbomachinery (in SI/Metric Units). 1978.

[10] Drtina, P.; Sallaberger, M. Hydraulic turbines—basic principles and state-of-the-art computational fluid dynamics applications. Proceedings of the Institution of Mechanical Engineers, Part C: Journal of Mechanical Engineering Science. 1999. doi: 10.1243/0954406991522202

[11] J. Thake, The Micro-hydro Pelton Turbine Manual - Design, manufacture and installation for small-scale hydropower. Practical Action Publishing 2000. ISBN 9781853394607

[12] Z. Zhang, Pelton Turbines. Springer 2016. ISBN: 978-3-319-31909-4

[13] Brekke, H. Hydraulic turbines design, erection and operation. Norwegian University of Science and Technology (NTNU) publications, 2001.

[14] Brekke, H.; Wu, Y.L.; Cai, B.Y. Design of Hydraulic Machinery Working in Sand Laden Water. 2003. doi: 10.1142/9781848160026_0004

[15] https://openmodelica.org/

[16] https://smart.fluidpower.it/

Biographies



Marco Rizzoli received the bachelor's degree in mechanical engineering from Modena and Reggio Emilia University in 2016 and the master's degree in mechanical engineering from Modena and Reggio Emilia University in 2019. He is currently working in the research field at the Vehicle Hydraulic Laboratory (LIV), Faculty of Engineering, Modena and Reggio Emilia University. His research area is the fluid power field, working involved with local SME to develop new technologies.

A Practical Numerical Method to Map the Energy Efficiency of Individual Electro-Hydraulic Drives

Damiano Padovani

Guangdong Technion-Israel Institute of Technology, Shantou, Guangdong, China
damiano.padovani@gtiit.edu.cn

Abstract.

Environmental and economic motivations require urgent improvements to the energy efficiency of hydraulics. In response, the ongoing tendency toward the electrification of fluid power is generating many individual, electro-hydraulic drives. Electric motors drive hydraulic pumps that control the motion of hydraulic actuators without using dissipative flow throttling. Energy efficiency is not constant but varies significantly across the operating range of any given drive and between different architectures. These changes are difficult to predict a priori, prevent a fair comparison between alternatives, and pose a challenge to the designer looking for the best arrangement. The solution is mapping the energy efficiency of the drive for all operating conditions to get a complete overview of its performance. This step is typically done by running countless high-fidelity simulations or experimentally testing the drive on a dedicated test-rig capable of adjusting the load applied to the actuator. Clearly, both approaches are not user-friendly and consume a long time. This research paper presents, therefore, a practical method to derive efficiency maps of electro-hydraulic drives. These maps are based on steady-state equations and require a limited number of parameters obtainable from the literature or published catalogs. The entire procedure does not require experiments, is quick to apply, and reveals the drive's performance and physical limitations with good approximation. The example presented in this study of a single-pump system shows that the drive's overall efficiency stays above 60% in a fairly wide region of the operating range.

Keywords. Efficiency map, energy efficiency, electric motor, inverter, pump, electro-hydraulic, actuator, modeling.

1. INTRODUCTION

Linear hydraulic actuators are crucial devices in many industries due to their distinctive characteristics, such as high-force capability and outstanding reliability. They are typically part of well-established, valve-controlled systems characterized by poor energy efficiency due to flow throttling and the absence of energy recovery [1]. Environmental and economic motivations require urgent improvements in this regard. Thus, the ongoing trends toward the electrification of hydraulics are strengthening the use of individual drives, where the

actuators are coupled to dedicated pumps. These drives can be displacement- or speed-controlled depending on the pump's control element (*i.e.*, its displacement setting or speed, respectively). Concerning the latter variant, multiple arrangements were already proposed involving, for instance, a single pump [2-3], two pumps [4-7], or even three units [8]. The resulting throttleless actuation enhances energy efficiency and enables energy recovery. These electro-hydraulic systems can easily replace conventional valve control in terms of dynamic response [9-10] and energy efficiency [11-12]. However, the energy efficiency is not constant across the drive's working range and varies based on the system architecture and component selection. These changes are difficult to predict a priori and prevent a fair comparison between alternatives. Therefore, a complete map of the system's energy efficiency is an essential tool (it is a chart similar to the ones commonly used for internal combustion engines or electric motors). It gives a good overview of the drive's performance and represents a helpful tool for sizing components. The required approach to obtain such a map is identifying the drive's energy efficiency for all operating conditions. This step is typically done by running countless high-fidelity simulations or experimentally testing the drive on a special test-rig capable of adjusting the external load applied to the actuator [13]. A much faster alternative approach derives the efficiency maps using steady-state mathematical models requiring a limited number of parameters obtainable from the literature or published catalogs. This idea was applied with special emphasis on components, namely a double-rod hydraulic cylinder [14] and a hydrostatic transmission [15], but not on the entire hydraulic system. A more comprehensive perspective was given when mapping the efficiency of a valve-controlled, load-sensing actuator [16], even if it does not involve any electric components. Furthermore, a 1-quadrant efficiency map of a variable-speed, variable-displacement power supply was recently developed [17], but the electric components were modeled with a simplified approach. Schmidt and Hansen derived some 1-quadrant efficiency maps with stress on the electric motor and pump [18]. Their focus was, however, on a study about the potentials of electro-hydraulic drives installed in networks so that the development of those maps was partially addressed.

Consequently, this research paper introduces a practical method to quickly derive efficiency maps, marked by reasonable approximation, of individual electro-hydraulic drives. The focus is on the piston extension against resistant loads, representing the most important working condition. The goal is to establish a generally applicable framework that can easily adjust to any electro-hydraulic drive. Such a comprehensive procedure was not traced in the technical literature despite the increasing popularity of this technology. Closing this gap is, therefore, crucial to fully understanding the system's performance under all operating states and supporting the sizing and selection of the components.

2. SYSTEM MODELING

The electro-hydraulic drive considered in this research is a single-pump system in closed-circuit configuration that requires a minimum number of components. Its layout, shown in Fig. 2.1, depicts the electric motor (EM) that drives the fixed-displacement hydraulic pump (P) used to control the motion of the single-rod hydraulic cylinder (C). The speed of the motor is adjusted by an inverter (I) connected to a DC supply. It can be a common DC-bus when multiple drives are used, or a rectifier if a unique drive is needed. Two pilot-operated check

valves (CVs) compensate for the differential flow of the cylinder. They are connected to a low-pressure line constituted, in this case, by a hydro-pneumatic accumulator (A). It represents a sealed reservoir so that the drive is self-contained (it only requires a wired connection to the electric power supply). Pressure-relief valves located on the actuator ports and a low-pressure filter are omitted for simplicity. These electro-hydraulic drives are capable of operating in four quadrants, if necessary, returning energy back to the DC supply when overrunning loads act on the actuator.

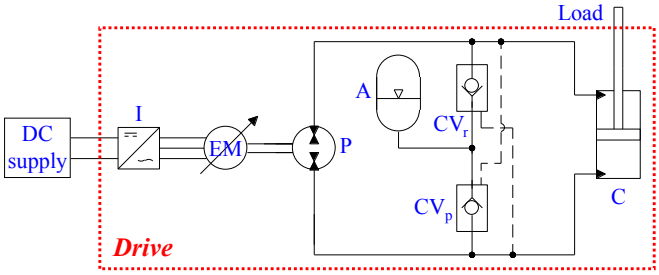

Figure 2.1. Simplified schematic of the individual electro-hydraulic drive chosen as the study case.

Before illustrating the drive's mathematical model, it is worth mentioning the power flows within the system and the different efficiencies. Fig. 2.2 addresses the standard functioning (the power flows from the DC supply to the load).

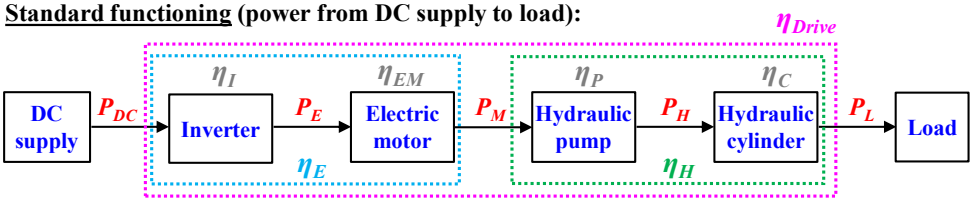

Figure 2.2. Block diagrams of the individual drive highlighting the power flow.

The following subsections describe the approach used to model the energy efficiency of the drive's components.

2.1. Hydraulic actuator

The steady-state force balance of the actuator recalls the hydraulic force (F_H), load force (F_L), and friction force (F_F)

$$F_H = F_L + F_F. \qquad (1)$$

The term F_H depends on the chamber pressures (p_p and p_r) acting on the respective areas (A_p and A_r), whereas the rod-side pressure is set by the low-pressure accumulator. The expression of F_F contains the coefficient of viscous friction (b), the actuator velocity (v), the Coulomb force (F_C), and a constant value (k_I) used to modulate the hyperbolic tangent:

$$F_H = p_p \cdot A_p - p_r \cdot A_r, \quad (2)$$

$$F_F = b \cdot v + \tanh(k_1 \cdot v) \cdot F_C. \quad (3)$$

The piston velocity is obtained by applying the flow conservation to the piston-side of the drive:

$$v = \left(Q_{P,e} - Q_{C,L}\right) \cdot \frac{1}{A_p}, \quad (4)$$

where the effective flow rate of the pump ($Q_{P,e}$) will be elucidated in the next subsection. The same principle enforced to the actuator's rod-side gives the flow through CV_r that is not needed for the purpose of mapping the efficiency. The actuator's mechanical power (P_L), namely the power delivered to the external load, is:

$$P_L = F_L \cdot v. \quad (5)$$

The hydraulic power (P_H) exchanged between the pump and the actuator is defined using the pump's effective flow rate together with the pressure drop (Δp) across the unit:

$$P_H = Q_{P,e} \cdot \Delta p = Q_{P,e} \cdot \left(p_p - p_r\right). \quad (6)$$

The flow leakages across the piston ($Q_{C,L}$) are a function of the pressure drop and a dedicated coefficient (k_L):

$$Q_{C,L} = k_L \cdot \Delta p \ = k_L \cdot \left(p_p - p_r\right). \quad (7)$$

The overall efficiency of the actuator (η_C) is given as:

$$\eta_C = \frac{P_L}{P_H} \cdot 100\%. \quad (8)$$

2.2. Hydraulic pump

The literature lists several analytical models to account for the losses of hydraulic pumps. The chosen approach is a physical-based, steady-state model built on the work of Olsson [19]. It defines the internal flow losses ($Q_{P,L}$) using the four terms in (9) that recall the dissipations due to laminar flow, turbulent flow, fluid compressibility, and constant leakages (Q_K), respectively:

$$Q_{P,L} = \frac{C_L \cdot D \ \cdot \Delta p}{2 \cdot \pi \cdot \mu} + C_T \cdot D^{\frac{2}{3}} \cdot \sqrt{\frac{2 \ \cdot \Delta p}{\rho}} + \frac{D \cdot n \ \cdot \Delta p}{\beta} + \ Q_K. \quad (9)$$

The parameters are the laminar coefficient (C_L), the displacement (D) of the hydraulic unit, the fluid's dynamic viscosity (μ), the turbulent coefficient (C_T), the fluid density (ρ_f), the shaft speed (n), and the fluid's bulk modulus (β).

Similarly, the torque losses ($T_{P,L}$) also include four terms:

$$T_{P,L} = \frac{C_F \cdot D \ \cdot \Delta p}{2 \cdot \pi} + C_D \cdot \mu \ \cdot D \cdot n + \frac{C_H \cdot \rho_f \cdot D^{\frac{5}{3}} \cdot n^2}{4 \cdot \pi} + \ T_K. \quad (10)$$

The latter equation utilizes the coefficients for dry friction (C_F), viscous friction (C_D), hydro-dynamic losses (C_H), and constant losses (T_K). These losses are combined with the theoretical quantities ($T_{P,th}$ and $Q_{P,th}$) to calculate the pump's effective flow rate ($Q_{P,e}$) and its effective torque ($T_{P,e}$):

$$Q_{P,th} = D \cdot n\,, \tag{11}$$

$$T_{P,th} = \frac{D \cdot \Delta p}{2 \cdot \pi} = \frac{D \cdot \left(p_p - p_r\right)}{2 \cdot \pi}, \tag{12}$$

$$Q_{P,e} = Q_{P,th} - Q_{P,L} = D \cdot n - Q_{P,L}, \tag{13}$$

$$T_{P,e} = T_{P,th} + T_{P,L} = \frac{D \cdot \Delta p}{2 \cdot \pi} + T_{P,L}. \tag{14}$$

Due to numerical reasons (*e.g*, the model fitting used to estimate the pump losses), a lower saturation sets to zero those negative values, if any, of F_L, v, $Q_{P,e}$, and $T_{P,e}$ so that the sign convention for the first quadrant is enforced.

Thus, both the theoretical and effective mechanical power of the unit (P_M) are derived:

$$P_{M,i} = T_{P,i} \cdot n\,, \qquad i = th, e. \tag{15}$$

Moreover, the efficiencies of the pump also become available, namely the volumetric ($\eta_{P,v}$), mechanical-hydraulic ($\eta_{P,mh}$), and overall ($\eta_{P,t}$) ones:

$$\eta_{P,v} = \frac{Q_{P,e}}{Q_{P,th}} \cdot 100\%, \tag{16}$$

$$\eta_{P,mh} = \frac{T_{P,th}}{T_{P,e}} \cdot 100\%, \tag{17}$$

$$\eta_{P,t} = \frac{P_H}{P_{M,e}} \cdot 100\% \; = \eta_{P,v} \cdot \eta_{P,mh}. \tag{18}$$

2.3. Electric motor

The procedure chosen here for the electric motor leads to an accurate model that requires parameters derived from datasheets (*e.g.*, the one of a PMSM [20]). The power dissipations in the electric machine ($P_{EM,L}$) are originated by three contributions accounting for the copper losses (the stray losses are neglected), iron losses (only in the core), and windage losses [21]:

$$P_{EM,L} = P_{Cu} + P_{Fe} + P_{Wi}, \tag{19}$$

$$P_{Cu} = \frac{1}{2} \cdot q \cdot R_{EM} \cdot \left(\frac{T_{P,th}}{K_T}\right)^2, \tag{20}$$

$$P_{Fe} = \left[K_h \cdot B^2 \cdot f + K_c \cdot B^2 \cdot f^2\right] \cdot m, \tag{21}$$

$$P_{Wi} = (k_2 \cdot n^2 - k_3 \cdot n + k_4) \cdot \pi \cdot \rho_a \cdot n^3 \cdot R_r^4 \cdot L_r. \tag{22}$$

These equations involve the number of phases (q), the winding resistance (R_{EM}), the torque constant (K_T), the coefficient of hysteresis loss (K_h), the frequency ($f = n \cdot z/60$) obtained through the shaft speed and the number of poles (z), the coefficient of classical eddy

current's loss (K_c), the peak flux density (B), the core mass of the machine (m), the skin friction coefficient - within brackets in (22) - derived using the constants $k_{2\to4}$, the air density (ρ_a), the rotor radius (R_r), and the rotor length (L_r). The electric power (P_E) and the efficiency of the motor (η_{EM}) result as

$$P_E = P_{M,th} + P_{EM,L}, \tag{23}$$

$$\eta_{EM} = \frac{P_{M,th}}{P_E} \cdot 100\%. \tag{24}$$

It should be noted the theoretical torque is involved. Introducing the effective torque in (20) as well as the effective mechanical power in (23) and (24) leads, in fact, to a slightly distorted efficiency map of the electric motor. The effective torque starts with non-zero values due to modeling the losses such as in (10), so the low-torque region is cut off from the efficiency estimation. Thus, a complete mapping of the motor efficiency is achieved by using the theoretical quantities since this step involves the electric motor alone.

2.4. Inverter

Physic-based modeling of the inverter is possible [22], but this method requires in-depth knowledge of elements, such as transistors, that are not always easily accessible. A simpler technique [23] helps those designers with core expertise in hydraulics. This modeling procedure does not introduce significant differences when compared to more complex approaches since inverters show very high efficiency in almost the entire working range [22].

The inverter's lost power ($P_{I,L}$) is a function of the EM's speed and theoretical torque. Its definition recalls three constant coefficients (c_i):

$$P_{I,L} = c_1 \cdot T_{P,th} + c_2 \cdot T_{P,th}^2 + c_3 \cdot \sqrt{P_{M,th}}\,. \tag{25}$$

The inverter's energy efficiency (η_I) is equal to

$$\eta_I = max\left\{\eta_{I,Min}, \frac{P_{M,th}}{P_{M,th} + P_{I,L}} \cdot 100\%\right\}, \tag{26}$$

where a lower saturation arbitrarily assigns the minimum value ($\eta_{I,Min}$). Again, the theoretical mechanical power of the motor is used for the abovementioned reasons about the map distortion. It is now possible to define the electric power (P_{DC}) drawn from the DC supply that enters the inverter as:

$$P_{DC} = \frac{P_{M,e}}{\eta_I \cdot \eta_{EM}} \cdot 100\%, \tag{27}$$

therefore, using the effective mechanical power of the electric motor, which is dictated by the pump's effective torque, combined with the proper maps of η_I and η_{EM}.

2.5. Drive

After discussing the different components separately, the combination of those partial results leads to the complete analysis of the drive. Its overall efficiency (η_D) includes all the power dissipations taking place in the system:

$$\eta_D = \frac{P_L}{P_{DC}} \cdot 100\% \; = \eta_E \cdot \eta_H = \eta_I \cdot \eta_{EM} \cdot \eta_{P,t} \cdot \eta_C. \quad (28)$$

Moreover, the performance of both the electric and hydraulic domains can be addressed distinctly by the electric efficiency (η_E) and the hydraulic efficiency (η_H):

$$\eta_H = \frac{P_L}{P_{M,e}} \cdot 100\% \; = \eta_{P,t} \cdot \eta_C, \quad (29)$$

$$\eta_E = \frac{P_{M,e}}{P_{DC}} \cdot 100\% \; = \eta_I \cdot \eta_{EM}. \quad (30)$$

3. DRIVE'S EFFICIENCY MAPS

The equations given in Section 2 are used to generate the numerical results presented in the sequel. Precisely, (1)-(19) and (23)-(30) constitute a set of 28 independent equations because (15) is repeated twice for the theoretical and effective magnitudes. They are characterized by 31 unknowns (F_F, F_H, F_L, n, P_{DC}, P_E, $P_{EM,L}$, P_H, $P_{l,L}$, P_L, $P_{M,e}$, $P_{M,th}$, p_p, p_r, $Q_{C,L}$, $Q_{P,e}$, $Q_{P,L}$, $Q_{P,th}$, $T_{P,e}$, $T_{P,L}$, $T_{P,th}$, v, η_C, η_D, η_E, η_{EM}, η_H, η_I, $\eta_{P,mh}$, $\eta_{P,t}$, $\eta_{P,v}$). Assigning numerical values to p_p, p_r, and n gives the numerical solution for the remaining 28 unknowns.

The individual drive discussed in [24] is taken as the study case, neglecting the load-holding valves. It controls a single-boom crane that dictates the load-carrying pressure on the piston-side chamber. The highest admitted pressure is 200 bar, the low-pressure side is characterized by $p_r \approx 0$ bar, and the maximum motor speed is assumed to be equal to 3800 rev/min. The vectors of p_p, p_r, and n are assigned using a fixed step for a total of 400 values. Finally, Table I in Appendix A lists all the other parameters required to simulate the system behavior.

3.1. Standard efficiency maps

The drive's overall efficiency is presented in Fig. 3.1 (all the values of the efficiencies are given as percentages). The envelope dictated by the S1 duty curve of the electric motor is also proposed to show the theoretical limit of the operating range (*i.e.*, working points would be

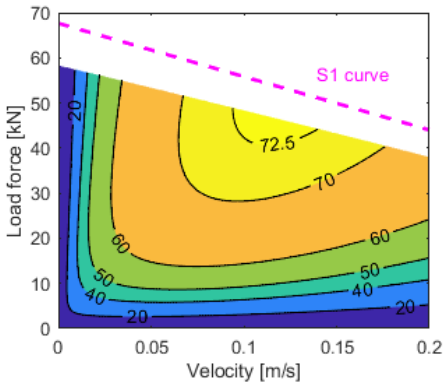

Figure 3.2. Drive's overall efficiency η_D (from DC supply to actuator load).

feasible up to this limit if the system were free of power dissipations). The efficiency's peak value of 73.4% takes place for medium velocity and high force of the actuator. Quantities above 60% are commonplace in a vast portion of the operating range, while poorer behavior is true for very-low piston velocities (<0.03 m/s) and low actuation forces (<15 kN). The global trend in Fig. 3.1 is comparable to the measured one for a similar single-pump system, even if the rectifier is included in that map [25]. It is then worth mentioning that such a performance is aligned with the one of electro-mechanical actuators [25]. In other words, electro-hydraulic drives represent a valid alternative that is also strengthened by other advantages, mainly the higher power output and the faster actuation capabilities [26].

Another asset of the proposed mapping procedure is the opportunity to address the effects of the different components on the drive's overall efficiency. The initial analysis can, for instance, focus on the two domains of the system, namely the electric and the hydraulic ones (Fig. 3.2). These charts show that the electric components have a global efficiency above 85% for a large range. The hydraulic elements, on the contrary, ensure a good combined efficiency above 75% only when the force delivered by the actuator is significant (at least one-third of the maximum). It should be noted that the top value of the hydraulic efficiency is approximately 80%; it refers to the conversion between the mechanical power of the pump's shaft and the one of the load. Such a result is encouraging when compared to valve-controlled systems; for instance, the hydraulic efficiency of a single, load-sensing actuator deteriorates faster when leaving the sweet spot [16].

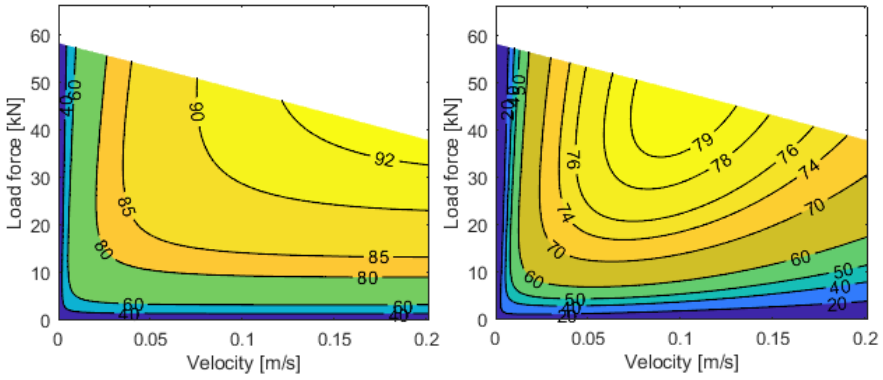

Figure 3.2. Drive's electric efficiency η_E on the left (from DC supply to electric motor's shaft) and hydraulic efficiency η_H (from motor's shaft to load).

Moving a step further, emphasis is placed on the efficiency of all components. Starting from the inverter (Fig. 3.3), its efficiency is well above 94%, with the only exception of the EM's low-speed operations. This behavior is true for popular Si-IGBT inverters, but improvements in that critical area are possible when selecting GaN-MOSFET inverters [22].

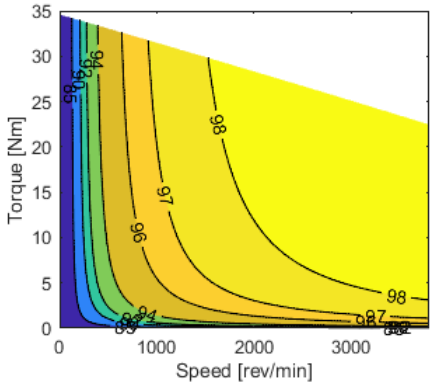

Figure 3.3. Inverter efficiency η_I (from DC supply to inverter outlet).

Then, the electric motor has a limited impact on the drive performance. Its efficiency remains sufficiently high, above 80%, on almost the entire range (Fig. 3.4). Those numbers can easily improve when the machine's rated power increases since it is well-known that powerful electric motors have higher efficiencies. Fig. 3.4 also reports the S1 duty curve of the PMSM. The upper limit of the speed in the plot (3800 rev/min) is the one leading to the maximum power output. For higher angular velocities up to the maximum admitted one (4200 rev/min), the outputted power drops down dramatically so that this portion of the operating range is ignored.

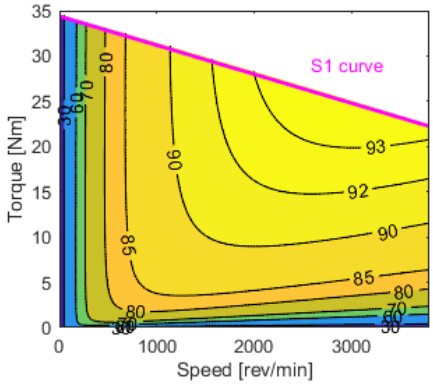

Figure 3.4. Electric motor's efficiency η_{EM} (from inverter outlet to motor shaft).

Moving to the hydraulic domain, the pump has a major impact on the drive performance (Fig. 3.5). Even if the pump's overall efficiency results are acceptable (it is greater than 60% almost everywhere for standard operations), its maximum value of 81.9% is limited. Such a behavior is representative of an axial-piston machine that does not employ the most recent findings being published to enhance efficiency and whose loss coefficients in (9) and (10) were tuned

to mimic the loss maps reported in [27]. Hydraulic units with newer designs will improve these numbers, as will machines with bigger displacements.

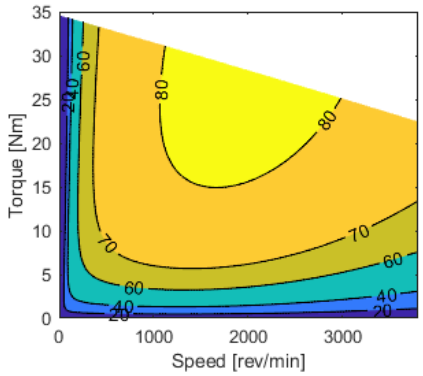

Figure 3.5. Pump's overall efficiency $\eta_{P,t}$ (from motor's shaft to pump outlet).

Finally, the influence of the hydraulic cylinder is minimal (Fig. 3.6). Its efficiency exceeds 90% in a wide range and stays above 95% for typical operations characterized by average velocities and medium-to-high forces.

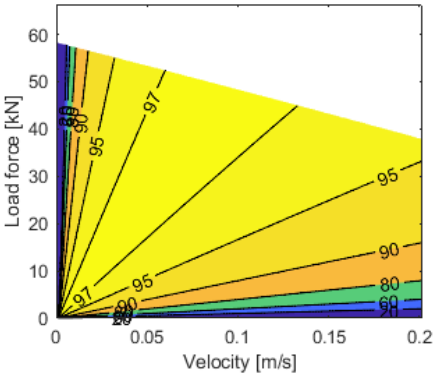

Figure 3.6. Actuator's efficiency η_C (from pump outlet to load).

3.2. Dimensionless efficiency maps

The possibility of plotting nondimensional magnitudes enables the most general understanding of the system behavior. The chart in Fig. 3.7, which depicts the drive's overall efficiency, was derived by dividing the magnitudes in the x and y directions with their maximum values (66.4 kN and 0.2 m/s). Reconstructing dimensional quantities via the inverse process can address similar drives of other sizes. This step offers an approximated estimation of the system performance without performing any simulations. However, this process will underestimate the efficiency of more powerful drives than the one used to derive the previous graphs (*i.e.*, installed power of 8.8 kW) for the already mentioned reasons about

the efficiency improvements as the size of the components grows. Lastly, the same approach can also be applied to the other maps in Fig. 3.2-Fig. 3.6, but it is omitted for brevity.

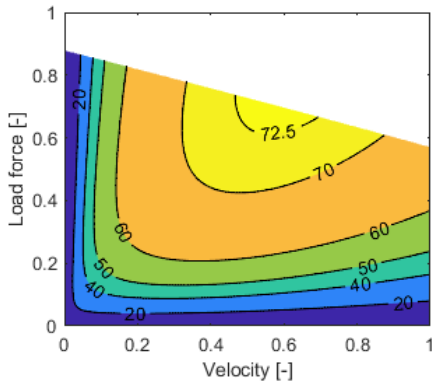

Figure 3.7. Dimensionless map of the drive's overall efficiency η_D (from DC supply to actuator load).

4. APPLICATIONS OF THE DRIVE'S EFFICIENCY MAP

4.1. Identifying the power limits

The efficiency maps derived before can also show the power managed by the drive. Useful insight is derived on the achievable power output and on the required power input. The plots in Fig. 4.1 clearly highlight the system limitations and are extremely valuable in predicting the suitability of the drive to perform a given task.

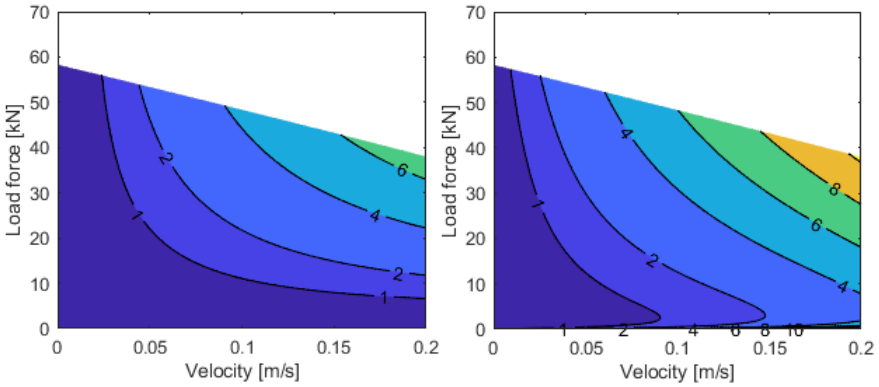

Figure 4.1. Power managed by the drive: mechanical power ouput P_L (left) and electric power input P_{DC} (right) in kW.

For the compact system assumed as the study case, the maximum outputted power is 6.9 kW, while the average values are within 3-5 kW for medium-to-high actuation velocities

and forces. Conversely, the electric power taken from the DC supply can increase up to 10.3 kW, even if it is often close to 4-7 kW during representative operations.

4.2. Supporting the component selection

This subsection shows another powerful application of the proposed method by considering an alternative component. Due to the impact of the pump on the overall performance, the effects of a more efficient hydraulic unit are predicted. For simplicity, the power losses of the original unit are reduced by 50% in any operating condition to arbitrarily consider feasible improvements. The new overall efficiency map of the pump in Fig. 4.2 displays that the peak efficiency increases up to 90.4%, as opposed to 81.9% of the initial set-up (Fig. 3.5). Most importantly, the efficiency is now above 70% almost everywhere, at least for standard operations (exceptions take place at very low torques and speeds).

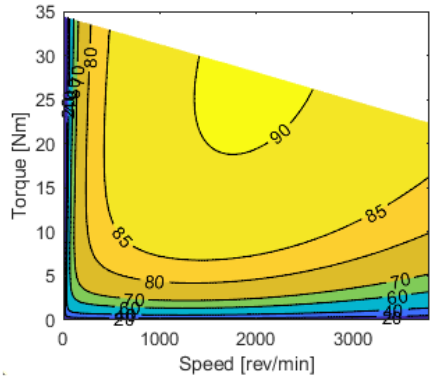

Figure 4.2. Hydraulic pump's overall efficiency $\eta_{P,t}$ for the alternative set-up.

The resulting improvements in the drive's overall efficiency and hydraulic efficiency emerge from Fig. 4.3.

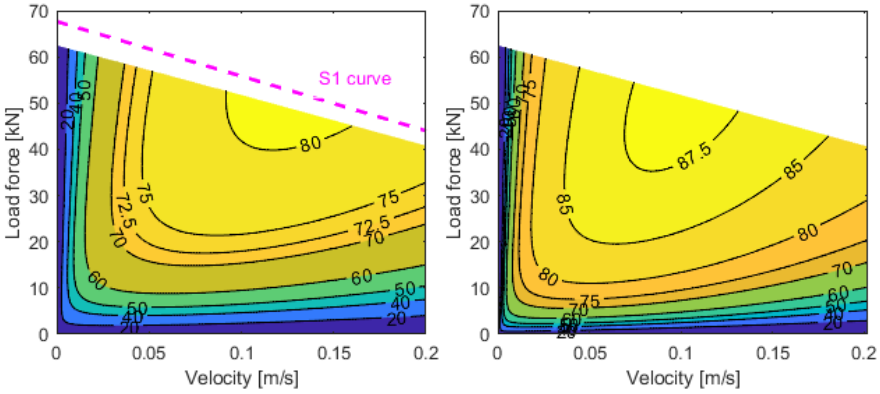

Figure 4.3. Drive's overall efficiency η_D (left) and drive's hydraulic efficiency η_H (right) for the alternative set-up.

First, the working area is expanded toward higher power levels (its upper margin is getting closer to the theoretical limit of the S1 curve). Values of at least 70% for the overall efficiency are commonplace, with the highest number at 80.8% as opposed to 73.4% for the original case. A similar benefit concerns the hydraulic efficiency that results superior to 80% in a wide range. However, it is worth noticing that both efficiencies do not improve greatly for unconventional operations characterized by very low actuation velocities (below 0.03 m/s) and medium-to-low actuation forces (under 15 kN, namely about one-fourth of the maximum transmissible force).

5. CONCLUSIONS

The ongoing trend toward the electrification of hydraulics requires user-friendly tools to further develop electro-hydraulic drives. This research paper contributes to increasing the understanding of those systems as follows:

- A generally applicable method is introduced to quickly derive efficiency maps for electro-hydraulic systems. This approach is defined as numerical because it is based on steady-state equations that use a limited number of parameters obtainable from the literature, or from catalogs (*i.e.*, experiments are not involved).
- It is possible to explore the behavior of the drive for all operating conditions and support the process of sizing and selecting the components. Efficiency maps of the single components are also obtained.
- The example of a single-pump drive confirmed that this throttleless technology is very promising. The peak efficiency of 73.4% was calculated when converting the electric power entering the inverter into the mechanical power leaving the actuator. It was also shown that the pump has the biggest influence on the overall efficiency, highlighting, therefore, a direction for future improvements.

In short, this generally applicable framework, which is adjustable to any electro-hydraulic drive, helps us better understand those energy-efficient solutions.

APPENDIX A

TABLE I. VALUES OF THE DRIVE'S PARAMETERS

A_p	3318.30	mm^2	K_c	$76.59/10^7$	$W/Hz/T^2/kg$
A_r	2356.20	mm^2	K_h	$56.26/10^3$	$W/Hz/T^2/kg$
b	8000.00	kg/s	k_L	$0.25/10^{12}$	$m^3/s/Pa$
B	1.30	T	K_T	2.05	Nm/A
c_1	2.00	kW/(Nm)	L_r	0.25	m
c_2	$5.00/10^4$	$kW/(Nm)^2$	m	16.20	kg
c_3	0.50	$kW/(Nm \cdot rad/s)^{1/2}$	q	3.00	-
C_D	$-11.32 \cdot 10^4$	-	Q_K	$15.39/10^2$	L/min

C_F	$56.46/10^3$	-
C_H	985.50	-
C_L	$57.94/10^5$	-
C_T	$95.07/10^6$	-
D	10.60	cm^3/rev
F_C	75.00	N
k_1	$5.00/10^3$	-
k_2	$87.07/10^{11}$	min^2/rev^2
k_3	$60.69/10^7$	min/rev
k_4	$19.18/10^3$	-

R_{EM}	0.79	Ω
R_r	$7.50/10^2$	m
T_K	20.34/10	Nm
z	4.00	-
β	3329.00	bar
$\eta_{I,Min}$	80	%
μ	$3.93/10^2$	Ns/m^2
ρ_a	10.09/10	kg/m^3
ρ_f	855.00	kg/m^3

6. REFERENCES

[1] D. Padovani, M. Rundo, and G. Altare, "The Working Hydraulics of Valve-Controlled Mobile Machines: Classification and Review," *ASME J. Dyn. Syst. Meas. Control*, vol. 142, no. 7, 2020.

[2] S. Michel and J. Weber, "Energy-efficient electrohydraulic compact drives for low power applications," *ASME/BATH Symp. Fluid Power Motion Control*, 2012.

[3] D. Padovani, S. Ketelsen, and L. Schmidt, "Downsizing the Electric Motors of Energy-Efficient Self-Contained Electro-Hydraulic Systems by Using Hybrid Technologies," *BATH/ASME Symp. Fluid Power Motion Control*, 2020.

[4] T. Minav, M. P. J.E. Heikkinenb, J. E. Heikkinen, and M. Pietola, "Direct driven hydraulic drive for new powertrain topologies for non-road mobile machinery," *Electr. Power Syst. Res.*, vol. 152, Nov. 2017.

[5] L. Schmidt, S. Ketelsen, D. Padovani, and K. Mortensen, "Improving the Efficiency and Dynamic Properties of a Flow Control Unit in a Self-Locking Compact Electro-Hydraulic Cylinder Drive," *ASME/BATH Symp. Fluid Power Motion Control*, 2019.

[6] G. Kolks and J. Weber, "Electro-Hydrostatic Compact Drives with Variable Transmission Ratio," *12th Int. Fluid Power Conf.*, 2020.

[7] S. Ketelsen, D. Padovani, M. K. Ebbesen, T. O. Andersen, and L. Schmidt, "A Gasless Reservoir Solution for Electro-Hydraulic Compact Drives with Two Prime Movers," *ASME/BATH Symp. Fluid Power Motion Control*, 2020.

[8] L. Schmidt, M. Groenkjaer, H. C. Pedersen, and T. O. Andersen, "Position Control of an Over-Actuated Direct Hydraulic Cylinder Drive," *Control Eng. Pract.*, vol. 64, 2017.

[9] D. Hagen, D. Padovani, and M. Choux, "A Comparison Study of a Novel Self-Contained Electro-Hydraulic Cylinder versus a Conventional Valve-Controlled Actuator — Part 1 : Motion Control," *Actuators*, vol. 8, no. 79, 2019.

[10] D. Padovani, "Adding Active Damping to Energy-Efficient Electro-Hydraulic Systems for Robotic Manipulators — Comparing Pressure and Acceleration Feedback," *IEEE 5th Int. Conf. on Robotics and Automation Engineering*, 2020.

[11] D. Hagen, D. Padovani, and M. Choux, "A Comparison Study of a Novel Self-Contained Electro-Hydraulic Cylinder versus a Conventional Valve-Controlled

Actuator — Part 2: Energy Efficiency," *Actuators*, vol. 8, no. 78, 2019.
[12] S. Qu, D. Fassbender, A. Vacca, and E. Busquets, "A High-Efficient Solution for Electro-Hydraulic Actuators with Energy Regeneration Capability," *Energy*, vol. 216, 2021.
[13] S. Qu, D. Fassbender, A. Vacca, and E. Busquets, "A Cost-Effective Electro-Hydraulic Actuator Solution with Open Circuit Architecture," *Int. J. Fluid Power*, vol. 22, no. 2, 2021.
[14] N. Manring, "Efficiency Mapping for a Linear Hydraulic-Actuator," *ASME J. Dyn. Syst. Meas. Control. Tech. Br.*, 2013.
[15] N. Manring, "Mapping the Efficiency for a Hydrostatic Transmission," *ASME J. Dyn. Syst. Meas. Control*, vol. 138, no. 3, 2016.
[16] L. Manring and N. Manring, "Mapping the Efficiency of a Double Acting, Single-Rod Hydraulic-Actuator Using a Critically Centered Four-Way Spool Valve and a Load-Sensing Pump," *ASME J. Dyn. Syst. Meas. Control*, vol. 140, no. 9, 2018.
[17] H. T. Phan and Y. Sato, "Improving the Overall Efficiency of an Electro-hydraulic Drive System by using Efficiency Maps," *JFPS Int. J. Fluid Power Syst.*, vol. 14, no. 1, 2021.
[18] L. Schmidt and K. V. Hansen, "Electro-Hydraulic Variable-Speed Drive Networks—Idea, Perspectives, and Energy Saving Potentials," *Energies*, vol. 15, no. 3, 2022.
[19] O. Olsson, "Matematisk Verkingsgradmodell (Mathematical Efficiency Model)," Institute of Technology, Linköping, Sweden, 1973.
[20] Bosch Rexroth AG, "Rexroth IndraDyn S MSK Synchronous Motors," Lohr a. Main, Germany, 2006.
[21] C. Huynh, L. Zheng, and D. Acharya, "Losses in High Speed Permanent Magnet Machines Used in Microturbine Applications," *ASME J. Eng. Gas Turbines Power*, vol. 131, no. 2, 2009.
[22] K. Kumar, "Efficiency Improvement of Three Phase Traction Inverter through GaN Devices for PMSM," *IEEE Int. Conf. on Power Electronics, Drives and Energy Systems*, 2016.
[23] A. Ritari, J. Vepsäläinen, K. Kivekäs, K. Tammi, and H. Laitinen, "Energy Consumption and Lifecycle Cost Analysis of Electric City Buses with Multispeed Gearboxes," *Energies*, vol. 13, no. 8, 2020.
[24] D. Padovani, S. Ketelsen, D. Hagen, and L. Schmidt, "A self-contained electro-hydraulic cylinder with passive load-holding capability," *Energies*, vol. 12, no. 2, 2019.
[25] S. Michel, "Elektrisch-Hydrostatische Kompaktantriebe mit Differentialzylinder für die Industrielle Anwendung," Technischen Universität Dresden, Germany, 2021.
[26] D. Hagen, D. Padovani, and M. Choux, "Guidelines to Select Between Self-Contained Electro-Hydraulic and Electro-Mechanical Cylinders," *IEEE 15th Conf. on Industrial Electronics and Applications*, 2020.
[27] D. Padovani, "Leveraging Flow Regeneration in Individual Energy-Efficient Hydraulic Drives," *ASME/BATH Symp. Fluid Power Motion Control*, 2021.

Biographies

Damiano Padovani joined the Guangdong Technion-Israel Institute of Technology in 2021. He received his B.Sc. and M.Sc. degrees in Mechanical Engineering from the Polytechnic University of Turin (Italy) and his Ph.D. degree in Engineering with a specialization in Fluid Power from Purdue University (USA). He worked as a post-doc researcher at Vanderbilt University (USA), as a faculty member at the University of Agder (Norway), and in the industry with Parker Hannifin (USA). His research interests focus on different aspects of fluid power, mainly embracing energy efficiency, mobile hydraulics, and applied control.

Development of a Bi-stable Mechanism for Efficiency Optimization of Pneumatic Pressure Boosters

Matthias Schmid, Olivier Reinertz, Katharina Schmitz

RWTH Aachen University
Institute of Fluid Power Drives and Systems (ifas)
Aachen, Germany, matthias.schmid@ifas.rwth-aachen.de

Abstract.

In hydrogen filling stations, pressure boosters are needed to increase the pressure from the level-dependent storage tank to a constant disposal pressure. Pneumatically driven pressure boosters can easily meet the special requirements of explosion protection in such applications. Thus, despite their actually low efficiency, they offer a worthwhile approach. The attractiveness can be further increased by optimizing the efficiency. In state-of-the-art units, a considerable part of the expansion energy in drive chambers is lost due to an unfavorable load over the stroke. By increasing the load at the beginning of the stroke by means of a bi-stable mechanism, the amount of previously unused expansion energy can be stored in it. This energy can be released again in the second half of the stroke. This reduces the pressure requirement at the end of the stroke, allows the air in the drive chamber to expand and thus lowers the air consumption and increases the efficiency. In the scope of this paper, an analytical representation of the pressure booster is shown for an understanding of the thermodynamic processes. On the basis of the simulation model, the load compensation is specified and a concept for the prototype is presented. The concept is based on the negative spring stiffness of a plate during mechanical snap-through. Subsequently, the developed mechanism is integrated into the simulation model and the results and achieved progress are elaborated. Finally, the outstanding measurements and already realized preparations are discussed.

Keywords. gas compression, mechanical snap-through, membrane buckling, spring stiffness, hydrogen

1. INTRODUCTION

For advancing the energy transition an increase in efficiency is also of great interest in pneumatic applications.

Lowering the network pressure is a simple and widely used approach to reduce losses in compressed air systems. However, the pressure demand of a small number of end devices often limits the realizable pressure reduction. To allow a lower system pressure and enhanced efficiency, the operation pressure required by these devices can be generated by

pressure boosters. However, only small boost factors are required for this. The system described in this paper is used for boost factors greater than 2.7.

In the context of the mobility revolution towards sustainable sources of fuel, another use case is emerging. For the use of hydrogen in automotive applications, a high pressure-level of the hydrogen of up to 700 bar is required [1]. Due to the special requirements for explosion protection in hydrogen applications, pneumatically driven systems for pressure boosting are an obvious choice, e.g., in hydrogen filling stations. Thus, pressure boosters offer a worthwhile approach to efficient energy use despite their actual low efficiency. The attractiveness of this device category can be further increased by an efficiency optimization.

In state-of-the-art devices, a significant share of the expansion energy supplied to their drive-chambers is lost due to unfavourable loading of the drive over the stroke. [2] By temporarily storing the previously unused expansion energy in pressure boosters within a bi-stable mechanism, overall efficiency can be increased [3]. A first concept, using a cam loaded by pistons, has already been presented by the co-author. Nevertheless, the presented design is not suitable for industrial application. The basic concept is patent pending. [4] Additionally, the concept of a bi-stabile mechanism has been postulated for usability in vacuum generator. In this paper the principle of a membrane will be used [5].

In the scope of this paper, at first, the examined pressure booster is abstracted for simulation. According to this structure, an analytical representation of the entire system is developed.

At the beginning of the stroke, the load is increased by the mechanical system. The energy thus stored in this mechanism is returned on the second half of the stroke, whereby an approximation to the optimal load profile is achieved. The system is intended to complement pressure boosters already in use, whereby an adaptive design is required to allow operation at varying driving pressures.

The focus of the current investigation is on the dynamic operation. In particular, the change in the stroke frequency caused by the mechanics has a considerable impact on the system´s usability. The aim is to increase efficiency without unreasonably reducing the delivered flow rate. In addition to the numerical simulations of the developed mechanical system, the designed prototype is presented.

The achieved increase in efficiency is shown by means of results from simulative investigation of the reference system compared to the modified device set-up. Finally, in relation to these results, the prototype design and measurement strategy for an experimental validation are discussed.

2. STATE OF THE ART

2.1. Pressure Booster

The principle of the pressure booster works according to Pascal´s Law. Low pressure can be converted into high pressure with the aid of a different area ratio. In the four Chambers shown in Figure 2.1, different thermodynamic processes take place.

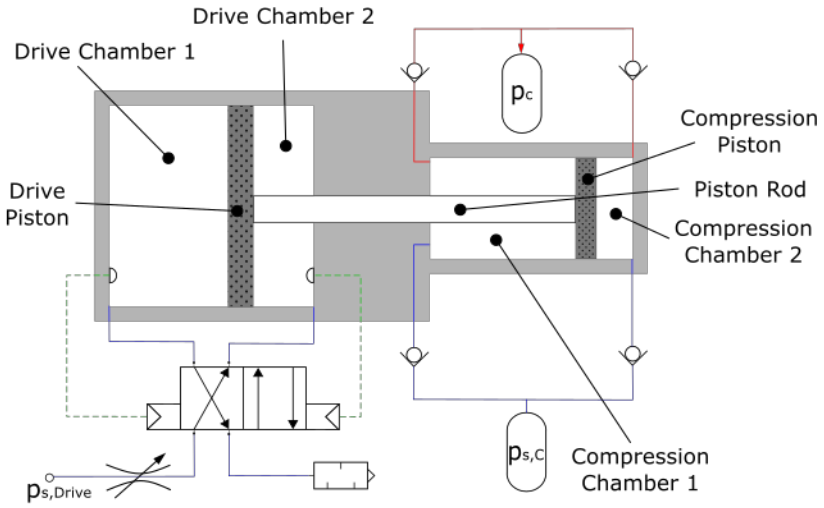

Figure 2.1: Function scheme of the pressure booster

In case of pistons movement to right direction, drive chamber 1 and compression chamber 2 are set as “active chamber”. In opposite direction these are “passive chambers”, as the other chambers are “active”. In the case of the compression chambers, the compression takes place in the first part of the stroke. This increases the resistance against the drive chamber. An isentropic compression is assumed. Once the outlet pressure is reached, a constant driving force is required to push the compressed gas through the corresponding check valve into the high pressure system. A small amount of the compressed gas stays in the dead volume of the chamber at strokes end. Therefore, the gas in the dead volume of the opposite compression chamber is expanded isentropically and supports the movement of the piston.

At the same time, venting to ambient pressure takes place in the directionally related passive drive chamber. The resultant force of the compression chambers and the passive drive chamber lead to a pressure profile of the active drive chamber. The exemplary pressure profile in Figure 2.2 shows an increasing pressure requirement at the end of the stroke. This determines the required pressure level. The aim is to store the pressure potential at the beginning of the stroke and to release it towards the end of the stroke in order to reduce the pressure requirement on the drive side.

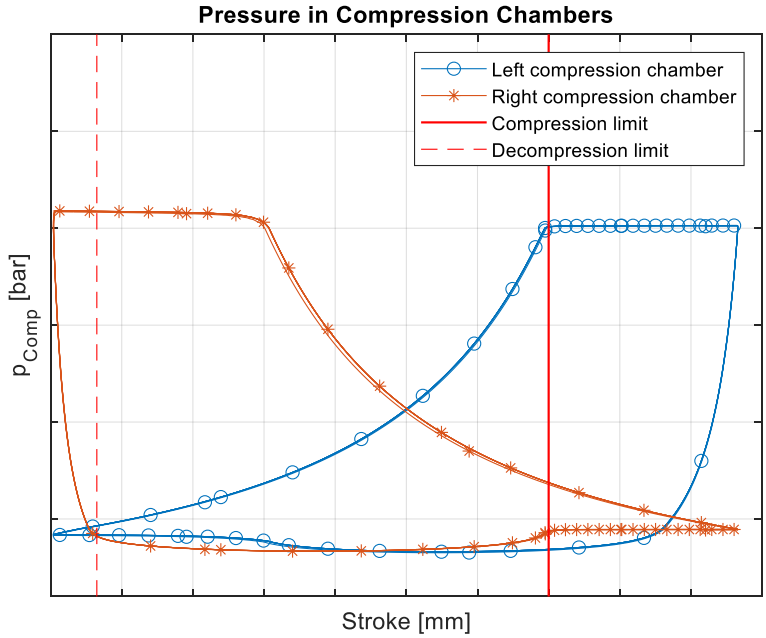

Figure 2.2: Pressure profiles of the compression chambers, 4,5 bar supply pressure, 20 bar compression pressure

In addition to the simulative investigation of the system explained later, an analytical description is presented in the following. This provides an approach to determine the force requirement and serves the general understanding of the process. The equations are based on the equation of motion for the piston. Pressure profiles are implemented in these for the force components corresponding to the piston surfaces. Assumptions are made for the pressure curves. In the case of the active drive chamber, the throttle equation is used for the description. For the complete description of the piston movement during a single stroke, three differential equations are used. The corresponding limits for these differential equations are marked in Figure 2.2. The first stroke section is limited by reaching the complete expansion of the dead volume from the passive compression chamber. This expansion acts supporting to the pistons movement. It is formulated in the fourth term of equation 2.1. At the same stroke section, an isentropic compression process takes place in the active drive chamber. The mathematical formulation is the third term of equation 1. The first term represents the throttle equation for the active drive chamber. For the passive drive chamber, ideal venting is assumed, whereby a constant pressure is added in the second term

$$M_P \cdot \ddot{h} = \frac{-b \cdot p_{S,D}}{\frac{A_{P,D1} \cdot \dot{h}}{C \cdot \rho_0 \cdot R \cdot T} - 1} \cdot A_{P,D1} + p_{D,passiv} \cdot A_{\mathrm{P},D2} + \frac{p_{C\mathrm{Comp}} \cdot {h_d}^{\kappa}}{(h_d + h)^{\kappa}} \cdot A_{\mathrm{P},C1}$$

$$- \frac{p_{S,C} \cdot (h_d + h_{max})^{\kappa}}{(h_d + h_{max} - h)^{\kappa}} \cdot A_{\mathrm{P},C2} \tag{2.1}$$

In the further course until the maximum compression pressure is reached, a constant pressure is established not only in the passive drive chamber but also in the passive compression chamber. The passive compression chamber is filled for the next stroke at the pre-pressure of the process gas. The compression process continues in the active compression chamber.

$$M_P \cdot \ddot{h} = \frac{-b \cdot p_{S,D}}{\frac{A_{P,D1} \cdot \dot{h}}{C \cdot \rho_0 \cdot R \cdot T} - 1} \cdot A_{P,D1} + p_{s,D} \cdot A_{\mathrm{P},D2} + p_{s,C} \cdot A_{\mathrm{P},C1}$$

$$- \frac{p_{s,C} \cdot (h_d + h_{max})^{\kappa}}{(h_d + h_{max} - h)^{\kappa}} \cdot A_{\mathrm{P},C2} \tag{2.2}$$

In the last section, the maximum compression pressure has already been reached, which means that a constant pressure is now also assumed here in the second term of equation 3.

$$M_P \cdot \ddot{h} = \frac{-b \cdot p_{S,D}}{\frac{A_{P,D1} \cdot \dot{h}}{C \cdot \rho_0 \cdot R \cdot T} - 1} \cdot A_{P,D1} + p_{s,D} \cdot A_{\mathrm{P},D2} + p_{s,C} \cdot A_{\mathrm{P},C1} - p_{C,\mathrm{max}} \cdot A_{\mathrm{P},C2} \tag{2.3}$$

For performing the experimental investigation, the pressure booster GPLV5 from Maximator is used [6]. The essential technical data are listed in Table 1

Drive stroke diameter	160 mm
Compression stroke diameter	70 mm
Piston rod diameter	20 mm
stroke	94mm
Supply pressure	1 – 10 bar
Maximal compression pressure	60 bar

Table 2.1: Essential technical Data of Maximator GPLV5

A peculiarity of this pressure booster is the mixed form between upstream and downstream throttling, due to the installed valve.

2.2. Bi-stable Mechanism

A bi-stable mechanism is developed for the pressure booster. According to the requirements, it shall store energy at the beginning of the stroke and release it at the end of the stroke. A possible solution to this problem is the use of a buckling shell. In this device energy is stored and returned in the same direction of pistons movement.

Such flexible mechanical structures can be distinguished between stable and unstable behaviour. An example for such structures is a Belleville spring. Figure 2.3 shows the force curve of a Belleville spring with an inner diameter of 80 mm, an outer diameter of 200 mm and a thickness of 0,8 mm. The transition between the two stable end positions leads to an unstable state during the stroke. In the case of the latter, in addition to the bifurcation, there is the snap-through. [7] Hereby the load-deformation curve shows a discontinuity. The area between the reversal points in Figure 2.3 can be understood as negative stiffness. The negative stiffness can be utilised by preloading and stroke limitation in this range [8] [9].

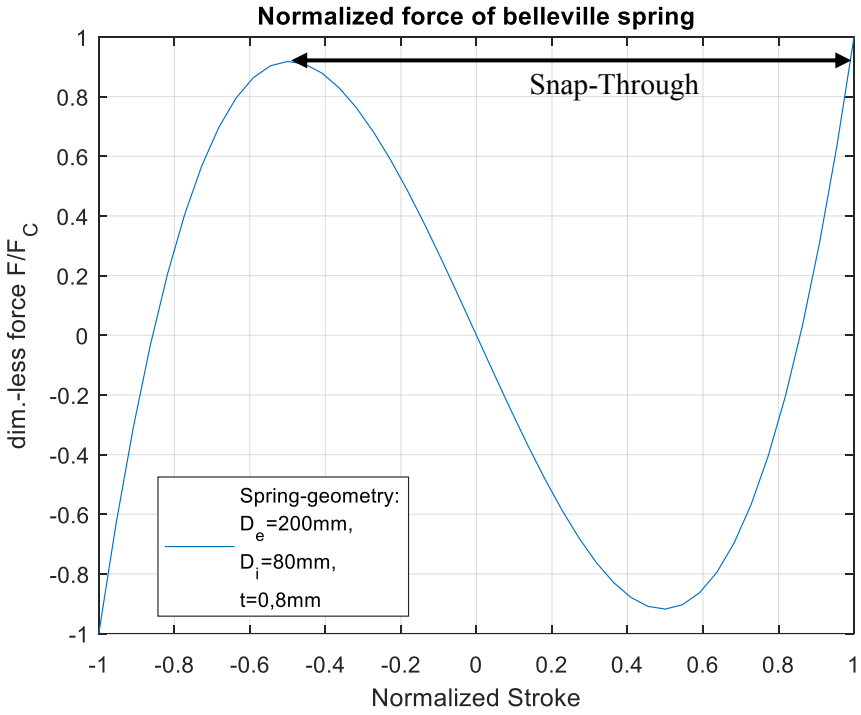

Figure 2.3: Characteristic force curve of a belleville spring according DIN 2092

Based on the simulation, the demand of force in the end positions can be estimated. As already described by Reinertz [3], a negative spring stiffness is required for load compensation.

3. METHODS

In the scope of this paper, the development process of the previously described bi-stable mechanism is explained. For the targeted development, the requirements are defined by means of the reference system. The design of the mechanism is iterated simulatively using FEM. The reference system is also experimentally analysed in preparation for carrying out tests with the new mechanism.

3.1. Determination of the Force Requirement

As stated before, the mechanism shall be used to modify the pressure demand over stroke. Therefore, the optimal force demand is estimated by simulation. The optimum curve is shown in Figure 3.1. In order to ensure functionality for the outward and return movement, the approximated spring stiffness, represented by the diagonal in the diagram, is aimed for.

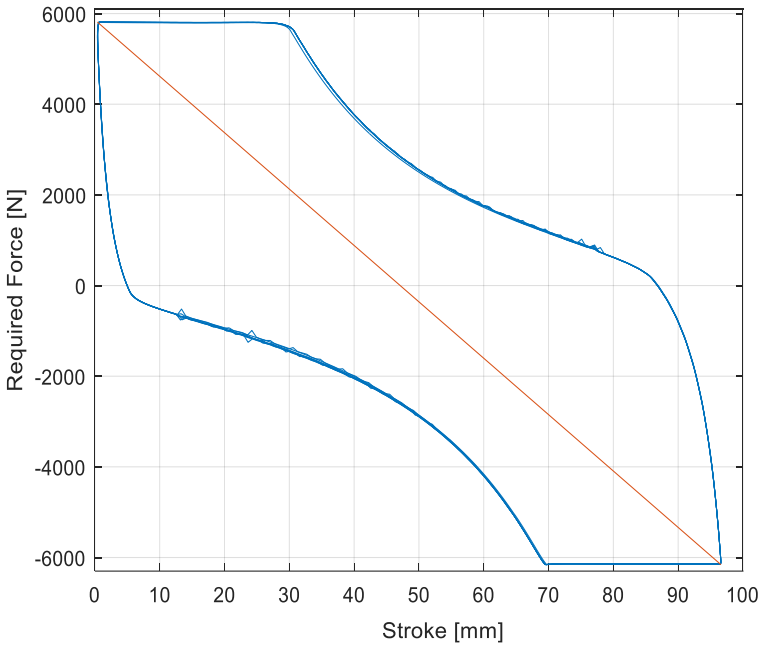

Figure 3.1: Force demand of the mechanics

With the spring described before, a similar force curve can be set. For this purpose, the spring is brought into a preloaded state and the range of movement lies between the force maxima and minima from Figure 3.1.

3.2. Design of Required Mechanism

A promising approach for rectified energy storage and release is mechanical snap-through. This is often realised with membranes First there is a circular plate, that is radially prestressed. This deforms the plate into a spherical shell. During the deformation of the membrane very large radial stresses occur. To circumvent this, the approach of a rectangular sheet is followed. In Figure 3.2 the result of ansys simulation is shown. Essential point of development is the critical stress. The colour steps refer to yield strength of steel 1.4410 and titan Grade 26. Thereof areas of plastic deformation can be identified.

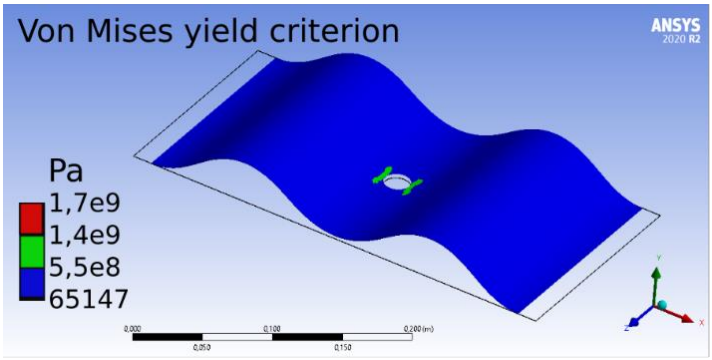

Figure 3.2: Large deformation simulation of rectangular sheet (thickness 0,4 mm) by means of Ansys

This sheet is firmly clamped on the two short sides. Simulatively, the geometry is optimised under the conditions of large deformations in transient dynamics. The main goal here is the reduction of stress. A first approach is to change the cross-section area and thereby the area moment of inertia. A balance between the reduction of the area moment of inertia and the resulting change in stiffness must be ensured. Increasing the size of the spring is another approach.

3.3. Experimental Setup

Two modifications to the commercial hardware are essential for the experimental setup. On the one hand, a way to attach the spring and on the other hand the conversion to upstream throttling. To insert the spring into the power flow, the piston rod on the existing pressure booster is extended on one side and guided outwards through the housing. The piston rod is extended on the drive side to influence the compression ratio as little as possible. The spring can be centrally fixed on the extended piston rod, while at the same time easy access to the pre-stressing of the spring is ensured. The attachment device with pressure booster is shown in figure 3.3.

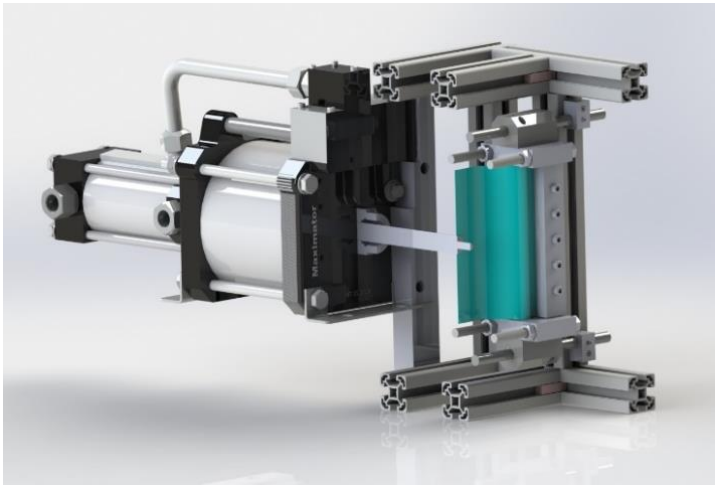

Figure 3.3: Attachment device on pressure booster

Apart from the higher efficiency of an upstream throttling itself, this is mandatory for the mechanics. The upstream throttling ensures that at the end of the stroke the required force from the mechanism takes place and that the drive pressure required up to that point actually decreases. So the drive chamber is not filled to the supply pressure again the drive chamber, as is also the case with the switchover at the end of the stroke. A closer look at the cross-sections of the exhaust air ducts reveals constrictions in the cross-section. Within the scope of the modification these cross-sections were enlarged in order to minimise the effect of downstream throttling.

4. RESULTS

In this section the simulation and measurement results are presented. First, the pressure profiles of the simulated devices are explained. Here, the results of later explanations are already anticipated in order to illustrate the necessity and the effect. Then the spring is described in more detail. The focus is on the geometry for the intended measurements. Finally, the measurement results from the standard device and after modification for upstream throttling are discussed.

4.1. Pressure Profile

The implementation of the negative stiffness in the existing simulation model shows a decreasing pressure demand at the end of the stroke. In contrast, the pressure required at the beginning of the stroke increases to the level of the supply pressure in the modified variant in figure 4.1. The approximately 10% lower pressure demand at the end position of the piston shows the desired effect.

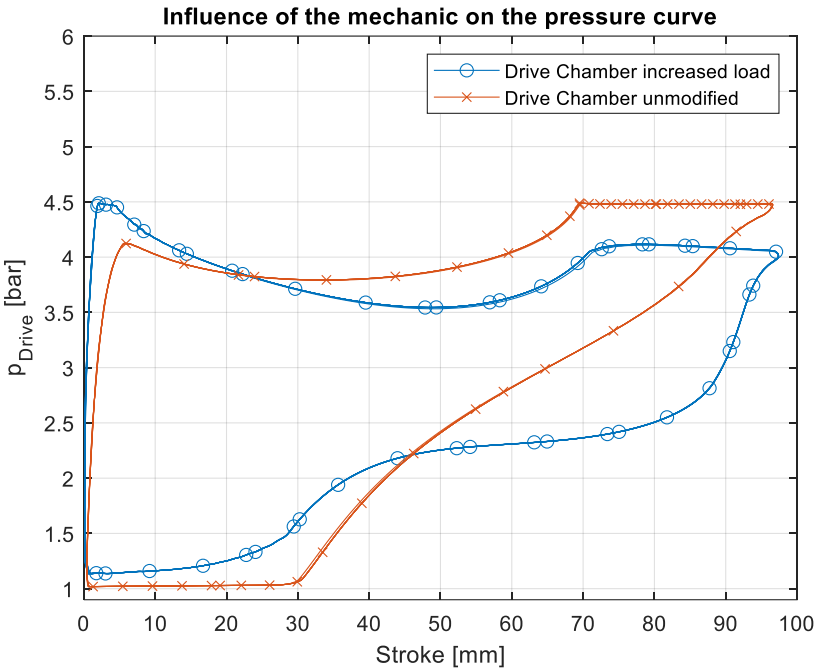

Figure 4.1: Simulated pressure profile of drive chambers with/ without developed mechanism; 4,5 bar supply pressure, 20 bar compression pressure

The additional force from the mechanism prevents the load-free high acceleration of the piston at the stroke begin. This effect can be seen in the time course of the stroke compared to the load-free variant, shown in Figure 4.2. At the same time, the movement of the piston of the unmodified system slows down considerably in the subsequent compression and delivery phase of the gas. The implemented mechanism has a supporting effect in this section, resulting in an approximately constant speed. Moreover, this modification also provides an increase in performance in addition to the energy savings shown above. Thy cycle time of the modified version is considerably shorter, which leads to an increase in delivered flow.

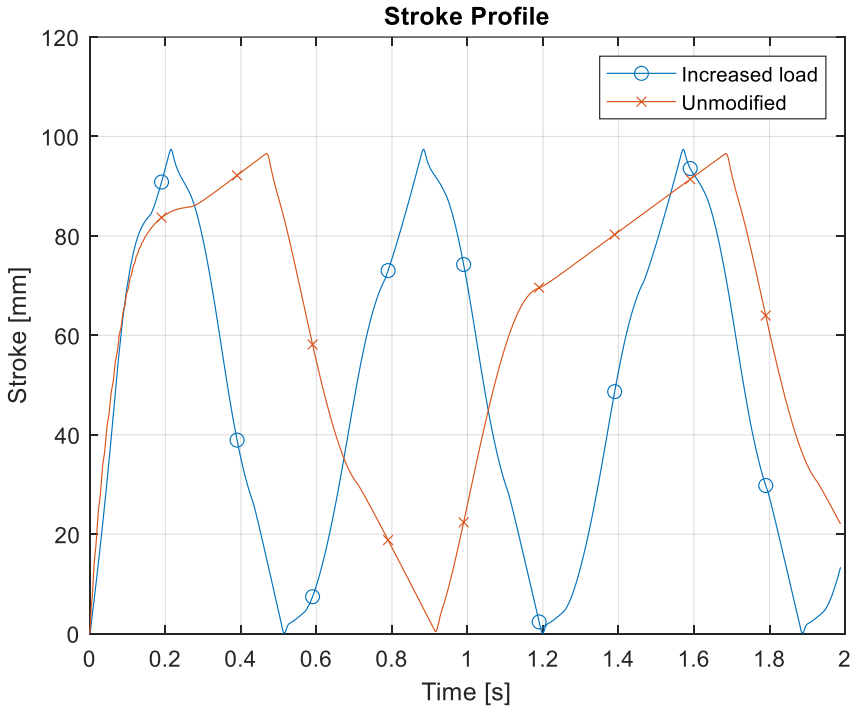

Figure 4.2: Simulated stroke curve with/without developed mechanism; 4,5 bar supply pressure, 20 bar compression pressure

4.2. FEM of the Spring in Snap-Through

Within the scope of the simulation of transient structural mechanics, the stress distributions and the strain behaviour are assessed. The starting point for the simulation procedure is a rectangular sheet. Titanium grade 5 alloy is assigned as the material. The described pre-stress is achieved by pushing the two short flanks together. Meanwhile, the centre of the sheet lifts. This boundary condition is implemented as a displacement in the simulation. Here, a non-linearity between the displacement of the flanks and the displacement of the centre need to be considered. Otherwise, undesired deformations already occur here. As a result, the stress level can exceed the yield strength or even the tensile strength. Compared to the linear displacement of the flanks, a degressive displacement must be applied to the centre. To keep the strains bearable at the large deformations, a sheet thickness between 0.2 mm and 0.3 mm is targeted. Due to the thin geometry, a one-element meshing over the thickness results for the meshing model as a solid shell. The force curve is of decisive importance. This is shown in Figure 4.3.

There is an asymmetry depending on the stroke direction. The cause is the buckling of the sheet. The buckling itself is already asymmetrical depending on the stroke direction. This shifts the zero crossing.

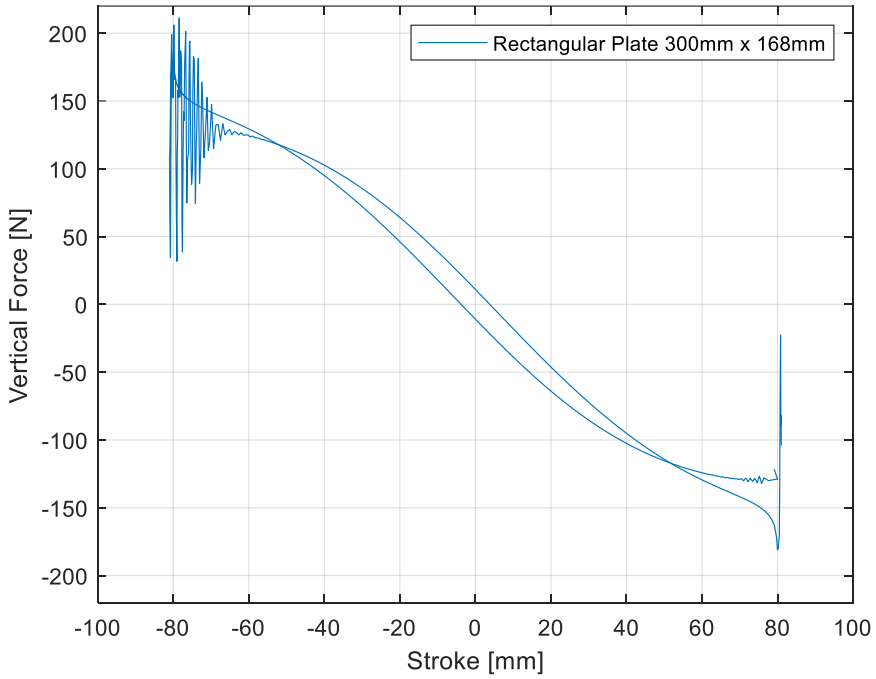

Figure 4.3: Simulated force curve of the spring in the preloaded state

Due to the poor availability of the chosen material, an investigation of available alternatives is necessary. The ferritic stainless steel 1.4410 shows a similar force curve in a first rudimentary simulation. In combination with the variation of the geometric dimensions, a suitable solution can be developed from this. However the maximum force is about 150 N, depends on available material, an individual count of springs are required.

4.3. Measurement Results

Figure 4.4 shows the pressure curve in a drive chamber in comparison between the original condition of the device and the modified version with upstream throttling. There is an improvement in the venting of the drive chamber. At the same time, this reduces the pressure requirement in the first stroke section in the active process. This results in a higher proportion of usable expansion energy. At the same time, the stroke frequency increases. This offers the approach of an additional external upstream throttling to further strengthen the previously mentioned effect.

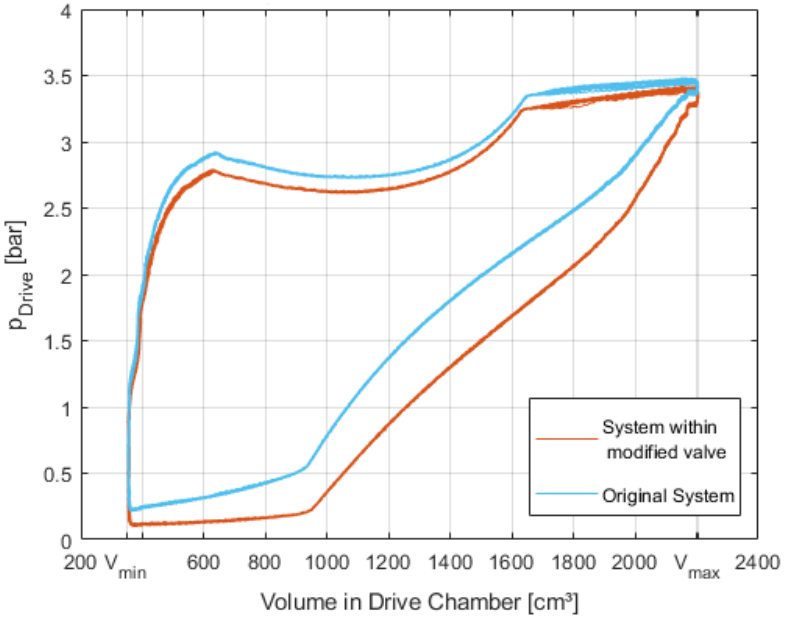

Figure 4.4: Measured pressure profile of drive chamber; effect of modification for upstream throttling

5. CONCLUSION AND OUTLOOK

5.1. Conclusion

Previous investigations in preparation for the measurements have shown that the usual throttling of the used pressure booster is unsuitable. A conversion to upstream throttling has been carried out. This has already shown an increase in performance. The simulative design of the spring was carried out using a grade 21 titanium alloy. Due to the availability on the market, a design was made for grade 5 titanium alloy and later on for stainless steel 1.4410. Due to the unfavourable stress position with a conical spring shape, the geometry was further developed in the direction of a rectangular plate. The resulting force curves were implemented in the simulation model. The results from this confirm the increase in efficiency due to the developed mechanics. The pressure level at the end of the stroke decreases as expected, which enables significant air savings. Due to the low-threshold load profiles of the springs, caused by the limitation of the stresses, several springs are required.

5.2. Outlook

To confirm the simulated results, measurements with the developed spring are pending. As soon as the current insufficient availability of titanium alloys, further simulations and measurements of the spring are necessary. The spring itself provides a corresponding maximum force depending on the preload. Since varying force levels are required depending on the supply pressure, the preload must be adapted to this. For initial tests, a mechanical

stressing mechanism via threaded rods is provided for this purpose. This tightens the clamping jaws and thus the edges of the spring. In the course of further work, this mechanism will be replaced by an adaptive alternative. A hydraulic system with transmission on the part of the supply pressure is conceivable here. This would make the system self-regulating. As soon as the test rig is available in its final configuration, the fatigue strength of the springs can be determined in order to assess the economic viability of the measure.

6. ACKNOWLEDGMENT

The research and development project Effipad - Efficient pneumatically driven pressure boosting - was funded by the European Union and the state of North Rhine-Westphalia. ifas would like to express its sincere thanks to all project partners, the European Regional Development Fund and the state of NRW.

7. NOMENCLATURE

$A_{P,D1}$	Area of piston in drive chamber (no. 1)
$A_{P,C1}$	Area of piston in compression chamber (no. 1)
b	Critical pressure ratio, 0.528
C	Sonic conductance
h	stroke
h_d	Stroke of dead volume
h_{max}	Maximal stroke
M_P	Mass of pistons including rod
p_C	Pressure in tank after compression
p_{Comp}	Pressure in compression chamber
$p_{D,passive}$	Pressure in Drive chamber during this is exhausted
$p_{s,D}$	Supply pressure for drive chamber
$p_{s,C}$	Supply pressure for compression chamber
R	Ideal gas constant
T	Temperature

8. REFERENCES

[1] K. Reddi, A. Elgowainy, N. Rustagi, E. Gupta, „Impact of hydrogen SAE J2601 fueling methods on fueling time of light duty fuel cell electric vehicles," Energy Systems Division, Argonne National Laboratory, South Cass Avenue, Argonne, 2017.

[2] F. Yang, K. Tadano, G. Li, T. Kagawa, „Analysis of the Energy Efficiency of a Pneumatic Booster Regulator with Energy Recovery," MDPI, Basel, August 2017.

[3] O. Reinertz, K. Schmitz, „Efficiency Optimized Pneumatic Pressure Booster," in *FPMC2019-1675, Symposium on Fluid Power and Motion Control*, Sarasota, October 2019.

[4] O. Reinertz, „Fluid-Driven Drive," WO, WO002020127886A1, 2020.

[5] O. Reinertz, K. Schmitz, „A Novel Exergy Efficient Pneumatic Vacuum Pump," in *FPMC2019-1675, 16. SICFP*, Tampere, Finland, May 2019.

[6] N.N., *Maximator Technical Data Sheet - Air Amplifier GPLV5, Release 03 / 2012 Page 1 of 3 • DB.01.02.01.04,* 2012.

[7] U. Risto, „Zur Charakterisierung und Anwendung des Durchschlagverhaltens von nachgiebigen rotationssymmetrischen Strukturen," Berichte der Illmenauer Mechanismentechnik (BIMT), TU Illmenau, Illmenau, October 2013.

[8] G. Arena, R. Groh, R. Theunissen, P. Weaver, A. Pirrera, „Adaptive Nonlinear Structures for Flow Regulation: Modelling Fluid-Structure Interactions with Coupled Eulerian-Lagrangian Meshes," in *SIMULIA UK Regional User Meeting*, 2016.

[9] L. Kashdan, C. Conner Seepersad, M. Haberman, P. Wilson, „Design, fabrication, and evaluation of negative stiffness elements using SLS," Mechanical Engineering Department and Applied Research Laboratory, University of Texas, Rapid Prototyping Journal, Austin, June 2011.

Biographies

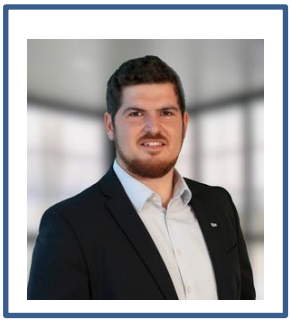

Matthias Schmid, received the bachelor's degree in mechanical engineering from Stuttgart University in 2016, the master's degree in mechanical engineering from Stuttgart University in 2020. He is currently working as a Research Associate at the Institute for Fluid Power Drives and Systems (ifas), RWTH Aachen University. His research areas include optimization of pneumatic systems focusing on energy efficiency and performance.



Olivier Reinertz received his diploma and his doctoral degree in mechanical engineering from RWTH Aachen University, Germany. He is currently Scientific Director at the Institute for Fluid Power Drives and Systems (ifas) at RWTH Aachen University. His research focuses on the model-based analysis of fluid power components and systems and the derivation and validation of innovative strategies for efficiency and performance optimization with an emphasis on compressed air and gas-powered systems.



Katharina Schmitz received a graduate's degree in mechanical engineering from RWTH Aachen University in 2010 and an engineering doctorate from RWTH Aachen University in 2015. She is currently the director of the Institute for Fluid Power Drives and Systems (ifas), RWTH Aachen University.

Influence of the Pressure-Viscosity Behavior of Different Base Oils on the Formation of Lubricating Films in Tribological Contacts

Sebastian Deuster, Achill Holzer, Katharina Schmitz

RWTH Aachen University, Institute for Fluid Power Drives and Systems (ifas), sebastian.deuster@ifas.rwth-aachen.de

Abstract.

Hydraulic fluids ensure power transmission and lubrication in hydraulic systems. The performance of hydraulic fluids primarily depends on their physical properties. The development of environmentally friendly hydraulic fluids has become more important. Depending on their chemical structure, these fluids have different physical properties, which influence the formation of load-bearing lubricating films in tribological contacts. In this paper, the influence of pressure-viscosity behavior on the formation of lubricating films in tribological contacts will be discussed by means of tribometric tests. For this purpose, hydraulic oils with different base oils are subjected to two test procedures. The tests are done for mineral oil based hydraulic oils (HLP) and biohydraulic oils based on synthetic esters (HEES). To determine the hydraulic fluids friction behavior, they are tested using a disc-on-disc tribometer. This test allows investigating the formation of load-bearing lubricating films of the oils. A comparison of the lubricant film formation at increasing rotational speeds is made. This allows evaluating the friction conditions and the influence of the oil's pressure-viscosity behavior based on Stribeck curves. To obtain a detailed statement on the formation of the lubricating film, tests are also carried out on a high frequency reciprocating rig (HFRR). The HFRR is an oscillating friction wear test, which provides information about the lubricity of fuels and lubricants.

Keywords. Biohydraulic oil, friction coefficient, load-lubricating film, pressure-viscosity behavior, synthetic ester, tribometer test, high-frequency reciprocating rig.

1. INTRODUCTION

The use of bio-based hydraulic oils is becoming more and more important due to increasing regulations regarding environmental protection. In some areas of application in which hydraulic systems are used, the utilization of biohydraulic oils is already regulated by law. For example, in forestry [1] or in shipping applications [2]. Other areas are expected to be affected by similar requirements in the future.

In addition to environmental benefits by using biohydraulic oils, the compatibility of the fluids used in the respective hydraulic system is of paramount importance for a safe and efficient operation of the respective machine. Furthermore, the physical properties of the hydraulic fluids used influence the operating behavior of the hydraulic components.

The properties and chemical structure of the base oil are decisive for the physical properties of hydraulic oils. The chemical composition of biohydraulic base oils differs from that of mineral oil based hydraulic fluids. Most hydraulic components, such as displacement pumps, have been developed with regard to the physical properties of mineral oil based fluids. A different behavior of biohydraulic oils can cause an insufficient formation of load-bearing lubricating films in tribological contacts for example in displacement pumps. In the worst case, this results in damage due to disproportionate wear. Experimental investigations in previous research works [3], detected higher leakage temperatures at the hydraulic pump when using biohydraulic oil instead of mineral oil, which indicates a less developed lubricating film in the tribological contacts.

In this paper, the influence of the pressure-viscosity behavior of different hydraulic oils on the formation of lubricating films in tribological contacts is analyzed. For this purpose, the performance of a synthetic ester (HEES) and a mineral oil based hydraulic oil (HLP) regarding the pressure-viscosity behavior is discussed by carrying out two test methods. The hydraulic oils are firstly subjected to a tribometer test in a disc-on-disc tribometer in which the conditions of real tribological contacts of hydraulic displacement units can be reproduced. Secondly, the wear and the lubricant film thickness is analyzed in a high frequency reciprocating rig (HFRR) at high contact pressures.

In previous research work dealing with the behavior of the tribological properties of biodegradable hydraulic oils, less practice-relevant contact conditions have been considered. The research of Castro [4] focused on the formation of tribological lubricating films in a pin-on-disc tribometer. Murakami [5] considered the tribological behavior of bio based hydraulic fluids using a four ball test. In this paper, contact mechanisms close to application are simulated with the help of a disc-on-disc tribometer, which increases the significance of the results for real powertrains of hydraulic displacement units.

The paper is structured as follows; first, the state of the art is described. For that, the fundamentals of lubrication film building will be described. Based on this, the influence of the different chemical structures of the base oils on the pressure-viscosity behavior is discussed. The two test methods are then presented and explained. The different test cycles are also described, as are the test parameters. The measurement results are then presented and analyzed. Particular attention is paid to analyzing the differences between the different hydraulic oils in terms of friction reduction and lubricant film formation. Furthermore, it will be discussed to which extend the results can be transferred to application-related hydraulic components and what influence they have on the operation of the respective components. Finally, the paper is concluded with a summary and an outlook on future research in this area.

2. STATE OF THE ART

Hydraulic fluids are important design elements in hydraulic systems. The specific properties of hydraulic fluids have a significant influence on the functionality, operational safety and environmental compatibility of hydraulic systems. In addition to the hydraulic power transmission, hydraulic fluids are subject to further function-maintaining tasks. One of the most important secondary tasks of hydraulic fluids is the reduction of friction and wear of components moving relative to each other. This is particularly important in components for power generation such as hydraulic displacement units. These contain highly stressed tribological contacts in which the surfaces are separated from each other by the hydraulic fluid.

The operating conditions and the loads imposed have a great influence on the friction-reducing behavior of hydraulic fluids. Viscosity is the most important physical property of hydraulic oils in terms of achieving a hydrodynamic or elastohydrodynamic lubricating (EHD) condition. It is a measure of the internal friction of the fluid.

According to Newton's law of friction (2.1), the shear stress τ formed between fluid layers is the product of the dynamic viscosity η and the shear rate S. [6]

$$\tau = \eta \cdot S \qquad (2.1)$$

The viscosity of hydraulic oils generally depends on various parameters, such as the shear gradient, temperature and pressure. For mineral oils and synthetic oils of comparable molecular masses, a Newtonian behavior is assumed. In this paper, the focus is on the viscosity-pressure behavior of hydraulic oils with different base oils.

2.1. Pressure-viscosity behavior

The oil's viscosity dependence on pressure can be explained based on its chemical structure. The branching and hydrocarbon chains, which move relative to each other, generate a resistance when sliding on each other, which represents the internal friction. If these chains are pressed closer together by applied pressure, a greater force is necessary to move them relative to each other. This means that the internal friction increases as the pressure rises. This applies to both mineral and synthetic oils. [7]

The first and still frequently used approach to describe the pressure-dependent viscosity is the exponential approach of Barus (2.2) [8]. The viscosity η_0 is obtained at a defined temperature under atmospheric pressure (p=0). α_0 is the pressure-viscosity coefficient, which will be discussed in more detail in the next chapter.

$$\eta(p) = \eta_0 \cdot \exp\left(\alpha_\eta \cdot p\right) \qquad (2.2)$$

Due to decreasing accuracy at very high pressures beyond approximately 5,000 bar, the Barus equation has been extended. In some approaches by various authors, the exponent of the Barus equation has been supplemented by potency and polynomial approaches [9]. A frequently used equation is the Roelands equation [10], which is often used to describe elastohydrodynamic contacts. In this paper, the Barus approach is considered because of its conciseness in the evaluations.

2.1.1. Pressure-viscosity coefficient

The pressure-viscosity coefficient described before is a fluid specific characteristic value and is mainly influenced by the composition (content of paraffin, naphthenic hydrocarbons and aromatics) of the base fluid. The added additives have a minor influence [11]. Since measured values for the coefficient are often not available, it is usually approximated. Pressure-viscosity coefficient estimates for ester-based and mineral oil-based are shown in **Table 2.1**. In general, the pressure-viscosity coefficient of mineral oils is higher than that of ester-based oils. This behavior was confirmed within the framework of the special research area 442 (SFB 442/German Research Foundation) [12] with the aid of a high-pressure viscometer.

The pressure-viscosity coefficient of a lubricant increases with increasing degree of branching and number of cyclic structures, presence of aromatics and increasing length of side chain branches. Naphthenic and paraffin-based mineral oils have extended branched chemical structures so that they interlock with increasing pressure, thus increasing the internal friction in the fluid. Ester molecules are composed of a flatter structure and have less extended branches, which causes a lower dependence on pressure. [13]

Table 2.1. Pressure-viscosity coefficient [14]

Oil type	Value	Unit
Paraffin-based mineral oils	$1.5 \ldots 2.4 \cdot 10^{-8}$	m^2/N
Naphten-based mineral oils	$2.5 \ldots 3.5 \cdot 10^{-8}$	m^2/N
Ester oils	$1.5 \ldots 2.0 \cdot 10^{-8}$	m^2/N

2.1.2. Previous investigations

Previous research also focused on the influence of the pressure-viscosity behavior of different base oils on the formation of lubricating films in tribological contacts. In [4] tests using a pin-on-disc tribometer showed an influence of the pressure-viscosity coefficient on the formation of the lubricating film. It was found that HEES formed a lubricating film of lower height compared to HLP, thus increasing the wear of the contact partners. [15] evaluated the wear of a hydraulic pump operated with the bio-based hydraulic oils HEES and HEPR compared to mineral oil. The best performance was achieved when tested with mineral oil, while a loss in efficiency could be identified when operating with HEES.

In this paper, the previous research work will be extended by different test procedures, which are presented in the following chapter.

3. TEST FLUIDS AND METHODS

In the following chapter, the test fluids and methods considered in this paper are presented, regarding setup, test properties and test evaluation.

3.1. Test Fluids

The test fluids of the investigations are a mineral oil based hydraulic oil (HLP) [16] and a biohydraulic oil based on a synthetic ester (HEES) [17]. The biohydraulic oil fulfils the

requirements of DIN 16807 [18]. The mineral oil tested contains zinc and is made of a paraffinic base oil. Some properties important for the investigations of the hydraulic oils are shown in Table **3.1**. Both hydraulic oils are of viscosity class ISO VG 49 according to DIN ISO 3448 [19].

Table 3.1. Fluid properties

Property	Mineral oil	Biohydraulic oil
Viscosity class [19]	46	46
Viscosity index (VI) [20]	105	190
Density (at 15 °C) [21]	875 kg/m³	920 kg/m³

3.2. Disc-on-disc tribometer

For tribological investigations, a disc-on-disc tribometer has been used. The tribometer represents an abstracted simulation of the contact mechanics of cylinder block/swash plate friction pairing. The comparability of the contact conditions of the tribometer used with those of hydraulic displacement units has already been investigated and confirmed in previous research work [22].

3.2.1. Setup and functions

Figure 3.1 shows a schematic drawing of the disc-on-disc tribometer. The type of tribometer test stand is also known as Siebel-Kehl tribometer [23]. The test rig consists of two test discs, stator and rotor, which are pressed onto each other. The corresponding pressure is generated by a hydraulic cylinder by initiating the compression force F_N. The rotor is driven by an electric motor at a rotational speed n and the torque M is transmitted to the stator. The corresponding torque is recorded at the stator with a torque sensor. The contact pair is operated in an oil bath whereby the contact surface is continuously supplied with oil. During the test, the oil bath temperature is regulated to a steady value. The tribometer was also used for investigations made in [24]. On optimization of the tribometer with regard to the avoidance of hysteresis during friction measurement was carried out within the work of [25].

The contact pairing consists of a hard-soft contact. The rotor is made of a 31CrMoV9 alloyed nitride steel. The stator is made of a non-ferrous metal with the designation CuZn40Al2Mn2Si. All counterparts have been lapped to a roughness of Ra 0.1.

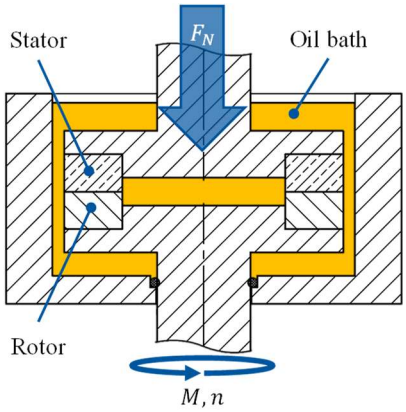

Figure 3.1. Disc-on-disc tribometer

The tribological measurement took place at an oil temperature of 60 °C, which was kept constant. Further technical parameters of the used test bench can be found in Table 3.2. The average contact diameter is 65 mm. The contact area is 1,021 mm² at a contact pressure of 1 MPa. During the test process, the rotational speed of 4,000 rpm is lowered until it comes to a standstill. The speed is reduced by 1 rpm per second. This makes it possible to reproduce a Stribeck curve of the test runs. Before the tests are carried out, the test specimens are run in at 1,000 rpm with a constant load of 1 MPa and 60 °C.

Table 3.2. Technical properties disc-on disc-tribometer

Parameter	Value	Unit
Mean contact diameter	65	mm
Area of contact	1,021	mm²
Friction track width	5	mm
Surface pressure	1	MPa
Rotational speed	0 to 4,000	1/min

3.2.2. Test evaluation

For evaluation, the frictional torque is recorded over the circumferential speed. This allows a Stribeck curve to be created and the frictional condition to be plotted as a function of speed. By plotting the friction coefficient, a statement can be made about the lubricity of the hydraulic oil.

3.3. High frequency reciprocating test (HFRR)

The test procedure using the high frequency reciprocating rig (HFRR) test is largely used to evaluate the lubrication properties of diesel fuels. The test is carried out according to the specifications of DIN EN ISO 12156-1 [26]. Due to the similar chemical structure of hydraulic oils and diesel fuels, the test method is used in this paper to identify the lubricity of hydraulic oils. The results obtained are analyzed with regard to the suitability of the test procedure according to [26] for evaluating the lubricating properties of hydraulic oils.

3.3.1. Setup and functions

Fig. 2 shows the test setup of the HFRR. An oscillating test ball with frequency f is pressed onto a stationary test plate under force F_G. The contact takes place in a temperature-controlled fluid bath. During HFRR testing, the machine's drive forces the ball to perform a sinusoidal movement.

The applied force creates a contact surface in the contact between the ball and the plate. Within this contact, a mixed friction condition occurs during the operation of the test rig. This means that solid contact occurs with simultaneous liquid friction. The proportion of the predominantly occurring friction condition depends on the lubricity of the respective lubricant. Among other effects, the formation of a load-bearing lubricant film is the decisive factor for the pressure viscosity behavior of the lubricant under investigation.

With the aid of the hertzian pressure theory, the contact pressure of the ball-on-disc contact can be calculated under steady-state contact conditions [27] The normal load induced by an attached 200 g weight creates a circular contact surface with a diameter of 67 µm. With (3.1), the maximum pressure of the ball disc contact can be calculated [6]. The force F_G applied to the contact amounts to 2.04 N. The two contact bodies are made of the steel ISO-683-17-100Cr6 [28]. The material-dependent characteristic values thus amount to a Poisson´s ratio ν of 0.3 and a modulus of elasticity E of 210,000 N/mm² [29]. This results in a maximum hertzian pressure of 835.68 N/mm². [30]

$$p_{max} = \frac{1}{\pi} \cdot \left[\frac{1.5 \cdot F_G}{r^2} \cdot \left(\frac{E}{1-\nu^2} \right)^2 \right]^{\frac{1}{3}} \qquad (3.1)$$

Due to the high loads on the contact, boundary friction occurs in the contact surface of the lubricated contact pair. This means that part of the load is carried by the lubricating fluid film, which is generated by hydrodynamic mechanisms. The other part is carried by solid contact of the test specimens.

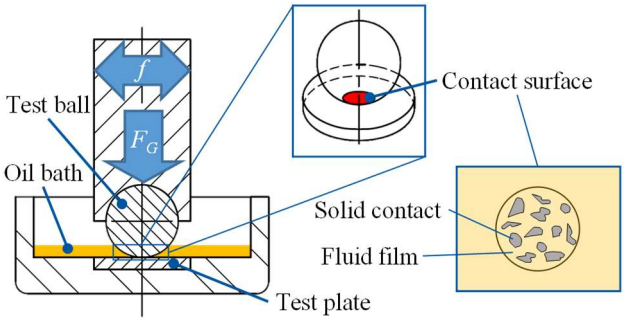

Figure 3.2. HFRR test setup

The test properties are chosen regarding DIN EN ISO 12156-1 (Table 3.3). The temperature of the oil bath is regulated to 60 °C during the testing process. The test fluid volume is 2 ml per fluid. The frequency of oscillation is 50 Hz, which results in a sliding speed of 0.05 m/s with a stroke length of 1 mm. The test procedure is carried out for 75 min for each run.

Table 3.3. Test setup HFRR

Parameter	Value	Unit
Oil temperature	60	°C
Fluid volume	2	mL
Frequency	50	Hz
Load	200	g
Stroke length	1	mm
Testing time	75	min

To analyze the lubricity of the fluid, the wear of the HFRR samples is determined after the tests have been carried out. For this purpose, the planar dimensions of the wear scar on the sample are recorded with an optical microscope. Then, the wear scar diameter (WSD) is calculated by averaging the length of the scar in sliding direction (y) and perpendicular (x) to it (3.2).

$$WSD = \frac{x+y}{2} \qquad (3.2)$$

4. TESTING RESULTS

In the following, the results of the tests executed are presented and discussed.

4.1. Disc-on-disc tribometer

4.1.1. Stribeck curves

To analyze the lubricity and the formation of a load-bearing lubricant film, the coefficient of friction μ is plotted against the rotational speed n, resulting in a so-called Stribeck curve. The coefficient of friction μ is calculated by dividing the frictional force F_R and the normal force F_N (4.1).

$$\mu = \frac{F_R}{F_N} \qquad (4.1)$$

Figure **4.1** shows the Stribeck curves of test runs in the disc-on-disc tribometer with HLP and HEES. The tests are recorded with a contact pressure of 1 MPa and at a regulated temperature at 60 °C. The tests were repeated three times to for every oil. The Stribeck curves obtained for all measurements of the different oils show in common the same trend. For this reason, two measurements are plotted as examples in Figure **4.1**.

The static friction (n≈0) when using HEES is significantly lower than when using HLP. This can be explained by the comparatively high polarity of the ester-based oil, which allows achieving a friction-reducing effect compared to HLP, especially in the boundary friction range. [31] When the speed is increased, the coefficient of friction drops significantly with HLP. With HEES, it drops less intensely. Thus, from 650 rpm, the coefficient of friction of HLP drops below that of HEES. From 2,750 rpm, both oils reach almost identical values again. All measurements taken show an abrupt reduction in coefficient of friction at 2,750 rpm, which makes it seem plausible that this is caused by factors related to the test

stand. In general, the Stribeck curve of HEES shows a much less pronounced trend than the curve of HLP. A notch point can be seen with the HEES from 2,300 rpm, but the coefficient of friction rises much more slowly (0.07 to 0.09) than with HLP (0.03 to 0.09). Which means that the fluid friction is much less developed by using HEES. The small difference between the coefficient of static friction and the coefficient of friction at high rotational speeds suggests that the contact pairing is operated in the mixed friction range for most of the test procedure. This indicates that the resulting lubricating film is smaller than when using HEES.

A possible explanation for this behavior is the lower pressure-viscosity coefficient of HEES. Especially at the high stressed roughness peaks, this can lead to solid body contact due to lower lubricant film thickness, which leads to a correspondingly higher coefficient of friction. Ongoing research underline this statement. This relationship is to be further investigated by the HFRR tests.

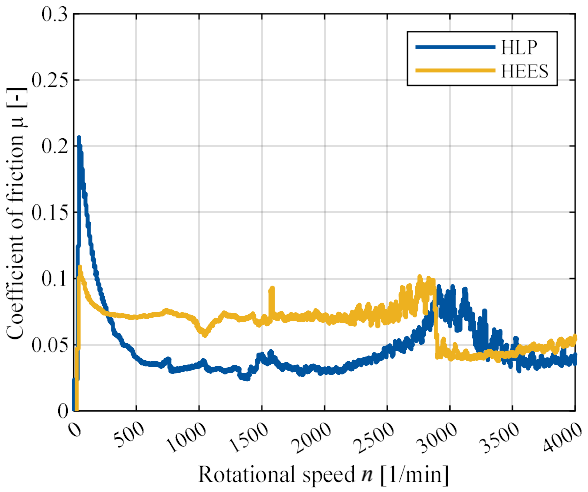

Figure 4.1. Stribeck curve at 1 MPa

4.2. High frequency reciprocating test (HFRR)

4.2.1. Wear scar diameter (WSD)

The WSD was determined over all tests carried out in accordance to [26]. For each fluid, five tests were performed. **Figure 4.2** shows the mean values of the wear calotte in x and y (sliding direction) coordinate and the respective standard deviations. The attached table shows the mean value for the WSD for the two hydraulic oils. The investigations show that in x and y direction, the wear area is larger when using HLP than when using HEES. On average, the wear area is about 15 % larger with HLP.

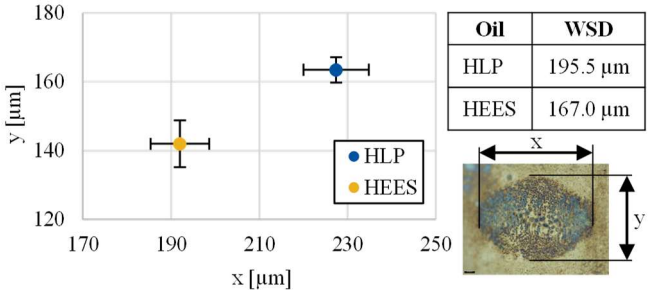

Figure 4.2. Wear scar diameter (WSD) with standard deviations

4.2.2. Wear examination

Following the test evaluation according to [26], the test specimens were examined under a 3D light microscope. For this purpose, the wear calotte was scanned 3-dimensionally and then the curvature was unwound and displayed as a flat surface. This makes it possible to display and analyze the surface profile of the test specimens. Figure **4.3** shows the surface profile of an HFRR test ball carried out with HLP and HEES. The geometry was recorded over a length of 130 µm in sliding direction. This is the area of greatest wear. In the adjacent areas, the wear is significantly less and mainly discoloration can be seen. Measurements were taken with a width of 20 µm and the mean value was calculated.

The contour of the resulting dome is similar when using both oils. An elliptical wear pattern is created with the long side in direction of the sliding movement. Three light-colored stripes can be seen in the center of the wear dome of the HEES test ball. All test specimens considered showed a similar pattern of wear. When observing this area under the 3D microscope, a significantly increased material removal could be detected in this area. This indicates an insufficiently formed lubricating film, which leads to solid body contact and increased wear. These grooves have a depth of up to 0.374 µm in relation of the ideal spherical shape (HLP: 0.254 µm). Beyond this significant wear in the center of the dome, less wear and abrasion can be observed on the rest of the dome when using HEES compared to HLP. In this area surrounding the contact point, which is subject of significantly lower loads, the higher viscosity of HEES due to the higher VI leads to an improved friction reduction compared to HLP, which may explain lower wear in this area.

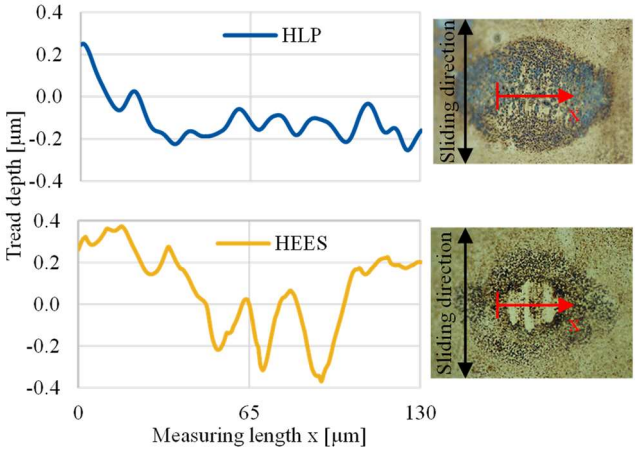

Figure 4.3. Wear contour ball HFRR

In addition, the discs used in the test were measured with the 3D light microscope. This procedure was also carried out by [30] in order to better describe the influence of diesel fuels. For this purpose, the surface profile of the worn area was recorded as in the previous investigations for the ball. Figure **4.4** shows the wear tracks for HLP and HEES as well as the surface profile transverse (x) to the sliding direction in the middle of the worn area. The disc operated with HLP is clearly more discoloured, which can possibly explained by different surface-active additives. When looking at the surface contour, it can be seen that contour with HLP has generally a deeper wear track than the disc operated with HEES. Furthermore, it can be seen that the wear contour of HLP is smoother than that of HEES, where some peaks can be seen, which can explain the groves that have formed in the ball.

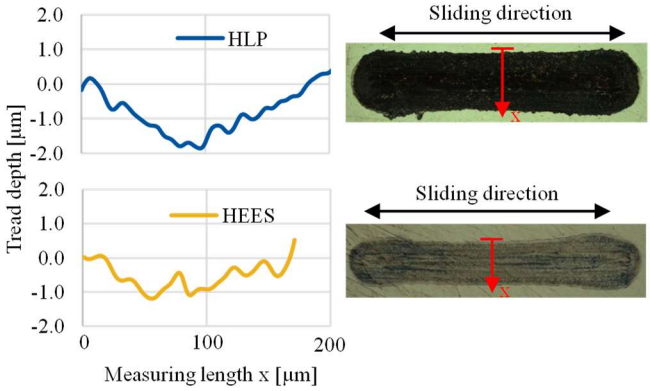

Figure 4.4. Wear contour disc HFRR

In general, the WSD results and the surface contours show contradictory results with regard to the wear properties of the fluids. On the one hand, the WSD of HEES is smaller than that of HLP. On the other hand, the test specimens of HEES show deep grooves of wear. In general, differences in the wear behaviour between the different fluids can be identified, so that the suitability for the wear testing of hydraulic fluids with the HFRR test method is

given. The extensive evaluation of the test with hydraulic oils represents a potential for further research work.

5. CONCLUSION AND OUTLOOK

The research carried out shows differences in the formation of load-bearing lubricating films between mineral oil based and ester-based lubricating films. Both the investigations in the disc-on-disc tribometer and the high frequency reciprocating (HFRR) test show differentiated results with respect to friction and wear of the two hydraulic oils considered.

Based on the results of the disc-on-disc tribometer test, an increased coefficient of friction was determined when using HEES compared to HLP. In the speed range between 600 and 2,300 rpm, the maximum coefficient of friction is 40 % higher than that of HLP. Furthermore, the flat course of the Stribeck curve of the HEES indicates that the contact pair is driven at boundary friction. For this reason, a possible explanation can be that the HEES formed a thinner lubricating film during investigations in the tribometer. In conclusion, the contact pair was operated in mixed friction over a wide speed range, whereas the formation of a hydrodynamic lubricating film can be identified from the measurement data when using HLP.

The results of the HFRR test showed that the use of HEES results in the formation of a 15 % smaller wear area (WSD) than with HLP. Further investigations using a 3D microscope showed that there is significantly deeper wear locally in the center of the dome of the ball, while using HEES. The grooves formed were almost twice as deep as with the use of mineral oil. A possible explanation for this could be the formation of an insufficient lubricating film due to the lower pressure viscosity dependence of the ester.

In general, it can be summarized that synthetic ester have different lubricating properties in relation to mineral oils. This must be taken into account especially when designing a hydraulic oil for use in systems in order to ensure safe and long-term failure-free operation. This leads to different friction conditions and challenges, especially in tribological contacts of hydraulic displacement units.

Subsequent research will relate to the influence of the results shown on the operation of hydraulic displacement units. Possible wear and losses occurring when using ester-based hydraulic oils will be analyzed. In addition to attributes during operation such as efficiency and heat emission, another necessary consideration is the service life and wear of the displacement units due to lubricant film formation in the tribological contacts. Furthermore, it is planned to increase the contact pressure during the disc-on-disc tribometer tests and to evaluate the influence on mineral oil based and ester-based hydraulic oils. These studies help to determine the performance characteristics of bio-based hydraulic oils identify possible development potential and make hydraulic systems more sustainable.

6. REFERENCES

[1] FSC Deutschland – Verein für verantwortungsvolle Waldwirtschaft e.V. *Deutscher FSC-Standard: Version 3-0;* FSC Deutschland – Verein für verantwortungsvolle Waldwirtschaft e.V.: Freiburg, **2018.** https://www.fsc-deutschland.de/preview.fsc-waldstandard-3-0.a-1208.pdf.

[2] Vessel General Permit for Discharges Incidental to the Normal Operation of a Vessel. In: *Federal Register*, **December 19, 2018**; Vol. *78*; pp. 1–8.

[3] Deuster, S.; Schmitz, K. Bio-Based Hydraulic Fluids and the Influence of Hydraulic Oil Viscosity on the Efficiency of Mobile Machinery. *Sustainability*, **2021**, *13,* 7570.

[4] Castro, R.d.M.; Curi, E.I.M.; Inácio, L.F.F.; Da Rocha, A.S. Analysis of the tribological performances of biodegradable hydraulic oils HEES and HEPR in the sliding of Cu–Zn/WC–CoCr alloys using the Stribeck curve. *J Braz. Soc. Mech. Sci. Eng.*, **2020**, *42,* 1–20.

[5] Murakami, T.; Sakamoto, H. Lubricating properties of vegetable oils and paraffinic oils with unsaturated fatty acids under high-contact-pressure conditions in four ball tests. *J. Synth. Lubr.*, **2003**, *20,* 183–201.

[6] Czichos, H. *Tribologie-Handbuch;* Springer Fachmedien: Wiesbaden, **2010**.

[7] Mang, T.; Dresel, W., Eds. *Lubricants and lubrication;* Wiley-VCH: Weinheim, Germany, **2017**.

[8] Barus, C. Isothermals, isopiestics and isometrics relative to viscosity. *American Journal of Science*, **1893**, *s3-45,* 87–96.

[9] Blume, J. Druck- und Temperatureinfluß auf Viskosität und Kompressibilität von flüssigen Schmierstoffen: Lehrstuhl und Institut für Maschinenelemente und Maschinengestaltung, Aachen, Techn. Hochsch., Diss., 1987: Aachen, **1987**.

[10] Roelands, C. *Correlational aspects of the viscosity-temperature-pressure relationship of lubricating oils*, **1966**.

[11] Klamann, D. *Schmierstoffe und verwandte Produkte: Herstellung, Eigenschaften, Anwendung. Unter Mitarb. von;* Verl. Chemie: Weinheim usw. Basel, **1982**.

[12] Murrenhoff, H. *Umweltverträgliche Tribosysteme: Die Vision einer umweltfreundlichen Werkzeugmaschine;* Springer-Verlag Berlin Heidelberg: Berlin, Heidelberg, **2010**.

[13] Totten, G.E.; Shah, R.J.; Forester, D.R., Eds. *Fuels and Lubricants Handbook: Technology, Properties, Performance, and Testing, 2nd Edition;* ASTM International: 100 Barr Harbor Drive, PO Box C700, West Conshohocken, PA 19428-2959, **2019**.

[14] Niemann, G.; Winter, H.; Höhn, B.-R.; Stahl, K. *Maschinenelemente 1: Konstruktion und Berechnung von Verbindungen, Lagern, Wellen,* 5th ed.; Springer Vieweg: Berlin, Heidelberg, **2019**.

[15] Majdan, R.; Tkáč, Z.; Kosiba, J.; Abrahám, R.; Jablonický, J.; Hujo, Ľ.; Mojžiš, M. Evaluation of tractor biodegradable hydraulic fluids on the basis of hydraulic pump wear. *Res. Agr. Eng.*, **2013**, *59,* 75–82.

[16] DIN Deutsches Institut für Normung e.V. *Pressure fluids - Hydraulic oils - Part 1: HL hydraulic oils, Minimum requirements;* Beuth Verlag GmbH: Berlin, **2017**.

[17] DIN Deutsches Institut für Normung e.V. *Schmierstoffe, Industrieöle und verwandte Produkte (Klasse L) – Familie H (Hydraulische Systeme) – Anforderungen für die Kategorien HETG, HEPG, HEES und HEPR (ISO 15380:2011);* Beuth Verlag: Berlin, **03.2012**.

[18] DIN Deutsches Institut für Normung e.V. *Flüssige Mineralöl-Erzeugnisse – Bio-Schmierstoffe – Kriterien und Anforderungen für Bio-Schmierstoffe und biobasierte Schmierstoffe (EN 16807);* Beuth Verlag: Berlin, **12.2016**.

[19] DIN Deutsches Institut für Normung e.V. *Flüssige Industrie-Schmierstoffe – ISO-Viskositätsklassifikation (ISO 3448:1992);* Beuth Verlag GmbH: Berlin, **2010**.

[20] DIN Deutsches Institut für Normung e.V. *Mineralölerzeugnisse Berechnung des Viskositätsindex aus der kinematischen Viskosität;* Beuth Verlag GmbH: Berlin, **2004 (Accessed** May 15, 2021).

[21] DIN Deutsches Institut für Normung e.V. *Bestimmung der Dichte: U-Rohr-Oszillationsverfahren;* Beuth Verlag GmbH: Berlin, **1997 (Accessed** March 14, 2022).

[22] Holzer, A.; Reetz, B.; Münch, T.; Schmitz, K. Experimentelle Untersuchungen zum Einlaufverhalten bleifreier Sondermessinglegierungen. *TuS*, **2022**, *69,* 16–32.

[23] Kehl, B.; Siebel, E. Untersuchungen über das Verschleißverhalten der Metalle bei gleitender Reibung. *Archiv für das Eisenhüttenwesen*, **1936**, *9,* 563–570.

[24] Stephan, K.; Holzer, A.; Megahed, S.; Ziegler, S.; Schleifenbaum, J.H.; Schmitz, K. Investigation of the coating of hydrodynamic plain bearing contact surfaces by means of Extreme High-Speed Laser Material Deposition (EHLA). *IOP Conf. Ser.: Mater. Sci. Eng.*, **2021**, *1097,* 12016.

[25] Holzer, A.; Schmitz, K. *Optimization of a disc-disc tribometer to avoid hysteresis during friction measurements:* Wien, **2019**.

[26] DIN Deutsches Institut für Normung e.V. *Diesel fuel – Assessment of lubricity using the high-frequency reciprocating rig (HFRR): Part 1: Test method (ISO 12156-1:2018);* Beuth Verlag GmbH: Berlin, **2018 (Accessed** February 7, 2022).

[27] Hertz, H. Ueber die Berührung fester elastischer Körper. *Journal für die reine und angewandte Mathematik (Crelles Journal)*, **1882**, *1882,* 156–171.

[28] DIN Deutsches Institut für Normung e.V. *Für eine Wärmebehandlung bestimmte Stähle, legierte Stähle und Automatenstähle - Teil 17: Wälzlagerstähle (ISO 683-17:2014); Deutsche Fassung EN ISO 683-17:2014;* Beuth Verlag GmbH: Berlin, **2015 (Accessed** March 7, 2022).

[29] Böge, A. *Technische Mechanik: Statik, Dynamik, Fluidmechanik, Festigkeitslehre ; mit 15 Tabellen, 22 Arbeitsplänen, 15 Lehrbeispielen und 40 Übungseinheiten,* 28th ed.; Vieweg + Teubner: Wiesbaden, **2009**.

[30] Weinebeck, A. *Einfluss der Schmierfähigkeit von Biokraftstoffen auf den Verschleiß in hoch belasteten Kontakten;* RWTH Aachen University, **2019**.

[31] Fatemimoughari, A. *Analysis of tribological properties for the design of synthetic biofuels;* Shaker: Aachen, **2012**.

Biographies



Sebastian Deuster received the bachelor's degree in mechanical engineering, specialising in energy technology from the University of Applied Sciences of Aachen in 2016. In 2018, he received the master's degree in product development in the field of mechanical engineering, also from Aachen University of Applied Sciences. He is currently working as a research associate at the Institute for Fluid Power Drives and Systems of RWTH Aachen University. His research interests include the testing of alternative and biobased lubricants in hydraulic applications.



Katharina Schmitz received a graduate's degree in mechanical engineering from RWTH Aachen University in 2010 and an engineering doctorate from RWTH Aachen University in 2015. Since 2018 she is the director of the Institute for Fluid Power Drives and Systems (ifas), RWTH Aachen University.

Topology optimization of fluid cooling systems for machine tools

Christoph Steiert[1*], Juliane Weber[1], Jürgen Weber[1]

[1]Chair of Fluid-Mechatronic Systems, Technische Universität Dresden, 01069 Dresden Germany
**Corresponding author: Christoph.Steiert@tu-dresden.de*

Abstract.

Fluid cooling systems for machine tools commonly operate with a constant speed drive pump and manual valves. The volume flow rate for cooling the components is set to a fixed value during commissioning and is not changed by the user during operation. Recent research proposes temperature control for machine tools. This requires variable speed drive pumps or proportional valves. A major obstacle to implementing such a system are material costs. This paper presents a method for designing such a system with minimal costs.

Keywords. optimization, machine tools, cooling systems, compensation, variable speed pumps, simulation, temperature (field), cost

1. INTRODUCTION

Usage of machine tools is indispensable especially for cutting, drilling and grinding. Therefore, they are widely spread in machine parks. In recent years' industry requests high quality production and higher productivity. Machine tools can meet the high demands, but during operation, heat is introduced to the machine tool. [1] mentions, that 75% of all geometric errors of machined workpieces can be attributed back to temperature variation of the machine.

Main heat sources in machine tools are spindles, linear drives, bearings and auxiliary units. Preventing the heat from spreading inside the machine tool, cooling circuits are installed. They absorb the heat near the source or prevent critical parts from varying temperature. When investigating the power,consumption of cooling and cooling lubricant systems, it is,observable that these systems consume about 45% of the overall electrical energy [2]–[4].

Various approaches to reducing energy consumption are being discussed in the scientific community. In projects such as EWOTek [2] optimization of components and load-dependent strategies for drives or the cooling unit are carried out. NCplus [3] investigates control strategies for the cooling unit besides other components and the NC control strategies.

Further approaches discuss load-dependent volume flow rate control for cooling channels in the machine tool. Kung-Ying Li et al. [5] focuses on the load-dependent supply of the main spindle. They investigate the deformation of the spindle depending on the temperature

difference of the cooling fluid, the spindle and the state of the cooling aggregate. In [6] different structures of the cooling system are shown. Here, each cooling circuit in the machine tool is controlled regarding the amount of coolant provided. This control strategy is enabled with variable speed drive pumps and/or proportional valves. In the system topology proposed by [6] each cooling circuit has its own actuator. For complex machine tools e. g. DMU 80 eVo by DMG, this leads to a large number of pumps or valves.

For installing a load-dependent cooling system with varying cooling fluid supply and low installation costs, it is necessary to identify cooling circuits that can be supplied by the same actuator. For this task, optimization algorithms are useful tools. In case of the topology of the cooling system a mixed-integer non-linear problem has to be solved. Related work can be found in [7], [8]. These works describe the optimization of the water distribution system of multi-storey buildings that need to be supplied with fresh water. This involves the use of different kind of pumps to optimize the overall costs.

2. SYSTEM DESCRIPTION

In this section the tempering system used for cooling the machine tool frame is described. First the system design and afterwards the physical behavior of the components are described.

2.1. Cooling system for a machine tool frame

Aim of the test rig is the evaluation of load dependent cooling structures. The system design of the tempering unit can be seen in Fig. 1. The tempering unit consists of ten centrifugal variable speed drive pumps (Wilo-Yonos PICOSTG 15/1-13-180) commonly used in heating systems of buildings. They generate the volume flow rate through each circuit. Sensors measure the physical quantities volume flow rate, pressure and temperature. They can be used to evaluate the state of the tempering unit. Seven of the ten fluid circuits pass through a machine tool frame in order to temper it. The other three circuits are bypasses and are only used to change the temperature of the fluid without passing it through the machine tool frame. The fluid temperature can be controlled with two different units. The first is a liquid-air cooling system called FLKS 5 EC from Hydac. The system is driven by a fan that passes air through a heat exchanger and cools the fluid to ambient temperature. The heat transfer capacity can be controlled by the speed of the fan. The 2nd system is a instantaneous water heater with a connected load of 2kW. It allows to raise the temperature of the fluid up to 35 ◦C. The fluid used is water-glycol with a ratio of 70% to 30%.

The machine tool frame used at the test rig is built by Framag Industrieanlagenbau GmbH. It consits of a steel hull that is poured with Hydropol. Hydropol is a special filling material designed to have better damping behavior than conventional mineral cast. For temperature monitoring, 30 PT100-sensors are integrated. Seven fluid circuits are installed inside of the machine tool frame to control the temperature. There are three types of fluid circuits: The circuit located on the floor is the longest, it has a length of 18 965mm. It is installed as a spiral, where flow and return running in parallel. The task of this fluid circuit is to thermally decouple the machine tool frame from the cold foundation. The two fluid circuits, called guiding have a length of 3656mm. Their function is to dissipate heat introduced by hot chips

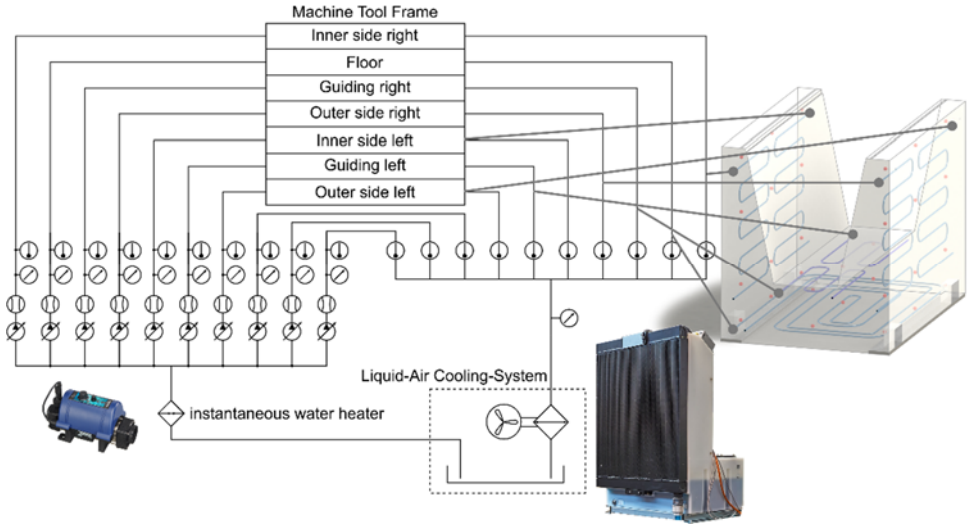

Figure 1. System design of the tempering unit

from the machine tool frame. For this purpose, the fluid circuits are placed in a meander under the collecting area. The remaining four fluid circuits have a length of 7105mm each

and are located in the sides of the machine tool frame. Their purpose is to minimize effects of environmental conditions such as solar radiation or changes in ambient temperature. Because of the usage of the machine tool frame as a demonstrator without production purpose, artificial heat sources are installed. In the area of the guiding, 20 heat mats with a power of up to 45W each are used. Second, there is an infrared light with a power of 1kW.

2.2. Mathematical description

A mathematical description of the system is given in the following section. It forms the basis for the optimization problem shown in section III.

To describe the heat flow ˙Q dissipated from the machine tool the following equation can be used

$$\dot{Q} = \dot{V} \cdot c_p \cdot \rho \cdot (T_{\text{return}} - T_{\text{flow}}). \quad (1)$$

The volume flow rate ˙V is measured with the integrated sensors. The specific heat capacity $c_p = 3849\,\text{J/kgK}$ and the density $\rho = 1044\,\text{kg/m}^3$ are material dependent properties. Both quantities are assumed to be temperature independent in the investigated range. The temperature difference $(T_{\text{return}} - T_{\text{flow}})$ between return and flow can also be measured with the installed sensors. The heat flow introduced by pressure losses is neglected. In addition to the heat flow transported by the tempering system, volume flow rate and pressure are important quantities because they determine the power consumption of the pumps. Calculating the pressure losses Δp depends on the volume flow rate ˙V of the cooling circuit and the hydraulic resistance R

$$\Delta p = R \cdot \dot{V}^2. \quad (2)$$

The resistance R of each fluid circuit is calculated from measurements and given in Table 1. With pressure losses and volume flow rate of each circuit it is possible to interpolate the necessary rotational speed of the pump, with the given diagram 2. A second diagram helps to calculate the power consumption of each pump.

Table 1: Hydraulic resistances of fluid circuits

Name	**Hydraulic Resistance in $\frac{\mathbf{kg}}{\mathbf{m^7}}$**
R_1	$9.6 \cdot 10^{11}$
R_2	$1.59 \cdot 10^{12}$
R_3	$6.9 \cdot 10^{11}$
R_4	$9.8 \cdot 10^{11}$
R_5	$8.9 \cdot 10^{11}$
R_6	$5.2 \cdot 10^{11}$
R_7	$1.05 \cdot 10^{12}$
R_8	$4.7 \cdot 10^{11}$

3. OPTIMIZATION MODEL

The optimization problem has to scenarios for that it is solved. The two scenarios chosen in this problem describe he active times of the heating elements during one day: The heating mats are active from 6:30 am till 9:00 pm. In addition, the infrared light is active from 12:00 pm till 3:00 pm. Scenario 1 lasts from 6:30 am to 12:00 pm and 3:00 pm to 9:00 pm. In total the duration of scenario 1 is 11.5 h. Scenario 2 lasts from 12:00 pm to 3:00 pm, with heating mats and infrared light active, and lasts 3.0 h. The loads are based on a two shift system. For implementing the optimization problem, a set of constant parameters will be used.

C_{elec}	Electricity price 0.19 €/kWh
P_i	Set of pumps $i \in \{1,2,3,4,5,6,7\}$
T_S	Temporal share of scenario $S \in \{1,2\}$
d	Work days per year $d = 250$ d
y	Number of years $y = 5$ years
S	Set of scenarios
C_{acq}	Acquisition costs per pump 250 €
R_j	Hydraulic Resistance of each fluid circuit

Besides these constant parameters, there are also two types of variables. First, those that are controlled by the solver of the optimization problem, and second, variables that contain physical quantities.

$x_i = \{0,1\}$	If pump i is used $x_i = 1$ otherwise $x_i = 0$
$x_{i,j} = \{0,1\}$	If pump I is connected to fluid circuit j $x_{i,j} = 1$ otherwise $x_{i,j} = 0$
$n_{i,S} \geq 0$	Rotational speed of pump i
$\dot{Q}_{cool\ j,S} \geq 0$	Necessary heat flow for fluid circuit j during scenario S
$P_{elec\ i,S} \geq 0$	Necessary electrical power of pump I during scenario S
$\dot{V}_{i,S} \geq 0$	Volume flow rate of pump I during scenario S
$p_{i,S} \geq 0$	Pressure head of pump I during scenario S
$R_i \geq 0$	Hydraulic resistance seen from pump i

3.1. Cost function

For solving the optimization problem, a cost function has to be implemented. The solver tries to minimize the cost function. For our problem the cost function is

$$\mathrm{C} = \sum_{i=1}^{7} (x_i \cdot C_{\mathrm{acq}}) + \sum_{S=1}^{2} \sum_{i=1}^{7} \left(P_{\mathrm{elec}\,i,S} \cdot T_S\right) \cdot d \cdot y \cdot C_{\mathrm{elec}}. \tag{3}$$

and returns a value in €. Equation (3) can be separated into two parts. The first part describes the acquisition costs for all necessary pumps. The second part gives the cost that occur during operation for y years. Here the energy consumption is for each scenario is calculated and multiplied with energy costs C_{elec}.

3.2. Constraints

Constraints describe the suitable range where the solver searches for a solution. They are designed specifically and need to be adapted for other topologies. In the following, some constraints are listed that describe the structural design of the fluid system:

$$\sum_{i=1}^{7} \mathrm{x_i} \leq 7 \tag{4}$$

$$\mathrm{x_{i,j}} \leq x_i \qquad \forall i \in \{1, \dots, 7\}, j \in \{1, \dots, 7\} \tag{5}$$

$$\sum_{i=1}^{7} x_{i,j} = 1 \qquad \forall j \in \{1, \dots, 7\} \tag{6}$$

$$\sum_{i=1}^{7} \sum_{j=1}^{7} \mathrm{x_{i,j}} = 7 \tag{7}$$

$$\mathrm{x_i} \leq \sum_{j=1}^{7} x_{i,J} \qquad \forall i \in \{1, \dots, 7\}. \tag{8}$$

The meaning of (4) is that in the optimal topology no more than seven pumps are used. Equation (5)ensures that the connection between pump i and fluid circuit j is active only when pump i is purchased. Otherwise, the connection must be inactive. Equation (6) defines that each fluid circuit is supplied by exactly one pump. In (7), the behavior is implemented that there are exactly seven connections between pumps and fluid circuits. To ensure that each pump supplies at least one fluid circuit, (8) is used. Besides these structural design constraints, it is necessary to develop some constraints that help to model the physical behavior of the system. It is necessary to calculate the electrical power of the pumps, which is needed for the cost function (3). To calculate the electrical power, pressure and volume flow rate must be known. The necessary volume flow rate for each fluid circuit is obtained by (1). Here, two assumptions are made. First, the temperature difference ($T_{\mathrm{return}} - T_{\mathrm{flow}}$) is constant at 0.4 K. This assumption is based on measurements performed at the test rig. The second assumption is a constant heat flow that is transported out of the machine tool frame by each fluid circuit. The heat flow is given in Table. 2.

Table 2: Heat Flow in W transferred out of the machine tool frame when heating elements are active

Fluid circuit	**Heating mat active**	**Infrared light active**
Inner side right	20	400
Floor	20	0
Guiding right	250	20
Outer side right	20	80
Inner side left	20	400
Guiding left	250	20
Outer side left	20	80

The rearranged equation (1) using the defined variables above gives the total volume flow rate that pump i must deliver during scenario S

$$\dot{V}_{i,S} = \frac{1}{c_p \cdot \rho \cdot (T_{\text{return}} - T_{\text{flow}})} \sum_{j=1}^{7} \dot{Q}_{\text{cool } j,S} \cdot x_{i,j}. \tag{9}$$

With the volume flow rate known, the pressure head $p_{i,S}$ of each pump can be calculated with help of (2). The hydraulic resistance R_i is the parallel circuit connected to pump i. It is calculated through:

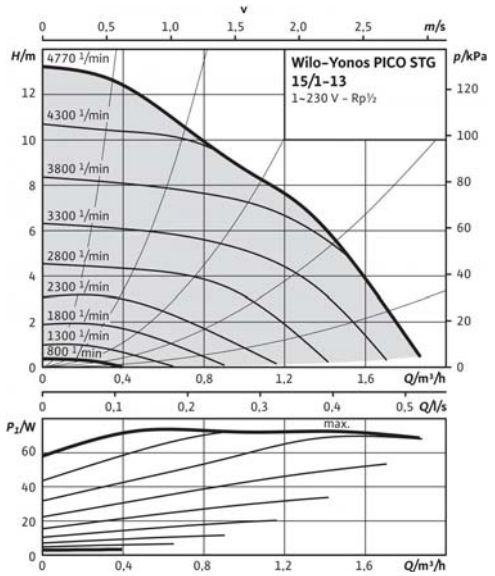

Figure 2: Diagram for pressure, volume flow rate, rotational speed and power of WIlo Yonos PICO STG 15/1-13

$$\frac{1}{\sqrt{R_i}} = \sum_{j=1}^{7} \frac{1}{\sqrt{R_i}} \cdot x_{i,j}. \tag{10}$$

The pressure head is now given by

$$\mathrm{p_{i,S}} = R_i \cdot \dot{V}_{i,S} + R_8 \cdot \sum_{i=1}^{7} \dot{V}_{i,S} \cdot x_i. \tag{11}$$

The first part of (11) represents the pressure loss of the parallel circuit supplied by pump i. The second part $\mathrm{R_8} \cdot \sum_{i=1}^{7} \dot{V}_{i,S} \cdot x_i$represents the pressure loss of the common used elements like the liquid-air cooling system.

Knowing pressure $p_{i,S}$ and volume flow rate $\dot{V}_{i,S}$, interpolation of the rotational speed $n_{i,S}$ of pump i is possible. The diagram is shown in the upper part of. 2. In the lower part of this figure, the relationship of volume flow rate $\dot{V}_{i,S}$, rotational speed $n_{i,S}$ and power consumption $P_{elec\,i,S}$ of pump i is given. With all these constraints in mind, it is possible to solve the mixed integer non-linear programming problem. The problem is mixed-integer because there are variables as x_i or $x_{i,j}$ that are integers, but there also exist variables being continuous, e.g. power consumption $P_{elec\,i,S}$. The problem is non-linear because of equations like (2).

3.3. Solving the problem

Having established the optimization problem, it has to be solved. For this purpose, the Yalmip Matlab Toolbox [9] is used. This toolbox delivers a method to implement the problem in a proper way and provides a variety of solvers. In this case the solver is called ”BMIBNB” and comes with the Yalmib toolbox. This algorithm is an implementation of the branchand-bound method [10] for the integer part of the optimization. The result of the optimization is a known relation between pump and fluid circuit as well as total cost of purchasing and operating the pumps. The optimization is done for a period of five years. The result is

$$\mathrm{x_i} = \begin{pmatrix} 1 \\ 1 \\ 1 \\ 1 \\ 0 \\ 0 \\ 0 \end{pmatrix} \tag{12}$$

and

$$\mathrm{x_{i,j}} = \begin{pmatrix} 0 & 0 & 1 & 1 & 0 & 0 & 0 \\ 0 & 0 & 0 & 0 & 0 & 1 & 1 \\ 1 & 1 & 0 & 0 & 0 & 0 & 0 \\ 0 & 0 & 0 & 0 & 1 & 0 & 0 \\ 0 & 0 & 0 & 0 & 0 & 0 & 0 \\ 0 & 0 & 0 & 0 & 0 & 0 & 0 \\ 0 & 0 & 0 & 0 & 0 & 0 & 0 \end{pmatrix}. \tag{13}$$

From (12), one can see that we must use four pumps for an cost-optimal system. The connection between pump i and fluid circuit j is given in (13). For example, the first row shows, that pump 1 is connected to fluid circuits 3 and 4. They represent guiding right and outer side right. Pump 2 supplies fluid circuits 6 and 7. Fluid circuit 6 is the guiding on the left side and fluid circuit 7 is for the outer side left. The inner side right and the floor, displayed with fluid circuits 1 and 2 are supplied by pump 3. This information is contained in row 3. The last pump is connected to fluid circuit 5, inner side left only. Rows five to seven contain only 0, so no connection from pumps 5, 6 and 7 to any fluid circuit is established. For x_i and $x_{i,j}$ all constraints mentioned in (4) to (8) are fulfilled. The result for the cost function (3) is 1325.14 €. The costs can be separated in purchasing costs with a value of 1000.00 € and energy costs of 325.14 €.

Besides the decision variables x_i and $x_{i,j}$, and the value of the cost function the optimization delivers e.g. rotational speed of pumps, pressure, volume flow rate and electrical power. These data can be used for further investigations.

4. SIMULATION MODEL

This section covers the simulation of the optimized topology of the cooling system and compares it with a cooling system consisting of seven pumps

4.1. Description of the model

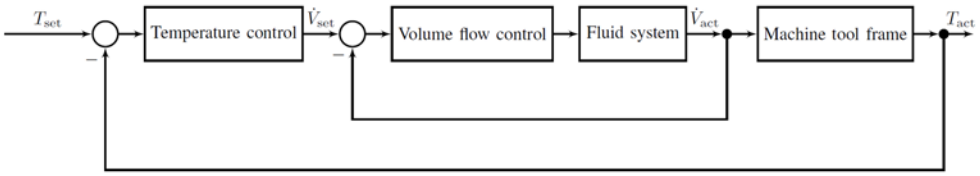

Figure 3: Schematic diagram of the control structure

The simulation model is implemented in Matlab/Simulink R2021a. It consists of a cascaded control loop where the machine tool frame is the plant. Fig. 3 shows the structural design. It is a cascaded controller with a fast volume flow rate control and a slower temperature control. Thus, this system design takes the different time constants between the fluid and the thermal system into account. In analogy, the plant is separated. One part is used to simulate the fluid system with calculation of volume and heat flow through the fluid. The second part is a thermal model of the machine tool frame. For this purpose, the machine tool frame is divided into seven regions according to the fluid circuits. It is implemented as a linear multi-input-multi-output system. Therefore to describe the machine tool frame, 49 transfer functions are necessary. They are based on measurements [11].

Both plants are coupled through the heat flow transported out of the machine tool frame. The heat flow is calculated using (1). However, since the temperature in the return depends on the wall temperature in the machine tool frame, it is given by:

$$T_{\text{return}} = T_{\text{wall}} \cdot \left(1 - \exp\left(-\frac{k}{c_p \cdot \rho \cdot \dot{V}}\right)\right) + T_{\text{flow}} \cdot \exp\left(-\frac{k}{c_p \cdot \rho \cdot \dot{V}}\right) \tag{14}$$

with

$$k = \pi \cdot L \cdot \left(\frac{1}{\alpha_i \cdot d_i} + \frac{1}{2 \cdot \lambda} + \frac{1}{\alpha_o \cdot d_o} \right)^{-1}. \quad (15)$$

The wall temperature T_{wall} comes from the thermal model of the machine tool frame. k contains geometrical and physical information. L is the length of the pipe with an inner diameter d_i and an outer diameter do. The heat transfer coefficients α_i and α_o indicate the capability to transfer heat from the fluid to the steel pipe and from the steel pipe to the machine tool frame. The thermal conductivity λ describes the ability to transfer heat through the wall of the pipe.

4.2. Simulation results

The simulated time is two days. Starting at 0:00 h the first load is applied at 06:30 h when the heat mats are activated with a thermal load of 30 W each. At 12:00 h the infrared light is switched on with a power of 1 kW for three hours. The heat mats are shut down at 21:00 h. This procedure repeats on the second day of the simulation. During the whole time the fluid cooling system is active and supplies the fluid circuits with coolant if it is necessary. The fluid temperature in the flow is constant at 20 °C. The set temperature for the machine tool frame is 21 °C. Independent PI-controller for every fluid circuit are controlling the temperature.

Comparing the temperature behavior of the machine tool frame in case of seven pumps see figure 4 and the optimized one in figure 5 shows the same characteristic. In addition, the temperature deviation from the set temperature is measured with the Euclidean norm also known as L^2-norm:

$$\mathrm{J} = \int_0^\infty e(t)^2 \, \mathrm{dt}. \quad (16)$$

with $e(t) = T_{\text{set}} - T_{\text{act}}$. The difference between the optimized structure and the initial situation is less than 1 %. An interesting point is that despite of a higher volume flow rate the heat flow out of the machine tool frame is constant. This is also observed on experiments performed on the machine tool frame. This behavior is explicable with the low heat conduction of the high performance concrete used to build the machine tool frame. Looking at the energy consumption of the pumps, there is a reduction from 14.82 kWh to 12.66 kWh. With the usage of four pumps the energy consumption can be reduced by 15 %. The power

of each pump is shown in figure 6 for the initial system with seven pumps and in figure 7 for the optimized system topology.

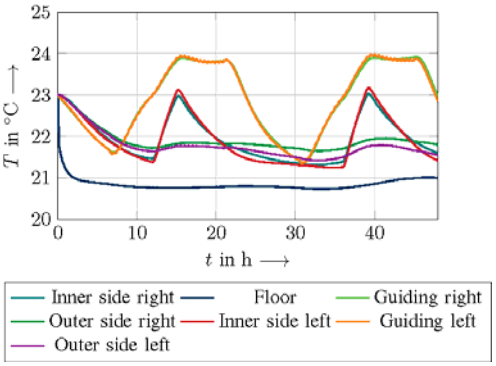

Figure 5: Temperature behaviour of the machine tool frame with seven pumps

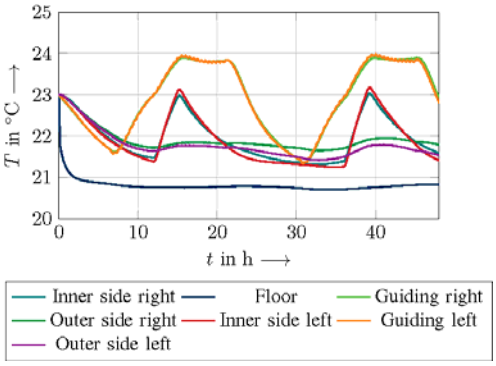

Figure 5: Temperature behaviour of the machine tool frame for optimized structure with four pumps

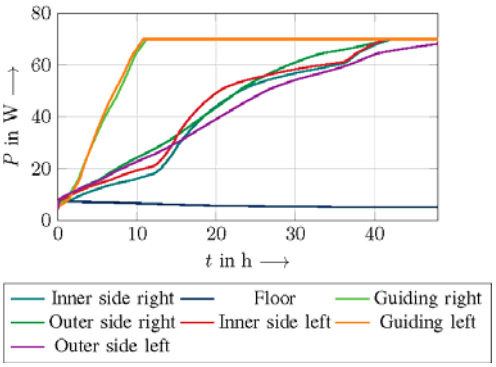

Figure 6: Power consumption for each of the seven pumps

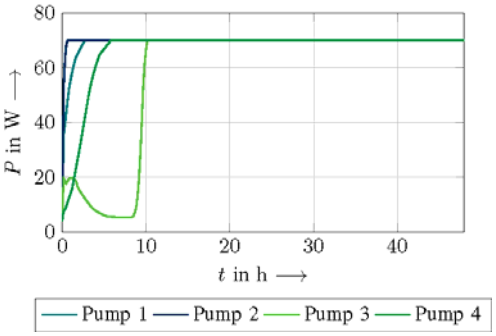

Figure 6: Power consumption for the four pumps of the optimized structure

5. OUTLOOK

In this paper, the optimal topology for a cooling system with seven cooling circuits of a machine tool frame is developed. The result is limited to one pump model. In further work, the number of pump models will be extended. With a variety of pumps, not only the number of them can be determined, but it is also possible to decide which pump is best regarding purchasing cost and energy consumption during operation.

The results are simulated and confirm the energy consumption and the ability to have no negative impact on the temperature field of the machine tool frame. A validation of the optimized structure at the test rig will be performed. Furthermore, an optimization regarding the temperature behavior is in discussion. This has to be performed with help of a FEMmodel of the machine tool frame.

6. REFERENCES

[1] Josef Mayr, Jerzy Jedrzejewski, Eckart Uhlmann, M Alkan Donmez, Wolfgang Knapp, Frank Härtig, Klaus Wendt, Toshimichi Moriwaki, Paul Shore, Robert Schmitt, et al. Thermal issues in machine tools. CIRP annals, 61(2):771–791, 2012.

[2] Christian Brecher, Stephan Bäumler, David Jasper, and Johannes Triebs. Energy efficient cooling systems for machine tools. In Leveraging Technology for a Sustainable World, pages 239–244. Springer, 2012.

[3] Berend Denkena and Thomas Garber. NCplus: Prozess- und wertschöpfungsorientiert gesteuerte Werkzeugmaschine; Abschlussbericht. PZH-Verlag, 2013.

[4] Juliane Weber, Jürgen Weber, Linart Shabi, and Harald Lohse. Energy, power and heat flow of the cooling and fluid systems in a cutting machine tool. Procedia Cirp, 46:99–102, 2016.

[5] Kun-Ying Li, Win-Jet Luo, Yu-Ru Zeng, and I-Hsing Huang. Increase in accuracy of a built-in spindle by adaptive cooling control with varied coolant volume and temperature. Sensors and Materials, 32(11):3689–3706, 2020.

[6] Linart Shabi. Thermo-energetisch optimierte Fluid-Systeme für Werkzeugmaschinen = Thermo-energetic optimized fluid systems for machine tools. Shaker Verlag, Düren, 2020.

[7] Lena C Altherr, Philipp Leise, Marc E Pfetsch, and Andreas Schmitt. Resilient layout, design and operation of energy-efficient water distribution networks for high-rise buildings using minlp. Optimization and Engineering, 20(2):605–645, 2019.

[8] T. M. Müller, Philipp Leise, Imke Lorenz, Lena C. Altherr, and P. F. Pelz. Optimization and validation of pumping system design and operation for water supply in high-rise buildings. Optimization and Engineering, 2020:1–43, September 2020.

[9] Johan Löfberg. YALMIP : A Toolbox for Modeling and Optimization in MATLAB. In In Proceedings of the CACSD Conference, Taipei, Taiwan, 2004.

[10] A. H. Land and A. G. Doig. An automatic method of solving discrete programming problems. Econometrica, 28(3):497–520, 1960.

[11] Sarah Mater. Demonstration verschiedener Strategien für die Temperaturregelung eines intelligenten Maschinengestells aus Hydropol. Diplomarbeit, Technische Univeristät Dresden, March 2021.

Acknowledgement:

The presented research activities are part of the project A04 ”Thermoenergetic description of fluid systems” founded by the German Research Foundation (Project-ID 174223256 - TRR96). The authors would like to thank the German Research Foundation (DFG) for the financial support.

Funded by
DFG Deutsche Forschungsgemeinschaft
German Research Foundation

Elastodynamic Performance Evaluation and Comparison in Hydraulic and Electromechanical Linear Actuator Driven Heavy-Duty Manipulators

Aleksi Vesterinen, Goran R. Petrovic´ and Jouni Mattila

Faculty of Engineering and Natural Sciences, Tampere University, Finland,
aleksi.vesterinen@tuni.fi
Faculty of Engineering and Natural Sciences, Tampere University, Finland,
goran.petrovic@tuni.fi
Faculty of Engineering and Natural Sciences, Tampere University, Finland,
jouni.mattila@tuni.fi

Abstract

Strict global regulations and initiatives like Paris Agreement 2015 for achieving low carbon dioxide emission via energy efficiency nowadays have already made the electrification of hydraulic working machines and manipulators an actual topic, invested heavily into. During the first wave, diesel engine powered vehicles are being replaced with more-electric or all-electric battery electric vehicles (BEVs). Electrification is an emerging topic, and, for example, Doosan Bobcat has recently introduced an all-electric T7X model where diesel power is entirely replaced with BEV technology. Hydraulic linear actuators for the bucketare replaced with electromechanical linear actuators (EMLA) by Moog, and the main drive motors are also electric. These modern trends also require the development and broadening of the underlying structural and dynamics analysis when electric actuators are used instead of hydraulic ones. From the control perspective, natural frequencies provide insight into the manipulator dynamics and achievable performance depending on the current working point. Elastodynamic performance, which directly relates to the manipulator stiffness, is one of the most important performance indicators, especially when considering manipulator positioning. Methods for calculating manipulator natural frequencies are well known in the case of

hydraulic manipulators, where the effect of hydraulic fluid compressibility (causing spring effect) has been studied in detail. This paper, among others, provides means for calculating natural frequencies of oscillation in an electrified EMLA-driven manipulator, and expression for the equivalent of hydraulic spring behaviour is given. The natural frequencies are compared between the two manipulator versions, of which the hydraulic already exists, and the electric one is in the design process. In addition, the applicability of EMLAs is discussed with respect to current mobile hydraulic working machine requirements.

1 Introduction

In the process of manipulator design, the choice of physical properties, like manipulator lengths and masses, is usually a solution to some mechanism optimisation problem. Each optimisation problem contains a relevant cost function to be minimised or maximised considering certain kinematic and dynamic limitations in the process. Since optimal solutions in different optimisation tasks may be different in each separate case, it is critical to identify relevant performance indices and combine them appropriately. Identifying and choosing pertinent performance indices may not be an easy task since these can be conflicting. For example, decreasing the manipulator's inertia will decrease the stiffness of the manipulator; thus, inertia minimisation and stiffness maximisation are contradictory goals, among many others available.

Different performance indices proposed over the years cover many dynamic behaviour aspects. These can comprehend workspace size, velocity transmission, inertia, stiffness, and eigenfrequencies [1]. Jacobian matrix, manipulability, condition number, isotropy, and global conditioning indices are also to be considered per [2]. In addition, the inertia torque index and centrifugal torque index can be found as proposed in [3].

Among many available indices, the natural oscillation frequencies are appropriate performance measures that incorporate both kinematic and dynamic properties, relating directly to mechanical vibrations. The lowest natural oscillation frequency can be chosen as a design objective, aiming at minimising vibrations and avoiding the existence of directions with zero gain [4]. Even this isolated task *per se* is not trivial considering that natural frequencies (NF) change from posture to posture, thus having different values during the manipulator operation. Because of this, there will undoubtedly exist manipulator configurations that are more favourable than others from the aspect of induced vibrations.

When discussing already available manipulator solutions, it may be intriguing to gain insight into the distribution of NFs over the workspace if the manufacturer does not provide that information. In many cases, particularly when interacting with the surroundings, manipulator vibrations that affect, for example, the positioning accuracy or cause tool wear, can be induced. By having a clear insight into how NFs change over the workspace, unfavourable manipulator postures can be avoided in the operation process. In this case, mathematical models in the form of linearized equations of motion can serve as a handy primary tool for preliminary analysis.

Apart from providing a preliminary insight into the distribution of NFs, the elastodynamic modelling of manipulators forms a solid basis for the eventual parameter identification procedures. Natural oscillation frequencies can also be directly estimated from experimentally obtained frequency response plots without any prior analysis. The problem is that they can be determined experimentally only for selected configurations because verification in the whole workspace would require an infinite number of experiments. This topic has been addressed in papers [5] – [7], where measurements have been performed in many different, carefully selected robot configurations. NFs for a serial, six-degree-of-freedom (DOF) industrial robot with only rotational joints (6R) have been provided, along with experimental verifications of NFs using impulse response tests. Impulse responses in carefully chosen postures have been used in [8], followed by identifying joints' stiffness and damping. Elastodynamic modelling and parameter identification have also been researched in [9] – [10]. In the study [11], NF surfaces showing the distribution of six NFs are provided with analytic verifications in eight manipulator poses for a parallel manipulator. Beforehand obtained prediction of the lowest NF of a hydraulic manipulator, using CAD software, was used in the adaptive control algorithm [12]. Minimum natural oscillation frequencies are also shown to be an essential factor when designing robust linear controllers for hydraulic manipulators [13]. In mobile manipulators, the manipulator arm's minimum NF is important when designing arm controller [14].

The change of actuation means will undoubtedly affect elastodynamics performance and NF distribution in the manipulator. Ongoing mega-trends in non-road mobile machinery (NRMM) focus on reducing greenhouse gasses [15] and bring in front electric and hybrid prime movers. Continuing development of hybrid and all-electric solutions for electromechanical actuators [16] provides a possibility of having capable all-electric NRMM. Many global competitors have already released all-electric solutions with imminent heavy investing to follow. In all of these all-electric NRMM solutions, elec-

tromechanical linear actuators (EMLAs) play an essential role. Their effect and what the change of actuation paradigm brings, in general, should be investigated in detail.

The present study compares natural oscillation frequencies in a heavy-duty manipulator for two considered cases of importance. Analysing the oscillations caused by the hydraulic oil spring effect and when EMLA is retrofitted to the same manipulator, this paper provides insight into one of the governing and widely accepted dynamic performance indices. The presentation of an EMLA mathematical model is followed by a good overview of expected achievable manipulator performance if electrification was to be carried out. Plots showing the distribution of NFs over the workspace are shown for both cases accompanied with appropriate time responses and power spectre densities, which validate the carried out analysis.

By tackling the all-present topic of today - electrification of heavy-duty machinery, this study provides a guide to analysing the effects of electrification on the elastodynamic performance of heavy-duty manipulators.

2 Mathematical Modelling

2.1 Preliminaries

All the manipulator links in the following analysis will be considered rigid. Every rigid body in the analysis will have at least one three-dimensional coordinate system $\{\mathbf{A}\}$ (called frame $\{\mathbf{A}\}$ in the following text) attached to it.

Let the linear and angular velocities as would be sensed in frame $\{\mathbf{A}\}$ be denoted throughout the paper as ${}^{\mathbf{A}}v = \begin{pmatrix} {}^{\mathbf{A}}v_{\mathrm{x}} & {}^{\mathbf{A}}v_{\mathrm{y}} & {}^{\mathbf{A}}v_{\mathrm{z}} \end{pmatrix}^T \in \mathbb{R}^{3\times 1}$ and ${}^{\mathbf{A}}\omega = \begin{pmatrix} {}^{\mathbf{A}}\omega_{\mathrm{x}} & {}^{\mathbf{A}}\omega_{\mathrm{y}} & {}^{\mathbf{A}}\omega_{\mathrm{z}} \end{pmatrix}^T \in \mathbb{R}^{3\times 1}$, respectively. The set of independent generalized coordinates represents the minimal number of geometric parameters which can be used to uniquely describe the motion of a mechanical system. In the following considerations the vector of generalized coordinates will be:

$$\xi = (\xi_1 \quad \xi_2 \quad \dots \quad \xi_i \quad \dots \quad \xi_n)^T \in \mathbb{R}^{n\times 1}, \tag{1}$$

and the corresponding generalized force vector will be:

$$\tau(\dot{\xi},\xi) = \left(\tau_1(\dot{\xi},\xi)\dots\tau_i(\dot{\xi},\xi)\dots\tau_n(\dot{\xi},\xi)\right)^T \in \mathbb{R}^{n\times 1}. \tag{2}$$

2.2 Choosing the Modelling Formalism

Different approaches for mathematical modelling of manipulator dynamics lead to different sets of equations, each having both specific advantages and downsides. Full-dynamics modelling of serial-parallel manipulators with little or no approximations, including the linear actuator masses and accounting for closed-loop kinematics relations, has been provided using the Lagrange formalism **MC**, in the Newton-Euler framework [17] and using Kane's equations obtained combining screw theory and the principle of virtual work [18].

The Lagrange approach based on kinetic and potential energies and the Newton-Euler approach based on the balance of all the forces acting on a rigid body is considered the most popular. The Newton-Euler approach is considered more fundamental and computationally efficient, [19]. With its very effective, recursive formulation, it enables subsystem-by-subsystem analysis and thus is indispensable in the VDC framework where the control action is formed on the subsystem level to guarantee the stability of the whole system [20]. It is also the most natural approach when reaction forces are included in the analysis [21]. The RNEA will effectively provide the identical inverse and direct dynamics calculations results as other methods would, but it will not lead directly to the most convenient form when performing the elastodynamic performance assessment. Except in simple cases, there will be more equations than degrees of freedom with RNEA. A potentially tedious procedure of combining equations might be needed when starting from RNEA to arrive at the manipulator dynamics description in the joint-space with the number of equations equalling the number of generalised coordinates. Formulating a system of linear equations like this is essential since it serves as the starting point in the elastodynamics performance analysis. The Lagrange approach leads directly to the same number of equations as is the number of generalised coordinates. These equations may be pretty complex, which is significantly magnified in the presence of the closed kinematic loops where the expressions for derivatives of the loop-closure function per generalised coordinates will usually introduce additional complexity. Still, their linearization results give the most direct path to the equations required in the considered context here, and thus, the dynamics of the manipulator analyzed here will be modelled using the Lagrange equations of the second kind. In the presented study, masses of linear actuator in rotational segments will be neglected when forming equations of motions since it will simplify the anal-

ysis and not reflect significantly on the elastodynamic performance analysis for the considered manipulator configuration with its underlying properties.

2.3 Equations of Motion

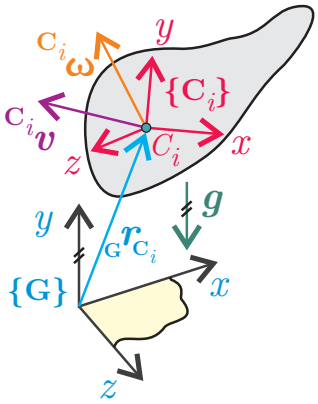

Figure 1 Considered rigid body.

Let us observe the i-th rigid body from Fig. 1, belonging to a multibody system. Kinetic energy of the i-th rigid body, labelled as $K_i(\dot{\xi},\xi) \in \mathbb{R}$, is per definition:

$$K_i(\dot{\xi},\xi) = \frac{1}{2} m_i v_{C_i}^T v_{C_i} + \frac{1}{2} {}^{\mathbf{C}_i}\boldsymbol{\omega}^T \left[{}^{\mathbf{C}_i}\mathbf{I}\right] {}^{\mathbf{C}_i}\boldsymbol{\omega}, \tag{3}$$

with $m_i \in \mathbb{R}$ being the body mass, $v_{C_i} \in \mathbb{R}^{3\times 1}$ is the considered COM velocity vector with respect to the inertial frame $\{\mathbf{G}\}$ and expressed in any convenient frame, $\left[{}^{\mathbf{C}_i}\mathbf{I}\right] \in \mathbb{R}^{3\times 3}$ denotes the tensor of inertia of the i-th rigid body about the axes of the $\{\mathbf{C}_i\}$ frame with its origin the the centre of mass (COM) C_i. Assuming that the gravity acceleration is constant and normal to the Earth-tangent plane Oxz, one way to define the potential energy $\Pi_i(\xi) \in \mathbb{R}$ of the considered i-th body is:

$$\Pi_i(\xi) = m_i g\, y_{C_i}(\xi), \tag{4}$$

where $g \in \mathbb{R}$ denotes the gravity acceleration magnitude and $y_{C_i}(\xi) \in \mathbb{R}$ denotes the y-coordinate value of the i-th rigid body COM with respect to the inertial frame $\{\mathbf{G}\}$, expressed in the $\{\mathbf{G}\}$ frame. If the Lagrange function is introduced by definition as the sum of difference between the kinetic and

potential energy of the whole rigid body system, which is composed of n rigid bodies, as:

$$\mathcal{L}(\dot{\xi},\xi) = \sum_{i=1}^{n} \left(K_i(\dot{\xi},\xi) - \Pi_i(\xi) \right), \tag{5}$$

then Lagrange equations of the second kind for a rigid body system can be written in the form of a system:

$$\frac{\mathrm{d}}{\mathrm{d}t}\left(\frac{\partial \mathcal{L}(\dot{\xi},\xi)}{\partial \dot{\xi}^i} \right) - \frac{\partial \mathcal{L}(\dot{\xi},\xi)}{\partial \xi^i} = \tau_i(\dot{\xi},\xi), \quad i = 1,...,n, \tag{6}$$

where $\tau_i(\dot{\xi},\xi) \in \mathbb{R}$ here denotes the generalized forces arising as the consequence of all the other forces acting upon the system, apart from the weight force which is comprehended through the potential energy. In the analyzed case, the generalized forces analysis will play an important role and will be addressed in more detail.

System of equations (6) can be rearranged and written in the form that is widely used:

$$\mathbf{M}(\xi)\,\ddot{\xi} + \mathbf{C}\left(\dot{\xi},\xi\right)\dot{\xi} + \mathbf{G}(\xi) = \tau\left(\dot{\xi},\xi\right), \tag{7}$$

with $\mathbf{M}(\xi) \in \mathbb{R}^{n\times n}$, denoting the real, symmetric and positive-definite mass matrix, $\mathbf{C}\left(\dot{\xi},\xi\right) \in \mathbb{R}^{n\times n}$ being the Coriolis/centrifugal matrix and $\mathbf{G}(\xi) \in \mathbb{R}^{n\times 1}$ representing the vector of gravity-related terms.

2.4 Linearized EOM and elastodynamic performance

Linearizing the equations of motion about the nominal manipulator posture in the resting state, determined with $\left(\dot{\xi},\xi\right) = (\mathbf{0},\xi_0)$ returns the system of linear ODEs:

$$\mathbf{E}_0(\xi_0)\,\Delta\ddot{\xi} + \mathbf{H}_0(\xi_0)\,\Delta\xi = \Delta\tau. \tag{8}$$

Assuming that generalized force perturbation term $\Delta\tau$ can be represented here in the general case as:

$$\Delta\tau = -\mathbf{F}_0(\xi_0)\,\Delta\dot{\xi} - \mathbf{K}_0(\xi_0)\,\Delta\xi, \tag{9}$$

leads to the common linearized form:

$$\mathbf{E}_0\,\Delta\ddot{\xi} + \mathbf{F}_0\,\Delta\dot{\xi} + (\mathbf{H}_0 + \mathbf{K}_0)\,\Delta\xi = 0, \tag{10}$$

where the matrix $\mathbf{E}_0(\xi_0)$ can be directly obtained from the mass matrix as:

$$\mathbf{E}_0(\xi_0) = \mathbf{M}(\xi_0), \tag{11}$$

matrix $\mathbf{F}_0(\xi_0)$ will be a consequence of dissipative friction forces and matrix $\mathbf{K}_0(\xi_0)$ will comprehend spring-like behaviour of linear actuators being considered here.

After choosing the state variables vector as:

$$\mathbf{x} = \left(\Delta\xi, \Delta\dot{\xi}\right)^T \in \mathbb{R}^{2n\times 1} \tag{12}$$

the system of equations from Eq. (10) can be rewritten as:

$$\dot{\mathbf{x}} = \mathbf{A}\left(\xi_0\right)\mathbf{x}, \tag{13}$$

with matrix $\mathbf{A}\left(\xi_0\right) \in \mathbb{R}^{2n\times 2n}$ being defined as:

$$\mathbf{A}\left(\xi_0\right) = \begin{pmatrix} \mathbf{O}_{n\times n} & \mathbf{I}_{n\times n} \\ -\mathbf{E}_0^{-1}\left(\mathbf{H}_0 + \mathbf{K}_0\right) & -\mathbf{E}_0^{-1}\mathbf{F}_0 \end{pmatrix}. \tag{14}$$

Eigenvalues and eigenvectors of matrix $\mathbf{A}\left(\xi_0\right)$ will determine the properties of unforced vibrations in the system, [22]. In the present study it is of interest to investigate how frequencies of unforced oscillations change when hydraulic linear actuators are replaced with electric counterparts. Thus, magnitudes of matrix $\mathbf{A}\left(\xi_0\right)$ eigenvalues will be investigated.

3 Spring-like Behaviour of Linear Actuators

While the matrices $\mathbf{E}_0(\xi_0)$ and $\mathbf{H}_0(\xi_0)$ from (10) can be fully determined by knowing the kinematic and mass properties of the considered manipulator, matrices $\mathbf{F}_0(\xi_0)$ and $\mathbf{K}_0(\xi_0)$ from (9) depend on the actuation type and actuator properties. In hydraulic systems at zero flow, and electromechanical systems, at nominal holding force/torque, motions exist due to the spring-like behaviour of the actuator.

3.1 Hydraulic Spring Effect

The effect of oil compressibility is known to cause the existence of "hydraulic spring" [23]. The existence of free oscillations can be attributed to the spring-like behaviour of the oil in cylinder chambers where the spring stiffness is varying.

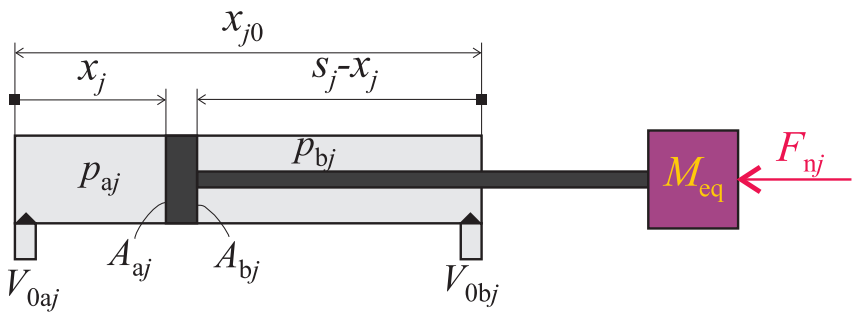

Figure 2 Linear hydraulic actuator.

Let us observe the j-th linear hydraulic actuator in Fig. 2. The linear momentum change of moving parts is:

$$M_{\mathrm{eq}j}\ddot{x}_j + C_{\mathrm{eq}j}\dot{x}_j = p_{\mathrm{a}j}A_{\mathrm{a}j} - p_{\mathrm{b}j}A_{\mathrm{b}j} - F_{\mathrm{n}j}, \tag{15}$$

where $M_{\mathrm{eq}j}$ is the equivalent mass of moving parts, $C_{\mathrm{eq}j}$ is the viscous damping coefficient and $F_{\mathrm{n}j}$ is the external force. Chamber pressures p_{aj} and p_{bj} create the actuation force by acting on piston areas A_{aj} and A_{bj}. At zero flows to both chambers, the pressures change as follows:

$$\dot{p}_{\mathrm{a}j} = -\frac{B_{\mathrm{a}j}A_{\mathrm{a}j}}{V_{0\mathrm{a}j} + A_{\mathrm{a}j}x_j}\dot{x}_j, \tag{16}$$

and:

$$\dot{p}_{\mathrm{b}j} = -\frac{B_{\mathrm{b}j}A_{\mathrm{b}j}}{V_{0\mathrm{b}j} + A_{\mathrm{b}j}\,(s_j - x_j)}\dot{x}_j, \tag{17}$$

with $B_{\mathrm{a}j}$ and $B_{\mathrm{b}j}$ representing the hydraulic fluid bulk moduli, and where the fluid volumes in hoses between the j-th direction valve and actuator chambers are $V_{0\mathrm{a}j}$ and $V_{0\mathrm{b}j}$.

Combining (15) – (17) one can arrive at the equation describing the motion of moving parts at zero flows as:

$$M_{\mathrm{eq}j}\dddot{x}_j + C_{\mathrm{eq}j}\ddot{x}_j + K_{\mathrm{hs}j}\dot{x}_j = -\dot{F}_{\mathrm{n}j}. \tag{18}$$

Once (18) is linearized about the equilibrium position determined with the piston position $x_{j\mathrm{N}}$, an equation describing motion in the vicinity of the nominal equilibrium point is:

$$M_{\mathrm{eq}j}\Delta\ddot{x}_j + C_{\mathrm{eq}j}\Delta\dot{x}_j + K_{\mathrm{hs}j\mathrm{N}}\Delta x_j = -\Delta F_{\mathrm{n}j}, \tag{19}$$

where the hydraulic spring stiffness $K_{\mathrm{hs}jN}$ is:

$$K_{\mathrm{hs}jN} = \frac{B_{\mathrm{a}j} A_{\mathrm{a}j}^2}{V_{0\mathrm{a}j} + A_{\mathrm{a}j}\, x_{jN}} + \frac{B_{\mathrm{b}j} A_{\mathrm{b}j}^2}{V_{0\mathrm{b}j} + A_{\mathrm{b}j}\,(s_j - x_{jN})}, \tag{20}$$

and the equivalent actuator stiffness $K_{\mathrm{h}j}$ is calculated from:

$$\frac{1}{K_{\mathrm{h}j}} = \frac{1}{K_{\mathrm{hs}jN}} + \frac{1}{K_{\mathrm{r}j}}, \tag{21}$$

with $K_{\mathrm{r}j}$ representing the j-th actuator rod stiffness.

3.2 Equivalent Spring Stiffness in EMLAs

Different mathematical models of EMLAs have been proposed over many years of extensive research [24] – [25]. They differ in form, complexity and methodology used. It is argued and shown through experiments that, as expected, higher-order models better capture the dynamic behaviour and predict the resonant peaks. Since the near-steady state behaviour is contemplated in the presented study, an adapted fourth-order model from [26] will be used, since it suffices for the overall picture that is to be presented here.

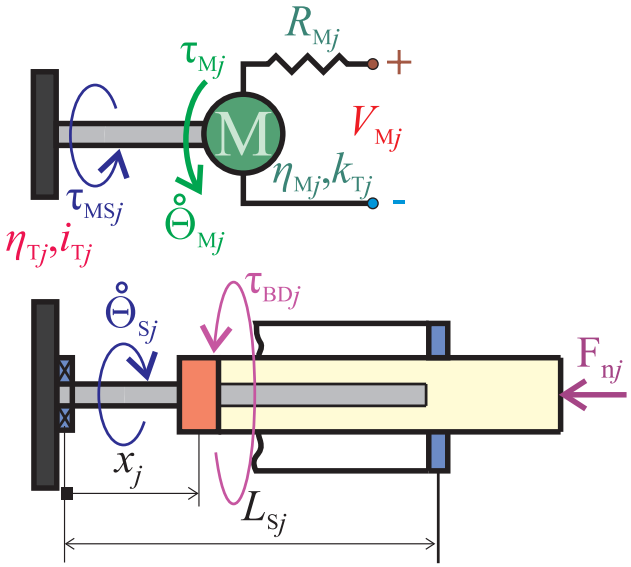

Figure 3 Schematic of an EMLA.

Let us observe the simplified schematics of an EMLA actuated with a DC motor in Fig. 3 and let us incorporate some of the modelling ideas from [27] for the sake of obtaining an insightful nonlinear model. If the inductivity of motor coils is neglected, the current flow $I_{\mathrm{M}j}$ in the windings of j-th EMLA can be approximately determined as follows:

$$V_{\mathrm{M}j} - k_{\mathrm{M}j}\,\dot{\Theta}_{\mathrm{M}j} = R_{\mathrm{M}j}\,I_{\mathrm{M}j}, \tag{22}$$

where $R_{\mathrm{M}j}$ is the resistance of coils, $V_{\mathrm{M}j}$ is the applied voltage, $\dot{\Theta}_{\mathrm{M}j}$ represents the motor shaft angular velocity, and $k_{\mathrm{M}j}$ is the back-electromotive force coefficient. The angular momentum change of the j-th DC motor shaft is:

$$J_{\mathrm{M}j}\,\ddot{\Theta}_{\mathrm{M}j} + C_{\mathrm{M}j}\,\dot{\Theta}_{\mathrm{M}j} + \tau_{\mathrm{MS}j} = \tau_{\mathrm{M}j}, \tag{23}$$

where $J_{\mathrm{M}j}$ represents the moment of inertia of motor rotating parts and motor shaft, $C_{\mathrm{M}j}$ is the viscous damping coefficient, $\tau_{\mathrm{MS}j}$ is the part of the motor actuation moment that is transferred to the load shaft. The j-th DC motor actuation moment $\tau_{\mathrm{M}j}$ can be calculated from:

$$\tau_{\mathrm{M}j} = \eta_{\mathrm{M}j}\,k_{\mathrm{T}j}\,I_{\mathrm{M}j}, \tag{24}$$

as a function of motor efficiency $\eta_{\mathrm{M}j}$ and torque constant $k_{\mathrm{T}j}$.

The transmission ratio $i_{\mathrm{T}j}$ relates angular velocities as:

$$\dot{\Theta}_{\mathrm{S}j}\,i_{\mathrm{T}j} = \dot{\Theta}_{\mathrm{M}j}, \tag{25}$$

where $\dot{\Theta}_{\mathrm{S}j}$ is the j-th EMLA shaft angular velocity.

Because it will be convenient to express certain following relations in terms of linear nut displacement $x_{\mathrm{n}j}$, the nut linear velocity $\dot{x}_{\mathrm{n}j}$ is related with load shaft angular velocity as:

$$\dot{x}_{\mathrm{n}j} = \frac{p_j}{2\pi}\,\dot{\Theta}_{\mathrm{S}j}, \tag{26}$$

where p_j is the j-th ballscrew pitch.

The load shaft rotates per relation similar to (23):

$$J_{\mathrm{S}j}\,\ddot{\Theta}_{\mathrm{S}j} + C_{\mathrm{S}j}\,\dot{\Theta}_{\mathrm{S}j} = i_{\mathrm{T}j}\,\tau_{\mathrm{MS}j} - \tau_{\mathrm{BD}j}, \tag{27}$$

where again as before, $J_{\mathrm{S}j}$ represents the moment of inertia of rotating parts on the load shaft, $C_{\mathrm{S}j}$ is the viscous damping coefficient, and $\tau_{\mathrm{BD}j}$ is the ballscrew back-drive moment:

$$\tau_{\mathrm{BD}j} = \frac{p_j}{2\pi}\left(C_{\mathrm{BS}j}\left(\dot{x}_{\mathrm{n}j} - \dot{x}_j\right) + K_{\mathrm{BS}j}\left(x_{\mathrm{n}j} - x_j\right)\right), \tag{28}$$

with the ballscrew equivalent stiffness $K_{\mathrm{BS}j}$, $C_{\mathrm{BS}j}$ denotes ballscrew damping coefficient, $\dot{x}_j$ and x_j are the velocity and position of the EMLA rod, respectively.

Combining equations (22)–(28), one can arrive at:

$$J_j^* \ddot{x}_{\mathrm{n}j} + C_j^* \dot{x}_{\mathrm{n}j} + C_{\mathrm{BS}j}(\dot{x}_{\mathrm{n}j} - \dot{x}_j) + K_{\mathrm{BS}j}(x_{\mathrm{n}j} - x_j) = K_j^* V_{\mathrm{M}j}, \tag{29}$$

where:

$$J_j^* = \left(J_{\mathrm{M}j} i_{\mathrm{T}j}^2 + J_{\mathrm{S}j}\right) \left(\frac{2\pi}{p_j}\right)^2, \tag{30}$$

$$C_j^* = \left(C_{\mathrm{M}j} i_{\mathrm{T}j}^2 + C_{\mathrm{S}j}\right) \left(\frac{2\pi}{p_j}\right)^2, \tag{31}$$

$$K_j^* = \frac{k_{\mathrm{T}j}\,\eta_{\mathrm{M}j}}{R_{\mathrm{M}j}} \frac{2\pi}{p_j}. \tag{32}$$

The motion of linearly moving EMLA parts follows:

$$M_j \ddot{x}_j + C_j \dot{x}_j + C_{\mathrm{BS}j}(\dot{x}_j - \dot{x}_{\mathrm{n}j}) + K_{\mathrm{BS}j}(x_j)(x_j - x_{\mathrm{n}j}) = -F_{\mathrm{n}j}. \tag{33}$$

Equivalent EMLA stiffness $K_{\mathrm{BS}j}(x_j)$ plays a cruicual role in determining NFs of a manipulator with EMLAs. This equivalent ballscrew stiffness of the j-th ballscrew is:

$$K_{\mathrm{BS}j} = \left(\frac{x_j}{K_{\mathrm{s}j}} + \frac{1}{K_{\mathrm{b}j}} + \frac{1}{K_{\mathrm{n}j}} + \frac{1}{K_{\mathrm{r}j}} + \frac{p^2 x_j}{4K_{\mathrm{rot}j}\pi^2}\right)^{-1} \tag{34}$$

if the EMLA shaft is fixed on one side, or:

$$K_{\mathrm{BS}j} = \left(\frac{L_{\mathrm{eff}j}}{K_{\mathrm{s}j}} + \frac{1}{2K_{\mathrm{b}j}} + \frac{1}{K_{\mathrm{n}j}} + \frac{1}{K_{\mathrm{r}j}} + \frac{p^2 x_j}{4K_{\mathrm{rot}j}\pi^2}\right)^{-1} \tag{35}$$

when the EMLA shaft is fixed on both sides. In both (34) and (35) term $K_{\mathrm{s}j}$ represents the axial stiffness of the j-th EMLA shaft, $K_{\mathrm{b}j}$ represents the bearing stiffness, $K_{\mathrm{n}j}$ stands for the stiffness of the nut, $K_{\mathrm{r}j}$ is the stiffness of the rod, and $K_{\mathrm{rot}j}$ is the rotational stiffness of the shaft. Term $L_{\mathrm{eff}j}$ is related to the effective length of the shaft and it can be calculated as:

$$L_{\mathrm{eff}j} = \left(\frac{x_j(L_{\mathrm{S}j} - x_j)}{L_{\mathrm{S}j}}\right), \tag{36}$$

where L_{Sj} is the distance between the bearings.

While (29) and (33) represent the governing nonlinear EMLA equations, their linearized versions will be investigated as was the case with hydraulic actuator. Choosing the state variables as deviations from the equilibrium:

$$\Delta x_{\mathrm{E}} = \begin{pmatrix} \Delta x_{\mathrm{n}j} \\ \Delta x_j \end{pmatrix}, \tag{37}$$

equations (29) and (33) can be linearized and written as:

$$\mathbf{M}_{\mathrm{E}j}\,\Delta\ddot{x}_{\mathrm{E}j} + \mathbf{C}_{\mathrm{E}j}\,\Delta\dot{x}_{\mathrm{E}j} + \mathbf{K}_{\mathrm{BS}j}\,\Delta x_{\mathrm{E}j} = \Delta\mathbf{u}_{\mathrm{E}j}, \tag{38}$$

where appropriate system matrices are:

$$\mathbf{M}_{\mathrm{E}j} = \begin{pmatrix} J_j^* & 0 \\ 0 & M_j \end{pmatrix}, \tag{39}$$

$$\mathbf{C}_{\mathrm{E}j} = \begin{pmatrix} C_j^* + C_{\mathrm{BS}j} & -C_{\mathrm{BS}j} \\ -C_{\mathrm{BS}j} & C_{\mathrm{BS}j} + C_j \end{pmatrix}, \tag{40}$$

$$\mathbf{K}_{\mathrm{BS}j} = \begin{pmatrix} K_{\mathrm{BS}j\mathrm{N}} & -K'_{\mathrm{BS}j\mathrm{N}}\,x_{j\mathrm{N}} - K_{\mathrm{BS}j\mathrm{N}} \\ -K_{\mathrm{BS}j\mathrm{N}} & K'_{\mathrm{BS}j\mathrm{N}}\,x_{j\mathrm{N}} + K_{\mathrm{BS}j\mathrm{N}} \end{pmatrix}, \tag{41}$$

and:

$$\Delta\mathbf{u}_{\mathrm{E}j} = \begin{pmatrix} K_j^*\,\Delta V_{\mathrm{M}j} \\ -\Delta F_{nj} \end{pmatrix}. \tag{42}$$

Considering the expected magnitudes of coefficients, an equivalent EMLA spring value calculated from (34) or (35) as $K_{\mathrm{BS}j\mathrm{N}} = K_{\mathrm{BS}j}(x_{j\mathrm{N}})$ can be used when addressing the effect of EMLA on the distribution of NFs over the workspace.

3.3 Linearized Force Moments in Revolute Joints

The equivalent spring stiffness is essential to calculate the spring-like force that an actuator produces when small-amplitude oscillations about the equilibrium are analyzed. These forces should be related to the angular motion exhibited by revolute joints as a final step.

Let us observe revolute joint actuated with linear actuator, shown in Fig. 4. For small angle displacements $\Delta\xi_j$, spring-like force is generated in the actuator per:

$$\Delta F_j = -k_j\,\Delta x_j = -k_j\,L_{\tau j}\,\Delta\xi_j, \tag{43}$$

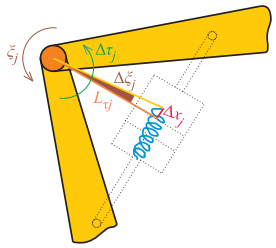

Figure 4 i-th revolute joint in a manipulator arm.

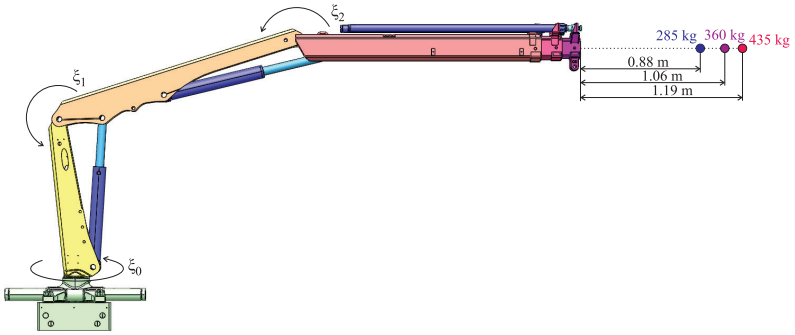

Figure 5 Considered manipulator arm, shown with linear hydraulic manipulators. Alongside are shown COMs of three different loads for which the analytic results are provided.

which after multiplying with the moment arm $L_{\tau j}$ gives the moment acting on the joint as:

$$\Delta\tau_j = -k_j L_{\tau j}^2 \Delta\xi_j. \tag{44}$$

In the case of prismatic joints, the modelling task is rather trivial, requiring just the force increment:

$$\Delta F_j = -k_j \Delta x_j. \tag{45}$$

Thus, the matrix $\mathbf{K}_0(\xi)$ has the following description:

$$\mathbf{K}_0(\xi) = \mathrm{diag}(k_{11}(\xi_1)\dots k_{ii}(\xi_i)\dots k_{nn}(\xi_n)), \tag{46}$$

where:

$$k_{ii} = \begin{cases} k_j & \text{if the joint is prismatic,} \\ k_j L_{\tau j}^2 & \text{if the joint is revolute.} \end{cases} \tag{47}$$

By modelling the friction as a locally linear function of velocity, matrix $\mathbf{F}_0$ can be written as:

$$\mathbf{F}_0 = \mathrm{diag}(f_{11}(\xi_1)\dots f_{ii}(\xi_i)\dots f_{nn}(\xi_n)), \tag{48}$$

with f_{ii} being a constant.

4 Comparing Distributions of Natural Oscillation Frequencies

Let us now analyze the heavy-duty manipulator from Fig. 5 based on the approaches described above. The effect of three different loads with different locations for their respective COMs will be investigated. Appropriate NF surfaces will be given for these three cases that can also be seen illustrated in Fig. 5 along with appropriate numeric values. Three generalized coordinates ξ_0, ξ_1, and ξ_2 will be used in the NF analysis. Although the base actuator stiffness will have different values as ξ_0 varies, the presented surfaces are provided for $\xi_0 = 0$. This suffices for the comparison needs.

Figures 6 - 8 show the distribution of $\omega_i, i = 0,1,2$ NFs in the case of hydraulic actuation over the $\xi_1 - \xi_2$ plane.

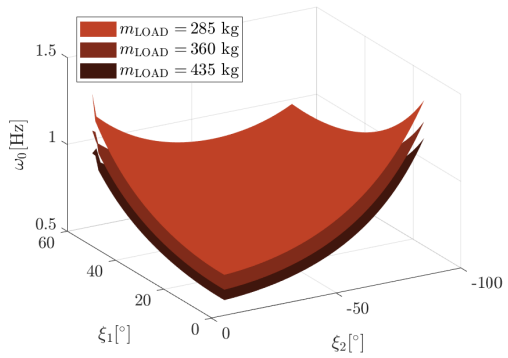

Figure 6 NF ω_0 distribution over the $\xi_1 - \xi_2$ plane (hydraulics).

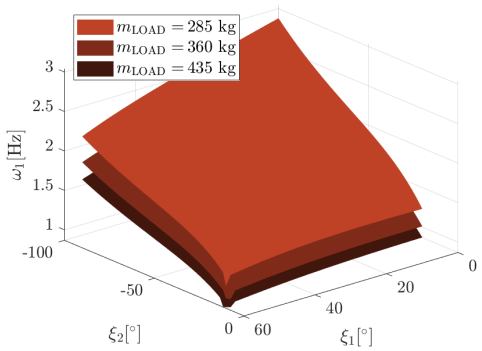

Figure 7 NF ω_1 distribution over the $\xi_1 - \xi_2$ plane (hydraulics).

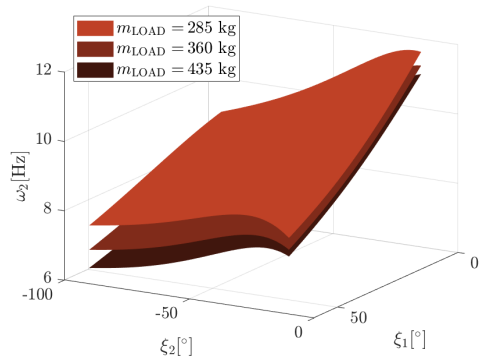

Figure 8 NF ω_2 distribution over the $\xi_1 - \xi_2$ plane (hydraulics).

Base rotation EMLA is designed such that two fixed supports restrain its motion, and the equivalent stiffness is calculated per (35). For EMLAs in the lift and tilt joint, the equivalent stiffness is calculated using (34). Figures 9 - 11 show the distribution of NFs in the case of electric actuation.

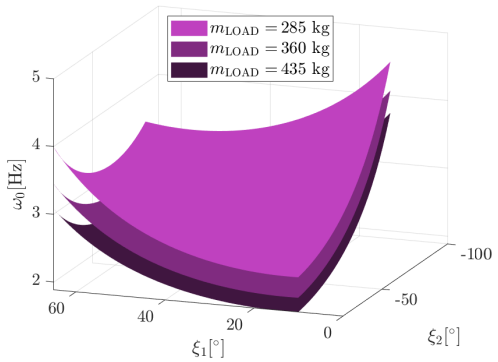

Figure 9 NF ω_0 distribution over the $\xi_1 - \xi_2$ plane (EMLA).

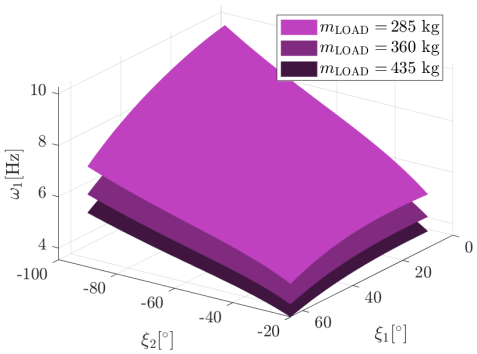

Figure 10 NF ω_1 distribution over the $\xi_1 - \xi_2$ plane (EMLA).

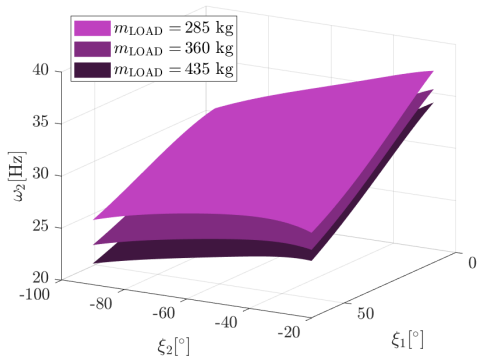

Figure 11 NF ω_2 distribution over the $\xi_1 - \xi_2$ plane (EMLA).

5 Conclusion

The near future is expected to bring an inevitable rise in all-electric heavy-duty manipulator solutions. These solutions will certainly induce new values for a palette of different important manipulator properties. Compared to all-hydraulic solutions, some of these may prove more favourable and will undoubtedly challenge hydraulics in certain aspects.

EMLAs can not outperform hydraulics in many aspects like high-speed actuation with high impact loads like in excavators, of which about 500.000 units are sold annually. Also, challenges regarding cooling are bound to exist in EMLAs, and these will require appropriate analyses.

In any case, addressing differences between hydraulically and electrically actuated manipulators where appropriate transition could occur and making relevant comparisons presents an essential investment to the knowledge base that is bound to gain more and more popularity as time goes by.

In hydraulic solutions, linear actuators are omnipresent, appearing both in prismatic and revolute segments. The same is expected to be encountered in all-electric solutions, leading to EMLAs playing an indispensable role. Since a ballscrew assembly often encountered in precision machining serves as one of the main constituting EMLA subsystems, the already existing and vast body of literature can serve as a foundation for analysis of heavy-duty manipulators with EMLAs.

The main mechanical properties of EMLAs that contribute to the equivalent stiffness are listed and analyzed in a fair amount of detail. Equations of motion for a complex and relevant manipulator arm configuration have

been derived and linearized in the vicinity of a general equilibrium point. Equivalent hydraulic stiffnesses of linear hydraulic and electric actuators have been used in the following analysis to replace the linear actuators with linear springs and calculate the frequencies of natural oscillations of a considered structure.

Based on the obtained results, it is expected that retrofitting EMLAs to existing heavy-duty manipulator arms or creating new all-electric ones will contribute to achieving overall higher values for minimum natural frequencies of manipulator oscillations. Higher values for this crucial structural quality indicator are favourable and could enable better positioning precision and the easier achieving of the higher closed-loop bandwidth. The presented study show that it is expected to achieve up to 3 times higher frequencies of natural oscillations.

Considering manipulator links as rigid bodies, the distribution of natural oscillation frequencies is plotted over the grid of generalized coordinates and will remain to serve as a road sign for future analyses.

References

[1] M. Krefft and J. Hesselbach, "Elastodynamic optimization of parallel kinematics," in *Proc. IEEE Inter. Conf. Autom. Sci. Eng.*, Edmonton, AB, Canada, Aug. 1–2, 2005, pp. 357–362, DOI: 10.1109/COASE.2005.1506795.

[2] J.-P. Merlet, "Jacobian, manipulability, condition number, and accuracy of parallel robots," *Journal of Mechanical Design*, vol. 128, no. 1, pp. 199–206, Jan. 2006, DOI: 10.1115/1.2121740.

[3] D. Liang, Y. Song, T. Sun, and G. Dong, "Optimum design of a novel redundantly actuated parallel manipulator with multiple actuation modes for high kinematic and dynamic performance," *Nonlinear Dynamics*, vol. 83, no. 1, pp. 631–658, Jan. 2016, DOI: 10.1007/s11071-015-2353-1.

[4] T. Sun, B. Lian, Y. Song and L. Feng, "Elastodynamic optimization of a 5-DoF parallel kinematic machine considering parameter uncertainty," *IEEE/ASME transactions on mechatronics*, vol. 24, no. 1, pp. 315–325, Feb. 2019, DOI: 10.1109/TMECH.2019.2891355.

[5] P. Glogowski, M. Rieger, J. B. Sun, and B. Kuhlenkötter, "Natural frequency analysis in the workspace of a six-axis industrial robot using design of experiments," *Advanced Materials Research*, vol. 1140, pp. 345–352, Aug. 2016., DOI: 10.4028/www.scientific.net/AMR.1140.345.

[6] A. Karim, J. Hitzer, A. Lechler, and A. Verl, "Analysis of the dynamic behavior of a six-axis industrial robot within the entire workspace in respect of machining tasks," in *Proc. IEEE Int. Conf. Adv. Intell. Mech. (AIM)*, Munich, Germany, Jul. 3–7, 2017, pp. 670–675, DOI: 10.1109/AIM.2017.8014094.

[7] J. Sun, W. Zhang, and X. Dong, "Natural Frequency Prediction Method for 6R Machining Industrial Robot," *Applied Sciences*, vol. 10, no. 22, art. no. 8138, Nov. 2020., DOI: 10.3390/app10228138.

[8] M. Bottin, S. Cocuzza, Silvio, N. Comand, and A. Doria, "Modeling and identification of an industrial robot with a selective modal approach," *Applied Sciences*, vol. 10, art. no. 4619, Jun. 2020., DOI: 10.3390/app10134619.

[9] A. Doria, S. Cocuzza, Silvio, N. Comand, M. Bottin, and A. Rossi, "Analysis of the compliance properties of an industrial robot with the Mozzi axis approach," *Robotics*, vol. 8, art. no. 80, Sep. 2019., DOI: 10.3390/robotics8030080.

[10] H. N. Huynh, H. Assadi, E. Riviere-Lorphevre, O. Verlinden, and K. Ahmadi, "Modelling the dynamics of industrial robots for milling operations," *Robotics and Computer-Integrated Manufacturing*, vol. 61, art. no. 101852, Jun. 2020., DOI: 10.1016/j.rcim.2019.101852.

[11] B. Lian, L. Wang, and X. V. Wang, "Elastodynamic modeling and parameter sensitivity analysis of a parallel manipulator with articulated traveling plate," *The International Journal of Advanced Manufacturing Technology*, vol. 102, no. 5, pp. 1583–1599, Jan. 2019., DOI: 10.1007/s00170-018-03257-x.

[12] J. Kovanen and H. Handroos, "Adaptive open-loop control method for a hydraulically driven flexible manipulator," in *Proc. IEEE/ASME Inter. Conf. Adv. Intell. Mech.*, Como, Italy, Jul. 8–12, 2001, pp. 942–947, DOI: 10.1109/AIM.2001.936805.

[13] L. Zhai, T. Virvalo, J. Mattila, and H. Saarinen, "Analysis and control of a water hydraulic manipulator for ITER divertor remote maintenance," *International Journal of Fluid Power*, vol. 11, no. 1, 2010., DOI: 10.1080/14399776.2010.10780997.

[14] M. Rigotti-Thompson, M. Torres-Torriti, F. A. Cheein, and G. Troni, "$\mathcal{H}_\infty$-Based Terrain Disturbance Rejection for Hydraulically Actuated Mobile Manipulators With a Nonrigid Link," *IEEE/ASME Transactions on Mechatronics*, vol. 25, no. 5, pp. 2523–2533, Oct. 2020., DOI: 10.1109/TMECH.2020.2983072.

[15] D. Vandenbroucke, A. Van Hyfte, and L. Francx, "Study in View of the Revision of Directive 97/68/EC on Non-Road Mobile Machinery (NRMM)," An Emissions Inventory and Impact Assessment, Final Report, 2010. [Online]. Available: https://op.europa.eu/s/vUdn

[16] G. Qiao, G. Liu, Z. Shi, Y. Wang, S. Ma, and T. C. Lim, "A review of electromechanical actuators for More/All Electric aircraft systems," *Proceedings of the Institution of Mechanical Engineers, Part C: Journal of Mechanical Engineering Science*, vol. 232, no. 22, pp. 4128–4151, 2018., DOI: 10.1177/0954406217749869.

[17] G. R. Petrović and J. Mattila, "Mathematical modelling and virtual decomposition control of heavy-duty parallel–serial hydraulic manipulators," *Mechanism and Machine Theory*, vol. 170, Art. no. 104680, pp. 1–26, Jan. 2022, DOI: 10.1016/j.mechmachtheory.2021.104680

[18] A. Cibicik and O. Egeland, "Dynamic modelling and force analysis of a knuckle boom crane using screw theory," *Mechanism and Machine Theory*, vol. 133, pp. 179–194, Mar. 2019., DOI: 10.1016/j.mechmachtheory.2018.10.019.

[19] R. Jazar, "Motion Dynamics," in *Theory of applied robotics: kinematics, dynamics, and control*, 2nd ed., New York, NY, USA: Springer, 2010, ch. 11, sec. 1–8, pp. 581–628, DOI: 10.1007/978-1-4419-1750-8

[20] W. H. Zhu, *Virtual decomposition control: toward hyper degrees of freedom robots*, 1st ed., Berlin Heidelberg: Springer-Verlag, 2010, DOI: 10.1007/978-3-642-10724-5

[21] G. R. Petrović and J. Mattila, "Analytic Solutions for Wheeled Mobile Manipulator Supporting Forces," *arXiv preprint arXiv:2202.10186*, Feb. 2022., DOI: 10.48550/arXiv.2202.10186

[22] L. Meirovitch, "Nonconservative systems. The nonsymmetric eigenvalue problem.," in *Principles and techniques of vibrations*, 1st ed., New Jersey, NJ, USA: Prentice Hall, 1997, ch. 4, sec. 8, pp. 189–195

[23] H. E. Merritt, "Valve controlled piston.," in *Hydraulic control systems*, John Wiley and Sons, 1967, ch. 6, sec. 2, pp. 145–150

[24] S. Frey, A. Dadalau, and A. Verl, "Expedient modeling of ball screw feed drives," *Production Engineering*, vol. 6, no. 2, pp. 205–211, Apr. 2012, DOI: 10.1007/s11740-012-0371-0

[25] I. Ansoategui, and F. J. Campa, "Mechatronics of a ball screw drive using an N degrees of freedom dynamic model," *The International Journal of Advanced Manufacturing Technology*, vol. 93, no. 1, pp. 1307–1318, Jun. 2017, DOI: 10.1007/s00170-017-0597-2

[26] R. Caracciolo and D. Richiedei, "Optimal design of ball-screw driven servomechanisms through an integrated mechatronic approach," *Mechatronics*, vol. 24, no. 7, pp. 819–832, Oct. 2014, DOI: 10.1016/j.mechatronics.2014.01.004

[27] M. S. Kim and S. C. Chung, "Integrated design methodology of ball-screw driven servomechanisms with discrete controllers. Part I: Modelling and performance analysis," *Mechatronics*, vol. 16, no. 8, pp. 491–502, Oct. 2006, DOI: 10.1016/j.mechatronics.2006.01.008

Evaluation of Nonlinear MIMO Controllers for Independent Metering in Mobile Hydraulics

Lukas Bachmann, André Sitte, Jürgen Weber

Chair of Fluid-Mechatronic Systems
Technische Universität Dresden
Dresden, Germany
lukas.bachmann@tu-dresden.de, fluidtronik@mailbox.tu-dresden.de

Hydraulic cylinder drives with coupled control edges suffer from inherent losses due to dependent meter-in and meter-out flow control. Velocity and pressure demands with different valve opening requirements collide and result in energy dissipation at the control edges. Independent metering technology provides individual actuation of inlet and outlet valves and leads to higher efficiency. The additional control input offers separate control of cylinder velocity, i.e. flow, and chamber pressure. However, the resulting nonlinear Multiple Input Multiple Output (MIMO) system poses several challenges for the control algorithm. Cross coupling between the system states requires multivariable control. Furthermore, the commonly used linearization approaches strongly depend on the current operating point of the hydraulic system. In mobile application, these operating points are usually difficult to predict and move across a wide range. Therefore, a nonlinear, multivariable control algorithm is required. This paper presents some frequently discussed nonlinear control approaches, namely flatness-based tracking control, sliding mode control and exact input/output linearization, and evaluates their performance and applicability in the mobile hydraulic context. Control variables are velocity and weighted chamber pressure of the cylinder. Previous research on these controller concepts showed promising results for simple nonlinear MIMO systems. However, more complex systems, incorporating modelling uncertainties and limited observability have rarely been studied thoroughly. Therefore, this study focuses on the validation of the controller implementa-

River Journal, 1–18.
© 2024 *River Publishers. All rights reserved.*

tion based on simplified models of a hydraulic valve-controlled manipulator with two joints. This is followed by an investigation of the performance on increasingly sophisticated and realistic models. Assessment criteria are robustness against parameter and model uncertainties, computational efficiency, communication delay and measurement effort.

Keywords: Nonlinear Control Theory, Flatness-based Control, Sliding Mode Control, Exact Input/Output Linearization, Independent Metering, Hydraulic Manipulator.

1 Introduction

The progress of automation and the demand for energy efficient hydraulic systems brings valve structures with decoupled control edges for independent flow and pressure control into focus. This principle is known for several decades as Independent Metering (IM). Past research at the Institute of Fluid-Mechatronic Systems [1, 2] has shown high energy saving potentials. Yet the technology has barely entered today's construction sites [3]. Main reason for the Original Equipment Manufacturer's (OEM) hesitancy is the increased control engineering effort and accompanying cost-intense sensor and valve equipment.

Hence, this paper seeks to evaluate some frequently discussed control strategies for the application in mobile hydraulic systems using IM technology. Given high pressure on costs and limited computational resources in mobile machinery, the realization and implementation is analyzed and questioned.

The control task of valve controlled hydraulic cylinder drives with IM-valve technology can be described as a nonlinear MIMO system. Sitte et al. [4, 5] analyze the decoupling effect of individual pressure compensators (IPC) on intrinsic coupling for the application of Single Input Single Output (SISO) controllers. The authors identified reduction of the coupling factor due to the usage of IPCs but also detected a strong dependency on the current state of operation. Thus, the applicability of SISO controllers is limited and multivariable control algorithms are required.

One strategy to control nonlinear systems is through nonlinear decoupling and linearization by feedback [6–9]. This is a simple and straight-forward solution which achieves good results if and only if the systems characteristic are known to a certain degree. Unknown or inaccurate system knowledge as well as parameter uncertainties will result in insufficient compensation of the systems nonlinearities and consequently poor performance.

The lack of robustness can be overcome by the introduction of so-called sliding surfaces [10]. The sliding mode controller (SMC) is motivated by the fact that a first degree system is easier controllable than a nth order system described by n^{th} order differential equations [11]. The transformation is done by attracting the system states toward a hyperplane or sliding surface, along which the system states are stabilized to a desired equilibrium state or trajectory.
Discontinuous switching laws reached good control performance for systems with model and parameter uncertainties [9, 12]. Unfortunately the use of such switching laws excites high frequency oscillations, known as the chattering phenomenon. This may result in premature aging or even damaging of the control actuators and can excite unmodeled high-frequency dynamics. Piecewise-continous switching laws [11–13] achieved slightly better performance and reduced strain on band-width limited actuators. The states are no longer drawn infinetisemally close towards the sliding surface but pulled inside a finite and bounded neighborhood.
The most promising results though were obtained using higher order sliding modes (HOSM) [14–20]. Beside the requirement to minimize the distance i.e. sliding variable s to the sliding surface, restrictions on the derivatives $s^{(n)}$, such as $s^{(n)} = 0$, are applied so that discontinuities appear at the n+1-th derivative at the earliest. This concept is known as the super twisting sliding mode controller (STSMC).
For a certain class of nonlinear systems another powerful control approach can be implemented. Exploiting the system characteristic of differential flatness [21] a dynamic, stabilizing state feedback can be realized by reconstructing the system states through a flat output y.

Definition 1.1. A system is called differentially flat if, and only if, a tuple of differentially independent quantities exists from which all other quantities of the system can be calculated without solving a differential equation. Such a tuple is called flat output.

Although Def. 1.1 seems restrictive, many physical systems meet these requirements and flatness-based tracking controllers (FTC) have been developed for various applications, among them hydraulic systems [1, 22–24].

2 System description

For the model-based controller design we consider the hydraulic system depicted in Fig. 1. The valve structure consists of two 2/2 leak-proof propor-

tional valves and one 4/3 switching valve. The latter is used for flow reversal at negative speeds while the proportional valves control pressure and cylinder velocity.

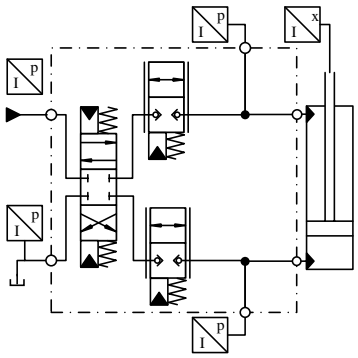

Figure 1 IM valve-controlled cylinder with sensor information

The force equilibrium at the hydraulic cylinder is given by

$$\mathrm{m_{cyl}} \cdot \ddot{z} + \mathrm{d_{cyl}}\left(\dot{z}\right) \cdot \dot{z} + F_{\mathrm{L}} = p_{\mathrm{A}} \cdot A_{\mathrm{A}} - p_{\mathrm{B}} \cdot A_{\mathrm{B}} \tag{1}$$

where F_{L} denotes the unknown load force at the mechanical connector of the cylinder. For the controller design the damping d_{cyl} is assumed linear proportional with respect to the cylinder velocity.
The pressure gradient inside the oil-filled volumes is expressed by

$$\dot{p}_{\mathrm{A}} = \frac{K'}{V_{\mathrm{A}} + A_{\mathrm{A}} z}\left(Q_{\mathrm{A}} - \mathrm{A_A}\dot{z}\right) \tag{2a}$$

$$\dot{p}_{\mathrm{B}} = \frac{K'}{V_{\mathrm{B}} + A_{\mathrm{B}}\left(h - z\right)}\left(\text{-}Q_{\mathrm{B}} + \mathrm{A_B}\dot{z}\right). \tag{2b}$$

For simplification the pressure-induced expansion of the piping system and the temperature influence on the bulk modulus K' are neglected. The pipe volumes V_{A} and V_{B} are constant while the variation of the chamber volume and the associated impact on the systems eigenfrequency and damping is considered.
We assume turbulent flow inside the valves and thereby define the flow characteristic with the following equation:

$$Q_i = K_{\mathrm{V}}(y_i) \cdot \mathrm{sign}\left(\Delta p_i\right) \sqrt{|\Delta p_i|}. \tag{3}$$

The opening gradient K_V of the valve orifice depends on the valve's nominal flow characteristic and on the normalized valve spool position y_i. For invertibility this is described as a polynomial curve and (3) is fitted to the valve characteristic depicted in Fig. 3.
Valve dynamics are neglected for the controller design. Especially in the case of large mobile machinery the dynamics of the kinematic chain are much slower than the valve dynamics.

3 Controller Design

Based on the system description we implemented four different control strategies. The control task involves velocity and pressure control. Since the control inputs can control two system states, only one chamber pressure is controllable. In order not to change the controlled state depending on the load situation, we introduce the weighted chamber pressure

$$p_\mathrm{K} = \frac{p_\mathrm{A} \cdot p_\mathrm{B}}{p_\mathrm{A} + p_\mathrm{B}} \tag{4}$$

as control variable in addition to the cylinder speed.

3.1 Exact Input/Output Linearization

With the definition of the state vector

$$\boldsymbol{x} = [\dot{z} \quad p_\mathrm{A} \quad p_\mathrm{B}]^\mathsf{T} \tag{5}$$

and output mapping using (4)

$$\boldsymbol{h}(\boldsymbol{x}) = [\dot{z} \quad p_\mathrm{K}]^\mathsf{T} \tag{6}$$

the simplified system governed by (1) to (3) can be represented as a nonlinear control-affine system of the form

$$\dot{\boldsymbol{x}} = \boldsymbol{f}(\boldsymbol{x}) + \boldsymbol{G}(\boldsymbol{x})\boldsymbol{u} \tag{7a}$$
$$\boldsymbol{y} = \boldsymbol{h}(\boldsymbol{x}) \tag{7b}$$

where the system state $\boldsymbol{x}$, the input $\boldsymbol{u}$ and output $\boldsymbol{y}$ are $n = 3$, $p = 2$ and $m = 2$ dimensional. The smooth vector fields $\boldsymbol{f}$ and $\boldsymbol{h}$ denote the autonomous part of the system and the output mapping. $\boldsymbol{G}$ is the square matrix-valued control sensitivity with according dimensions.

With exact input/output linearization, the nonlinearity of the system is compensated by an inverse, nonlinear control law. For this, the system output must be derived until at least one of the system inputs comes up:

$$y_i^{(r_i)} = \pounds_{\boldsymbol{f}}^{r_i} h_i + \sum_{j=1}^{m} \pounds_{\boldsymbol{g}_i} \pounds_{\boldsymbol{f}}^{r_i-1} h_i u_j \tag{8}$$

Definition 3.1. The derivation degree r_i for which

$$\pounds_{\boldsymbol{g}_i} \pounds_{\boldsymbol{f}}^{r_i-1} \neq 0 \wedge \pounds_{\boldsymbol{g}_i} \pounds_{\boldsymbol{f}}^{k} = 0, \quad k \in \{0, \ldots, r_i - 2\}$$

holds, is called relative degree [25]. $\boldsymbol{g}_i$ are the row vectors of $\boldsymbol{G}$.

For a MIMO system this is explicitly shown in (9), where $\boldsymbol{G}^*$ is called decoupling matrix [25].

$$\begin{bmatrix} y_1^{(r_1)} \\ \vdots \\ y_m^{(r_m)} \end{bmatrix} = \begin{bmatrix} \pounds_{\boldsymbol{f}}{}^{r_1} h_1 \\ \vdots \\ \pounds_{\boldsymbol{f}}{}^{r_m} h_m \end{bmatrix} + \begin{bmatrix} \pounds_{\boldsymbol{g}_1} \pounds_{\boldsymbol{f}}{}^{r_1\text{-}1} h_1 & \cdots & \pounds_{\boldsymbol{g}_m} \pounds_{\boldsymbol{f}}{}^{r_1\text{-}1} h_1 \\ \vdots & \ddots & \vdots \\ \pounds_{\boldsymbol{g}_1} \pounds_{\boldsymbol{f}}{}^{r_m\text{-}1} h_m & \cdots & \pounds_{\boldsymbol{g}_m} \pounds_{\boldsymbol{f}}{}^{r_m\text{-}1} h_m \end{bmatrix} \boldsymbol{u}$$
$$\boldsymbol{y}^{\boldsymbol{r}} = \boldsymbol{f}^* + \boldsymbol{G}^* \boldsymbol{u} \tag{9}$$

Exact input/output linearization is achieved by introducing the virtual control inputs ω_i and solving (9) for $\boldsymbol{u}$:

$$\boldsymbol{u} = (\boldsymbol{G}^*)^{\text{-}1} \left[\boldsymbol{\omega} - \boldsymbol{f}^* \right], \qquad \omega_i = y_i^{(r_i)}. \tag{10}$$

For the virtual inputs ω_i, linear error dynamics can be specified according to the respective relative degree r_i. Thereby, the linearizing feedback is supplemented by a stabilizing one.
For the studied hydraulic system the corresponding relative degrees are $r_v = 2$ for velocity control and $r_{p_\mathrm{K}} = 1$ for pressure control. The linear error dynamics are thus stabilized by

$$\omega_v = \ddot{v}_\mathrm{d} \qquad -k_{v,1} \left(\dot{v} - \dot{v}_\mathrm{d} \right) - k_{v,0} \left(v - v_\mathrm{d} \right) \tag{11a}$$
$$\omega_{p_\mathrm{K}} = \dot{p}_{\mathrm{K,d}} \qquad -k_{p_\mathrm{K},0} \left(p_\mathrm{K} - p_{\mathrm{K,d}} \right) \tag{11b}$$

with all gains $k_{i,j} > 0$ as the necessary condition is also sufficient for first and second degree polynomial equations.

3.2 Sliding Mode Control

Definition 3.2. Consider the control-affine system (7). For each of the m control variables we define a sliding surface of the kind:

$$s_i(\boldsymbol{z},t) = \left(\frac{\mathrm{d}}{\mathrm{d}t} + \lambda_i\right)^{r_i-1} \tilde{y}, \quad \lambda > 0, \quad i = 1, \cdots, m. \tag{12}$$

The relative degree r_i is determined as described in Def. 3.1 and the positive constant λ_i determines exponential convergence on s_i.

With two sliding surfaces as in Def. 3.2 for v and p_K the decoupled r_i^{th}-order system (9) can be transformed in two 1st-order stabilization problems in s_i [13]. In the s_i-space the relative degree is reduced to one, as the input per definition already appears after one derivation.
For an asymptotic attraction towards the sliding surface the positive definite and radially unbounded Lyapunov function

$$V_i(s_i) = \frac{1}{2}s_i^2 \qquad \dot{V}_i(s_i,\dot{s}_i) = \frac{1}{2}\frac{\mathrm{d}}{\mathrm{d}t}\left(s_i^2\right) \overset{!}{<} 0 \tag{13}$$

is chosen. In order to reach s_i in finite time $t \leq |s_i(0)|/\eta_i$ [13], the following tightening of (13) shall apply:

$$\dot{V}(s_i,\dot{s}_i) = s_i\dot{s}_i \overset{!}{\leq} \text{-}\eta||s_i||, \qquad \eta_i > 0. \tag{14}$$

The positive constant η_i governs the attracting speed towards the sliding surface s_i. Inserting (9) in (14) results in an inequality equation which can be simplified by introducing a piecewise continuous discontinuous control law yielding

$$\boldsymbol{u} = (\boldsymbol{G}^*)^{\text{-}1}\left[\boldsymbol{\omega} - \boldsymbol{f}^* - \boldsymbol{k}\cdot\mathrm{sat}(\boldsymbol{s}/\boldsymbol{\epsilon})\right] \tag{15}$$

where the virtual control input equals $\omega_i = s_i - y_i^{(r_i)}$.
The additional parameter ϵ denotes the tolerance width around the sliding surface where no control action is performed to reduce chattering [13].
In contrast to the control strategy of 3.1 model uncertainties of the kind

$$\left|\tilde{f}_i^* - f_i^*\right| \leq F_i \tag{16a}$$

$$\boldsymbol{G^*} = (\boldsymbol{I} + \boldsymbol{\Delta})\tilde{\boldsymbol{G}}\boldsymbol{^*} \tag{16b}$$

can be incorporated in (15) by solving

$$(1-\delta_{ii})k_i + \sum_{j\neq i}\delta_{ij}k_j = F_i + \sum_{j=1}^{\mathrm{M}}\delta_{ij}\left|\omega_i^{(r_i-1)} - \tilde{f}_i^*\right| + \eta_i \tag{17}$$

Table 1 Parametric uncertainties for valve controlled cylinder drive

Parameter	**Nominal Value**	**Range**
F_{L}	$0\,\mathrm{kN}$	-40 kN $\cdots$ +80 kN
K'	$14\,000\,\mathrm{bar}$	$8000\,\mathrm{bar}$ $\cdots 16\,000\,\mathrm{bar}$
$\partial K_{\mathrm{V}}/\partial y^{\mathrm{a}}$	$1.527 \times 10^{-4}\,\sqrt{\mathrm{m}^7/\mathrm{kg}}$	$\pm 10\,\%$
d_{cyl}	$150\,\mathrm{kNs/m}$	+75 kNs/m $\cdots 300\,\mathrm{kNs/m}$
m_{cyl}	$3000\,\mathrm{kg}$	$2500\,\mathrm{kg}$ $\cdots 3500\,\mathrm{kg}$

[a] For simplification the mean linear gradient is varied.

for k_i as proposed by [9, 13]. The maximum relative deviations of $\boldsymbol{G}^*$ are denoted by $\delta_{ij} \geq |\Delta_{ij}|$.
For the given use case (Fig. 1) geometric quantities are considered well known while external influences like load force and pressure and temperature sensitive parameters like the bulk modulus are assigned with an uncertainty range denoted in Table 1.

3.3 Super Twisting Sliding Mode Control

Another approach to reduce chattering is the use of HOSM [14,15]. A second order implementation of HOSM is known as the STSMC.
Again sliding surfaces of relative degree $r_i = 1$ are defined according to (12) and decoupling and input assignment of the virtual control law is given by the inversion of the input sensitivity:

$$\boldsymbol{u} = (\boldsymbol{G}^*)^{\text{-}1}\left[\boldsymbol{\omega} - \boldsymbol{f}^*\right]. \tag{18}$$

Referring to possible implementations [14] of the virtual control input, we select the following system of differential equations for $\boldsymbol{\omega}$:

$$\omega_i = \text{-}k_{i,1}\sqrt{|s_i|}\mathrm{sign}\,(s_i) - k_{i,2}s_i + \Omega_i \tag{19a}$$

$$\dot{\Omega}_i = k_{i,3}\mathrm{sign}\,(s_i) - k_{i,4}s_i. \tag{19b}$$

There exist publications [14, 18, 26] considering the estimation of the control parameters $k_{i,j}$ for robust stability against additive disturbances on (9). To the authors knowledge there has been no methodology do determine the gains $k_{i,j}$ for a class of parameter and model uncertainties like (16) thus, the parameters were determined empirically for this study.

3.4 Flatness-based Tracking Control

Exploiting the system property of flatness, as defined in Def. 1.1, the system can be stabilized and controlled along a reference trajectory by a state feedback law.
First, flatness must be proven for the considered system output (6). This is achieved by systematically expressing the system's states through a flat output $\boldsymbol{\eta}$ and its derivatives[1]. For the sake of clarity the following expressions are abbreviated and only the occurring derivation orders are listed.

$$x_1 = \psi_1(\eta_1) = \eta_1 \tag{20a}$$
$$x_2 = \psi_2(\eta_1, \dot{\eta}_1, \eta_2) \tag{20b}$$
$$x_3 = \psi_3(\eta_1, \dot{\eta}_1, \eta_2) \tag{20c}$$

(20a) follows directly from (6) and (20b) and (20b) result from rearranging (1) and inserting (6). Also the flow rate can be expressed by using the derivatives of (20b) and (20c) respectively with (2a) and (2b). Hence, it is proven that simply by measuring the system's flat output, all system states can be computed. The system is *input/state linearizable*[2] and consequently the required system input can be obtained for a desired system state expressed by $\boldsymbol{\eta}$:

$$u_\mathrm{A} = \varphi_1(\eta_1, \dot{\eta}_1, \ddot{\eta}_1, \eta_2, \dot{\eta}_2) \tag{21a}$$
$$u_\mathrm{B} = \varphi_2(\eta_1, \dot{\eta}_1, \ddot{\eta}_1, \eta_2, \dot{\eta}_2) \tag{21b}$$

Equation (21) can be considered as a feed forward control with the inverse system characteristic. To compensate disturbances and modeling uncertainties an additional control through state feedback is introduced. Choosing η_i as new states x_i' and the highest derivatives of η_i as virtual control inputs ω_i a linear, classical[3] state space model in Brunovský normal form [22] is created where the highest derivatives of the flat output are chosen as virtual system

[1] The symbol $\boldsymbol{\eta}$ is used to distinguish the flat output from the general system output $\boldsymbol{y}$.

[2] For SISO systems this approach is in fact identical to the input/output linearization.

[3] As long as no derivatives of the system input $\boldsymbol{u}$ appear in (22) the state space model is classic and static state feedback can be implemented, otherwise dynamic feedback is mandatory [25].

inputs for the control law.

$$\dot{x}'_{1,1} = x'_{1,2} \qquad = \dot{\eta}_1 \tag{22a}$$

$$\dot{x}'_{1,2} = \varphi_1(x'_{1,1}, x'_{1,2}, x'_{2,1}, u) \qquad \stackrel{!}{=} \omega_1 \tag{22b}$$

$$\dot{x}'_{2,1} = \varphi_2(x'_{1,1}, x'_{1,2}, x'_{2,1}, u) \qquad \stackrel{!}{=} \omega_2 \tag{22c}$$

A linear, time-invariant error dynamics of the tracking error $\tilde{\boldsymbol{\eta}} = \boldsymbol{\eta} - \boldsymbol{\eta}_{\mathrm{ref}}$ is specified for the virtual inputs.

$$\ddot{\tilde{\eta}}_1 + k_{1,1}\dot{\tilde{\eta}}_1 + k_{1,0}\tilde{\eta}_1 = 0 \tag{23a}$$

$$\dot{\tilde{\eta}}_2 + k_{2,0}\tilde{\eta}_2 = 0, \quad k_{i,j} > 0 \tag{23b}$$

Like (11) controller gains $k_{i,j}$ are determined by pole placement and the resulting control law including state feedback is given by:

$$u_{\mathrm{A}} = \varphi_1(\eta_1, \dot{\eta}_1, \ddot{\tilde{\eta}}_{\mathrm{ref},1} - k_{1,1}\dot{\tilde{\eta}}_1 - k_{1,0}\tilde{\eta}_1, \eta_2, \dot{\tilde{\eta}}_{\mathrm{ref},2} - k_{2,0}\tilde{\eta}_2)$$
$$u_{\mathrm{B}} = \varphi_2(\eta_1, \dot{\eta}_1, \ddot{\tilde{\eta}}_{\mathrm{ref},1} - k_{1,1}\dot{\tilde{\eta}}_1 - k_{1,0}\tilde{\eta}_1, \eta_2, \dot{\tilde{\eta}}_{\mathrm{ref},2} - k_{2,0}\tilde{\eta}_2)$$

4 Simulation Study

Since the objective of this work is the applicability of the controllers on a mobile hydraulic systems, the control performance is analyzed on the hydraulic system of a large material handler. To mimic the typical framework of controller hardware for mobile applications, the communication interval between controller and actuators is limited to $\Delta t = 10\,\mathrm{ms}$. This influences the controller parametrization. For pole placement of the FTC (11) and input/output linearization (23) the numerical stability ranges of the solver have to be considered. In order to achieve conservative[4] stability for recursive Euler the poles s_i are chosen in such a way that $|1 + \Delta t s_i| < 1$ holds. In particular, fixed step euler integration is used to simulate the sliding regime as other solvers result in integration error as stated by Utkin [28].
A challenging test regime (Fig. 2) with a rectangular load force profile with amplitude $F_{\mathrm{L}} = 30\,\mathrm{kN}$ is applied to evaluate the performance of the controllers.

[4] Other numerical integration methods possess larger and more complex stability areas [27]. For conservative stability the Euler stability range is considered.

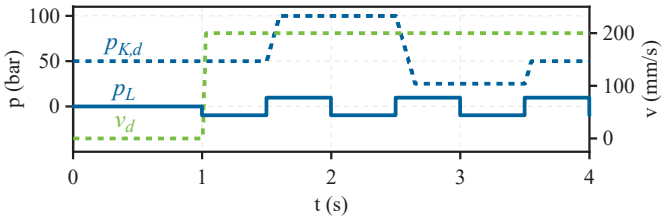

Figure 2 Test regime

4.1 Simulation models

Two models are created for validation and evaluation of the parametrized controllers. The simplified model is designed in *Matlab/Simulink* and mostly coincides with the model equations used for the controller design. Additionally, it includes measurement noise and nonlinear cylinder friction. Model simplifications are constant bulk modulus, no pressure drop across the pipes, constant supply pressure, neglected temperature influence, no valve dynamics and a linear valve opening characteristic.

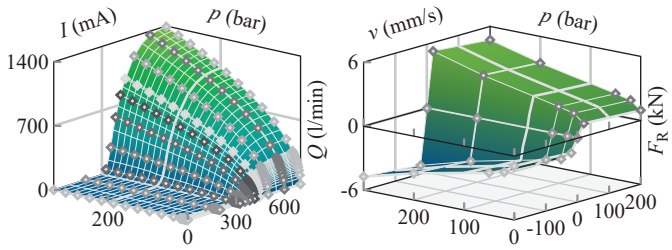

Figure 3 Valve flow characterstic (left) and nonlinear cylinder friction (right)

The complex model is based on the hydraulic system of a large two link mobile manipulator. The system modeled in *ETI ISI SimulationX* incorporates a complex hydraulic fluid model, realistic valve characteristics and friction models shown in Fig. 3. As with the simplified model the hydraulic pump is simplified and modeled as a constant pressure source.

4.2 Controller Adaption

During parametrization and evaluation of the controllers some minor adaptions were performed to enhance the controller performance: Firstly, to take into account the nonlinear valve orifice gradient in (3) a sixth degree polynomial is fitted to the valve characteristic and inverted for the control laws. And secondly, the error dynamics of the FTC (11) and input/output linearization (23) which originally incorporate proportional and derivative terms were extended by an integral error term, reducing static deviations through load force and other unmodeled influences.
We performed the controller parametrization using a cost function on trajectory tracking for each of the two controlled states. Parameter ranges were, if applicable obtained by definition equations 17 or pole placement, else determined empirically during simulation.

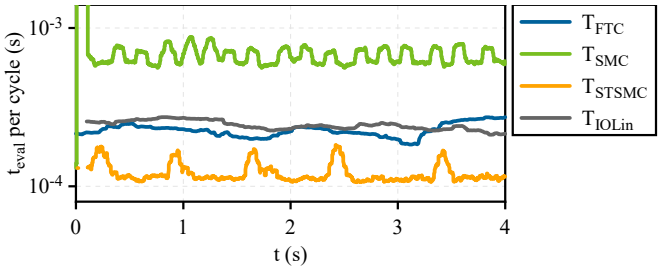

Figure 4 Computation time of controller per cycle

The design of the control laws of each of the four controllers requires complex symbolic computations as shown in Section 3. These were performed offline and the results are callable functions for online evaluation. As the expressions are very complex and lengthy the evaluation time per control cycle was measured during simulation (Fig. 4). The relevance of the absolute evaluation times is low as *Matlab* uses internal optimization and caching for faster evaluation, but it can be observed, that the SMC requires considerably more time per cycle to evaluate the control law than the other algorithms. This can be explained by the high switching frequency[5] at the sliding surface as zero-crossings present a common bottle-neck for function evaluation using discrete switching laws. The STSMC overcomes this issue by requesting

[5] The chattering in discrete time implementations of the SMC is caused by finite time switching limited to the sampling rate and not only a result of unmodeled dynamics [28].

$\dot{s} = 0$ and thus reducing chattering. This can be observed comparing velocity and pressure signals (v, p_{K}) in Fig. 5b to 5c.

4.3 Controller Evaluation

Fig. 5a to 5d show the simulation results of the controlled states for the model validation (v, p_{K}) and evaluation (v^*, p_{K}^*). The simulation is initialized with prestressed chambers and the switching valve opens at $t = 1\,\mathrm{s}$.
On the simplified model all controllers achieve very satisfactory results on pressure control. Slight differences are observable at velocity tracking: While the FTC (Fig. 5d) shows little control errors and good disturbance rejection, the other controllers indicate slightly slower dynamics (Fig. 5a), small static errors and oscillations (Fig. 5b) and imperfect disturbance rejection (Fig. 5c). Generally speaking, independent control of p_{K} and v was accomplished by all four controllers. However, the relatively slow communication frequency negatively affects the performance of the sliding regime controllers as the communication interval limits the switching frequency and thus introduces high frequency chattering.
Moving on to the manipulator's hydraulic system, significant increase of the control error can be observed on all four controllers. Only the combination of feed-forward control (21) and additional PID-like control through (24) of the FTC still obtains acceptable control results, though significant degradation in the form of overshooting and slower transient behavior is observable. The decoupling properties of the other algorithms are obviously reduced. This is especially problematic as the chamber pressure on both sides drops to $p_{\mathrm{T}} = 1\,\mathrm{bar}$ at the beginning of the motion thereby influencing the velocity tracking.

5 Conclusion

In this paper we evaluated four different control strategies for a nonlinear MIMO control problem. Specifically, the objective of this study was to investigate the applicability of these complex algorithms on mobile hydraulic systems. Challenging aspects in this field are parametric and model uncertainties, limited computational capacities and low communication frequency. Foundation for the model-based design is a simplified model of the valve controlled cylinder drive. This incorporates easily identifiable parameters such as geometric parameters as well as approximations of nonlinear model properties like friction and valve characteristic.

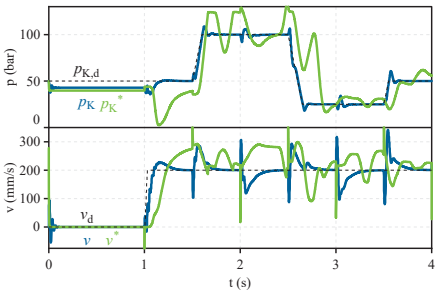

(a) Input/output linearization results for simple (v, p_K) and complex hydraulic model (v^*, p_K^*)

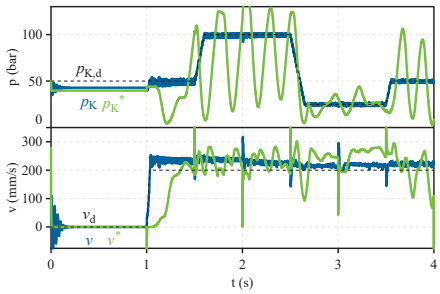

(b) SMC results for simple (v, p_K) and complex hydraulic model (v^*, p_K^*)

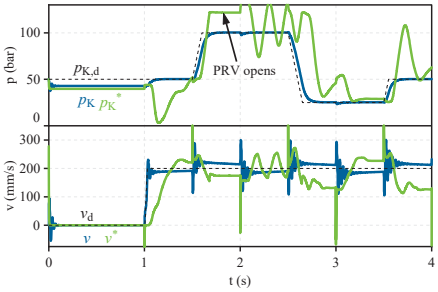

(c) STSMC results for simple (v, p_K) and complex hydraulic model (v^*, p_K^*). At approx. 1.6 s the pressure relieve valve (PRV) opens as p_B exceeds 370 bar.

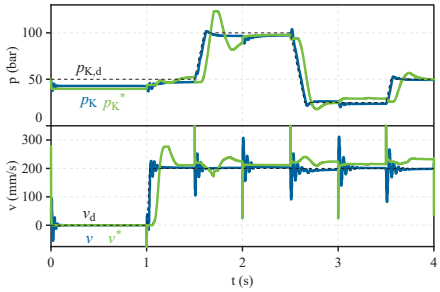

(d) FTC results for simple (v, p_K) and complex hydraulic model (v^*, p_K^*)

Figure 5 Simulation results for velocity and weighted chamber control

Validation is performed on a simplified model, where the FTC and input/output linearization approach showed good follow-up behavior, disturbance rejection and decoupling of the two control variables. But also the sliding regime controllers reached satisfactory results with slight deterioration on the validation model.

Unfortunately, only one controller could reach comparable results on the more complex model. The deterioration was expected for input/output linearization approach as it depends on the inversion of the system model and is susceptible to model and parameter uncertainties. But also the more robust sliding mode controllers could not adequately control the given system. Main reason is the bandwidth limitation and deadtime of the actuating valves as real sliding theoretically requires infinitely fast actuators. Furthermore, the fixed

communication time limits the switching frequency and thus creates chattering not due to unmodeled dynamics but due to discrete sampling. Only the flatness-based tracking controller achieved acceptable results. Although the feed-forward part of the controller is susceptible to parametric uncertainties and unmodeled dynamics, the additional linear controller is able to stabilize the system along the given trajectory.

We demonstrated in this study that a high modeling accuracy is mandatory for the considered control algorithms. Additionally, the low communication frequency of the controller poses a further source of chattering for the sliding based controllers and generally contributes to delayed control performance. However, these requirements are in contrast to the available resources. The controller design already requires the accurate measurement of the system output up to the second derivative. Qualified measurement results are highly questionable and more complex system models incorporating e.g. valve dynamics and variable bulk modulus will further increase the number of derivations necessary.

Lastly, the parametrization of the controllers represented a great challenge. Even though some control gains could be chosen by pole placement and with regard to the used sampling frequency others needed time-consuming empirical tuning with optimization tools.

Acknowledgment

The work reported in this paper was performed within the project: “Development and testing of load- and motion-decoupled actuator structures using nonlinear, model-based control algorithms” funded by the DFG (German Research Society GZ: WE 4828/8-1 Transfer Project). The permission for publication is gratefully acknowledged.

Funded by
DFG Deutsche Forschungsgemeinschaft
German Research Foundation

Nomenclature

Designation	Denotation	[Unit] / Dim.
$A_\mathrm{A}, A_\mathrm{B}$	Piston- and rod-side area of cylinder	$[\mathrm{m}^2]$
d_cyl	Linear damping coefficient	$[\mathrm{s/m}]$
$\boldsymbol{f}$	Autonomous system part	$\mathbb{R}^n$
F_L	External load force	[N]
$\boldsymbol{G}$	Control-affine system part	$\mathbb{R}^{m\times p}$
$\boldsymbol{h}$	Output function	$\mathbb{R}^m$
h	Maximum cylinder stroke	$[\mathrm{m}]$
$k_{i,j}$	Control gains	[-]
K'	Effective bulk modulus	[Pa]
K_V	Valve orifice gradient	$[\mathrm{m}^3\mathrm{s/kg}]$
m_cyl	cylinder mass	$[\mathrm{kg}]$
$p_\mathrm{A}, p_\mathrm{B}$	Chamber pressure	[Pa]
p_K	Weighted chamber pressure	[Pa]
$p_{i,\mathrm{d}}$	Desired pressure	[Pa]
p_0	Supply pressure	[Pa]
p_T	Reservoir pressure	[Pa]
$Q_\mathrm{A}, Q_\mathrm{B}$	Flow	$[\mathrm{m}^3/\mathrm{s}]$
r_i	Relative degree	[-]
s_i	Sliding surface	[-]
$\boldsymbol{u}$	Controller Output / System input	$\mathbb{R}^p$
$\boldsymbol{x}$	System state	$\mathbb{R}^n$
$\boldsymbol{y}$	General system output	$\mathbb{R}^m$
v_d	Desired cylinder velocity	$[\mathrm{m/s}]$
$V_\mathrm{A}, V_\mathrm{B}$	Constant pipe volume	$[\mathrm{m}^3]$
z	Cylinder position	$[\mathrm{m}]$
$\mathcal{L}$	Lie-derivative	[-]
ϵ	Saturation dead zone	[-]
$\boldsymbol{\eta}$	Flat system output	$\mathbb{R}^m$
η	Control parameter for asymptotic convergence towards sliding surface	[-]
λ	Control parameter for exponential convergence on sliding surface	$[1/\mathrm{s}]$
φ_i	Transformation between flat output and input	[-]
$\boldsymbol{\psi}$	Transformation between flat output and state	[-]
$\boldsymbol{\omega}$	Virtual control input	[-]

References

[1] G. Kolks and J. Weber, "Modiciency-Efficient industrial hydraulic drives through independent metering using optimal operating modes," in *Proc. of the 10th International Fluid Power Conference (10. IFK)*, vol. 1, Dresden, 2016, pp. 105–120.

[2] J. Lübbert, A. Sitte, and J. Weber, "Neue Lösungen für elektrohydraulische Steuerungssysteme mobiler Arbeitsmaschinen mit aufgelösten Steuerkanten," DFG, Final Report WE 4828/1-1, May 2016.

[3] Volvo CE Europe, "Large Crawler Excavators: Volvo EC530E/EC550E," Jul. 2021. [Online]. Available: https://www.volvoce.com/europe/en/products/excavators/ec550e/

[4] A. Sitte and J. Weber, "Structural design of independent metering control systems," in *Proc. of the 13th Scandinavian International Conference on Fluid Power*. Linköping, Sweden: Linköping University Electronic Press, 2013, pp. 261–270.

[5] A. Sitte, B. Beck, and J. Weber, "Design of independent metering control systems," in *Proc. of the 9th International Fluid Power Conference*, Aachen, 2014.

[6] A. Isidori, A. J. Krener, C. Gori-Giorgi, and S. Monaco, "Nonlinear Decoupling via Feedback: A Differential Geometric Approach," in *Proc. of IEEE Transactions on Automatic Control*, vol. 26, no. 2, 1981, pp. 331–345.

[7] A. J. Krener, A. Isidori, and W. Respondek, "Partial and Robust Linearization by Feedback," in *Proc. of the 22nd IEEE Conference on Decision and Control*, 1983, pp. 126–130.

[8] A. Isidori, "Exact Linearization Methods," in *Nonlinear control systems*, 1st ed. Berlin: Springer, 1985, pp. 178–253.

[9] T. I. Fossen and B. A. Foss, "Sliding Control of MIMO Nonlinear Systems," *Modeling Identification and Control*, vol. 12, no. 3, pp. 129–138, 1991.

[10] V. I. Utkin, *Sliding modes in control and optimization*, 1st ed. Berlin: Springer DE, 1992.

[11] J.-J. E. Slotine and S. S. Sastry, "Tracking Control of non-linear systems using sliding surfaces, with application to robot manipulators," *International Journal of Control*, vol. 38, no. 2, pp. 465–492, 1983.

[12] K. D. Young, V. I. Utkin, and U. Özgünür, "A control engineers guide to sliding mode control," in *Proc. of IEEE Transactions on Control Systems Technology*, vol. 7, no. 3, 1999, pp. 328–342.

[13] J.-J. E. Slotine and W. Li, *Applied Nonlinear Control*. Englewood Cliffs, New Jersey: Prentice Hall, 1991.

[14] A. Levant, "Sliding order and sliding accuracy in sliding mode control," *International journal of control*, vol. 58, no. 6, pp. 1247–1263, 1993.

[15] L. Fridman and A. Levant, "Higher order sliding modes as a natural phenomenon in control theory," in *Robust control via variable structure and Lyapunov techniques*. London: Springer, 1996, pp. 107–133.

[16] G. Bartolini, A. Ferrara, E. Usai, and V. I. Utkin, "On Multi-Input Chattering-Free Second-Order Sliding Mode Control," in *Proc of IEEE Transactions on Automatic Control*, vol. 45, no. 9. IEEE, 2000, pp. 1711–1717.

[17] J. Davila, L. Fridman, and A. Levant, "Second-Order Sliding-Mode Observer for Mechanical Systems," in *Proc. of IEEE Transactions on Automatic Control*, vol. 50, no. 11, 2005, pp. 1785–1789.

[18] J. Rivera, L. Garcia, C. Mora, J. J. Raygoza, and S. Ortega, "Super-Twisting Sliding Mode in Motion Control Systems," *Sliding Mode Control*, vol. 1, pp. 237 – 254, 2011.
[19] J. A. Moreno and M. Osorio, "Strict Lyapunov Functions for the Super-Twisting Algorithm," in *Proc. of IEEE Transactions on Automatic Control*, vol. 4, no. 57, 2012, pp. 1035–1040.
[20] T. Gonzalez, J. A. Moreno, and L. Fridman, "Variable gain super-twisting sliding mode control," in *Proc. of IEEE Transactions on Automatic Control*, vol. 57, no. 8, 2012, pp. 2100–2105.
[21] M. Fliess, J. Lévine, P. Martin, and P. Rouchon, "On differntially flat nonlinear systems," in *Nonlinear Control Systems Design 1992*, Bordeaux, France, 1992, pp. 159–163.
[22] R. Rothfuß, "Application of flatness-based analysis and control of nonlinear MIMO systems," PhD thesis, 1997. [Online]. Available: http://dx.doi.org/10.18419/opus-4118
[23] R. Bindel, R. Nitsche, R. Rothfuß, and M. Zeitz, "Flatness Based Control of a Two Valve Hydraulic Joint of a Large Manipulator," in *Proc. of IEEE European Control Conference (ECC)*, Karlsruhe, Germany, 1999, pp. 3190–3195.
[24] G. Kolks and J. Weber, "Controller Design for Precise and Efficient Industrial Cylinder Drives Using Independent Metering Valves," in *Proc. of the 9th FPNI Ph.D. Symposium on Fluid Power*, vol. 50473. Florianópolis, SC, Brazil: ASME, 2016.
[25] K. Röbenack, *Nichtlineare Regelungssysteme - Theorie und Anwendung der exakten Linearisierung*, 1st ed. Springer Vieweg, 2017.
[26] I. Nagesh and C. Edwards, "A multivariable super-twisting sliding mode approach," *Automatica*, vol. 50, no. 3, pp. 984–988, 2014.
[27] K. Janschek, *Systementwurf mechatronischer Systeme*. Springer, 2010, vol. 1.
[28] V. I. Utkin, A. Poznyak, Y. V. Orlov, and A. Polyakov, "Discrete-Time Systems," in *Road Map for Sliding Mode Control Design*. Springer, 2020, vol. 1, no. SpringerBriefs in Mathematics, pp. 91–97.

Biography



Lukas Bachmann is a research assistant at TUD University of Technology Dresden, where he has been working at the Chair of Fluid-Mechatronic systems since 2021. He holds a diploma engineer degree in electrical engineering from the TUD University of Technology Dresden. His areas of expertise include nonlinear control theory, automation, robotics and multi-domain simulation. At the Chair of Fluid-Mechatronic systems, as leader of the mobile applications group, his current studies are focused on control and automation of mobile hydraulic systems incorporating independent metering valve technology.

Combined multidimensional approaches for the simulation of flow trough a wall-flow particulate filter

A. N. Impiombato[1] G.Discepoli[1] F. Paltrinieri[1] M. Milano[2] L. Montorsi [2]

luca.montorsi@unimore.it

https://orcid.org/0000-0002-4910-5693

[1]*Department of Science and Methods for Engineering,*
University of Modena and Reggio Emilia 42121 Reggio Emilia, Italy

[2]*Department of Science and Methods for Engineering-Centro En&Tech*
University of Modena and Reggio Emilia 42121 Reggio Emilia, Italy

Abstract.

The paper proposes a combined CFD and 1D approach for the numerical analysis of porous media typical of particulates filters. Due to the geometric complexity of the filter, the model combined the CFD flow simulation upstream the porous medium with the lumped and distributed parameter simulation of the elemental cells of the porous medium. The proposed mathematical model for solving the flow within the porous medium considers the exhaust gas flow within a single three-dimensional trap cell taking continuity and momentum balance into account. The non-linear set of equations of the elements encompassing the porous medium are solved numerically using a one-dimensional approach and combined iteratively with the CFD solution. The pressure drop due to the crossing of the elemental cell walls composed by the particulate layer and the porous medium is modeled using the Darcy's law. The predictive capabilities of the proposed numerical approach are addressed by comparing the numerical results of the model with the data available in literature for a reference geometry

.**Keywords**. Computational Fluid Dynamics, Star CCM+, Particulate Filter, Porous Media, Pressure Drop

1. INTRODUCTION

The exhaust gases generated by the internal combustion engines are among the main causes of pollution as they carry out in the form of aerosols quantities of pollutants harmful to the environment and human health [1], [2]. To lower the pollutants level, automotive companies, in addition to various control systems on the quality of engine combustion, adopt exhaust fumes filtering systems [3]. A Broad field of research is also carried out on the development

of fully sustainable vehicles (such as innovative electric buses [4] or solar-powered vehicles for [5], [6]).

The most commonly used filter is the one with wall-flow geometry, in which the exhaust gases are forced to pass between the filter cells and throughout the porous matrix that separates the different cells. Obviously, the insertion of the monolith in the flue gas exhaust duct produces a pressure drop that the engine has to perform a higher job to ensure that the fumes overcome it. This affects the engine performance, especially the fuel efficiency. Therefore, the ability to accurately predict the back pressure caused by the filter monolith has become very important for automotive companies in optic to optimizing their vehicles [7].

The first fundamental study on the regenerative process of the filter was proposed by Bisset [8] in 1984; the author proposes a one-dimensional model of mass balance, momentum and energy equations. This work was the starting point of subsequent works which had the purpose of predicting the pressure drop in different working conditions. Prantoni et al. [9] adopted the Bisset model [8] in the hypothesis of fluid dynamic interaction between the cells that make up the entire wall-flow filter. While Aleksandrova et al. [10] used the Bissett model [8] to characterize particulate filters for diesel and gasoline engines under different flow conditions but at a fixed temperature. Furthermore, Koltsakis et al. [11] and Yang et al. [12] report further examples of application of the Bissett model [8] for the characterization of particulate filters. In a previous work [13] the dimensionless model of the filter for determining the pressure drop was obtained. Most of these models are based on a scaling approach so that the filter pressure drop can be modeled considering a simplified geometry that includes a single inlet and outlet channel. According with the literature ([7], [9], [13]), the approximation introduced by the scaling approach can be justified when the velocity profile entering the filter is constant so that the mass flow rate is the same in all channels, and when the ratio between the hydraulic diameter of the cell and the filter diameter is very small ($d / D_{filter} \ll 1$). In other words, the full coupling between open and closed channels is negligible on the scale of the entire filter. It is worth mentioning that the applicability of the scaling approach is also limited to filters with homogeneous properties, i.e. all the cells have the same hydraulic diameter, all the porous walls have the same permeability, and soot is distributed homogeneously.

Depending on how the soot is deposited inside the filter cells, the efficiency of the filter also changes. Simulating the filter in this scenario requires the modeling of the interaction events between particles and the porous matrix (Lattice-Boltzmann method), with a high computational cost ([14]–[16]). Another problem that affects the simulation of a real porous medium is the modelling of geometry. On this regard,

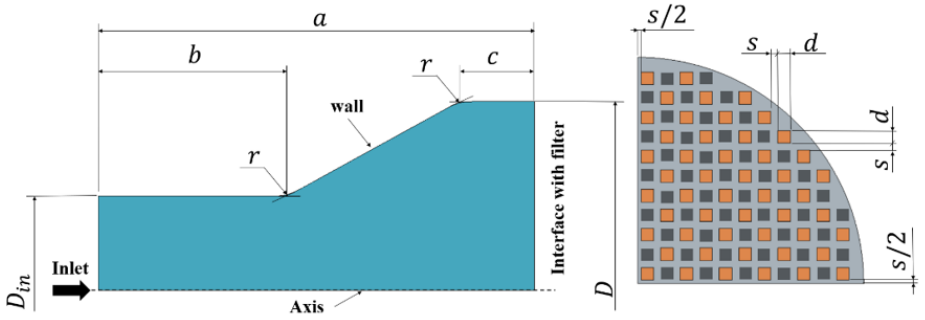

Symbol	D_{in}	D	a	b	c	r	s	d
Value	25.00	50.00	50	25	10	5	0.76	1.40
Unit	mm	mm	mm	mm	mm	mm	mm	mm

Figure.1. CFD computational domain (left); frontal view (right): the open cells are coloured in orange and the closed cells are coloured in black. Geometry measure (bottom).

some authors used the Voronoi tessellation (as reported in [17], [18]), while others used real images obtained from an X-ray [19].

This work analyzes how the fluid dynamics upstream of the filter is influenced inside the duct considering the entire geometry of the monolith. To do this the Computational Fluid Dynamics (CFD) was used to determine the flow field before the monolith and, once the inlet velocity conditions to the individual cells have been obtained, an external code was used to obtain the pressure value in the individual faces of the cells in which the fluid enters. To arrive at the final solution, an iterative process was established between the CFD software and the external code. It is important to specify that, in this work, an ideal gas maintained at fixed temperature of *953.15 K* was considered and no model is used to describe the particulate matter. The results show that the pressure distribution upstream of the filter is not uniform and this affects the velocity range in a way that is not easily predictable.

2. CFD MODEL

In order to demonstrate the coupling between the CFD simulation and the code for solving the governing equations inside the filter channels, the pipe is described in Fig.1. Only the open cells (orange) represent the outlet sections from the fluid domain (i.e. entering the filter). The closed cells (black), on the other hand, have been shown for the sake of clarity, but they are not part of the CFD domain. These, together with the gray part of Fig.1, are seen as a single wall. This assumption is a simplification, as in reality the closed cells (black) are obstructed by a plug. This assumption does not affect the final result as Prantoni M, et al. [9] demonstrated. The geometrical symmetry along the axis permits to consider only a quarter of the entire physical domain, this resulting in a lower computational cost, thus without any loss of information.

In the fluid domain, the Standard k-ω turbulence model [20] (an explanation of the model is provided in Appendix A) was solved using Star-CCM+ [21] considering the set-up of Tab.1.

A velocity inlet of 1 m/s of hot air gas was prescribed at the geometry inlet section. The filter is not included in the computational domain, but the entrance faces of the inlet channels are included (orange cells in Fig.1) and set up as pressure outlets. The value of the pressure for each channel is

Table 1. StarCCM+ set-up parameters

Parameter	**Model**
Domain	3-D
Time	Steady state
Flow solver	Segregated flow
Viscous regime	Turbulent
Model	*k-ω*
Temperature	Isothermal, *T=953.15 K*
Equation of state	Ideal gas law
Fluid	Air
Viscosity	Sutherland's law

determined from the multi-channel model and is discussed in the next section. The remaining boundary surfaces are set-up as no slip walls.

As shown in Fig.2, a polyhedral mesh was used with 5 boundary layers near the pipe wall to achieve *y+* value below 1. A mesh independence stud has been carried out to ensure a mesh-independent solution.



Figure 2. Polyhedral mesh of CFD domain.

3. MULTI-CHANNEL MODEL

Prantoni M, et al. [9] have developed a method for the identification of open cells and closed cells. As shown in Fig.3, the trap cells was identified by two indices (i, j), as each open cell (orange cells) has an even sum of the indices, while the closed cells (black cells) have an

odd sum of the indices. According to the notation shown in Fig.3, the governing flow equation are defined as mass (Eq.1) and momentum (Eq.2) balance [9]:

$$\frac{d}{dx}\left(\rho_{i,j}u_{i,j}\right) = -(-1)^{i+j}\frac{1}{d_h}\,\rho_{i,j}\left(v_{i,j} + w_{i,j} + v_{i+1,j} + w_{i,j+1}\right) \qquad (1)$$

$$\frac{d}{dx}\left(\rho_{i,j}\,u_{i,j}^2\right) = -\frac{d}{dx}\left(p_{i,j}\right) - F\,\frac{\mu}{d^2}u_{i,j} \qquad (2)$$

where u_{ij} is the velocity in the (i,j) channel, p_{ij} is the pressure drop in the (i,j) channel, v_{ij} and w_{ij} are the filtration velocities trough the vertical and horizontal filter walls, ρ_{ij} is the gas density in the (i,j) channel evaluated trough the ideal gas low ($\rho_{ij}=p_{ij}/(R\,T)$ where R is the specific gas constant), μ_{ij} is the gas dynamic viscosity, F arise from the laminar theory in a square pipe [22] and it is equal to *28.454*, d_h is the cell hydraulic diameter and x is the axial coordinate varying from 0 (at the entrance from the filter) to L at the exit of the filter.

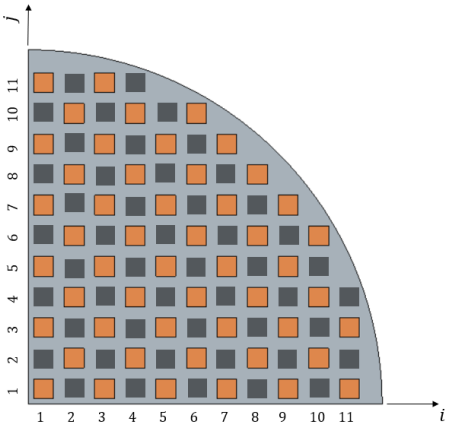

Figure 3. Cell index scheme.

In order to account for the pressure drop variation across the porous wall, the Darcy's law was used to determine the filtrations velocities that arises in Eq.1:

$$v_{i,j} = \frac{k}{\mu\, s}\left(p_{i,j} - p_{i-1,j}\right) \qquad (3)$$

$$w_{i,j} = \frac{k}{\mu\, s}\left(p_{i,j} - p_{i,j-1}\right) \qquad (4)$$

$$v_{i+1,j} = \frac{k}{\mu\, s}\left(p_{i,j} - p_{i+1,j}\right) \qquad (5)$$

$$v_{i,j+1} = \frac{k}{\mu\, s}\left(p_{i,j} - p_{i,j+1}\right) \qquad (6)$$

Substituting Eq.s.3-6 in Eq.1, and considering the ideal gas law, is it possible to define the following system of equations:

$$\frac{d}{dx}\left(p_{i,j}u_{i,j}\right) = -\frac{k}{d_h\,\mu\,s}\,p_{i,j}\left[\left(p_{i,j}-p_{i-1,j}\right)+\left(p_{i,j}-p_{i,j-1}\right)+\left(p_{i,j}-p_{i+1,j}\right)+\left(p_{i,j}-p_{i,j+1}\right)\right] \quad (7)$$

$$\frac{1}{R\,T}\frac{d}{dx}\left(p_{i,j}\,u_{i,j}^2\right) = -\frac{d}{dx}\left(p_{i,j}\right) - F\,\frac{\mu}{d_h^2}u_{i,j} \quad (8)$$

According to Prantoni M, et al. [9], the boundary conditions for the system use the known velocity entering in the inlet channel, zero velocity at the end of the inlet channel and beginning of the outlet channel, and a known pressure at the end of the outlet channel:

Inlet channels (*i* + *j* = even)

$$u_{i,j}(x=0) = U_{i,j} \quad (9)$$

$$u_{i,j}(x=L) = 0 \quad (10)$$

Outlet channels (*i* + *j* = odd)

$$u_{i,j}(x=0) = 0 \quad (11)$$

$$p_{i,j}(x=L) = p_{out} \quad (12)$$

where $U_{i,j}$ is the mean axial velocity at the entrance of the inlet channel (*i,j*), and p_{out} is the pressure at the exit of the outlet channel.

Eq.s.7-12 were solved through Matlab [23] and a boundary value problem solver '*bvp5c(...)*' has been used. The solver is a finite difference code that implements the four-stage Lobotto 3°a formula [24]. The CFD coupling methodology was explained in the next section.

4. COUPLING CFD AND MULTI-CHANNEL MODEL

The CFD and the Multi-Channel models were coupled through the front faces of the inlet channels (Fig. 4), and an iteration procedure was used to obtain a converged solution in both domains (see Fig.5).

As Prantoni M, et al. [9] demonstrated, Fig.6 shows the solution algorithm for the coupling between Star-CCM+ [21] and Matlab [23]. The procedure consists of:

1) setup CFD simulation with the pressure values at the inlet cells with an initial guess value.

2) Run the CFD simulation until convergence.

3) Extract the mean cross-sectional velocity entering each channel (Ui,j).

4) Use these velocities as inlet boundary conditions defined in Eq.9 for solving the boundary value problem using Matlab. The pressure pout defined in Eq.12 is setup as ambient pressure.

5) Extract the pressure at the entrance of each inlet channel from Matlab solution.

6) Update the outlet pressure condition of each entrance face of the inlet channels in the CFD simulation.

7) Repeat n times the steps 2) to 6) until the differences in backpressure is less than 10-6.

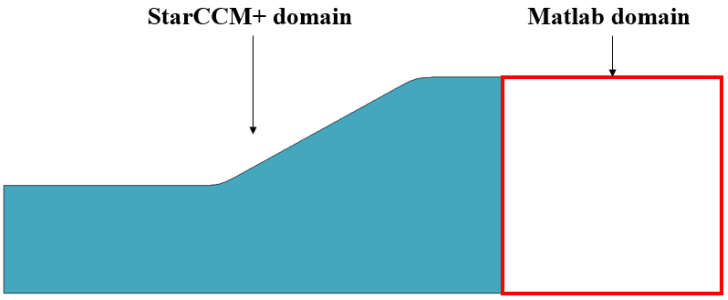

Figure 4. Computational domain in StarCCM+ and Matlab.

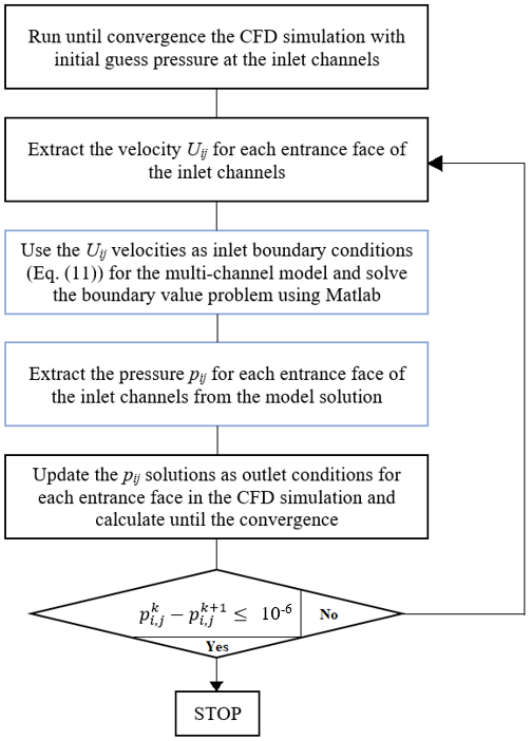

Figure 5. Algorithm.

5. RESULTS

For Matlab [23] numerical resolution the following filter properties have been considered:

- Filter length: $L=0.125\ m$
- Porous media permeability: k=5.5 10^{-3} m^2
- Hydraulic dyameter: $d=0.0014\ m$
- Pressure outlet: $p_{out}=0\ Pa$

Fig. 6 shows the last results of the iterative process. In particular, the velocity and the pressure range on a longitudinal section of the entire pipe is shown. It can be seen how the geometry of the pipe influences the fluid dynamics of the system. In fact, the areas of interface with the filter that are closest to the axis undergo a greater impact by the fluid, generating an overpressure around them, while the areas further away from the axis are little affected by the violence of the fluid impact. In Fig. 6 the velocities and pressures in the open cells are also shown. As it is easy to notice, the cells that undergo a higher input velocity are those halfway between the central units and those farthest from the axis.

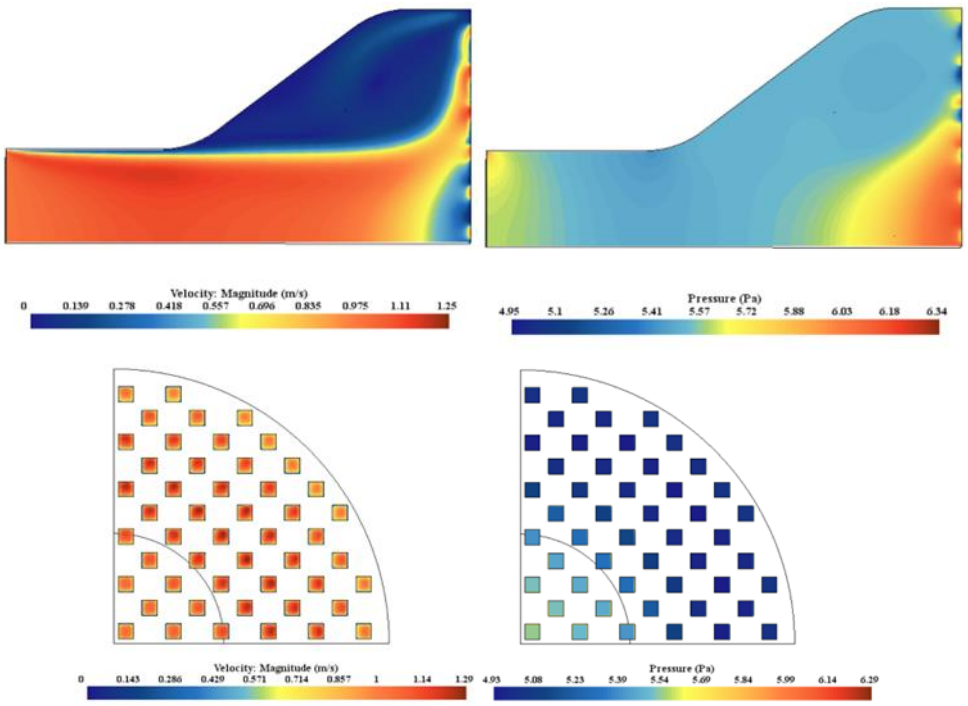

Figure 6. Velocity contour and relative pressure contour on longitudinal and frontal section.

It is however interesting to note that the pressure is not constant upstream of the filter and the geometric configuration influences the entire fluid dynamics as also demonstrated by Prantoni M, et al. [9]. To better visualize the areas where vortices were formed, a convolution integral on the velocity field has been shown in Fig. 7.

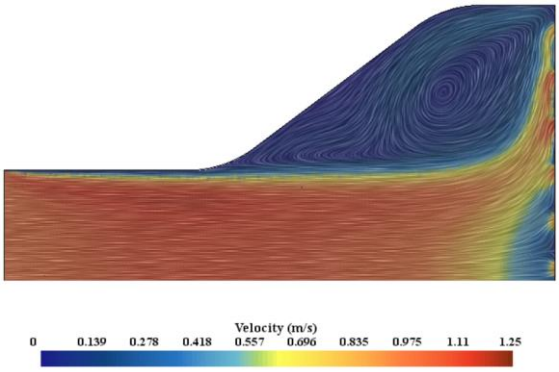

Figure 7. Velocity integral convolution for vortex visualization.

6. CONCLUSION

In this manuscript an alternative method for solving a fluid dynamics problem has been proposed. In particular, the influence of a wall-flow particulate filter it was studied on the fluid dynamics upstream of it. The conformation of the filter forces the fluid to pass through the small cells. This can lead into a numerical problem when one takes into account the real filters with a very high number of cells per mm^2 as it is necessary to create meshes that from large become very small. It is possible to get rid of this problem if the computational domains are separated: the fluid dynamic part upstream of the filter was solved through a classic CFD; the fluid dynamic part in the filter was solved externally by solving the equations that characterize the filter. The numerical coupling between the two different domains was carried out through an iterative procedure, which derives the input velocity to the filter cells from the CFD calculation and uses this as boundary conditions of the boundary value problem in the filter domain to derive the new pressure to be imposed in the outlet sections of the CFD domain. The results show that upstream of the filter the pressure distribution is not uniform. This means that the engine that pushes the exhaust fumes has to do more work to expel them.

The focus of the presented study was to demonstrate a software coupling methodology. The hypotheses made have a big weight on the final result:

- It was assumed that the relative pressure downstream of the filter was known (set equal to zero), but this value does not conform to reality. The actual conditions deviate from reality and this has an impact on the filter itself which must be taken into account.
- The soot accumulation or an initial soot layer in contact with the filter walls was not considered: this modifies the porous media permeability which will no be longer a continuous medium, but will be formed by layers of different material.

- A constant temperature has been assumed but, in reality, the temperature changes during the process and will result in changes in density, mass flow and pressure. This influence will be further explored in future works.

APPENDIX A

The standard *k*- ω model is an empirical model based on model transport equations for the turbulent kinetic energy, *k*, and the specific dissipation rate, ω. These quantities are obtained from the following transport equations:

$$\frac{\partial}{\partial x_i}(\rho k u_i) = \frac{\partial}{\partial x_j}\left(\Gamma_k \frac{\partial k}{\partial x_j}\right) + G_k - Y_k \quad (1.A)$$

$$\frac{\partial}{\partial x_i}(\rho \omega u_i) = \frac{\partial}{\partial x_j}\left(\Gamma_\omega \frac{\partial \omega}{\partial x_j}\right) + G_\omega - Y_\omega \quad (2.A)$$

Where ρ is the fluid density, u_i is the fluid velocity component, G_k and G_ω represents the generation of k and ω, Γ_k and Γ_ω represent the effective diffusivity ok *k* and ω, Y_k and Y_ω represent the dissipation ok *k* and ω due to turbulence. More information can be found in the literature for a better understanding.

7. REFERENCES

[1] R. Niessner, 'The many faces of soot: Characterization of soot nanoparticles produced by engines,' Angewandte Chemie - International Edition, vol. 53, no. 46, pp. 12366–12379, Nov. 2014, doi: 10.1002/anie.201402812.

[2] J. Tollefson, 'Soot a major contributor to climate change,' Nature, Jan. 2013, doi: 10.1038/nature.2013.12225.

[3] A. J. Torregrosa, J. R. Serrano, F. J. Arnau, and P. Piqueras, 'A fluid dynamic model for unsteady compressible flow in wall-flow diesel particulate filters,' Energy, vol. 36, no. 1, pp. 671–684, 2011, doi: 10.1016/j.energy.2010.09.047.

[4] C. Fragassa, 'Electric City Buses with Modular Platform: A Design Proposition for Sustainable Mobility,' Smart Innovation, Systems and Technologies, vol. 68, pp. 789–800, 2017, doi: 10.1007/978-3-319-57078-5_74.

[5] G. Minak, C. Fragassa, and F. V. de Camargo, 'A Brief Review on Determinant Aspects in Energy Efficient Solar Car Design and Manufacturing,' Smart Innovation, Systems and Technologies, vol. 68, pp. 847–856, 2017, doi: 10.1007/978-3-319-57078-5_79.

[6] G. Minak, T. M. Brugo, C. Fragassa, A. Pavlovic, F. v. de Camargo, and N. Zavatta, 'Structural Design and Manufacturing of a Cruiser Class Solar Vehicle,' JoVE (Journal of Visualized Experiments), vol. 2019, no. 143, p. e58525, Jan. 2019, doi: 10.3791/58525.

[7] M. Prantoni et al., 'Modelling Pressure Losses in Gasoline Particulate Filters in High Flow Regimes and Temperatures,' 2019.

[8] E. J. Bissett, 'Mathematical Model Of The Thermal Regeneration Of A Wall-Flow Monolith Diesel Particulate Filter,' 1984.

[9] M. Prantoni, S. Aleksandrova, H. Medina, and S. Benjamin, 'Multi-channel modelling approach for particulate filters,' Results in Engineering, vol. 5, Mar. 2020, doi: 10.1016/j.rineng.2019.100077.

[10] S. Aleksandrova et al., ‘Turbulent Flow Pressure Losses in Gasoline Particulate Filters,’ Source: SAE International Journal of Engines, vol. 12, no. 4, pp. 455–470, 2019, doi: 10.2307/26897923.

[11] G. Koltsakis, O. Haralampous, C. Depcik, and J. C. Ragone, ‘Catalyzed diesel particulate filter modeling,’ Reviews in Chemical Engineering, vol. 29, no. 1, pp.161,Feb.2013,doi:10.1515/REVCE20120008/MACHINEREADABLECITATION/RIS.

[12] S. Yang, C. Deng, Y. Gao, and Y. He, ‘Diesel particulate filter design simulation: A review:,’ http://dx.doi.org/10.1177/1687814016637328, vol. 8, no. 3, pp. 1–14, Mar. 2016, doi: 10.1177/1687814016637328.

[13] A. N. Impiombato, C. Biserni, M. Milani, and L. Montorsi, ‘Prediction Capabilities of a One-dimensional Wall-flow Particulate Filter Model,’ J. Appl. Comput. Mech, vol. 8, no. 1, pp. 245–259, 2022, doi: 10.22055/JACM.2021.38708.3270.

[14] U. Lantermann and D. Hänel, ‘Particle Monte Carlo and lattice-Boltzmann methods for simulations of gas–particle flows,’ Computers & Fluids, vol. 36, no. 2, pp. 407–422, Feb. 2007, doi: 10.1016/J.COMPFLUID.2005.10.005.

[15] L. P. Wang, C. Peng, Z. Guo, and Z. Yu, ‘Lattice Boltzmann simulation of particle-laden turbulent channel flow,’ Computers & Fluids, vol. 124, pp. 226–236, Jan. 2016, doi: 10.1016/J.COMPFLUID.2015.07.008.

[16] C. Rettinger and U. Rüde, ‘A coupled lattice Boltzmann method and discrete element method for discrete particle simulations of particulate flows,’Computers&Fluids, vol.172, pp. 706–719, Aug. 2018, doi:10.1016/J.COMPFLUID.2018.01.023.

[17] H. Wei, J. S. Chen, and M. Hillman, ‘A stabilized nodally integrated meshfree formulation for fully coupled hydro-mechanical analysis of fluid-saturated porous media,’ Computers & Fluids, vol. 141, pp. 105–115, Dec. 2016, doi: 10.1016/J.COMPFLUID.2015.11.002.

[18] J. Huang, F. Xiao, H. Dong, and X. Yin, ‘Diffusion tortuosity in complex porous media from pore-scale numerical simulations,’ Computers & Fluids, vol. 183, pp. 66–74, Apr. 2019, doi: 10.1016/J.COMPFLUID.2019.03.018.

[19] K. Yamamoto, S. Satake, H. Yamashita, N. Takada, and M. Misawa, ‘Fluid simulation and X-ray CT images for soot deposition in a diesel filter,’ Eur. Phys. J. Special Topics, vol. 171, pp. 205–212, 2009, doi: 10.1140/epjst/e2009-01030-x.

[20] D. WILCOX, ‘A half century historical review of the k-omega model,’ Jan. 1991, doi: 10.2514/6.1991-615.

[21] Siemens Digital Industries Software, ‘Simcenter STAR-CCM+, version 2021.1.1.’ 2021.

[22] N. C. Markatos, ‘Transport processes in chemically reacting flow systems,’ International Journal of Heat and Mass Transfer, vol. 33, no. 5, p. 1039, May 1990, doi: 10.1016/0017-9310(90)90087-B.

[23] MATLAB, ‘R2022a.’ The MathWorks Inc. Natick, Massachusetts, 2022.

[24] L. Shampine, J. Kierzenka, and L. F. Shampine, ‘A BVP solver that controls residual and error A BVP Solver that Controls Residual and Error 1,’ European Society of Computational Methods in Sciences and Engineering (ESCMSE) Journalof Numerical Analysis, Industrial and Applied Mathematics (JNAIAM), vol. 3, no. 2, pp. 27–41, 2008, Accessed: Mar. 29, 2022. [Online]. Available: https://www.researchgate.net/publication/228748602

Biographies



Luca Montorsi received the master's degree in mechanical engineering from University of Modena and Reggio Emilia in 1999, and the philosophy of doctorate degree in Materials Engineering from University of Modena and Reggio Emilia in 2003, respectively. He is currently working as an Full Professor at the Department of Sciences and Methods for Engineering, Faculty of Engineering, University of Modena and Reggio Emilia. His research areas include Fluid Power and System for Energy Conversion and Environment. He has been serving as a reviewer for many highly-respected journals.

Using nonlinear observers as virtual sensors in hydraulically actuated equipment in Industrial IoT systems

Victor Zhidchenko, Yashar Shabbouei Hagh, Egor Startcev, Heikki Handroos

Mechanical Engineering Department, LUT University, Lappeenranta, Finland
victor.zhidchenko@lut.fi

Abstract.

Real-time state observation of hydraulically actuated equipment requires powerful computational resources. The reason is the high sampling rate needed to capture dynamics of the hydraulic systems and additional computational complexity introduced by nonlinear estimators. In Industrial IoT applications, this problem is exacerbated by network delays. This paper considers the problem of improving the computational performance of the two popular nonlinear observers—Unscented Kalman Filter and Particle Filter—in IoT applications for hydraulic equipment. For the example case of a mobile log crane, the paper demonstrates several ways of building remote observers for IoT applications. Multi-body model of the crane coupled with the model of its hydraulic system allows capturing crane dynamics with different sets of sensors. Parallel computing on multi-core CPUs and GPUs is used to speed up calculations. Experimental results demonstrate the performance of the observers executed on a desktop computer and on an edge-computing device. The paper concludes with general guidelines for implementing nonlinear observers in these execution environments. The results can be applied in the remote and autonomous operation of hydraulically actuated equipment and maintenance activities for such machines.

Keywords. Observation, observer, Unscented Kalman Filter, Particle Filter, hydraulics, Internet of Things.

1. INTRODUCTION

Recent advancements in sensor and telecommunication technology allowed obtaining continuous information about remote equipment state. The benefits of processing this information within the Industrial Internet of Things (IIoT) and Digital Twin concepts are limited by the availability and cost of computing resources that can be allocated to each piece of equipment. At the time of writing, statistical and machine learning methods dominated in equipment fleet management systems. Physics-based methods, being widely used in simulation in the machine design phase, were not so popular in the operation and

maintenance phase. The reasons include the difficulty of precise model creation for each instance of equipment and the computational complexity of such methods, especially when a small time step is required. Since physics-based methods can enrich information by calculating unmeasured values and providing confident results, their integration into IIoT and Digital Twin concepts is an important task.

Observation techniques facilitate the application of physics-based models by decreasing the modeling errors related to the non-perfect fit of the model to a real object [1, 2]. They can also extend virtual sensor capabilities by parameter estimation by finding the values for which explicit formulas are not present in the model. Due to nonlinearity of models used for hydraulically actuated equipment simulation, nonlinear filters should be used to observe such equipment. This paper considers two widely used nonlinear filters, the Unscented Kalman Filter (UKF) and the Particle Filter (PF). Applying these methods for hydraulically actuated machines further increases the high computational complexity of the physics-based models. However, the capability of the model to provide results in real time is essential, even if there is no real-time connection with the machine. For IIoT and digital twin applications, it ensures that the model results are provided concurrently with the machine operation and no latency accumulates over time.

The goal of the presented work is to study real-time capabilities of computer programs that implement nonlinear filtering for the hydraulic models coupled with multi-body models of heavy equipment. Such programs can be used in IIoT systems to build digital twins of mobile working machines. Using a hydraulic log crane as an example, this paper considers real-time application of UKF and PF and demonstrates some techniques for improving their computational performance. The paper contributes to the development of IIoT and Digital Twin concepts by presenting possible ways of integrating physics-based models into the information processing pipelines for hydraulic equipment. For hydraulic cranes, such integration can facilitate crane operation [3] (especially remote and autonomous operation), remote surveillance, predictive maintenance, and fatigue life estimation [4].

The rest of the paper is organized as follows. Section II gives a brief literature review on the topic of the paper. The methodology used in this paper is addressed in Section III. Section IV introduces the experimental setup of the considered log crane. The results are discussed in Section V. Conclusions are presented in the final section.

2. RELATED WORK

Due to computational complexity, nonlinear filters have traditionally been used in application areas where the sampling interval is relatively large. For example, in position detection and some manufacturing and chemical processes, the measurements can be made once in several seconds [5]. The works considering nonlinear filtering in multi-body dynamics are more recent.

The computational efficiency of a program implementing model-based nonlinear filtering for multi-body systems depends primarily on the time needed to calculate a system state at each time step. The computational complexity of different multi-body formulations varies from $O(N^4)$ to $O(N)$, where N is the number of bodies [6]. Sometimes, it is impossible to choose the formulation because it is prescribed by the software used for multi-body modeling. If there is an opportunity to choose, the formulation with lower computational

complexity will give more freedom for the efficient filter implementation. Another important aspect is the possibility to represent the multi-body model in a state-space form, which is required for applying the filtering techniques.

The application of the nonlinear Kalman filters, such as the Extended Kalman Filter (EKF) and Unscented Kalman Filter (UKF), in real-time state estimation of different nonlinear systems has gained significant attention in the past years. For instance, [7, 8] proposed a new version of the EKF algorithm named indirect EKF based on multi-body models. Using different methods to calculate the Jacobian matrix, it has been shown that the proposed EKF could achieve the same level of accuracy as UKF but with less computational cost. However, by reducing the sampling rate of sensors, the quality of the estimations degrades faster than with UKF. Nevertheless, computing the Jacobian matrix might not be an easy task, especially for systems with severe nonlinearity. Furthermore, [9] applied the nonlinear Kalman filters state estimation using multi-body models. To this end, EKF, UKF, and spherical simplex UKF (SSUKF) are applied to a 5-bar linkage mechanism. Emphasizing on the computational cost of the UKF-based filters, these filters resulted in more accurate estimations than the EKF. On the other hand, it has been mentioned that the easy implementation of the UKF and its ability to use parallel computing are the reasons that make UKF capable to run in real time.

Representing a subset of Monte Carlo methods, particle filters support parallelization. A generic parallel algorithm for particle filter was presented in [10]. Experiments on different computers using the Message Passing Interface (MPI) technology demonstrated an ability to implement the algorithm in real time for the simple synthetic tasks of position estimation. A survey on early developments in distributed estimation with particle filtering can be found in [11]. The paper considered the particle filter a viable alternative for real-time implementations in the near future. Nonetheless, a decade later, the method was still used primarily in low-sampling rate applications.

Attempts to improve the computational efficiency of particle filtering by using GPUs appeared immediately with the rise of this technology. One of the early works [12] considered a general approach for parallelizing the particle filter on GPUs. In more recent works, GPU-accelerated particle filters were applied to the tasks of controlling the robotic arm [13] and manufacturing processes [5].

3. METHODOLOGY

3.1. Multi-body Model of the Crane

This paper studies the application of nonlinear filtering to the multi-body system state estimation using a simple real machine. Mobile hydraulic log crane PATU655 installed in the laboratory of intelligent machines of LUT University was used as a test system (Figure 3.1). The crane consists of a pillar, a main boom, and a jib boom. A grapple was not attached to the crane for safety reasons. Constrained space in the laboratory did not allow to rotate the pillar. Therefore, the crane could only move in two dimensions by rotating the main and the jib booms. Two hydraulic cylinders actuated the booms. The jib boom was connected to the cylinder by a four-bar mechanism.

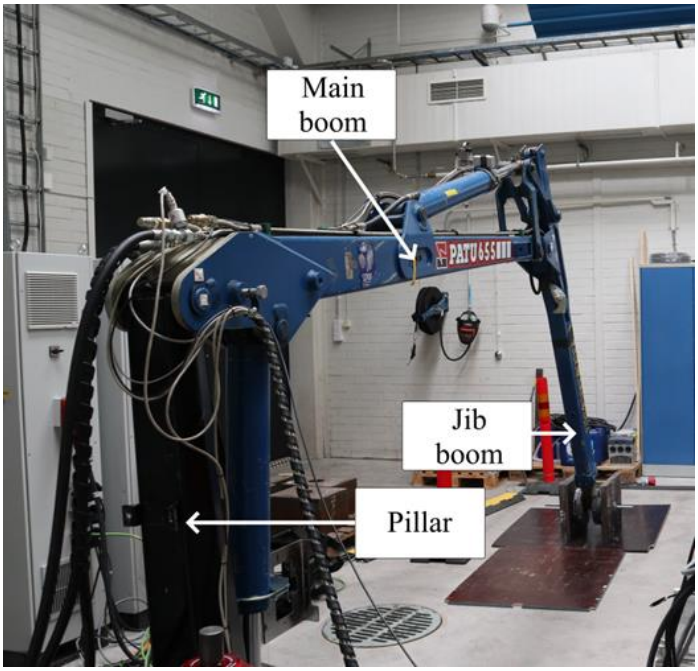

Figure 3.1. The mobile hydraulic log crane considered in the paper

The multi-body model based on the Iterative Newton-Euler Formulation (INEF), which was developed and described in [3] and [4], was used to simulate the crane dynamics. The model considers four states: the angle of the main boom, the angular velocity of the main boom, the angle between the main and the jib boom, and the angular velocity of the jib boom relative to the joint between the booms. The forces produced by the hydraulic cylinders are calculated from the pressure in the cylinder chambers, the geometry of the cylinders, and the speed of the cylinder motion.

For state estimation problems, the state-space representation of the dynamic model offers a general framework. Thus, in this paper, the state-space formulation is utilized to introduce the filtering algorithms.

Consider a discrete-time nonlinear system as:

$$\begin{aligned} x_k &= \mathcal{F}(x_{k-1}, u_{k-1}) + w_{k-1} \\ y_k &= \mathcal{H}(x_k) + v_k \end{aligned} \tag{3.1}$$

in which x_k denotes the state vector of the system with the dimension of n_x, and u_k represents the input control signal. $\mathcal{F}(x_{k-1}, u_{k-1})$ represents the dynamic system function. The observation is denoted by y_k with dimension of n_y and measurement sensitivity matrix of $\mathcal{H}(x_k)$. The nonlinear system is under an additive Gaussian process and measurement noise. $w \sim \mathrm{N}(0, \mathcal{Q})$ and $v \sim \mathrm{N}(0, \mathcal{R})$ represent the process and the measurement noises with zero-mean and the covariance matrix of $\mathcal{Q}$ and $\mathcal{R}$, respectively.

3.2. Unscented Kalman Filter

As an alternative to the conventional EKF with deficiencies due to linearization, which can be found in the literature [14], the UKF algorithm was proposed to address these drawbacks [15]. This algorithm is based on a sampling technique named Unscented Transform, which generates a set of sample points known as sigma-points to capture the true mean and covariance of the random variable [16, 17].

The algorithm is initialized with $k = 0$ values of the error covariance matrix as $P_{0|0} = E[(x_0 - \hat{x}_0)(x_0 - \hat{x}_0)^T]$ and the state estimation as $\hat{x}_{0|0} = E[x_0]$. Based on these assumptions the sigma-points are calculated for $k = 1$ as:

$$\chi^{(j)}_{k-1|k-1} = \left[\hat{x}_{k-1|k-1}, \hat{x}_{k-1|k-1} + \sqrt{n_x + \Gamma}\sqrt{P_{k-1|k-1}}, \hat{x}_{k-1|k-1} - \sqrt{n_x + \Gamma}\sqrt{P_{k-1|k-1}}\right] \tag{3.2}$$

in which $j = 0, \dots, 2n_x$, $\sqrt{\cdot}$ denotes the square root of the Cholesky decomposition using its lower triangular matrix and $\Gamma = \alpha^2(\mathrm{n_x} + \kappa) - \mathrm{n_x}$. α and κ are the scaling parameters in which $0 \leq \alpha \leq 1$ controls the spread of the sigma-points and $\kappa \geq 0$ guarantees positive semi-definiteness of the covariance matrix. Then, based on the dynamic system function defined in Eq.(3.1), the generated sigma-points should be propagated as:

$$\gamma^{(j)}_{k|k-1} = \mathcal{F}\left(\chi^{(j)}_{k-1|k-1}, u_{k-1}\right), j = 0,1,\dots,2n_x \tag{3.3}$$

Now, using the predefined set of weights as $\omega_0^{(m)} = \Gamma/(n_x + \Gamma)$, $\omega_0^{(c)} = \omega_0^{(m)} + (1 - \alpha^2 + \beta)$, $\omega_j^{(c)} = \omega_j^{(m)} = 1/2(n_x + \Gamma)$, the *a priori* estimation of the mean and the covariance can be calculated using the following formulations:

$$\begin{aligned} \hat{x}_{k|k-1} &= \textstyle\sum_{j=0}^{2n_x} \omega_j^{(m)} \gamma^{(j)}_{k|k-1} \\ \mathrm{P}_{k|k-1} &= \textstyle\sum_{\mathrm{j}=0}^{2\mathrm{n_x}} \left\{\omega_{\mathrm{j}}^{(c)} \left(\gamma^{(j)}_{k|k-1} - \hat{x}_{k|k-1}\right)\left(\gamma^{(j)}_{k|k-1} - \hat{x}_{k|k-1}\right)^{\mathrm{T}}\right\} + \mathcal{Q}_{\mathrm{k\text{-}1}} \end{aligned} \tag{3.4}$$

in which β as the secondary scaling factor is set to be 2 as an optimal choice for Gaussian noise distributions. In order to correct the *a priori* estimations, a new set of sigma-point should be generated as:

$$\chi^{(j)}_{k|k-1} = \left[\hat{x}_{k|k-1}, \hat{x}_{k|k-1} + \sqrt{n_x + \Gamma}\sqrt{P_{k|k-1}}, \hat{x}_{k|k-1} - \sqrt{n_x + \Gamma}\sqrt{P_{k|k-1}}\right] \tag{3.5}$$

then, each column of the generated sigma-points will propagate through the measurement sensitivity matrix as:

$$\mathcal{Y}^{(j)}_{k|k-1} = \mathcal{H}\left(\chi^{(j)}_{k|k-1}\right), \quad j = 0,1,\dots,2\mathrm{n}_x \tag{3.6}$$

Based on the propagated sigma-points the predicted measurements, innovation covariance, and the cross-covariance of the predicted measurement can then be computed as follows:

$$\begin{aligned} \hat{\mathcal{Y}}_{k|k-1} &= \textstyle\sum_{\mathrm{j}=0}^{2\mathrm{n}_x} \omega_j^{(m)} \mathcal{Y}^{(j)}_{k|k-1} \\ P_k^{xy} &= \textstyle\sum_{\mathrm{j}=0}^{2\mathrm{n}_x} \omega_j^{(c)} \left(\gamma^{(j)}_{k|k-1} - \hat{x}_{k|k-1}\right)\left(\mathcal{Y}^{(j)}_{k|k-1} - \hat{\mathcal{Y}}_{k|k-1}\right)^{\mathrm{T}} \\ P_k^{yy} &= \textstyle\sum_{\mathrm{j}=0}^{2\mathrm{n}_x} \left\{\omega_j^{(c)} \left(\mathcal{Y}^{(j)}_{k|k-1} - \hat{\mathcal{Y}}_{k|k-1}\right)\left(\mathcal{Y}^{(j)}_{k|k-1} - \hat{\mathcal{Y}}_{k|k-1}\right)^{\mathrm{T}}\right\} + \mathcal{R}_k \end{aligned} \tag{3.7}$$

Based on P_k^{xy} and P_k^{yy}, the Kalman gain K_k can be calculated, which is used to calculate the *a posteriori* mean state vector $\hat{x}_{k|k}$ and the covariance matrix $P_{k|k}$ as:

$$\begin{aligned} K_k &= P_k^{xy}\left(P_k^{yy}\right)^{-1} \\ \hat{x}_{k|k} &= \hat{x}_{k|k\text{-}1} + K_k\left(y_k - \hat{y}_{k|k-1}\right) \\ P_{k|k} &= P_{k|k\text{-}1} - K_k P_k^{yy} K_k^{\mathrm{T}} \end{aligned} \tag{3.8}$$

The equations from Eq. (3.2) to Eq. (3.8) are calculated for each new time step. This loop is repeated until the stop criteria are met.

3.3. Particle Filter

The particle filter algorithm, which is based on the Monte Carlo method, uses a set of randomly chosen samples (particles) with associated weights to estimate the posterior probability density function (PDF) [18, 19]. The idea of representing the posterior PDF with a set of samples and weights is referred to as the sequential importance sampling (SIS) algorithm. This posterior PDF can be approximated as $p[x_k|y_k] \approx \sum_{i=1}^{N} w_k^i\, \delta\left[x_k - x_k^i\right]$, in which x_k^i is the set of random samples, N is the number of samples, w_k^i are the associated weights, and $\delta[\cdot]$ is the Dirac delta measure. This sampling procedure from the true posterior PDF is usually impossible, hence an importance density as $q\left[x_k^i|x_{k-1}^i, y_k\right]$ is used. Therefore, at each sampling instant, a sample is drawn from the importance density rather than the true posterior PDF. To compensate for the difference between these two densities, the associated weights can be calculated in a sequential case as:

$$\tilde{w}_k^i = \tilde{w}_{k\text{-}1}^i \frac{p\left[y_k|x_k^i\right]p\left[x_k^i|x_{k-1}^i\right]}{q\left[x_k^i|x_{k-1}^i, y_k\right]} \implies w_k^i = \frac{\tilde{w}_k^i}{\sum_{j=1}^{N} \tilde{w}_k^j} \tag{3.9}$$

One major issue with the SIS filter is known as weight degeneracy. In this case, after some iterations, only a few particles have non-zero importance weights. In other words, after some iterations, some particles will have zero contribution to the approximation of $p[x_k|y_k]$. A resampling step is introduced to resolve this drawback, which is based on the sampling importance resampling particle filter (SIR-PF) algorithm. This step discards the samples with low importance using different methods such as: residual sampling [20], systematic sampling [18], stratified sampling [21]. However, owing to the simplicity and efficiency of systematic resampling, this is a common choice in an SIR method. The algorithm of this resampling method is given in [22]. The SIR-particle filter algorithm can be summarized as follows:

- Step (1): Initialization: For $k = 0$ generate initial particles x_0^i and the associated weights w_0^i for $i = 1, \ldots, N$ from the *a priori* distribution;
- Step (2): Importance sampling: Generate prior particles, $x_k^{i,-}$, from the importance sampling density function;
- Step (3): Weighting: Calculate the weights of each particle once a new measurement is available using Eq. (3.9);
- Step (4): Resampling: Based on the calculated weightings and resampling method of systematic resampling, calculate the *a posteriori* particles x_k^i;

- Step (5): Estimation: Estimate the state by calculating $\hat{x}_k = \sum_{i=1}^{N} w_k^i \, x_k^i$. Set $k = k + 1$ and go back to Step (2).

3.4. Particle Filter Implementation on a GPU

This study used Nvidia CUDA technology to accelerate particle filter implementation. Three features of Nvidia GPUs were utilized to minimize calculation time: a substantial amount of device memory, asynchronous memory transfers, and streams. Since the function $\mathcal{F}(x, u)$ derived from INEF formulation was implemented as a custom C function, it was converted to a kernel function to generate particles concurrently at step (2) of the particle filter algorithm. Another kernel function performed weighting at step (3) of the algorithm.

The most time-consuming operations in a particle filter are the calculation of the system function $\mathcal{F}(x, u)$ and the generation of the pseudo-random numbers. The latter operation was performed in a batch mode when many random values were generated by a single function call and stored in the device memory as a lookup table. Instead of calling a time-consuming random generator at each time step, the values from the table were used across several time steps to create particles. When the lookup table with random numbers was consumed, it was generated again. System function calculation and random number generation were performed in different streams. These measures allowed to implement real-time particle filter for the crane model with 1024 particles. The accuracy of the filter was considered sufficient, and the resampling step was not performed on the GPU.

4. EXPERIMENTAL SETUP

The log crane used in the experiments was instrumented with pressure sensors for the piston side and the rod side of each cylinder, position sensors measuring the length of each cylinder, and the gyroscopes attached to each boom. The sensors were connected to the dSPACE 1005 data acquisition system, which transmitted the data to the computer installed in the lab using the local area network connection. A Python script was used to save the data on disk and send them to a remote computer in LUT University by the UDP protocol.

Two sets of experiments were performed. In the first set, the accuracy and computational performance of the UKF and particle filters were evaluated. The particle filter was implemented by a custom-made C program using Nvidia CUDA technology for GPU computing. The C program implementing the UKF filter was automatically generated from a custom MATLAB script using the MATLAB Coder tool. Both programs read the measurement data from a CSV file, estimated the system state using a full or constrained set of sensors, and saved the results to another CSV file. Measurement data consisted of the boom angles calculated from the cylinder linear displacement measurements, angular velocity of the booms measured by gyroscopes, and pressure in the cylinder chambers measured by pressure sensors. Calculations were performed on a desktop computer equipped with the Intel Core i9-9820X 3.3GHz CPU and NVIDIA GeForce RTX 2080 SUPER GPU. The program implementing the UKF filter was also compiled and executed on a Raspberry Pi 4 Model B microcomputer. Optimizing compilation was not used in the experiments. Each program version was executed 30 times on the same data set. Between the executions, 15 seconds breaks were made to decrease the influence of other programs on CPU load. Execution time was measured using the omp_get_wtime() function of the OpenMP library. Other capabilities of the OpenMP technology were not used in the experiments.

In the second set of experiments, the nonlinear filters were used for the real-time visualization of the crane motion. A remote computer in LUT University connected to the crane measurement system by the local area network represented an IoT system. CAD drawings of the crane were used to visualize its motion in the Unity environment. The programs implementing UKF and particle filters were modified to receive the input data by UDP protocol instead of reading them from a CSV file. The Python script executed on the computer located near the dSPACE system transmitted the measurement data to the remote computer. The sensor data were transmitted with a sampling rate of 1000 samples per second. The programs implementing the filtering were calculating the boom angles and sending them to the Unity program 40 times per second. The user interface of the Unity program allowed to choose the measured states by setting the checkboxes in real time, during the program execution. A 3D model of the crane was displayed in real time on-top of the video stream from a camera installed in the laboratory near the crane. While one researcher was operating the crane, the second researcher watched the concurrent motion of the crane and its 3D model on a video wall located in another laboratory of LUT University. The second researcher was also able to select the measured states in real time using the checkboxes. The experimental environment is presented in Figure 4.1.

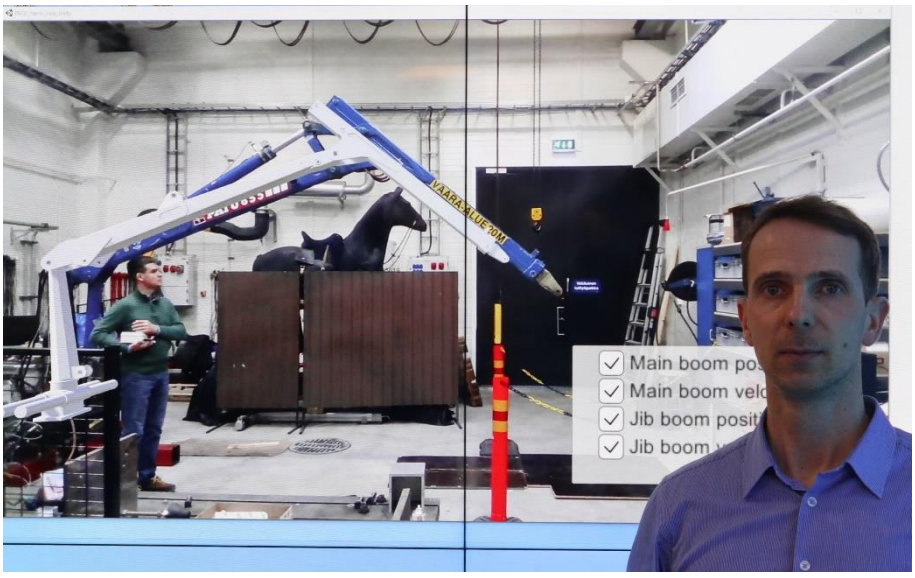

Figure 4.1. Experimental environment

5. RESULTS

The results of the first set of experiments are presented in Table 1 and Figure 5.1. Table 1 presents the execution time of different programs analyzing the data set obtained during the 39.992 s of measurements. The execution duration of the program implementing the UKF filter was 14.7 times smaller than the duration of the analyzed period, even on the Raspberry Pi microcomputer (denoted in the table as RPi). The program implementing the particle filter was able to fit the analyzed period duration using GPU and 1024 particles.

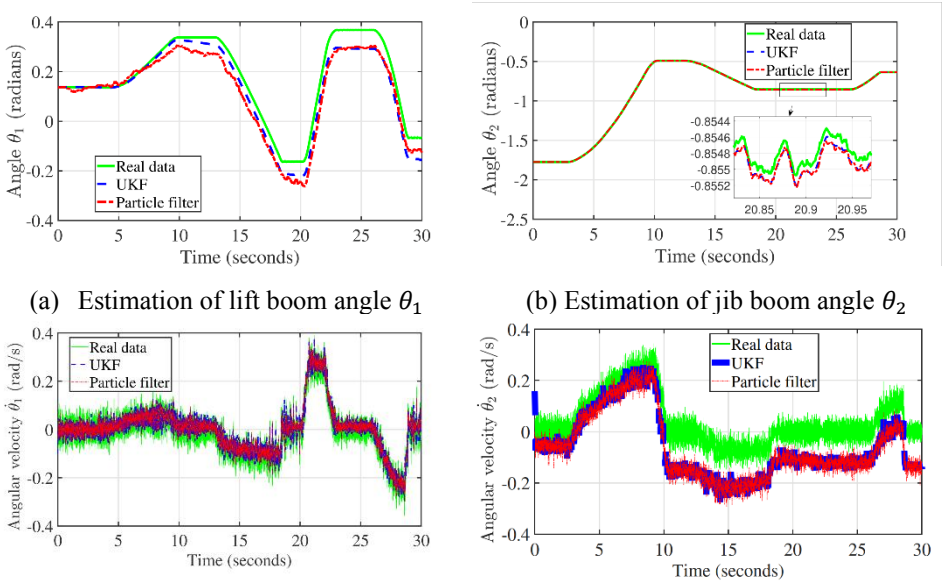

(a) Estimation of lift boom angle θ_1 (b) Estimation of jib boom angle θ_2

(c) Estimation of lift boom velocity $\dot{\theta}_1$ (d) Estimation of jib boom velocity $\dot{\theta}_2$

Figure 5.2. Estimation of the hydraulically actuated log crane states using the UKF and Particle filter

Figure 5.1 shows the measured and estimated states using the UKF and particle filter for the same input data that was used in the first set of experiments. In this example, the angular velocity of the main boom $\dot{\theta}_1$ and the angle of the jib boom θ_2 calculated from the position of the jib cylinder were used as measurements. The angle of the main boom θ_1 and the angular velocity of the jib boom $\dot{\theta}_2$ were estimated by the filters.

As for the estimation accuracy of the two approaches, Figure 5.1 indicates that both methods are capable to estimate the true states of the model. To have a better metric on how these methods perform, root mean square error (RMSE) is calculated for all four states. The RMSE of the UKF are: $\theta_1 = 0.2174\,rad$, $\theta_2 = 0.0203\,rad$, $\dot{\theta}_1 = 0.0001\,rad/s$, $\dot{\theta}_2 = 0.1401\,rad/s$ and the RMSE of the particle filter method are: $\theta_1 = 0.2684\,rad$, $\theta_2 = 0.0212\,rad$, $\dot{\theta}_1 = 0.0001\,rad/s$, $\dot{\theta}_2 = 0.1448\,rad/s$. It can be seen that the performance of the UKF method is slightly better than the particle filter.

Table 1: Execution time of different observer implementations

	UKF	**Particle filter**		
	PC	**RPi**	**GPU**	**CPU**
Total time (s)	0.654	2.718	13.844	80.510
Reading from file (s)	0.505	2.062	1.354	1.359
Calculations (s)	0.086	0.480	12.176	78.840
Writing to file (s)	0.046	0.105	0.312	0.309

6. CONCLUSION

The presented study demonstrated the possibility of using nonlinear observers for the real-time state estimation of hydraulically actuated equipment in Industrial IoT systems. The capability of the observation techniques to estimate unmeasured states allows using them as virtual sensors and decreasing the number of sensors installed on the equipment. It should be noted that due to the nonlinear nature of the hydraulically actuated systems, observer parameter tuning might be required for each type of equipment, taking into account its operating conditions.

The experiments performed in the current study showed that the UKF-based observer was able to run up to 142 times faster than the particle filter implemented on GPU while providing similar estimation accuracy. The result favors the use of UKF for virtual sensor implementation in Industrial IoT systems.

A combination of UKF and PF in a single observer for an IIoT system could be considered for future research. For the most common operating conditions, a fast UKF-based estimator could be used. For the periods with high nonlinearity detected using additional information on a particular machine, a PF-based estimator could be applied. Another research topic would be an improvement of an observer's performance by using the measurement data for a period of the machine operation. In the presented experiments, each sample was transmitted separately, while in practice, it is more efficient to transmit a sequence of samples in an IIoT system at once. Processing such sets of data could improve observer performance while preserving its real-time capabilities.

7. REFERENCES

[1] D. Simon, Optimal state estimation: Kalman, H infinity, and nonlinear approaches. Nashville, TN: John Wiley & Sons, 2006.

[2] J. V. Candy, Bayesian signal processing: Classical, modern, and particle filtering methods, 2nd ed., ser. Adaptive and Cognitive Dynamic Systems: Signal Processing, Learning, Communications and Control. Nashville, TN: John Wiley & Sons, 2016.

[3] I. Malysheva, H. Handroos, V. Zhidchenko, and A. Kovartsev, “Faster than real-time simulation of a hydraulically actuated log crane,” in 2018 Global Fluid Power Society PhD Symposium (GFPS). IEEE, 2018, pp. 1–6.

[4] V. Zhidchenko, H. Handroos, and A. Kovartsev, “Application of digital twin and IoT concepts for solving the tasks of hydraulically actuated heavy equipment lifecycle management,” International Journal of Engineering Systems Modelling and Simulation, vol. 11, no. 4, pp. 194–206, 2020.

[5] F. Lopez, L. Zhang, J. Beaman, and A. Mok, “Implementation of a particle filter on a GPU for nonlinear estimation in a manufacturing remelting process,” in 2014 IEEE/ASME International Conference on Advanced Intelligent Mechatronics. IEEE, 2014, pp. 340–345.

[6] R. Featherstone and D. E. Orin, “Robot dynamics: equations and algorithms,” Proceedings 2000 ICRA. Millennium Conference. IEEE International Conference on Robotics and Automation. Symposia Proceedings (Cat. No.00CH37065), vol. 1, pp. 826–834 vol.1, 2000.

[7] E. Sanjurjo, D. Dopico, A. Luaces, and M. Á. Naya, “State and force observers based on multibody models and the indirect Kalman filter,” Mechanical Systems and Signal Processing, vol. 106, pp. 210–228, 2018.

[8] A. J. Rodríguez, E. Sanjurjo, R. Pastorino, and M. Á. Naya, “State, parameter and input observers based on multibody models and Kalman filters for vehicle dynamics,” Mechanical Systems and Signal Processing, vol. 155, p. 107544, 2021.

[9] R. Pastorino, D. Richiedei, J. Cuadrado, and A. Trevisani, “State estimation using multibody models and non-linear Kalman filters,” International Journal of Non-Linear Mechanics, vol. 53, pp. 83–90, 2013.

[10] O. Brun, V. Teuliere, and J.-M. Garcia, “Parallel particle filtering,” Journal of Parallel and Distributed Computing, vol. 62, no. 7, pp. 1186– 1202, 2002.

[11] A. Simonetto and T. Keviczky, “Recent developments in distributed particle filtering: towards fast and accurate algorithms,” IFAC Proceedings Volumes, vol. 42, no. 20, pp. 138–143, 2009.

[12] G. Hendeby, R. Karlsson, and F. Gustafsson, “Particle filtering: the need for speed,” EURASIP Journal on Advances in Signal processing, vol. 2010, pp. 1–9, 2010.

[13] M. Chitchian, A. Simonetto, A. S. van Amesfoort, and T. Keviczky, “Distributed computation particle filters on GPU architectures for Real-Time control applications,” IEEE Trans. Control Syst. Technol., vol. 21, no. 6, pp. 2224–2238, Nov. 2013.

[14] T. Fiorenzani, C. Manes, G. Oriolo, and P. Peliti, “Comparative study of unscented Kalman filter and extended Kalman filter for position/attitude estimation in unmanned aerial vehicles,” Inst. for Systems Analysis and Computer Science (IASI-CNR), Rome, Italy, Rept, pp. 08–08, 2008.

[15] S. J. Julier and J. K. Uhlmann, “Unscented filtering and nonlinear estimation,” Proceedings of the IEEE, vol. 92, no. 3, pp. 401–422, 2004.

[16] Y. S. Hagh, R. M. Asl, and V. Cocquempot, “A hybrid robust fault tolerant control based on adaptive joint unscented Kalman filter,” ISA transactions, vol. 66, pp. 262–274, 2017.

[17] M. Mohammadi, Y. S. Hagh, X. Yu, H. Handroos, and A. Mikkola, “Determining the State of a Nonlinear Flexible Multibody System using an Unscented Kalman Filter,” IEEE Access, 2022.

[18] M. S. Arulampalam, S. Maskell, N. Gordon, and T. Clapp, “A tutorial on particle filters for online nonlinear/non-Gaussian Bayesian tracking,” IEEE Transactions on signal processing, vol. 50, no. 2, pp. 174–188, 2002.

[19] X. Han and X. Li, “An evaluation of the nonlinear/non-Gaussian filters for the sequential data assimilation,” Remote Sensing of environment, vol. 112, no. 4, pp. 1434–1449, 2008.

[20] J. S. Liu and R. Chen, “Sequential Monte Carlo methods for dynamic systems,” Journal of the American statistical association, vol. 93, no. 443, pp. 1032–1044, 1998.

[21] P. Fearnhead et al., “Sequential Monte Carlo methods in filter theory,” University of Oxford, 1998.

[22] A. Tulsyan, R. B. Gopaluni, and S. R. Khare, “Particle filtering without tears: A primer for beginners,” Computers & Chemical Engineering, vol. 95, pp. 130–145, 2016.

Biographies



Victor Zhidchenko received the D.Sc. (Tech.) degree from LUT University, Lappeenranta, Finland, in 2019, and the Candidate of Sciences degree from Samara National Research University, Russia. He is currently working as a Postdoctoral Researcher at LUT University. His research interests include computer simulation, cyber-physical systems, digital twins for heavy equipment, big data, cloud computing, and the Internet of Things.



Yashar Shabbouei Hagh received his M.Sc. degree in Control Engineering from the University of Tabriz, Iran, in 2016. In 2023, he obtained his doctoral degree in Mechanical Engineering from LUT University, Finland. At the time of the conference, he was a Junior Researcher at the Laboratory of Intelligent Machines, Department of Mechanical Engineering, LUT University. His research focuses on synergetic control theory and the state and parameter estimation of multibody dynamic systems, with applications to digital twins. His interests include fault detection and diagnosis systems, fault-tolerant controls, sliding mode controllers, synergetic control, nonlinear Kalman filtering, and robotic manipulators.



Egor Startcev received an Engineering degree in computing machines, complexes, systems, and networks from Samara State Technical University, Russia, in 2003. He is a former Microsoft Most Valuable Professional (MVP) for Data Protection Manager in 2011 and Cloud and Datacenter Management from 2012 to 2013. He has 15 years of experience in managing the IT department of a large construction holding. He is currently working as a Junior Researcher at LUT University. His research interests include cloud computing, digital twins, virtualization technologies, and the Internet of Things.



Heikki Handroos received the M.Sc. (Eng.) and D.Sc. (Tech.) degrees from the Tampere University of Technology in 1985 and 1991, respectively. He has been a Professor of machine automation at LUT University since 1992. He has also been a Visiting Professor at the University of Minnesota, Minneapolis, MN, USA; Peter the Great St. Petersburg Polytechnic University, Saint Petersburg, Russia; and the National Defense Academy, Japan. He has published about 250 international scientific papers and supervised around 20 D.Sc. (Tech.) theses. He has led several important domestic and international research projects. His research interests include modeling, design, and control of mechatronic transmissions to robotics and virtual engineering. He has been an Associate Editor of the Journal of Dynamic Systems, Measurement, and Control since 2014.

Dynamic fluid simulation of hydraulic oil flow inside fatigue cracks during transient loads

Lukas Michiels*, Marcus Geimer

Institute of Mobile Machines (Mobima), Karlsruhe Institute of Technology (KIT), Karlsruhe, German, lukas.michiels@kit.edu, marcus.geimer@kit.edu

ABSTRACT

Fatigue damage plays an important role in mobile hydraulics as all components are subject to varying and highly transient loads. Transient loads lead to complex damage accumulation processes and, thereby, difficulties in design and testing. Estimation of fatigue damage during complex load cycles allows efficient design and maintenance cycles, besides being the groundwork for real-time damage monitoring in the future. The interaction between pressurized fluid and crack faces is supposed to have a significant effect on the fatigue crack growth of hydraulic components. It prevents crack closure and contact of the crack faces during unloading. In this paper, we introduce a simplified simulation for the fluid flow in narrow cracks. Coupling the fluid simulation with a mechanical solver to account for elastic pressure-related deformation is difficult in terms of numeric stability. Instead of artificially modifying the fluid properties to increase the dynamic dampening effects of the fluid, we simplify the mechanical deformation matrix and introduce damping to the mechanical deformation to improve the overall solution stability. Our results show that dynamic effects do influence the fluid flow inside cracks and, thereby, fatigue crack growth.

Keywords. Fatigue, fluid dynamics, damage accumulation, mobile hydraulics.

1. INTRODUCTION

Increasing fuel costs and the aim to reduce CO_2 emissions have driven the development of more energy-efficient hydraulic power systems in recent decades. While electrification can reduce CO_2 emissions even further, the power density of hydraulic actuators cannot be reached by electric components, [1]. For this reason, the electric hydraulic hybrid concepts are considered as alternatives to purely electric drivetrains, [2], [3], [4]. Electric and hydraulic energy storage is highly limited and improving the efficiency of all drive components is becoming even more important, [5].

Mobile machines are used in rough and challenging environments and undergo varying and highly transient loads, [6]. Due to the recurrent loading, hydraulic components are subject to wear and eventually failure when the fatigue limit is reached. Through damage accumulation, even a few events can have a negative influence on the lifetime and lead to failure before the expected life-time end, [7]. Reducing weight and improving efficiency requires knowledge of the fatigue mechanism to predict damage accumulation and define service intervals. The fatigue of hydraulic components is influenced by fluid-structure interaction (FSI). The fluid pressure represents a supplementary fatigue stress when oil is

flowing into a crack. In addition, the fluid's viscosity opposes fast volume changes and, hence, fast crack closure. In this paper, we focus on the simulation of the fluid flow inside the fatigue cracks to simulate the fluid pressure during highly transient loads. Additional fluid effects, e.g. oil wedging, need to be taken into account to calculate accurate stress amplitudes to predict fatigue damage. In the literature, several similar approaches from related fields can be found.

The experiments of Davis and Ellison, [8], showed a small decrease in crack propagation rate when submerging specimens in high viscose oil. The reduced crack propagation was explained by the decreased stress amplitude due to hydrodynamic pressure inside the crack (oil wedging). Lower crack propagation rates were also reported by [9], whereas Tzou et al., [10], reported increased crack growth for low fatigue levels of submerged specimens. Contrary to specimens in pressure-free fluids, static ambient pressure led to increased crack growth in [11].

The interaction of fluids and fatigue cracks caught the attention of researchers working on driven-over rail systems. It is assumed that fluids assist crack propagation due to surface contact pressure, [12], [13], [14]. Bower states in [12] that crack growth on rails occurs especially in combination with fluid, e.g. water, and only in the direction of movement. Two main effects are assumed to contribute to this effect. One aspect is that fluid lubricates the crack flanks, leading to increased Mode II crack growth. On the other hand, when the crack is directed in the direction of movement, the fluid is pressed into the crack and the pressure of the enclosed fluid is increasing due to the wheel's load. The additional stress is, in these cases, caused by the external wheel load and no internal oil wedging.

The Flow regime inside fatigue cracks came to attention with the "lead before break" (LBB) concept. If fatigue cracks lead to leakage of pressure reservoirs without causing rupture, fatigue damage can be sensed by the leakage. The research is mainly focused on large-scale applications in the power industry. However, similarities to hydraulic applications can be found in the leakage of pressurized cylinders, [15], [16], [17]. The experiments by Clarke et al., [15], showed a dependency of the fluid flow on the grain size. If the grain size is smaller than the crack width, a laminar flow model corresponds well, while for smaller cracks, modelling the turns and bends due to grain size is more accurate. A simplified computational fluid dynamics model was used by Bagshaw et al., [16], to simulate flow rates in narrow cracks less than 3 times the size of the surface roughness. In contrast to the presented approach, these studies focused on a constant flow through an established crack under the assumption of a constant intern load pressure of a cylinder, neglecting fluid compressibility and inertia.

The paper is structured as follows: in Section 2, a simplified fluid flow simulation is presented. In the following Section 3, the coupling of the simplified simulation with a structural simulation is described. The simplified simulation was validated based on the one-way coupled computational fluid dynamics simulation presented in Section 4. The results are discussed in Section 5, before the paper is concluded in Section 6.

2. FLUID FLOW SIMULATION

2.1. Laminar fluid model

In the following, we assume laminar flow between the crack faces. The time variable t is divided into discrete time-steps t_k with temporal resolution Δ t. The crack is subdivided into N spatial control volumes (sections), which are indicated by the incremental subscript i. The volumes are of length l_i, width b and height $h_i(\bar{p}(t))$. The height $h_i(\bar{p}(t))$ of the flow area corresponds to the mean crack opening displacement of the section. Figure 2.1 shows one section and the corresponding flow between neighboring sections. The volume flow between each section is defined as $Q_i(t)$ in the positive i direction.

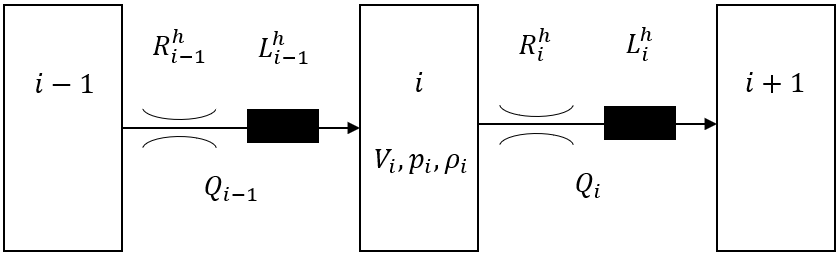

Figure 2.1. Fluid flow between discrete sections $i-1$, i, and $i+1$ with fluid volume V_i, density ρ_i, pressure p_i, and volume flow $Q_i(t)$ at section i.

The volume flow between consecutive sections is modeled using the electronic-hydraulic analogy, providing a simple and understandable dynamic model. The hydraulic flow resistance $R_i^{h(t)}$ is calculated based on the assumption of a laminar flow between two parallel plates, [18], as

$$R_i^{h(t)} = \left(12\eta \frac{l_i}{b\, h_{i(t)}^3}\right), \tag{2.1}$$

The fluid inertia of the flow between the sections i and $i+1$ characterize the hydraulic inductance $L_i^{h(t)}$ which is defined as

$$L_i^h\,(t) = \rho_i(t) \frac{l_i}{b h_i(t)}. \tag{2.2}$$

Assuming isothermal compression, the Tait equation of state is used to calculate the density for a given pressure, [19]. The bulk modulus K and the reference density ρ_0 are material constants depending on the oil. For a density exponent of $n = 1$, the density is linear proportional to the pressure change and can be calculated as

$$\rho_i(t) = \rho_0 \cdot \left(1 + \frac{p_i(t)}{K}\right). \tag{2.3}$$

Following the analogy shown in Figure 2.1, the pressure difference between sections i and $i+1$ is the total of the pressure losses at the hydraulic resistance $R_i^h(t)$ and the hydraulic inductance $L_i^h(t)$:

$$p_i(t) - p_{i+1}(t) = L_i^h(t)\frac{\delta Q_i(t)}{\delta t} + Q_i(t)R_i^h(t) \tag{2.4}$$

The pressure loss of the inductance accounts for the fluid inertia. The fluid inertia opposes fast changes in the volume flow. The time discrete solution of (2.4) for time-steps t_{k-1} and t_k is, [20],

$$\begin{aligned} Q_i(t_k) &= \widehat{Q}_i(t_k) - \left[\widehat{Q}_i(t_k) - Q_i(t_{k-1})\right]e^{-\frac{\Delta t}{\tau}} \\ &= \widehat{Q}_i(t_k)\left(1 - e^{-\frac{\Delta t}{\tau}}\right) + Q_i(t_{k-1})e^{-\frac{\Delta t}{\tau}} \end{aligned} \tag{2.5}$$

with

$$\widehat{Q}_i(t = t_k) = \frac{1}{R_i^h(t)}\left(p_i(t) - p_{i+1}(t)\right), \tag{2.6}$$

and the time factor τ_i defined as

$$\tau_i(t) = \frac{L_i^h(t)}{R_i^h(t)}. \tag{2.7}$$

The volume flow Q_{i-1} is calculated based on the fluid density ρ_{i-1} at section $i-1$. Given the conservation of mass,

$$\rho_{i-1}[Q_{i-1}]_{at\ Sec.\ i-1} = \rho_i[Q_{i-1}]_{at\ Sec.\ i}, \tag{2.8}$$

the same mass flow at section i with density ρ_i is,

$$[Q_{i-1}]_{at\ Sec.\ i} = \frac{\rho_{i-1}}{\rho_i}[Q_{i-1}]_{at\ Sec.\ i-1}. \tag{2.9}$$

In the following, Q_i is always calculated based on the density of the corresponding section i and the subscript "at Sec. i" is omitted. The volume flows at section i sum up as

$$\Delta V_i(t_k) = V_i(t_k) - V_i(t_{k-1}) = \left[\frac{\rho_{i-1}}{\rho_i}Q_{i-1}(t_k) - Q_i(t_k)\right]\Delta t. \tag{2.10}$$

The resulting pressure change dp_i is

$$\Delta p_i(t_{k+1}) = p_i(t_{k+1}) - p_i(t_k) = \frac{1}{C_i^h(t_k)}\left(\Delta V_i(t_k) - \Delta h_i(t_k)\ b\ l_i\right), \tag{2.11}$$

with the hydraulic capacity

$$C_i^h = \frac{1}{K}l \cdot h_i\left(\bar{p}(t_k)\right)b \tag{2.12}$$

The second part of (2.11) is the volume change of the section due to the motion of the crack faces $\Delta\, h_i(t_k)$:

$$\Delta h_i(t_k) = h_i\left(\bar{p}(t_k)\right) - h_i\left(\bar{p}(t_{k-1})\right). \tag{2.13}$$

A decreasing crack size $\Delta\, h_i(t_k) < 0$ is increasing the fluid pressure.

Given (2.11), the pressure at the next time-step $k+1$ is

$$p_i(t_{k+1}) = p_i(t_k) + \Delta p_i(t_k). \tag{2.14}$$

At this point, one time-step is completed, and the calculation continues with the next time-step $t = t_{k+1}$. The simulation is a pure forward model and is not iterated towards a semi-stationary steady state.

Several boundary conditions have been defined. At the last element, there is no volume flow to the next element and $Q_N(t) = 0$. The load pressure $p_0(t)$ is known for all time-steps. The simulation is initialized at time $t_0 = 0$ under the assumption of a constant pressure $p_i(t_0) \cong \sim p_0(t_0)$ throughout the crack. A structural model of the part is required to calculate the crack opening displacement $h_i\big(\bar{p}(t_k)\big)$, depending on the fluid pressure inside the crack $\bar{p}(t_k)$, the load pressure outside the crack $p_0(t)$, and any external loads.

2.2. Structural Deformation

The structural deformation can be divided into a parallel and an orthogonal component compared to the crack's orientation. The parallel component does not change the flow area inside the crack. The orthogonal component, however, changes the crack opening displacement $h_i\big(\bar{p}(t)\big)$. Under the assumption of an ideal-linear elastic material, the crack opening displacement can be defined as

$$\bar{h}\big(\bar{p}(t)\big) = \bar{h}_0\big(\bar{p}_0(t)\big) + \boldsymbol{A}\bar{p}(t) - \boldsymbol{M}\frac{\delta^2\bar{h}\big(\bar{p}(t)\big)}{\delta t^2} \tag{2.15}$$

with a stiffness matrix $\boldsymbol{A}$, an inertial matrix $\boldsymbol{M}$ and the crack opening displacement due to external loads h_0.

Both, $\boldsymbol{A}$ and $\boldsymbol{M}$ does depend on the structural surrounding of the crack but are not to be confused with the stiffness and mass matrix of the finite-element method. The stiffness matrix $\boldsymbol{A}$ can be derived from a static finite-element solution. The inertial matrix, on the other hand, is damping the structural deformation. Even as the crack closing rapidly, the structural deformation is remaining small. As $\boldsymbol{M}\,\frac{\delta^2\bar{h}(p(t))}{\delta t^2} \ll \boldsymbol{A}\,\bar{p}(t)$ the inertial dampening can be neglected. In the time-discrete simulation, an under-relaxation factor of α is used instead of the inertial matrix of $\boldsymbol{M}$ to induce inertial damping and achieve numeric stability. The crack opening displacement h_i is replaced by an under-relaxed term $\hat{h}_i$ as

$$\hat{h}_i(t_{k+1}) = \hat{h}_i(t_k) + \alpha\left[h_i\left(\bar{p}\big(t_{(k+1)}\big)\right) - \hat{h}_i(t_k)\right]. \tag{2.16}$$

The under-relaxation corresponds to a low-pass filter with smoothing factor $\alpha = \frac{\Delta t}{T_{lp}}$ with time advancement Δt and time constant T_{lp}. Hence, the time constant T_{lp} of the filter must been significantly smaller than the timescale of the expected deformations.

In the simulations, the number of sections was set to $N = 100$, the time advancement $\Delta t = 2 \cdot 10^{-9}\,s$, and the total step count to 10^7 steps. A small-time advancement was required to attain the intended accuracy. The time constant of the low-pass filter was chosen as $T_{lp} = 1 \cdot 10^{-7}\,s$ resulting in an under-relaxation factor of $\alpha = 0.02$.

3. FEM SIMULATION MODEL

The elastic deformation of the crack region is simulated with the commercial Finite-Element-Method Solver Ansys in a 3D simulation. The mesh consists of a single layer and symmetry conditions in the third direction, resulting in a quasi-2D simulation. The solid regions are meshed with hexahedron and prism elements with linear basis functions, see Figure 5.4. The base element size is 0.5 mm, being refined around the crack with an element size of 0.05 mm and 0.01 mm at the crack tip, leading to a total of approximately 28,000 elements. The material of the loaded part is modelled with a linear elastic material behavior and a Young's modulus of $E = 210\ GPa$ and a Poisson's ratio of $\nu = 0.3$.

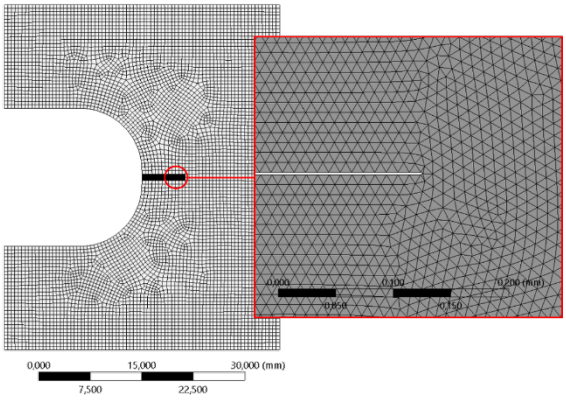

Figure 3.1. Overview of finite-element mesh and refined mesh around the crack tip

According to Section 2.1, the crack is divided into N partial subsection with a surface pressure boundary condition $\bar{p} = [p_1, \dots, p_N]$. The deformation of the crack, also referred to as crack opening displacement, is denoted as $\bar{h} = [h_1, \dots, h_N]$.

The objective of the structural analysis is to derive the stiffness matrix $\boldsymbol{A}$ of the crack region. Dividing the crack into N sections lead to a matrix $\boldsymbol{A} = [a_{i,j}]$ of shape NxN. N independent pressure distributions $\bar{p}^j$ are required to calculate the coefficients $a_{i,j}$. A lower triangular matrix with arbitrary pressure level p satisfy all required conditions:

$$\begin{aligned} \boldsymbol{P} &= [\bar{p}^1 \quad \bar{p}^2 \quad \dots \quad \bar{p}^{N-1} \quad \bar{p}^N] \\ &= \begin{bmatrix} p & p & \cdots & p & p \\ 0 & p & \dots & p & p \\ \vdots & \vdots & \ddots & \vdots & \vdots \\ 0 & 0 & \cdots & 0 & p \end{bmatrix} \end{aligned} \tag{3.1}$$

Solving the N static load cases, gives N crack deformation profiles $\boldsymbol{H}$:

$$\begin{aligned} \boldsymbol{H} &= [\bar{h}^1 \quad \bar{h}^2 \quad \dots \quad \bar{h}^{N-1} \quad \bar{h}^N] \\ &= \begin{bmatrix} \mathrm{h}_1^1 & \mathrm{h}_2^1 & \cdots & \mathrm{h}_{\mathrm{N}-1}^1 & \mathrm{h}_{\mathrm{N}}^1 \\ \mathrm{h}_1^2 & \mathrm{h}_2^2 & \dots & \mathrm{h}_{\mathrm{N}-1}^2 & \mathrm{h}_{\mathrm{N}}^2 \\ \vdots & \vdots & \ddots & \vdots & \vdots \\ \mathrm{h}_1^N & \mathrm{h}_2^N & \cdots & \mathrm{h}_{\mathrm{N}-1}^N & \mathrm{h}_{\mathrm{N}}^N \end{bmatrix} \end{aligned} \tag{3.2}$$

Following (2.15) $\boldsymbol{A}$ is calculated as

$$\boldsymbol{A} = \boldsymbol{P}^{-1}\boldsymbol{H}. \tag{3.3}$$

Additional equations are required to calculate the crack stiffness due to external loads. In this case, the load pressure is the only applied external load leading to

$$\bar{h}_0\big(p_0(t)\big) = \boldsymbol{B}p_0(t), \tag{3.4}$$

where $\boldsymbol{B}$ is an $1xN$ matrix. The FEM model with the zero-pressure loading inside the crack ($\bar{p}(t) = \bar{0}$) and the external pressure level ($p_0(t) = p^e$) as boundary conditions gives the deformation $\bar{h}^0$ due to these external loads. The linear deformation matrix $\boldsymbol{B}$ follows as:

$$\boldsymbol{B} = \frac{\bar{h}^0}{p^e} \tag{3.5}$$

4. COUPLED FLUID SIMULATION

Since experimental studies of the fluid flow inside fatigue cracks are difficult, the simplified simulation described in Section 2.1 was compared to a CFD analysis. For the analysis, the commercial CFD software Ansys Fluent was used. Table 4.1 gives an overview of the analysis's parameters.

The fluent area was meshed with hexahedron elements with $N = 100$ elements in the direction of the crack and 20 elements in the orthogonal direction. In the third direction, only one element with symmetric boundary conditions was used, resulting in a quasi-2D simulation. The boundary conditions were a pressure inlet at the crack mouth and the symmetry conditions in the z-direction. The inlet pressure corresponded to the external load pressure.

Table 4.1. Summary of CFD analysis

Program	Ansys Fluent 2020R2
Solver	Coupled
Base Function	Quadratic
Number of elements	2000
Boundary conditions	Pressure inlet, Grid Motion
Time-Steps	1000 à 0.02 ms

The wall motion of the crack faces was modelled as an additional boundary condition. The crack deformation was precalculated using the simplified simulation described in Section 2.1 and was imposed as a boundary condition to the simulation. Before the simulation, a DEFINE_GRID_MOTION function for Ansys Fluent was written in a UDF file defining the wall motion, and the mesh was updated at every time-step to account for the wall motion. Therefore, the CFD-Simulation was one-way coupled to the structural analysis. A direct coupling of the CFD simulation with the structural analysis is difficult in terms of stability and greatly increases simulation time.

The CFD simulation was only used for validation. If the assumption of a laminar flow between two parallel plates holds true, the simulated pressure inside the crack should be identical to the pressure simulated by the CFD simulation. The volume flow is imposed by

the wall motion and the compressibility of the fluid and is therefore identical in both analyses.

In addition to the wall motion due to the structural deformation, the mesh was pre-deformed to simulate bent cracks. Each node was randomly displaced orthogonal to the crack's direction, leading to a more realistic crack structure. Figure 4.1 depicts the crack structure for a mean nodal displacement of 20 μm. The nodal displacement could be compared to a possible grain structure. The simplified simulation accounts for the nodal displacement by increasing the section length l_i to correspond to the effective crack length.

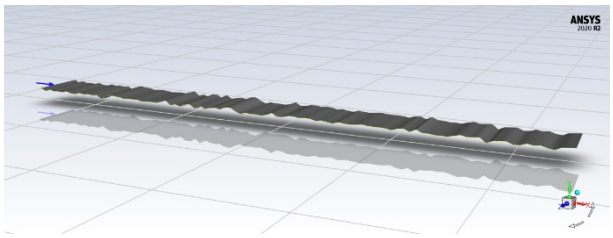

Figure 4.1. Crack structure with a mean nodal displacement of 20 μm and pressure inlet on the left side.

5. RESULTS AND DISCUSSION

5.1. Setup

The simplified simulation was used in the following to simulate the fluid flow and the structural deformation during a single pressure pulse. The load pressure was defined as a time sequence based on the pressure rise rate (positive temporal pressure gradient), the upper-pressure level, and the pressure drop rate (negative temporal pressure gradient). A rise rate of $\Delta p_r = 100\ kbar/s$ and an upper pressure level $p_{max} = 300\ bar$ were used for all simulations. The hold time of the upper and lower pressure resulted from the overall pulse length of one pulse of $t = 0.02\ s$. The used pulse length results in a pulse frequency of $f = 50hz$ which is significantly faster than current pulse experiments. However, in each pulse, the crack is filled with oil, and therefore, an increased pulse length would not change the results. In comparison with a two-way coupled fluid-structure interaction simulation, the simplified simulation significantly decreases simulation time. The total amount of 10^7 time-steps were solved on an AMD Epyc Rome server system in about 5 to 10 minutes. Three drop rates were compared in the simulations, $\Delta p_d = 50, 250, 300\ kbar/s$.

5.2. Results

Oil wedging occurs when oil is trapped inside a crack due to its high flow resistance. The magnitude of this effect increases with high pressure drop rates. Figure 5.1a shows the absolute crack tip pressure in dependence of the drop rate. For pressure drop rates lower than $50\ kbar/s$ oil wedging was not significant, and the crack tip pressure did not exceed the load pressure. In the case of high pressure drop rates, however, the crack tip pressure did exceed the load pressure by a factor of up to three. This high pressure was located at the crack tip after the release of the load pressure and decreased with time, see Figure 5.2.

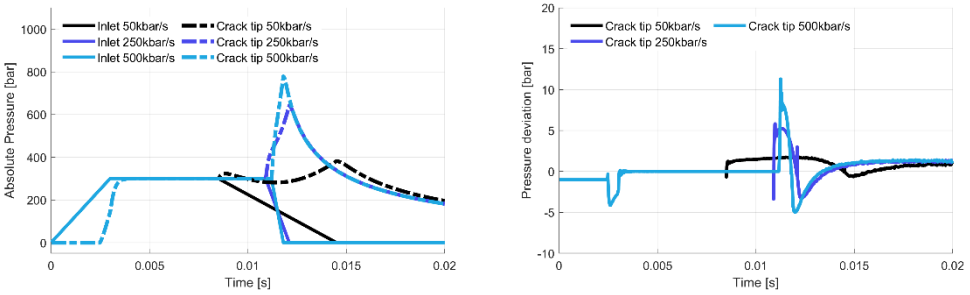

a) Simulated crack tip pressure.

b) Crack tip pressure deviation compared to non-simplified CFD.

Figure 5.1. Crack tip pressure of the FSI-simulation over one pulse at drop rates of $50, 250,$ and $500\ kbar/s$ with a nominal load pressure of $300\ bar$.

The results of the simplified simulation were compared to the results of the CFD simulation for validation. In the case of a straight crack, the simulated pressure corresponded well to the CFD simulation, as can be seen in Figure 5.1b. Contrary to the simplified simulation, the CFD simulation accounts for fluid flow orthogonal to the crack. The orthogonal component (y-direction) of the velocity, however, remains insignificantly small inside the crack, and therefore, neglecting it does not significantly change the overall fluid flow. The existing deviations could be explained by the spatial and temporal discretization and numeric effects.

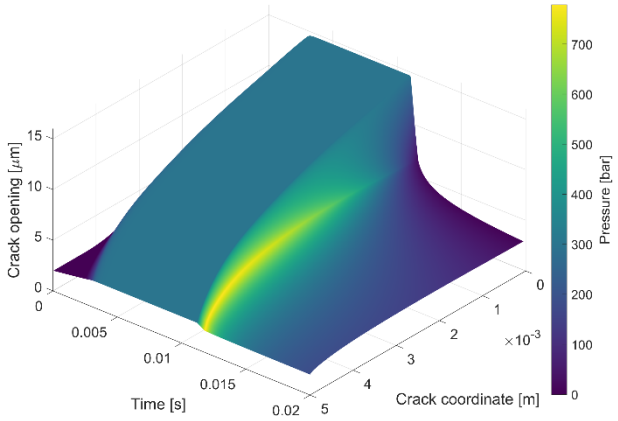

Figure 5.2. Pressure distribution and crack opening displacement during one pulse at a drop rate of $500\ kbar/s$ and a load pressure of $300\ bar$.

The focus on the electronic-hydraulic analogy was motivated by a simple integration of fluid inertia and compressibility. In Figure 5.3a the minimal and maximal density inside the crack is shown. As the crack opened, cavitation inside the crack occurred, and gaseous liquid fluid was inside the crack. As the crack closed, the fluid was compressed by the closing crack. Fluid pressure and density increased significantly. The compressibility of the oil was opposed to the increasing pressure, leading to lower pressure levels inside the crack.

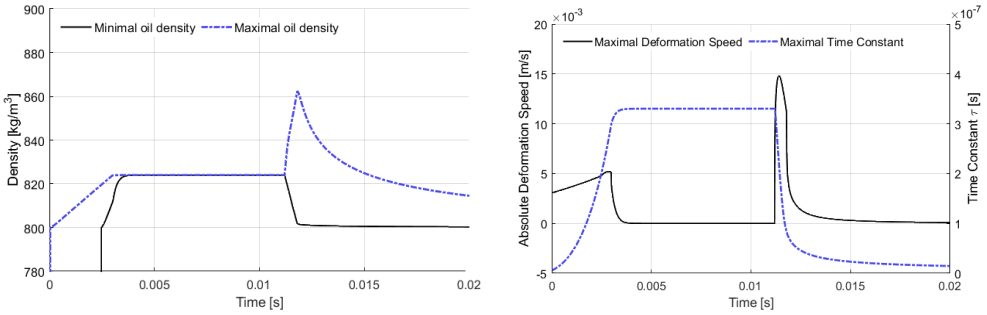

a) Minimal and maximal oil density (isothermal compression).

b) Structural deformation speed and electronic-hydraulic time constant.

Figure 5.3. Compression and dynamic properties of the simulated crack at a drop rate of 500 $kbar/s$ and a load pressure of 300 bar.

In contrast to the pressure, the fluid inertia did not play a significant role. In Figure 5.3b, the time factor and the structural deformation speed are shown. The time factor ($\tau \approx 0.35\ \mu s$) is small in comparison to the simulation timescale ($t = 0.02\ s$). The same holds true for the inertia of the structure. While the deformation occurred in a short time ($t = 0.02\ s$), it's magnitude ($\Delta h \approx 5 - 10\ \mu m$) was significantly smaller. As a result, the deformation speed remained low ($v_{def} < 0.015\ \frac{m}{s}$), and the inertia can be neglected.

The pressure inside the crack increased with the nodal displacement of the crack mesh, see Figure 5.4. This pressure increase can be explained by the increasing effective crack length and the decreasing flow area. On the other hand, the accuracy of the simplified simulation decreases as the discrepancy between the theoretic background of parallel plates and the crack geometry increases.

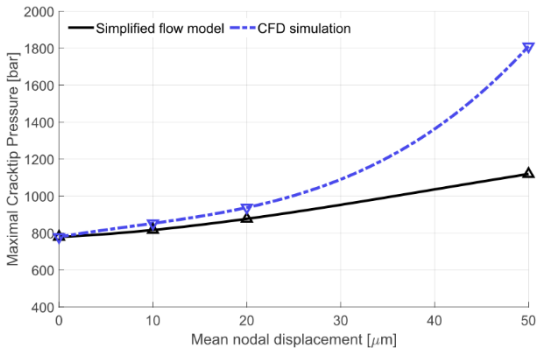

Figure 5.4. Crack tip pressure in relation to the mean nodal displacement of the mesh. The simplified simulation (black) is compared to the CFD simulation (blue). At a drop rate of 500 $kbar/s$ and a load pressure of 300 bar.

6. CONCLUSION

Fluid flow inside fatigue cracks is changing the fatigue properties of hydraulic power systems. Ignoring the fluid inside the crack leads to an underestimation of the fatigue stress. On the other hand, fluid flow properties, especially the fluid's flow resistance, lead to superposed impacts like oil wedging that reduce the effective stress amplitude. Accurate simulations of the fluid pressure and the crack displacement are required to determine stress amplitudes and fatigue crack growth.

In this paper, we developed a simplified simulation, assuming laminar flow, to simulate fluid flow inside fatigue cracks of hydraulic components. The electronic-hydraulic analogy allows one to derive a laminar flow model which accounts for fluid compressibility and inertia. The simplifications lead to a significant reduction in computational time compared to two-way coupled fluid-structure interaction simulations.

The results show that the assumption of laminar flow between two parallel plates holds true for straight cracks. A more complex crack geometry with turns and bends, e.g. caused by grain boundaries, has been simulated by a nodal displacement of the fluid mesh. In these cases, the simplified flow simulation does not lead to identical results, and the deviations increase with higher distortion. The simulations showed that the fluid inside the crack has a significant influence on the crack opening displacement and, therefore, on the resulting fatigue stress.

Besides, the distortion of the crack is modelled as a smooth wall. In future work, crack geometries should be measured in experiments and integrated into the fluid simulation. Direct validation of the fluid flow inside the crack is difficult due to the crack's dimensions. Experiments could be performed and compared to the simulations in terms of deformation and fatigue crack propagation. Additionally, the structural analysis could be extended to account for non-linear plastic deformation at the crack tip.

7. REFERENCES

[1] Y. Tanaka, S. Sakama, K. Nakano, and H. Kosodo, “Comparative Study on Dynamic Characteristics of Hydraulic, Pneumatic and Electric Motors,” in *ASME/BATH 2013 Symposium on Fluid Power and Motion Control*, Sarasota, Florida, USA: American Society of Mechanical Engineers, Oct. 2013. doi: 10.1115/FPMC2013-4459.

[2] K.-E. Rydberg, “Energy Efficient Hydraulic Hybrid Drives,” presented at the 11:th Scandinavian International Conference on Fluid Power, SICFP’09, June 2-4, Linköping, Sweden, 2009.

[3] G. Niu, F. Shang, M. Krishnamurthy, and J. M. Garcia, “Design and Analysis of an Electric Hydraulic Hybrid Powertrain in Electric Vehicles,” *IEEE Transactions on Transportation Electrification*, vol. 3, no. 1, pp. 48–57, Mar. 2017, doi: 10.1109/TTE.2016.2628792.

[4] A. Lajunen, P. Sainio, L. Laurila, J. Pippuri-Mäkeläinen, and K. Tammi, “Overview of Powertrain Electrification and Future Scenarios for Non-Road Mobile Machinery,” *Energies*, vol. 11, no. 5, Art. no. 5, May 2018, doi: 10.3390/en11051184.

[5] S. Hui, Y. Lifu, and J. Junqing, “Hydraulic/electric synergy system (HESS) design for heavy hybrid vehicles,” *Energy*, vol. 35, no. 12, pp. 5328–5335, Dec. 2010, doi: 10.1016/j.energy.2010.07.027.

[6] L. Brinkschulte, *Assistenzsysteme zur Reduktion des Schädigungsverhaltens von Komponenten einer mobilen Arbeitsmaschine*, vol. 90. Karlsruhe: KIT Scientific Publishing, 2021. doi: 10.5445/KSP/1000130176.

[7] S. K. Paul and S. Tarafder, “Cyclic plastic deformation response at fatigue crack tips,” *International Journal of Pressure Vessels and Piping*, vol. 101, pp. 81–90, Jan. 2013, doi: 10.1016/j.ijpvp.2012.10.007.

[8] F. H. Davis, E. G. Ellison, and W. J. Plumbridge, “Effects of Hydrostatic Pressure on the Rate of Fatigue Crack Growth,” *Fatigue & Fracture of Engineering Materials & Structures*, vol. 12, no. 6, pp. 511–525, 1989, doi: https://doi.org/10.1111/j.1460-2695.1989.tb00560.x.

[9] C. J. Polk, W. R. Murphy, and C. N. Rowe, “Determining Fatigue Crack Propagation Rates in Lubricating Environments through the Application of a Fracture Mechanics Technique,” *A S L E Transactions*, vol. 18, no. 4, pp. 290–298, Jan. 1975, doi: 10.1080/05698197508982771.

[10] J.-L. Tzou, S. Suresh, and R. O. Ritchie, “Fatigue crack propagation in viscous environments,” in *Mechanical Behaviour of Materials*, J. CARLSSON and N. G. OHLSON, Eds., Pergamon, 1984, pp. 711–717. doi: 10.1016/B978-1-4832-8372-2.50090-7.

[11] W. J. Plumbridge, P. J. Ross, and J. S. C. Parry, “Fatigue crack growth in liquids under pressure,” *Materials Science and Engineering*, vol. 68, no. 2, pp. 219–232, Jan. 1985, doi: 10.1016/0025-5416(85)90411-2.

[12] A. F. Bower, “The Influence of Crack Face Friction and Trapped Fluid on Surface Initiated Rolling Contact Fatigue Cracks,” *Journal of Tribology*, vol. 110, no. 4, pp. 704–711, Oct. 1988, doi: 10.1115/1.3261717.

[13] M. Akama and T. Mori, “Boundary Element Analysis of Effects of Crack Face Friction and Trapped Fluid on Rolling Contact Fatigue Cracks,” *QR of RTRI*, vol. 46, no. 4, pp. 231–237, 2005, doi: 10.2219/rtriqr.46.231.

[14] D. I. Fletcher, P. Hyde, and A. Kapoor, “Modelling and full-scale trials to investigate fluid pressurisation of rolling contact fatigue cracks,” *Wear*, vol. 265, no. 9, pp. 1317–1324, Oct. 2008, doi: 10.1016/j.wear.2008.02.025.

[15] L. V. Clarke, H. Bainbridge, S. B. M. Beck, and J. R. Yates, “Measurement of fluid flow rates through cracks,” *International Journal of Pressure Vessels and Piping*, vol. 71, no. 1, pp. 71–75, Apr. 1997, doi: 10.1016/S0308-0161(96)00056-7.

[16] N. M. Bagshaw, S. B. M. Beck, and J. R. Yates, “Identification of fluid flow regimes in narrow cracks,” *Proceedings of the Institution of Mechanical Engineers, Part C: Journal of Mechanical Engineering Science*, vol. 214, no. 8, pp. 1099–1106, Aug. 2000, doi: 10.1243/0954406001523542.

[17] C. Hong, Y. Asako, and J.-H. Lee, “Estimation of Leak Flow Rates Through Narrow Cracks,” *Journal of Pressure Vessel Technology*, vol. 131, no. 5, Sep. 2009, doi: 10.1115/1.3147984.

[18] B. S. Massey, *Mechanics of fluids*. Van Nostrand Reinhold, 1989.

[19] G. A. Neece and D. R. Squire, “Tait and related empirical equations of state,” *J. Phys. Chem.*, vol. 72, no. 1, pp. 128–136, Jan. 1968, doi: 10.1021/j100847a024.

[20] S. H. Russ, “Circuit Elements: Resistance, Capacitance, and Inductance,” in *Signal Integrity: Applied Electromagnetics and Professional Practice*, S. H. Russ, Ed., Cham: Springer International Publishing, 2022, pp. 43–63. doi: 10.1007/978-3-030-86927-4_4.

Biographies



Lukas Michiels studied mechanical engineering at the Karlsruhe Institute of Technology and the Institut national des sciences appliquées de Lyon, with a focus on robotics and computer science. Since 2021, he is a PhD student at the institute for mobile machinery at KIT, focusing on the fluid simulation in the context of hydraulic drives of mobile machines.

Implementation of a Variational Autoencoder for Dimension Reduction of a Hydraulic System

Faras Brumand-Poor*; Faried Makansi; Jiakun Liao; Katharina Schmitz

RWTH Aachen University, Institute for Fluid Power Drives and Systems (ifas), Campus-Boulevard 30, D-52074 Aachen, Germany,*
** Corresponding author: Tel: +49 241 80 47743 E-Mail:*
faras.brumand@ifas.rwth-aachen.de

Abstract

Hydraulic systems are often equipped with a great number of actors and sensors to monitor and enable the control of a system. For continuous monitoring, a vast amount of data needs to be recorded and frequently stored. Prediction based on this big database is often not directly comprehensible by a human and requires preprocessing. With the development of computational power, machine learning becomes a promising approach to handle these huge amounts of data and offers to be a possible solution for the automated processing of raw machine data. In this paper, a deep unsupervised learning (UL) model, the variational autoencoder (VAE), is implemented. The VAE is used for the reduction of high dimensional time series of a simulation of a reference system, a hydraulic press. To handle the time dependency of the dataset, the VAE contains long short-term memory (LSTM) layers. The high dimensional input data matrix is compressed by the first part of the VAE, the encoder, into the latent. This low dimensional representation of the time series is then used by the counterpart of the encoder, the decoder, to reconstruct the original time series. The VAE achieves a compression rate of 99,94 % with a small deviation compared to the original input. This contribution shows the possibilities of compressing big data from a hydraulic system into a low dimensional representation. The compressed data can be used as input for

River Journal, 1–17.
© 2024 *River Publishers. All rights reserved.*

condition monitoring (CM) algorithms, with the benefit that it doesn't contain any redundant information.

Keywords: Data-based condition monitoring, deep unsupervised learning, hydraulic system, VAE.

1 Introduction

In production, safety and efficiency are two essential factors to be ensured. For a well-organized production strategy, the condition of the plant needs to be well monitored. In real life, the plant needs to be examined by an experienced engineer regularly, in case of defective components. These have to be replaced, to avoid potential risks for production. In recent years, data-based condition monitoring has been applied to fluid power systems [1] - [6]. Data-based condition monitoring relies on a constant generation of data by the plant's sensors and actors. Predicting the machine state directly from the unprocessed measurements often exhibits limited performance. This is due to two main reasons: Firstly, the process is fairly complex and needs to be simplified for an algorithm to be able to conclude. Secondly, the dataset is such vast in size, that the algorithm is not able to detect the particular data points for the required prediction. For a specific task in CM, often certain data points of particular sensors/actors are decisive. Therefore a preprocessing of the big data needs to be done, to discover the most crucial information, such that the CM algorithm can achieve the best performance.
One approach to preprocessing is to reduce the size of the original data before further analysis. Hereby, the reduction needs to be done with a minimal information loss and a maximal compression rate. There are several techniques for data reduction, which can be distinguished by the amount of data required to obtain good performance. A good performance means that the algorithm is able to compress the original data in a meaningful representation for further application. Statistical methods achieve reasonable performance with a smaller amount of data [7]. However, the amount depends heavily on the dataset (e.g. complexity, number of dimensions, etc.). Machine Learning algorithms, especially Deep Learning (DL) ones, normally require a greater amount of data compared to classical approaches. For the case, that a plant consistently generates data or a simulation of the reference system is available, machine learning is a good solution for the data reduction task. In order to validate the compression of a DL method, the algorithm is often validated by a counterpart, which aims to reconstruct the

original data with minor error.

The scope of this paper is the dimension reduction of high dimensional time series data of a simulation of a hydraulic press and the investigation of the reconstructed data. A deep unsupervised learning model, the variational autoencoder, is implemented and compresses the input matrix into a reduced vector containing the crucial information of the press, which can be used for further applications like condition monitoring, predictive monitoring or system control.
In section 2, the state of the art of data-based condition monitoring in fluid power systems as well as the VAE are presented. In section 3, the implementation of the model is described. Subsequently, the results of the model are shown. In the last section, the conclusion and the outlook are given.

2 State of the Art

2.1 Data-Based Condition Monitoring in Fluid Power Systems

During the production process, the machine state has to be monitored to detect system anomalies. CM can be applied to fluid power systems to automate potential failure detection. One approach for CM is developing a mathematical model of the plant. The fault detection algorithm predicts the machine state by comparing the outputs of the plant and the model [8] - [10]. These model-based approaches require knowledge of the machine and complex modeling, especially if nonlinearities need to be considered.

Data-based CM is another method for CM, which bases its prediction on the data provided by a machine or a simulation of it [1], [7]. Investigations have been carried out on firstly compressing the time series data of the plant using statistical approaches before the application of fault classification machine learning models [11] - [14].

Research has been conducted on unsupervised learning algorithms for the compression of data in hydraulic systems. UL models aim to reduce the size of a given dataset by omitting irrelevant particulars while ensuring a minimal loss of information. Statistical analysis like principal component analysis have been applied to hydraulic systems to reduce a dataset provided by the plant [15] - [17]. In other studies, neural networks are used for the reduction and prove to be efficient for the fault detection of a hydraulic simulation

model [18]. In most cases a classification algorithm is implemented for the actual fault detection, however, Krogerus et. al. directly used an UL method for the working condition of a worn spool of a valve [19].
In recent years, more advanced UL models, the autoencoder (AE) and the stacked autoencoder, have been applied for dimension reduction of data of hydraulic systems [20], [21]. The autoencoder is an UL model especially suitable for dimension reduction [22]. A minimum loss of information is ensured by the AE aiming to reconstruct the original data from the low-dimensional representation. In most recent studies, Mallak et. al. have implemented an AE with long short-term memory, which store information over extended time intervals, to handle time dependencies in their machine data. The data was reconstructed with a small loss of information [21].

2.2 The Variational Autoencoder

The variational autoencoder is an AE that aims to learn a mathematical meaningful encoding [23]. The AE compresses a dataset in an incomprehensible latent representation. The main goal is to achieve high compression. Compared to the AE, the VAE aims to create a meaningful latent space. This is beneficial for CM since the actual machine state prediction is based on the latent space, which is mathematically comprehensible in the case of the VAE. The VAE consists of two parts, the encoder, and the decoder. The first compresses the original input into a low-dimensional representation, which is called the latent. The decoder aims to reconstruct the original input through the latent. The compression quality is normally investigated based on the similarity of original and reconstructed data.

3 Material and Methods

3.1 The Hydraulic Press

The dataset is provided by [1], and the reader is advised to refer to this work for more detailed information. The dataset is obtained by a simulation of a hydraulic reference system, which is displayed in Fig. 1. The simulation is built according to a physical demonstrator machine. The main components are a hydraulic power supply, a proportional directional control valve and a single acting hydraulic cylinder. Additionally, a ram is attached to the cylinder rod and acts against a load force. The load force represents the reaction force of a workpiece. The hydraulic press moves the ram to a defined position while working against a load force. Fig. 2 shows the progressions of the cylinder's

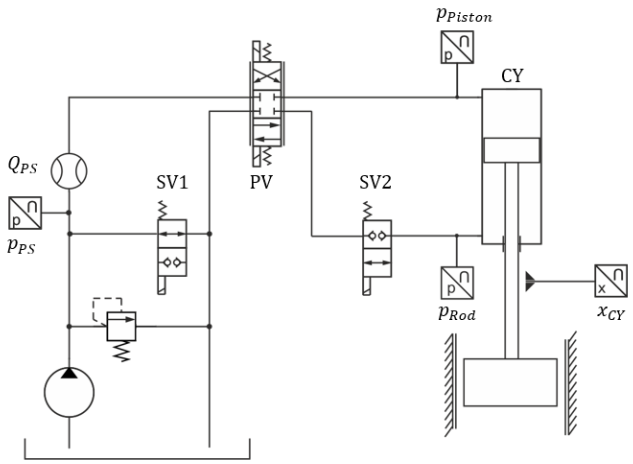

Figure 1: Circuit diagram of the considered hydraulic system

position, piston side pressure and the volume flow of the pressure supply. The cycle starts in idle mode. After 1 second, the ram moves towards the workpiece without external load. During this phase, there is no restriction on the velocity. As soon as the ram reaches a defined distance to the workpiece, the velocity is limited through the control signal and the volume flow to the cylinder, respectively. When the ram is in contact with the workpiece, the piston side pressure increases proportionally to the cylinder stroke. As a fixed position is reached, the backstroke is initiated. After the retraction is finished, the press is in idle mode for the rest of the cycle. Regarding the dataset: There is no empty entry, and it is normalized for better performance in the training process. The dataset contains different working conditions (e.g. internal, external cylinder leakage, no leakage). All features are continuous, except y_{SV1} and y_{SV2}, which are discrete between 0 and 1. The duration of each cycle is 18 seconds, with a sampling frequency of 100 Hz, thus one cycle has the length of 1801. The 9 features are denoted in Table 1 with their abbreviation and physical meaning.

3.2 The Implementation of the Variational Autoencoder

First, the structure of the encoder, which is shown in Fig. 3, is elucidated. The batch size (bs) is set to one for a better demonstration and is the number of

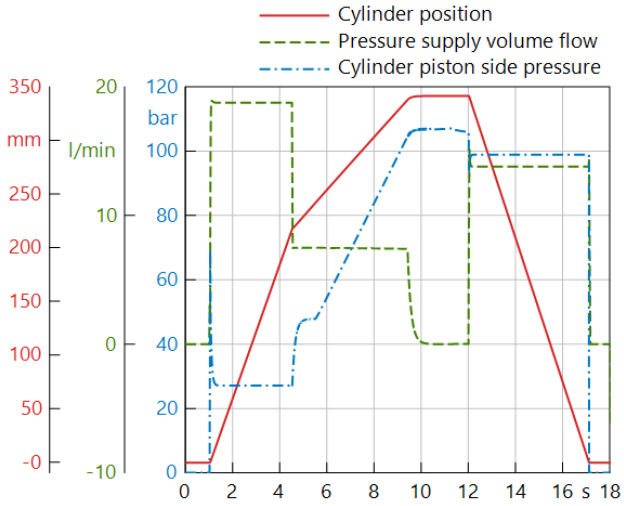

Figure 2: Working Cycle of the hydraulic press

Table 1: The features and their physical meaning

Feature	Physical meaning
x_{CY}	Cylinder position
p_{PS}	Power Supply
p_{Piston}	Piston pressure
p_{Rod}	Rod side pressure
u_{PV}	Control signal propotional valve
y_{PV}	Position propotional valve
Q_{PS}	Volumetric flow rate
$y_{SV1,2}$	Position switching valves SV1,2

bundles of 9 time series utilized in one training iteration, which is denoted as one epoch. As it has been stated before, the input is time series data. The latent size is set to the number of features, 9, thus the time series are completely compressed to one value, respectively. The first two layers consist

of LSTMs in order to consider time dependencies between the data points. The LSTM considers the prior input by storing the information in its hidden state, which is used for computing the output for the subsequent input. In

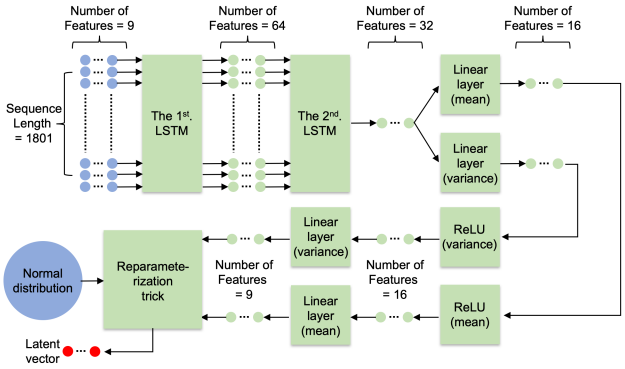

Figure 3: The detailed structure of the encoder

machine learning, a rule of thumb for the layer size is in the power of two. In the first LSTM layer, the input is processed sequentially. For each time step, the measurement features together with the hidden state from the last time step are used to generate the hidden state of the current time step. The size of the generated hidden state is set to 64. So the output of the first LSTM is a sequence of the hidden states in the length of 1801, and the number of features is 64. It is then fed to the second LSTM neural network. In this LSTM, instead of using the whole list of hidden states as output, only the hidden state in the last time step is provided. The size of the generated hidden state is then compressed to 32.

In order to compute a mean (μ) and a variance (Σ), which are eventually used to obtain the latent z, after the LSTM layers, two parallel linear layers are implemented. Each layer has a rectified linear unit (ReLU) as the activation function. Mean (μ) and variance (Σ) vectors are generated after another sequence of linear layers. The data dimension is eventually reduced to 9.
The latent z is randomly sampled by the distribution obtained by μ and Σ, therefore the gradient can not be calculated. This problem is solved by using the reparameterization trick. A random node, which samples a random vector ϵ from a standard normal distribution, is added. The latent space is then calculated by: $z = \mu + \Sigma \odot \epsilon$, with $\odot$ being the Hadamard operator which means a component-wise multiplication. With this function, the gradient can

be calculated by the derivatives of $\frac{\partial z}{\partial \mu}$ and $\frac{\partial z}{\partial \Sigma}$ and used for the optimization of the VAE parameter. The reparametrization trick allows the relocation of the randomness of z to ϵ. However, this is only necessary during the training process. For the validation of the model, the latent vector z is directly assigned with μ. The latent vector generated from the encoder is then fed to the decoder. The structure of the decoder is shown in Fig. 4. The first three layers are reversely arranged compared to the encoder. The latent vector, provided by the encoder is fed to the linear layers and expanded to a size of 32. The repeater loops the input vector 1801 times. In this way, it generates a series of data with a constant trajectory size, which is then fed to the LSTM layers, which eventually computes the reconstructed time series.

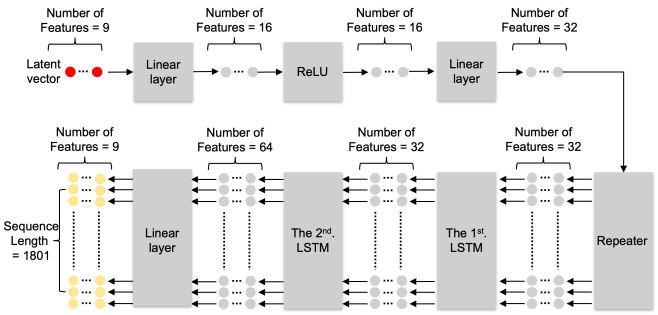

Figure 4: The detailed structure of the decoder

4 Results

This section presents the training and testing results. Firstly, the losses are presented. To obtain a better understanding, the loss is modified. The system parameters are normalized between 0 and 1, except for u_{PV}, y_{PV} and Q_{PS} which are normalized between -1 and 1. Therefore, the loss can be expressed as a percentile number by being computed relatively to these intervals. Secondly, the original and reconstructed time series of Q_{PS} is plotted. Q_{PS} is chosen, since the cylinder velocity is proportional to the volume flow and therefore provides an insight on the dynamic behaviour of the press. Besides, an error plot is given. Since the original dataset contains several entries with a value of 0, the error plots are created by the relative percentage difference (RPD) [24]. The RPD is used to compare two quantities if the original value

is zero. Normally, the error is calculated by dividing the absolute difference of both values with the original value. In the RPD the denominator is the absolute maximum of both values. Lastly, the original and reconstructed time series are quantified by several characteristics, which are given in 2. A detailed description of the features investigated can be found in [25]. Transferring raw data to a new representation is helpful for the interpretability and comprehensibility of a trained ML model, since now the performance of the model can be quantified by more than just the loss. Furthermore, the whole time series are divided into four sections, where each represents a different state of the hydraulic press which were explained in fig. 2. For each section, the characteristics are calculated, weighted, and averaged.

4.1 Results of the variational autoencodder

The VAE is trained with several different sets of hyperparameters in a heuristic approach. The best-performing settings are introduced in the following section.
The best results are obtained with a VAE, which has a batch size of 25 and a learning rate l_r of 10^{-4}. The learning rate is a dimensionless value, since the data is normalized, and is used for the actual tuning of the VAE's parameters during the training process. To detect overfitting, which is that the model learns the training data too well to the extent that it negatively impacts the performance on new data, the VAE is evaluated on a testing dataset. During the testing, the VAE is not optimizing its parameters.
Fig. 5 shows the progress of the mean error for the training and testing data. For a better understanding of the training process, the loss is modified, as described at the beginning of this section, such that a percentile number is obtained. The loss starts at around 216 % and decreases 95.5 % to eventually settle at around 9.5 % after 640 epochs. The testing loss follows the training loss closely, which means that no overfitting occurs during the optimization.
Fig. 6 display the original, reconstructed, and the relative percentage error of the volume flow. The reconstructed time series displays a similar trajectory compared to the original data. As it can be seen, the error is the lowest in the extracting and retracting part of the cycle and increases in the first and last sections. The mean RPD for the whole time serie is 3.8 %. The mean RPD for the other features is displayed in Table. 2 and shows small errors for the remaining ones. Table. 2 shows the characteristics of the 9 features. For each feature, the characteristic is computed for the four sections of the time series, and mean and standard deviation of the percentile error are cal-

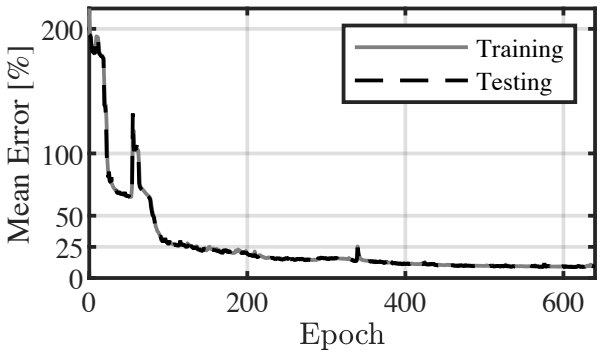

Figure 5: The detailed structure of the vanilla decoder

culated. The empty entries mean, that the error can not be determined, since the characteristic of the original time series is zero, thus the percentile deviation is not defined. Overall, the characteristics show a low error. There are certain outliers; The minimum value of the cylinder position displays a rather high deviation, which is mostly dominated by the second section's deviation. Nevertheless, the other characteristics of x_{CY} display a much smaller error, and besides the mean RPD for the whole cycle is 7.7 %. Furthermore, more extreme values can be observed in the locations of minimum and maximum values of a section. u_{PV}, y_{PV}, and Q_{PS} have high deviation, whereas the other characteristics have low errors with y_{SV1} and y_{SV2} reaching nearly 0. Regarding Q_{PS}, the maximum value also shows a higher deviation, but the other features display good performance.

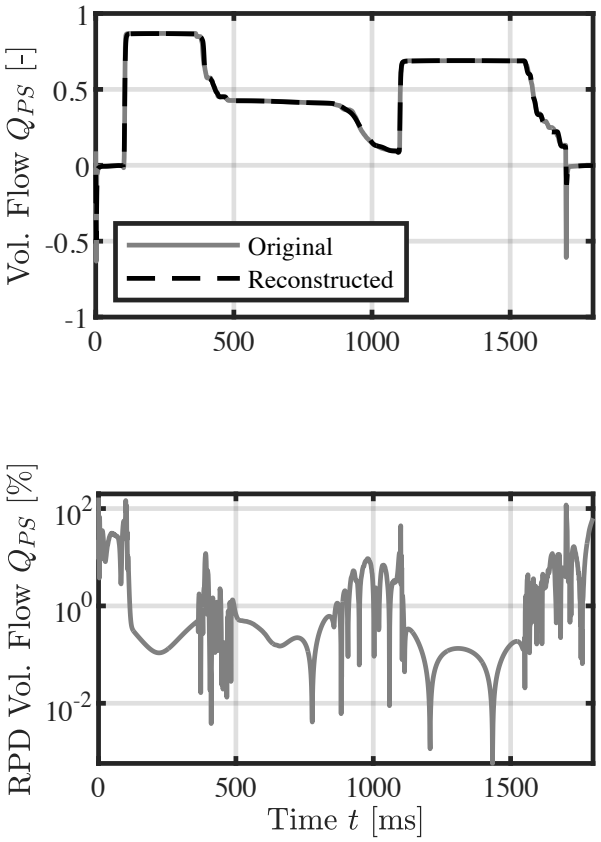

Figure 6: The original (solid grey), the reconstructed (dashed black) volume flow and the RPD plot

The error of most characteristics of y_{SV1}, y_{SV2}, and u_{PV} can not be computed. However, the RPD for all three is smaller than 4 %. Especially, for the control signal of the proportional valve, the RPD is as low as 1.6 % and 1.3 % for the extracting and retracting part, respectively.

5 Conclusion and Outlook

5.1 Conclusion

In this paper, a deep unsupervised learning model with LSTM layers was presented, which reduces the machine data of a hydraulic press into a low dimensional representation and afterwards reconstructs the original input. The quality of the reconstruction is examined by three approaches: Firstly, by the training process. Secondly by plots of the original, reconstructed volume flow and the relative percentage difference error and lastly by several characteristics describing the time series. Regarding the characteristics, the time series are divided into four sections based on the four modes of a working cycle of the hydraulic press. The characteristic for each section is computed and a mean and a standard deviation for the whole time series for each of the 9 features is calculated.

The variational autoencoder has been implemented for the data compression task. In order to handle the time series, the VAE contain long short-term memory layers. The training achieves a 95.5 % decrease and the RPD plot of the volume flow shows good performance, especially in the extracting and retracting phase of the cycle. The characteristics also show rather small deviations, with some outliers. Features like Q_{PS} and x_{CY} have a small number of characteristics with higher deviation but show a good performance regarding the remaining characteristics. Furthermore, the mean RPD of both is also low. Especially for y_{SV1}, y_{SV2} and u_{PV}, where most characteristics can not be computed, the RPD shows good performance, especially in sections 2 and 3 and an overall RPD of less than 4 %. The input matrix has a size of 1801×9 and is reduced to a latent size of 9 with a small information loss. Therefore a compression rate of 99.94 % is successfully obtained.

5.2 Outlook

In future work, the VAE model will be combined with a classification algorithm in order to perform fault detection and diagnosis. The preprocessing of the original data by the VAE is crucial for a good classification. Through the compression into the highly reduced representation, the classification model is provided with the most important information of the machine. Without the data reduction, the classification can't completely focus on the actual fault detection task, since it also needs to filter out redundant data points itself. The combination with a classification model requires an intensive investigation of the latent space. Especially, the trade-off between dimension reduction and

the actual fault detection needs to be examined. With greater latent size, the amount of unique and redundant information for the classification algorithm increases. An optimum size depending on the prediction tasks needs to be found. Furthermore, the VAE creates a mathematical meaningful latent, thus the investigation of the compressed representation in combination with the classification provides a more comprehensive workflow compared to an AE.

Acknowledgement

The authors thank the Research Association for Fluid Power of the German Engineering Federation VDMA for its financial support. Special gratitude is expressed to the participating companies and their representatives in the accompanying industrial committee for their advisory and technical support.

References

[1] Makansi, F.; Schmitz, K., A. Simulation-Based Data Sampling for Condition Monitoring of Fluid Power Drives. IOP Conf. Ser.: Mater. Sci. Eng. 1097 012018, 2021.

[2] Duensing, Y. (Corresponding author); Rodas Rivas, A.; Schmitz, K. Machine Learning for failure mode detection in mobile machinery Drives. In: 11. Kolloquium Mobilhydraulik : Karlsruhe, 10. September 2020.

[3] Zachrison, A. Fluid Power Applications Using Self-Organising Maps in Condition Monitoring., 2008.

[4] Wang, Z.; Lu, C.; Liu, H.; Chen, Z. Performance Assessment of Hydraulic Servo System Based on Radial Basis Function Neural Network and Mahalanobis Distance. Applied Mechanics and Materials. 764-765. 613-618. 10.4028/www.scientific.net/AMM.764-765.613, 2015.

[5] Chawathe, S. S. Condition Monitoring of Hydraulic Systems by Classifying Sensor Data Streams. 0898-0904. 10.1109/CCWC.2019.8666564, 2019.

[6] Siyuan, L.; Linlin, D.; Wanlu, J. Study on application of Principal Component Analysis to fault detection in hydraulic pump. 10.1109/FPM.2011.6045752, 2011.

[7] Helwig, N., Andreas Schütze, Detecting and compensating sensor faults in a hydraulic condition monitoring system. In Proc. Sensor 17th International Conference on Sensors and Measurement Technology, 2015.

[8] Münchhof, M. Model-Based Fault Detection for a Hydraulic Servo Axis. Autom., 2007.

[9] Isermann, R. Fault-Diagnosis Applications: Model-Based Condition Monitoring: Actuators, Drives, Machinery, Plants, Sensors, and Fault-tolerant Systems., 2011.

[10] Stammen, C. Condition Monitoring für intelligente hydraulische Linearantriebe., Dissertation, 2005.

[11] Jegadeeshwaran, R.; Sugumaran, V. Fault diagnosis of automobile hydraulic brake system using statistical features and support vector machines. Mechanical Systems and Signal Processing. 52. 10.1016/j.ymssp.2014.08.007., 2015.

[12] Helwig, N.; Andreas Schütze, A. Detecting and compensating sensor faults in a hydraulic condition monitoring system. in Proc. SENSOR 2015 - 17th International Conference on Sensors and Measurement Technology, oral presentation D8.1, Nuremberg, Germany., May, 2015.

[13] Schneider, T.; Helwig, N.; Andreas Schütze. Automatic feature extraction and selection for classification of cyclical time series data. pp. 198–206. doi: 10.1515/teme-2016-0072, 2017.

[14] Lurette, C.; Lecoeuche, S. Unsupervised and auto-adaptive neural architecture for on-line monitoring. Application to a hydraulic process. Engineering Applications of Artificial Intelligence. 16. 441-451. 10.1016/S0952-1976(03)00064-2., 2021.

[15] Sudarshan S. Chawathe, "Condition Monitoring of Hydraulic Systems by Classifying Sensor Data Streams",, doi: 978-1-7281-0554-3/19., 2019.

[16] Liu S., Ding linlin, Jiang Wanlu, "Study on Application of Principal Component Analysis to Fault Detection in Hydraulic Pump", doi: 978-1-4244-8452-2/11, 2011.

[17] Schneider, T.; Helwig, N.; Andreas Schütze. "Automatic feature extraction and selection for classification of cyclical time series data."tm - Technisches Messen 2017, 84(3), 198–206. doi: 10.1515/teme-2016-0072, 2017.

[18] Zhenya. W., Chen L., Jian. M., Hang. Y., Zihan. C., "Novel method for performance degradation assessment and prediction of hydraulic servo system", SCI IRAN, 22 1604-1615., 2015.

[19] Korgerus T., Vilenius J., Liimatainen J. and Koskinen K.T., "Self-Organizing Maps with Unsupervised Learning for Condition Monitoring of Fluid Power Systems", 2006.

[20] Huijie, Z.; Ting, R.; Xinqing, W.; You, Z.; Hu-sheng, F. "Fault diagnosis of hydraulic pump based on stacked autoencoders" In Proceedings of the 2015 12th IEEE International Conference on Electronic Measurement & Instruments (ICEMI), Qingdao, China, 16–18 July 2015.

[21] Mallak A., Fathi M., "Sensor and Component Fault Detection and Diagnosis for Hydraulic Machinery Integrating LSTM Autoencoder Detector and Diagnostic Classifiers", doi: https://doi.org/10.3390/s21020433, 2021.

[22] Baldi, P., "Autoencoders, Unsupervised Learning, and Deep Architectures." Proceedings of ICML Workshop on Unsupervised and Transfer Learning, in Proceedings of Machine Learning Research 27:37-49 Available from https://proceedings.mlr.press/v27/baldi12a.html., 2012.

[23] Diederik P. Kingma and Max Welling, "An Introduction to Variational Autoencoders", in Machine Learning., 2019.

[24] Törnqvist L., Vartia P. & Yrjö O., "How Should Relative Changes be Measured?", The American Statistician, 39:1, 43-46, DOI: 10.1080/00031305.1985.10479385., 1985.

[25] M. Christ, A. W. Kempa-Liehr, M. Feindt, "Distributed and parallel time series feature extraction for industrial big data applications", https://arxiv.org/pdf/1610.07717., 2016.

Table 2: Deviation (mean, standard deviation) of characteristics between original and reconstructed data for all 9 features.

Features	x_{CY}	p_{PS}	p_{Piston}	p_{Rod}	u_{PV}	y_{PV}	Q_{PS}	y_{SV1}	y_{SV2}
Max	(-11, 21)	(1.5, 1.6)	(-0.1, 3.7)	(-1.2, 2.6)	(-, -)	(-10.1, 211)	(117, 230)	(-, -)	(-, -)
Min	(486, 983)	(4, 6.4)	(10, 15)	(-0.8, 1.3)	(-, -)	(-, -)	(18.5, 18.7)	(-, -)	(-, -)
Mean	(0.8 , 1.8)	(0.5, 1)	(0.1, 1.3)	(0.4, 0.6)	(-, -)	(-0.06, 0.7)	(0.5, 1.5)	(-, -)	(-, -)
Median	(1.2 , 2.3)	(0.1, 0.4)	(-0.02, 1)	(1.4, 2.6)	(-, -)	(-, -)	(-0.5, 1.3)	(-, -)	(-, -)
Standard deviation	(-10.9, 13)	(-2.4, 8)	(0.1, 2.1)	(-0.4, 0.7)	(-, -)	(1.9, 3.8)	(1.1, 1.8)	(-, -)	(-, -)
Variance	(-68.3, 90)	(-7, 18.7)	(0.04, 4.2)	(-0.9, 1.5)	(-, -)	(3.4, 6.8)	(1.6, 1.7)	(-, -)	(-, -)
Skewness	(4.6, 6.1)	(31, 62)	(1.8, 2.1)	(-2.4, 6.1)	(-, -)	(1.4, 1.3)	(0.8, 1.7)	(-, -)	(-, -)
Kurtosis	(-0.2, 3)	(-95, 193)	(0.4, 0.6)	(-0.4, 3)	(-, -)	(1, 2.8)	(2.4, 2)	(-, -)	(-, -)
Abs. energy	(-6.3, 12.2)	(1.7, 2.1)	(0.04, 3)	(0.6, 1.1)	(-, -)	(0.1, 1.1)	(1.5, 2.3)	(-, -)	(-, -)
Mean abs. change	(1.2, 3)	(-18.8, 42)	(2.2, 2.5)	(8.5, 13.2)	(-, -)	(-5.3, 20.4)	(8.4, 6.8)	(-, -)	(-, -)
Abs. sum change	(1.2, 3)	(-18.8, 42)	(2.2, 2.5)	(8.5, 13.2)	(-, -)	(-5.3, 20.4)	(8.4, 6.8)	(-, -)	(-, -)
First minimum	(-26, 32)	(0.4, 0.9)	(5.7, 9)	(0, 0)	(-188, 251)	(-31.1, 38.9)	(-7.6, 13.5)	(-0.01, 0)	(0, 0)
First maximum	(-5.5, 18)	(-1.1, 2.9)	(-0.9, 1.3)	(-1.3, 2.8)	(-48e2, 96e2)	(803, 1.6e3)	(-172, 254)	(0, 0)	(-0.01, 0)
Last minimum	(-26.1, 32)	(0.4, 0.9)	(5.7, 9)	(0, 0)	(-188, 251)	(-31.1, 38.9)	(-7.6, 13.5)	(-0.01, 0)	(0, 0)
Last maximum	(-5.5, 18.6)	(-1.1, 2.9)	(-0.9, 1.3)	(-1.3, 2.8)	(-48e2, 96e2)	(803, 1.6e3)	(-172, 254)	(0, 0)	(-0.01, 0)
RPD	(7.7)	(1.9)	(4.5)	(2.5)	(3.1)	(12.3)	(3.8)	(0.05)	(0.05)



Faras Brumand-Poor received a bachelor's degree in electrical engineering from RWTH Aachen University in 2017, a master's degree in electrical engineering from RWTH Aachen University in 2019, a master's degree in automation engineering from RWTH Aachen University in 2020, respectively. He is currently working as a Research Associate at the Institute for Fluid Power Drives and Systems at RWTH Aachen University. His research areas include deep learning, physics-based learning, fluid transmission lines, and virtual sensory.



Faried Makansi graduated in mechanical engineering at TU Darmstadt with a Master of Science degree. Since 2019, he has been working as a research assistant at the Institute for Fluid Power Drives and Systems (ifas) of the RWTH Aachen University. His general research concerns leveraging digital technologies for fluid power applications, with a special focus on data-driven methods for condition monitoring.



Katharina Schmitz received a graduate's degree in mechanical engineering from RWTH Aachen University in 2010 and an engineering doctorate from RWTH Aachen University in 2015. She is currently the director of the Institute for Fluid Power Drives and Systems (ifas), RWTH Aachen University.

CFD simulations of Flow Field in Flapper-Nozzle Pilot Valve with Vortex Generators

Tong Li
dept. of fluid control and automation
Harbin Institute of Technology
Harbin, China
18b908121@stu.hit.edu.cn

Jinghui Peng*
dept. of fluid control and automation
Harbin Institute of Technology
Harbin, China
jpeng@hit.edu.cn

Songjing Li*
dept. of fluid control and automation
Harbin Institute of Technology
Harbin, China
lisongjing@hit.edu.cn

Abstract.

For the flapper-nozzle servo valve, the existence of the flow separation phenomenon in the pilot stage may lead to self-excited oscillation, which is a hidden danger to the stability of the servo valve. Aiming at improving the flow state and the stability of the flow field in the pilot stage, a new structure of flapper with vortex generators without disturbing the control performance of the pilot stage is designed. The flow separation phenomenon in the pilot stage is confirmed by analyzing the flow with traditional flapper under different inlet pressures. The flow field in the pilot stage is explored using vortex generators compared to traditional one, the results show that the flow state of the pilot stage flow field is changed by the novel flapper with vortex generators, the flow separation phenomenon is well controlled, the number of vortices in the flow field is significantly reduced, and the flow field is more stable. Therefore, the compact and effective vortex generators have a good effect on improving the stability of the flow field in the pilot stage of flapper-nozzle servo-valve. The primary parameters of vortex generators, height and location, are also taken into account, it is found that when the height of vortex generators h=0.2 and the location size l=0.4, it is more suitable for the actual situation.

Keywords. Flapper-nozzle pilot valve; flow field; flow separation; vortex generators

1. INTRODUCTION

Electro-hydraulic servo technology is an important drive and transmission technology widely used in aerospace, national defense and modern production fields. As an indispensable core component of electro-hydraulic servo system, the stability of servo valve has a vital influence on the reliable operation of the whole servo system. Many studies show that the stability of servo valve is closely related to the flow field of the pilot stage.

The pilot stage flow field refers to the area formed by nozzle, flapper and fixtures, the jet from the nozzle impinging on the flapper and then flows to the outlet. Different from the ordinary impingement jet, the flapper in the pilot stage is neither a flat plate nor a cylinder,

but a combination of cylinder and plane. However, to the best of the author's knowledge, few attentions are paid to this type of impingement jet. Experimental and numerical investigations of cavitation phenomenon appearing in the flow field between the flapper and nozzle of an electrohydraulic servo-valve are carried out in [1], one of their discoveries is that at lower Reynolds numbers, such as Re=630 and Re=1060, the flow moves around the flapper, however, with the increase of Reynolds number, the flow gradually separates from the flapper surface, and cavitation is more obvious. Cavitation phenomenon causes pressure pulsation in flow field and increases the possibility of self-excited oscillation. Furthermore, according to [2], separation of flow and a relative motion between solids contacting in liquid are two possible ways for cavitation. The flow separation is the reason of the large-amplitude oscillation of the flow fields around the inverted flag as in [3], Therefore, it is necessary to research the method of controlling flow separation.

Flow separation phenomenon is very common, such as cylinder flow and aircraft stall phenomenon. The vortex generator (VG), as one of the most successful designs in aviation history, has been highly regarded since its invention in the 1940s and has been applied in many fields. In order to improve the aerodynamic performance of tilt-rotor aircraft, the flow characteristics of V-22 airfoil without and with two rows of parallel vortex generators are studied by numerical simulation [4]. The role of vortex generator in controlling and suppressing dynamic stall on a wind turbine airfoil under unsteady conditions is studied in [5]. Aiming at the problem of excessive propeller excitation force and hull vibration noise of a ship, a triangular vortex generator is designed and installed on the surface of ship stern [6]. The counter-rotating streamwise vortices induced by micro-VGs had a rectifying effect on the near-wall flow and withstood the flow disturbance in the spanwise direction [7].

From the above research, it can be seen that the vortex generator has a good role in delaying flow separation. Therefore, based on the special flow field structure and the flow state of flapper-nozzle pilot stage, a new flapper with vortex generators arranged in pairs at certain angles on its surface is proposed.

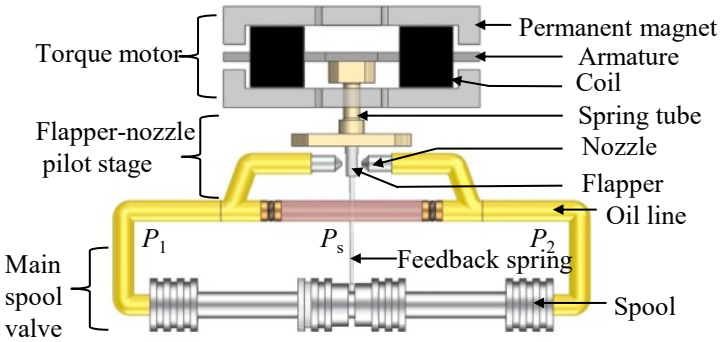

Figure 1.1. Structure of flapper-nozzle servo-valve

2. THE STRUCTURE OF FLAPPER-NOZZLE SERVO-VALVE

Double flapper-nozzle servo-valve is one of the most widely used servo-valve structures. Figure 1.1 is the structure schematic diagram of the servo-valve in the null position. The servo-valve is mainly composed of two parts, electromagnetic part and hydraulic part. The

electromagnetic part, also known as torque motor, including permanent magnet, armature, coil, etc. The role of torque motor is to convert the control signal into mechanical movement. The hydraulic part includes a flapper-nozzle pilot stage and a power stage of spool valve. The pilot stage includes nozzle, flapper, spring tube, feedback spring, etc., and the power stage is mainly composed of spool and valve sleeve. The combination of armature, flapper, spring tube and feedback spring is called armature component.

3. FLOW FIELD OF THE PILOT STAGE

The flow field of the pilot stage is the area surrounded by nozzle, flapper and wall. When the servo valve is in operation, the high-pressure oil is emitted from the nozzle, after a short distance of free jet flow, it impinges on the flapper and then flows in all directions with the stagnation point as center, at this point, the flow state is equivalent to wall jet flow, a small part of the fluid flows to the outlet along the flapper plane, and at the same time, most of the fluid flows away from the flapper to the housing wall, and then reverse. The fluid is separated when it impacts the housing wall and flows in the reverse direction, part of the fluid is affected by the incoming flow, the housing wall and the nozzle wall and rotates in the counterclockwise direction, the other part of the fluid flows under the constraint of the cylindrical wall and then couplings with the fluid emitted from the opposite nozzle, under the influence of the flapper wall, a vortex is formed. Flow separation occurs approximately after the fluid leaves the flapper.

4. VORTEX GENERATOR

The basic principle of vortex generator to control flow separation is to generate streamwise vortices with high energy. Such streamwise vortices are mixed with the downstream low-energy boundary layer flows, and the energy is transferred to the boundary layer, so that the boundary layer flow field in adverse pressure gradient can continue to attach to the body surface without separation after obtaining additional energy, as see in Figure 4.1.

In order to control the flow separation phenomenon, the vortex generator is adopted in this paper. Shape, size and installation position are three key parameters of vortex generator design. In terms of shape, the geometric shape of vortex generator includes airfoil, rectangular plate, triangular plate and dipole surface [6]. Combined with the installation space and the effect of delaying separation, the triangular vane vortex generator is selected in this paper, and the size of the vortex generator is set according to [8]. The installation form and specific size are shown in Figure 4.2(a). Vortex generator arrangement is determined based on five parameters: height h, length m, pair distance n, local flow incidence angle β and distance l relative to the center line of the nozzle, as shown in Figure 4.2(b). Relevant research shows that the height and installation position of vortex generator are particularly important among vortex generator parameters [5,8,9]. Therefore, the height and installation position of vortex generator are studied in this paper.

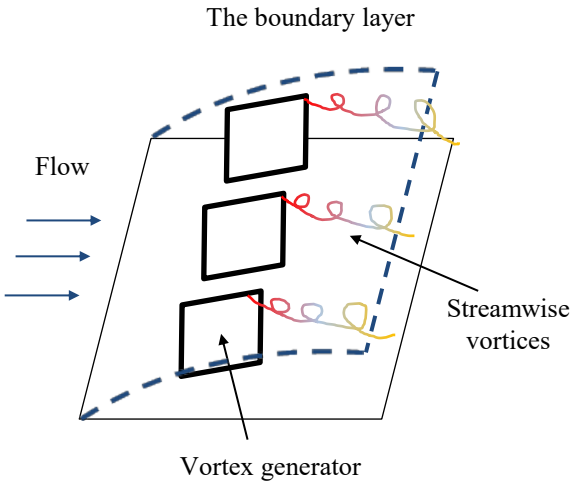

Figure 4.1. Vortex generator

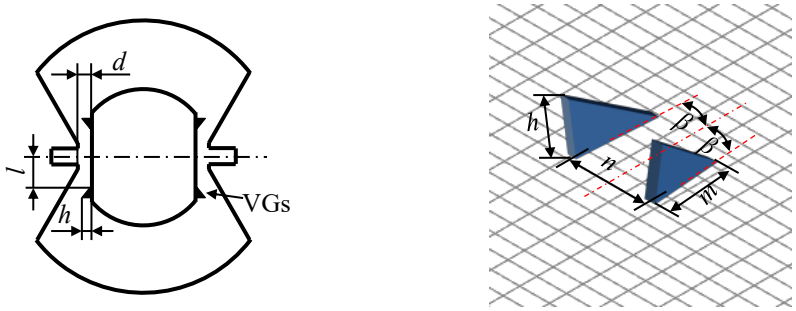

(a) (b)

Figure 4.2. Structure of vortex generator: a. Schematic diagram of installation position of vortex generators; b. Triangular vane type vortex generator.

4.1. Determination of vortex generator height h

Vortex generators transfers momentum from the external flow to the near wall region, so that the flow is well attached to the wall. Therefore, the height of vortex generators is usually related to the local boundary layer thickness [4].The boundary layer thickness of impinging jet on smooth surface and low Reynolds number is as follows [10]:

$$\frac{z(u_{\max})}{D} = \frac{3.2}{\sqrt{Re_1}}\sqrt{\frac{rW_{jet}}{Du_{\max}}} \quad \text{for } Re_1 < 2.5\times10^4 \qquad (4.1)$$

where $z(u_{\max})$ is the distance from plate corresponding to maximum radial mean velocity, m; D is diameter of the jet pipe, m; Re_1 is local Reynolds number, r is the radius from the stagnation point, m; W_{jet} is axial jet velocity at the center of the pipe outlet, m/s; $u_{\max}$ is the maximum radial mean velocity for a specified r, m/s.

$$Re_1 = ru_{\max} / v \quad (4.2)$$

where v is the kinematical viscosity, m^2/s.
It is estimated that when the inlet pressure is 4MPa, the local boundary layer thickness ($z(u_{\max})$) at r=0.3 is 1.8×10^{-5}m. For nozzle-flapper pilot stage, the size of vortex generator is affected by various factors, flow field space($d\approx2\times10^{-4}$m), manufacturing feasibility, and boundary layer thickness. From this, the influence of different vortex generator heights (h=0.05, 0.1, 0.2mm) on the delay of flow separation is investigated in this paper.

4.2. Determination of other shape parameters of vortex generator

The installation form of vortex generators are shown in Figure 4.2. As only the vortex generator is added to the flapper, other dimensions are the same as before. The diameter of the flapper is 2mm, and the width of the flapper plane is about 1.32mm. In addition, to prevent impact on the impingement jet, the vortex generators should be arranged outside the projection area of the nozzle on the flapper plane, so the installation position of the vortex generator should meet the following relationship.

$$l > D/2 \quad (4.3)$$

$$l + m < 1.32/2 = 0.66\text{mm} \quad (4.4)$$

In this paper, the length of vortex generator m is set to 0.15mm, and the diameter of the nozzle D is 0.3mm, Therefore, the range of installation position parameter l of vortex generator is 0.15 ~ 0.51mm, and l = 0.3, 0.4 and 0.5 are selected to study the influence of the installation position of vortex generators on delaying flow separation. The vane thickness is set to the ideal state, which is 0.01mm. The pair distance n is set to 0.1mm, and the local flow incidence angle β is 15°.

5. IMPLEMENTATION OF NUMERICAL STUDY

5.1. Geometry model and computational domain of pilot stage

The overall size of the flow field of the pilot stage is small and the experiment is complicated, it will cost a lot of time and money to conduct experimental research on the influence of all different parameters on the flow field. Therefore, simulation research is necessary, and which is performed with Star-ccm+ software.

5.2. Meshing and boundary conditions

The structure of the whole model is symmetrical, in order to save computing resources and time, half of the model is used for simulation. The turbulence model and the detailed parameters are set according to the previous work [1]. Star-ccm+ software is used to complete the mesh division of the model, and the overall mesh size is 0.1mm. Since the vortex generator structure is mainly used to generate vortices in the boundary layer, this paper considers the influence of boundary layer and refines the boundary layer near the flapper wall. The thickness of boundary layer is set to 33% of the basic grid size, i.e. 0.03mm, the number of inner boundary layer is set to 10, and the growth rate of boundary layer is set to 1.5. In addition, the grid size in the boundary layer is set to 0.025mm. Boundary conditions are also considered, the two inlet types are set as stagnation inlet with pressure of 2,4,6,8Mpa, respectively; and the two outlet types are pressure outlet with pressure of 0MPa; the middle

surface (x=0) type is set as symmetry plane; the other surfaces are wall, as shown in Figure 5.1. In addition, the viscosity of oil is 0.0085kg/ms, the density of oil is 850kg/m^3.

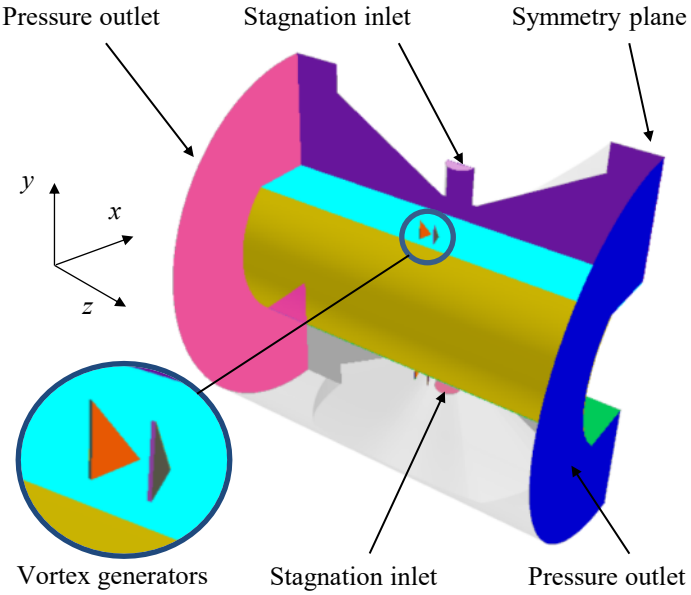

Figure 5.1. 3D model and boundary type setting

6. RESULTS AND DISCUSSION

6.1. Flow field under different inlet pressures

Figure 6.1 shows the velocity scalar diagram of the flow field in the pilot stage under different inlet pressures. As can be seen from the figure, when the inlet pressure p_i is 2MPa, the pressure energy is small, the kinetic energy of jet is relatively small, and the liquid flow velocity is small, the maximum velocity is 66.8m/s. After leaving the flapper plane, the liquid flow along the cylinder wall of the flapper, which is consistent with the Coanda Effect. With the increase of inlet pressure, when p_i is 4MPa, the pressure energy, kinetic energy and flow velocity increase, and the maximum velocity is 94.4m/s, after leaving the flapper plane, most of the fluid still flows along the cylinder wall of the flapper, and a small part of the liquid flows away from the flapper wall, resulting in flow separation. When p_i is 6MPa, the maximum velocity reaches 116m/s, most of the liquid continues to flow along the original flow direction after leaving the flapper plane, and a small part flows along the cylinder wall. When p_i is 8MPa, the maximum velocity reaches 134m/s, the flow field is roughly divided into four parts, and the flow separation phenomenon is more obvious. This is consistent with previous research [1].

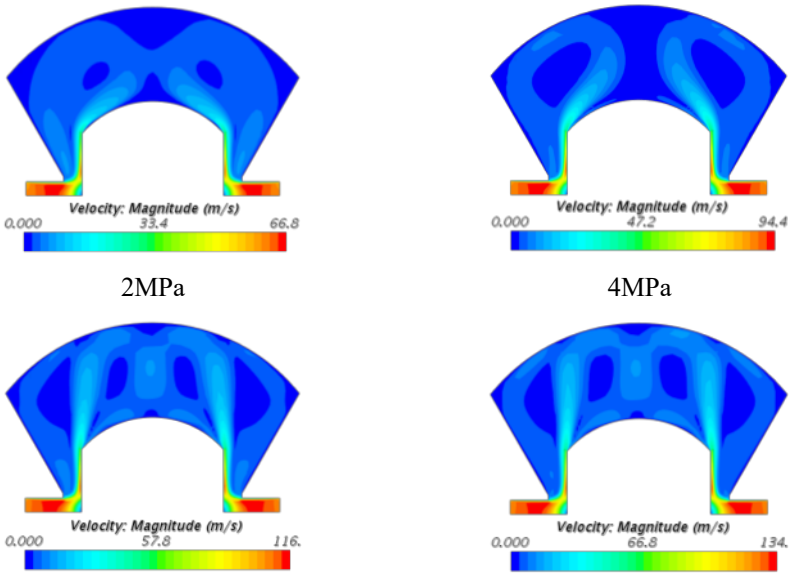

Figure 6.1. Velocity scalar diagram of pilot stage flow field under different inlet pressures based on conventional flapper

6.2. Flow separation delay

For the sake of suppress the flow separation phenomenon, the vortex generators are introduced in this paper, and the effect of the vortex generators are studied.

Figure 6.2 shows the flow state comparison diagram of flow field in the pilot stage with vortex generators and smooth. The inlet pressure p_i of both is 6MPa, and the parameters of the vortex generators are h =0.2 and l =0.4. Figure 6.2(a) and (b) are velocity scalar diagrams of flow field with vortex generators and smooth respectively. As can be seen from the figure, when the vortex generators are installed on the flapper plate, the oil flow still flows along the flapper surface after passing through the junction of plane and camber of the flapper, and the flow state is more stable than that without vortex generators.

Figure 6.2(c) and (d) are velocity vector diagrams of flow field with vortex generators and smooth respectively. It can be seen more clearly from the vector figure that when there are no vortex generators, the oil flow is separated at the junction of plane and camber of the flapper, thus four vortices are formed in the flow field, in which A and C are counterclockwise, B and D are clockwise, and the four vortices almost occupy the whole flow field. However, in the flow field with vortex generators installed, the liquid flow continues to flow along the flapper camber, and only two small vortices are formed in the flow field, E in the counterclockwise direction and F in the clockwise direction. The flow field is relatively more stable.

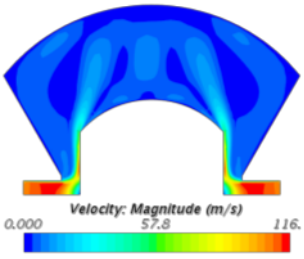

(a)smooth

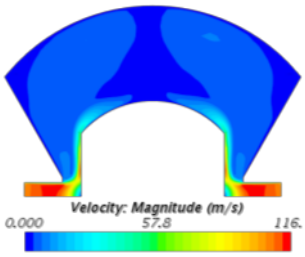

(b)with VGs

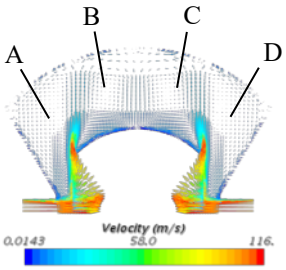

(c) smooth

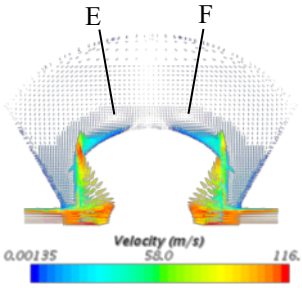

(d) with VGs

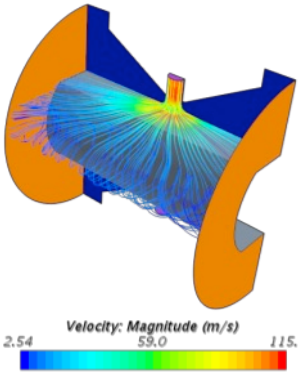

(e) smooth

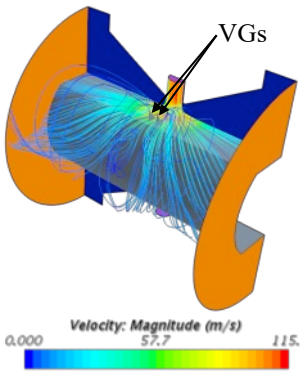

(f) with VGs

Figure 6.2. Comparison of flow state with or without vortex generators

Figure 6.2 (e) and (f) is the 3d flow diagram of the flow field, from which the flow state of the fluid can be clearly seen. As can be seen from Figure 6.2(e), the fluid continues to flow in the original direction after breaking away from the flapper plane, and after hitting the housing wall, it reenters and forms a counterclockwise vortex coupled with the flow from the other inlet. While in Figure 6.2(f), with the presence of vortex generators, the fluid continues to flow close to the cylinder wall of the flapper after leaving the flapper plane and forms a clockwise vortex coupled with the flow from the other inlet.

6.3. Pressure distribution and vortices

Figure 6.3 shows pressure and vorticity field of flow field with vortex generators and smooth. The pressure is still 6MPa, and the parameters of the vortex generator are h =0.2, l =0.4. As can be seen from Figure 6.3(a) and (b), a low pressure area appears behind the junction of flapper plane and camber in the flow field with or without vortex generator, A1 in Figure 6.3(a) and A2 in Figure 6.3(b), which are equivalent to wakes in the flow field. A low pressure area also appears at B in Figure 6.3(b) due to the presence of the vortex generators. In addition, it can be seen from Figure 6.3(a) that there are four large low-pressure areas in the flow field, which are formed by vortices in the flow field, corresponding to Figure 6.2(c). The two areas with low relative pressure in Figure 6.3(b) correspond to Figure 6.2(d), which is also caused by vortices in the flow field. Figure 6.3(c) and (d) are vorticity fields. The vortices in Figure 6.3(c) correspond to Figure 6.2(c) and Figure 6.3(a). Flow separation generates vortices and the formation of vortices generates a low pressure area. In the flow field with vortex generators, the flow separation phenomenon is suppressed, the number of vortices is reduced, and the flow field is more stable, as shown in Figure 6.3(d).

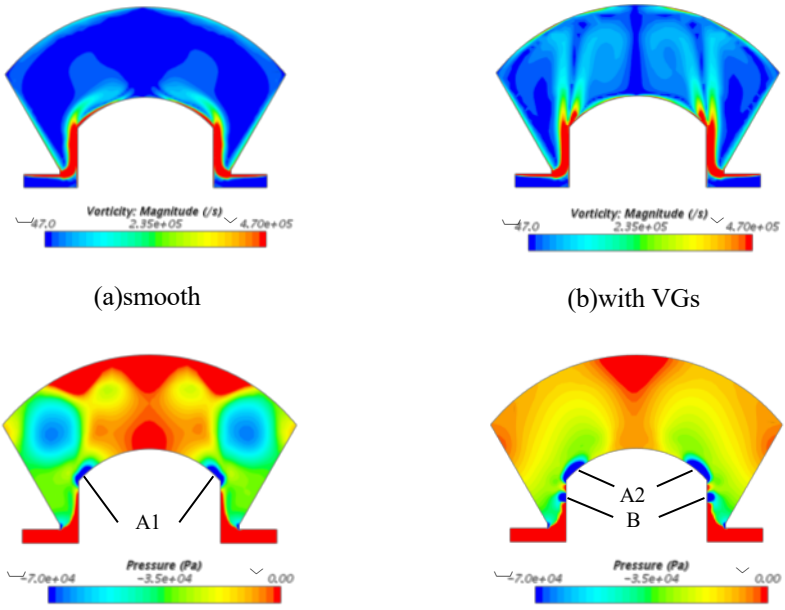

(a)smooth (b)with VGs

(c)smooth (d)with VGs

Figure 6.3. Pressure field and vorticity field

6.4. Effect of vortex generator dimension

The instability in the flow field of the pilot stage is mainly caused by the turbulent flow, so the turbulent kinetic energy is selected in this paper to represent the influence of the vortex generators parameters on the flow field. In order to fully express the flow field, six points are taken as detection points in the flow field to study the stability of the flow field, as shown in Figure 6.4. And the coordinates of the detection points are shown in Table 6.1.

The influence of the height and location of the key geometric parameters on the effect of the vortex generator is simulated. The inlet pressure is set as 6MPa, and the l =0.4 is selected for the position of vortex generators. The average value of turbulent kinetic energy within 0.01s after the flow field is stabilized is taken as the data point to plot. Figure 6.5. shows the turbulent kinetic energy of flow field with different vortex generators height (h =0.05, 0.1, 0.15, 0.2). As can be seen from the figure, compared with the traditional flapper, the turbulent kinetic energy of the flow field with vortex generators at points P2 and P5 decreases substantially by about 80%. Meanwhile, the turbulent kinetic energy at points P1, P3, P4 and P6 does not change much, so the vortex generators play a role in improving the stability of the flow field in the pilot stage. In the flow field with vortex generators, the overall turbulent kinetic energy of the flow field decreases with the increase of the height of the vortex generators, and the flow field is relatively more stable. If the height of vortex generators is too small, it is difficult to be machined; if the height is too large, it may interfere with the wall and cannot be assembled. Therefore, h =0.2 is relatively appropriate.

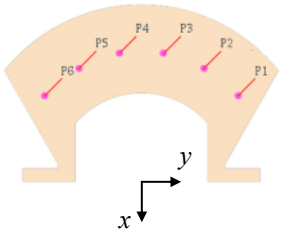

Figure 6.4. Detection points

Table 6.1. The coordinates of the detection points

coordinates	P1	P2	P3	P4	P5	P6
x(mm)	-0.97	-1.28	-1.45	-1.45	-1.28	-0.97
y(mm)	1.1	0.71	0.25	-0.25	-0.71	-1.1
z(mm)	0	0	0	0	0	0

In order to study the influence of vortex generator location on the flow field, the inlet pressure p_i is still set as 6MPa. If the height h of the vortex generator is too large, the height of the vortex generator is the main influence, which is not conducive to analyzing the influence of the vortex generator location on delaying flow separation, therefore, the height h is selected as 0.05 here. The location parameters of vortex generators are l=0.3, 0.4 and 0.5, respectively. It can be seen from Figure 6.6. that the location of vortex generators also has an influence on the flow field, and when l =0.3, the turbulent kinetic energy is minimum, while when l =0.5, compared with the traditional flapper, the impact is very small. Here is why: The flow separation point is at the intersection of plane and camber of the flapper, when l = 0.3, vortex generators are in front of the separation point, the vortex generators can very good play, when l = 0.4, vortex generators also ahead of the separation point, flow separation is also delayed, but the effect is a bit poor, when l = 0.5, the tail of the vortex generators are near the separation point, the vortex generators are basically not functioning, as a result, the effect of delaying flow separation is the worst. If the vortex generator is too close to the nozzle, the jet flow of

the nozzle will be affected. The installation position of the vortex generator l should be relatively large, so l =0.4 is better.

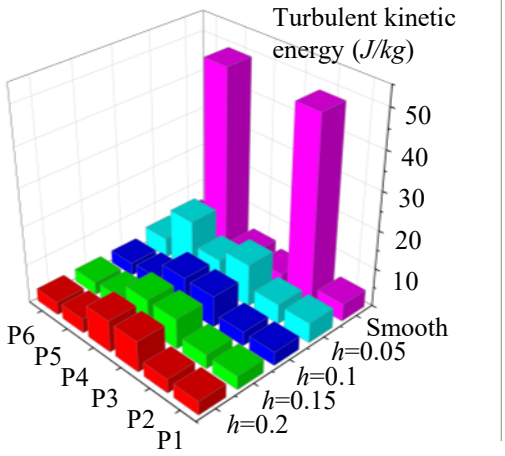

Figure 6.5. Turbulent kinetic energy of flow field corresponding to different vortex generator heights

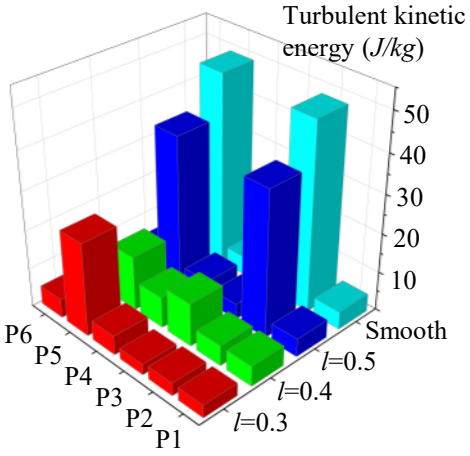

Figure 6.6. Turbulent kinetic energy of flow field corresponding to different vortex generator location

7. CONCLUSION

In this paper, a new flapper structure with vortex generators is proposed, which has the function of controlling the flow separation phenomenon of the pilot stage flow field and improve the stability of the flow field in flapper-nozzle pilot valve. The effectiveness of the vortex generators has been tested by CFD simulation method, and the conclusions can be summarized as follows.

The flow separation phenomenon exists in Flapper-nozzle pilot valve, and the greater the pressure is, the more obvious the flow separation phenomenon is.

Flow separation is delayed when the vortex generators are installed on the flapper. The larger the height of the vortex generator is, the more obvious the effect is. The vortex generator needs to be positioned in front of the separation point to function.

By controlling the flow of fluid, the vortex generators improve the stability of the flow field of pilot stage.

8. REFERENCES

[1] Li S, Aung N, Zhang S, Cao J, Xue X. Experimental and numerical investigation of cavitation phenomenon in flapper–nozzle pilot stage of an electrohydraulic servo-valve. Comput Fluids 2013;88:590-8.

[2] Washio S , Kikui S , Takahashi S . Nucleation and subsequent cavitation in a hydraulic oil poppet valve[J]. ARCHIVE Proceedings of the Institution of Mechanical Engineers Part C Journal of Mechanical Engineering Science 1989-1996 (vols 203-210), 2010, 224(4):947-958.

[3] YaoWei Hu,JiangSheng Wang,JinJun Wang,Christian Breitsamter. Flow-structure interaction of an inverted flag in a water tunnel[J]. Science China(Physics, Mechanics & Astronomy), 2019, 62(12):61-71.

[4] Chen H , Chen B . Aerodynamic Performance Enhancement of Tiltrotor Aircraft Wings Using Double-Row Vortex Generators[J]. International Journal of Aeronautical and Space Sciences, 2021:1-11.

[5] Tavernier D D , Ferreira C , A Viré, et al. Controlling dynamic stall using vortex generators on a wind turbine airfoil[J]. Renewable Energy, 2021(3).

[6] Li L , Zhou B , H Huang, et al. Vortex generator design and numerical investigation for wake non-uniformity and cavitation fluctuation pressure reduction[J]. Ocean Engineering, 2021, 229:108965.

[7] Che B , Chu N , Cao L. et al. Control effect of micro vortex generators on attached cavitation instability [J]. Physics of Fluids, 2019, 31(6): 064102.

[8] Daniel B , Carlos F , De T D , et al. Experimental parameter study for passive vortex generators on a 30% thick airfoil[J]. Wind Energy, 2018, 21.

[9] Baldacchino D , Manolesos M , Ferreira C , et al. Experimental benchmark and code validation for airfoils equipped with passive vortex generators[C]// Journal of Physics: Conference Series. 2016.

[10] Xu Z , Hangan H . Scale, boundary and inlet condition effects on impinging jets[J]. Journal of Wind Engineering & Industrial Aerodynamics, 2008, 96(12):2383-2402.

Biographies



Li Tong received the master's degree in mechanical engineering from Hunan University in 2017, He is currently studying for his doctorate at Harbin Institute of Technology with a research direction of servo valves.

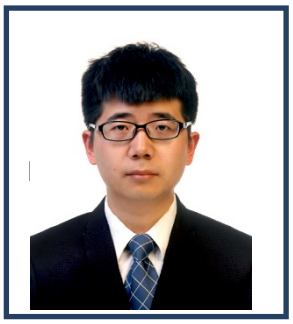

Jinghui Peng received the master's degree and the philosophy of doctorate degree in mechatronics engineering from the Harbin Institute of Technology in 2011 and 2016, respectively. He is currently working as a Professor in the School of Energy Science and Engineering, Harbin Institute of Technology. His research areas include functional fluids, electrohydraulic servo-valve, fluid-structure interaction, vibration and noise suppression, and microfluidic microbial fuel cells.

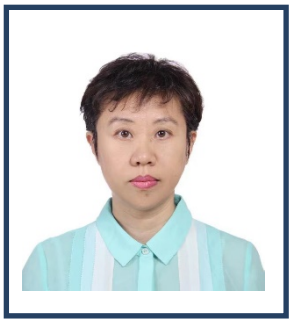

Songjing Li received the Ph.D. from the Harbin Institute of Technology (HIT), China, in 1998. She is currently a Professor and the Head of the Department of Fluid Control and Automation, School of Mechanical Engineering, Harbin Institute of Technology. Her research topics include CFD for fluid power components and systems, microfluidic chips and systems, self-excited noise in hydraulic servo-valves and water generator from air.

Study of a dual layout Input-to-Output Coupled hydromechanical transmission

Antonio Rossetti[1] Nicola Andretta[2] Alarico Macor[2]

1-Istituto per la Tecnologia della Costruzione - CNR
Consiglio Nazionale delle Ricerche - Padova, ITALY, antonio.rossetti@itc.cnr.it

2-Dipartimento di Tecnica e Gestione dei Sistemi industriali (DTG) - Università degli Studi di Padova - Padova, ITALY, nicola.andretta.1@phd.unipd.it, alarico.macor@unipd.it

Abstract.

Hydromechanical three-shaft transmissions, the well-known Input Coupled and Output Coupled, require additional mechanical ranges in order to cover the usual speed ranges of off-highway vehicles. This increases the costs and also the complexity of the transmission.

This work proposes a new configuration that does not require additional mechanical ranges. It consists of a single three-shaft hydromechanical unit, which is operated in dual mode through the action of some clutches: as an IC transmission at low speeds and as an OC transmission at high speeds. In this way the speed range the transmission can cover is doubled.
The performance comparison of the dual layout with that of the Input Couped and Output Coupled transmissions showed that the former maintains high efficiency values for wider vehicle speed ranges than the other two, while reaching the same efficiency peaks.

Keywords. Hydromechanical transmission, dual layout transmission, power split transmission, ICtoOC.

1. INTRODUCTION

The hydromechanical transmission, introduced in the agricultural sector in the 90s, is an interesting alternative to the power-shift transmission, since it offers greater driving comfort and the possibility of optimal engine management [1, 2]. The performance of a hydromechanical transmission, intended both as efficiency and as a functional capacity to meet speed and torque requirements, are strongly conditioned by its layout, which can take a simple or complex forms. The former are the well-known Input Coupled (IC) and Output Coupled (OC), having a single planetary gear; the latter are known as Dual Stage and Compound, having complex planetaries [3] and additional mechanical gears.

However, simple layouts cannot cover the usual vehicular speed ranges without operating at low efficiency conditions. Therefore, they too must adopt additional gears [2]. For example:

Vario from Fendt (OC + 3 gears), HVT R2 from Dana Rexroth (IC + 3 gears) [4], ZF cPower (OC + 2 gears) [5].

Simple hydromechanical transmissions have been the subject of numerous studies aimed at the design [3, 6, 7, 8] and at the optimization of the transmission [9], as well as at the optimal management of the powertrain enabled by the continuous speed variation [10, 11].

The multirange solutions were proposed in the 70's by Orshansky [12] who analysed the functioning of the hydromechanical transmissions with 3 planetary gears and three gear steps, and showed their advantages. Jarchow in his patent [13] proposed a compound scheme with *n* additional ratios. Petterson [14] will take up this pattern by transforming the design method for complex hydromechanical transmissions in an multiobjective optimization problem, whose objective functions are the energy efficiency and the installed displacements. The design method was applied to a heavy wheel loader.

Subsequently various multirange solutions were proposed, based on simple and complex layouts, applied to different off-highway vehicles.

Xia et al. [15] proposed a Compound in power recirculation showing that at the start the transmission provides a high torque value. The solution was applied to a tractor whose parameters were optimized using the multi-objective genetic algorithm [16].

Wan et al. [17] established the characteristic equations of the IC layout and applies them to the case of a four step gear transmission for a wheel loader.

Liu et al. [18] presented a new design method for the study of a multi-range hydro-mechanical transmission. It was based on dual stage IC layout and its gear ratio extension was obtained by means of another planetary gear.

Zu et al. [19] studied a composite powertrain for tractors consisting of a hydromechanical transmission with 4 planetaries and two energy sources: thermal and electrical energy. They defined an optimal energy management criterion and achieved significant consumption reductions compared to the power-shift and hydromechanical power-split tractor of the same power.

Apparently secondary aspects of hydromechanical transmissions, but essential in their functioning, have also been studied. For example, Samorodov et al. [20], studying the braking phase of an OC transmission for a mine locomotive, found some situations of excessive overpressure in the hydrostatic group during the braking phase.

From the above, the need to cover wide speed ranges implies the use of complex planetary gears and additional gears, with construction complications and cost increase.

In this work we propose a solution based on the idea that the same hydromechanical group, thanks to the action of some clutches, can switch from the IC driving mode to the OC driving mode. In this way the speed range can be practically doubled without excessive complications.

Since the shift between the two operating modes can only take place from IC to OC, the proposed layout has been called ICtoOC.

Even if this solution reduces the constructive complexity, it does not guarantee a priori better performances with respect to the two parent layouts. Therefore, in the paper the potential of

this configuration will be studied through some performance comparisons with the IC and OC applied to the same vehicle.

The forklift is the reference vehicle, whose low speeds do not require additional gears to the IC and OC. In this way the forklift does not privilege one solution over another.

The work will develop in the following way. Section 2 will present the transmission and define its sizing criteria; in Section 3 the design and the models of the transmissions to be compared will be illustrated; in Section 4 comparisons will be made between the three configurations operating along a constant load cycle.

2. THE ICTOOC TRANSMISSION

The scheme of the ICtoOC transmission is shown in Figure 2.1. At zero vehicle speed, clutches A and B are closed, C and D open; the transmission is in IC driving mode and in power recirculation mode [2]. The solar and the ring rotate in the opposite direction and the carrier is stationary. By reducing the displacement of unit 1, D_1, the speed of the ring decreases and the speed of the carrier, i.e. the vehicle speed, increases. The power transferred through the hydrostatic transmission is reduced as the vehicle speed increases, thus reaching the full mechanical point, where all the power is transferred through the mechanical branch. Beyond this point the transmission still works in IC, but in additive mode, up to the change speed (V_{shift}). At this point, clutches C and D close and A and B open, and the transmission begins to work in OC driving mode and in power additive mode, until it reaches the second full mechanical point at maximum speed.

The transmission is managed by adjusting only the displacement of unit 1.

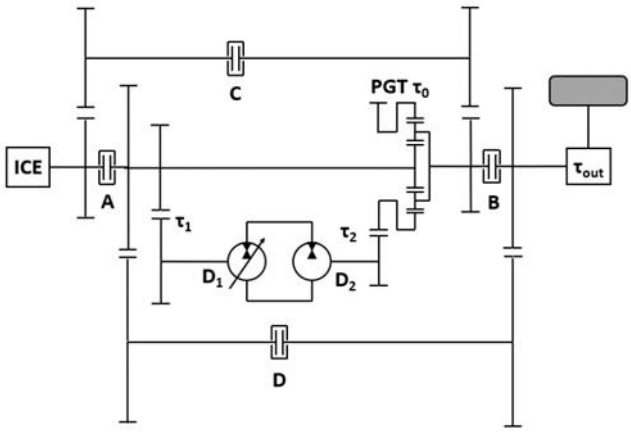

Figure 2.1. Scheme of the ICtoOC transmission.

2.1. Sizing the ICtoOC transmission

The ICtoOC power split transmission can be sized accordingly to the standard procedure used to design IC and OC powertrain, except that the shifting point has to be accounted for and each element has to be verified both in the IC and in the OC driving mode.

Given the constitutive velocity equation of the planetary gear of (1), the full mechanical point is obtained when the ring shaft speed is null reducing (1) to (2).

$$\tau_0\ \omega_s + (1 - \tau_o)\omega_c + (-1)\omega_r = 0 \tag{1}$$

$$\tau_0\ \omega_s + (1 - \tau_0)\omega_c = 0 \tag{2}$$

where ω is angular velocity, r, c, s stand for ring, carrier, and solar of the planetary, respectively.

When the IC driving mode is selected, the sun and the ICE are rigidly connected to each other and the carrier velocity is proportional to the vehicle speed:

$$\omega_s = \omega_{ice} \tag{3}$$

$$\omega_c = \frac{\omega_{out}}{\tau_{out}} = \frac{1}{\tau_{out}} \frac{V}{2\pi\ R_{tire}} \tag{4}$$

On the opposite, when the OC driving mode is selected, the engine is connected to the carrier shaft while the sun drives the output shaft:

$$\omega_c = \omega_{ice} \tag{5}$$

$$\omega_s = \frac{\omega_{out}}{\tau_{out}} = \frac{1}{\tau_{out}} \frac{V}{2\pi\ R_{tire}} \tag{6}$$

Combining the couples of equations (3) and (4) and (5) and (1) with (2), which express the full mechanical point condition, the two full mechanical point velocities V_{fmp}^{IC} and V_{fmp}^{OC} can be computed:

$$V_{fmp}^{IC} = \frac{\tau_0}{(\tau_0 - 1)} \omega_{ice} \tau_{out}\ 2\pi\ R_{tire} \tag{7}$$

$$V_{fmp}^{OC} = \frac{\tau_0 - 1}{\tau_0} \omega_{ice} \tau_{out}\ 2\pi\ R_{tire} \tag{8}$$

Equations 7 and 8 can then be used to define the standing gear ratio τ_0 of the planetary gear and the axle gear ratio τ_{out} once the two full mechanical points of the transmission are chosen. The full mechanical point velocity of the OC configuration V_{fmp}^{OC} can be assumed equal to the maximum vehicle speed as usually done in OC layout. The V_{fmp}^{IC} can be set to optimize the average efficiency of the IC mode or to favour a specific velocity. As a general

rules the IC full mechanical point is designed at one third of the maximum speed as this has proved to lead to the best efficiency for this layout [9]. This design rule can be applied considering, instead of the maximum speed, one third of the shifting speed, which is the maximum speed realized using the IC driving mode (see (10)).

The request for a synchronous shift between the IC and the OC modes leads to the identity between the solar and the carrier shaft $\omega_s = \omega_c$. This condition, along with (1), defines the shift condition as the one where all the planetary gear shafts move synchronously as in the power split node:

$$\omega_s = \omega_c = \omega_r \tag{9}$$

As at the shifting point all the planetary shafts are synchronous, this rotational speed has to match the ICE speed, no matter if the IC (3) or the OC configuration (5) is selected, leading to identify the shifting speed, using (4) or (6):

$$V_{shift} = \omega_{ice}\tau_{out}\, 2\pi\, R_{tire} \tag{10}$$

Is interesting to notice here that the shifting speed V_{shift} corresponds to the geometric average of the IC and OC mechanical points

The gear ratios τ_1 and τ_2 are designed to limit the speed of the hydraulic units below the design value $\omega_{Hy\,Max}$. For the hydraulic unit connected to the power split node, the maximum of the ICE speed (connected during IC mode) and the speed at maximum velocity V_{max} has to be verified:

$$\tau_1 = \frac{\omega_{Hy\,Max}}{\max\left(\omega_{ICE}, \frac{1}{\tau_{out}}\frac{V_{max}}{2\pi\, R_{tire}}\right)} \tag{12}$$

For the hydraulic unit connected to the power merge node (i.e. the planetary gear), the highest velocity of ω_c, whichever it occurs at zero speed, at shifting speed V_{shift} or maximum velocity V_{max} has to be verified:

$$\tau_2 = \frac{\omega_{Hy\,Max}}{\max\left(\omega_c \middle| \begin{matrix} V=0 \\ V_{shift} \\ V_{max} \end{matrix}\right)} \tag{13}$$

Once the gears ratios τ_1 and τ_2 are known, the hydraulic units can be sized. Each unit has to be sized to maintain the hydraulic system pressure below the maximum design value and to provide a coherent flow rate between the two units:

$$D_1 = \frac{2\pi\, T_1}{\Delta P_{max}}, \quad D_2 = \frac{2\pi\, T_2}{\Delta P_{max}} \tag{14}$$

$$\alpha_1\, \omega_1 D_1 = \omega_2 D_2 \text{ with } \alpha_1 < 1 \tag{15}$$

To calculate the torques T_1 and T_2, the most severe condition has to be identified for the specific vehicle considering the two following situations:

- Vehicle still, maximum pulling force, IC mode;
- Shifting speed, maximum power, OC mode.

3. SIZING AND MODELLING OF THE TRANSMISSIONS

The three transmissions under comparison were sized according to the suggestions of Section 2. They are designed for a 5 t forklift with 75 kW, whose characteristics are shown in Table 3.1.

Table 3.1. Characteristic data of the vehicle

	Value	Unit
Engine Power	75	[kW]
Engine Speed	2400	[rpm]
Maximum Wheel Torque	17290	[Nm]
Maximum Vehicle Speed	24	[km/h]
Wheel Radius	0.38	[m]

Figure 3.1 shows the schemes of the IC and OC transmissions, while the scheme of the ICtoOC is in Figure 2.1. The sizing of the IC transmission requires the assumption of V_{fmp}. Since the full mechanical point is the highest efficiency point, the value of its speed has been chosen equal to the one with the highest use frequency of the forklift, which is around 4 km/h.

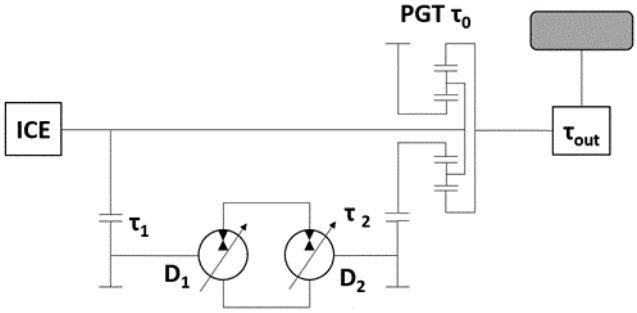

(a)

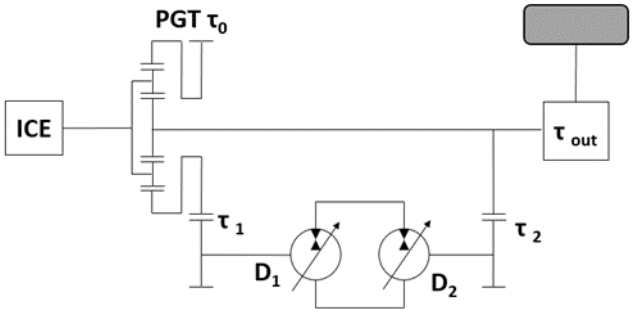

(b)

Figure 3.1. Scheme of the IC (a) and OC (b) transmissions

The full mechanical point speed for the OC transmission, on the other hand, is assumed to be equal to the maximum speed of the vehicle, as is usually done in order to prevent the power recirculation mode.

The ICtoOC sizing maintains the two previous full mechanical point speeds and assumes the shift speed equal to their geometric mean, as established in Section 2.

Table 3.2 summarizes the values of the full mechanical point and shift speeds together with the parameters produced by the sizing. It should be noted that the reduction in the speed range due to the change from IC to OC mode in the ICtoOC layout reduces the overall displacement of the hydraulic units, potentially leading to a more compact CVT unit.

The three transmissions were modeled through Amesim [21] (Figure 3.2). Particular attention was given to the definition of the loss models of the two hydraulic units, since the performance of the transmission essentially depends on their energy losses. The volumetric losses and the hydromechanical losses of the hydraulic machines have been described by a polynomial model derived from experimental measurements [22]. Losses in ordinary gears were defined by an average efficiency equal to 0.98, while for the epicyclical gears, an average efficiency of 0.97 was assumed for each pair of engaged gears.

For the sake of simplicity, the internal combustion engine has been replaced by a constant speed input. Each of the three transmissions is managed by a PI-type control system that tracks the vehicle speed by acting on the displacement of unit 1 (see Figure 2.1).

Table 3.2. Functional data of the transmissions

	IC	OC	ICtoOC
V_{fmp} [km/h]	4	24	4 and 24
V_{shift} [km/h]	/	/	9,8
D_1 [cc]	55	160	110
D_2 [cc]	140	80	40
τ_1	1.25	0.477	0.51
τ_2	0.77	1.25	1.26
τ_{out}	14	40	35
τ_0	-5.1	-1.8	-1.5
ΔP_{max} [bar]	400	400	400

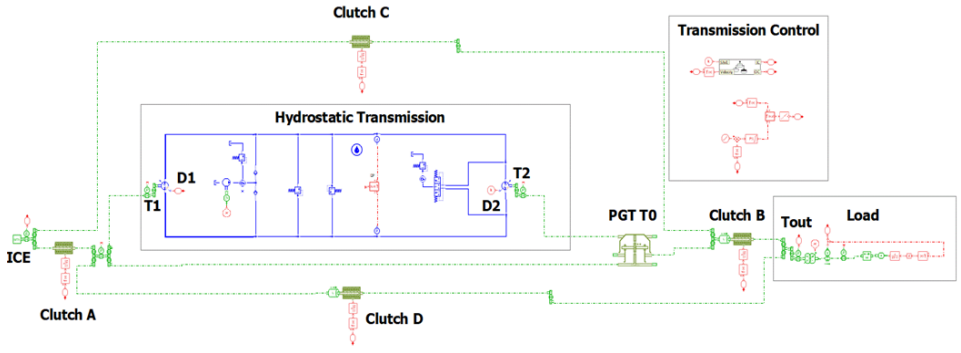

Figure 3.2. Amesim model of the ICtoOC transmission.

4. PERFORMANCE COMPARISON

The comparison between the three transmissions was carried out by means of two quantities: the energy consumption, i.e. the energy supplied by the engine, and the transmission efficiency, defined as the ratio between the power at the wheels and the power supplied by the engine. The calculations were carried out at maximum power condition, with gradually increasing speed between zero and the vehicle maximum speed.

Figure 4.1 shows the trend of the displacement and the speed of the hydraulic machines of the ICtoOC transmission along with the truth table of the clutches (Table 4.1).

The energy consumptions of the three transmissions are shown in Figure 4.2. IC is the least efficient layout, while the OC and the ICtoOC have lower consumption by 5.2% and 9% respectively. These results are the consequence of the losses in the three transmissions. While IC and OC layouts have only one full mechanical point, 4 km/h and 24 km/h respectively, the ICtoOC has two at the same speeds, as shown by the efficiency curve in figure 4.3. It is worth remembering that full mechanical point is the functional condition with maximum efficiency, since here all the power is transmitted via the most efficient mechanical path, and not via the hydraulic path, which is always the site of a double energy conversion. Furthermore, the ICtoOC benefits from the small size of the hydraulic machines, which leads to fewer losses.

As expected then, the ICtoOC can take the best response from the two configurations.

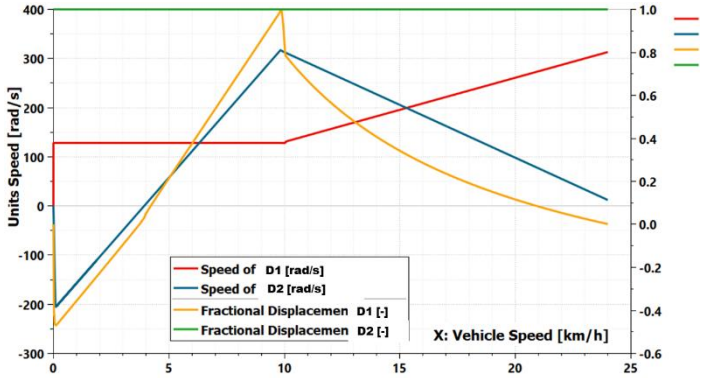

Figure 4.1. Displacements and speeds of the hydraulic units of ICtoOC transmission.

TABLE 4.1. Truth table of the clutches of the ICtoOC transmission.

	A	B	C	D
0 - V_{shift}	✓	✓	×	×
V_{shift} - V_{max}	×	×	✓	✓

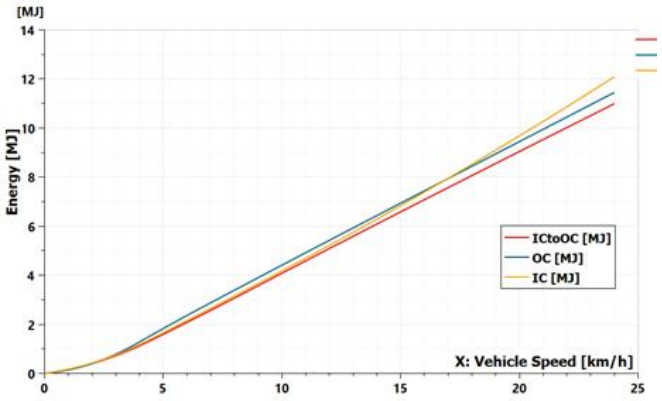

Figure 4.2. Energy consumption of the transmissions.

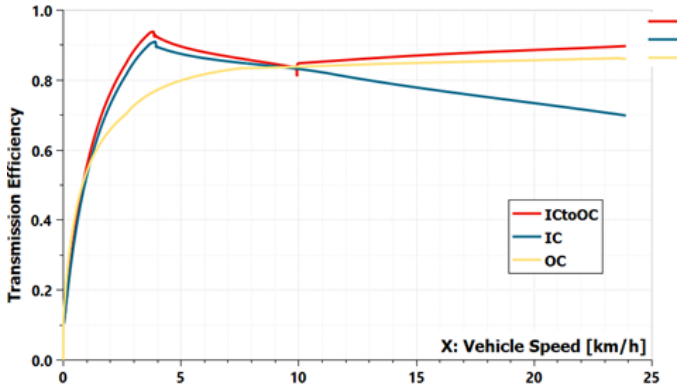

Figure 4.3. Efficiency of the transmissions.

5. CONCLUSIONS

The paper proposes a new three-shaft layout in which a single hydromechanical group (planetary + hydrostatic group) can switch from the IC layout to the OC layout, thereby extending the vehicle's speed range without adding mechanical gears. The powertrain is designed so to realize the shift between the IC and the OC layout at synchronous condition between the engaging shafts, to avoid discontinuity in the vehicle speed and to reduce the friction engaging time.

With this solution some advantages can be obtained:

- the layout has two full mechanical points, in which the power is transmitted only mechanically, therefore with high efficiency;

- the prevalent operation of the transmission is the additive mode, the most efficient, except at start-up in which the mode is power recirculation;

- the overall displacement of the hydraulic units is reduced compared to the corresponding one for the IC and OC layouts, with advantages in terms of losses, costs and encumbrance.

The simplification due to the lack of additional ranges is partially offset by the need to introduce four clutches (three considering one still present between engine and transmission).

The new layout was compared with IC and OC layouts applied to the case of a fork-lift. Under maximum power condition, the energy consumption of ICtoOC resulted 4% and 9% lower than the one of IC and OC layouts respectively.

Future developments of this solution will have to include simulations on realistic loading and unloading cycles and the optimal sizing to adapt the design parameters to the characteristics of the vehicle. Further interaction between this solution and possible energy recovery strategies will be also analysed.

6. REFERENCES

[1] J.H. Kress, 'Hydrostatic power-splitting transmissions for wheeled vehicles. Classification and theory of operation' SAE Paper No.680549; 1968.

[2] K. T. Renius and R. Resch, 'Continuously Variable Tractor Transmissions' In: ASAE Distinguished Lecture Series Tractor Design. 29. 2005.

[3] C. Blake, M. Ivantysynova, K. Williams, 'Comparison of operational characteristics in power split continuously variable transmissions', In Proceedings of the SAE 2006 Commercial Vehicle Engineering Congress & Exhibition, Rosemont/Chicago, IL, USA, 31 October–2 November 2006.

[4] S. Mercati, F. Panizzolo and G. Profumo, 'Power split hydro-mechanical variable transmission (HVT) for offhig,hway application', 10th International Fluid Power Conference, Dresden, Germany 2016.

[5] J. Legner, W. Rebholz, and R. Morrison, 'ZF cPower – Hydrostatic-Mechanical Powersplit Transmission for Construction and Forest Machinery', 10th International Fluid Power Conference. Dresden 2016.

[6] P. Casoli, A. Vacca, G. Berta, S. Meleti, and M. Vescovini, 'A numerical model for the simulation of Diesel/CVT power split transmission', SAE paper n. 2007-24-137, SAE-NA ICE2007, 17-20 Settembre, 2007 Capri-Napoli. ISBN: 978-88-900399-3-0. DOI: 10.4271/2007-24-0137

[7] P. Linares, V. Mendez, and H. Catalan, 'Design parameters for continuously variable power-split transmissions using planetaries with 3 active shafts', Journal of Terramechanics, 47 (2010) 323–335

[8] S. Xiong, G. Wilfong, and J. Lumkes Jr., ' Components sizing and performance analysis of hydro-mechanical power split transmission applied to a wheel loader' Energies2019,12, 1613; doi:10.3390/en12091613.

[9] A. Rossetti, A. Macor, 'Continuous formulation of the layout of a hydromechanical transmission', Mechanism and Machine Theory 133 (2019) 545–558. https://doi.org/10.1016/j.mechmachtheory.2018.12.006

[10] A. Rossetti, A. Macor, A. Benato, 'Impact of control strategies on the emissions in a city bus equipped with power-split transmission', Transportation Research Part D: Transport and Environment, Volume 50, 1 January 2017, Pages 357-371. DOI: 10.1016/j.trd.2016.11.025. Scopus code: 2-s2.0-85000426786.

[11] A. Rossetti, N. Andretta, and A. Macor, 'On the use of the Disability-adjusted Life Year (DALY) estimator as a metric to optimally manage ICE emissions', Energies 2022, 15, 4386. https://doi.org/10.3390/en15124386

[12] E. Orshansky and W.E., Weseloh, 'Characteristics of Multiple Range hydromechanical transmissions', SAE paper 720724,Warrendale, PA: Society of Automotive Engineers, 1972.

[13] F. Jarchow, 'Leistungsverzweigte Getriebe' (Power split transmissions), Vdi-Z 1964, 106, 196–205.

[14] K. Pettersson and P. Krus. 'Design Optimization of Complex Hydro-mechanical Transmissions', Journal of Mechanical Design 135.9 (2013). doi: 10.1115/1.4024732.

[15] Y. Xia and D. Sun, 'Characteristic analysis on a new hydro-mechanical continuously variable transmission system', Mechanism and Machine Theory Volume 126, August 2018, pp. 457-467. https://doi.org/10.1016/j.mechmachtheory. 2018.03.006

[16] Y. Xia, D. Sun, D. Qin, and X. Zhou, 'Optimisation of the power-cycle hydro-mechanical parameters in a continuously variable transmission designed for agricultural tractors', Biosystems Engineering, vol. 193, May 2020, pp. 12-24. https://doi.org/10.1016/j.biosystemseng.2019.11.009

[17] L. Wan, H. Dai, Q. Zeng, Z. Sun, and M. Tian, 'Characteristic Analysis and Co-Validation of Hydro-Mechanical Continuously Variable Transmission Based on the Wheel Loader', Appl. Sci. 2020, 10, 5900; doi:10.3390/app10175900

[18] F.X. Liu, W. Wu, J.B. Hu, and S.H. Yuan, 'Design of multi-range hydro-mechanical transmission using modular method,' Mech. Syst. Signal. Proc. 2019, 126, pp.1–20.

[19] Z. Zhu, Y. Yang, D. Wang, Y. Cai, and L. Lai, 'Energy Saving Performance of Agricultural Tractor Equipped with Mechanic-Electronic-Hydraulic Powertrain', System.Agriculture 2022, 12, 436. https://doi.org/10.3390/ agriculture12030436

[20] V. Samorodov, A. Bondarenko, I. Taran, and I. Klymenko, 'Power flows in a hydrostatic- mechanical transmission of a mining locomotive during the braking process', TRANSPORT PROBLEMS 2020 volume 15 issue 3. doi: 10.21307/tp-2020-030.

[21] AMESim 2021, 2021-2. Siemens Industry Software NV

[22] N. Andretta, 'Design methods for hybrid hydro-mechanical transmissions of heavy-duty vehicles', Ph.D. thesis, Supervisors: A. Macor, A. Rossetti. Padua University, Italy, 2022.

Biographies



Antonio Rossetti is a Researcher at the Construction Technologies Institute (ITC) of the Italian National Research Council (CNR). His actual research interests focus on the thermo-fluid dynamic aspects of the cold-chain field at different TRL levels involving numerical, experimental, and on-site activities. At present, he is mainly involved in the study of natural fluids applications for the refrigerated transport sector and sustainable mobility solutions. He graduated in 2005 at Padua University in Mechanical Engineering obtaining a Ph.D. in Industrial Engineering in 2009. Since then, he has published more than 60 research papers in the fields of HVAC&R, turbomachinery, computational fluid dynamics and powertrain management and design.



Nicola Andretta received the bachelor's degree in Mechanical Engineering in 2016, Master's Degree in Product Innovation in 2018, and Ph.D. in Mechatronics and Product Innovation Engineering at Padua University in 2022. His research areas include industrial and mobile fluid power, design and optimization of hydromechanical hydraulic hybrid transmissions, publishing 10 articles on these topics. In 2019 he received the award for the best degree thesis from the Italian Fluid Power Society.



Alarico Macor graduated in Mechanical Engineering and obtained a PhD in Energy Engineering from the University of Padua. He is an associate professor of Fluid Machines and Fluid Power Systems also teaching at the Graduate School of Mechatronics. His recent research topics concern biofuels and the impact of their emissions, the design, optimization, and management of hydromechanical transmissions. He is the author of over 100 articles covering energy systems, biofuels, hydraulic hybrid systems, and power-split hydromechanical transmissions.

Simulation model of hydraulic generator with variable flow direction

Kacper Dąbek, Krzysztof Kędzia, Piotr Osiński

Kacper Dąbek, MSc. Eng. Wroclaw University of Science and Technology, Poland
kacper.dabek@pwr.edu.pl

Krzysztof Kędzia, PhD. Eng. Wroclaw University of Science and Technology, Poland
krzysztof.kedzia@pwr.edu.pl

Piotr Osiński, Prof. Eng. PhD. Wroclaw University of Science and Technology, Poland
piotr.osinski@pwr.edu.pl

Abstract.

The paper presents a simulation model of a hydraulic pump generator with variable flow direction. Current solutions are based on a steady flow of hydraulic fluid. This article presents the results of simulations for a system in which the flow will have a sinusoidal (alternating) progression. The simulation will be performed using MatLAB Simulink. The results of the simulations will be used in the next phase to develop the design assumptions and make a prototype system. Ultimately, the prototype of the hydraulic system will be used in a hydrostatic transmission with oscillating flow. The subject of the dissertation will be the assessment of the hydraulic and dynamic properties of the prototype transmission with the oscillating flow.

Keywords. Hydrostatic drive system, generator with variable flow direction, simulation model

1. INTRODUCTION

The natural resources of the Earth are limited. Their excessive use has a negative impact on ecology [1]. In recent years, more and more emphasis has been placed on renewable energy sources. Regulations aimed at reducing carbon dioxide emissions are a good example. As a result, there is again a dynamic development of the industry related to recuperation and efficient energy storage. Many concepts of hybrid drives are developing in the automotive industry. In most of them, the vehicle's kinetic energy is recuperated on the electric way [2, 3] during braking [8, 9]. There are many solutions and configurations. Last time the Audi company introduced into production vehicles with energy recuperation from shock absorbers. The principle of operation is presented in Fig.1. An innovative solution based on

an electromechanics system. The maximum power that this solution could generate is up to 600 Watts [4].

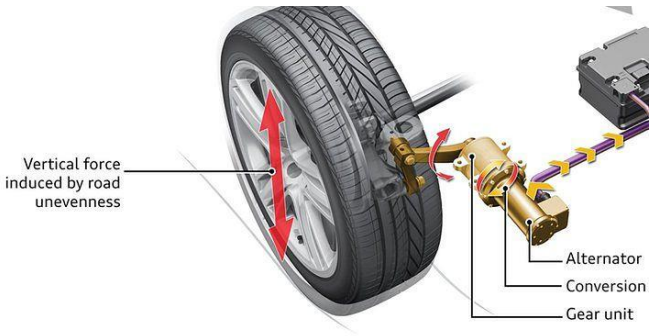

Figure 1.1. The operating principle of the Audi erupt system [4]

This paper aims to present a simplified simulation model of an oscillating hydrostatic transmission that allows to recuperate energy from shock absorbers of civil vehicles.

2. MATHEMATIC MODEL

The simulated hydraulic system is shown in Fig. 2. The drawing alludes to the patent application [10]. It consists of a double-acting cylinder, four check valves, a hydraulic motor and two maximum valves. The check valve system creates a hydraulic rectifier, which is characterized by the ability to straighten the direction of the flow of the working fluid [5, 11]. A number of simplifications have been made to the model:

- no oil temperature change,
- perfect forcing the actuator,
- no line and local losses,
- no inertia in valves,
- is no included loading on the piston rod, such as spring, inertia, friction.

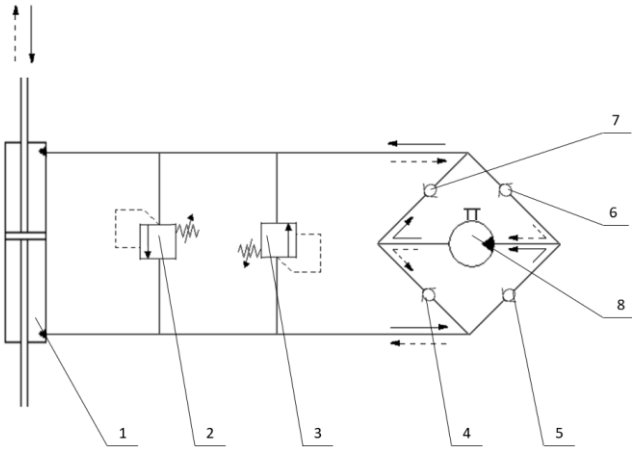

- Figure 2.1. Hydraulic system scheme; 1- double-acting hydraulic cylinder, 2,3- pressure relief valve, 4-7- check valve, 8- hydraulic motor [10]

2.1. Double-acting hydraulic cylinder

As the first element in the system, it is the source of stream energy. The compulsion is the ideal shift model. Any kind of leakage, internal or external, is not taken into account.

2.2. Hydraulic motor

A hydraulic motor as an element that converts the energy of steady flow of the working fluid into a mechanical rotary motion. The engine model takes into account the losses: mechanical and volumetric. Volumetric losses are related to internal leakages between the engine inlet and the engine outlet. The described mechanical losses are related to internal friction. The hydraulic motor model has the ability to impart inertia. These dependencies are described by the following formulas [6, 7].

Rated flow:

$$q_{Real} = q_{Ideal} + q_{Leak} \quad (1)$$

where:

q_{Real} - real volumetric flow rate

q_{Ideal} - ideal volumetric flow rate

q_{Leak} - internal leakage volumetric flow rate

Torque:

$$\tau = \tau_{Ideal} - \tau_{Friction} \quad (2)$$

where:

τ - net torque

τ_{Ideal} - ideal torque

$\tau_{Friction}$ - friction torque

Ideal volumetric flow rate:

$$q_{Ideal} = D\omega, \quad (3)$$

where:

D - the value of the hydraulic motor displacement

ω - instantaneous angular velocity of the rotary shaft

Ideal generated torque:

$$\tau_{Ideal} = D\Delta p \quad (4)$$

where:

Δp - instantaneous pressure drop from inlet to outlet

Leakage:

$$q_{leak} = K_{HP}\Delta p \quad (5)$$

where:

K_{HP} – Hagen-Poiseuille coefficient for laminar pipe flow

2.3. Check valve

The check valve allows the working liquid flow in one direction. Due to the design, exist a minimum pressure, above which the valve opens. The opening is linear until the maximum value of the valve area is reached. Leakage for a closed valve was determined as a constant value for the leakage area. The dependencies are shown in Fig. 3.

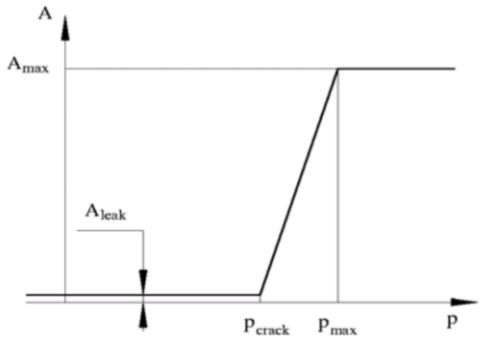

Figure 2.2. Dependence of pressure and area [7]

Check valve equation:

$$\Delta p = p_A - p_B \tag{6}$$

where:

p_A – pressure before valve

p_B – pressure after valve

Flow area:

$$A(p) = \begin{cases} A_{leak} & \text{for } p \leq p_{crack} \\ A_{leak+k\cdot(p-p_{crack})} & \text{for } p_{crack} < p < p_{max} \\ A_{max} & \text{for } p_{max} \leq p \end{cases} \tag{7}$$

where:

A_{max} - fully open passage area

A_{leak} - closed valve leakage area

p_{crack} - valve cracking pressure

p_{max} - fully open pressure

2.4. Pressure relief valve

The system is protected by two maximum valves. They allow the working liquid to flow into a parallel line in case of too much load on the hydraulic motor. The dependencies of pressure and passage are shown in Fig. 3.

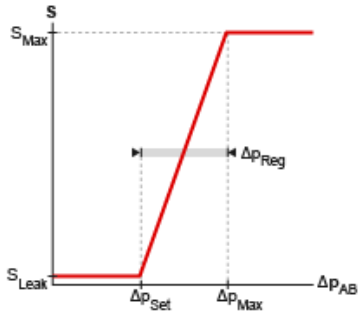

Figure 2.3. Dependence of pressure and area in pressure relief valve [7]

Leakage for a closed valve was determined as a constant value for the leakage area. The opening is linear according to the following equation:

$$S(\Delta p_{AB}) = S_{leak} + k(\Delta p_{AB} - \Delta p_{set}) \qquad (8)$$

where:

$S(p_{AB})$ – relief valve opening area

S_{leak} – leakage area

Δp_{set} – valve pressure setting

Δp_{AB} – pressure drop from port A to B

2.5. Inertia

The inertia was modeled for the hydraulic motor model. It is expressed as follows:

$$T = J\frac{d\omega}{dt} \qquad (9)$$

where:

T - inertia torque.

J - inertia.

ω - angular velocity.

t - time.

3. SIMULATION

The MatLAB Simulink program with the Simscape extension was used to create the simulation model. After selecting the simulation parameters, the input was implemented. The source that drives the entire system is an external displacement source connected to a double-actuator cylinder. The input force is a sinusoidal function.

3.1. Simulation without inertia

The simulation is shown in Fig. 5. which presents the velocity of the double-actuator cylinder. Fig. 6. shows the dependence of the rotational speed of the hydraulic motor shaft. Fig. 7. shows the flow rate of the hydraulic motor as a function of time.

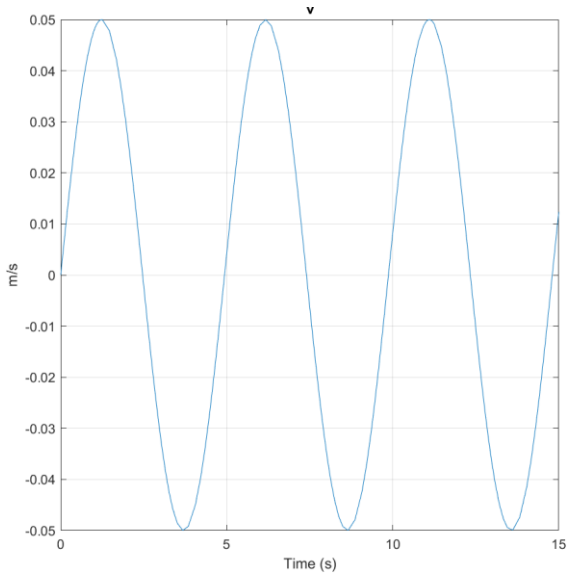

Figure 3.1. Simulation without inertia – extortion signal

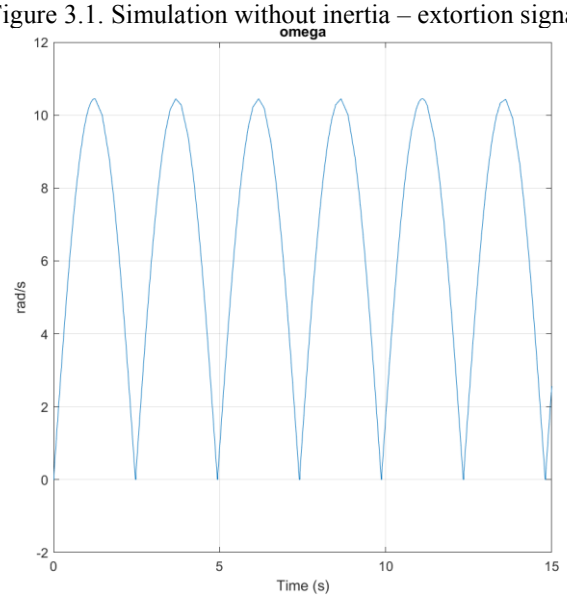

Figure 3.2. Simulation without inertia - *motor* rotational *speed.*

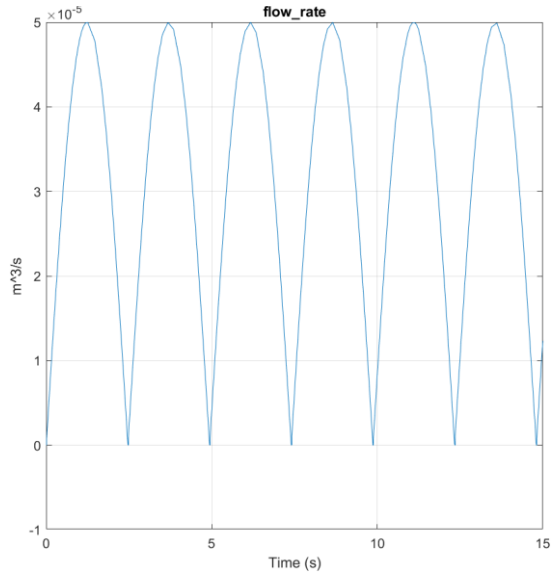

Figure 3.3. Simulation without inertia – flow rate.

3.2. Simulation with inertia

The simulation was carried out with joined inertia. Similar to the simulation without inertia: Fig. 8. shows the velocity of a double-actuator cylinder, Fig. 9. shows the dependence of the rotational speed of the hydraulic motor shaft, and Fig. 10. shows the flow rate shown in hydraulic motor as a function of time.

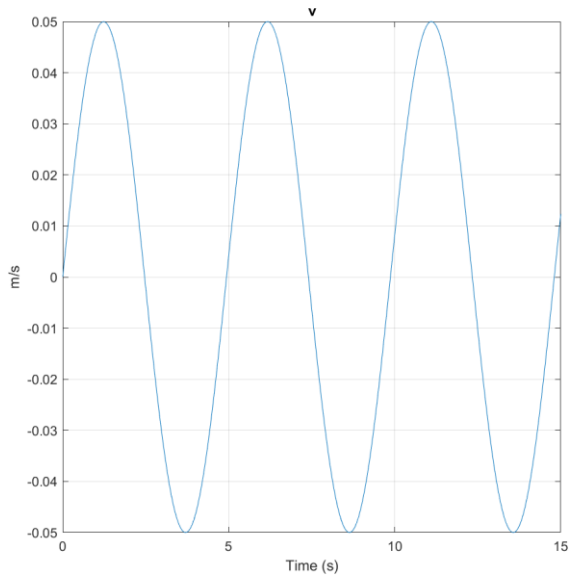

Figure 3.4. Simulation with inertia – extortion signal.

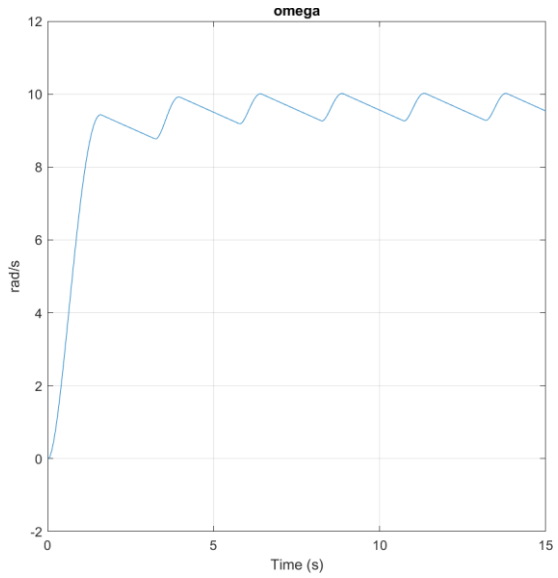

Figure 3.5. Simulation with inertia – rotational speed of the motor.

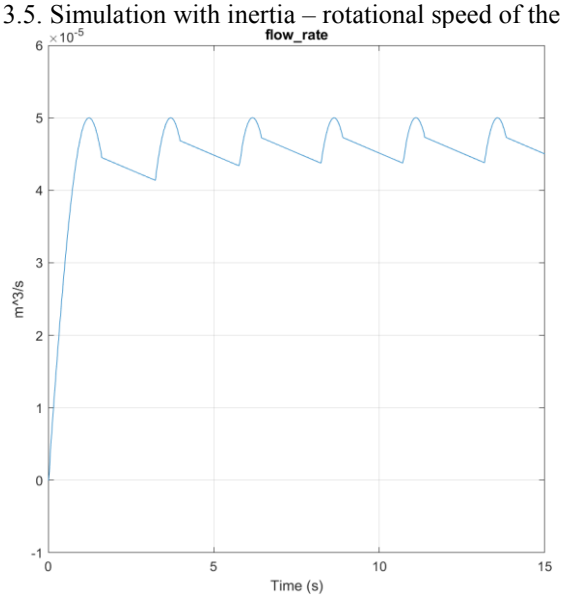

Figure 3.6. Simulation with inertia – flow rate.

3.3. Simulation with inertia and high frequency

The simulation was carried out with joined inertia. Similar to the simulation without inertia: Fig. 11. shown velocity of the double actuator cylinder, Fig. 12. shown dependence

of the rotational speed of the hydraulic motor shaft, Fig. 13. the flow rate shown in the hydraulic motor in the function of time.

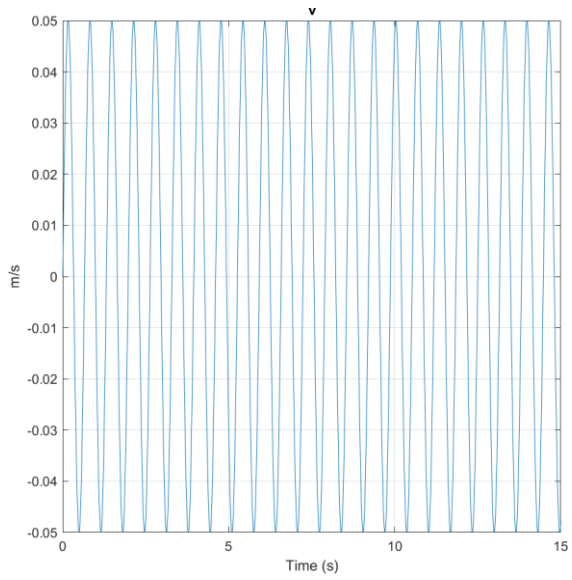

Figure 3.7. Simulation with inertia and high frequency – extortion signal.

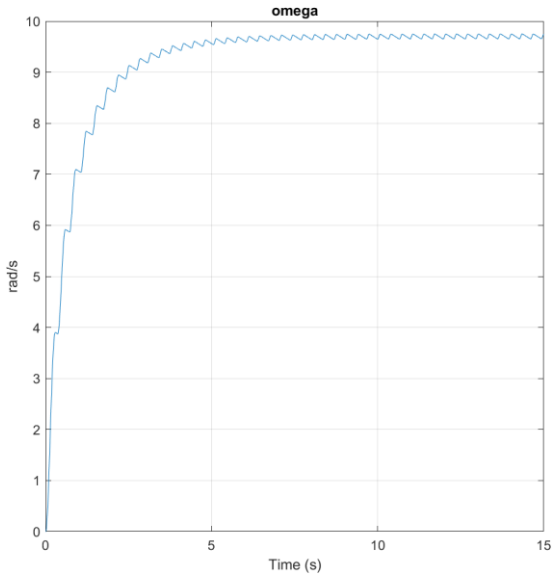

Figure 3.8. Simulation with inertia and high frequency – rotational speed of the motor.

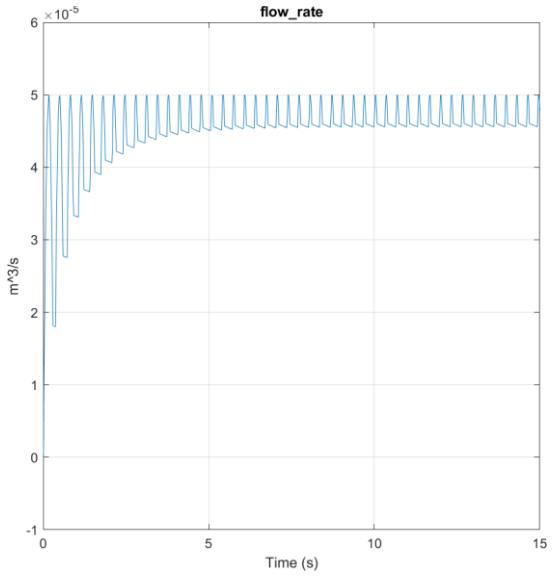

Figure 3.9. Simulation with inertia and high frequency – flow rate.

4. CONCLUSIONS

The results obtained in the simulation process presented in the article are preliminary. They do not consider many important physical phenomena. The next step will be to reduce the simplifying assumptions. The most important step in reducing simplification assumptions will be to remove the inertia of the check valves. This will allow the system to be checked at high frequencies. To verify the simulation model, it is planned to test the real system during the experimental tests. The experimental research will be performed on the real object for validation (checking) of the adopted mathematical model. Comparison of the experimental results with the calculation values will allow us to determine the impact of the simplifications adopted.

By analyzing Fig. 5, 6, and 7 it can be concluded that the hydraulic motor without inertia moves as expected.

If inertia (Fig. 8, 9, and 10) and high frequency of forcing (Fig. 11, 12, and 13) are taken into account, the cylinder speed is the same as the input speed.

For the rotational speed of a hydraulic motor, the influence of inertia is significant; after a few rotations, the value of the rotational speed or flow rate value does not drop below the specified value.

Hydraulic generator with variable flow direction as the first step to create a system to recuperating energy from dampers in vehicles, ultimately consisting of four actuators and one receiver. The results show that a hydraulic re-approval system can be created, allowing more environmentally friendly vehicles to be built.

5. REFERENCES

[1] IPCC report, Climate Change 2022 Summary, and Policymakers,

[2] B. M. Al-Alawi, T. H. Bradley, Review of hybrid, plug-in hybrid, and electric vehicle market, Renewable and Sustainable Energy Reviews 21, 2013, pp. 190–203

[3] P. Slowik, N. Lutsey, Expanding the electric vehicle marker in U.S. cities, the ICCT, 2017, pp. 7.

[4] V. Jacota, M. Matache, Calibration of a system capable to recover the dissipated energy into an automobile suspension, U.P.B Sci. Bill., 2018, pp. 100-101

[5] C. Li, R. Zhu, M. Liang, S. Yang, Integration of shock absorption and energy harvesting using a hydraulic rectifier, Journal of Sound and Vibration, 2014, pp. 3904-3906

[6] MatLAB v. R2021b help on-line documentatoion

[7] N. D. Manring, R. C. Fales, Hydraulic Control Systems, University of Missouri–Columbia, 2020

[8] Z. Domagała, K. Kędzia, M. Stosiak, Ways to improve energy efficiency in hydraulic drives (Sposoby zwiększenia efektywności energetycznej w napędach hydraulicznych), Oficyna Wydawnicza Politechniki Opolskiej, 2019. pp. 39-51

[9] K. Kędzia, An algorithm for the determination of the control parameters of a multisource drive system, Czasopismo Techniczne-Technical Transactions. 2017, pp. 173-182.

[10] P. Osiński, K. Kędzia, K. Dąbek, Hydraulic close transmission with hydraulic bridge rectifier (Przekładnia hydrostatyczna zamknięta z hydraulicznym mostkiem prostowniczym), patent application: P.440311, 2022

[11] Z. Domagała, K. Kędzia, M. Stosiak, The use of innovative solutions improving selected energy or environmental indices of hydrostatic drives, IMTech 2019 Scientific and Technical Conference, 2019, Szczyrk, pp. 1-12.

Biographies



Kacper Dąbek is PhD student at the Wrocław University of Science and Technology. In the research work, he analyzes pressure pulsations and hydrostatic transmissions with an oscillating flow. Co-author of three patent applications and speaker at two international scientific conferences. Multiple medalist of the Polish Academic Championships in Karate WKF.



Piotr Osiński works at the Faculty of Mechanical Engineering of the Wrocław University of Science and Technology. Specializes in the following areas: hydraulic drive and control, and vibroacoustics of machines and devices. Since 2013 he has been the head of the Laboratory of Hydraulic Drives and Vibroacoustics of Machines (www.lhiw.pwr.edu.pl). The acquired construction experience and mastered measuring workshop in the field of diagnostics of hydraulic systems and vibroacoustic measurement resulted in his participation as a project manager or main contractor in several research projects financed by the Ministry of Science and Higher Education and NCBR. The author has about 250 works in his scientific achievements, of which over 110 have been published in periodicals and books of national and international reach, other works are research and design and technological studies carried out in cooperation with industry. Close cooperation with industry has resulted in numerous implementations, including the introduction of PZ4 and PC series pumps into production. The developed constructions have been awarded many times at trade fairs, both domestic and foreign.



Krzysztof Kędzia is assistant professor at the Department of Technical Systems Operation and Maintenance Faculty of Mechanical Engineering Wrocław University of Science and Technology. Deals with drives and control of multi-source drive systems, in particular hydrostatic ones. As part of his scientific activity, he deals with building simulation models (Matlab SIMULINK) and their analysis. Author and co-author of over 70 publications and articles. Also the president of the Chamber of Commerce for Components and Technology, vice-president of the Corporation of Hydraulic and Pneumatic Drives and Controls, scuba diving instructor and president of the PIRANIA Academic Scuba Diving Club, editor in the Hydraulika i Pneumatyka magazine, member of the board of the Hydraulics Section of the Association of Polish Engineers and Mechanics.